# 2022 International Forum on Big Data for Sustainable Development Goals

# Collection of Selected Abstracts

September 6-8, 2022 Beijing, China

# Contents

# SDG 2 (Zero Hunger): Developing Sustainable Food Systems

# Monitoring and Evaluation of Improvement and Utilization of Saline-alkali soil in western Jilin Province from 1985 to 2020

Xiaojie Li[1], Yingye Li [1, 2], Bin Wang [1]

[1] Northeast Institute of Geography and Agroecology, Chinese Academy of Sciences, No. 4888 Shengbei Street, Gaoxinbei District, Changchun 130102, China
Email: lixiaojie@iga.ac.cn
Email: 854596107@qq.com

[2] University of Chinese Academy of Sciences, No.19(A) Yuquan Road, Shijingshan District, Beijing, 100049, China
Email: liyingye21@mails.ucas.ac.cn

## 1. INTRODUCTION

Soil salinization and secondary salinization have become constraints to the sustainable development of agriculture in the world. Soil salinization has led to the decline of soil fertility, inhibited the normal growth of crops, and destroyed the ecological balance. With the change of climatic conditions, the trend of soil salinization continues to expand. In recent years, the government has adopted a series of saline-alkali land control measures (such as rice cultivation in saline-alkali land, leaching and physical and chemical improvement methods) and a series of major projects (such as the river and lake connection project in western Jilin Province, and the major land consolidation project in western Jilin Province), which have led to continuous changes in the state of soil salinization in recent decades [1-3]. Therefore, it is of great significance to realize large-scale dynamic monitoring of saline-alkali soil in this area and obtain the evolution information of saline-alkali soil in time for evaluating the effect of soil improvement and rationally developing and utilizing land.

The Landsat-5 TM and Landsat-8 OLI satellites, launched in 1984 and 2013, have been widely used for moderate-resolution (30m) improved global environmental and safety monitoring. Bannari et al. used Landsat TM, ETM+ and OLI data to assess the impact of climate change on the dynamics of soil salinity in arid landscapes in the state of Kuwait in the northwestern Arabian Peninsula from 1987 to 2017 [4]. These studies demonstrate that it is feasible to monitor soil salinity dynamics using the Landsat series of satellites. However, there are significant differences in soil characteristic spectra of different genesis and different salinity species, which makes it impossible to establish a general soil salinity inversion model [5].

The saline soil in western Jilin belongs to the inland Saline-Sodic Soil, and the salt is mainly sodium carbonate and sodium bicarbonate. Even the spectral response of the soil salinity index was not obvious, which challenged the determination of soil salinization degree in this area. In the past few decades, due to the influence of natural conditions and artificial transformation, the area and degree of soil salinization in western Jilin Province have undergone great changes. We studied the temporal and spatial characteristics of soil salinization, and analyzed the factors that affect soil salinization, which is of great significance for saline soil reclamation and protection of agricultural ecological environment. Specifically, this study aims to:

1) Establish a remote sensing inversion model of Saline-Sodic Soil Electrical conductivity (EC).

2) Inverse and classify soil EC from 1985 to 2020 based on Landsat TM/OLI data.

3) Monitor and map the temporal and spatial changes of soil salinization from 1985 to 2020.

4) Analyze the correlation of meteorological, environmental, social, groundwater and other factors with salinity and calculate the variable importance measure (VIM).

## 2. MATERIALS AND METHODS

### *2.1 Data collection*

### *2.1.1 In situ soil EC measurements*

In order to obtain the electrical conductivity data of saline soil in western Jilin Province, we conducted a field sampling experiment from June 20 to 28, 2019, including a total of 328 sampling points.

### *2.1.2 Satellite imagery data*

We divided the period from 1989 to 2019 into eight periods, with five years interval between each period. Landsat TM and OLI are used as data sources. In this study, we used random forest algorithm to identify saline-alkali soil with high precision from 1985 to 2020. The samples of saline-alkali soil (8674) and non-saline-alkali soil (7068) obtained through the field sampling and the third soil survey were used as training samples.

### *2.1.3 Acquisition of environment data*

We obtained daily data sets of meteorological element station observations in China on the resource and environment data cloud platform (http://www.resdc.cn/). The population data, grain output, and meat output of each county and city are all taken from the County Statistical Yearbook. Digital Elevation Model (DEM) and slope data come from the "MERIT/DEM/v1_0_3" dataset of the GEE platform. The groundwater level and the difference of groundwater level in the dry-peak season come from the measured data. The Land-Use and Land-Cover Change (LUCC) data comes from the Chinese LUCC dataset from the University of Chinese Academy of Sciences since 1980 [6].

### *2.2 Methods*

The soil EC inversion models from 1985 to 2010 and 2015 to 2020 were established by using the field survey sampling data and satellite remote sensing multi-period image data set [7-9]. The degree of soil salinization was graded based on THE USDA standard [10]. Finally, combining with land use data, the paper analyzes the feature transformation of saline-alkali land and the importance of meteorological and geomorphological factors to the change of saline-alkali land area.

## 3. RESULTS

### *3.1 Temporal variation of saline-alkali land area in western Jilin Province*

According to the change of the total area of salinized soil, we can divide the three decades into two stages: the total area of salinized soil showed an increasing trend from 1985 to 2000, and the total area of salinized soil showed a decreasing trend from 2000 to 2020. According to the government's implementation period of saline soil reconstruction project, it can be divided into natural state (1985-2000) and transformed state (2000-2020). In a word, the total area of natural salinized soil showed an increasing trend, while the total area of reformed salinized soil showed a decreasing trend.

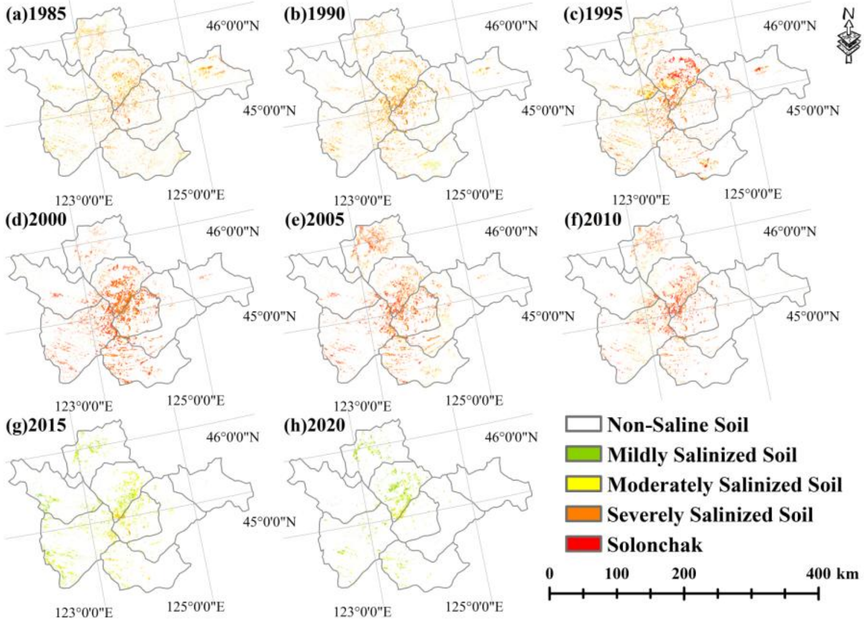


**Fig. 1.** Distribution of saline-alkali soil in western Jilin Province from 1985 to 2000

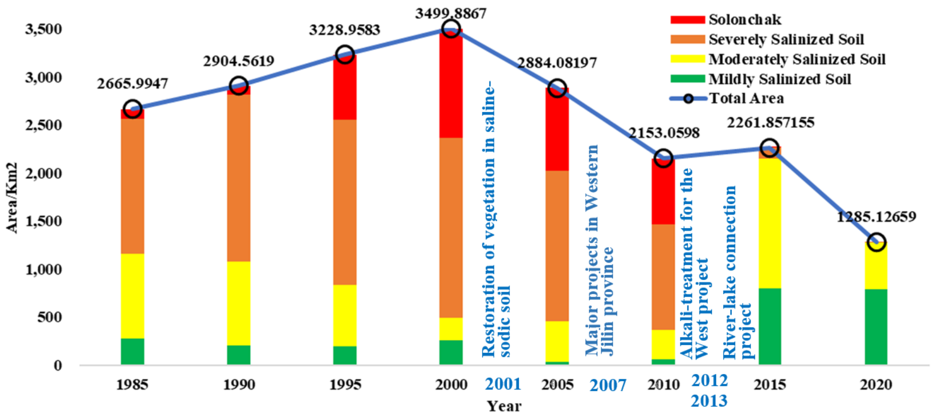


**Fig. 2.** Temporal changes of saline-alkali soil area in western Jilin province from 1985 to 2020

### *3.2 Analysis of change rate of saline-alkali land*

According to area change, the total area of saline-alkali land increased the most from 1990 to 1995, and decreased the most from 2015 to 2020. The area of saline soil/alkaline soil and severely saline soil increased from 1985 to 2000, but decreased after 2000. The area of lightly saline soil decreased before 2010 and increased after 2010. According to the dynamic attitude of area change, salinized soil/alkaline soil had the greatest change from 1990 to 1995, and lightly salinized soil had the greatest change from 2010 to 2015.

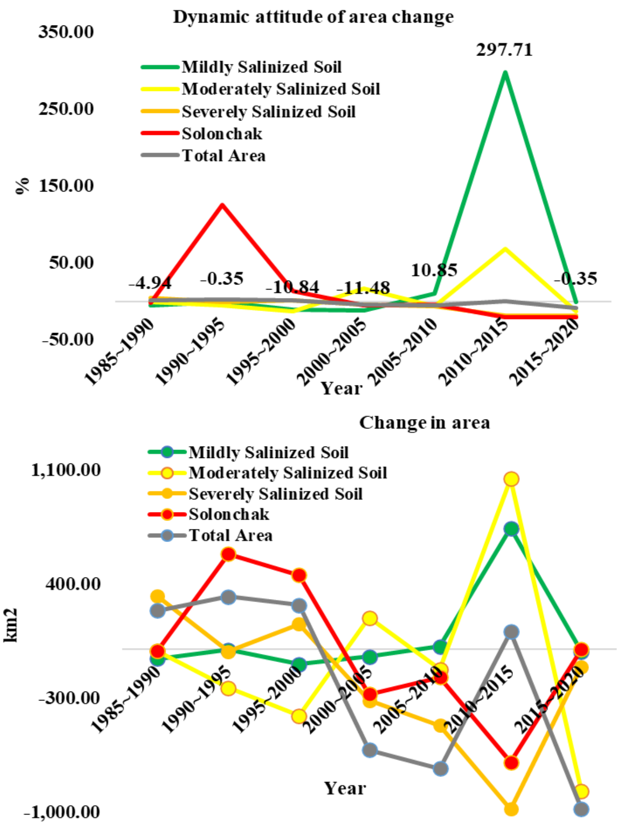


**Fig. 3.** Variation and dynamic attitude of saline-alkali land area

### *3.3 Analysis of saline-alkali land and land use conversion*

The changing regions of saline-alkali soil and non-saline-alkali soil were superimposed with land use data to analyze the direction of saline-alkali soil transfer. Combined with the two stages of total area change of saline-alkali land: natural state (1985-2000) and transformed state (2000-2020), the area percentage of mutual transformation between different land features and saline-alkali land in these two stages was obtained.

**Table 1.** Conversion between saline-alkali land and land use types

| | Cropland | Grassland | Water | Forest | Impervious surface | Paddy field |
|---|---|---|---|---|---|---|
| 1985~2000 to saline soil | 26.93% | 56.71% | 12.26% | 2.37% | 1.55% | 0.18% |
| 2000~2020 from saline soil | 55.59% | 23.51% | 6.18% | 9.34% | 3.96% | 1.42% |

Table 1 shows that 56.71% of the increase in saline-alkali land from 1985 to 2000 was due to the conversion of grassland and cropland, which affected the development of animal husbandry and agriculture and would cause social and economic losses if not controlled. From 2000 to 2020, 55.59 percent of saline-alkali land was converted to cropland and 23.51 percent to grassland.

### *3.4 Influencing factors of saline-alkali land area*

Taking saline-alkali land area as dependent variable and population, evaporation, precipitation, evapotranspiration ratio, groundwater level, groundwater level difference, DEM and slope as independent variables, a random forest model was established and the importance of variables was calculated. The results are shown in Fig. 4. By comparing the natural state (1985-2000) with the transformed state (2005-2020), we found that the importance of all meteorological factors, groundwater and geomorphic factors decreased except the total population at the end of the year. These data show that in the natural state, these factors have a great impact on the area of saline-alkali land. On the contrary, in the transformed state, due to artificial disturbance, the importance of these factors is reduced, which is also consistent with the objective reality.

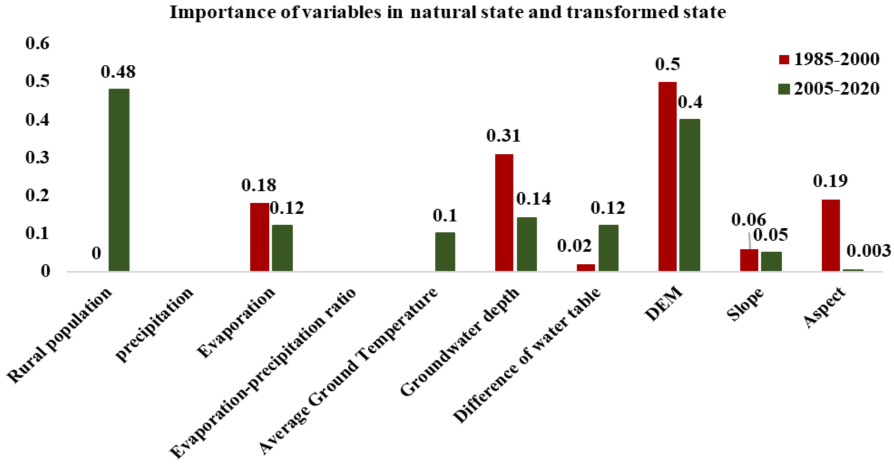


**Fig. 4.** Importance of each factor to saline-alkali land area

## 4. SUMMARY

In this study, saline-alkali land recognition and soil EC inversion algorithms were developed to realize the mapping of grade distribution of saline-alkali land in western Jilin province from 1985 to 2020, which can provide important scientific data for SDG 2.4 evaluation.

The results show that: (1) The area of saline-alkali land in western Jilin increased significantly during 1985-2000 (natural state), and decreased during 2000-2020 (transformed state), indicating that the effect of saline-alkali land treatment project is significant. (2) Cropland and grassland were the main features that were frequently converted to saline-alkali land. (3) Natural conditions (including geomorphic elements and groundwater) are important factors causing soil salinization, and the participation of human activities can reduce the influence of these factors. To sum up, we suggest increasing positive transformation activities and reducing destructive activities such as overgrazing.

## References

[1] Wang S., Xu J., Wang Q., Cheng D. (2020) Modeling of wetting deformation of coarse saline soil with an improved von Wolffersdorff model, Bulletin of Engineering Geology and the Environment, 79(9): 4783-4804.

[2] Talat N. (2020) Alleviation of soil salinization and the management of saline soils, climate change, and soil interactions, Climate Change and Soil Interactions, Elsevier, 305-329 pp.

[3] Zhao F., Chang L., Zhang W., Kou G., Liu H. (2019) Study on dynamic stress-strain response law of frozen saline soil, IOP Conference Series: Earth and Environmental Science, 267(3): 032013.

[4] Bannari A., Al-Ali Z. (2020) Assessing climate change impact on soil salinity dynamics between 1987-2017 in arid landscape using Landsat TM, ETM+ and OLI data, Remote Sensing, 12(17): 2794.

[5] Howari F., Goodell P., Miyamoto S. (2002) Spectral properties of salt crusts formed on saline soils, Journal of Environmental Quality, 31(5): 1453-1461.

[6] Yang X., Jin X., Yang Y., Song J., Zhang T., Zhou Y. (2022) Spatially explicit changes of forestland in Taiwan Province from 1910 to 2010, Journal of Geographical Sciences, 32(3): 441-457.

[7] Li X., Sun Y., Chen X., Li Y., Jiang T., Liang Z. (2022) Saline-Sodic Soil EC Retrieval Based on Box-Cox Transformation and Machine Learning, IEEE Journal of Selected Topics in Applied Earth Observations and Remote Sensing, 15: 1692-1700.

[8] Dong X., Li X., Zheng X., Jiang T., Li X. (2020) Effect of Saline Soil Cracks on Satellite Spectral Inversion Electrical Conductivity, Remote Sensing, 12(20): 3392.

[9] Li X., Ren J., Zhao K., Liang Z. (2019) Correlation between spectral characteristics and physicochemical parameters of soda-saline soils in different states, Remote Sensing, 11(4): 388.

[10] Richards L. (1954) Diagnosis and improvement of saline and alkali soils, Lippincott William&Wilkins, Vol. 78, No. 2, 154 pp.

# Contributing to SDG 2: Rice Area Monitoring in Southeast Asia with Time Series SAR

Lu Xu[1,2], Hong Zhang[1,2,*], Chunling Sun[1,2,3] , Chao Wang[1,2,3]

[1] International Research Center of Big Data for Sustainable Development Goals, Beijing 100094, China
Email: hongzhang@radi.ac.cn
Email: xulu@aircas.ac.cn
Email: sunchunling19@mails.ucas.ac.cn
Email: wangchao@radi.ac.cn
[2] Key Laboratory of Digital Earth Science, Aerospace Information Research Institute, Chinese Academy of Sciences, Beijing 100094, China
[3] University of Chinese Academy of Sciences, Beijing 100049, China.

## 1. INTRODUCTION

A rational allocation of agricultural resources is the key to maintain the balance of food supply and plays a vital role in the safeguarding of human livelihood. As the requirement of The United Nations 2030 Agenda for Sustainable Development Goal 2.4 (*"By 2030, ensure sustainable food production systems and implement resilient agricultural practices that increase productivity and production, that help maintain ecosystems, that strengthen capacity for adaptation to climate change, extreme weather, drought, flooding and other disasters and that progressively improve land and soil quality"*), it is necessary to conduct long-term agricultural monitoring to effectively assess the agricultural productivity at national, regional and even global scales, to promote the innovations in agricultural infrastructures and technologies, and thus contribute to the elimination of hunger.

Rice is one of the most important grains for human, which accounts for 9% of world crop production (FAO, 2020). As the main staple food for the populations in Asia, Southern Europe, and parts of America and Africa, the timely monitoring of rice cultivation is direct related to the stability of food supply and quality of human nutrition. The Southeast Asia is a major rice producing and exporting area in the world, where the warm and humid climates create favorable conditions for multi-seasonal rice production. Due to the differences in economic policy orientations and cultivation traditions, Southeast Asia countries differ in agricultural productivity levels. The complicated topography also brings obstacles to field surveys. As a result, the distributions and the spatial-temporal patterns of rice in Southeast Asia are difficult to assess using traditional methods.

As a reliable technology to gather large-scale earth surface information, remote sensing has been proved to be a promising solution to many environment problems. In the past decades, agricultural monitoring based on optical remote sensing data has been well developed in terms of theory, methods, and applications. However, optical remote sensing images covering the Southeast Asian region are difficult to be acquired stably and consistently due to frequent cloudy and rainy weather, and optical image-based rice extraction methods are often difficult to implement in the Southeast Asian region. Meanwhile, despite the thriving of large-scale land-cover-land-use (LULC) products in recent years [1-3], specialized information about rice distribution is still rare. Also, the annual or seasonal updating is hardly to achieve because of the difficulties in data updating.

The progress in Synthetic Aperture Radar (SAR) instruments has provided with new opportunities for the monitoring in tropical and subtropical regions for its all-weather and all-day imaging ability. The Sentinel-1 satellite, launched by ESA in 2014, has improved the spaceborne SAR revisit cycle to 12 days (or 6 days, if use both S1A and S1B satellites), allowing a more detailed depiction of rice growth patterns [4-7]. Meanwhile, the thriving in deep learning, cloud computing and parallel architectures have brought new inspirations to remote sensing data processing [8-10]. Many deep learning models have been introduced into various SAR applications to deal with big data problems. In agricultural field, some preliminary results were achieved in Southeast Asian countries [11, 12], but the application of intelligent models in large-scale rice mapping still need further research.

Inspired by previous studies, this research intends to explore the feasibility of SAR in large-scale rice monitoring. The purpose is to produce the annual rice cultivation area product of Southeast Asia in resolution of 20m, on the basis of multitemporal Sentinel-1 GRD images. Targeting this task, the multitemporal backscattering features of rice fields were analyzed, and the U-Net segmentation model was introduced to learn the distinctive information of rice to achieve an accurate extraction of rice fields in Southeast Asia counties. This product is potential to offer cross validations for the multisource statistical data. As the supplement information for the LULC datasets, it will contribute to the assessment of rice planting intensity, and serve the stabilization of global grain prices.

## 2. MATERIALS AND METHODS

### *2.1 Dataset*

The purpose of this research is to generate the annual rice cultivation area dataset from 2019 to 2021 in the major rice production countries of Southeast Asia, including Thailand, Vietnam, Laos, Cambodia, and Myanmar. The difficulty of paddy rice mapping in these countries can be attribute to two factors: 1) the favorable climate for rice growing, which leads to a long cultivation time window; 2) the cultivation system that dominated by small-holder, which leads to casual cultivation practices. As a result, to fully capture the annually rice mapping conditions, all the available data during the whole year should be involved. In total, 2140 S1A and 554 S1B images that belonged to 91 frames of 12 orbits were collected, with 12-day revisit cycle and the 250km swath width (IW mode).

Necessary preprocessing was conducted to the time-series data of each frame using the SNAP software provided by ESA. After thermal noise removal, registration, and multitemporal filtering, the 30m resolution Shuttle Radar Topography Mission (SRTM) DEM data was used for the radiometric calibration and geocoding. Finally, the backscattering sequences of VH and VV polarizations ($\sigma^0_{VH}$ and $\sigma^0_{VV}$), were generated with a grid size of 20m, according to which the analysis of sowing and harvest patterns can be carried out.

### *2.2 Methodology*

The topographical terrain in Southeast Asia is complex, and some cultivated plots are small in size and fragmented in shape, so that the spatial characteristics should be taken into consideration to depict the rice distribution accurately. To effectively combine the spatio-temporal information of time-series SAR, in our previous studies, we analyzed the backscattering responses of rice and non-rice land covers [13]. To make full use of continuously observed time-series SAR data and meanwhile avoid the difficulties of generating backscattering evolution models, three temporal statistical features that highlight the most distinctive features during the growing of rice were extracted from the time-series of $\sigma^0_{VH}$, and were stacked in to the U-Net sematic segmentation model for rice recognition [14].

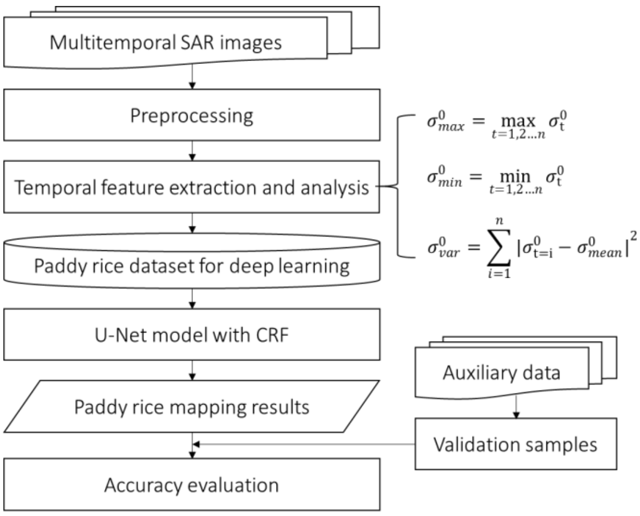


$$\sigma^0_{max} = \max_{t=1,2\ldots n} \sigma^0_t$$

$$\sigma^0_{min} = \min_{t=1,2\ldots n} \sigma^0_t$$

$$\sigma^0_{var} = \sum_{i=1}^{n} |\sigma^0_{t=i} - \sigma^0_{mean}|^2$$

**Fig. 1.** Flow chart of the rice mapping method.

The proposed method groups the spatio-temporal information of time-series SAR. The consistence of temporal statistical features in different years and different areas were tentatively validated in our recent research [15]. In other words, the classification models can be trained by a group of representative samples and then directly extended to the whole country. In this research, we used the training dataset mentioned in our previous study [14], which contained 15659 image patches with size of 224×224.

## 3. RESULTS

Fig.2 shows the preliminary results of the annual rice cultivation product in 2019. For now, the product includes Thailand, Vietnam, Laos, and Cambodia. The processing of the Myanmar datasets is in progress. Simultaneously, auxiliary data including Google Earth optical image, Sentinel-2 optical data, official statistics data and LULC products were collected, to inspect the quality of the rice extraction results. Compared with the validation dataset (which was composed of 2894554 pixels from 2021 ground parcels), the overall accuracy for the product in Thailand reached 91%, which displayed good consistence with the FROM-GLC global cover dataset. We are also working on the expansion of training dataset to improve the performance of the model. Hopefully, the formal version of the 20m annual rice cultivation product in 2019 covering 5 Southeast Asia countries could be released in the end of this year.

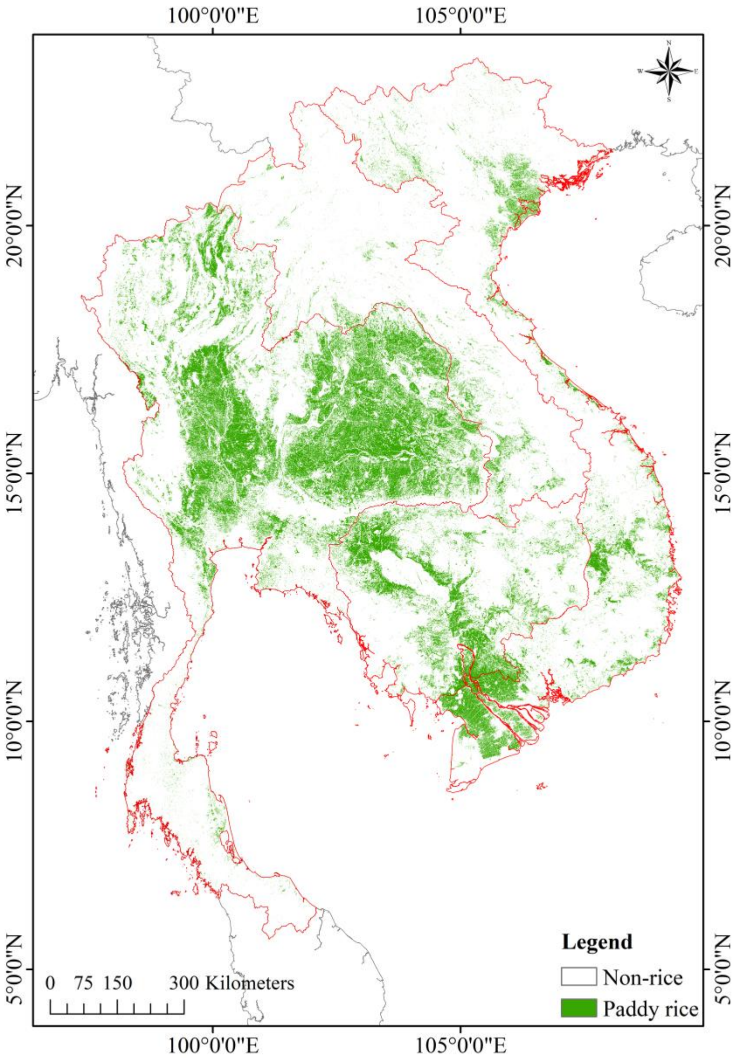


**Fig. 2.** Preliminary result: the annual rice distribution map of Thailand, Vietnam, Laos, and Cambodia in 2019.

## 4. SUMMARY

This research intends to generate an annual rice cultivation product from 2019 to 2021, based on the time-series Sentinel-1 data. Considering of the difficulties caused by the complex cultivation calendar and the irregular land parcels, a large-scale rice mapping scheme based on temporal statistic features and U-Net model was proposed to capture the key information of rice growth. The preliminary results of Thailand, Vietnam, Laos, and Cambodia in 2019 is displayed in this paper, and the result of Myanmar is on the way. The initial accuracy assessment in Thailand validated the potential of the result. Now we are working on the refinement of the details and the enrichment of the training dataset. Meanwhile, the annual rice area product in 2020 and 2021 are in preparation. We expect that the product can serve SDG 2 by providing information of grain production in Southeast Asia, which assists land management, policy formulation and price stabilization.

## References


[1] Yu, L., Wang, J., Clinton, N., et al.. 2013. FROM-GC: 30 m global cropland extent derived through multisource data integration. International Journal of Digital Earth, 6, 521-533.

[2] Chen, J., Chen, J., Liao, A.P., et al. 2015. Global land cover mapping at 30 m resolution: A POK-based operational approach. ISPRS Journal of Photogrammetry and Remote Sensing, 103, 7-27.

[3] Zhang, X., Liu, L., Chen, X., et al. 2019. Fine Land-Cover Mapping in China Using Landsat Datacube and an Operational SPECLib-Based Approach. Remote Sensing, 11, 1056.

[4] Asilo, S., de Bie, K., Skidmore, A., et al. A. 2014. Complementarity Of Two Rice Mapping Approaches: Characterizing Strata Mapped By Hypertemporal MODIS And Rice Paddy Identification Using Multitemporal SAR. Remote Sensing, 6, 12789–12814.

[5] Rossi, C., Erten, E. Paddy-Rice Monitoring Using TanDEM-X. 2015. IEEE Transactions on Geoscience and Remote Sensing, 53, 900-910.

[6] Fikriyah, V.N., Darvishzadeh, R., Laborte, A., et al. 2019. Discriminating transplanted and direct seeded rice using Sentinel-1 intensity data. International Journal of Applied Earth Observation and Geoinformation, 76, 143-153.

[7] Bazzi, H., Baghdadi, N., El Hajj, et al. 2019. Mapping Paddy Rice Using Sentinel-1 SAR Time Series in Camargue, France. Remote Sensing, 11.

[8] Kussul N, Lavreniuk M, Skakun S, et al. 2017. Deep learning classification of land cover and crop types using remote sensing data. IEEE Geoscience and Remote Sensing Letters, 14(5): 778-782.

[9] Ndikumana E, Ho Tong Minh D, Baghdadi N, et al. 2018. Deep recurrent neural network for agricultural classification using multitemporal SAR Sentinel-1 for Camargue, France. Remote Sensing, 10(8): 1217.

[10] Teimouri N, Dyrmann M, Jørgensen R N. 2019. A novel spatio-temporal FCN-LSTM network for recognizing various crop types using multi-temporal radar images. Remote Sensing, 11(8): 990.

[11] Clauss, K., Ottinger, M., Leinenkugel, P., Kuenzer, C., 2018. Estimating rice production in the Mekong Delta, Vietnam, utilizing time series of Sentinel-1 SAR data. International Journal of Applied Earth Observation and Geoinformation 73, 574-585.

[12] Minh, H.V.T., Avtar, R., Mohan, G., Misra, P., Kurasaki, M., 2019. Monitoring and Mapping of Rice Cropping Pattern in Flooding Area in the Vietnamese Mekong Delta Using Sentinel-1A Data: A Case of An Giang Province. ISPRS International Journal of Geo-Information 8, 22.

[13] Sun, C., Zhang, H., Ge, J., et al. 2022. Rice Mapping in a Subtropical Hilly Region Based on Sentinel-1 Time Series Feature Analysis and the Dual Branch BiLSTM Model. Remote Sensing, 14, 3213.

[14] Xu, L., Zhang, H., Wang, C., et al. 2021. Paddy Rice Mapping in Thailand Using Time-Series Sentinel-1 Data and Deep Learning Model. Remote Sensing, 13, 3994.

[15] Xu, L., Zhang, H., Wang, C., et al. 2022. Consistency Study Of The Time-Series SAR Responses In Rice Fields Of Southeast Asia. The International Geoscience and Remote Sensing Symposium (IGARSS) 2022, Kuala Lumpur, Malaysia.

# SDG 6 (Clean Water and Sanitation): Integrated Management for Water Resources

# Cryospheric Water Resources Present Opportunities and Challenges for Crop Water Stress in the Tarim River Basin

LIU Shiwei[1]

[1] State Key Laboratory of Earth Surface Processes and Resources Ecology, Beijing Normal University, Beijing, 100875, China
email: 11132022609@bnu.edu.cn

## 1. INTRODUCTION

Ensuring access to 'Clean Water and Sanitation' by 2030 (SDG 6) is one of the 17 UN Sustainable Development Goals (SDGs) to address water scarcity, of which SDG 6.4.2 is an indicator of 'level of water stress': the ratio of total fresh water withdrawn by all sectors to the water availability (WS, water stress). Water stress arises when the amount of water resources available does not meet water demand to a certain extent. It is estimated that more than 4 billion people worldwide face a blue water shortage for at least one month of the year [1], and that available surface and subsurface freshwater resources are not sufficient to meet human withdrawals. The commonly used method for evaluating WS is WSI (water stress index): the ratio of water consumption to the water availability. However, in order to consider the efficiency of water use, the ratio of water withdraw to the water availability is gradually being used more often. Further, Environmental flow requirements (EFR) is usually taken into account in the WS as well [2]. WSI below 0.25 can be considered safe in any instance, whereas on the other, values above 0.25 should be regarded as potentially and increasingly problematic and should be qualified and/or reduced [3].

The data needed for this calculation are often difficult to obtain at the regional scale, especially in regions with unique water resources endowments that do not fully take into account their water resources characteristics. In order to study WS at finer spatial and temporal scales, hydrological models have become effective tools. Many studies have performed WSI simulations at the watershed scale and raster scale [4,5]. Furthermore, to better reflect the actual situation, Liu et al. simulate the WSI by considering the upstream and downstream relationship. It is found that considering the confluence and up and down has a greater effect on WS [6]. Nevertheless, due to the lack of data on irrigation facilities, the water withdrawal methods used in the simulations nowadays are generally able to take only the runoff from local grid or use the rule of sub-basin leveling to divert water for irrigation. Lack of irrigation network may make WS overestimated in some areas. Furthermore, irrigation return flows are often assessed or ignored using the coefficient method, which may underestimate the available water resources in areas with high intensity irrigation. All these aspects will bias the local and regional WS assessments.

In 2019, the national average WSI of China is 0.43, but there is significant variability between regions, e.g., WSI in Xinjiang is around 0.6 [7], which would be in an extreme water stress state if environmental flows are considered. Focusing on finer spatial scales, the WSI exceeds 1.0 in most of northern and northwestern China [6]. Water resources are scarce in the arid zone of northwest China, and cryospheric water resources are irreplaceably important to downstream oases. The Tarim River basin relies on oasis agriculture and is one of the regions with the strongest water tower functions and services, which is characterized by the human-water relationship of 'water defining the oasis, water defining the city, and water defining the industrial structure., and it is of great scientific and practical significance to assess the future sustainable development of oasis in the region. The study shows that the Tarim River basin is characterized by a 'warming and wetting' of the climate and an overall increase in water resources due to increased glacial ablation, but the increase in temperature and population will also lead to an increase in agricultural water demand. It is important to study how the WS of the Tarim River basin will change under the combined climate, cryosphere, and agriculture scenarios.

## 2. MATERIALS AND METHODS

### *2.1 Materials*

The data used in this thesis include both natural and crop components. The data information is shown in Table 1.

**Table 2.** Data information

| Name | Data | Period | Temporal resolution | Spatial resolution |
|---|---|---|---|---|
| Altitude | STRM | / | / | 1km |
| Soil | FAO | / | / | 1km |
| Glaciers | GLIMS | 2006 | / | / |
| Meteorological data | CRU | 1980-2016 | monthly | 0.5 ° |
| Runoff reference | GRUN | 1980-2014 | monthly | 0.5 ° |
| Glacial runoff and area | PyGEM | 1980-2016 | monthly | / |
| Crop land | ESA | 1992-2015 | annual | 300m |
| Crop structure | Farming the planet:2 | 2000 | annual | 5 arcmin |
| Crop calendar | MIRCA2000 | 2000 | / | 5 arcmin |
| Irrigation efficiency | statistical yearbook | 1993-2016 | / | / |
| RCPs | CMIP5 | 2006-2099 | / | / |

The forcing data are downscaled by the Delta method, and processed with interpolation and bias correction processing.

### *2.2 Methods*

Figure 1 shows a schematic diagram of the framework of the coupled WAPABA-AGR model. The irrigation withdrawal model couples the hydrological model (WAPABA) with the water balance of the agricultural model. The irrigation process connects the water demand of the agricultural model (GAEZ) with the actual irrigation of the hydrological model, thus changing the water balance of the downstream under irrigation conditions and affecting the actual evapotranspiration, soil water, groundwater and the corresponding hydrological processes. At the same time the downstream diversion irrigation module allows irrigation to affect river runoff downstream of the basin, thus changing the amount of water available downstream.

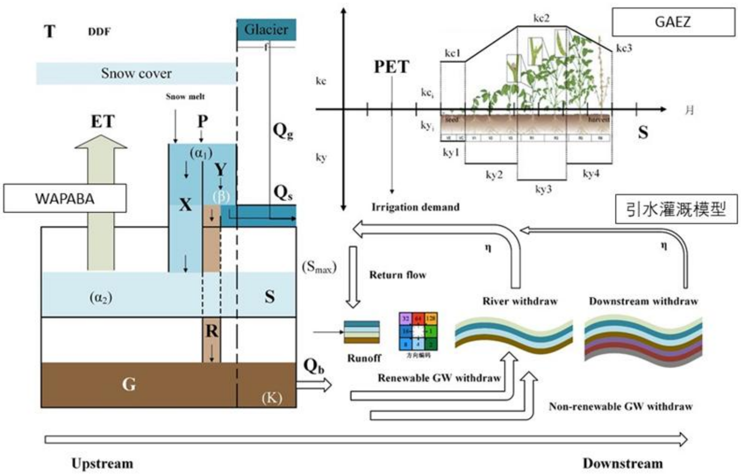

**Fig. 1.** Schematic diagram of the framework of the coupled WAPABA-AGR model

Based on the MCMC approach to calibrate hydrological modelling, the watershed water resource composition was first assessed and further simulated for irrigation, and finally WSI.

## 3. RESULTS

### *3.1 Water resources changes in the Tarim River basin*

The runoff is divided into glacier runoff, snowmelt runoff, rainfall runoff, and baseflow respectively. The results show that the average natural discharge of Tarim River from 1980 to 2016 is close to 360 × $10^8$ $m^3$/a, and the increase rate over the past 37 years reached 0.8 × $10^8$ $m^3$/a (Figure 2). Glacial runoff contributes significantly to the total runoff, with an average annual contribution of 28%, and together with snowmelt runoff contributes about 33%. The upper reaches of the Aksu, Yarkant and Hotan rivers account for an even higher percentage, with some area even exceeding 50% or more.

As shown in Figure 2, the increase in annual natural discharge is mainly caused by increased glacial discharge, which increases in a rate of 0.57 × $10^8$ $m^3$/a. Although snowmelt and rainfall runoff show increasing trends, the trends are insignificant and have no significant effects on total discharge. The increase in precipitation due to warming and humidification has a small effect on the increase in runoff from the watershed, but the effect of increasing temperature on glaciers is significant.

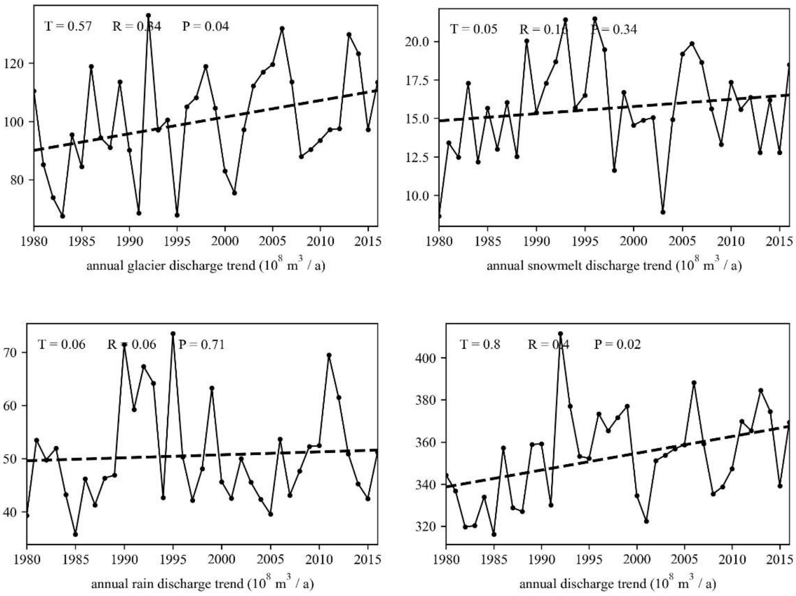


**Fig. 2.** Natural discharge changes in the Tarim River from 1980 to 2016

As shown in Figure 3, the intra-annual distribution of natural discharge shows a unimodal pattern, with glacier and rainfall discharge being the main sources of summer flooding, while snowmelt plays a lesser role. From the changes in the two periods (1980-2000 & 2000-2016), no major shift in the intra-annual runoff process occurred, with a higher increase in runoff in August.

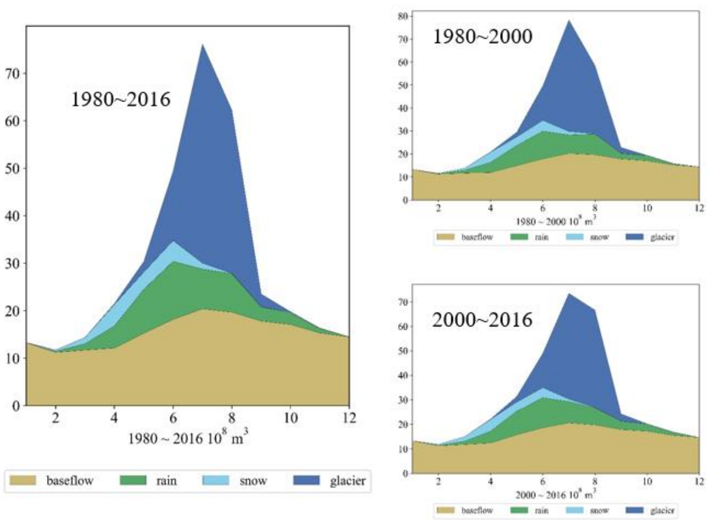


**Fig. 3.** Changes in the intra-annual distribution of natural discharge in the Tarim River from 1980 to 2016

### *3.2 Water stress index characteristics*

As shown in Figure 4, irrigation network can effectively alleviate the problem of high WSI in most areas. In the local abstraction scenario, only the main river with high discharge has low WSI, while the majority of oasis areas produce little or no runoff, which would overestimate the WSI in most areas if irrigation facilities are not considered. On the other hand, the construction of irrigation facilities in the Tarim River basin has been effective in relieving water stress problems in most regions. However, the water stress problem in Kashgar and Hotan may require solutions in terms of significant improvements in irrigation efficiency and control the extent of arable land.

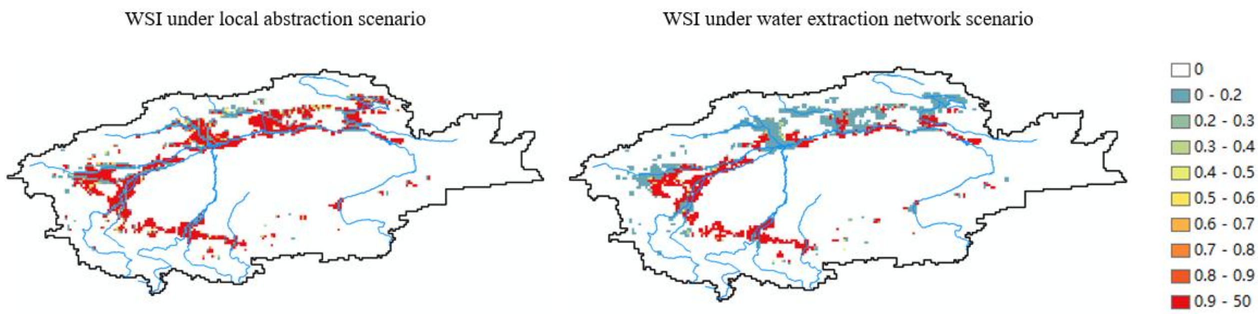


**Fig. 4.** Distribution of WSI under local abstraction scenario and irrigation network scenario

As shown in Figure 5, basin average WSI is on a downward trend. The WSI prior to 2000 was generally greater than 1.0, and the entire basin was at severe water stress levels. There was a gradual downward trend after 2000. The graph shows that the improvement in irrigation efficiency plays an important role in the decline of WSI. Of course, the increase in water resources also plays an integral role. However, there is still some distance to go compared to safe water pressure levels, but the progress over the past 37 years has been remarkable.

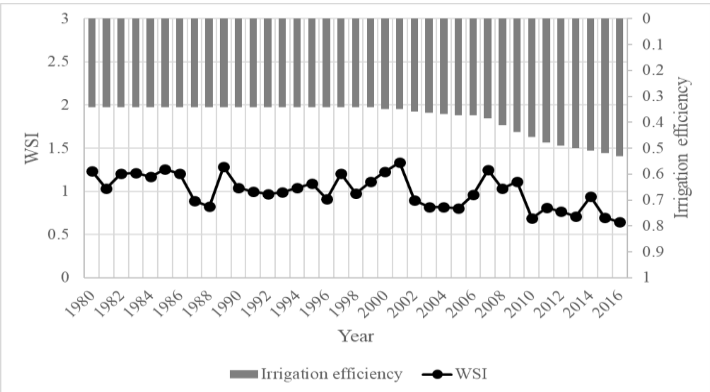


**Fig. 5.** Distribution of WSI under local abstraction scenario and irrigation network scenario

### *3.3 Cryospheric water resources relieve water stress*

As shown in Figure 6, The cryospheric water resources provided more than 30% of the irrigation water in July and averaged 21% throughout the year. With annual recharge rates increasing from about 20% to about 30% over the past 37 years, cryospheric water resources are playing a more important role in relieving water stress.

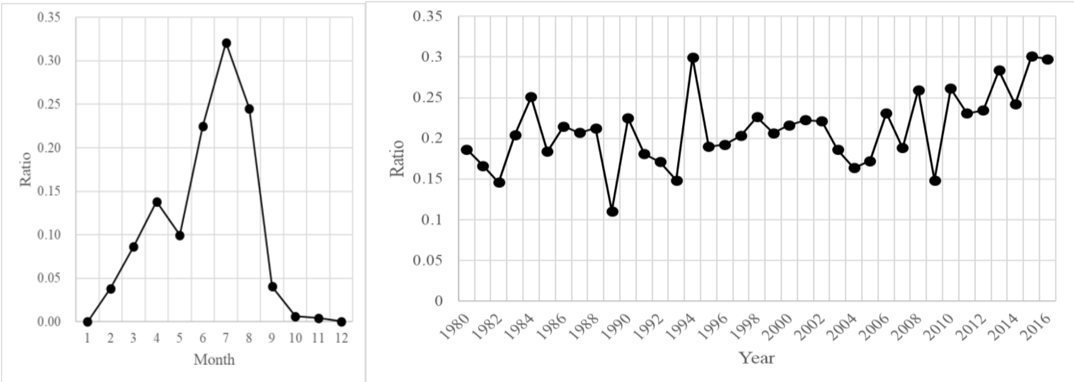


**Fig. 6.** Ratio of cryospheric water resources to water withdraw in inter-annual scale and annual scale in Tarim River Basin from 1980 to 2016

### *3.4 Cryospheric water resources changes in future present opportunities and challenges on water stress*

Under the climate scenario, changes in climatic conditions and the cryosphere will have an impact on water resources. As shown in Figure 7, glacial discharge will experience tipping points at different times under different RCP scenarios, which will affect the tipping pattern of total discharge. Before the tipping point, total discharge will increase by about 5% to 20%, which will relieve some of the water stress and can bring some opportunities for agricultural development and ecological restoration of the oasis. However, it should be noted that after the tipping point, there will be a decline in water resources, and by the end of the century there will even be less total discharge than present, which will challenge the water stress and put agriculture and ecology at risk.

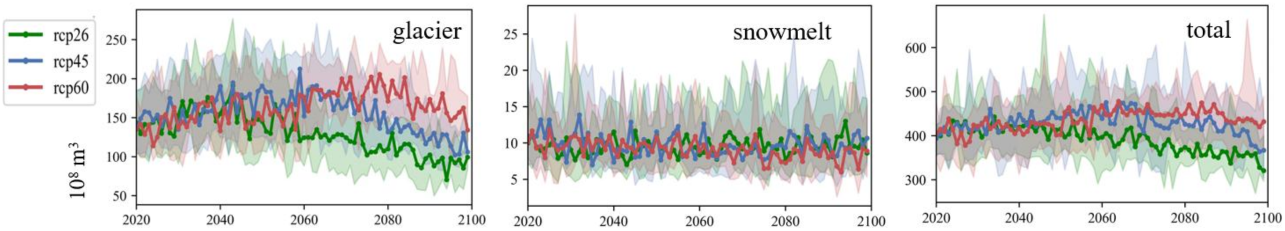


**Fig. 7.** Natural discharge projections in the Tarim River under RCPs

## 4. SUMMARY

Tarim River basin is characterized by a 'warming and wetting' of the climate and an overall increase in water resources due to increased glacial ablation, but the increase in temperature and population will also lead to an increase in agricultural water demand. It is important to study how the WS of the Tarim River basin will change under the combined climate, cryosphere, and agriculture scenarios. A new developed coupled WAPABA-AGR model was used to investigate historical change of WSI in Tarim River Basin. Results indicates basin average WSI a downward trend, the WSI prior to 2000 was generally greater than 1.0, and the entire basin was at severe water stress levels. There was a gradual downward trend after 2000. The results shows that the improvement in irrigation efficiency plays an important role in the decline of WSI. Furthermore, the cryospheric water resources provided more than 30% of the irrigation water in July and averaged 21% throughout the year. With annual recharge rates increasing from about 20% to about 30% over the past 37 years, cryospheric water resources are playing a more important role in relieving water stress. Future projections indicate that cryospheric water resources will present opportunities for oasis development in the mid-century, but will present challenges towards the end of the century.

## References

[1] Mekonnen M M, Hoekstra A Y. Four billion people facing severe water scarcity[J]. Science advances, 2016, 2(2): e1500323.
[2] Vanham D, Hoekstra A Y, Wada Y, et al. Physical water scarcity metrics for monitoring progress towards SDG target 6.4: An evaluation of indicator 6.4. 2 “Level of water stress”[J]. Science of the total environment, 2018, 613: 218-232.
[3] FAO and UN Water. 2021. Progress on Level of Water Stress. Global status and acceleration needs for SDG Indicator 6.4.2, 2021. Rome. https://doi.org/10.4060/cb6241en
[4] Biancalani R, Marinelli M. Assessing SDG indicator 6.4. 2 ‘level of water stress’ at major basins level[J]. UCL Open: Environment, 2021: 1-17.
[5] Wada Y, Van Beek L P H, Viviroli D, et al. Global monthly water stress: 2. Water demand and severity of water stress[J]. Water Resources Research, 2011, 47(7).
[6] Liu X, Tang Q, Liu W, et al. A spatially explicit assessment of growing water stress in China from the past to the future[J]. Earth's Future, 2019, 7(9): 1027-1043.
[7] Zhao X, Liu J, Liu Q, et al. Physical and virtual water transfers for regional water stress alleviation in China[J]. Proceedings of the National Academy of Sciences, 2015, 112(4): 1031-1035.

# Coastal Bangladesh, risk estimation, and natural disasters: accounting for probabilities with local peoples' perception

MD. ABUL KALAM AZAD[1]

[1] Doctoral student and Graduate Research Assistant, Natural Resources Institute, University of Manitoba, Canada

email: azadmak@myumanitoba.ca; azad.socio@gmail.com

## 1. INTRODUCTION

Risk perception is an imperative predictor that influences the functionalities of disaster risk mapping and its associated decision-making process. This disaster risk-sensitive perception building on judgment and experience empowers self-efficacy, risk reduction efficiency, self-preparedness, and the anticipation capacity of hazards. However, understanding of risk perception and implications for risk estimation is poorly documented in disaster literature. With this context, the study aimed to (i) identify and map the ranking of natural hazards in local communities by the residents; (ii) develop a comparative hazards profile using a place-based model, and (iii) estimate the potential impacts of or severity of hazards on coastal communities of Bangladesh.

## 2. MATERIALS AND METHODS

This study attempted to develop a perception-based risk profile of a coastal community by applying a mixed-method research design. For assessing risks of the coastal communities, we selected four villages using a simple random sampling procedure to nine unions of Dacope Upazila – Phankhali-1 and Khatail villages of Phankhali union, Kamarkhola village of Kamarkhola union, and Tildanga village of Tildanga union. A semi-structured interview schedule was administered among 159 of the hazard-prone households. For understanding risk perception, following Nirupama (2012), we used the Risk Perception Index as: $[RI\text{cp} = PH\ X(V\ X\ CP)]$; where RI = Risk Index, PH=the probability of a hazard, V= the degree of severity, and CP=Community perception on the consequences of hazards.

## 3. RESULTS

The results of the Risk Index$_{cp}$ revealed that the coastal community's perception of environmental pressures was profoundly modified by both biophysical and social systems – especially the factors associated with social, economic, and health domains. The average likelihood of hazards ranged from 4.626 (frequent or very likely) to 1.497 (a highly unlikely or rare event); community perception of risk ranged between 12% and 100%. The findings of Risk Index$_{cp}$ further revealed that the community was highly exposed to hydro-meteorological hazards, such as cyclone, storm surge, salinity intrusion, coastal floods, waterlogging, and heavy precipitation; the probability of occurrences of these hazards was calculated to be "very likely" (every 1 – 5 years).

## 4. SUMMARY

In the context of natural disasters, the RI$_{cp}$ suggests that a comprehensive risk assessment approach needs to integrate peoples' perception into risk identification, risk estimation so that the outputs could be used in risk reduction measurements or interventions. Such inclusivity of local community members' perspectives will strengthen the conventional probabilistic disaster-risk calculation. The Bangladesh's coastal community case study demonstrates a successful application of this newer approach.

## References

[1] Azad, M. A. K., & Khan, M. M. (2015). Post disasters social pathology in Bangladesh: a case study on AILA affected areas. *Sociology and Anthropology*, *3*(2), 85–94. https://doi.org/10.13189/sa.2015.030203

[2] Choudhury, M. U. I., Uddin, M. S., & Haque, C. E. (2018). “Nature brings us extreme events, some people cause us prolonged sufferings”: the role of good governance in building community resilience to natural disasters in Bangladesh. *Journal of Environmental Planning and Management*, *0*(0), 1–21.

[3] Ferrier, N., & Haque, C. E. (2003). Hazards risk assessment methodology for emergency managers: A standardized framework for application. *Natural Hazards*, *28*(2–3), 271–290. https://doi.org/10.1023/A:1022986226340

[4] Haque, C. E., & Etkin, D. (2007). People and community as constituent parts of hazards: The significance of societal dimensions in hazards analysis. *Natural Hazards*, *41*(2), 271–282. https://doi.org/10.1007/s11069-006-9035-8

[5] Nirupama, N. (2012). Risk and vulnerability assessment: A comprehensive approach. *International Journal of Disaster Resilience in the Built Environment*, *3*(2), 103–114. https://doi.org/10.1108/17595901211245189

# Assessment of sustainable utilization of water resources in Central Asia based on water resources carrying capacity

LIU Wenhua[1], WANG Yizhuo[1,2], JIA Shaofeng[1,3], ZHU Wenbin[1]

[1] Key Laboratory of Water Cycle and Related Land Surface Processes, Institute of Geographic Sciences and Natural Resources Research, Chinese Academy of Sciences, Beijing, China
email: liuwh@igsnrr.ac.cn
email: wangyizhuo8044@igsnrr.ac.cn
email: jiasf@igsnrr.ac.cn
email: zhuwb@igsnrr.ac.cn

[2] University of Chinese Academy of Sciences, Beijing, China
[3] School of Geographical Sciences, Qinghai Normal University, Xining, China

## 1. INTRODUCTION

Water is not only equal to life but also a strategic resource for sustainable development of regional economy and ecological environment [1,2]. Today about 2.4 billion people worldwide live in highly water-stressed areas, because of the uneven temporal and spatial distribution of available renewable freshwater resources. This issue is especially acute in Central Asia. Climate change has already accelerated the rate of evaporation, causing inland lakes such as the Aral Sea and Lake Balkhash to dry up and threatening the normal water supply [3-5]. In 1991, the independence of Central Asia meant the collapse of the economic system and the ensuing widespread socioeconomic upheaval [6]. The region's major rivers also became transboundary rivers. This has left a legacy of international transboundary disputes over water allocation due to conflicting interests between upstream hydropower generation by Tajikistan and the downstream water needs of Turkmenistan and Uzbekistan for cotton, rice and wheat irrigation [7,8]. In addition, due to the population explosion, urban migration human activities including change in land use and dam construction, water resource allocation in Central Asia has become a big and complicated problem.

A reliable and adequate supply of water is one of the key elements addressed by the Sustainable Development Goals (SDGs) agreed by the United Nations in 2015. To better monitor progress towards the target of sustainable utilization of water resources, two indicators are used: Indicator 6.4.1 measuring water use efficiency and 6.4.2 measuring the level of water stress. However, the two indicators do not directly describe the relationship between the sustainable use of water resources in various countries with the population and economy, nor do they combine this relationship to propose corresponding improvement measures from the perspective of water resources management. Therefore, we choose water resources carrying capacity (WRCC) that can scientifically understand the water resources carrying capacity threshold and overload risk to assess the sustainable utilization of water resources. As an innovative concept, WRCC was first put forward by the Xinjiang Water Resource Soft-Science Research Group in 1989. Currently, WRCC is defined as the maximum socioeconomic scale or water resource availability that can be carried by water resources under various constraints [9]. In this paper, we define it as the maximum population size in a region that can be supported by water availability a certain level of economy, technology and welfare, following the principle of the sustainable development. In this paper, we apply WRCC to the assessment of sustainable utilization of water resources in Central Asia to quantitatively reveal the cross-country differences and to promote sustainable development in countries along the Belt and Road.

## 2. MATERIALS AND METHODS

### *2.1 Materials*

The data related to water resources used in this paper, which include water resources and water withdrawal (1995-2020), were obtained from the United Nations Food and Agriculture Organization

(FAO). GDP, GDP per capita and total population of the five countries of Central Asia (1990-2020) were acquired from the World Bank. And the indicator domestic water withdrawal as % of total water withdrawal (%) was obtained from a report produced by the Organization for Economic Cooperation and Development (OECD).

### *2.2 Methods*

After meeting the water demand of ecosystem, the maximum population was taken as the object function, and water use efficiency and social welfare were set as the constraints. The related equations are given as follows:

$$AR = \text{Total renewable water resources} - \text{Environmental flow requirements} \quad (1)$$

$$\text{Total water withdrawal} = \text{Domestic water withdrawal} + (\text{Agricultural water withdrawal} + \text{Industrial water withdrawal} + \text{Service water withdrawal}) \quad (2)$$

$$pDU = \text{Domestic water withdrawal} / Pop \quad (3)$$

$$tPU = (\text{Agricultural water withdrawal} + \text{Industrial water withdrawal} + \text{Service water withdrawal}) / GDP \quad (4)$$

where *AR* [$10^9$ $m^3$ $year^{-1}$] is the available water resources; The units of *Total renewable water resources, Environmental flow requirements, Total water withdrawal, Domestic water withdrawal, Agricultural water withdrawal, Industrial water withdrawal*, and *Service water withdrawal* are all [$10^9$ $m^3$ $year^{-1}$]; *Pop* [-] is the total population; *GDP* [current US$] is the Gross Domestic Product; *pDU* [$m^3$ $year^{-1}$]is the domestic water withdrawal per capita; *tPU* [$m^3$ $US\$^{-1}$ $year^{-1}$] is water use efficiency. Substituting Eqs. (2) – (4) into Eq. (1), the WRCC can be written as:

$$WRCC = \frac{AR \times 10^9}{pDU + tPU \cdot pGDP} \quad (5)$$

where *pGDP* [current US$]is the GDP per capita. In order to evaluating the WRCC, we used water resources carrying capacity index (WRCI) to represent the six carrying types as shown in Table 1. And the WRCI can be represented as follows:

$$WRCI = \frac{Pop}{WRCC} \quad (6)$$

**Table 3.** Division criterion of WRCI

| WRCI | Types |
|---|---|
| Highly surplus | (0, 0.6) |
| Moderate surplus | [0.6, 0.8) |
| Lowly surplus | [0.8, 1.0) |
| Lowly overload | [1.0, 1.2) |
| Moderate overload | [1.2, 1.4) |
| Highly overload | [1.4, +∞) |

## 3. RESULTS

### *3.1 Evaluation of WRCC*

Based on the available water resources, technical level, and social welfare, the population that the water resources of Central Asia could carry in 1995, 2000, 2005, 2010, 2015 and 2020 were calculated by using Eq. (1)-(5). The results are shown in Fig. 2. Kazakhstan had a significantly higher WRCC than the other four countries, up to 15 times higher. The WRCC of all five Central Asian countries was increasing due to the improvement of water use efficiency.

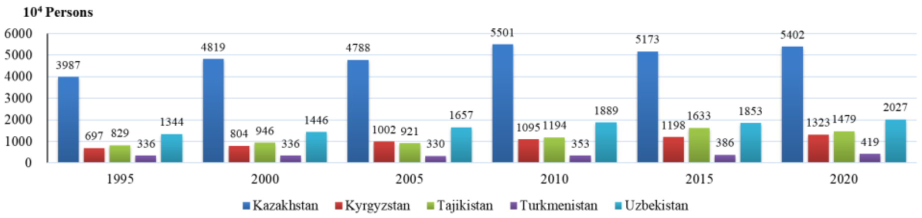


**Fig. 2.** The calculated WRCC of Central Asia in 1995, 2000, 2005, 2010, 2015 and 2020

### *3.2 Evaluation of WRCI*

Based on the population in each year and the calculated population carried by the water resources, the WRCI in each area in Central Asia was obtained, as given in Fig. 3. There were significant differences in the WRCI of the five Central Asian countries, with Kazakhstan and Kyrgyzstan as highly surplus, Tajikistan as moderate surplus, and Turkmenistan and Uzbekistan as highly overload. In terms of temporal changes, the sustainable utilization of water resources in Central Asia was increasing, but not significantly.

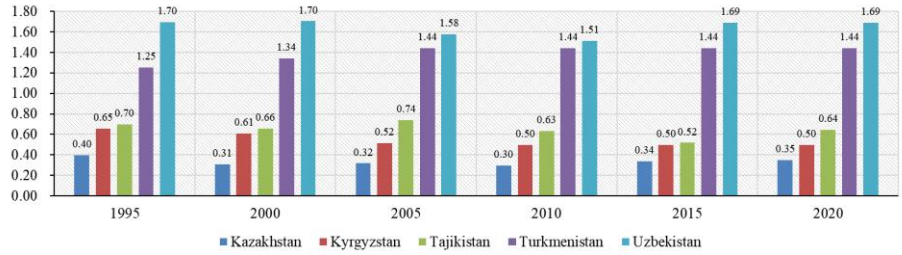


**Fig. 3.** The calculated WRCI of Central Asia in 1995, 2000, 2005, 2010, 2015 and 2020

## 4. SUMMARY

Through the analysis of the main data related to water resources and water withdrawal and the main indicators of the World Development for Central Asia, we can conclude that Kazakhstan had the most sustainable utilization of water resources, while Turkmenistan and Uzbekistan were facing a huge water crisis during 1995-2020. Therefore, we assume that the maximum population that can be carried by water resources in each year is 1 time, 1.25 times and 1.67 times as the total population of the year, the tPU can be calculated as Table 2. Because tPU of Kazakhstan can be as low as 0.14 under the Status Quo, the tPU we calculated for Turkmenistan and Uzbekistan can be achieved. The government can take measures to reduce the production water withdrawal in order to reach these goals.

**Table 2.** The calculated tPU Turkmenistan of Uzbekistan and after adjusting WRCI level

| Year | Turkmenistan | 1.0 | 0.8 | 0.6 | Kazakhstan | Kyrgyzstan | Tajikistan |
|---|---|---|---|---|---|---|---|
| 1995 | 9.59 | 7.60 | 6.04 | 4.48 | 1.34 | 5.89 | 8.14 |
| 2000 | 8.78 | 6.48 | 5.15 | 3.81 | 1.16 | 6.66 | 11.01 |
| 2005 | 3.37 | 2.32 | 1.84 | 1.36 | 0.38 | 3.13 | 4.59 |
| 2010 | 1.21 | 0.83 | 0.66 | 0.49 | 0.14 | 1.54 | 1.59 |
| 2015 | 0.76 | 0.53 | 0.42 | 0.31 | 0.13 | 1.10 | 0.89 |
| 2020 | 0.54 | 0.37 | 0.30 | 0.22 | 0.14 | 0.95 | 1.12 |
| Year | Uzbekistan | 1.0 | 0.8 | 0.6 | Kazakhstan | Kyrgyzstan | Tajikistan |
| 1995 | 4.21 | 2.39 | 1.87 | 1.35 | 1.34 | 5.89 | 8.14 |
| 2000 | 4.10 | 2.32 | 1.81 | 1.30 | 1.16 | 6.66 | 11.01 |
| 2005 | 3.66 | 2.24 | 1.76 | 1.27 | 0.38 | 3.13 | 4.59 |
| 2010 | 1.00 | 0.64 | 0.50 | 0.36 | 0.14 | 1.54 | 1.59 |
| 2015 | 0.65 | 0.37 | 0.29 | 0.20 | 0.13 | 1.10 | 0.89 |
| 2020 | 0.93 | 0.53 | 0.41 | 0.29 | 0.14 | 0.95 | 1.12 |

## References

[1] Batisha A. (2022). Horizon scanning process to foresight emerging issues in Arabsphere's water vision. Scientific Reports, 12(1): 12709.
[2] Han Y., Jia S. (2022). An assessment of the water resources carrying capacity in Xinjiang. Water, 14(9): 1510.

[3] Duan W., Zou S., Chen Y., Nover D., Fang G., Wang, Y. (2020). Sustainable water management for cross-border resources: The Balkhash Lake Basin of Central Asia, 1931–2015. Journal of Cleaner Production, 263: 121614.
[4] Lioubimtseva E., Henebry G.M. (2009). Climate and environmental change in arid Central Asia: Impacts, vulnerability, and adaptations. Journal of Arid Environments, 73(11): 963-977.
[5] Yang X., Wang N., Chen A., He J., Hua T., Qie Y. (2020). Changes in area and water volume of the Aral Sea in the arid Central Asia over the period of 1960–2018 and their causes. CATENA, 191: 104566.
[6] Severskiy I.V. (2004). Water-related problems of central Asia: some results of the (GIWA) International Water Assessment Program. Ambio, 33(1-2): 52-62.
[7] Bernauer T., Siegfried T. (2012). Climate change and international water conflict in Central Asia. Journal of Peace Research, 49(1): 227-239.
[8] Jalilov S.M., Amer S.A., Ward F.A. (2013). Water, Food, and Energy Security: An Elusive Search for Balance in Central Asia. Water Resources Management, 27(11): 3959-3979.
[9] Jia S., Zhou C., Yan H., Zhou H., Tang Q., Zhang J. (2004). Estimation of usable water resources and carrying capacity in Northwest China. Advances in Water Science, 15(6): 801-807.

# SDG 7 (Affordable and Clean Energy): Transitioning to Low-carbon Energy

# Quantification of the effects of aerosols and clouds on solar energy over China using WRF-Chem

GAO Yi [1], ZHANG Yanqing [2], ZHANG Meigen [2], Han Xiao [2]

[1] State Key Laboratory of Atmospheric Boundary Layer Physics and Atmospheric Chemistry (LAPC), Institute of Atmospheric Physics, Chinese Academy of Sciences, Beijing 100029, China
email: ygao@mail.iap.ac.cn

[2] State Key Laboratory of Atmospheric Boundary Layer Physics and Atmospheric Chemistry (LAPC), Institute of Atmospheric Physics, Chinese Academy of Sciences, Beijing 100029, China
email: zhangyanqing19@mails.ucas.edu.cn
email: mgzhang@mail.iap.ac.cn
email: Hanxiao@mail.iap.ac.cn

## 1. INTRODUCTION

The promotion of renewable energy as a substitute for fossil fuels is the key solution to achieving the goals agreed on by the member countries during the UN Climate Change Conference in Glasgow (COP26), that is, to phase down coal power and achieve net-zero carbon emissions. Among the various renewable energy sources, solar energy is an attractive option that will have a significant effect on the future of energy supply and energy use. In this study, we evaluated the solar energy simulated by the WRF-Chem during 2016–2020 and quantified the relative contributions of the aerosol direct effect (ADE), aerosol indirect effect (AIE), and cloud radiation effect (CRE) to solar energy.

## 2. MATERIALS AND METHODS

An online-coupled meteorology–chemistry model, WRF-Chem v4.2, was used to simulate the transformation of chemical species (both trace gases and aerosols) as well as meteorological fields and their interactions [2][4]. The horizontal resolution of the model domain is 36 km, with a total of 160 × 123 grid points in the east–west and south–north directions covering the whole country of China. The vertical direction has been divided into 36 vertical levels extending from the surface to 10 hPa. The meteorological initial and boundary conditions were derived from the European Centre for Medium-Range Forecasts Reanalysis v5 (ERA5, $0.25° \times 0.25°$) [6]. The chemical initial and boundary conditions were obtained from the output of the Community Atmosphere Model with Chemistry (CAM-chem) in the NCAR Community Earth System Model (CESM2.0) [1]. Numerical experiments were conducted from December 1, 2015, to January 1, 2021. The carbon bond mechanism (CBMZ) [10] for gas-phase chemistry, and 4-bin version of the model for simulating aerosol interactions and chemistry (MOSAIC) [11] for aerosols are used. The anthropogenic emissions of CO, NOx, SO2, VOC, BC, OC, PM2.5, and PM10 in 2016 were based on Tsinghua University's 2016 monthly emission inventory [7][12]. The anthropogenic emissions from 2017 to 2020 were calculated based on the 2016 emissions using the annual emission factor [9]. Biogenic emissions were calculated online by using a model of emissions of gases and aerosols from nature (MEGAN) [5]. Dust emissions were calculated online according to the method of [8]. Sea salt emissions were calculated online according to the method of [3]. We conducted four sensitivity experiments by turning the ADE, AIE, and CRE on/off to quantify the contributions of the ADE, AIE, and CRE to the change in solar energy trends. Table 1 lists the sensitivity experiments. The difference between the EXP_CTRL and EXP_NOADE represents the impact of ADE on solar energy trends. The difference between the EXP_CTRL and EXP_NOAIE represents the impact of AIE. The difference between the EXP_CTRL and EXP_NOCRE represents the impact of CRE on solar energy trends.

**Table 1**. Configurations of the model sensitivity experiments.

| Experiments | ADE | AIE | CRE |
|---|---|---|---|

| | | | |
|---|---|---|---|
| EXP_CTRL | ON | ON | ON |
| EXP_NOADE | OFF | ON | ON |
| EXP_NOAIE | ON | OFF | ON |
| EXP_NOCRE | ON | ON | OFF |

Equation (1) was used to calculate the contributions of the ADE, AIE, and CRE to solar energy trends:

$$Relative\ Contribution\ Percent = \frac{\Delta Trend_i}{\sum|\Delta Trend_i|} \times 100\%, \tag{1}$$

where $\Delta Trend_i$ is the change in the solar energy trends due to the ADE, AIE, and CRE. When the relative contribution percent is higher than 0, it represents a positive contribution, which means that the solar trends increase when ADE, AIE or CRE is turned on. When the relative contribution percent is below 0, it represents a negative contribution, which means that the solar trends decrease when ADE, AIE, or CRE is turned on.

## 3. RESULTS

The aim of our study was to quantify the contributions of aerosols and clouds to solar energy trends in China by applying the WRF-Chem model to the period 2016–2020. Figure 1 shows the relative contributions of the ADE, AIE, and CRE to solar energy trends calculated by using Equation (1). The relative contributions of aerosols and clouds to solar energy trends are different in horizontal distribution. Figure 9(a) shows that the ADE positively affects the solar energy trends in China, with the largest contribution exceeding 70% in northern China and ~60% in several regions of Xinjiang. High PM2.5 concentrations (exceeding 80 μg m-3) and significant decreases (-6 μg m-3 yr-1) during 2016–2020 contribute to the increase in the solar energy in northern China. The increase in the CF (<0.4% yr-1) is too small to affect the solar energy during 2016–2020 in northern China (Figure 7). The positive contribution of the ADE to solar energy in several parts of Xinjiang during 2016–2020 is also due to the significant decrease in the PM2.5 (4 μg m-3 yr-1). The ADE affects the solar energy by absorbing and reflecting solar radiation; thus, the decrease in the PM2.5 leads to an increase in the solar energy during 2016–2020 in northern China and parts of Xinjiang. Figure 9(b) shows that the AIE positively affects the solar energy, mainly in Guangxi and the southern Qinghai–Tibet Plateau, with a maximum contribution of 60%. The decrease in PM2.5 leads to a decrease in the clouds through the AIE during 2016–2020. Therefore, the solar radiation reflected by clouds decreases, leading to an increase in the solar energy. Negative contribution of the AIE to solar energy in several parts of the northern China and northern Xinjiang, with a maximum contribution of -40%. Figure 9(c) shows that the contribution of the CRE to solar energy differs in different regions. A positive contribution can be mainly observed in Guangdong, Xinjiang, and Tibet, where the PM2.5 concentration is low (60%, 70%, and 80%, respectively). The CF significantly decreases from 2016–2020 in Guangdong, Guiyang, Xinjiang, and Tibet, with a value of -2%, -1%, -0.4%, and -0.6% yr-1, respectively (Figure 7). The decrease in the CF leads to less solar radiation being reflected or absorbed by clouds and thus results in an increase in the solar energy from 2016–2020 in these regions. The negative contribution of the CRE to the solar energy can be mainly observed in the Sichuan Basin and Northeast China, with the largest contributions exceeding -70% and -50%, respectively. In these two regions, the CF significantly increases (1.5% yr-1 and 0.3% yr-1) from 2016–2020. The increase in the CF brings about more solar radiation to be absorbed or reflected by clouds, resulting in a decrease in the solar energy from 2016–2020 in the Sichuan Basin.

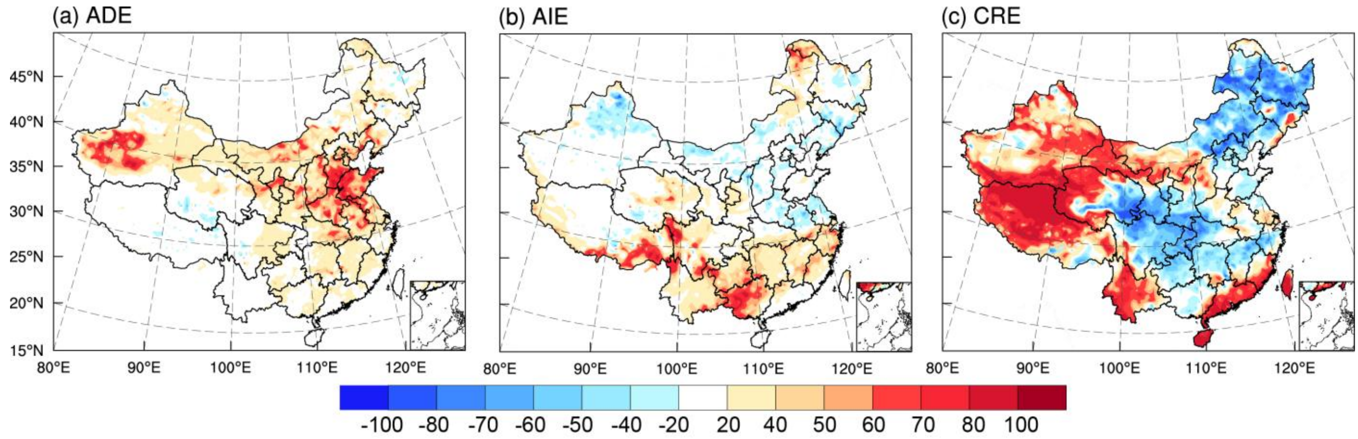


Fig. 1. Relative contributions of the ADE, AIE, and CRE to the solar energy (%) during 2016-2020 in China.

## 4. SUMMARY

We selected the period of 2016–2020 during which the aerosol concentration gradually decreased due to strict pollutant control measures to evaluate solar energy simulations based on the Weather Research Forecast-Chemistry (WRF-Chem) model. We also analyzed the contributions of the aerosol direct effect (ADE), aerosol indirect effect (AIE), and cloud radiation effect (CRE) to solar energy trends by conducting sensitivity experiments. The results show that the WRF-Chem model performs well for the 2 m temperature (T2), cloud fraction, PM2.5, solar energy trends during 2016–2020. There are regional and seasonal differences in the contributions of ADE, AIE, and CRE to solar energy trends, with a decrease in ADE contributions and an increase in CRE contributions from north to south in China, and the AIE contribution being relatively slight. On an annual scale, ADE is the main contributor to the increase in solar energy trends in the Beijing-Tianjin-Hebei (89%) and Fenwei Plains (83.9%) from 2016 to 2020, which is related to the horizontal distribution of PM2.5. In the Yangtze River Delta and other regions, ADE and CRE contributed equally to the increase in solar energy trends, about 40%. In the Pearl River Delta and Sichuan Basin, the contribution of CRE is larger than that of AIE and ADE, the Pearl River Delta region is the largest contributor of CRE to the annual solar energy trends among the five major urban agglomerations, with a contribution of 78.4%, and Sichuan basin is the only region where CRE has a negative contribution to the annual solar energy trends (-59.1%). On the seasonal scale, the contribution of CRE is dominant except for the greater positive contribution of ADE to the solar energy trends in spring, summer, and autumn in Beijing-Tianjin-Hebei and in autumn in Fenwei Plain.

## References

[1] Emmons, L., Schwantes, R., Orlando, J., Tyndall, G., Kinnison, D., Lamarque, J.F., Marsh, D., Mills, M., Tilmes, S., Bardeen, C., Buchholz, R., Conley, A., Gettelman, A., Garcia, R., Simpson, I., Blake, D., Meinardi, S., Pétron, G. (2020) The Chemistry Mechanism in the Community Earth System Model version 2 (CESM2), J. Adv. Model. Earth Syst., 12, e2019MS001882.

[2] Fast, J., Gustafson, W., Easter, R., Zaveri, R., Barnard, J., Chapman, E., Grell, G., Peckham, S. (2006) Evolution of Ozone, particulates, and aerosol direct radiative forcing in the vicinity of Houston using a fully coupled meteorology-chemistry-aerosol model, J. Geophys. Res., 111, 305.

[3] Gong, S., Barrie, L., Blanchet, J.P. (1997) Modeling sea-salt aerosols in the atmosphere 1. Model development, J. Geophys. Res., 102: 3805–3818.

[4] Grell, G.A., Peckham, S.E., Schmitz, R., McKeen, S.A., Frost, G., Skamarock, W.C., Eder, B. (2005) Fully coupled "online" chemistry within the WRF model, Atmos. Environ., 39: 6957–6975.

[5] Guenther, A., Karl, T., Harley, P., Wiedinmyer, C., Palmer, P., Geron, C. (2006) Estimates of global terrestrial isoprene emissions using MEGAN (Model of Emissions of Gases and Aerosols from Nature), Atmos. Chem. Phys., 6: 3181–3210.

[6] Hersbach, H., Bell, B., Berrisford, P., Hirahara, S., Horányi, A., Muñoz Sabater, J., Nicolas, J., Peubey, C., Radu, R., Schepers, D., Simmons, A., Soci, C., Abdalla, S., Abellan, X., Balsamo, G., Bechtold, P., Biavati, G., Bidlot, J., Bonavita, M., Thépaut, J.-N. (2020) The ERA5 global reanalysis, Q. J. R. Meteorol. Soc., 146: 1999–2049.

[7] Lei, Y., Zhang, Q., He, K., Streets, D. (2011) Primary anthropogenic aerosol emission trends for China, 1990–2005, Atmos. Chem. Phys., 11: 931–954.

[8] Shao, Y., Ishizuka, M., Mikami, M., Leys, J. (2011) Parameterization of size-resolved dust emission and validation with measurements, J. Geophys. Res, 116, D08203.

[9] Tong, D., Cheng, J., Liu, Y., Yu, S., Yan, L., Hong, C., Qin, Y., Zhao, H., Zheng, Y., Geng, G., Li, M., Liu, F., Zhang, Y., Zheng, B., Clarke, L., Zhang, Q. (2020) Dynamic projection of anthropogenic emissions in China: methodology and 2015–2050

emission pathways under a range of socio-economic, climate policy, and pollution control scenarios, Atmos. Chem. Phys., 20: 5729–5757.
[10] Zaveri, R., Peters, L. (1999) A new lumped structure photochemical mechanism for large-scale applications, J. Geophys. Res. Atmos., 104: 30387–30415.
[11] Zaveri, R.A., Easter, R.C., Fast, J.D., Peters, L.K. (2008) Model for Simulating Aerosol Interactions and Chemistry (MOSAIC), J. Geophys. Res. Atmos., 113.
[12] Zhang, Q., Streets, D., Carmichael, G., He, K., Huo, H., Kannari, A., Klimont, Z., Park, I., Reddy, E.S., Fu, J., Chen, D., Duan, L., Lei, Y., Wang, L., Yao, Z. (2009) Asian emissions in 2006 for the NASA INTEX-B mission, Atmos. Chem. Phys., 9: 5131–5153.

# Remote sensing monitoring of power consumption along the China-Pakistan Economic Corridor

BIAN Jinhu[1], LI Ainong[1], LEI Guangbin [1]

[1] Research Center for Digital Mountain & Remote Sensing Application,Institute of Mountain Hazards and Environment, CAS
bianjinhu@imde.ac.cn
ainongli@imde.ac.cn
leiguangbin@imde.ac.cn

## 1. INTRODUCTION

Pakistan is a fast developing but also an extremely short of electricity country, with weak power infrastructure (Valasai et al. 2017). A nationwide blackout on January 9, 2021 plunged Pakistan into darkness at night and further focused global attention on the country's power shortages. The power problems in Pakistan are mainly reflected in four aspects: the contradiction between the accelerated modernization process and the increase of power consumption demand, the unreasonable structure of industrial power consumption and household power consumption, the unreasonable structure of fossil fuels and clean energy, and the huge gap between the rich and the poor in power consumption (Alter and Syed 2011). The construction of energy projects is the key priority of CPEC, including power stations and transmission projects, which will greatly alleviate power shortages in Pakistan (Mirza et al. 2019). Estimation of China-Pakistan economic corridor construction since the electric power consumption, understanding the power consumption of time and space change pattern, and analyzing the energy changes in Pakistan power consumption before and after the completion of the project will have great significance on optimizing investment programs and power plant and reasonable layout. It will also be helpful for the adjustment of the energy structure, energy future cooperation with Pakistan electric power sustainable development to provide data support and decision-making basis.

## 2. MATERIALS AND METHODS

To provide a consistent dataset of EPC in Pakistan and a comprehensive assessment of changes in its spatiotemporal patterns during the last decades, we used NASA NPP/VIIRS DNB black marble product to estimate the monthly and yearly EPC in Pakistan at a 15 arc second spatial resolution for the period 2013 to 2020. We then analyzed the spatiotemporal pattern variation by CPEC.

### *2.1 1. NASA Black marble nighttime light Product for EPC estimation*

The NASA black marble nighttime light product were used in this study. The product retrieval strategy uses a novel “Turning off the Moon” approach that combines cloud-free, atmospheric-, terrain-, vegetation-, snow-, lunar-, and stray light-corrected nighttime VIIRS DNB radiances, daytime DNB surface reflectance, bidirectional reflectance distribution function (BRDF)/albedo, and lunar irradiance values to minimize the influence of extraneous artifacts and biases

### *2.2 2. GTWR model to estimate EPC from nighttime light product*

The GTWR model was employed to model the space-time relationship between electricity consumption and nighttime light radiance. GTWR model considers both the spatial nonstationary of geographic data and temporal effects in the calculation model. Formally, GTWR can be expressed as Equation (1).

$$Y_i = \beta_0(u_i, v_i, t_i) + \sum_{k=1}^{K} \beta_k(u_i, v_i, t_i) X_{ik} + \varepsilon_i \tag{1}$$

For each observation $i$ ($i$=1,2,…$n$), $Y_i$ is the dependent variable, whereas $X_{ik}$ is the $k$th explanatory variable. ($u_i$,$v_i$,$t_i$) represents the space-time coordinates of observation $i$. $u_i$ and $v_i$ are the spatial coordinates, whereas $t_i$ is the temporal coordinate. $\beta_0(u_i, v_i, t_i)$ is the intercept value, and $\beta_k(u_i, v_i, t_i)$ denotes the regression coefficient.

## 3. RESULTS

### *3.1 Spatial distribution pattern of power consumption in Pakistan*

Overall, Pakistan's electricity consumption is mainly concentrated in the eastern plain region, and the eastern region is higher than the western region. The direction of power consumption in Pakistan is obvious, with a northeast - southwest distribution. Most of Pakistan's mountainous areas have an average of zero power consumption and are mostly sparsely populated areas with no lights at night. The socio-economic activities in these regions showed fewer characteristics of low power consumption. In Pakistan, the area with average power consumption greater than 0 is about 121,480 $km^2$, accounting for 14.84% of the land area. In terms of administrative divisions, the consumption of electricity in Punjab and Sindh provinces of Pakistan is significantly higher than other regions. Punjab and Sindh are important economic and cultural centers of Pakistan. Big cities such as Lahore, Karachi and Sukkur consume a lot of electricity. The two provinces occupy a large proportion of industrial enterprises, education, economic and other areas of good development. Islamabad area is the capital of Pakistan, and is the cultural and political center of the country, electricity consumption of the country's top cities. The spatial distribution characteristics of power consumption in Pakistan are closely related to the overall distribution of the country and the development degree of each region.

### *3.2 Temporal and spatial patterns of power consumption in Pakistan from 2013 to 2020*

The change slope of time series of power consumption can reflect the change trend of power consumption. The larger the change slope is, the faster the regional economy develops. Overall, power consumption in Pakistan increased rapidly from 2013 to 2020. In 2020, compared with 2013, power consumption increased by 2.7684 billion Kwh, with an average annual increase of nearly 350 million Kwh. Power consumption showed an increasing trend from west to east. The area with a change slope of 0 accounted for 45.42% of the total area from 2013 to 2020, while 6.46% of the area saw a significant increase in power consumption. Specifically, the increase in power consumption is mainly concentrated in large and medium-sized cities in Pakistan, such as Islamabad, Karachi and Lahore. The economic and cultural development and the power generation and transmission resources of the China-Pakistan Economic Corridor power station are the main reasons for the increase in power consumption. In the urban area, the urban spatial change area is mainly concentrated in the urban periphery area rather than the urban center area, and the increase of power consumption in suburban area is higher than that in the central area.

## 4. SUMMARY

This study developed the high spatial resolution EPC datasets based on the night light data and statistical data of power consumption from 2013 to 2020. The spatio-temporal variation patterns of the electricity consumption in Pakistan since China Pakistan economic corridor power project construction were then analyzed. It can provide important scientific data support for the monitoring of realization process the SDG 7 affordable and clean energy and SDG 11 sustainable community.

## References


[1]. Alter, N. and S. H. Syed (2011). "An Empirical Analysis of Electricity Demand in Pakistan." International Journal of Energy Economics and Policy 1(4): 116-139.

[2]. Mirza, F. M., N. Fatima and K. Ullah (2019). "Impact of China-Pakistan economic corridor on Pakistan's future energy consumption and energy saving potential: Evidence from sectoral time series analysis." Energy Strategy Reviews 25: 34-46.

[3]. Valasai, G. D., M. A. Uqaili, H. R. Memon, S. R. Samoo, N. H. Mirjat and K. Harijan (2017). "Overcoming electricity crisis in Pakistan: A review of sustainable electricity options." Renewable and Sustainable Energy Reviews 72: 734-745.

# Satellite-based Compliance Monitoring for Enforcing Pollution Control Policies: Coal-fired Power Plants in China

YAN Xiaoxi[1], XU Yuan [1,2]

[1] Department of Geography and Resource Management, The Chinese University of Hong Kong, Shatin, NT, Hong Kong, China
email: yanxiaoxi@link.cuhk.edu.hk

[2] Institute of Environment, Energy and Sustainability, The Chinese University of Hong Kong, Shatin, NT, Hong Kong, China
email: yuanxu@cuhk.edu.hk

## 1. INTRODUCTION

China is one of the top emitters of most key air pollutants. Most of China's major cities cannot meet the recently upgraded ambient air quality guidelines from the World Health Organization, while the major pollutants are $PM_{2.5}$ and ozone [1, 2]. $SO_2$ and $NO_x$ are critical precursor pollutants $PM_{2.5}$ and ozone. Energy consumption dominates the anthropogenic emissions of $CO_2$, $SO_2$ and $NO_x$.

Various policies have been enacted to tackle the mounting environmental problems and a large quantity of facilities has been installed. China has witnessed its average thermal efficiency of coal-fired power sector surpassing that of the United States, largely through shutting down inefficient small plants and building efficient large ones [3]. However, bottom-up studies have reported significant overestimation [4] and underestimation of China’s emissions [5]. At the end of 2012, about 95% coal-fired power plants had installed Flue-Gas Desulfurization (FGD) facilities for $SO_2$ mitigation and about one-third had Selective Catalytic Reduction (SCR) facilities for $NO_x$ mitigation, both capable of avoiding over 90% emissions [6]. The operation and maintenance of these facilities are very expensive (over 1 million RMB per day for one coal-fired power plant with four 600 MW generators). One critical factor to encourage their normal operation is to catch enough non-compliance cases and issue severe enough penalty [7].

The current emission data reporting system in China is largely bottom-up, which could potentially suffer from two major problems. First, energy and environmental monitoring and reporting in China at present generally have to pass through, and inspected by, polluting firms and various levels of local government and relevant agencies before reaching the central government. Most of environmental policy implementation capacity, such as personnel and governmental expenditure, is in local governments, while the central government is mainly in charge of policy making. Emissions of $CO_2$, $SO_2$ and $NO_x$ are generally calculated via bottom-up energy consumption data and emission factors [4, 8, 9]. This approach is often subject to the influence of intentional distortions for the interest of stakeholders along the path [10]. China has been exerting increasingly high pressure on local governments and energy-intensive firms to achieve top-down energy and emission control goals from the central government. In comparison to the technologically challenging, economically expensive, and politically difficult tasks of actual mitigation, it could be much easier and convenient to twist the reported numbers. Furthermore, another shortcoming is the potentially high costs. Because of China’s sheer size, the large system involves numerous personnel and occupies substantial resources. In the 12th Five-Year Plan (2011-2015) alone, the Chinese government planned to invest 40 billion RMB (~US$6.3 billion) to enhance related environmental regulation capacity [11].

Adopting an economic theory on crime and punishment [12, 13], enforcement models explain why a polluting firm complies, or does not comply, with an environmental policy based on the economic calculation of costs and benefits responding to enforcement activities. A key research question is how to deter environmental non-compliance effectively. With different data and methodology, studies have concluded that detection probability is more important [14], punishment severity is more important [15], and both are important [16]. Studies found that policing strategies are of only minor significance, while the number of police – total monitoring, reporting and verification (MRV) expenditure – may explain a large proportion of the crime rate change [17].

Environmental non-compliance is one of the most important reasons that lead to earlier environmental crises in China [7]. Non-compliance cannot be deterred without a high enough proportion of cases being caught and punished [7]. Catching non-compliance could be achieved through various means. Different MRV techniques may have different detection probabilities of non-compliance cases. Continuous emission monitoring systems (CEMSs) have been widely used in the United States to provide accurate data on $SO_2$ emissions and monitor compliance [18], while the poorer quality of CEMSs in China often fail to achieve such accuracy and they are mainly used to provide guidance for occasional site inspections [7, 19].

Remote sensing technologies have become increasingly important in environmental non-compliance monitoring with the potential to alleviate the above two shortcomings of the current data reporting system. First, remote sensing technologies could circumvent various levels of local governments and polluting sources to provide top-down, objective data without subjective distortions [20]. Second, remote sensing technologies could potentially provide a relatively low-cost means to monitor polluting sources. Although each satellite observing the Earth's $CO_2$ and air quality could cost a few hundred million US dollars, such as the newly launched OCO-2 satellite for $CO_2$ monitoring by NASA with a price tag of US$465 million, its wide spatial and regular coverage could substantially reduce the average costs per polluting source [21]. Remote sensing technologies using satellites could provide large-scale spatial coverage of multiple pollutants [22]. The measurement extends to areas either inaccessible or beyond the current ground monitoring network, while the spatial resolution is coarse [22]. Remote sensing data have been successfully applied in China to examine the impacts of environmental policies on pollutant emissions from coal-fired power plants [23, 24]. However, the objective data have not been systematically integrated with governmental institutions to examine when and why environmental policies are effectively enforced to encourage active enforcement and honest compliance.

Satellite data can provide important complements with objective observations and much lower monitoring costs per polluting source, but their accuracy has not reached a level to replace the MRV system. This study is aimed at integrating the informative yet imperfect data to screen form possible violations, and then using MRV or environmental inspections to target those suspicious polluters or regions for confirming environmental compliance statuses before issuing penalty[25].

## 2. MATERIALS AND METHODS

### *2.1 Data*

#### *2.1.1 OMI satellite observations*

The Ozone Monitoring Instrument (OMI) on-board Aura, launched in 2004, is a nadir-viewing Ultraviolet/Visible spectrophotometry imaging spectrograph with its wavelength ranging from 270 to 500 nm [26]. The spatial resolution of OMI ranges from 13km x 24 km at the nadir to 28 km x 150 km at the outermost swath angle [26]. Tropospheric $NO_2$ (OMNO2) and planetary boundary layer $SO_2$ (OMSO2) of level 2 swath products are used [27, 28]. Pixels affected by “row anomalies” (see http://www.knmi.nl/omi/research/product/rowanomaly-background.php) are excluded and only sky data with a cloud radiance fraction of each scene less than 20% are used [29, 30].

#### *2.1.2 Data of coal-fired power plants*

Data of coal-fired power plants is derived by combining Global Coal Plant Tracker and the lists of sulfur and nitrogen control facilities for coal-fired generation units published in July 2014 by the Ministry of Ecology and Environment of the People's Republic of China [31, 32]. In total, 1225 coal-fired power plants are included.

### *2.2 Methods*

#### *2.2.1 Time-series of emission level of coal-fired power plants*

Since the spatial resolution of OMI observations is relatively low, the emission level of coal-fired power plants is represented by the observations in a moving space-time window with the spatial radius of 2km and the time length of one year. The emission level of coal-fired power plant *i* at time *t* is represented as the mean value of observations with its distance from *i* no more than 2km and its time difference from *t* no more than a half year.

### *2.2.2 Subtracting local background value*

To minimize the impact from local background value on the emission signals, the signals are represented by VCD enhancements by subtracting background value from the original observations. Coal-fired power plants are clustered using a DBSCAN method to derive the local background areas of coal-fired power plants and coal-fired power plants clusters, and the calculation details can be found in [33].

### *2.2.3 Compliance status*

One coal-fired power plant can go through various compliance statuses over time after it was equipped with FGDs and SCRs. In this study, we divided compliance statuses into three statuses: improving status indicating a good compliance behavior, worsening status indicating a non-compliance behavior and maintenance status indicating a status with no significant difference from the previous one. The improving status is determined by a significant decreasing trend (negative slope and $p <= 0.1$) over the period, the worsening status is determined by a significant increasing trend (positive slope and $p <= 0.1$) over the period, and the maintenance status is determined by a not significant trend ($p > 0.1$) over the period.

### *2.2.4 Selective implementation*

Sometimes, polluters may define their emission control tasks based on their own cost-benefit analysis and perform differently between environmental policies that must be executed and those they can ignore, which is called “selective implementation”. Based on the emission levels of $SO_2$ and $NO_2$, we can further derive a signal of selective implementation by finding the periods of good control of one pollutant while maintaining bad control with the other one, as shown in table 1.

**Table 4.** Selective implementation determination

| | $SO_2$ good control | $SO_2$ bad control |
|---|---|---|
| $NO_2$ good control | Good environmental control | Selective implementation (NO2) |
| $NO_2$ bad control | Selective implementation (SO2) | Bad environmental control |

## 3. RESULTS

### *3.1 Dynamic compliance of large coal-fired power plants (>=600MW)*

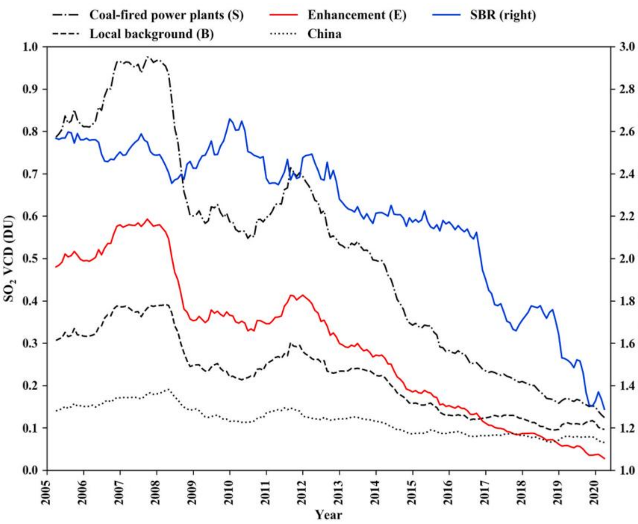


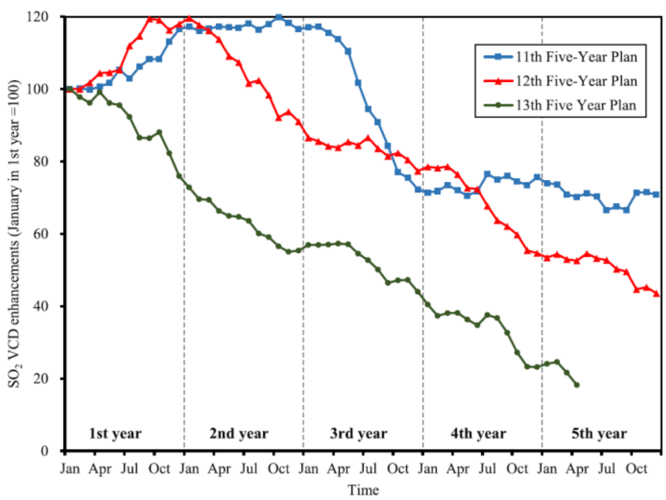


**Fig. 1** **Fig. 2**

**Fig. 1.** Pixel average $SO_2$ VCD over coal-fired power plants, local background and enhancement, as well as for entire China, and the curve for SBR.

**Fig. 2.** $SO_2$ VCD enhancements over three Five-Year Plans (taking $SO_2$ VCD enhancements of January in 1st year as 100)

Signal-to-background ratio (SBR) of coal-fired power plants is calculated as the ratio between S and its corresponding B, indicating the impacts of $SO_2$ emissions from a coal-fired power plant on its VCD, which is expected to be greater than 1. SBR fluctuated between 2.3 and 2.7 before 2013, and showed a continuous downward trend after 2013.

$SO_2$ VCD enhancements of coal-fired power plants decreased by 94.33 % or 0.466 DU from 0.494 DU on 1st January 2006 to 0.028 DU on 1st April 2020. However, most of the reduction took place in only two short periods, being 0.221 DU in 2008 and 0.149 DU in 2013-2015, corresponding to two crucial environmental policies. One policy was the "management on desulfurization electricity price of coal-fired generating units and the operation for desulfurization facilities (Trial)" entered into force on 1st July 2007[34]. The other policy was the "upgrading and retrofitting action plan for energy conservation and pollution mitigation in the coal-fired power sector" (here after "ultra-low emission" policy), carried out in September 2014. However, some regions might have started renovating its coal-fired power plants earlier than the "ultra-low emission" policy. That's because the state council carried out the policy "Action Plans on Air Pollution Prevention and Control" on 10th September 2013 to control $PM_{10}$ and $PM_{2.5}$, in which renovating coal-fired power plants and controlling $SO_2$ emissions of coal-fired power plants were also important tasks[35]. Thus, regions like Beijing-Tianjin-Hebei area, Yangtze River Delta and Pearl River Delta, which were main monitoring regions of $PM_{10}$ and $PM_{2.5}$, may have started the task since September 2013[35].

### *3.2 Compliance circle over Five-Year Plans*

Five-Year Plans demonstrated profound impacts on $SO_2$ mitigation. On the one hand, their stringent goals of $SO_2$ mitigation and environmental clean-up guide active policy making and implementation[25]. On the other hand, not every year is equally important. Goals in China's Five-Year Plans generally compare the final year in the current Five-Year Plan with the final year in the previous one. The incentives for goal attainment are also mainly applied for the final year. As a result, a compliance cycle may demonstrate more noncompliance in the first year to reflect more relaxed enforcement efforts (Fig.2). As the first years of the 11th and 12th Five-Year Plans respectively, 2006 and 2011 registered 17.3% and 19.6% increases of $SO_2$ VCD enhancements to confirm the existence of such compliance cycles. However, although 2016 was the first year of the 13th Five-Year Plan, it showed a steady reduction of $SO_2$ VCD enhancements. This may indicate that the 13th Five-Year Plan has better alleviated such compliance cycle, but 2021 as the first year of the 14th Five-Year Plan should be carefully watched to confirm that compliance has been successfully established as a routine outcome.

### *3.3 Selective implementation*

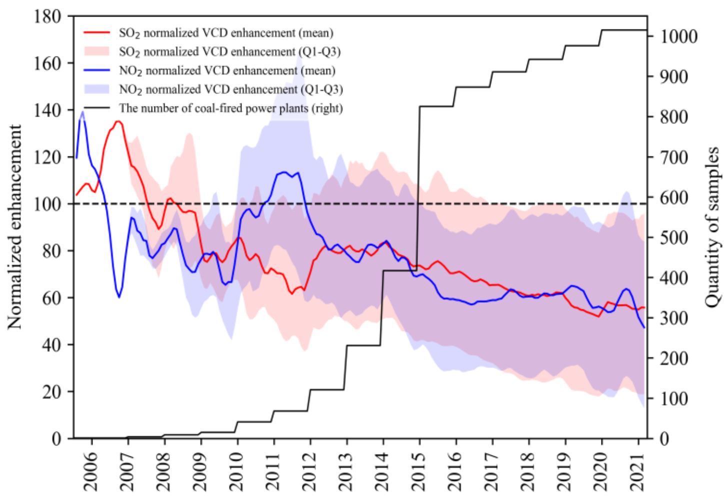


**Fig. 3.** Pixel average $SO_2$ VCD over coal-fired power plants, local background and enhancement, as well as for entire China, and the curve for SBR.

By normalizing the $NO_2$ and $SO_2$ by setting 100 as the emission level before installing SCRs and FGDs, it is found that from 2010 to the middle of 2012, the signal of $NO_2$ suddenly went upwards and exceeded 100 for many coal-fired power plants while $SO_2$ signal for most coal-fired power plants was less than 100. This two and a half year can be regarded as a typical period of selective implementation of $SO_2$, after which both signals were maintained to basically lower than 100 for several years, although a small gap between $SO_2$ and $NO_2$ control can still be observed in 2015 to the middle of 2017. By comparison, the proportion of coal-fired power plants with selective implementation decreased from around 68% in 2010-June 2012 to around 35% in 2018-2020, which indicates a reduction of selective implementation.

## 4. SUMMARY

The attainment of good environmental control of air pollutants is not s straightforward process, not only for multiple species together but also for single species each. Polluters may have the incentives to choose a "right time" to execute environmental policies and choose to only execute the policies under strict supervision while choosing to "safely ignore" the others to maximum their outcome, both economically and environmentally. Good environmental control cannot be maintained without strict and continuous supervision. Satellite data could potentially be a useful and cheap way to assist current compliance monitoring systems by screening possible non-compliance behaviors.

## References


[1] World Health Organization (2021), WHO global air quality guidelines. Particulate matter (PM2.5 and PM10), ozone, nitrogen dioxide, sulfur dioxide and carbon monoxide.: Geneva.

[2] Schraufnagel, D.E., et al. (2019), Air Pollution and Noncommunicable Diseases: A Review by the Forum of International Respiratory Societies' Environmental Committee, Part 1: The Damaging Effects of Air Pollution. Chest. **155**(2): 409-416.

[3] Xu, Y., C.J. Yang, and X.W. Xuan (2013), Engineering and optimization approaches to enhance the thermal efficiency of coal electricity generation in China. Energy Policy. **60**: 356-363.

[4] Liu, Z., et al. (2015), Reduced carbon emission estimates from fossil fuel combustion and cement production in China. Nature. **524**(7565): 335-+.

[5] Guan, D.B., et al. (2012), The gigatonne gap in China's carbon dioxide inventories. Nature Climate Change. **2**(9): 672-675.

[6] MEP (2014), The lists of $SO_2$ scrubbers and SCR/SNCR facilities.

[7] Xu, Y. (2011), Improvements in the Operation of SO2 Scrubbers in China's Coal Power Plants. Environmental Science & Technology. **45**(2): 380-385.

[8] Lu, Z., Q. Zhang, and D.G. Streets (2011), Sulfur dioxide and primary carbonaceous aerosol emissions in China and India, 1996-2010. Atmospheric Chemistry and Physics. **11**(18): 9839-9864.

[9] Zhang, Q., et al. (2007), $NO_x$ emission trends for China, 1995-2004: The view from the ground and the view from space. Journal of Geophysical Research-Atmospheres. **112**(D22): -.

[10] Tsinghua University (2010), A study on the management system of environmental pollution data collection in China: Beijing, China.

[11] MEP (2013), The 12th Five-Year Plan on Capacity Building of Environmental Regulations.

[12] Glaeser, E.L. (1999), An overview of crime and punishment, Harvard University and NBER.

[13] Becker, G.S. (1968), Crime and Punishment - Economic Approach. Journal of Political Economy. **76**(2): 169-217.

[14] Grogger, J. (1991), Certainty Vs Severity of Punishment. Economic Inquiry. **29**(2): 297-309.

[15] Friesen, L. (2009), Certainty of Punishment versus Severity of Punishment: An Experimental Investigation, in Working paper.

[16] Earnhart, D. and L. Friesen (2012), Environmental Management Responses to Punishment: Specific Deterrence and Certainty versus Severity of Punishment, in Working paper.

[17] Levitt, S.D. (2004), Understanding why crime fell in the 1990s: Four factors that explain the decline and six that do not. Journal of Economic Perspectives. **18**(1): 163-190.

[18] Stranlund, J.K. and C.A. Chavez (2000), Effective enforcement of a transferable emissions permit system with a self-reporting requirement. Journal of Regulatory Economics. **18**(2): 113-131.

[19] Pan, L., Z. Wang, and Z. Wang (2005), Present Status and Countermeasure Suggestion for Thermal Power Plants CEMS in China. Research of Environmental Sciences. **18**(4): 42-45.

[20] Yan, X. and Y. Xu (2021), SO2 mitigation in China's coal-fired power plants: A satellite-based assessment on compliance and enforcement. Atmospheric Environment. **254**: 118396.

[21] Wall, M. (July 2, 2014). NASA Launches Satellite to Monitor Carbon Dioxide. Available: http://www.space.com/26403-nasa-oco2-carbon-dioxide-satellite-launch.html

[22] Streets, D.G., et al. (2013), Emissions estimation from satellite retrievals: A review of current capability. Atmospheric Environment. **77**: 1011-1042.

[23] Zhang, Q., et al. (2009), Asian emissions in 2006 for the NASA INTEX-B mission. Atmospheric Chemistry and Physics. **9**(14): 5131-5153.

[24] Li, C., et al. (2010), Recent large reduction in sulfur dioxide emissions from Chinese power plants observed by the Ozone Monitoring Instrument. Geophysical Research Letters. **37**.

[25] Xu, Y. (2020), Environmental Policy and Air Pollution in China: Governance and Strategy, Taylor & Francis. p. 212.

[26] Levelt, P.F., et al. (2006), The ozone monitoring instrument. IEEE Transactions on Geoscience and Remote Sensing. **44**(5): 1093-1101.

[27] Li, C., et al. (2020), Version 2 Ozone Monitoring Instrument SO2 Product (OMSO2 V2): New Anthropogenic SO2 Vertical Column Density Dataset. Atmospheric Measurement Techniques Discussions. **13**(11): 6175–6191.
[28] Nickolay A. Krotkov, L.N.L., Sergey V. Marchenko, Eric J.Bucsela, William H. Swartz, Joanna Joiner and the OMI core team (2019), OMI/Aura Nitrogen Dioxide (NO2) Total and Tropospheric Column 1-orbit L2 Swath 13x24 km V003, O.A.N.D.N.T.a.T.C.-o.L.S.x.k. V003, Editor: Greenbelt, MD, USA, Goddard Earth Sciences Data and Information Services Center (GES DISC).
[29] Fioletov, V.E., et al. (2016), A global catalogue of large SO2 sources and emissions derived from the Ozone Monitoring Instrument. Atmospheric Chemistry and Physics Discussions. **16**(18): 11497–11519.
[30] Fioletov, V., et al. (2011), Estimation of SO2 emissions using OMI retrievals. Geophysical Research Letters. **38**(21).
[31] Ministry of Environmental Protection (2014), Announcement on National Desulphurization and Denitrification Facilities of Coal-fired Generation Units and other Key Air Pollution Mitigation Projects.
[32] Global Energy Monitor (2021). Global Coal Plant Tracker. Available: https://globalenergymonitor.org/projects/global-coal-plant-tracker/ (14-April-2021).
[33] Yan, X. and Y. Xu (2021), SO2 mitigation in China's coal-fired power plants: A satellite-based assessment on compliance and enforcement. Atmospheric environment (1994). **254**: 118396.
[34] National Development and Reform Commission and State Environmental Protection Administration (2007), Management on desulfurization electricity price of coal-fired generating units and the operation for desulfurization facilities (Trial).
[35] State Council (2013), Action Plans on Air Pollution Prevention and Control.

# SDG 11 (Sustainable Cities and Communities): Green and Resilience City

# A New Perspective to Map the Supply and Demand of Artificial Night Light Based on Loujia1-01 and Urban Big Data

Yang Ye[1,2], Haijun Bao [1,2], Yun Shao[1,3]

[1] Institute of Spatial Information for City Brain, Zhejiang University City College, Hangzhou 310015, China
email: yeyang@zucc.edu.cn

[2] School of Spatial Planning and Design, Zhejiang University City College, Hangzhou 310015, China
email: baohaijun@zucc.edu.cn

[3] Laboratory of Radar Remote Sensing Application Technology, Institute of Remote Sensing and Digital Earth (RADI), Chinese Academy of Sciences, Datun Road, Chaoyang District, Beijing 100101, China
email: isicagz@zucc.edu.cn

## 1. INTRODUCTION

In the last decade, artificial night light (ANL) has rapidly increased both in intensity and density, accompanied by the rapid development of urbanization [1], [2]. The multiple sources of ANL include street lighting, lighting from buildings and advertising, vehicles, etc. [3], [4]. ANL has some clear benefits for humans, including illumination, recreation in festivals, extension of human activities into the night, and promotion of production activities [5], [6]. However, several concerns have been raised about its negative influence, especially for ANL in open areas. Selecting the U.S. as an example, approximately 120 terawatt-hours of energy is consumed by outdoor lighting in an average year, mostly to illuminate streets and parking lots, and at least 30% of outdoor lighting is wasted, which releases 21 million tons of carbon dioxide per year [7]. Hence, there is an urgent need to study how to satisfy human activity demands and establish effective lighting regulations simultaneously to alleviate the disruptive effects of ANL [8], as well as to achieve the sustainable urban goal.

Most studies have confirmed that the satellites-recorded ANL has a great potential in modelling demographic and socioeconomic variables. However, few studies have evaluated the ANL status from the human perspective, and most employed ANL data in previous studies are too coarse to meet the requirements of light regulation in urban areas. Specifically, the Defense Meteorological Satellite Program/-Operational Linescan System (DMSP/OLS) and Visible Infrared Imaging Radiation Suite (VIIRS) have provided the longest publicly available time series of ANL data [9]–[11]. But the coarse spatial resolution of DMSP/OLS (2.7 km) and VIIRS (740 m) data limits their capacity to accurately depict the spatial pattern of the ANL supply within the urban environment [12], [13]. However, the recently launched Luojia1-01 satellite provides a new generation of ANL imagery with a higher spatial resolution (130 m) [14]–[16], which allows detailed analysis of various illumination mechanisms among different functional zones at the block scale [16], [17].

This paper aims to map the supply and demand of ANL from the human perspective, and thus provides a new tool for planners and researchers to deeply understand the relationship between the ANL and PD for further making optimal decisions in urban management. To achieve this objective, this study has to (1) assess the overall spatial pattern between the ANL and PD; (2) delineate mismatch and match regions at the block scale; (3) validate the mapping results by field investigation; and (4) analyze the underlying mechanism of the delineation results to formulate light regulation recommendations.

## 2. MATERIALS AND METHODS

### *2.1 Study area and data*

Hangzhou, the capital city of Zhejiang Province, was selected to implement the proposed method. To achieve the mapping of supply and demand status, four kinds of data were used in this study: (1) ANL imagery. Loujia1-01 is a new generation of nighttime light remote sensing satellites, with a higher spatial resolution of 130 m and radiometric quantization of 14 bits, which makes it possible to show more detailed information inside the city; (2) Population density. PD data were obtained from Tencent's big data platform named *Easygo* through crawling techniques, with a spatial resolution of nearly 25 m. (3) Road network. This data were employed to generate the blocks that were the basic analysis elements in the study. (4) Land use type (LUT). The land use survey map contains eight major LUTs, i.e., non-development, public services, commercial, residential, industrial, transportation, green space, and municipal utilities areas

### *2.2 The flowchart of the methodology*

The step-by-step procedures in Fig. 1 were implemented to study the supply and demand status of ANL from the human perspective. First, raw ANL and PD datasets were generated as layer stacking raster data after calibration and resampling, respectively. Second, the block was adopted to integrate all the geo-information. Blocks generation was achieved by the morphologic operations of dilation and thinning of the road networks. Third, the study applied bivariate clustering to assess the overall spatial aggregation between the ANL and PD, and divided all blocks into four clusters. Then, the specific delineation of mismatch regions was achieved by the template matching technique based on the clustering results. In this way, a map of the supply and demand was obtained, which was further validated by field investigation.

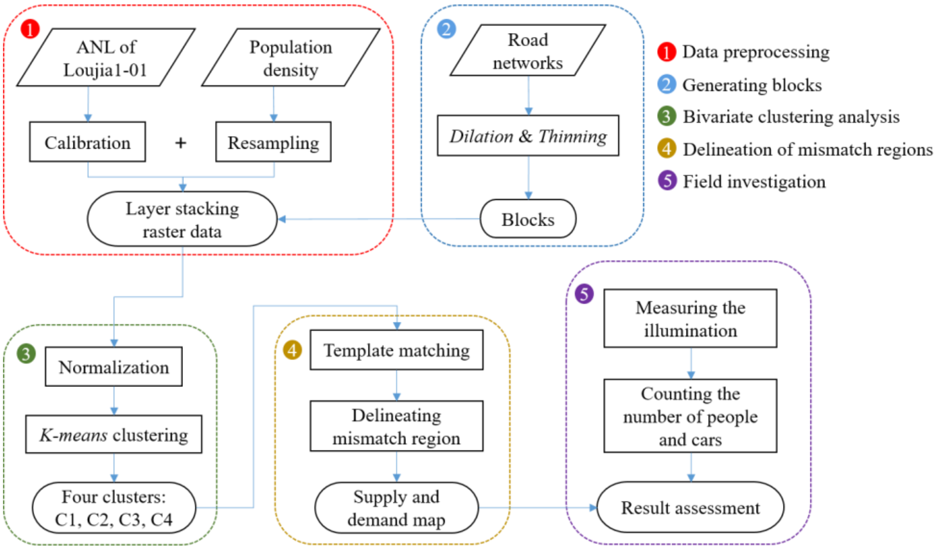


Fig. 1. The flowchart of the methodology

### *2.3 Delineation of the mismatch regions*

The spatial intensities of ANL and PD could differ among certain blocks. Hence, a classical template matching technique, i.e., normalized cross-correlation (NCC), was introduced to match the corresponding templates of ANL and PD based on their similarity based on the following equation [18]:

$$R(x,y)=\frac{\sum_{i=0}^{m-1}\sum_{j=0}^{m-1}\left[A(x+i,y+j)-\overline{A_{x,y}}\right]\left[P(x+i,y+j)-\overline{P_{x,y}}\right]}{\sqrt{\sum_{i=0}^{m-1}\sum_{j=0}^{m-1}\left[A(x+i,y+j)-\overline{A_{x,y}}\right]^2\left[P(x+i,y+j)-\overline{P_{x,y}}\right]^2}}$$
$$\overline{A_{x,y}}=\frac{1}{mm}\sum_{i=0}^{m-1}\sum_{j=0}^{m-1}[A(x+i,y+j)]$$
$$\overline{P_{x,y}}=\frac{1}{mm}\sum_{i=0}^{m-1}\sum_{j=0}^{m-1}[P(x+i,y+j)] \quad (1)$$

where $m$ is the window size of the template (Fig. 5); $\overline{A_{x,y}}$ is the template average of ANL; $\overline{P_{x,y}}$ is the template average of PD; and $R(x, y)$ ($R\in[-1,1]$) records the NCC value at the central pixel $(x, y)$ of the template.

The mismatch regions were delineated based on the results of template matching and spatial clustering. Specifically, two types of mismatch regions, i.e., regions with high supply but low demand

(HSLD) ANL status and the low supply but high demand of (LSHD) ANL status, and two types of match regions, i.e., regions with the high supply and high demand (HSHD) ANL status and the low supply and low demand (LSLD) ANL status, were defined in this study.

### *2.4 Field investigation*

Shown as Fig. 2, twenty typical blocks were selected to validate the results of the delineated mismatch regions (HSLD or LSHD). The lighting intensity was measured with a digital illuminance meter (DIM), as shown in Fig. 2b. In each selected block, at least three points were chosen to measure the illumination, including the highest intensity, median intensity, and lowest intensity. The average was utilized as a representative value of the corresponding block. Additionally, the number of people and cars within ten minutes was counted as an index to indicate the human activities within a certain block. Finally, all the data recorded in the field were compared to the ANL and PD data to assess the linear correlations.

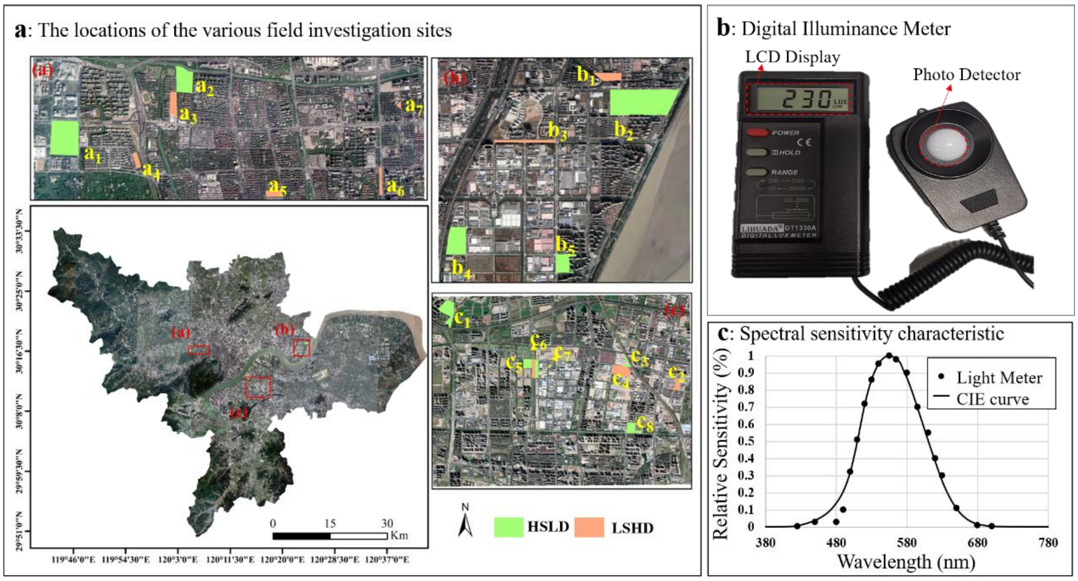


Fig. 2. (a) The locations of the various field investigation sites. (b) The DIM applied in the study; (c) spectral sensitivity characteristic of the DIM, available in the instrument specification.

## 3. RESULTS

### *3.1 Delineation results of the mismatch regions*

The final delineations of the mismatch and match regions are shown in Fig. 3a. The total area of the mismatch regions (HSLD and LSHD) was more than 100,000 hectares, among which the HSLD status was the leading component with more than 65,000 hectares. The percentages of the four statuses among the eight LUTs were analyzed by stacked bar diagrams, as shown in Fig. 3b. Considered together, several points are generated: (1) the HSLD status was mainly distributed in the city center, whereas non-development and industrial land areas occupied a considerable absolute area in the HSLD regions; (2) the proportion of the HSLD was notable in the public services (44%), commercial (40%), industrial (39%), transportation (56%), and green space areas (53%), which calls for increased attention because the ANL there could far exceed the demand; (3) the LSLD regions covered the largest absolute area due to the very large cardinality of non-development land; and (4) over time, the total HSLD area was greatly increased (946 hectares), which indicated that the negative effects of ANL would be more notable.

### *3.2 Field investigation*

The linear relationship between the measured light intensity and satellite-recorded ANL is compared, of which the $R^2$ coefficient value is 0.75, suggesting that the goodness of linear fit is relatively high. For the linear relationship between the PD and the measured number of people and cars, the R2 value is 0.62, which still indicates a high positive correlation.

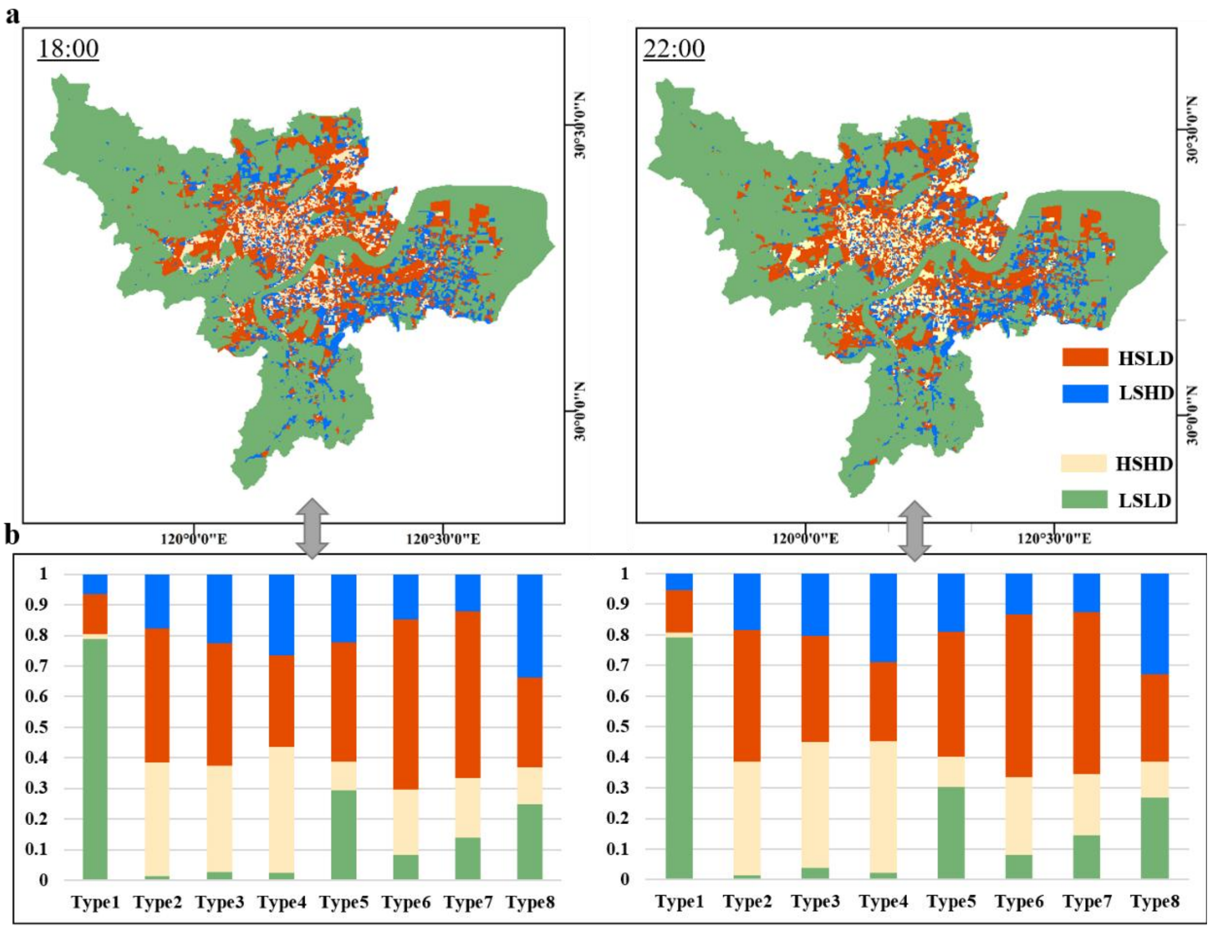


Fig. 3. (a) Delineation of the four supply and demand statuses at 18:00 and 22:00. (b) The stacked bar diagrams indicate the percentages of the four different statuses (HSLD, LSHD, HSHD and LSLD) in eight LUTs (Type1: non-development; Type 2: public services; Type 3: commercial; Type 4: residential; Type 5: industrial; Type 6: transportation; Type 7: green space; Type 8: municipal utilities.).

## 4. SUMMARY

This study proposed a novel perspective to map the supply and demand of ANL in open areas via the latest released ANL imagery of Loujia1-01 and fine-scale PD data, which bridged the research gap in this area and provided a new tool for light regulation. All the methods employed have clear logic and mathematical foundations to guarantee rational and credible research. Moreover, the nighttime imagery of Loujia1-01 has been confirmed to be more advanced than its predecessors in terms of a fine resolution and high radiometric quantization, and all these improvements enable the estimation of the supply and demand of the ANL at the block scale. In contrast with the PD from traditional censuses, social media derived PD data can represent dynamic human activities on a fine scale and thus play an increasingly important role in urban management. This research chose Hangzhou as a typical area to demonstrate the mapping method, but it can also be implemented in other cities since the applied data are available in most cities in China.

## References

[1] C. C. M. Kyba et al., "Artificially lit surface of Earth at night increasing in radiance and extent," Sci. Adv., vol. 3, no. 11, p. e1701528, 2017, doi: 10.1126/sciadv.1701528.

[2] S. Chang, J. Wang, F. Zhang, L. Niu, and Y. Wang, "A study of the impacts of urban expansion on vegetation primary productivity levels in the Jing-Jin-Ji region, based on nighttime light data," J. Clean. Prod., vol. 263, p. 121490, 2020, doi: 10.1016/j.jclepro.2020.121490.

[3] K. J. Gaston, J. P. Duffy, and J. Bennie, "Quantifying the erosion of natural darkness in the global protected area system," Conserv. Biol., vol. 29, no. 4, pp. 1132–1141, 2015, doi: 10.1111/cobi.12462.

[4] Y. Katz and N. Levin, “Quantifying urban light pollution - A comparison between field measurements and EROS-B imagery,” Remote Sens. Environ., vol. 177, pp. 65–77, 2016, doi: 10.1016/j.rse.2016.02.017.
[5] P. R. Boyce, “The benefits of light at night,” Build. Environ., vol. 151, no. January, pp. 356–367, 2019, doi: 10.1016/j.buildenv.2019.01.020.
[6] K. J. Gaston, S. Gaston, J. Bennie, and J. Hopkins, “Benefits and costs of artificial nighttime lighting of the environment,” Environ. Rev., vol. 10, no. May, pp. 1–10, 2014, doi: 10.1139/er-2014-0041.
[7] International Dark-Sky Association, “https://www.darksky.org/,” 2020. .
[8] K. J. Gaston, “Sustainability: A green light for efficiency,” Nature, vol. 497, no. 7451, pp. 560–561, 2013, doi: 10.1038/497560a.
[9] D. Fehrer and M. Krarti, “Spatial distribution of building energy use in the United States through satellite imagery of the earth at night,” Build. Environ., vol. 142, no. December 2017, pp. 252–264, 2018, doi: 10.1016/j.buildenv.2018.06.033.
[10] Q. Zhang, B. Pandey, and K. C. Seto, “A Robust Method to Generate a Consistent Time Series From DMSP / OLS Nighttime Light Data,” IEEE Trans. Geosci. Remote Sens., vol. 54, no. 10, pp. 5821–5831, 2016, doi: 10.1109/TGRS.2016.2572724.
[11] B. Yu et al., “Urban built-up area extraction from log-transformed NPP-VIIRS nighttime light composite data,” IEEE Geosci. Remote Sens. Lett., vol. 15, no. 8, pp. 1279–1283, 2018, doi: 10.1109/LGRS.2018.2830797.
[12] Q. Zheng et al., “A new source of multi-spectral high spatial resolution night-time light imagery—JL1-3B,” Remote Sens. Environ., vol. 215, no. October 2017, pp. 300–312, 2018, doi: 10.1016/j.rse.2018.06.016.
[13] N. Levin, K. Johansen, J. M. Hacker, and S. Phinn, “A new source for high spatial resolution night time images - The EROS-B commercial satellite,” Remote Sens. Environ., vol. 149, pp. 1–12, 2014, doi: 10.1016/j.rse.2014.03.019.
[14] X. Li, L. Zhao, D. Li, and H. Xu, “Mapping Urban Extent Using Luojia 1-01 Nighttime Light Imagery,” Sensors (Basel)., vol. 18, no. 11, pp. 1–18, 2018, doi: 10.3390/s18113665.
[15] G. Zhang, L. Li, Y. Jiang, X. Shen, and D. Li, “On-orbit relative radiometric calibration of the night-time sensor of the luojia1-01 satellite,” Sensors (Switzerland), vol. 18, no. 12, 2018, doi: 10.3390/s18124225.
[16] G. Zhang, X. Guo, D. Li, and B. Jiang, “Evaluating the potential of LJ1-01 nighttime light data for modeling socio-economic parameters,” Sensors (Switzerland), vol. 19, no. 6, pp. 1–13, 2019, doi: 10.3390/s19061465.
[17] W. Jiang et al., “Potentiality of using luojia 1-01 nighttime light imagery to investigate artificial light pollution,” Sensors (Switzerland), vol. 18, no. 9, 2018, doi: 10.3390/s18092900.
[18] William K.Pratt, Digital image processing, no. 13. Los Altos: A Wiley-Interscience Publication, 2001.

# HERI-GRAPHS: Constructing Semi-supervised Machine Learning Datasets of Heritage Values and Attributes for Sustainable Urban Heritage Management using Social Media Data

BAI Nan[1], NOURIAN Pirouz[2], LUO Renqian[3], PEREIRA RODERS Ana[1]

[1] UNESCO Chair in Heritage and Values: Heritage and the Reshaping of Urban Conservation for Sustainability, Delft University of Technology, Delft, the Netherlands
n.bai@tudelft.nl; a.r.pereira-roders@tudelft.nl

[2] Genesis Lab of Generative Systems and Sciences, Delft University of Technology, Delft, the Netherlands
p.nourian@tudelft.nl

[3] Machine Learning Group, Microsoft Research Asia, Beijing, China
renqianluo@microsoft.com

## 1.INTRODUCTION

Values (why to conserve) and Attributes (what to conserve) are essential concepts of cultural heritage to detail its cultural significance, especially in the context of UNESCO World Heritage Convention[1-3]. However, the heritage values and attributes are not only to define the significance of Outstanding Universal Value (OUV) in the particular context of World Heritage List (WHL), but all kinds of significance, ranging from listed to unlisted, natural to cultural, tangible to intangible, and from global to national, regional and local[4-7]. Moreover, the 2011 UNESCO Recommendation on the Historic Urban Landscape (HUL) stressed that heritage should also be recognized through the lens of civic society, calling for tools of civic engagement and knowledge documentation[8]. In the past decade, User-Generated Content (UGC) from social media platforms have been actively used to collect the public opinions and to map heritage values and attributes conveyed by various stakeholders[9-12]. However, it is rare to connect heterogeneous modalities of images, texts, geo-locations, timestamps, and social network structures to mine the semantic and structural characteristics therein[13-15]. This study presents a methodological workflow for constructing multi-modal datasets using posts and images on Flickr for graph-based semi-supervised machine learning (ML) tasks concerning heritage values and attributes. By combining the abundant information in various modalities with its socio-economic and spatiotemporal context[16-18], one can better reveal and understand the pattern of collective perception of the online community formed with concerned citizens[15]. The workflow could be further applied in global cases, which has both scientific relevance for ML research[19-21], and societal interests for Urban and Heritage Studies. Such understanding is strongly aligned with the Sustainable Development Goal (SDG) 11, with its ultimate objective of making the urban heritage management processes more inclusive[15].

## 2.MATERIALS AND METHODS

### *2.1 Selection of Case Studies*

Without loss of generality, this research selected three cities in Europe and China that are related to UNESCO WHL and HUL as case studies: Amsterdam (AMS), the Netherlands; Suzhou (SUZ), China; and Venice (VEN), Italy. All three cities either are themselves entirely or partially inscribed in the WHL, or contain WHL in multiple spots of the city, showcasing different spatial typologies of cultural heritage in relation to its urban context[22-23], all of which strongly demonstrate the relationship between urban fabric and water systems.

### *2.2 Data Collection and Processing Workflow*

*FlickrAPI* python library was used to access the Application Programming Interface (API) methods provided by Flickr, which has been a popular social media platform for constructing open-source datasets in the field of deep learning [24]. A maximum of 5000 geo-tagged images covering the major urban areas of the case study cities were queried, to make the datasets from the three cities comparable and compatible. To test the scalability of the workflow, another larger dataset not limiting the amount of images was also collected in Venice (VEN-XL). Only images marked as '*downloadable*' by the Flickr users were collected, respecting their privacy and copyrights. For each downloadable image, the following information was collected: owner's ID; provided title, description, and tags (textual fields); geo-tag of the image; timestamp marking when the image was taken; and the $150 \times 150$ px small-size image. The textual fields of posts are cleaned to only contain valid information, translated into English, and merged together. With pre-trained state-of-the-art deep learning models[25-26], the raw images and texts were embedded as vectors of float numbers, producing visual features $X^{\text{vis}}_{982\times K} \in [0,1]^{982\times K}$ , and textual features $X^{\text{tex}}_{771\times K} \in [0,1]^{771\times K}$, respectively, where $K$ denotes the sample size of a city. Furthermore, under the idea of transfer learning[27], the images and texts were also fed into thoroughly-trained classifiers on heritage attributes (in terms of the depicted urban scenes[10,28]) and heritage values (in terms of the OUV selection criteria [26]) to generate the pseudo-labels $Y^{HA}_{9\times K} \in [0,1]^{9\times K}$ and $Y^{HV}_{11\times K} \in [0,1]^{11\times K}$ for each post, where each row of the label matrices would add up to 1, being effectively a soft label as probability distribution for each post. The data processing workflow for an exemplary post could be seen in Fig.1. Moreover, the temporal, spatial, and social relationship among the posts are modelled as a multi-graph $\mathcal{G} = (\mathcal{V}, \{\mathcal{E}^{\text{TEM}}, \mathcal{E}^{\text{SPA}}, \mathcal{E}^{\text{SOC}}\})$ , where $\mathcal{V} = \{v_1, v_2, \ldots, v_K\}$ is the node set of all posts, and $\mathcal{E}^{\text{TEM}}, \mathcal{E}^{\text{SPA}}, \mathcal{E}^{\text{SOC}} \subset \mathcal{V} \times \mathcal{V}$ are the link sets of each relationship type among the posts. Therefore, the graph-based multi-modal semi-supervised learning problem based on the constructed datasets could be formulated as:

$$f: X^{\text{vis}}, X^{\text{tex}}, \mathcal{G} \mapsto Y^{HA}, Y^{HV} \qquad (1)$$

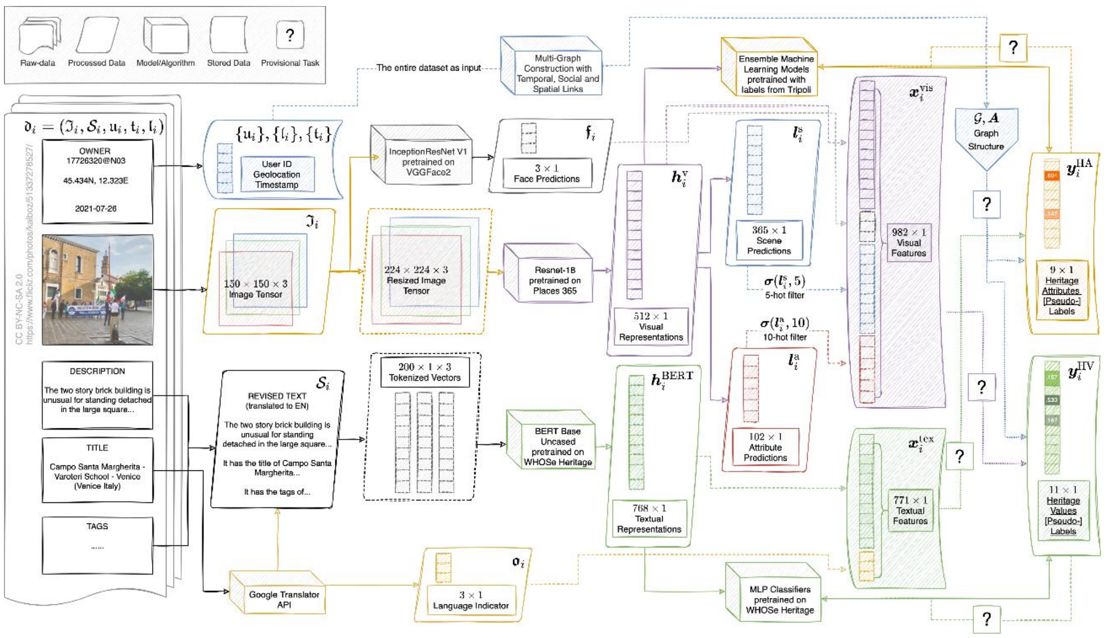


**Fig. 1.** The workflow of multi-modal feature generation process of one sample post in Venice, while graph construction requires all data points of the dataset. The question marks in the right part indicate some provisional tasks for this dataset.

## 3.RESULTS

### *3.1 Graph Structure of the Social Media Posts*

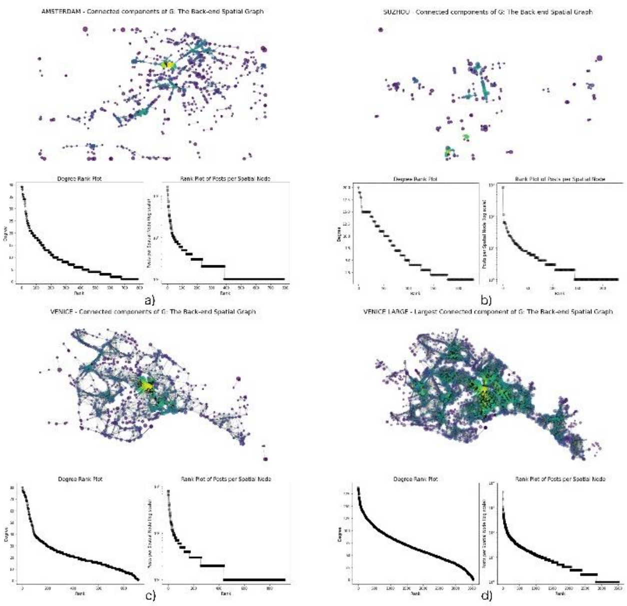

**Fig. 2.** The geographical networks for three case studies, respectively showing the graph structure, degree ranking distribution, and the ranking distribution of posts per geo-spatial node (on a logarithm scale) in Amsterdam, Suzhou, Venice, and Venice-XL. The sizes of nodes denote the number of nearby posts allocated to the nodes, and the colours of nodes illustrate the degree of the node on the graph. Each link connects two nodes reachable to each other within 20 minutes.

Fig.2 visualizes the spatial structure of the posts in all case studies. The urban fabric is more visible in Venice than the other two cities. This is possibly related to the distribution of tourism destinations, which is also consistent with the zoning typology of WHL property concerning urban morphology[22-23]. Furthermore, the two types of rank-size plots showing respectively the degree distribution and the posts-per-node distribution showed similar patterns, the latter being more heavy-tailed, a typical characteristic of large-scale complex networks. Furthermore, the multi-graph structure statistics listed in Table 1 demonstrate that the three case studies are compatible with each other, even though each of them may have heterogeneous characteristics.

**Table 5.** The statistics for the generated multi-graphs in the three case studies

| Graph Features | AMS | SUZ | VEN | VEN-XL |
|---|---|---|---|---|
| #Nodes | 3727 | 3137 | 2951 | 80,963 |
| #Nodes with valid *Textual Features* | 2904 | 754 | 1761 | 49,823 |
| #Nodes with *Heritage Values* and *Attributes* Labels | 639 | 118 | 361 | 11,569 |
| Label Rate | .171 | .038 | .122 | .143 |
| #Temporal Links | 692,839 | 293,328 | 249,120 | 35,527,354 |
| #Spatial Links | 135,079 | 415,049 | 221,414 | 101,046,098 |
| #Social Links | 877,584 | 602,821 | 242,576 | 38,527,354 |
| #All Links | 1,271,171 | 916,496 | 534,513 | 145,005,270 |
| Graph Density with all Links | .183 | .186 | .123 | .044 |

### *3.2 Semi-supervised Learning Dataset*

During the pseudo-label generation, only data samples with high prediction agreement and confidence are considered as ‘labelled’. Note the label rates of the datasets shown in Table 1 are also comparable with common datasets used in graph-based semi-supervised learning tasks[19-21]. Fig.3 demonstrates the distribution of ‘labelled’ data about heritage attributes in each city. It is remarkable that although the models were only pre-trained and never fine-tuned on the three case study cities, they performed reasonably well in previously unseen data samples in Amsterdam, Suzhou, and Venice, capturing typical scenes of monumental buildings, architectural elements, and gastronomy, etc. According to the bar plots, the distributions of Venice and Venice-large are similar to each other, suggesting a good representativeness of the sampled small dataset. Similar patterns could be observed with the case of heritage values predicted from the textual description of posts.

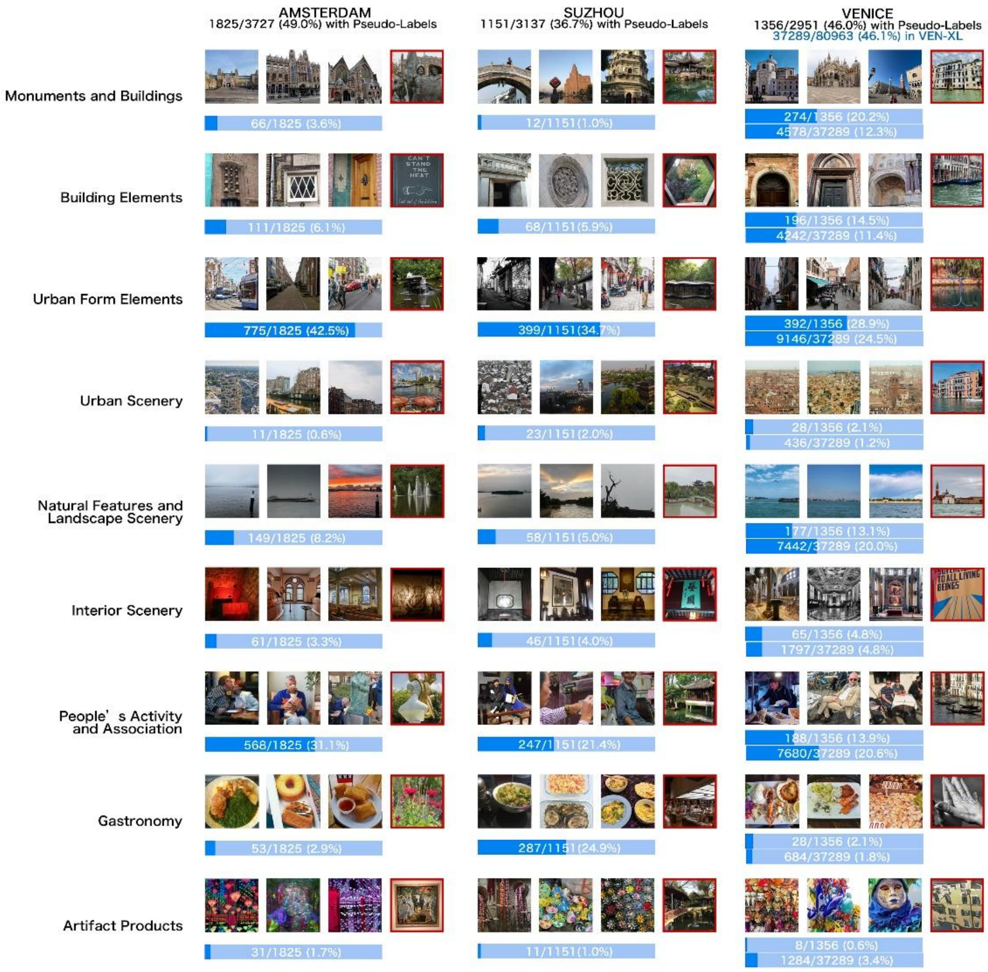


**Fig. 3.** Typical image examples in each city labelled as each heritage attribute category (depicted scene) and bar plots of their proportions in the datasets (length of bright blue background bars represent 50%).

## 4.SUMMARY

This study introduced a novel workflow to construct graph-based multi-modal datasets Heri-Graph concerning heritage values and attributes using data from social media platform Flickr. State-of-the-art machine learning models have been applied to generate multi-modal features and pseudo-labels. Three case study cities Amsterdam, Suzhou, and Venice containing UNESCO World Heritage properties are tested with the workflow. Such datasets have the potentials to be applied by both machine learning and urban data scientists to answer questions with scientific and social relevance in response to the Sustainable Development Goals, which could also be applied around the globe for inclusive heritage planning and management processes. The dataset collected in this study could be accessed at https://github.com/zzbn12345/Heri_Graphs.

## References

[1] UNESCO. (1972) Convention Concerning the Protection of the World Cultural and Natural Heritage, UNESCO World Heritage Centre, Technical Report, https://whc.unesco.org/en/conventiontext/
[2] UNESCO. (2021) Operational Guidelines for the Implementation of the World Heritage Convention, UNESCO World Heritage Centre, Technical Report, https://whc.unesco.org/document/190976
[3] Veldpaus L. (2015) Historic Urban Landscapes: Framing the Integration of Urban and Heritage Planning in Multilevel Governance, PhD thesis, Technische Universiteit Eindhoven, https://research.tue.nl/files/3914913/798291.pdf
[4] Rakic T., Chambers D. (2008) World Heritage: Exploring the Tension Between the National and the 'Universal', Journal of Heritage Tourism, 2 (3):145-155.
[5] Tarrafa Silva A., Pereira Roders A. (2010) The cultural significance of World Heritage cities: Portugal as case study, Heritage 2010: Heritage and Sustainable Development, Évora, Portugal. 255-263.

[6] Bonci A., Clini P., Martin R., Pirani M., Quattrini R., Raikov A. (2018) Collaborative Intelligence Cyber-Physical System for the Valorization and Re-Use of Cultural Heritage, Journal of Information Technology in Construction, 23 (1):305-323.
[7] Pereira Roders A. (2019) The Historic Urban Landscape Approach in Action: Eight Years Later, Reshaping Urban Conservation, Springer, 21-54.
[8] UNESCO. (2011) Recommendation on the Historic Urban Landscape, UNESCO World Heritage Centre, Technical Report, https://whc.unesco.org/uploads/activities/documents/activity-638-98.pdf
[9] Monteiro V., Henriques R., Painho M., Vaz E. (2014) Sensing World Heritage An Exploratory Study of Twitter as a Tool for Assessing Reputation. Computational Science and its Applications - ICCSA 2014, 404-419.
[10] Ginzarly M., Pereira Roders A., Teller J. (2019) Mapping Historic Urban Landscape Values through Social Media, Journal of Cultural Heritage, 36:1-11. https://doi.org/10.1016/j.culher.2018.10.002
[11] Gomez R., Gomez L., Gibert J., Karatzas D. (2019) Learning from #Barcelona Instagram Data What Locals and Tourists Post About Its Neighbourhoods, Computer Vision – ECCV 2018 Workshops, Munich, Germany. 530-544.
[12] Kang Y., Cho N., Yoon J., Park S., Kim J. (2021) Transfer Learning of a Deep Learning Model for Exploring Tourists' Urban Image Using Geotagged Photos, ISPRS International Journal of Geo-Information, 10 (3):137.
[13] Aggarwal CC. (2011) An Introduction to Social Network Data Analytics. Social Network Data Analytics, Chapter 1, 1-15.
[14] Baltrusaitis T., Ahuja C., Morency LP. (2019) Multimodal Machine Learning: A Survey and Taxonomy. IEEE Transactions on Pattern Analysis and Machine Intelligence, 41 (2):423-443.
[15] Bai N., Nourian P., Luo R., Pereira Roders A. (2021) Global Citizens and World Heritage: Social Inclusion of Online Communities in Heritage Planning. The International Archives of the Photogrammetry, Remote Sensing and Spatial Information Sciences, XLVI-M-1-2021:23-30.
[16] Batty M. (2013) The New Science of Cities, MIT Press, 496 pp.
[17] Cheng T., Wicks T. (2014) Event Detection using Twitter: A Spatiotemporal Approach. PloS One, 9 (6):e97807. https://doi.org/10.1371/journal.pone.0097807
[18] Zhang Y., Cheng T. (2020) Graph Deep Learning Model for Network-based Predictive Hotspot Mapping of Sparse Spatiotemporal Events. Computers, Environment and Urban Systems, 79:101403. https://doi.org/10.1016/j.compenvurbsys.2019.101403
[19] Zhou Z., Li M. (2010) Semi-supervised Learning by Disagreement. Knowledge and Information Systems, 24 (3):415–439.
[20] Kipf TN., Welling M. (2016) Semi-supervised Classification with Graph Convolutional Networks. arXiv preprint, https://doi.org/10.48550/arXiv.1609.02907
[21] Ma Y., Tang J. (2021) Deep Learning on Graphs, Cambridge University Press, 320 pp.
[22] Pereira Roders A. (2010) Revealing the World Heritage Cities and their Varied Natures. Heritage 2010: Heritage and Sustainable Development, Évora, Portugal. 245-253.
[23] Valese M., Noardo F., Pereira Roders A. (2020) World Heritage Mapping in a Standard-based Structured Geographical Information System. The International Archives of the Photogrammetry, Remote Sensing and Spatial Information Sciences, XLIII-B4-2020:81–88.
[24] Deng J., Dong W., Socher R., Li LJ., Li K., Li F. (2009) ImageNet: A large-scale Hierarchical Image Database. IEEE conference on computer vision and pattern recognition, Miami, United States of America. 248-255.
[25] Zhou B., Lapedriza A., Xiao J., Oliva A., Torralba A. (2017) A 10 million image database for scene recognition. IEEE transactions on pattern analysis and machine intelligence, 40 (6):1452-1464.
[26] Bai N., Luo R., Nourian P., Pereira Roders A. (2021) WHOSe Heritage: Classification of UNESCO World Heritage Statements of "Outstanding Universal Value" with Soft Labels. Findings of the Association for Computational Linguistics: EMNLP 2021, Punta Cana, Dominican Republic. 366-384.
[27] Pan SJ., Yang Q. (2009) A Survey on Transfer Learning. IEEE Transactions on knowledge and data engineering, 22 (10):1345-1359.
[28] Bai N., Nourian P., Luo R., Pereira Roders A. (2022) Heri-Graphs: A Workflow of Creating Datasets for Multi-modal Machine Learning on Graphs of Heritage Values and Attributes with Social Media. arXiv preprint, https://arxiv.org/abs/2205.07545

# Interference and SDG measurement of the World Cultural Heritage Sites

TANG Yunwei[1,2], CHEN Fulong [1,2,3]

[1] International Research Center of Big Data for Sustainable Development Goals, Beijing 100094, China

[2] Key Laboratory of Digital Earth Science, Aerospace Information Research Institute, Chinese Academy of Sciences, Beijing 100094, China

[3] International Centre on Space Technologies for Natural and Cultural Heritage under the Auspices of UNESCO, Beijing 100094, China

email: tangyw@aircas.ac.cn

email: chenfl@aircas.ac.cn

## 1. INTRODUCTION

World Cultural Heritage Sites (WCHS) are commonly acknowledged to be of great significance and outstanding universal value (OUV), the effective risk management and assessment of WCHS are therefore extremely important. In recent years, the uprising conflict between urban development and heritage conservation has drawn attention [1]. SDG 11.4 aims to strengthen efforts to protect and safeguard the world's cultural and natural heritage [2]. Only one indicator (SDG 11.4.1) based on the expenditure per capita is to support SDG 11.4, which is an oversimplification and not effective to achieve this goal [3]. Other complementary indicators should be developed to quantify the preservation status of WCHS [4]. Even so, the first data collection on SDG 11.4.1 in 2020 has shown that the availability of data is still limited [5]. SDG 11.4 has put forward the urgent demand of acquiring global data to support heritage conservation, the space observation provides an effective measure to achieve this target.

This study proposed an indicator named interference degree and an SDG measurement to quantify land cover changes in WCHS. This indicator reflects the degree of interference of human activity and natural factors at the protected area within a time period. A global dataset of interference degree was produced based on remotely sensed images at a sub-meter resolution from 2015 to 2020, thus providing elaborate monitoring data and a complementary indicator to achieve SDG 11.4.

## 2.MATERIALS AND METHODS

### *2.1 Datasets*

The core zone and the buffer zone consist of the main protected area of a heritage site. The boundary data of the core zone and buffer zone for 628 WCHS were manually delineated according to documents published by UNESCO [6]. A small part of the WCHS lacked boundary information. The area error of the boundary data is less than 15%.

The high-resolution Google Earth images were used as base maps for monitoring land cover changes at WCHS. The acquisition time was in 2015 and 2020, some bias exists due to the unavailability of data at the desired time. For our study, over 90% of the images are with a sub-meter resolution, and the average resolution is around 0.5 m. In total, 586 pairs of images at WCHS were processed.

The population and Gross Domestic Product (GDP) data in 2015 and 2020 provided by the Population Dynamics, Department of Economic and Social Affairs of the United Nations were also acquired.

### *2.2 Method*

Land cover changes at the WCHS were extracted from Google Earth images in 2015 and 2020 to derive the interference degree and SDG measurement. The flowchart is shown in Fig. 1, and the step-by-step illustration is as follows.

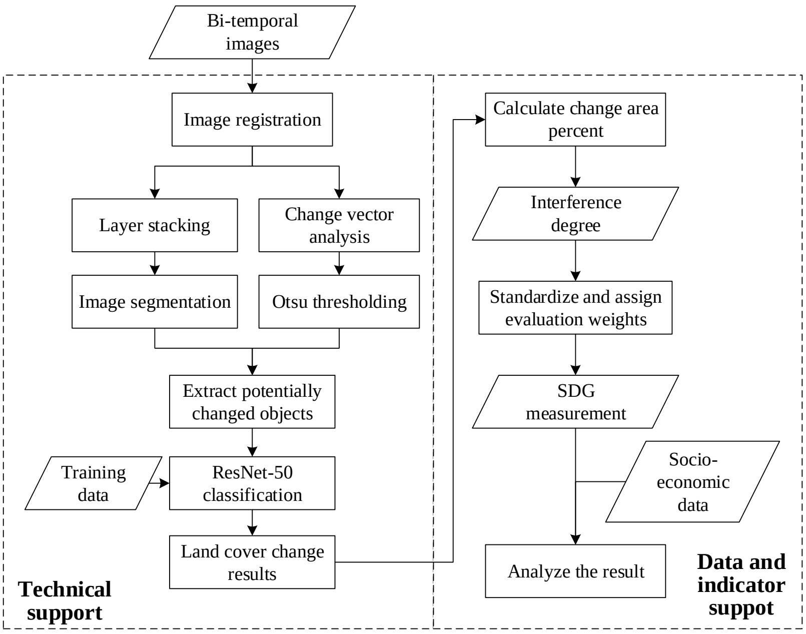


**Fig. 1.** Flowchart of the developed interference degree and SDG measurement for elaborate monitoring at WCHS.

1. The bi-temporal images were co-registered and stacked, and multi-resolution image segmentation was performed on the stacked images, dividing the images into homogenous objects. By applying change vector analysis, the difference image was derived. The Otsu segmentation algorithm was used to conform a threshold that divided changed/unchanged objects, thus extracting potentially changed objects.

2. A deep learning method was applied to classify the potentially changed objects into five land cover classes: water, barren land, built-up land, farmland, and vegetation. Built-up land and farmland are closely related to human activity, whereas water, barren land, and vegetation mainly contribute to the natural factors affecting sites. ResNet-50 [7] was used for the classification. The training data were derived from Google Earth and some public scene datasets, and the total number of training data exceeded 60,000 after augmentation. The final results were derived by comparing classes per object for the bi-temporal images, where the object with the different class labels was categorized as the changed object.

3. The interference degree was calculated by the percentage of the changed area at the core zone and buffer zone, respectively. We evaluated whether the changes are positive or negative for each WCHS at the buffer zone. Positive changes are beneficial to cultural sites such as utilization of new energy, improvements on the environments and construction of museum, and negative changes may cause damages to heritage sites such as urban development and forest degradation. The interference degree was standardized between 0 and 1, and an evaluation weight 1 (positive changes) or -1 (negative changes) was assigned to each WCHS to derive the SDG measurement. Therefore, the SDG measurement close to 1 means a suitability measurement for the cultural site, and otherwise the value is close to -1.

4. The SDG measurement in the cultural heritage countries and global regions was calculated by taking the mean value of each WCHS. Then the SDG measurement and per capita GDP were compared and analyzed, revealing the impacts of the economic level on the sustainable development of WCHS.

## 3.RESULTS

According to UNESCO and the heritage community [6], a core zone has strict protection status, where human intervention must be kept to a minimum. A buffer zone may set limits to protect views, settings, land uses, and other aspects but may also positively encourage developments that would be beneficial to the site and community [8]. Therefore, a high interference degree in the core zone usually implies a high risk to the heritage site. A high value in the buffer zone indicates the heritage site needs to be further evaluated to assess whether these changes have strengthened or weakened the relationship between humans and heritage. Fig. 2 presents the interference degree of the cultural heritage countries.

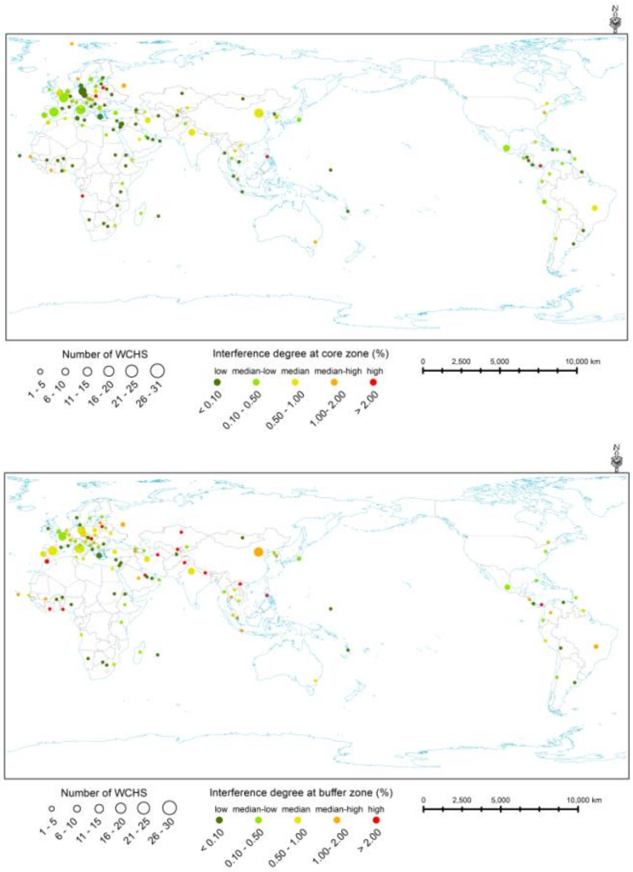


(a) (b)

**Fig. 2.** Interference degree of the cultural heritage countries at the core zone (a) and buffer zone (b).

Results can be revealed as follows. I) In European countries, the interference degree at the core zone remains at a low (<0.1%) to median-low level (0.1%~0.5%), where some countries shown an uneven distribution. The value at the buffer zone is at a median-low level (0.5%~1.0%), where a few countries have a high value (>2.0%). II) In most Asian countries, the interference degree at the core zone ranges from a low to median level, where China has a median value. Difference has shown at the buffer zone, where some countries have a high value caused by the natural disaster and human intervene. China has a median-high value (1.0%~2.0%), mainly contributed by the environmental improvement. III) Most American countries have a low to median interference level at the core zone with only two exceptions. North American countries are at a low interference level at the buffer zone, and Central and South American countries appear a few high values. IV) African countries are generally with a low interference level at the core zone, and with a median-low level at the buffer zone, only some West African countries show high values.

Fig. 3 shows the SDG measurement and GDP per capita growth from 2015 to 2020 in each country and region of the world. The SDG measurements for most WCHS are near 0, indicating that most countries follow the principle to keep human intervention to a minimum. However, the number of countries with negative changes is more than that with positive changes, suggesting a conflict between economic development and heritage protection exits. For those countries with a negative SDG measurement, most of which have a sluggish or even negative GDP growth, revealing the importance of capital investment to the sustainable development of WCHS. According to the SDG measurement in different regions, Central Asia is the only region that has a positive SDG measurement. In the developing countries represented by China, the interference at WCHS are most caused by positive changes such as emptying residential, building management facilities and museums to improve the condition of heritage sites. Most developed countries such as North America, Europe and Oceania do not show a significant interference, only Southeast Asia has a high negative SDG measurement. The interference in the less developed countries such as Central America and North Africa leads to negative SDG measurements, mainly caused by construction works of buildings and roads for the economic development, and thus are unsustainable for the heritage protection.

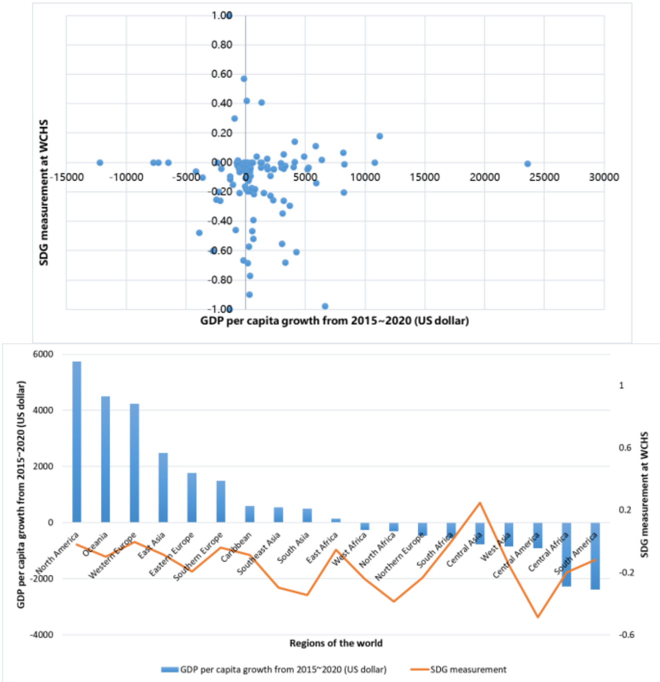


(a) (b)

**Fig. 3.** The relationship between SDG measurement and GDP per capita growth at each cultural heritage country (a) and regions of the world (b).

## 4.SUMMARY

This study proposed an interference degree and an SDG measurement to monitor the elaborate land cover changes at WCHS. This indicator can directly reflect the amount of changes and trends of the heritage environment, thus providing data for SDG 11.4 from the cultural heritage site level to the country level. A state-of-the-art deep learning method for processing big earth data was developed and demonstrated an effective technological solution to periodically monitor the WCHS in the future. This study provided the first-hand global scientific data and a complementary indicator for the sustainable development of the WCHS.

## References


[1] Ashrafi B., Kloos M., Neugebauer C. (2021) Heritage impact assessment, beyond an assessment tool: a comparative analysis of urban development impact on visual integrity in four UNESCO World Heritage Properties. Journal of Cultural Heritage, 47: 199-207.

[2] United Nations. (2015) Transforming our world: the 2030 Agenda for Sustainable Development. Division for Sustainable Development Goals: New York, NY, USA, https://sustainabledevelopment.un.org/post2015/transformingourworld.

[3] Nocca F. (2017) The role of cultural heritage in sustainable development: Multidimensional indicators as decision-making tool. Sustainability, 9: 1882.

[4] Tang Y., Chen F., Yang W., Ding Y., Wan H., Sun Z., Jing L. (2022) Elaborate monitoring of land-cover changes in cultural landscapes at heritage sites using very high-resolution remote-sensing images. Sustainability, 14: 1319.

[5] United Nations Statistics Division. (2021). SDG indicator metadata, https://unstats.un.org/sdgs/metadata/files/Metadata-11-04-01.pdf.

[6] World Heritage Centre. (2009) World Heritage and Buffer Zones. Proceedings of the International Expert Meeting on World Heritage and Buffer Zones, Davos, Switzerland, 11-14 March 2008; Martin, O., Piatti, G., Eds.; UNESCO—World Heritage Centre: Paris, France, 25 pp.

[7] He K., Zhang X., Ren S., Sun J. (2016) Deep residual learning for image recognition. Proceedings of the IEEE conference on computer vision and pattern recognition, 770-778.
[8] UNESCO. (2005) Operational Guidelines for the Implementation of the World Heritage Convention. Paris, France: UNESCO World Heritage Centre.

# Heritage zoning and urbanisation: An assessment of urban densification of world heritage using Land cover and land use change detection

KATONTOKA Moses[1], RODERS Ana [2], NOURIAN Pirouz[3], ESCH Thomas[4], FULONG Chen[5]

[1] Delft University of Technology, Netherlands
email: m.katontoka@tudelft.nl

[2,3] Delft University of Technology, Netherlands
email: A.R.Pereira-Roders@tudelft.nl
email: P.Nourian@tudelft.nl
[4] German Aerospace Centre, German
email: thomas.esch@dlr.de
[5]International Research Centre of Big Data for Sustainable Development Goals, China
email: chenfl@aircas.ac.cn

## 1. INTRODUCTION

Urbanization has triggered the rapid change of landscapes, altering land cover and land-use type for better or for worse. For example, Urban sprawl competes with areas that act as carbon sinks and spaces meant for agricultural purposes[1]. On the other hand, compact urbanization leads to the densification and consolidation of detached urban spaces turning them into concrete jungles[2]. The challenge of rapid urbanization leads to an uncontrolled expansion of cities, the shrinking of green spaces[1] and subsequently threatens World Heritage properties(WH)[3]. These transformations may convert WH core zones into completely different landscapes without any resemblance to the rich human heritage embedded in them that defines and tells tales of our past. The results of this transformation may be seen in the observable changes in the spatial orientation of land cover, land-use types, loss of habitats, densification of core zones and eventually loss of World Heritage authenticity[3]. The loss of heritage can be observed through the delisting of properties by United Nations Educational, Scientific and Cultural Organization (UNESCO) as in the case of Dresden Elbe Valley which was delisted because of a four-lane bridge that was constructed in the core zone, or the Arabian Oryx Sanctuary (Oman) which had lost 90% of the protected area under Omani Law[4]. Specifically, Udeaja et al.[5], notes that rapid urbanization and land-use change are threatening cultural heritage at an alarming rate. In addition to urbanization, Mariani & Guizzardi[6], notes that UNESCO's designation as World Heritage seems to create a complicated relationship between tourism and preservation which is characterized by dependence and conflict. While tourism has multiple positive impacts on heritage such as generating funds for the management of the WH site, the negative impacts that come with extra development threaten the very values by which the properties were inscribed into the WH list[7].

The idea that heritage zoning guarantees the conservation of areas of Outstanding Universal Value(OUV) and is expected to disable urbanization within and around core zones has been theorized in several studies[8–10]. Globally, UNESCO recognizes heritage properties of exceptional value to humanity and adds them to a list called the World Heritage list (WH list). Valese et al.[9] defined WH List as a tool to foster heritage conservation worldwide by operationalizing the 1972 Convention Concerning the Protection of the World Cultural and Natura Heritage. As demand from various stakeholders increases for land, accommodation, water and tourism, urban landscapes are increasingly changing to meet this demand. In the process, the role of Heritage zoning in conserving heritage characteristics is ignored[11]. In times of rapid urbanization and dynamic urban environments[12], How urban is heritage? is an important question to explore. Thus, this research investigated the impact of heritage zoning on urbanization. The investigation utilized a relatively larger sample than ever used before to quantify the amount of land cover and land use type change in WH properties. Additionally, we utilized global satellite imagery data for land-cover and land-use change detection.

## 2.MATERIALS AND METHODS

### *2.1 Case study*

Global cases of 158 cultural heritage sites were used as a sample. The properties are grouped into five (5) UNESCO regions as seen in Figure 1.

### *2.2 Materials*

The material that was considered included vectors layers, point location of WH(x,y), raster data and PDF maps of WH. Specifically, 158 Vector data of area extents of WH properties which also represented the case studies. The raster data included preprocessed satellite images with advanced digital technology from DLR. Additional, raster data of World Human Settlement (WHS) and Global Urban Footprints (GUF), were used to assess the urban footprint and where human beings live at a global scale relative to world heritage. The World Human Settlement layer was generated using an advanced classification system combining open, free optical and radar satellite imagery and is available at 10m resolution and at global scale.

### *2.3 Methodology*

The methodology compromised three steps i.e., Data assessment, Inclusion and exclusion criteria and the land use and land cover change detection (LULC). Firstly, seven (7) digital platforms associated with geospatial WH data were queried and the database from the International Research Center on Space technologies of Natural and Cultural Heritage was relatively more reliable for the assessment. Multiple thematic layers were overlaid to assess how each performed against the other in QGIS. Secondly, the State of Conservation Information system by UNESCO was used to include and exclude properties with urbanization as a threat. LULC detection was used to quantify landcover and land-use type change. QGIS was used to integrate GIS, Remote sensing and WH List data while exploiting advanced image processing technology from German Aerospace Center. The nomination year of the WH property were used as reference years.

## 3.RESULTS

### *3.1 Data assessment*

The results from online platforms showed that there was relatively enough effort towards the generation of WH data which gives a general view of the WH properties. Further, the data quality was context-based and was used based on the purpose of the digital platform. To quantify WH areas and the changes impacting them, one must be conscious of the limitations of the current geospatial data in many WH geospatial platforms.

### *3.2 Inclusion and exclusion criteria*

A total of 426 properties under threat were identified from SOC. This represented 37% of 1154 UNESCOs WH properties. Additionally, the results of the data assessment of the properties suggested that a total of 376 properties have been mapped while 52 out of 426 properties have not yet been mapped.

### *3.3 Harmonization of Data assessment and the inclusion and exclusion criteria*

The data harmonization between the inclusion and exclusion criteria and the available area extents of the WH properties process resulted in a smaller sample of One Hundred fifty-eight (158) properties being read for reuse at the time of this study. The properties were then divided into regions and cultural categories as seen in figure 1.


Fig. 1. The UNESCO regions and cultural sub-categories of case studies.

## 4.SUMMARY

As urban needs are being met, the threat to WH is incredibly concerning and the threat is expected to continue increasing. The challenge of geospatial data operability in heritage is still very prominent. There is a need for UNESCO and individual partners to find ways to improve the Operability and Reusability of Geospatial WH data. Collaboration between UNESCO and other institution such as HIST, DLR and academics are necessary to increase the availability of WH Digital Data. Additionally, a lack of a standardized map format that state parties can use mapping properties makes the data transformation more challenging.

Concerning the management of world heritage, transfer of management practices from one region to another is needed in order to reduce the threat of urbanization. State parties must be able to be transparent and document the threats of urbanization on WH for effective management. The high number of WH properties under threat in developed regions does suggests that, as developing regions with high urbanization rates begin to equal the developed regions, the number of WH properties under threat will also continue to increase. Lastly, more attention on individual regional management practices must be given as there could be under or over documentation of urban threats on WH properties by state parties.

## References


[1] Esch T., Asamer H., Bachofer F., Balhar J., Boettcher M., Boissier E, et al. (2020) Digital world meets urban planet–new prospects for evidence-based urban studies arising from joint exploitation of big earth data, information technology and shared knowledge, International Journal of Digital Earth, 13(1):136–57.

[2] Wilson J., Bayón M. (2015) Concrete Jungle: The Planetary Urbanization of the Ecuadorian Amazon, Human geography, 8(3):1–23.

[3] Guzmán A., Roders P. (2014) Bridging the gap between urban development and cultural heritage protection . International association for impact assessment 14 Conference Proceedings, Viña del Mar, Chile.

[4] Eike A., Bénédicte G. (2015) Procedure for delisting a site from the world heritage list: Is delisting with consent or against the wish of a state party possible?, Journal of tourism and hospitality management, 3(1):15–21.

[5] Udeaja C., Trillo C., Awuah K.G.B., Makore B.C.N., Patel D.A., Mansuri L.E, et al. (2020) Urban heritage conservation and rapid urbanization:Insights from Surat, India, Sustainability, 12(6):2172.

[6] Mariani M.M., Guizzardi A. (2020) Does designation as a UNESCO World Heritage site influence tourist evaluation of a local destination?, Journal of travel research, 59(1):22–36.

[7] Borges M.A., Carbone G., Bushell R., Jaeger T. (2011) Sustainable tourism and natural World Heritage: Priorities for action. Internationa union of conservation of nature, Gland, Switzerland.

[8] Jones T.E., Bui H.T., Ando K. (2020) Zoning for world heritage sites: dual dilemmas in development and demographics, Tourism geographies, 24(1):33–55.

[9] Valese M., Noardo F., Pereira Roders A. (2020) World heritage mapping in a standard-based structured geographical information system, international archives of the photogramme remote sensing spatial information science, 43(B4):81–8.

[10] Zamarbide U., Satoh S. (2017) A comparative analysis on the morphology of "World Heritage" zoning, Journal Architecture and Planning, 82(733):667–76.

[11] Kiruthiga K., Thirumaran K. (2019) Effects of urbanization on historical heritage buildings in Kumbakonam, Tamilnadu, India, Frontiers of architectural research, 8(1):94–105.

[12] Agapiou A. (2021) UNESCO World Heritage properties in changing and dynamic environments: Change detection

methods using optical and radar satellite data, Heritage science, 9(1):1–15.

# China Land Surface Deformation Dynamics Monitored with Satellite InSAR Technology

WANG Chao[1,2,3], TANG Yixian [1,2,3], ZHANG Hong [1,2,3], DONG Longkai[1,2,3], YOU Haihang[4,3], ZHANG Weikang[4], ZHANG Yan[5]

[1] International Research Center of Big Data for Sustainable Development Goals, Beijing 100094, China
email: wangchao@radi.ac.cn, tangyx@aircas.ac.cn, zhanghong@aircas.ac.cn

[2] Key Laboratory of Digital Earth Science, Aerospace Information Research Institute, Chinese Academy of Sciences, Beijing 100094, China

[3] College of Resources and Environment, University of Chinese Academy of Sciences, Beijing 100049, China

[4] Institute of Computing Technology, Chinese Academy of Sciences, Beijing 100190, China

4 Computer Network Information Center, Chinese Academy of Sciences, Beijing 100083, China

## 1. INTRODUCTION

The UN general assembly adopted resolution on the 2030 Agenda for sustainable development in 2015. The 17 sustainable development goals (SDGs) and 169 targets were put forward in the 2030 Agenda [1]. All countries and all stakeholders, acting in collaborative partnership, will implement this plan. New technologies are required to ensure its implementation, and to review, at the national, regional and global levels, in relation to the progress made in implementing the Goals and targets over the coming years.

Synthetic aperture radar (SAR), which transmits radar signals to the earth in regardless of light illumination and weather conditions, is a powerful earth observation technique, especially the interferometric SAR (InSAR) technique, which could measure the millimeter deformation of the earth surface. The earth surface dislocation is related to natural earth movement and human-induced earth surface height change. The topographic changes could threaten environmental, economic and social development of human society, hence impede the implementation of SDGs. With the help of satellite InSAR technology, the process of surface movement could be monitored, and its impact to infrastructures and human societies could be assessed.

Sponsored by the “the Big Earth Data Science Project” of the Strategic Science and Technology Pioneer Program of Chinese Academy of Science, the supercomputing InSAR processing system on the CASEarth platform was developed. The European Sentinel-1 SAR data was processed to monitor the land surface deformation from 2019-2020 in China. In this paper, the preliminary results are shown on the change and its impact of the surface deformation in China.

## 2. DATASETS AND METHODS

The European Sentinel-1 SAR data is used in this study. 10985 scenes of data are processing, covering 368 frames and 33 orbits. The time-series InSAR algorithm is used. The processing is performed on the CASEarth supercomputing platform [2]. The technical details are described before [3].

## 3.RESULTS

The annual mean deformation veolocity in 2021 is derived from Sentinel-1 SAR data using time-series InSAR algorithm as shown in Fig. 1. The area with velocity larger than 30mm/year is considered as severe deformation region. In 2020, the severe region is 6261 $km^2$. In 2021, the severe deformation region is 6168 $km^2$, reducing 1.49%. Overall speaking, the deformation situation of the whole country eases a little bit. However, some regions become worse, such as in the lower Yangtze River regions. The North China Plain remains the main subsidence region in China, which occupies 68.47% of the total severe subsidence region in China.

Combined the subsidence data with the WorldPop data, it is shown that the exposed population of severe subsidence regions with 3 km buffer zones are 84.3263 million. The exposed population in North China Plain is 32.0708 million, about 38.03% of total exposed population in China.

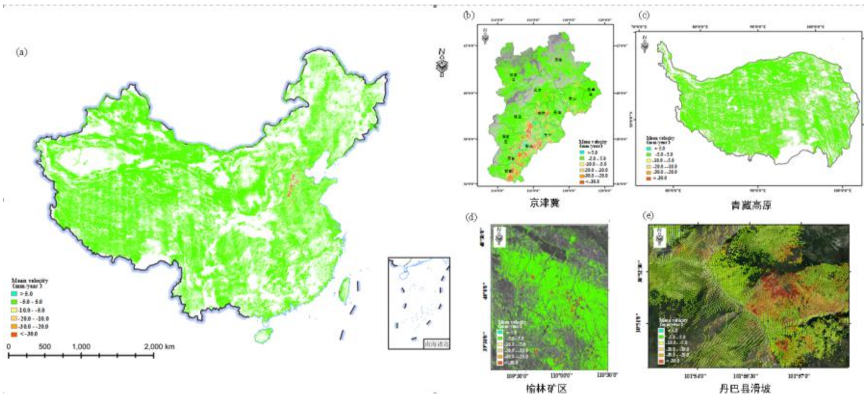


**Fig. 1.** The 2021 annual mean deformation velocity of China measured by satellite InSAR technolog (velocity direction: light of sight).

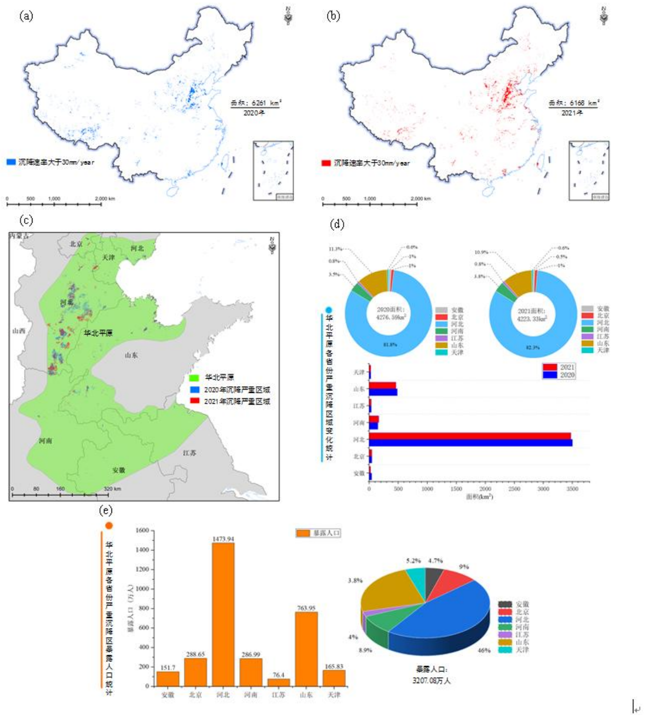


**Fig. 2.** The Spatial and temporal change of severe deformation regions in China between 2020 and 2021.

## 4.SUMMARY

The China surface deformation is measured using time-series InSAR technique and European Sentinel-1 SAR data on the CAS Earth supercomputing platform. The subsidence change in China between 2020 and 2021 is shown. The exposure population is estimated using WorldPop data.

The annual surface deformation in China will be monitored continuously in the future, providing technical support for assessment and implementation of UN SDGs, the Global Development Proposal and China sustainable development agenda.

**Acknowledgements:** This work is supported by the Big Earth Data Science Engineering Project of the Strategic Priority Research Program (Category A) of the Chinese Academy of Sciences, and the National Natural Science Foundation of China under Grants 41930110.

## References

[1] UN (2015) Transforming Our World: The 2030 Agenda for Sustainable Development, Available: https://sdgs.un.org/2030agenda (2022-01-26)
[2] Computer Network Information Center, Chinese Academy of Sciences. (2018) CAS Earth Cloud, The Big Earth Data Science Engineering Project of the Strategic Priority Research Program (Category A) of the Chinese Academy of Sciences. Available: http://portal.casearth.cn/en/ (2022-07-19)
[3] Wang C., Tang Y., Zhang H., et al. (2021) First mapping of China surface movement using supercomputing interferometric SAR technique, Science Bulletin, 66(16): 1608-1610.

# Long-term variation of population exposure to PM2.5 in Eastern China: A perspective from SDG 11.6.2

ZHANG Yuheng [1], ZHOU Qi [1], CHANG ke [1]

[1] School of Geography and Information Engineering, China University of Geosciences, Wuhan, P.R.China
email: hengxin@cug.edu.cn; zhouqi@cug.edu.cn; changk@cug.edu.cn

## 1. INTRODUCTION

Air pollution has a significantly negative effect on human health. It has been estimated that in 2015 more than 4.2 million premature deaths worldwide were attributed to air pollution [1], especially due to exposure to fine particulate matter with a diameter less than 2.5 microns (PM2.5). The level of population exposure to PM2.5 has also been selected by the United Nations as an indicator in Sustainable Development Goals (SDGs), i.e., SDG 11.6.2: "Annual mean levels of fine particulate matter (e.g., PM 2.5 and PM 10) in cities (population weighted)", in order to achieve the Goal 11: "Make cities and human settlements inclusive, safe, resilient and sustainable" [2]. It is therefore desirable for various countries to perform a long-term monitoring of this indicator at not only national but also city levels.

Extensive studies have paid attention to the analysis of PM2.5 concentration for a long time span (e.g., over decades) [3-5]. For instance, Zhao et al. (2019) analyzed the temporal-spatial variation of PM2.5 concentration in China during the period 1999-2016 [3]. However, these studies did not take the distribution of population into consideration. Some studies have assessed the level of population exposure to PM 2.5 [6-9]. But, most of these assessments were carried out at a national or regional level rather than at a city level; on the other hand, most of them only involved a short time span (e.g., a calendar year) for analysis. To be best of our knowledge, few studies have employed the SDG indicator 11.6.2 to perform a city-level analysis and also for a long time span.

To fill this research gap, this study aims to investigate the long-term (2000-2020) variation of population exposure to PM 2.5 in Eastern China (including 318 prefecture-level cities). We selected China as the study area because the number of PM2.5-realted premature deaths in this country was estimated to 1.1 million in 2015, which accounted for 26% of the number (4.2 million) in the world [1]. Therefore, a long-term monitoring of population exposure to PM2.5 in China has received much attention worldwide [3,5,8,10]. More important, a high-resolution and long-term PM2.5 data product has recently been published for conducting this study.

## 2. Materials and methods

### *2.1 Study area and Data*

The study area includes 318 prefecture-level cities in Eastern China. Specifically, this study area has a population of 1.36 billion, which accounts for 94.8% of the total population in China. Moreover, both high-resolution and long-term PM2.5 and population data are freely acquirable for this study area.

Three categories of data sources were involved for the analysis.

1) PM2.5 data: A high-resolution and long-term yearly PM2.5 data product was recently made for public use [5]. The data product covers the region of Eastern China. Also, it has a spatial resolution of 1km, and it includes a long time series of datasets during 2000-2020.

2) Population data: The global 100m-resolution population data product (Worldpop) was acquired [11,12]. The data product also includes a long time series of datasets during 2000-2020. Moreover, it has been used for the evaluation of SDG 9.1 [13] and SDG 11.7 [14,15]. Thus it is possible to investigate the variation of population exposure to PM2.5 not only for decades (21 years) but also in the recent years.

3) City boundary data: The administrative boundary data of the 318 prefecture-level cities were freely acquired from the National Catalogue Service For Geographic Information.

### *2.2 Methods*

The SDG indicator 11.6.2 denotes the population-weighted annual mean PM2.5 concentration (*PWAM* ). This indicator can be calculated as follows:

$$PWAM = \frac{\sum_{i=1}^{k} p_i \times c_i}{\sum_{i=1}^{k} p_i} \quad (1)$$

where, $c_i$ denotes the PM2.5 concentration in the 1km grid cell *i*. $p_i$ denotes the total population in the same grid cell *i*, i.e., it equals to the total population in 100m-resolution population grids whose centroids are located inside the grid cell *i*. *k* denotes the number of 1km grid cells in a geographical region. The *PWAM* can be calculated at a regional level (e.g., the whole study area) and also at a city level (e.g., each prefecture-level city).

The specific experiment steps include: First, the *PWAM* was calculated for the whole study area during 2000-2020. Second, the *PWAM* for each of the 318 prefecture-level cities was also calculated and mapped for these years. Third, all the prefecture-level cities were divided into five different intervals (i.e., 0-35; 35-50; 50-75; 75-100; ＞100 μg/m$^3$), and the population percentages of various intervals were plotted for the whole study area during 2000-2020.

## 3. Results

Figure 1 plots the variation (2000-2020) of the *PWAM* for the whole study area. This figure shows that: the variation has approximately passed through three phases: In the first phase (2000-2003), the *PWAM* increases from around 60 μg/m$^3$ (in 2000) to 70 μg/m$^3$ (in 2003). In the second phase (2004-2013), the *PWAM* fluctuated slightly around 70 μg/m$^3$, and it reaches to the maximum (72 μg/m$^3$) in 2011. In the third phase (2014-2020): the *PWAM* decreases year by year, and it decreases to 34 μg/m$^3$ in 2020. It should be noted that the *PWAM* is for the first time lower than the interim target-1 (35 μg/m$^3$) defined by the WHO (World Health Organization ) [16].

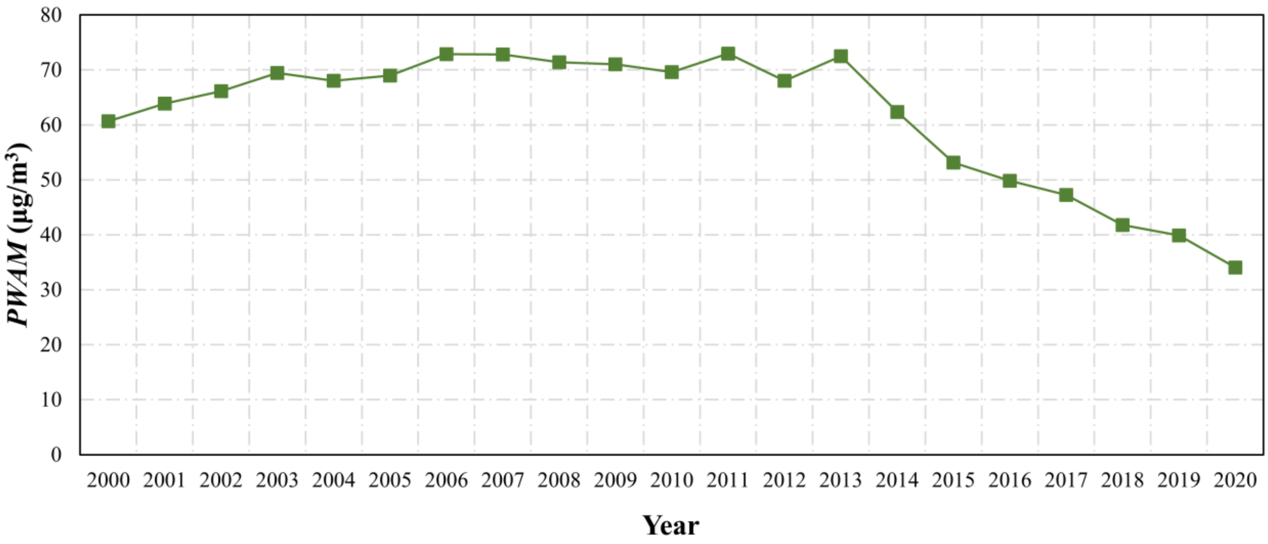


**Fig. 1.** The variation (2000-2020) of the *PWAM* for the whole study area.

Figure 2 shows the temporal-spatial variations (2001-2020) of the 318 prefecture-level cities. This figure shows that: In 2001, the *PWAM* is higher than 75 μg/m$^3$ for 45 out of the 318 prefecture-level cities. This number of such cities increases to the maximum (100) in 2011. But in 2020, there is no prefecture-level city whose *PWAM* is higher than 75 μg/m$^3$. On the contrary, in 2020, the *PWAM* is lower than the interim target-1 for 214 of the 318 prefecture-level cities. The above results indicates a considerable decrease of the *PWAM* in most of the prefecture-level cities.


**Fig. 2.** Temporal-spatial variation (2001-2020) of the *PWAM* for the 318 prefecture-level cities.

Figure 3 plots the population percentages of various PM2.5 concentration intervals for the whole study area during 2000-2020. In 2000, 65% of the total population are located in the prefecture-level cities whose *PWAM* is higher than 50 μg/m$^3$. Such a percentage has reached to the maximum (88%) in 2011.

However, in 2020, this percentage has been decreased to 3%. On the contrary, less than 3% of the total population are located in the prefecture-level cities whose *PWAM* is lower than 35 μg/m$^3$. But in 2020, this percentage has been increased to 67%. This indicates a considerable improvement of population exposure to PM2.5 in Eastern China.

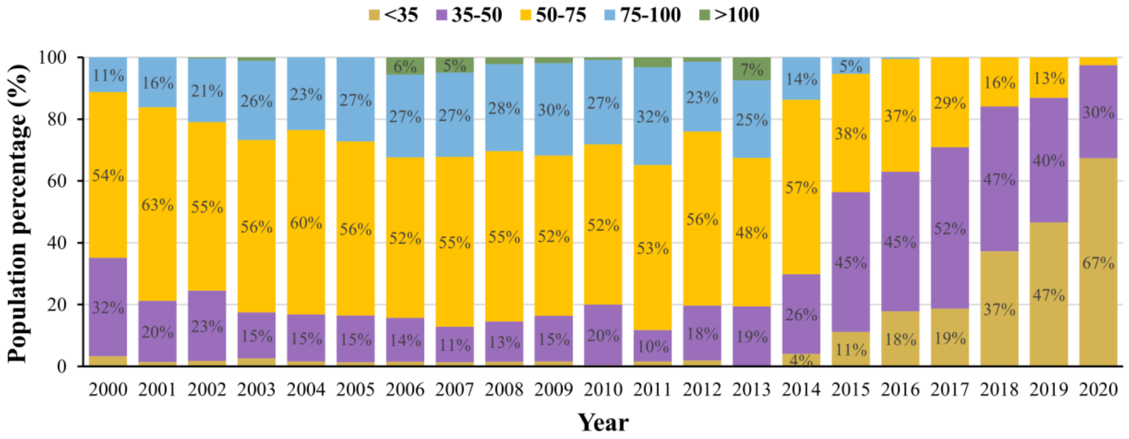


**Fig. 3.** The variations (2000-2020) of population percentages of various PM2.5 concentration intervals for the whole study area.

## 4. Summary

This study conducted a case study of using the SDG indicator 11.6.2 to perform a long-term (2000-2020) analysis of population exposure to PM2.5 in Eastern China. Specifically, the population-weighted annual mean PM2.5 concentration (*PWAM* ) was employed for the analysis. Not only the whole study area, but also each of its 318 prefecture-level cities were analyzed. We found that: 1) a considerable decrease of the  has been observed during 2014-2020. 2) In 2020, the *PWAM* is lower than 35 μg/m$^3$, not only for the whole study area but also for 214 of its prefecture-level cities, which accounts for 67% of its total population. The results indicates a considerable improvement of air quality in Eastern China. More important, this study verifies the feasibility of using open geospatial data to monitor the SDG indicator 11.6.2, which may be applied to other countries and regions.

## References


[1] Cohen, A. J., Brauer, M., Burnett, R., Anderson, H. R., Frostad, J., Estep, K., et al. 2017. Estimates and 25-year trends of the global burden of disease attributable to ambient air pollution: an analysis of data from the Global Burden of Diseases Study 2015. THE LANCET, 389:1907-1918.

[2] Klopp, J. M., and Petretta, D. L. 2017. The urban sustainable development goal: Indicators, complexity and the politics of measuring cities. Cities, 63:92-97.

[3] Zhao, J., Wang, X., Song, H., Du, Y., Cui, W., and Zhou, Y. 2019. Spatiotemporal Trend Analysis of PM2. 5 Concentration in China, 1999–2016. Atmosphere, 10(8): 461.

[4] Lim, C. H., Ryu, J., Choi, Y., Jeon, S. W., and Lee, W. K. 2020. Understanding global PM2. 5 concentrations and their drivers in recent decades (1998–2016). Environment International, 144:106011.

[5] Wei, J., Li, Z., Lyapustin, A., Sun, L., Peng, Y., Xue, W., et al. 2021. Reconstructing 1-km-resolution high-quality PM2. 5 data records from 2000 to 2018 in China: spatiotemporal variations and policy implications. Remote Sensing of Environment, 252:112136.

[6] Yao, L., and Lu, N., 2014. Particulate Matter Pollution and Population Exposure Assessment Over Mainland China in 2010 With Remote Sensing. International journal of environmental research and public health, 11(5):5241-5250.

[7] Zhang, Y. L., and Cao, F., 2015. Fine particulate matter (PM 2.5) in China at a city level. Scientific reports, 5(1):1-12.

[8] Guo, H., Cheng, T., Gu, X., Wang, Y., Chen, H., Bao, F., et al. 2017. Assessment of PM2. 5 concentrations and exposure throughout China using ground observations. Science of the Total Environment, 601:1024-1030.

[9] Chen, J., Zhou, C., Wang, S., and Hu, J. 2018. Identifying the socioeconomic determinants of population exposure to particulate matter (PM2.5) in China using geographically weighted regression modeling. Environmental Pollution, 241:494-503.

[10] Zhang, Q., Zheng, Y., Tong, D., Shao, M., Wang, S., Zhang, Y., et al. 2019. Drivers of improved PM2. 5 air quality in China from 2013 to 2017. Proceedings of the National Academy of Sciences, 116(49):24463-24469.

[11] Lloyd, C. T., Chamberlain, H., Kerr, D., Yetman, G., Pistolesi, L., Stevens, F. R., et al. 2019. Global spatio-temporally harmonised datasets for producing high-resolution gridded population distribution datasets. Big Earth Data, 3(2):108-139.

[12] Zhang Y. H., Zhou, Q., Brovelli, M. A., and Li, W. J. 2022. Assessing OSM building completeness using population data. International Journal of Geographical Information Science, 36(7): 1443-1466.

[13] Li, W. J., Zhou, Q., Zhang Y. H., and Chen, Y. J. 2022. Visualising rural access index and not served rural population in Africa. Environment and Planning A: Economy and Space, 54(2): 215-218.

[14] Long, X. J., Chen, Y. J., Zhang Y. H., and Zhou, Q. 2022. Visualizing green space accessibility for more than 4,000 cities across the globe. Environment and Planning B: Urban Analytics and City Science, 49(5): 1578-1581.
[15] Zhou, Q., Liao, Y. M., and Wang J. 2022. Mapping global urban greenspace: An analysis based on open land-cover data. Urban Forestry & Urban Greening, 74: 127638.
[16] World Health Organization. 2006. Air quality guidelines for particulate matter, ozone, nitrogen dioxide and sulphur dioxide. Available from: https://www.who.int/publications/i/item/WHO-SDE-PHE-OEH-06-02 (accessed in July 2022).

# Research on infrared and low light level data quality improvement in Guangdong-Hong Kong-Macao Greater Bay Area

Hao Chang[1,2],Changmiao Hu[1]

[1] Aerospace Information Research Institute， Chinese Academy of Sciences， Beijing 100094， China

email: changhao211@mails.ucas.ac.cn

[2] School of Electronic， Electrical and Communication Engineering， University of Chinese Academy of Sciences， Beijing 100049， China

email: hucm@aircas.ac.cn

## 1. INTRODUCTION

Based on the breakthrough of automatic matching technology of low-light and thermal infrared images, this study aims to explore the classification detection ability and information extraction ability of population density, fishery, shipping and oil and gas exploitation through the low-light + thermal infrared observation mode. The correlation between the busyness of Marine activities in the Guangdong-Hong Kong-Macao Greater Bay Area and economic indicators and carbon emissions is analyzed.

SDGSAT-1 is equipped with thermal infrared, low-light and multi-spectral loads, and has a low-light data resolution of 10m, which makes it possible to detect nighttime maritime targets based on light data. It provides an average of 12 views of thermal infrared data and 9 views of low-light data per month.

## 2. DATA AND METHODS

### *2.1 Data*

SDGSAT-1 remote sensing image of the Guangdong-Hong Kong-Macao Greater Bay Area was taken from February to June in 2022. The data source was the International Research Center for Big Data for Sustainable Development. The obtained data had been pre-processed with radiometric correction, atmospheric correction and geometric correction. At present, thermal infrared and low-light level data have been obtained, including 61 thermal infrared data and 45 low-light level data.

### *2.2 Data processing method*

Through the analysis of the downloaded data, it is found that there are problems such as local registration precision jitter of data from different sources in the same region and obvious noise of low-light image, as shown in Figure 1 and Figure 2.

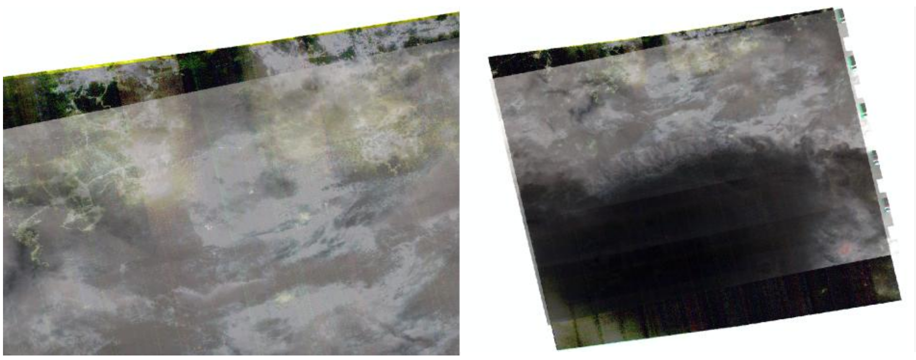

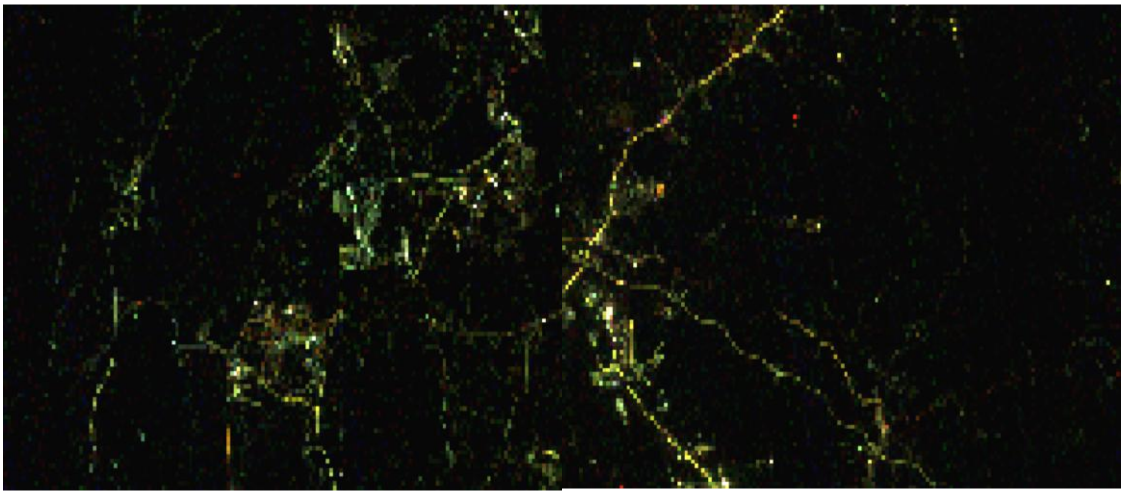

**Fig. 1.** May and June low-light and infrared data overlay rendering (partial on the left, overall on the right)

**Fig. 2.** Noise of low - light image

In order to further improve the data quality, the preliminary project team carried out preliminary experiments on the pre-processing of downloaded data, mainly including the high-precision matching of low-light and thermal infrared data and the improvement of low-light image quality.

The methods to improve the quality of low-light image mainly include removing noise and improving image contrast. In this study, the median filtering method is mainly used to denoise. A sliding window with odd points is used to replace the gray value of the specified point with the median gray value of each point in the window. Gray stretching and gray equalization are the main methods to improve image contrast. Gray stretching method is to transform the gray concentration part of the image through linear transformation, so that the gray contrast of the transformed image is higher than the original image, so that the image becomes clearer. Gray equalization is a nonlinear stretching of the image, redistributing the pixel value of the image so that the number of pixels in a certain range is roughly the same, so that the image brightness can be better distributed on the histogram.

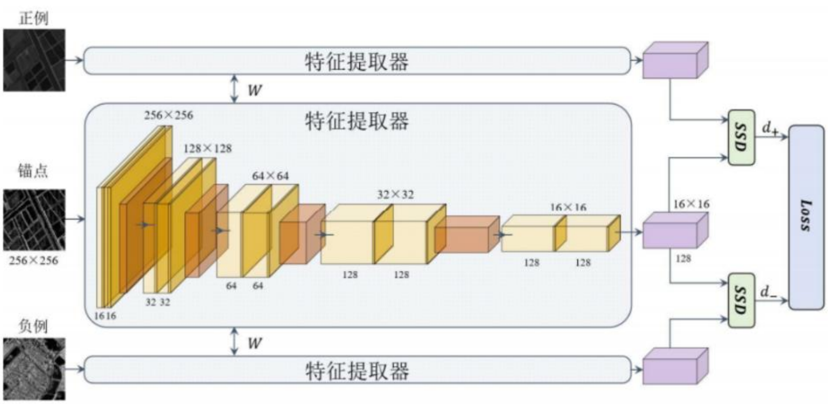


**Fig. 3.** Frame diagram of matching algorithm based on triplet twin network

The automatic registration of thermal infrared and low light level mainly adopts deep learning method. Firstly, the multi-modal image block pair sample library is constructed by combining the artificial method with the sample expansion method based on generative adversarial network. Secondly, sample expansion is made to the preliminary sample data. Traditional methods include image rotation, image flipping, changing contrast, brightness, saturation or hue, adding color disturbance, etc. The sample augmentation method based on generative adversarial network can make the model automatically generate a large number of unknown samples. Finally, an image block based on triplet twin network is constructed to match the similarity judgment network, and Fourier transform is used to accelerate the reasoning speed of the image block matching network. The algorithm flow diagram is shown in Figure 3.

The triplet twin network selects a pair of samples from the sample base, which are called the anchor point and the positive example respectively, and then randomly selects other heteromorphic image blocks unpaired with the anchor points from the sample base as negative examples. Feature extractor uses deep convolutional network to extract texture features of image blocks. After the three input image blocks are entered into the same feature extractor, the corresponding 3D feature tensor is obtained respectively as the eigenvalue of similarity calculation. The similarity between features is calculated using error square and SSD:

$$SSD = \sum_{c=1}^{C} \sum_{h=1}^{H} \sum_{w=1}^{W} (X(c,h,w) - Y(c,h,w))^2 \qquad (1)$$

Where, C, H and W are the number of channels, height and width of the feature tensor, and X and Y represent two feature tensors. The SSD of anchor point and positive example is $SSD_+$, and the SSD of anchor point and negative example is $SSD_-$. After Softmax normalization, $d_+$ and $d_-$ are obtained respectively, as shown in Eq. (2).

$$d_+ = \frac{e^{SSD_+}}{e^{SSD_+} + e^{SSD_-}}, d_- = \frac{e^{SSD_-}}{e^{SSD_+} + e^{SSD_-}} \qquad (2)$$

On this basis, the loss function is calculated as Eq. (3).

$$Loss(d_+, d_-) = \ ||(d_+, d_- - 1)||_2^2 = const d_+^2 \qquad (3)$$

Makes the network to determine different modal image block of similarity, and as a multimodal image registration of the same name point search tools, complete the image registration. In addition, Fourier transform is used to accelerate the inference speed based on image block matching network.

The noise of low-light imaging mainly comes from the imaging characteristics of devices. For low-light image with large pixel size, we try to use the de-noising algorithm based on BM3D frame to deal with it. The algorithm framework is shown in Figure 4.

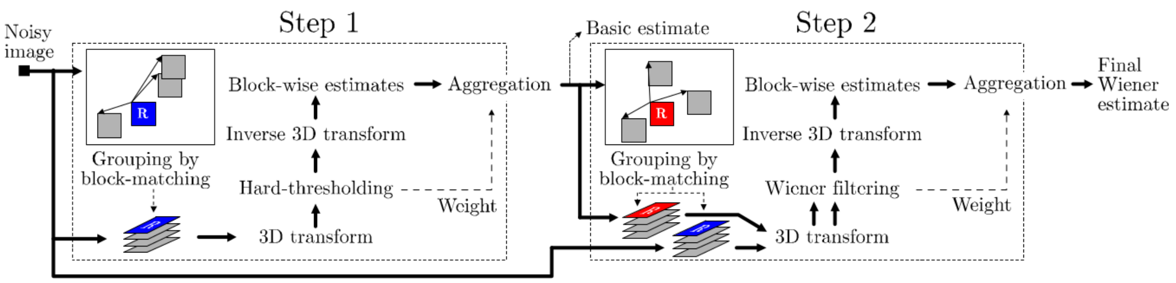


**Fig. 4.** Block diagram of BM3D algorithm

The process operation of BM3D framework is complex, especially with the increase of image pixel size, the computational complexity of sliding matching window will increase rapidly. In order to adapt to the application of low-light image denoising with large pixel size, the optimization algorithm will be studied under the premise of ensuring the denoising quality.

## 3. RESULTS

The preliminary experimental results show that the local geometric registration accuracy can be improved to pixel level, and the low light level image denoising can significantly eliminate the image noise, while preserving the object boundary.

## 4. SUMMARY

The observation mode of low light level + thermal infrared can significantly improve the ability of target identification and detection at night, which is of great significance to the detection of night activities. The activity intensity of sea targets can be calculated by identifying and classifying sea targets at night. Based on these calculation results, regression analysis can be carried out with the data of Marine production and other data, and correlation relationship can be further established with the economic indicators such as gross Marine product and trade volume with countries along the Maritime Silk Road. Finally, the GDP, population density and carbon emission of the study region can be estimated.

## References


[1] Zhi-jie deng. Extraction of multi-source remote sensing of luminous city proper research [D]. Donghua university of science and technology, 2021. The DOI: 10.27145 /, dc nki. GHDDC. 2021.000127.

[2] Song Jiayi. Infrared image detection and positioning of target and the sea to deal with the fog [D]. Shenzhen university, 2020. The DOI: 10.27321 /, dc nki. Gszdu. 2020.000046.

[3] Zhao J M.Spatial-temporal characteristics of regional economic development in the Yangtze River Delta based on night-light remote sensing [J]. Surveying and mapping, 2021 (S1) : 109-113. The DOI: 10.13474 / j.carol carroll nki. 11-2246.2021.0525.

[4] Wang C X.Analysis and characteristics of urban agglomeration spatial structure based on night light remote sensing data [D]. East China normal university, 2021. DOI: 10.27149 /, dc nki. Ghdsu. 2021.000500.

[5] Huang Tie-Lan, LUO Jing, GAO Zhao-zhong, HUANG Fei-ni. Urban spatial pattern evolution in the Guangdong-Hong Kong-Macao Greater Bay Area based on DMSP-OLS and Luojia no.1 night-light remote sensing image [J]. Bulletin of surveying and mapping, 2021 (12) : 10-15. DOI: 10.13474 / j.carol carroll nki. 11-2246.2021.364.

[6] He J. Rapid detection and recognition of maritime targets based on visible light remote sensing images [D]. Changchun university of Chinese Academy of Sciences, China (Chinese Academy of Sciences institute of optical precision machinery and physical), 2020. The DOI: 10.27522 /, dc nki. GKCGS. 2020.000122.

[7] Deng Haojian, LI Hengkai, XIONG Yongzhu, ZHENG Chunyan, LI Yingshuang. Spatial-temporal evolution of urban agglomerations in the Guangdong-Hong Kong-Macao Greater Bay Area in the past 20 years [J]. World regional studies,2020,29(06):1181-1189.

# Assessing progress toward achieving the transport dimension of the SDGs in China

Liu Xiaofei[1, 2], Yuan Minmin[1, 2]

[1] Research Institute of Highway Ministry of Transport, Beijing, China 100088

[2] National Environmental Protection Engineering and Technology Center for Road Traffic Control, Beijing, China 100088

email: xf.liu@rioh.cn

## 1. INTRODUCTION

The global indicator framework for measuring the progress of SDGs included 231 unique indicators [1]. With objectives such as universal access, improved resilience, and greater efficiency, transport is an important factor in sustainable development [2,3]. Transport promotes regional economic development and improves social welfare by ensuring convenient travel and efficient transportation of goods. Research has revealed that transport infrastructure has a great impact on land, urban development, and human life [4,5] and is an important factor in ensuring regional economic growth [6,7]. However, transport also has adverse effects. For example, it leads to high levels of carbon emissions [8], direct harm to human health from polluting gases emitted by motor vehicles [9,10], and habitat fragmentation and loss of biodiversity resulting from road construction [11]. Additionally, traffic accidents are the main cause of death in developing countries [12].

In China, such information is urgently needed as the promulgation of *the Outline for Building China's Strength in Transport* policy, which aims to build a safe, convenient, efficient, green, and economically modern comprehensive transport system, is put in place. These goals coincide with SDGs. A spatiotemporal analysis of SDGs is useful for the transport sector, allowing the recognition of its current developmental advantages and limitations and judging the focus of sustainable development in the future [13-15]. The localized transport evaluation system constructed according to the SDG framework provides information for other regions to assess the sustainable development of the transport sector [13,16].

## 2. MATERIALS AND METHODS

### *2.1 Transport indicators for SDG targets and data sources*

We selected the following quantifiable SDG indicators directly related to transport: SDG 3.6 (halve the number of global deaths and injuries from road traffic accidents), SDG 7.2 (substantially increase the share of renewable energy in the global energy mix), SDG 8.2 (achieve higher levels of economic productivity), SDG 9.1 (develop quality, reliable, sustainable, and resilient infrastructure), SDG 11.2 (provide safe, affordable, accessible, and sustainable transport systems for all), SDG 11.6 (reduce the adverse per capita environmental impact of cities), SDG 12.2 (achieve sustainable management and efficient use of natural resources), SDG 13.2 (integrate climate change measures into national policies, strategies, and planning), and SDG 15.1 (ensure the conservation, restoration, and sustainable use of terrestrial and inland freshwater ecosystems).

### *2.2 Selection of upper and lower bounds*

### *2.3 Normalization*

The reference Equation (1) used is as follows:

$$x' = \frac{X_i - X_{min}}{X_{max} - X_{min}} \times 100 \quad (1)$$

where x is the raw data value; max and min denote the bounds for the best and worst performance, respectively; and x' is the normalized value after rescaling.

The larger the value of the indicator, the closer it is to the target, and Equation (2) is used as follows:

$$x' = \frac{X_i - X_{2.5}}{X_{max} - X_{2.5}} \times 100 \tag{2}$$

For the indicator with the smaller value, the closer it is to the target, Equation (3) is used as follows:

$$x' = \frac{X_i - X_{97.5}}{X_{max} - X_{97.5}} \times 100 \tag{3}$$

where $X_i$ represents the corresponding indicator value in the original data, $X_{max}$ represents the upper bounds; $X_{2.5}$ and $X_{97.5}$ represent the percentile values corresponding to the sorting of all data across provinces and years from small to large. If the percentile value is between two values, the value with better performance would be taken; that is, if the indicator value is preferably smaller, the larger value close to the 2.5 percentile would be taken; if the indicator value is preferably greater, the smaller value close to the 97.5 percentile would be taken.

## 3. RESULTS

### *3.1 Transport SDG scores*

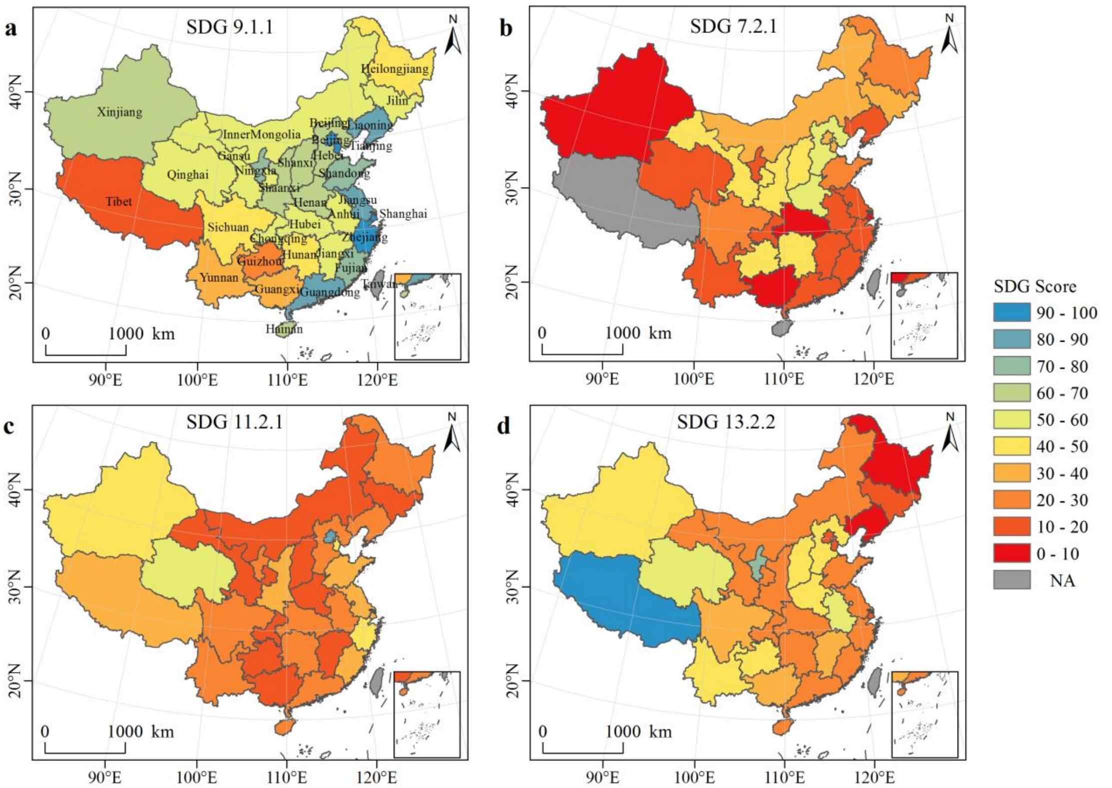


**Fig. 1.** Average performance of provinces on SDGs. a. SDG 9.1.1 proportion of near-road population; b. SDG 7.2.1 clean energy proportion of transport, warehousing, and postal industry; c. SDG 11.2.1 bus ownership among 10,000 people; d. SDG 13.2.2 performance of transport CO2 emissions.

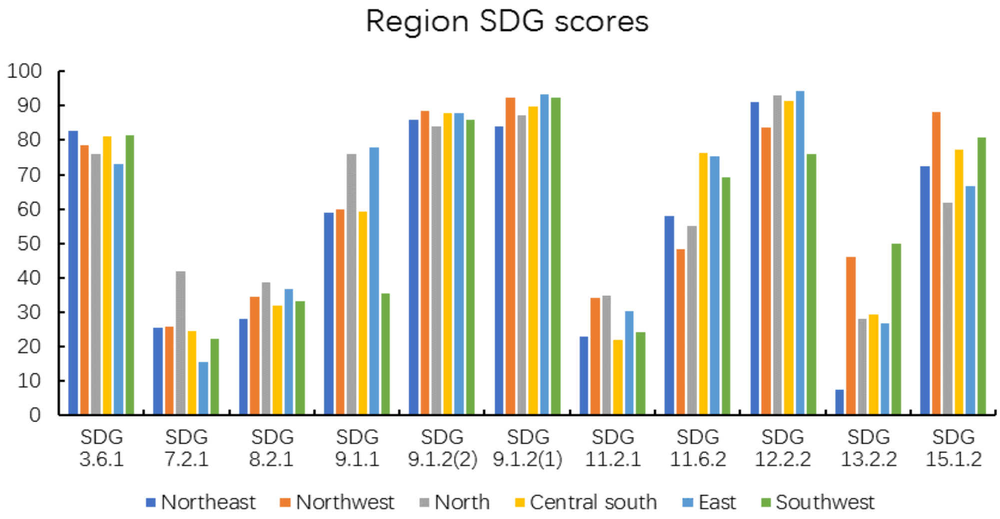


**Fig. 2.** Average SDG scores of six regions

### *3.2 Trade-off analysis*

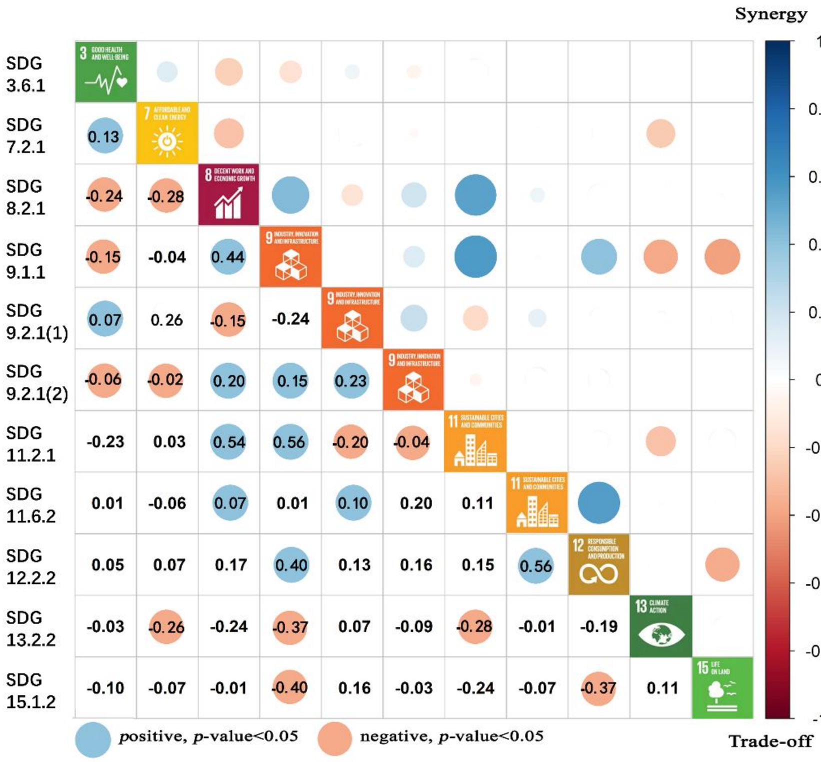


**Fig. 3.** Correlation coefficient of SDG performance. Spearman correlation coefficient was used.

## 4. SUMMARY

Transport is an important service industry in the national economy. Sustainable transportation is central to sustainable development. Currently, investigating the sustainable development process and trade-offs in China’s transportation sector is urgent. In this study, 11 transport indicators were selected and constructed for the sustainable development goals (SDGs) under the UN indicator framework. The scores of each indicator were calculated, and spatiotemporal patterns and correlations were analyzed. The results revealed that China's transport infrastructure performed well in large transportation volumes and guaranteed traffic safety and strict land use control, with scores above 75. However, China’s transport sector currently faces a challenge in using clean energy, and a more balanced development of bus ownership among the provinces is expected. The correlation analysis revealed that both the significant trade-off and synergy relationships among the selected indicators accounted for approximately half, indicating that China's transport sector had prioritized achieving specific sustainable development objectives and that sustainable transport should be fully realized in the future. We suggest that more SDG indicators with indirect impacts should be included in future transport SDG research, and there should be further developments of trade-off and synergy research methodologies for SDG indicators.

## References


1 United Nations. *Global indicator framework for the Sustainable Development Goals and targets of the 2030 Agenda for Sustainable Development*, <https://unstats.un.org/sdgs/indicators/indicators-list/> (2021).

2 China's State Council Information Office. Sustainable Development of Transport in China, white paper. (Beijing, 2020).

3 United Nations. Sustainable transport, sustainable development. Interagency report for second Global Sustainable Transport Conference. (2021).

4 Liu, J. *et al.* Systems integration for global sustainability. *Science* **347**(2015).

5 Wang, L., Xue, X., Zhao, Z. & Wang, Z. The Impacts of Transportation Infrastructure on Sustainable Development: Emerging Trends and Challenges. *International Journal of Environmental Research and Public Health* **15**(2018).

6 Prus, P. & Sikora, M. The Impact of Transport Infrastructure on the Sustainable Development of the Region-Case Study. *Agriculture-Basel* **11**(2021).

7 Jiang, X., Zhang, L., Xiong, C. & Wang, R. Transportation and Regional Economic Development: Analysis of Spatial Spillovers in China Provincial Regions. *Networks & Spatial Economics* **16**, 769-790(2016).

8 Chen, X., Shuai, C., Wu, Y. & Zhang, Y. Analysis on the carbon emission peaks of China's industrial, building, transport, and agricultural sectors. *Science of The Total Environment* **709**, 135768(2020).

9 Rosofsky, A., Levy, J. I., Zanobetti, A., Janulewicz, P. & Fabian, M. P. Temporal trends in air pollution exposure inequality in Massachusetts. *Environmental Research* **161**, 76-86(2018).

10 Amini, H. *et al.* Long-term exposure to air pollution and stroke incidence: A Danish Nurse cohort study. *Environment International* **142**, 105891(2020).

11 Kang, D. W. *et al.* Evaluating the effects of roads on giant panda habitat at two scales in a typical nature reserve. *Science of the Total Environment* **710**(2020).

12 Sapsirisavat, V. & Mahikul, W. Drinking and Night-Time Driving May Increase the Risk of Severe Health Outcomes: A 5-Year Retrospective Study of Traffic Injuries among International Travelers at a University Hospital Emergency Center in Thailand. *International Journal of Environmental Research and Public Health* **18**(2021).

13 Tremblay, D. *et al.* A Systemic Approach for Sustainability Implementation Planning at the Local Level by SDG Target Prioritization: The Case of Quebec City. *Sustainability* **13**(2021).

14 Huan, Y., Li, H. & Liang, T. A New Method for the Quantitative Assessment of Sustainable Development Goals (SDGs) and a Case Study on Central Asia. *Sustainability* **11**(2019).

15 Xu, Z., Chau, S. N., Chen, X., Zhang, J. & Liu, J. Assessing progress towards sustainable development over space and time. *Nature* **577**, 74-78(2020).

16 Xu, Z. *et al.* Impacts of international trade on global sustainable development. *Nature Sustainability* **3**, 964-971(2020).

# Urban thermal comfort and Local Climate Zones in Milan Metropolitan City

VAVASSORI Alberto [1], PUCHE Mathilde [2], BROVELLI Maria Antonia [3]

[1, 2, 3] Department of Civil and Environmental Engineering, Politecnico di Milano, Piazza Leonardo da Vinci 32, 20133 Milano, Italy

email: [1] alberto.vavassori@polimi.it, [2] mathildedanielle.puche@mail.polimi.it, [3] maria.brovelli@polimi.it

## 1. INTRODUCTION

Nowadays, cities host more than 55% of the world's population, while about 75% of European citizens live in urban areas [1]. Cities concentrate people, infrastructures, activities, and resources, making them particularly vulnerable to the effects of climate change. This challenge is explicitly addressed by the United Nations (UN) Sustainable Development Goal (SDG) 11 "Make cities inclusive, safe, resilient and sustainable". With the rapid expansion of cities, natural and green areas are being increasingly replaced by artificial surfaces with different thermal capacities and conductivities, thus affecting urban heat fluxes and ultimately local climate [2]. As a result, the Urban Heat Island (UHI) effect has intensified, leading to an increased impact on the health and welfare of citizens due to their persistent exposure to extreme thermal conditions [3].

UHIs can be measured through a climate-based classification system called Local Climate Zones (LCZ), that defines 17 unique area types based on the physical and thermal properties of their surface [4]. This classification explains the contribution of urban surface characteristics to heat fluxes and is therefore widely employed for urban climate-related studies. LCZ maps are typically derived from the supervised classification of satellite imagery, by leveraging ancillary Earth Observation products and geospatial data to define suitable training datasets. A detailed and comprehensive protocol established by the World Urban Database and Access Portal Tools (WUDAPT) and formalized by [5] provides guidelines on how to perform the LCZ classification.

With this background, this work contributes to the investigation of the climate of the Metropolitan City of Milan (MCM). Landsat 8 satellite imagery is leveraged for computing a detailed LCZ map of the study area as well as to assess the relationship between LCZs and Land Surface Temperature (LST). Outcomes provide preliminary evidence on the effect of land surface features and temperature distribution, pointing out how natural surfaces can significantly contribute to buffering extreme temperatures in urban areas.

## 2. MATERIALS AND METHODS

### *2.1 Study area and data collection*

The analysis developed in this study is focused on the Metropolitan City of Milan (MCM), located in the Lombardy Region (Northern Italy). With more than 3 million inhabitants [6] and an area of 1,575 km$^2$, it is the second most populous metropolitan city in the nation. The area experiences cold winters as well as humid and hot summers, with poor wind circulation, which makes it susceptible to persistent UHIs and therefore a suitable test area for investigating local climate effects. Average temperatures range from -0.9 ℃ to 5.9 ℃ in January and from 18.0 to 29.2 ℃ in July, but maxima higher than 35 ℃ are becoming increasingly frequent during summer [7].

Landsat 8 was selected among available missions as it provides global coverage, freely available, and high spatial resolution imagery through two main sensors, an optical sensor (the Operational Land Imager, OLI), and a thermal one (the Thermal Infrared Sensor, TIRS). This study was carried out by exploiting the Collection 2 Level 2 (C2L2) product of the Landsat 8 mission, which provides analysis-ready Bottom-of-Atmosphere (BOA) reflectance data. Specifically, bands 1 to 7 (with 30m resolution) were employed with the aim of generating LCZ maps. To account for seasonality and increase classification accuracy, 5 images were selected in the different seasons of 2021, namely 16 March, 19 May, 6 July, 24 September, and 5

December, all acquired at 10:10 a.m. Greenwich Mean Time. The thermal band 10 (30m resolution) was used to derive the LST map. In order to detect the highest temperatures experienced across the study area, the image of 22 July 2021 was selected. The choice of specific images was restricted to dates with a maximum cloud coverage of 5% over the study area.

Ancillary geospatial datasets, including soil consumption data (*Carta Nazionale Consumo del Suolo*), building height data (obtained from the Lombardy Region Topographic database), and Google Satellite images, were leveraged for creating suitable training and testing datasets.

### *2.2 LCZ classification*

As C2L2 Landsat 8 products provide BOA reflectance values, no additional atmospheric correction is required. Therefore, bands 1 to 7 were merged into a single multispectral raster for deriving the LCZ classification map. The building height dataset was converted into a raster dataset and added to the multispectral image as a new band in order to improve the classifier performance.

The Random Forest (RF) algorithm was used for the classification. A single training set was applied to each of the five Landsat 8 images in order to obtain the LCZ maps. The training set was created through a combined analysis of soil consumption and building height layers as well as Google Satellite imagery photo-interpretation. An independent testing set was similarly created for the classification accuracy assessment. Only 8 of the 17 original LCZs were identified in the area of interest. Specifically, 5 built-up classes - namely Compact Mid-Rise (class 2) Compact Low-Rise (class 3), Open Mid-Rise (class 5), Open Low-Rise (class 6), Large Low-Rise (class 8) -, and 3 non-built-up classes - namely Scattered Trees (class 102), Low Plants (class 104), and Water (class 107).

The RF algorithm was run on each satellite image, resulting in 5 LCZ maps for 2021. Maps were post-processed with a majority filter and combined using majority voting to obtain one single LCZ map. The small percentage of pixels for which no majority was found was left with no-data value. Finally, the test dataset was used to assess the classification accuracy by using standard metrics derived from the confusion matrix.

### *2.3 LST mapping and relation with LCZ*

The Landsat 8 ST product is derived from the Collection 2 Level 1 TIRS band 10 and generated from the single channel algorithm [8]. To retrieve the LST from the L2C2 image, a linear transformation of the digital number (DN) was performed as shown in Eq. (1) and (2):

$$LST_{Kelvin} = 0.00341802 \cdot DN + 149 \tag{1}$$

$$LST_{Celsius} = LST_{Kelvin} - 273.15 \tag{2}$$

As documented in [9], the presence of clouds may cause large negative errors in the LST distribution. To avoid this issue, the north-eastern portion of the MCM with significant cloud coverage was removed. The resulting LST map was used together with the final LCZ map to compute the mean temperature of each class and disclose the effect of urban texture and land cover composition on the surface temperature.

## 3. RESULTS

The final LCZ is depicted in Fig. 1 while the accuracy assessment results are reported in Table 1. With an overall accuracy (OA) of 94%, the achieved LCZ map is one of the most accurate maps available in the World Urban Database. The building height dataset allowed to properly differentiate Mid-Rise from Low-Rise classes, resulting in user accuracy (UA) and producer accuracy (PA) values higher than 82% for all the classes (and higher than 90% for most of the classes).

The derived LST distribution for 22 July 2021 (see Fig. 2) depicts temperatures ranging from 12 to 63 °C, with an average of 40.5 °C and a standard deviation of 5.6 °C. By computing the mean temperature per class, natural classes turn out to have cooler temperatures than built-up classes (see Fig. 3) with mean LST ranging from 43.7 to 46.2 °C and from 33.9 to 39.1 °C, respectively. This first experiment thus provides pieces of evidence about the importance of natural areas in mitigating summer extreme temperatures.

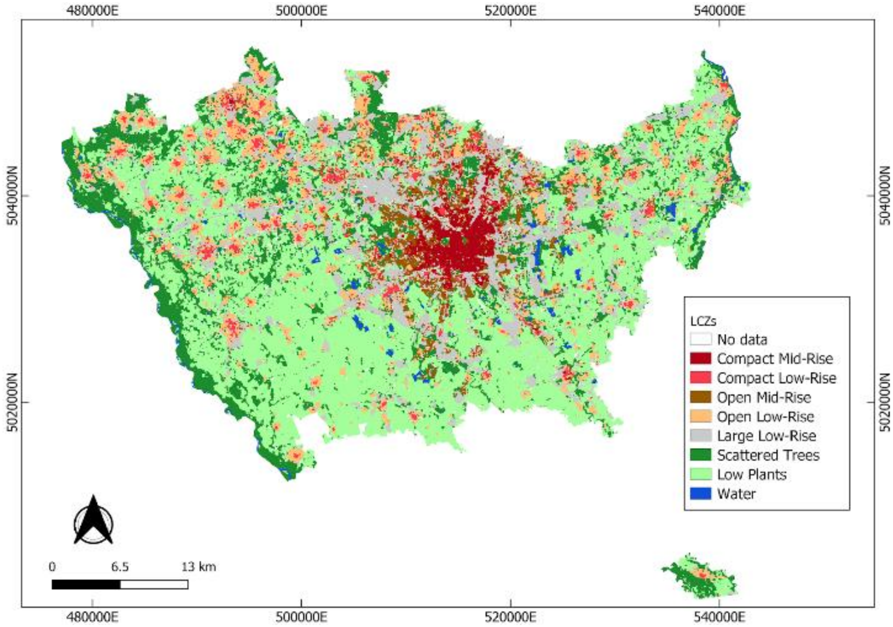


**Fig. 1.** Final LCZ map (2021) at 30m resolution.

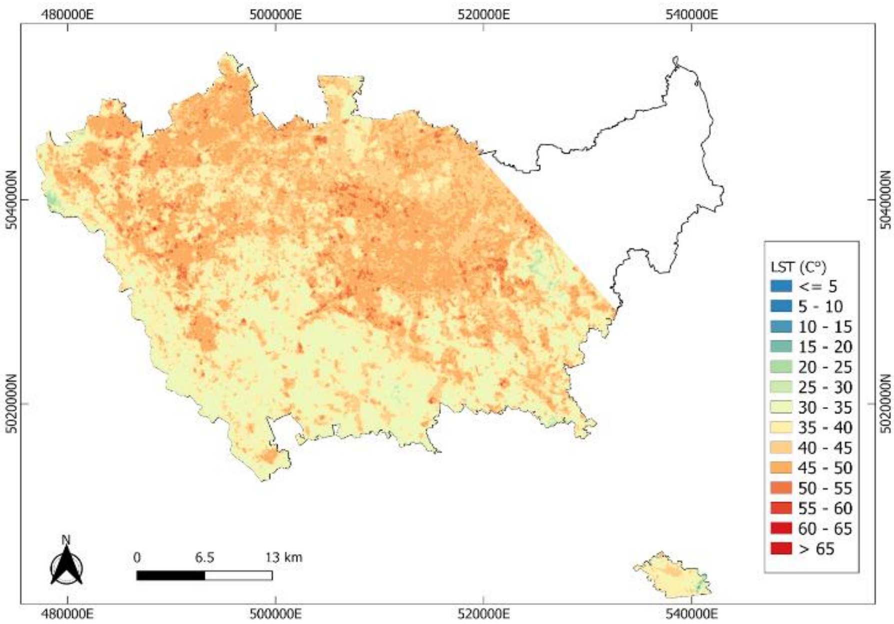


**Fig. 2.** LST map (22 July 2021) at 30m resolution.

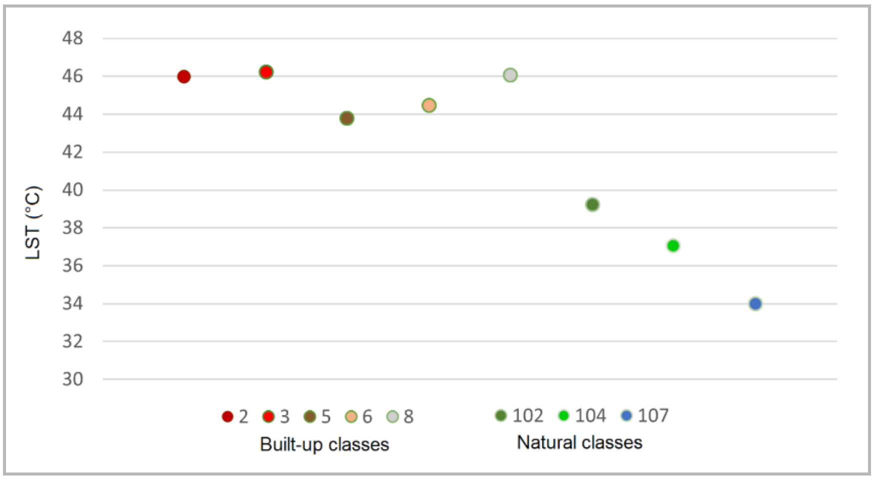


**Fig. 3.** Mean LST per class.

**Table 6.** LCZ final accuracies.

| CLASS | 2 Compact Mid-Rise | 3 Compact Low-Rise | 5 Open Mid-Rise | 6 Open Low-Rise | 8 Large Low-Rise | 102 Scattered Trees | 104 Low Plants | 107 Water |
|---|---|---|---|---|---|---|---|---|
| PA [%] | 97.9 | 82.8 | 82.5 | 90.9 | 97.7 | 99.0 | 99.2 | 99.4 |
| UA [%] | 95.7 | 89.6 | 94.4 | 85.9 | 95.1 | 95.3 | 98.5 | 99.6 |
| OA [%] | 94.0 | | | | | | | |

## 4. SUMMARY

This study exploits high-resolution satellite imagery and ancillary geospatial datasets to investigate the effect of urban morphology and land cover composition on the local climate, using the MCM as a case study. Satellite imagery from Landsat 8 mission was used to derive a detailed LCZ map depicting urban texture, morphology, and land cover composition across the study region. Five cloud-free and analysis-ready images for the year 2021 were processed and classified with the RF algorithm to derive a set of LCZ maps that were finally merged to achieve a single synthetic LCZ map. The OA of 94% and single-class accuracies higher than 82% point out a satisfying performance of the tested procedure for the LCZ mapping.

A preliminary experiment for the assessment of the LCZ effect on the urban climate was run by computing the LST distribution across the MCM. A single Landsat 8 image of July 2021 was selected and processed to point out temperature extremes in summer and to perform a preliminary correlation analysis between LCZ and LST distribution. Results show an underlying relationship between the LCZ and the LST for the chosen study area, with the built-up climate zones experiencing a higher mean temperature (ranging between 44 and 46 ℃) than the non-built-up zones (where average temperatures range between 34 and 40 ℃).

The proposed LCZ mapping approach looks promising for improving the available WUDAPT classification for the study region. The resulting map may be employed for further investigations of the urban climate at a local scale, including the analysis of a relevant climate-related variable, i.e., air temperature, and its relationship with the LCZs. The correlation between LCZs, LST, and air temperature for different seasons and day hours - foreseen as a future development of this work - will provide insights into the influence of urban morphology and human footprint on the local climate.

## References

[1] European Environment Agency (2021) Urban sustainability: how can cities become sustainable? Available: https://www.eea.europa.eu/themes/sustainability-transitions/urban-environment (accessed on 18/07/2022)
[2] Salazar A., Baldi G., Hirota M., Syktus J., McAlpine C. (2015) Land use and land cover change impacts on the regional climate of non-Amazonian South America: A review, Global and Planetary Change, 128:103-119

[3] Avashia V., Garg A., Dholakia H. (2021) Understanding temperature related health risk in context of urban land use changes, Landscape and Urban Planning, 212:104107
[4] Stewart I.D., Oke T.R. (2012) Local Climate Zones for Urban Temperature Studies, Bulletin of the American Meteorological Society, 93(12):1879–1900
[5] Bechtel B., Alexander P.J., Böhner J., Ching J., Conrad O., Feddema J., Mills G., See L., Stewart I. (2015). Mapping Local Climate Zones for a Worldwide Database of the Form and Function of Cities, ISPRS International Journal of Geo-Information 4(1):199–219
[6] Eurostat (2022) Population on 1 January by age groups and sex - cities and greater cities. Available: https://ec.europa.eu/eurostat/web/products-datasets/-/MIGR_POP1CTZ  (accessed on 18/07/2022)
[7] Aeronautica Militare (2022) Tabelle climatiche 1971-2000 della stazione meteorologica di Milano Linate dall'Atlante Climatico 1971-2000 del Servizio Meteorologico dell'Aeronautica Militare. Available: https://it.wikipedia.org/wiki/Stazione_meteorologica_di_Milano_Linate (accessed on 18/07/2022)
[8] Sayler K. (2022) Landsat 8-9 Collection 2 (C2) Level 2 Science Product (L2SP) Guide. USGS, Available: https://www.usgs.gov/media/files/landsat-8-9-collection-2-level-2-science-product-guide (accessed on 18/07/2022)
[9] Cook M., Schott J.R., Mandel J., Raqueno N. (2014) Development of an Operational Calibration Methodology for the Landsat Thermal Data Archive and Initial Testing of the Atmospheric Compensation Component of a Land Surface Temperature (LST) Product from the Archive, Remote Sensing, 6(11):11244-11266

# Analysing $NO_2$ pollution with Sentinel 5P and ground sensors

CEDENO JIMENEZ, J. R. [1] ; PUGLIESE VILORIA, A. [1] ; BROVELLI, M. A. [1]

[1] Department of Civil and Environmental Engineering, Politecnico di Milano, Milan, Italy
email: (jesusrodrigo.cedeno, angellyde.pugliese, maria.brovelli)@polimi.it

## 1. INTRODUCTION

Air quality deterioration has recently become a pressing topic for local, regional and global authorities. Nitrogen Dioxide ($NO_2$) is an atmospheric pollutant that causes health problems like Chronic Obstructive Pulmonary Disease (COPD)[1]. The combination of $NO_2$ impact on health and global warming has encouraged organizations such as the European Union (EU) to measure and monitor atmospheric pollutants[2]. Additional to these guidelines and to promote global engagement, the UN established the Sustainable Development Goals (SDGs). In particular, SDG 11 addresses the topic of pollution and Sustainable Cities and Communities. One of the targets of this goal is to reduce the adverse per capita environmental impact of cities, by paying special attention to air quality and municipal and other waste management[3]. As reported by Pinder et al (2019) air quality monitoring in High-Income countries, like the USA, has been implemented in the last 50 years. Moreover, according to the same paper, this has been achieved through the investment of millions of dollars to install, maintain and use monitoring stations. Unfortunately, this is not the case in Low- and Middle-Income Countries (LMICs), where air quality monitoring is poor or not present[4].

The main purpose of this work is to present a solution to this problem by enabling LMICs to monitor ground air quality without the need of making a financial investment to install ground stations. This issue has already been partially addressed with the development of satellite technology. An example is the Sentinel-5P from the Copernicus programme developed by the European Commission, the European Space Agency (ESA) and the European Organisation for the Exploitation of Meteorological Satellites (EUMETSAT). This programme is mainly designed to provide European citizens with open data about the Earth. Sentinel-5P is a satellite equipped with a state-of-the-art sensor capable of measuring atmospheric pollution concentrations at a spatial resolution of 5 km x 3.5 km. Although satellite data has a good correlation with ground sensor measurements in some cases (like mountain regions) these measurements have a weak correlation[5]. For this reason, this work describes an Artificial Intelligence (AI) trained model to provide ground-level measurements starting from the satellite data.

As a case study for this work, we considered analysing atmospheric $NO_2$ concentrations in the Lombardy region in the North of Italy. $NO_2$ was selected due to its close relationship to human transportation. This can serve for authorities to implement measures to improve the situation. According to the EEA, transportation is the main cause of this pollutant's concentration in ambient air[6], therefore, we focus on air quality in urban areas. Lombardy is considered a pollution hotspot and due to its topographic characteristics, it was selected as the area of interest. The presence of the Alps in the North and West, and the Apennines in the south promotes the wind to get entrapped in the area. Frequent thermal inversions, prevent correct atmospheric pollution dispersion[7]. Additional to this, Facebook mobility data provided by the crisis portal Data for Good were used to relate atmospheric pollution with anthropogenic dynamics in the area.

Given that building a pollution measurement model is sophisticated, this work was divided into two phases. The former (described in this document) uses both a combination of satellite data and ground sensor data to train the algorithm. Future work will be focused on the exclusive use of satellite data.

This document will be divided as follows, in the following section, the materials and methods will be described, as well as the computational model used. In the third section, the preliminary results will be presented and described. The final section includes a summary of the work performed, as well as future steps that will be developed.

## 2. MATERIALS AND METHODS

The Lombardy Regional Environment Protection Agency (ARPA Lombardia) provides citizens, companies, and organisations with constant air quality and meteorological measurements. Measurements are obtained using a ground network composed of 84 fixed stations with a 10-minute temporal resolution. After data is obtained, it is shared through its data portal (http://dati.lombardia.it) in an open and accessible fashion. Even though the agency provides data for all of the Lombardy Region, this work is focused on pollution measurement in urban areas, therefore only sensors present in Milan were used. The ground sensor data from ARPA used in this study were $NO_2$ ground concentrations, ambient temperature, wind speed, precipitation, global radiation and relative humidity. Data is provided in Comma-Separated Values (CSV) format.

For the satellite component, data from tropospheric $NO_2$ Sentinel-5P measurements were used. The reason for this is that this satellite is currently the one that provides the highest spatial resolution for $NO_2$ tropospheric measurements among satellites. An example of this is the OMI satellite from the National Aeronautics and Space Administration (NASA) which has a spatial resolution of 13 km × 24 km and daily time resolution[8]. Sentinel-5P data is provided with a daily temporal resolution and in NetCDF format. Due to the current incapability of ESA's web portal (https://s5phub.copernicus.eu/dhus) to provide Sentinel-5P data downloads in batch mode, the CREO DIAS (https://creodias.eu/) was used.

Facebook (now Meta) developed a service to deliver information to the scientific community in response to crises and emergencies. This service is offered through the Facebook Data for Good platform (https://dataforgood.facebook.com/). We used the Facebook Mobility Maps for this project to consider Facebook users' movements and understand the influence of anthropogenic dynamics on $NO_2$ emissions.

### *2.1 Computational Model*

Estimating daily atmospheric $NO_2$ concentrations at ground level is the final goal of this model. Through a Long Short Term Memory (LSTM) artificial neural network, we employed a neural network Non-Linear Multivariate Autoregressive Model. Many of the issues with other networks are solved by the supervised learning prediction architecture known as LSTM. This can carry long-term dependencies into the future[9].

The Python programming language was used to implement the LSTM neural network. It was chosen as the programming language since it has been the site of the creation of numerous scientific libraries. TensorFlow and SciKit-learn were the scientific libraries utilized in this work (https://www.tensorflow.org/ and https://scikit-learn.org/, respectively). TensorFlow was used to generate the LSTM model, while SciKit-learn was used to prepare the data to be utilized as an input to the model.

### *2.2 Methodology*

Three steps made up the methodology used for this project (data processing, training, testing and validation). A little more than 80% of the project's time was spent on data processing. The end product was a Python processing pipeline that automatically introduces and processes each dataset. A dataset containing movement from Facebook and weather data from ARPA Lombardia was used for the training process. The ARPA $NO_2$ ground average reading for each day of the year was provided as the searched output. In this manner, the LSTM could comprehend that a particular set of variables will lead to a particular ground $NO_2$ measurement. The testing phase consisted in generating a predicted $NO_2$ measurement and comparing it with the real results (i.e. the RMSE was used as a measure of error)[10].

## 3. RESULTS

Results show that the daily $NO_2$ forecasts from the LSTM model are reasonably close to the actual observed values at the ground level. Thus, both satellite and meteorological indicators can help to explain a portion of the ARPA atmospheric $NO_2$ data. In this instance, the RMSE is on the order of 2.5 $g/m^3$ units. Original data ranges from a minimum of about 10.97 $g/m^3$ to a maximum of 58.96 $g/m^3$ with a mean of 32.2 $g/m^3$ and a standard deviation of 10.52 $g/m^3$. The RMSE measurement shows that the predicted values enhance the satellite $NO_2$ estimation, but it is still unclear whether they can be utilized as a preliminary benchmark for ground air quality. The data trend shows that the model can produce values that are reasonably close to reality. It can also be observed that, by now, the algorithm is not predicting well days with abnormal concentrations.

## 4. SUMMARY

In this work, we have created a computational model that calculates ground $NO_2$ air concentrations starting from April 2020 until April 2022. We used an artificial neural network LSTM algorithm that enables the system to be trained with long time series of data. This work can be used as a baseline for future studies of pollution prediction by using a combination of Sentinel-5P and pollution ground measurements. Future steps will focus on estimating air quality based only on meteorological satellites and Sentinel-5P.

## References


[1] Z. Zhang, J. Wang, and W. Lu, "Exposure to nitrogen dioxide and chronic obstructive pulmonary disease (COPD) in adults: a systematic review and meta-analysis," Environ. Sci. Pollut. Res., vol. 25, no. 15, pp. 15133–15145, May 2018, doi: 10.1007/s11356-018-1629-7.

[2] EEA, "Health impacts of air pollution in Europe, 2021," Eionet, 2021. https://www.eea.europa.eu/publications/air-quality-in-europe-2021/health-impacts-of-air-pollution (accessed Jun. 07, 2022).

[3] United Nations, "The sustainable development goals report 2020." 2020. [Online]. Available: https://sdgs.un.org/goals

[4] R. W. Pinder, J. M. Klopp, G. Kleiman, G. S. W. Hagler, Y. Awe, and S. Terry, "Opportunities and challenges for filling the air quality data gap in low- and middle-income countries," Atmos. Environ., vol. 215, p. 116794, Oct. 2019, doi: 10.1016/j.atmosenv.2019.06.032.

[5] D. Oxoli, J. C. Jimenez, and M. Brovelli, "ASSESSMENT OF SENTINEL-5P PERFORMANCE FOR GROUND-LEVEL AIR QUALITY MONITORING: PREPARATORY EXPERIMENTS OVER THE COVID-19 LOCKDOWN PERIOD," Int. Arch. Photogramm. Remote Sens. Spat. Inf. Sci., vol. 44, no. 3/W1, 2020.

[6] EEA, "Emissions from road traffic and domestic heating behind breaches of EU air quality standards across Europe," Eionet, Feb. 16, 2022. https://www.eea.europa.eu/highlights/emissions-from-road-traffic-and (accessed Jun. 08, 2022).

[7] H. Diémoz et al., "Transport of po valley aerosol pollution to the northwestern Alps–Part 1: Phenomenology," Atmospheric Chem. Phys., vol. 19, no. 5, pp. 3065–3095, 2019.

[8] N. Earth Science Data Systems, "OMI," Earthdata, 2022. http://www.earthdata.nasa.gov/sensors/omi (accessed Jun. 09, 2022).

[9] A. Nielsen, Practical time series analysis: Prediction with statistics and machine learning, First. O'Reilly Media, 2019.

[10] T. Hastie, R. Tibshirani, and J. Friedman, The Elements of Statistical Learning: Data Mining, Inference, and Prediction, 2nd ed. Springer, 2017. [Online]. Available: https://hastie.su.domains/ElemStatLearn/printings/ESLII_print12_toc.pdf

# Low-light-level Detection of Migrant Worker Population Flow in Anhui and Henan Provinces During Spring Festival

WANG Zhao

Aerospace Information Research Institute, Chinese Academy of Science, Beijing, 100094, China
email: wangzhao21@mails.ucas.ac.cn

## 1. INTRODUCTION

Migrant workers are the main force driving China's industrialization and urbanization. They have become the main body of industrial workers in China. They are a strong support for "Made in China" to go to the world, and they have made a huge contribution to economic and social development.

Studying the population flow of migrant workers can provide ideas for solving migrant workers' problems and promoting rural revitalization. Since the Reform and Opening Up, with the improvement of the urbanization, migrant workers are mainly flowing from the countryside to the city. The rural revitalization strategy has been proposed in recent years, many migrant workers prefer to return home to start their own businesses. Sorting out the flow of migrant workers is of great significance to explore its driving mechanism and promote coordinated development [1].

Anhui and Henan are populous provinces of migrant workers. To solve the problem of how to construct noctilucent data based on low-light sensor to model population flow, this project detects migrant workers' population flow in Anhui and Henan provinces during the Spring Festival by using high spatial resolution low-light-level image, establishes the relationship between urban information and population spatial distribution based on the automatic matching of low-light-level image and multi-spectral image, and explores the relationship between migrant workers' return to their hometown and rework and regional lighting changes during the Spring Festival.

## 2. MATERIALS AND METHODS

In this study, SDGSAT-1 low-light-level data and multispectral image data of Anhui and Henan before and after Spring Festival in recent five years were used. These data are provided by the SDGSAT-1 remote sensing satellite from the International Research Center of Big Data for Sustainable Development Goals. The data have been preprocessed by radiometric, atmospheric, and geometric correction. The range width of low-light-level image is 300km, and the spatial resolution of panchromatic and color low-light data is divided into 10m and 40m. The multispectral image has a range width of 300 km and a resolution of 10m.

### *2.1 Low-light-level image filtering*

Low-light-level image can obtain the intensity and partial information of light efficiently, but it has the disadvantages of small dynamic range, low contrast, and low signal-to-noise ratio. Therefore, it is necessary to preprocess the low light level image with enhancement and denoising.

### *2.2 High precision automatic registration for low-light-level and hyperspectral images method*

Low-light-level image and multispectral image are from different sensor. The multispectral image can detect the distribution and type of buildings in the target area. The low-light-level image can detect the population and distribution according to the light. The main content of this project is to 1) carry out automatic registration and fusion of data of two modes. 2) Study the detection ability of low-light-level image on population migration. 3) Superimpose human living area extracted from multi-spectral image and population distribution extracted from low-light image to analyze the general changes of population in the target area.

This method mainly includes three parts:

(1) Construction of the multi-modal image block pair sample library by using artificial production combined with sample expansion based on Generative Adversarial Network (GAN).

Firstly, we choose some typical multi-modal images with different terrain, different season, different surface coverage of the area. We select the same name points for multi-modal images and then use classical correction models such as polynomial models and rational number models for registration. Then we crop the multimodal image block pairs with a certain size. Each sample contains blocks of the same size with different modal data in the same area, which means that the center point of each modal block is consistent in geographical location. Finally, build a preliminary sample database with certain number of collected samples.

Traditional methods and Deep Learning can be used to expand the sample database. Traditional methods include image rotation, image flipping, changing contrast, adjusting brightness, transforming saturation, adding color perturbation, etc. The sample augmentation method based on GAN can make the model automatically generate abundant unknown samples and increase the scene complexity of samples in the sample base.

(2) Construction of image block pair similarity judgment network based on triplet twin network

The structure of the triplet twin network is shown in Fig.1. A pair of samples were selected from the sample base, which were called anchor points and positive examples respectively, and then other unpaired hetero-modal image blocks were randomly selected from the sample base as negative examples. Feature extractor uses deep convolutional network to extract texture features of image blocks, such as VGG and U-Net. After the three input image blocks enter the same feature extractor, the corresponding 3d feature tensor is obtained as the eigenvalue of similarity calculation. The similarity between features can be measured by the Sum of Squared Difference (SSD). The smaller the SSD between two features, the more similar they are.  Combined with the ternary loss training network model, make the distance from the positive example to the anchor tends to 0, make the distance from the negative example to the anchor tends to infinity. This means that if two image blocks with different modes correspond to the same geographical location, the features learned by the network are similar. Otherwise, the features learned have no similarity at all. This enables the network to judge the similarity of image blocks of different modes. Then serve as a homonym search tool for multi-mode image registration to complete image registration.

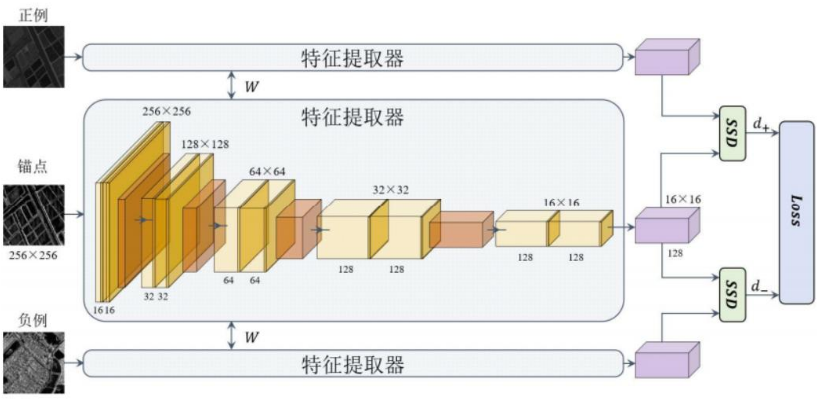


**Fig. 1.** Captions should be placed below the figure. Please use graphics fonts large enough to be clearly readable. Figures captions should be 9pt. Times New Roman, centred, numbered with Arabic numbers.

(3) Acceleration of inference speed of image block matching network using Fourier Transform (FT).

The matching method based on image block uses sliding window to generate similarity hot map. It takes the most similar point as the result. FT can Transform the sliding window from space domain into frequency domain. It will greatly reduce the time and space overhead required to match points with the same name.

### *2.3 Detection of population distribution*

There are three main technical routes for population detection:

(1) Extraction of luminance value (DN value) of low light level data

The extraction of DN value requires the desaturation of noctilucent image first. The nighttime light brightness in the urban center far exceeds the maximum brightness of the sensor, resulting in serious oversaturation in the central area where the lights are concentrated. Some classical noctilucent index desaturation, such as the index of Nighttime Light (NTL), Index of Corrected Nighttime Light (CNTL), Vegetate on Adjust NTL Urban Index (VANUI) and other indexes can fix this problem [2]. Then, exclude some light information of non-human habitation by using maximum entropy threshold segmentation. When entropy is maximum, the uncertainty between foreground and background is maximum. Then set it as the threshold of the image.

(2) Construction of population parameter

The low-light-level sensor of SDGSAT-1 consists of a panchromatic band and RGB bands. The color bands can describe some radiation indices closely related to human activities, such as the brightness of construction land, water area, arable land, and forest land. These parameters can be used as independent variables in population distribution modeling.

(3) Spatial modeling of population distribution

Studies have shown that there is a strong correlation between population distribution and light intensity characterization at night [3-4]. Two sets of independent variable indexes could be established by statistically analyzing the area with light, area without light and total radiation brightness of various land use types. Pearson correlation analysis will tell the degree of correlation between selected indicators and population size. The closer the coefficient is to 1, the stronger the correlation between variables. In this project, lighting statistics of various plots at the township scale were taken as independent variables and demographic values as dependent variables. Using Pearson correlation analysis to fit the regression parameters. According to the correlation between brightness statistics and population distribution.

The population migration of the target area can be analyzed by superposing the residential layer extracted from the multi-spectral data and the population distribution map extracted from the low-light-level data. Based on the mask of residence, different accommodation indexes are set for different buildings. Then the accommodation distribution map with the same spatial grid size as the population distribution map can be calculated. Superimposed on the estimated population map, the vacancy rate can be further calculated. Combined with the statistical yearbook of the local government, the data of migrant workers in the target area and their spatial distribution can be analyzed. Thus, we can roughly figure out the rate of migrant workers going out to work and returning home during the Spring Festival in the target region.

## 3. RESULTS

The low-light-level detector can get information about the intensity and distribution of lights at night. Traditional methods for demographic or economic surveys based on low-light-level images do not have high spatial resolution. Therefore, the method of modeling the correlation between low-light-level images and population or economic factors in a large-scale grid is mainly used. SDGSAT-1 has high spatial resolution noctilucent data. It can directly model the spatial distribution of population, but the modeling ability needs to be further explored.

## 4. SUMMARY

Preliminary results of the experiment suggest that the accuracy of geometric registration of low-light-level image and multispectral image can be locally improved to pixel level. Median filtering can eliminate image noise and preserve object boundary. The low-light-level data can detect population spatial distribution and population flow.

## References

[1] Jiang Z., Wang J., Yin W., Zhu Y. (2022) Spatio-temporal preference and driving mechanism of migrant workers' mobility in China: based on the data of the National floating population dynamic monitoring survey from 2011 to 2018 [J]. Journal of Central China Normal University (Natural Sciences), 47(01):1-13
[2] Zhang X., Hu Y., Fan Y. (2015) The Detection of Urbanization Process by VANUI Index in Jing-Jin-Ji Area from 2001~2012[J]. Remote Sensing Technology and Application, 30(6):1153-1159.
[3] Li P., Hong H. (2015) Estimation of Urban Population in Guangdong Province Based on DMSP-OLS Lighting Data [J]. Journal of South China Normal University (Natural Science Edition), 47(02): 102–107.
[4] Wang X., Ning X., Zhang H., et al. (2022) Population spatialization by integrating LJ1-01 nighttime light and WeChat positioning data—taking Beijing city as an example [J]. Science of Surveying and Mapping, 47(2):173-183.

# Inversion of Urban Aerosol Optical Depth Based on SDGSAT-1 Night-Time Light Imagery

JIANG Yichen [1,2,3], TANG Yunwei [1,2], JING Linhai [1,2]

[1] Key Laboratory of Digital Earth Science, Aerospace Information Research Institute, Chinese Academy of Sciences, Beijing 100094, China

[2] International Research Center of Big Data for Sustainable Development Goals, Beijing 100094, China

[3] College of Resource and Environment, University of Chinese Academy of Sciences, Beijing 100094, China

email: jyc350802@gmail.com
email: tangyw@aircas.ac.cn
email: jinglh@aircas.ac.cn

## 1. INTRODUCTION

In 2015, 17 Sustainable Development Goals (SDGs) were proposed to support the 2023 Agenda for Sustainable Development. Among them, SDG 11.6 aims to reduce per capita negative environmental impacts in cities [1], with a particular attention to the air quality (SDG 11.6.2). Aerosols in the atmosphere not only affect the Earth's climate and ecosystem through direct and indirect radiative forcing, but also can enter the respiratory tract with human respiratory activities and partially deposit in the lungs, thus causing lesions and threatening human health [2]. The Aerosol Optical Depth (AOD) is an important parameter to characterize the degree of aerosol effect [3]. The inversion of AOD can help understand the urban pollution and climate change.

Many studies calculated AOD from night-time light images [4, 5]. Currently, the widely available night-time light images such as Defense Meteorological Satellite Program's Operational Line-Scan System (DMSP/OLS) and Suomi National Polar-Orbiting Partnership Satellite's Visible Infrared Imaging Radiometer Suite (Suomi NPP/VIIRS) are not enough to reflect the human activity at a fine resolution [5]. The Sustainable Development Science Satellite 1 (SDGSAT-1) is the world's first science satellite dedicated to serving the 2030 Agenda. The Glimmer Imager for Urbanization (GIU) of SDGSAT-1 includes a panchromatic band and three multicolor bands (RGB), with the spatial resolution of 10 m and 40 m, respectively. As the first multicolor GIU with a high spatial resolution, it can serve for the elaborate monitoring of air pollution, and thus is especially suited to the inversion of the urban AOD.

In this study, we estimated the urban AOD using the 10 m GIU of the SDGSAT-1 satellite. The AOD result was compared with that derived from the VIIRS imagery and verified by the Aerosol Robotic Network (AERONET) site data. This study demonstrates an effective measure for the inversion of the AOD product from SDGSAT-1 GIU data, and thus provides a technical solution to monitor the urban pollution at the fine scale so as to achieve SDG 11.6.2.

## 2. MATERIALS AND METHODS

### *2.1 Study area and data*

The study area is located in the center of the Beijing City, the capital of China. The panchromatic images of SDGSAT-1 GIU were used for the inversion of the AOD, with a spatial resolution of 10 m. The AOD inversion method relies on the multi-temporal images to provide a base map (see the detailed method in Subsection 2.2). Therefore, three GIU images were involved for the AOD inversion, with the acquisition dates of November 26, 2021, January 3, 2022 and February 4, 2022. The VIIRS/Day-Night Band (DNB) data, with a spatial resolution of 400 m, were used in the same way to provide a benchmark result. The three VIIRS/DNV images were acquired on November 26 to 28, 2021. Only one image on November 26, 2021 was used for comparison. Two site data (Beijing and Beijing-RADI) were available on that day from the AERONET to provide verification data.

### *2.2 Method*

The urban AOD is calculated by the following equation [5].

$$\tau = -\mu \ln\left(\frac{\Delta I_{sat}}{\Delta I_a}\right)$$

where $\tau$ denotes the urban AOD, $\mu$ denotes the zenith angle, $\Delta I_{sat}$ denotes the spatial deviation of the radiation, and $\Delta I_a$ represents the inherent spatial deviation of the urban lighting under the conditions of no aerosol, no cloud and no moonlight.

McHardy [5] indicated that standard deviation can be a substitute of the spatial deviation. Therefore, this study used the standard deviation in a local spatial template to represent the spatial deviation of urban light. To derive $\Delta I_a$, the standard deviation was calculated for each of the multi-temporal images, and the maximum value was used as the inherent spatial deviation to provide a base map. $\Delta I_{sat}$ was directly calculated through standard deviation from each image. Since the inversion of AOD is only suited to the urban area, it is necessary to determine the urban pixels from the GIU data. Suggested by McHardy [5], the pixels with the radiation value greater than 1.5 times the overall average are assumed as the urban pixels.

## 3. RESULTS

### *3.1 Inversion results*

Fig. 1 shows the original night-time light images of SDGSAT-1 and VIIRS/DNB, and their AOD inversion results on November 26, 2021.

(a) Panchromatic image of SDGSAT-1 GIU

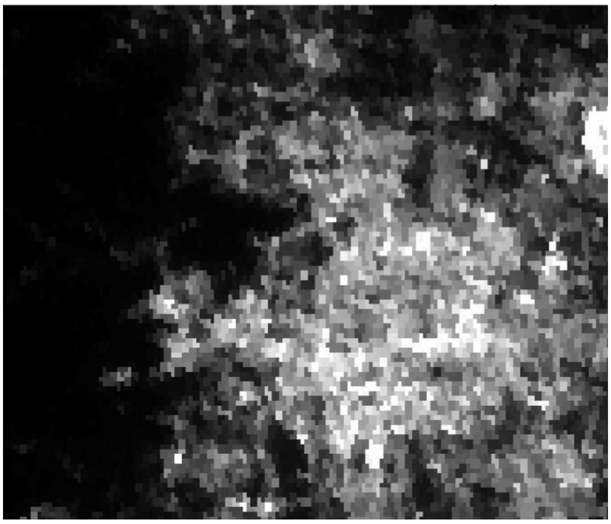

(b) VIIRS/DNB image

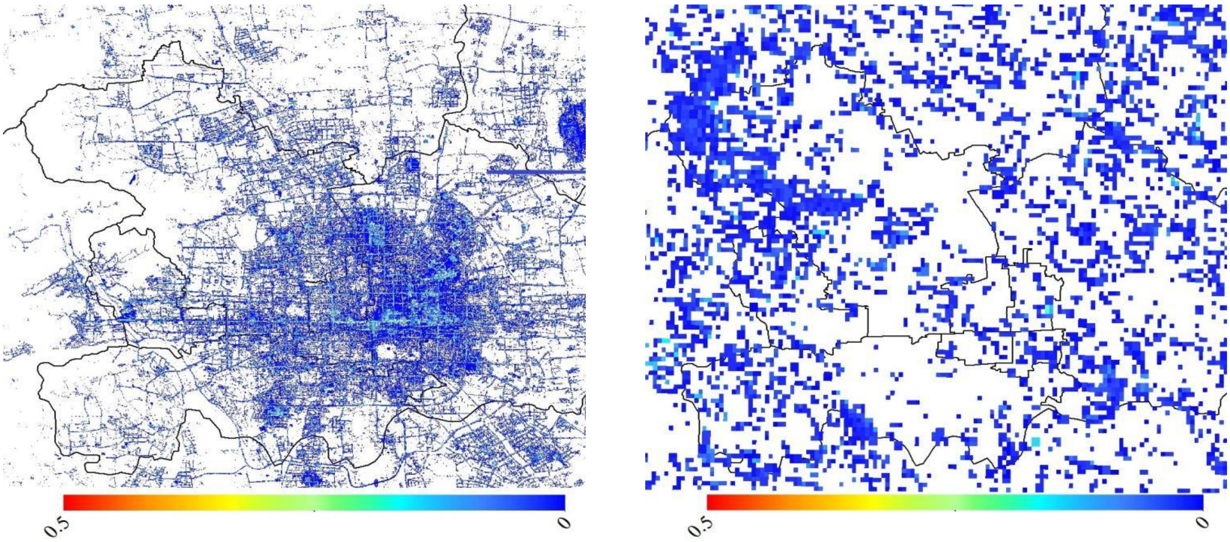


(c) AOD inversion result based on SDGSAT-1 GIU data (d) AOD inversion result based on VIIRS/DNB data

**Fig. 1.** SDGSAT-1 GIU and VIIRS/DNB and the AOD inversion results

It can be seen that the AOD results of both show high values in the city center and low values in the surroundings, which accords with the general rule: the city center tends to have turbid the atmosphere and low atmospheric transmittance, whereas the suburbs of city are with cleaner atmosphere and higher atmospheric transmittance. Due to the limitation of the spatial resolution of the VIIRS/DNB data, its AOD result cannot accurately reflect spatial details of the city. In contrast, the AOD result based on the SDGSAT-1 shows stronger spatial continuity within the same value range, which can retrieve the AOD details of buildings and streets at an unprecedented fine scale.

### *3.2 Comparison with AERONET AOD data*

Two AERONET site data were available on November 26, 2021 and February 4, 2022 (although with 4 hours' difference with the satellite transit time). Fig. 2 shows the correlation between AOD products retrieved from SDGSAT-1 GIU data and AERONET site data. The squared Pearson correlation coefficient ($R^2$) was assessed. The goodness of fit $R^2$ between inversion results and AERONET data is 0.71. In Wang's results [6], the goodness of fit ($R^2$) between AOD products produced by the VIIRS/DNB data and AERONET site data was 0.69. The result shows that the correlation of AOD products derived from SDGSAT-1 was higher than that from the VIIRS / DNB data.

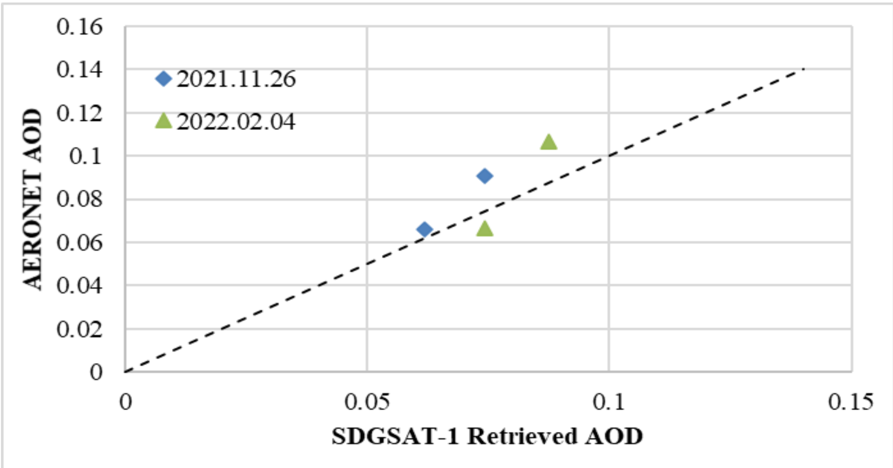


**Fig. 2.** Comparison of AOD inversion results of two phases with AERONET site data.

## 4. SUMMARY

In this study, the AOD product in the Beijing city was retrieved from the SDGSAT-1 GIU data. Compared with the AOD result based on the VIIRS/DNB data and AERONET site data, this study proved that the AOD result based on the SDGSAT-1 GIU data not only has a higher accuracy, but also includes richer spatial details. This AOD inversion method can accurately reflect the status of urban pollution, and can be extended to the other city areas to provide elaborate global monitoring data for the implementation of SDG 11.6.2.

## References


[1] United Nations. (2015) Transforming our world: the 2030 Agenda for Sustainable Development. Division for Sustainable Development Goals: New York, NY, USA, https://sustainabledevelopment.un.org/post2015/transformingourworld.

[2] 姜梦蝶, 陈林, 何玉青, 胡秀清, 刘明奇, 张鹏. (2022) 利用 NPP/VIIRS 微光数据反演夜间气溶胶光学厚度. 遥感学报, 26 (3): 493-504.

[3] Li, Z., He, X. (2018) Analyzing the relationship between aerosol optical depth and GDP in China by integrating MODIS and nighttime light data. In 2018 7th International Conference on Agro-geoinformatics, 1-6.

[4] Johnson, R. S., Zhang, J., Hyer, E. J., Miller, S. D., Reid, J. S. (2013) Preliminary investigations toward nighttime aerosol optical depth retrievals from the VIIRS Day/Night Band. Atmospheric Measurement Techniques, 6 (5): 1245-1255.

[5] McHardy, T. M., Zhang, J., Reid, J. S., Miller, S. D., Hyer, E. J., Kuehn, R. E. (2015) An improved method for retrieving nighttime aerosol optical thickness from the VIIRS Day/Night Band. Atmospheric Measurement Techniques, 8: 4773-4783.

[6] Li, X., Li, X., Li, D., He, X., Jendryke, M. (2019) A preliminary investigation of Luojia-1 night-time light imagery. Remote Sensing Letters, 10 (6): 526-535.

[7] 王锋. (2017) 基于微光数据的夜间亮目标表观反射率特性和城市光学厚度反演研究. 硕士论文, 国防科技大学.

# Smart and Resilient Cities Leveraging on Open Data

Mogire[1], Wafula[2], Waweru[3]
[1]South Eastern Kenya University, P.O. Box 170, Kitui, 90200, Kenya
email: omogire@seku.ac.ke
[2,3]Jomo Kenyatta University of Agriculture and Technology, P.O. Box 62,000, Juja, 00200, Kenya
email: [2]muliaro@icsit.jkuat.ac.ke ;[3]waweru_mwangi@icsit.jkuat.ac.ke

## 1. ABSTRACT

Cities have become attractive destination to many people who are at their prime age looking for employment and quality lifestyle. They are hot beds of economic growth, innovations and cultural melting pots. According to International Telecommunication Union (ITU) report, by 2050, more than 70% of the world's population is projected to live in cities with high urbanization expected in Asia and Africa. This unprecedented urbanization brings with it a number of resources and sustainability challenges. Goal no 11 in the 17 Sustainable Development Goals (SDGs) of 2015; successors of the 8 Millennium Development Goals (MDGs) of 2000, unveiled by UN emphasizes on smart data to leapfrog building smart, resilient and sustainable cities by 2030. Smart open data, can be used to plan, implement, monitor the progress towards this envisaged dream in 2030 agenda. The UN recognized vitality of open data by embodying data revolution principles which emphasizes on open data that meets FAIR principle (**F**indability, **A**ccessibility, **I**nteroperability and **R**eusability) towards 2030 vision. Towards this end, many smart cities initiatives have been launched around the world aimed at arresting impending city challenges in order to actualize the global dream. Yet, the potential of open data is not yet fully leveraged in these initiatives due to its newness and ecosystem challenges. This research sought to underscore the significance of "smart" open data to leapfrog smart and sustainable cities. Synthesis of findings from research literature review through quantitative and qualitative analysis based on narrative reviews of scientific publications, case studies and interviews with expert underscore disintegrated and uncoordinated city initiatives, hence proposes an integrated novel smart city framework leveraging on "smart" open data to build inclusive, safe, resilient, sustainable cities as envisaged in vision 2030.

Keywords: Open Data, Smart Data, Smart Cities, Sustainable Cities, SDG11

## 2. INTRODUCTION

Smart cities have been painted as the "magic bullet" to all urbanization challenges and envisaged opportunities [1, 2]. As such, they are indispensable to nations, hot beds of economic growth, innovations and are cultural melting pots. Up to 80percent of world's GDPs is generated in cities, making them engines of economies [3, 4, 5, 6, 7]. This is an indication that cities have salient features and a cultural identity as well as present a multitude of opportunities for business, entrepreneurs, innovations, and quality life [6]. Given these attributes, cities attract people from rural areas seeking employment opportunities and excellence lifestyle [4]. As such, cities continue to witness megatrends of population growth, with more than 50 percent of world population living in cities currently and projected to reach 70 percent by 2050 [19]. This is an indication that cities is bound to face serious challenges from sustainability of infrastructure to environment to effective service delivery if no action is taken [3, 4, 5, 10, 11, 12, 13, 19]. For example, cities demand two thirds of the global energy at the same time producing up to 7 percent of the global greenhouse gas emissions. Buildings alone accounts 40 percent of the world's energy use producing a $1/5^{th}$ of the world's $CO_2$ emissions. At the same time, 75 percent of global natural resource consumption happens in cities while a third of people in developing countries living in cities live in slums [14]. In addition, there has been a proliferation of cases of social instability in some cities around the world due to unemployment, widening income inequalities and marginalization. Inadequate and lack of affordable housing, proliferation of informal dwellings, as well as sewerage and sanitation problems, air and water pollution, traffic congestion, urban violence and crime also constitute major challenges to urban governments and policymakers [8]. In 2016, 91% of the urban population globally were breathing air that did not meet the World Health Organization (WHO) air quality guidelines value for Particulate Matter

(PM 2.5). More than half were exposed to air pollution levels at least 2.5 times higher than that safety standard and is estimated that 4.2 million people died as a result of high levels of ambient air pollution [27]. Consequently, smart solutions have been championed to reverse this trend and tackle myriad city challenges, although many of these solutions are neither leveraging IoT nor smart open data generated by citizens hence they are not aligned with sustainability targets envisaged in 2030 agenda, thereby generating the concept of smart sustainable cities [15]. A smart sustainable city is an innovative city that uses ICT technologies and other means to improve quality of life, efficiency of urban operation and services, and competitiveness, while ensuring that it meets the needs of present and future generations with respect to economic, social, environmental as well as cultural aspects [16]. Smart cities has the ability to leverage on technology and use big data generate by citizens every second to achieve convenience and efficiency by optimizing resources. A smart city targets energy savings and adopts environmentally-friendly technologies, which helps promoting sustainable development. All successful smart cities benefit from the monetization of municipal services. It can range from installing paid parking meters, to collecting public macro-data such as car parking spaces, congestion, bins, energy and water use, satellite imagery, population density, and crime statistics. The data is then converted into useable information, accessible through subscriptions. In the wake of unprecedented urbanization challenges, intelligent technologies anchored in smart open data must be leveraged to ensure smart sustainable development envisaged in the UN 2030 agenda. The UN SDGs are the 17 ambitious goals envisaging poverty eradication, systematic tackling of climate change through Sendai framework, building peaceful, resilient, equitable and inclusive societies.This study sought to review literature with case studies in urbanization and associated challenges, smart cities, open data and SDGs, specifically goal no. 11 that has branded smart cities as a "magic bullet" to all urbanization challenges and opportunities. The Analysis of the findings is then used to propose an integrated novel framework towards intelligent and sustainable cities leveraging on open data. The research output adds to the existing body of knowledge about smart cities and open data and acts as a guide to policy makers and city governments for emerging cities in order to leapfrog into 21st century sustainable development agenda and beyond.

## 3. METHODOLOGY

This research methodology used sought to underscore the significance of open data to leapfrog smart and sustainable cities. Synthesis of findings from research literature review through quantitative and qualitative analysis based on narrative reviews of scientific publications, case studies and interviews with expert underscore disintegrated and uncoordinated city initiatives, hence proposes an integrated novel conceptual smart city framework leveraging on open data to build inclusive, safe, resilient, sustainable cities as envisaged in vision 2030.This is visualized in Fig. 1. Based on the inputs obtained from literature review and case studies a conceptual framework to underpin planning, implementation, monitoring and evaluation of Smart cities is developed. Fig. 2 shows the methodology for building conceptual smart sustainable city framework.

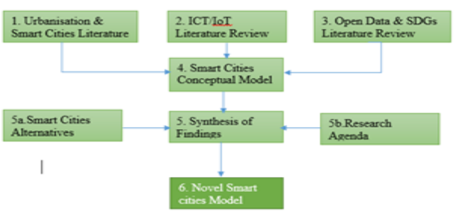


Fig.1 Research methodology adopted

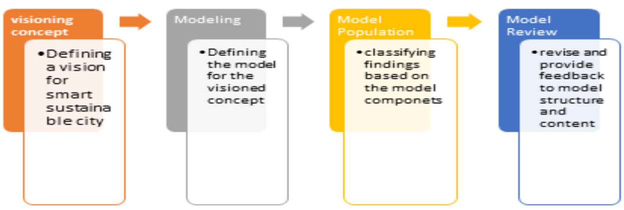


Fig. 2. Methodology for building conceptual smart sustainable city Framework

## 4. CITIES AND URBANIZATION

Over 80 percent of the GDPs is generated in cities [4, 6]. By 2020, cities will create huge business opportunities with a market value of $1.5 Trillion [4, 6]. Cities leveraging on open data catalyzed by IoT technologies by 2025, a cross-sector, will have a total potential impact of $3.9 trillion–11.1 trillion per year, as distributed in Fig. 3 [17]. Thus, cities present many socio-economic benefits and have gained traction globally. By 2014, 54% of the world's population lived in urban areas with Asia hosting 53%of the world's urban population, Europe 14%, and Latin America and the Caribbean 13%. The current trend shows that in every one second, urban population increases by 2 people [18]. Globally by the year 2050, approximately 70% of global population that is projected to be 9.6 billion will live in cities, with the fastest growing cities of less than 1 Million inhabitants being in Asia and Africa [12, 18, 19]. Albeit, cities the way they are planned and governed, are not prepared to cope up the ongoing demographic changes and related challenges. This situation, has the potential to become critical and irreversible in the near future if not acted upon urgently. Nevertheless, data generated from citizens and IoT in urban development, if aptly used, have the potential to become the driving force underpinning smart cities envisaged in the global agenda of 2030; SDGs goal no. 11 thereby reversing the trend. Accordingly, there is a desperate need for the cities to get smarter to handle this large-scale urbanization, challenges, manage complexities, increase efficiency, reduce cost, and improve quality of life. Smart Cities is the route to sustainable development envisaged in 2030 agenda if Open Data is well leveraged. By “smart”, we mean that the city is more sustainable, livable and efficient. The smart city market is estimated to reach an annual spending of about $16 billion (Fig.3.) by the year 2020 [9].

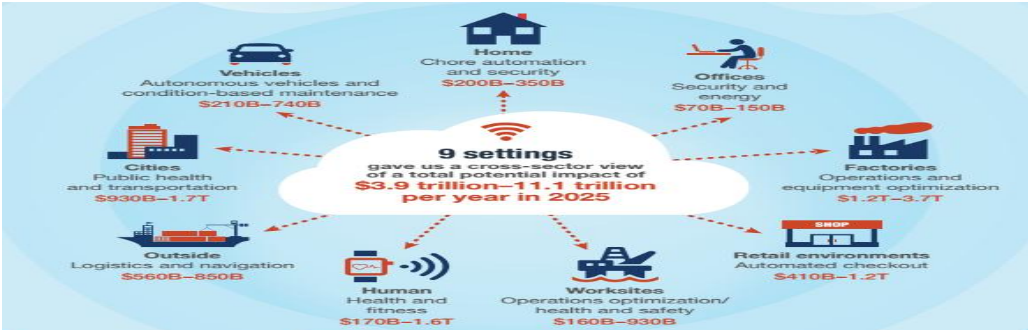


*Fig 3.* The Potential of IoT by 2025 in various sectors [17]

Research indicates that 62% of the Sub-Saharan Africa urban population and 43% of the urban population of South-Central Asia lives in temporary housing. One in four urban citizens does not have access to improved sanitation. Again 27% of the urban population in the developing world has no access to piped water at home. Further cities account for about 67 % of the global energy demand. Buildings represent about 40% of the total energy consumption. Cities are responsible for up to 70% of harmful greenhouse gases [18, 25, 26]. Further, a third of people in developing countries living in cities live in slums, and as the world continues to urbanize, sustainability challenges will be increasingly affect cities, particularly in Africa and Asia. Persistent urban issues over the last 20 years include urban growth, changes in family patterns, growing number of urban residents living in slums, informal settlements, and the challenge of providing urban services. Connected to these persistent issues are newer trends in the urban governance and finance. Emerging urban issues include climate change, exclusion and rising inequality, rising insecurity and upsurge in international migration [19]. For example in South Africa, Enkanini, Stellenbosch slum was established in the year 2006, and by 2015 the population was of 80,000 while Mathare in Nairobi Kenya was established in 1963 and by 2017-2018 the population was 190,000 [20].

### *4.1. Cities and Sustainability*

The new urban agenda should promote smart and environmentally sustainable cities, resilient, inclusive, safe and violence-free, economically productive, better connected to and contributing towards sustained rural transformation. This is in line with the 2030 agenda for sustainable Development, especially Goal 11; to make cities and human settlements inclusive, safe, resilient and sustainable [19]. Such cities will lay the foundation for a better future—a future where cities care for environment, people, the earth, air, water and other natural resources based on the urbanization trends and challenges explained earlier. A city is smart and sustainable if it promotes the four strands of development- Social, Economical, Environmental and Institutional. Towards this goal, the concept of smart cities has emerged as a “magic bullet” to tackle urban sustainability challenges towards 2030 agenda [1-3]. The concept of ‘Smart’ and ‘Sustainable’ City varies among cities and around the globe. There can be no single approach for making a city both smart and more sustainable [6]. Each city is unique, with a unique economic, environmental and social context, and will have to determine a unique path to becoming smart and sustainable [12]. One in eight of the world's urban citizens lives in one of the 28 mega cities with more than 10 million inhabitants [12]. As envisaged in SDG 11 of the 17 SDGs that was unveiled 2015, presents a holistic approach to global sustainability by embracing economic, social and environmental developments. Goals 6, 7,11,12,15 and 17 shown in fig 10, relates to environment and unban developments envisaged to create smart and sustainable cities using innovative initiatives.

### *4.2 Data Revolution for Smart Sustainable Cities*

Smart city paradigm is associated with ICT technologies, IoT and Big data. However, little research on big data-open data role in smart cities is scanty. FAIR principles requires that open data be Findable: have sufficiently rich metadata and a unique and persistent identifier; Accessible: retrievable by humans and machines through a standard protocol; open and free; authentication and authorization where necessary; Interoperable: metadata use a 'formal, accessible, shared, and broadly applicable language for knowledge representation'; Reusable: metadata provide rich and accurate information; clear usage license; detailed provenance [21]. The open data in cities can be related to the environment, water, health, buildings, transport, weather, transport and traffic, statistics and finance. Open data helps in ensuring transparency across systems, driving the participation of citizens in governance and improving service delivery by virtue of leveraging data for the welfare of people at large. With open data, governments may fuel the set-up of groundbreaking services and businesses that render commercial and social value. Additionally, open data will facilitate coordination among multiple departments and increase the visibility of city coordinates for the delivery of services. Vision 2030, an ambitious agenda envisaging poverty eradication, systematic tackling of climate change, building peaceful, resilient, equitable and inclusive societies emphasizes on data release, data use and value addition and urgently calls everyone to mobilize the data revolution for all people and the whole planet in order to monitor SDGs progress, hold governments accountable and foster sustainable development [23]. Open data could help to accelerate the development of smart cities by connecting the people most capable of creating smart city solutions with the data needed to generate and support them. Smart Cities have a lot of potential to improve the circumstances of both developed and developing countries. Open Data Inventory and the 1st UN World Data Forum in 2017 Global Plan for Sustainable Development Data identified serious gaps in data and various levels of openness. A number of challenges in data availability to track progress towards implementation of SDG 11 also present significant barriers to assessing global progress on the goal. Numerous open data impediments that are legal, political, social, economic, institutional, operational and technical in nature that needs to be addressed using open data policy to fully leverage city sustainable developments envisaged in 2030 agenda. To move towards a new urban agenda, urbanization needs to be integrated, inclusive, resilient and sustainable. In realization of 2030 agenda, several approaches have been proposed towards smart and sustainable developments globally. The focus being on urban areas where the cities are concentrated. The novel integrated conceptual framework for smart city presented here is universal and adaptable to different national circumstances, based on key urbanization challenges and opportunities shared by all countries. Implementation of the framework must be integrated to address the inter linkages between the, social, economic, environmental and city governance objectives of sustainable development. To move towards more inclusive, resilient and sustainable cities in the all regions, global data revolution is key to attain effective and results-based implementation and monitoring of the new urban agenda at the local, national and global levels. Fig.4. Integrated smart sustainable Conceptual framework. The architecture including: (i) ICT infrastructure, IoT, Big Open data, and governance

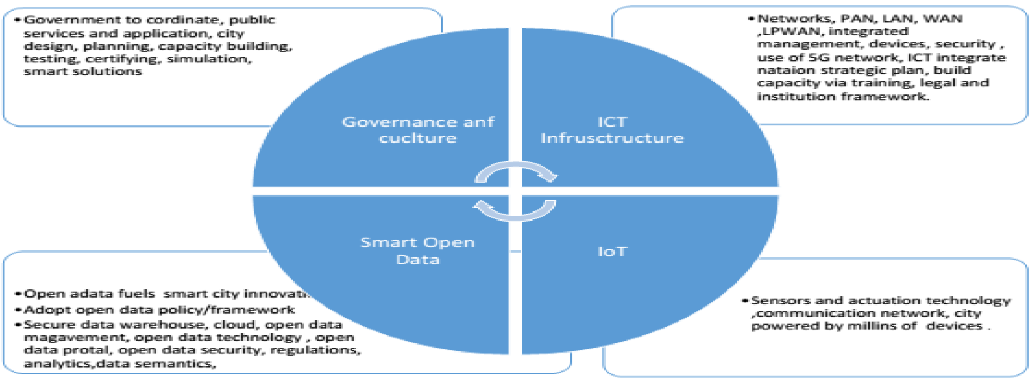

*Fig. 4.* An Integrated Novel Conceptual framework

## 5. SUMMARY

To move towards a new urban agenda, urbanization needs to be integrated, inclusive, resilient and sustainable. In realization of this agenda, several approaches have been proposed towards smart and sustainable developments globally as envisaged in 2030 agenda, however the role of open data in the same is scanty. Thus, the proposed framework provides an alternate to smart city design, planning, development, and monitoring by leveraging open data to enable policy makers to make informed decision. The novel conceptual framework for smart city presented here is universal and adaptable to different national circumstances, based on key urbanization challenges and opportunities shared by all countries. Implementation of the framework must be integrated to address both social, economic, environmental and city governance challenges. The need to move towards more inclusive, resilient and sustainable cities in the all regions, global data revolution is key to attain effective and results-based implementation and monitoring of the new urban agenda at the local, national and global levels.

## REFERENCES


[1] Shelton, T.; Zook, M.; Wiig, A ( 2014) The 'actually existing smart city'. Camb. J. Reg. Econ. Soc. pg, 8, 13–25.

[2] Paroutis, S.; Bennett, M.; Heracleous, L.(2014) A strategic view on smart city technology: The case of ibm smarter cities during a recession. Technol. Forecast. Soc. Chang. pg, 89, 262–272.

[3] ITU (2016). ICT policies and plans for transition to smart and Sustainable Development in Arab region

[4] United Nations, Department of Economic and Social Affairs, Population Division (2014).World Urbanization Prospects: The 2014 Revision, Highlights (ST/ESA/SER.A/352).www.worldgovernmetsummit.org

[5]United Nations. World Urbanization Prospects. United Nations, Department of Economic and Social Affairs, Population Division: the 2011 Revision: Highlights. 2012

[6] ITU-T Focus Group on Smart Sustainable Cities. (2015). Retrieved from: http://www.itu.int/en/ ITU T/focusgroups/ssc/Pages/default.

[7] Currid, E. (2006). New York as a global creative hub: A competitive analysis of four theories on World cities. Economic Development Quarterly, 20(4), 330–350. https://doi.org/10.1177/0891242406292708.

[8] PWC, "Making cities smart and sustainable," Inf. Exch. Group's Summit, 2015.

[9] Pike Research on Smart Cities [dedicates entire section to World sensing].Available: http://www.pikeresearch.com/research/smart-cities.

[10] Y. Sun et al.(2016). IoT and Big Data Analytics for SCCs. IEEE Access

[11] David, D. (2017). Environment and urbanization. The International Encyclopedia of Geography, 24(1), 31–46. https://doi.org/10.1002/9781118786352.wbieg0623

[12] Estevez, E., Lopes, N. V., & Janowski, T. (2016). Smart sustainable cities. Reconnaissance Study, 330.

[13] Han, J., Meng, X., Zhou, X., Yi, B., Liu, M., & Xiang, W.-N. (2016). A long-term analysis of urbanization process, landscape change, and carbon sources and sinks: A case study in China's Yangtze River Delta region. Journal of Cleaner Production, 141, 1040–1050

[14] Cities and climate change: global report on human settlements (2011). United Nations Human Settlements Programme

[15] Vinod Kumar, T. M., & Dahiya, B. (2017). Smart Economy in smart cities. In T. M. VinodKumar (Ed.). Smart economy in smart cities. International Collaborative Research:Ottawa, St.Louis, Stuttgart, Bologna, Cape Town, Nairobi, Dakar, Lagos, New Delhi,Varanasi, Vijayawada, Kozhikode, Hong Kong (pp. 3–76). Singapore: Springer. https://doi.org/10.1007/978-981-10-1610-3_1.

[16] UNECE (2015). Key performance indicators for smart sustainable cities to assess the achievement of sustainable development goals, 1603 ITU-T L.1603.

[17] Mckinsey Global Institute, The Internet Of Things: Mapping The Value Beyond The Hype 2015

[18] United Nations, Department of Economic and Social Affairs, Population Division (2015). World Population Prospects: The 2015 Revision, Key Findings and Advance Tables. Working Paper No. ESA/P/WP.241.

[19] United Nations Human Settlements Programme (UN-Habitat); Urbanization and Development: emerging Futures; 2016

[20] Conceptualising slum in an urban African context; Smit S, Musango JK, Kovacic Z, Brent AC (2017).

[22] https://www.europeandataportal.eu/en/using-data/benefits-of-open-data

[23] Transforming Our World: The 2030 Agenda for Sustainable Development.http://www.un.org

[24] Zuiderwijk, A. and Janssen, M. 2013 Open data policies, their implementation and impact: a framework for comparison. Government Information Quarterly, Vol. 31 No. 1

[25] The World Bank. 2014. "Energizing Green Cities: Solutions to Meet Demand and Spark Economic Growth." 2014–15

[26] UN-HABITAT. 2011. A Global Report on Human Settlement. Retrieved (http://mirror.unhabitat.org/downloads/ docs/E_Hot_Cities.pdf).

# SDG 13 (Climate Action): Accelerating Climate Change Mitigation and Adaptation

# Reduced Risks of Temperature Extremes From 0.5 ℃ less

## Global Warming in the Earth's Three Poles

DUAN Anmin [1,2,3], TANG Bin[1,2], HU Wenting[1,2], GAO Kailun[4], PENG Yuzhuo[1,2]

[1] State Key Laboratory of Numerical Modeling for Atmospheric Sciences and Geophysical Fluid Dynamics (LASG), Institute of Atmospheric Physics, Chinese Academy of Sciences, Beijing, China
email: amduan@lasg.iap.ac.cn

email: tangbin@mail.iap.ac.cn

email: hwt@lasg.iap.ac.cn

email: yuzhuo@lasg.iap.ac.cn

[2] University of Chinese Academy of Sciences, Beijing, China
[3] State Key Laboratory of Marine Environmental Science, College of Ocean and Earth Sciences, Xiamen University, Xiamen, China
[4] Beijing Municipal Climate Center, Beijing, China
email: gaokl@lasg.iap.ac.cn

### 1. INTRODUCTION

The Arctic (north of 60°N), Antarctica (south of 60°S), and the so-called "Third Pole," the Tibetan Plateau (TP; 25°–45°N, 65°–105°E; altitude >2,000 m), together termed "Earth's three poles", are highly sensitive to global warming (Li et al., 2020; Gao et al., 2019; Rintoul et al., 2018; Sui et al., 2017). Climate change in these regions may trigger a series of climatic responses that can lead to global consequences (Fang et al., 2021; You et al., 2021; Li et al., 2020). For instance, the decline in sea ice under global warming in the Arctic and Antarctica will likely cause a rise in sea level in the coming centuries, thus affecting corresponding plans or measures to adapt to and mitigate against such changes (Rintoul et al., 2018). Likewise, warming in the TP region may affect water resources in downstream areas (Pithan, 2010; You et al., 2016). Since enormous challenges are inevitable in polar regions in terms of sustainable development alongside increasing human activities, efforts to understand and project climate change over the Earth's three poles under global warming scenarios are crucial for risk assessment and policymaking aimed at coping with future climate change (Siegert, 2016; Ford et al., 2015; IPCC, 2014).

### 2. MATERIALS AND METHODS

#### *2.1 Observations and CMIP6 Model Outputs*

Daily gridded minimum and maximum temperature data at a resolution of 0.5°×0.5° provided by the European Center for Medium-Range Weather Forecasts (ECMWF) Interim Re-Analysis (ERA-Interim) data set were employed as observational data to evaluate the historical simulations of CMIP6 models in this study (Dee et al., 2011). In order to have as many models as possible, the outputs of future projections under SSP2–4.5 and SSP5–8.5 during 2015–2100 as well as the historical simulations during 1979–2014 derived from 25 CMIP6 models were used in this study. The variables used in this study were the daily maximum and minimum temperature and the monthly mean temperature.

#### *2.2 Extreme Temperature Indices*

Following the definitions from the Expert Team on Climate Change Detection and Indices (ETCCDI; X. Zhang et al., 2011), four extreme temperature indices were used in this study, including coldest night (TNn), warmest night (TNx), coldest day (TXn), and warmest day (TXx). More details of these extreme temperature indices can be found on the ETCCDI website (http://etccdi.pacificclimate.org/list_27_indices.shtml).

### *2.3 Bias Correction Method*

Since there is model bias in simulating extreme temperature, particularly in polar and mountain regions, bias correction is needed for CMIP6 model simulations (Gumindoga et al., 2019; Peng et al., 2019; Teutschbein and Seibert, 2012; Sperna et al., 2010). We utilized a variance scaling method in this study, as it can guarantee that the climatological mean and standard deviation of the model simulations are the same as those of the observations during the reference period, while the model biases are time-variant.

### *2.4 Response of extreme temperature indices to global warming and signal-to-noise ratio*

To investigate the response of extreme temperature indices to global warming, we obtain the time series of the projected extreme temperature indices averaged over the Earth's three poles and global mean temperature by applying a 5-year overlapping mean over decadal periods and calculate the response rate.

The signal-to-noise ratio (SNR) was used to measure the credibility of the projected results in this study. The SNR is defined as the ratio of the multimodel ensemble median and the intermodel standard deviation. The projected results are robust when SNRs are greater than 1.

### *2.5 Avoided Intensification of Extreme Temperature Indices Between the 1.5 ℃ and 2 ℃ Global Warming Levels*

The avoided intensification (Li et al.,2018) is defined as follows:

$$\text{Avoided intensification} = \frac{C_{2.0}-C_{1.5}}{C_{2.0}} \times 100\% \qquad (1)$$

In this formula, $C_{1.5}$ and $C_{2.0}$ indicate the changes in extreme temperature indices at the 1.5 ℃ and 2 ℃ global warming levels with respect to the pre-industrial period, respectively.

## 3. RESULTS

### *3.1 Response of extreme temperature indices to global warming*

Figure 1 shows the response rates and SNRs of the extreme indices over the Earth's three poles to the changes in global mean surface air temperature under the SSP2-4.5 and SSP5-8.5 scenarios. As all the SNRs are larger than 1 under both SSP2-4.5 (Figure 1b) and SSP5-8.5 (Figure 1d), these responses are all robust against the model spread. For the cold indices (TNn and TXn), the SNRs in the TP region are always the largest, while the largest SNRs of the warm indices (TNx and TXx) occur in Antarctica under both scenarios (Figures 1b, 1d). This indicates that the changes in the cold indices in the TP region and the changes in the warm indices in Antarctica, are relatively more credible.

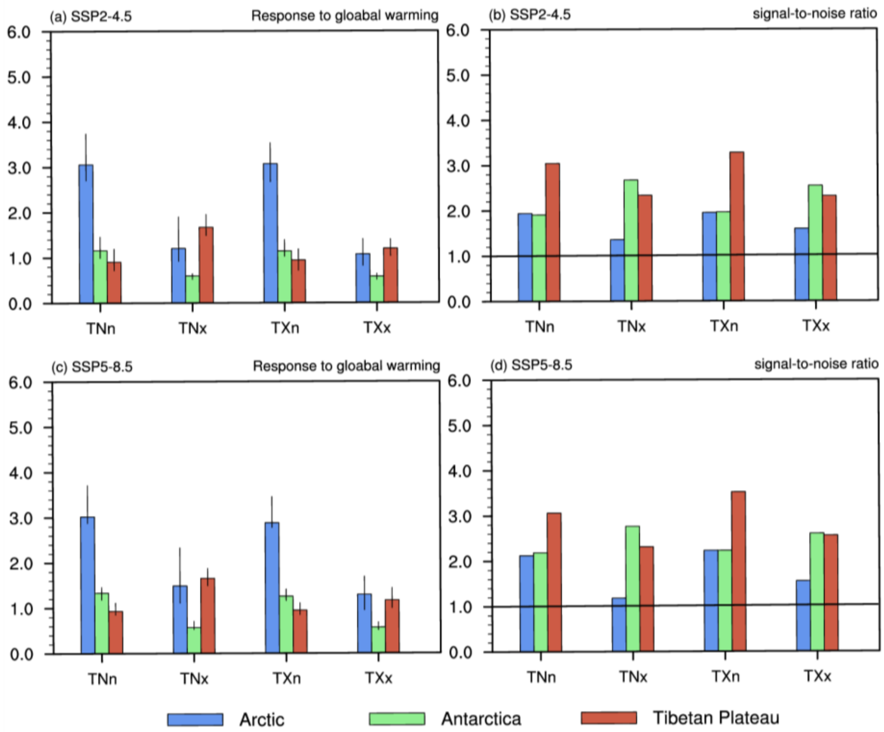


**Fig. 1.** (a, c) Response rates of the extreme indices over the Arctic, Antarctica and the TP to the changes in global mean surface air temperature under the SSP2-4.5 and SSP5-8.5 scenarios. The MME medians and the 25%–75% uncertainties are denoted by histograms and vertical black lines, respectively. (b, d) SNRs of the temperature extremes under the SSP2-4.5 and SSP5-8.5 scenarios. The horizontal black line in (b, d) indicates that the SNR is 1.

### *3.2 The avoided intensification from 0.5 ℃ less warming*

The avoided intensification of extreme temperature indices in the Earth's three poles from 0.5 ℃ less warming was further quantified and the results are shown in Figure 2. If global warming can be limited to 1.5 ℃ instead of 2 ℃, all of the indices in the Arctic (Figure 2a), the TNx and TXx in Antarctica (Figure 2b), and the TNn and TXx in the TP region (Figure 2c) are projected under SSP2–4.5 to benefit from a consistently avoided intensification, since there is the same sign of changes in more than 70% of the models (solid circles). However, under SSP5–8.5, only the TXn, TXn, and TXx in the Arctic (Figure 2a), and the TXx in Antarctica and the TP (Figures 2b and 2c) will benefit from a consistently avoided intensification. In summary, the TNx in the TP region and TXx in Antarctica show the largest avoided intensification from 0.5 ℃ less warming under SSP2–4.5 and SSP5–8.5, respectively. Meanwhile, scenario–and region–dependence also exist for the avoided intensification of extreme temperature indices. Since the multimodel medians of avoided intensification are positive for all four extreme temperature indices, the risk of temperature extremes over the Earth's three poles is likely to decrease when global warming is limited to 1.5 ℃ instead of 2 ℃ under both SSP2–4.5 and SSP5–8.5.

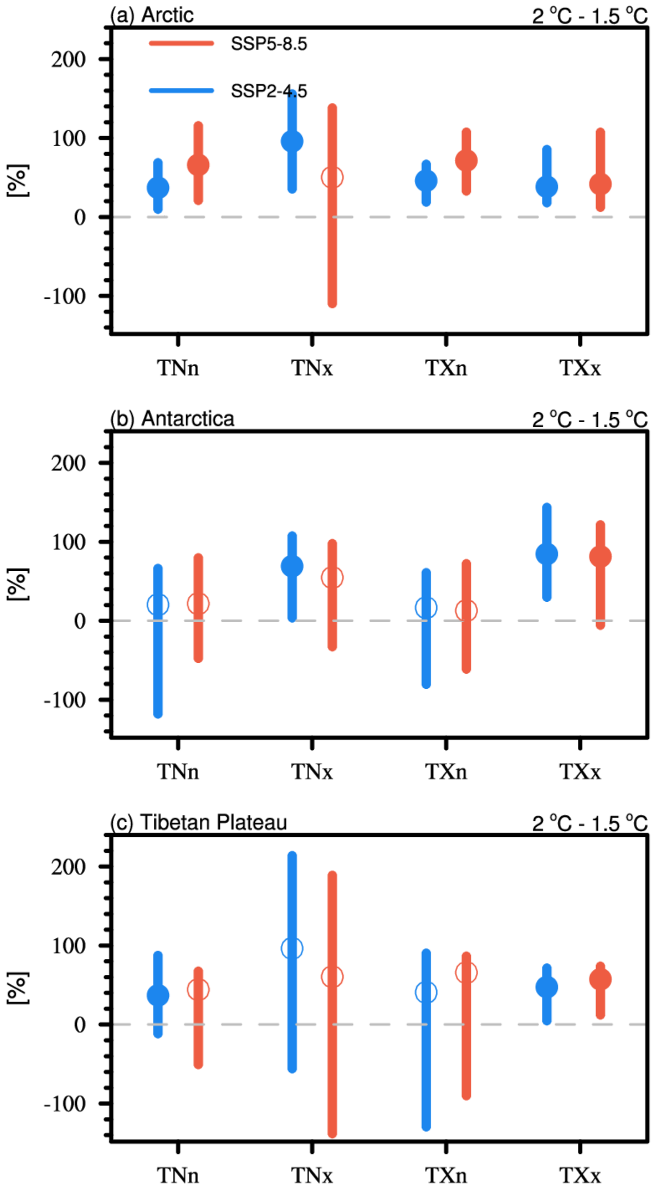


**Fig. 2.** Avoided intensification from 0.5 ℃ less warming over the Arctic, Antarctica, and the Third Pole-Tibetan Plateau under the Shared Socioeconomic Pathway (SSP)2–4.5 (blue bars) and SSP5–8.5 (red bars) scenarios. The circles and bars indicate the multimodel medians and the 25%–75% uncertainties, respectively. Solid (open) circles indicate that more (less) than 70% of the models agree on the sign of the changes.

## 4. SUMMARY

### *4.1 A lower warming target is necessary for reducing the risks of extreme temperature over the three poles.*

Efforts to understand and project climate change over the Earth's three poles (the Arctic, Antarctica, and Third Pole-Tibetan Plateau) under global warming scenarios are crucial for risk assessment and policymaking aimed at coping with future climate change. This study reports the future change of four extreme temperature indices over the Earth's three poles based on the observational datasets and outputs from models of phase 6 of the Coupled Model Intercomparison Project (CMIP6) with bias correction. We find that the increase of four extreme temperature indices in the Earth's three poles with global mean temperature is linear. Although the future changes in extreme temperature indices under a 1.5 ℃ or 2 ℃ warming world are not uniform in space, the risk of temperature extremes over the Earth's three poles is likely to decrease when global warming is limited to 1.5 ℃ instead of 2 ℃ under both SSP2-4.5 and

SSP5-8.5. This means that a lower warming target is necessary for reducing the risks of extreme temperature over the three poles.

## Citation

Tang, B., W. T. Hu, A. M. Duan, K. Gao, and Y. Peng, 2022: Reduced risks of temperature extremes from 0.5 ℃ less global warming in the Earth's three poles, Earth's Future, 10, e2021EF002525. https://doi.org/10.1029/2021EF002525

## References

[1] Dee, D.P., Uppala, S.M., Simmons, P., Berrisford, P., Poli, S., Kobayashi, U., Andrae, M.A., Balmaseda, G., Balsamo, P., Bauer, P., et al. (2011) The ERA-Interim reanalysis: configuration and performance of the data assimilation system. Quart. J. Roy. Meteor. Soc. 137, 553–597.

[2] Fang, K., Zhang, P., Chen, J., Chen, D. (2021) Co-varying temperatures at 200 hPa over the Earth's three poles. Sci. China Earth Sci. 64, 340–350.

[3] Ford, J.D., Mcdowell, G., Pearce, T. (2015) The adaptation challenge in the Arctic. Nat. Clim. Chang. 5, 1046–1053.

[4] Gao, K., Duan, A., Chen, D., Wu, G. (2019) Surface energy budget diagnosis reveals possible mechanism for the different warming rate among Earth's three poles in recent decades. Sci. Bull. 64, 1140–1143.

[5] Gumindoga, W., Rientjes, T., Haile, A.T., Makurira, H., Reggiani, P. (2019) Performance of bias-correction schemes for CMORPH rainfall estimates in the Zambezi river basin. Hydrol. Earth Syst. Sci. 23, 2915–2938.

[6] IPCC, (2014) Climate change 2014: impacts, adaptation, and vulnerability. Part B: Regional aspects. Contribution of Working Group II to the Fifth Assessment Report of the Intergovernmental Panel on Climate Change. Cambridge University Press, Cambridge, United Kingdom and New York, NY, USA.

[7] Li, D., Zhou, T., Zou, L., Zhang, W., Zhang, L. (2018) Extreme high-temperature events over east Asia in 1.5°C and 2°C warmer futures: analysis of NCAR CESM low-warming experiments. Geophys. Res. Lett. 45, 1541–1550.

[8] Li, X., Che, T., Li, X.W., Wang, L., Duan, A.M., Shangguan, D.H., Pan X.D., Fang, M., Bao, Q. (2020) CASEarth Poles: Big data for the Three Poles. Bull. Amer. Meteorol. Soc. 101, E1475–E1491.

[9] Peng, D., Zhou, T., Zhang, L., Zhang, W., Chen, X. (2019) Observationally constrained projection of the reduced intensification of extreme climate events in Central Asia from 0.5 ℃ less global warming. Clim. Dyn. 53, 543–560.

[10] Rintoul, S.R., Chown, S.L., DeConto, R.M., England, M.H., Fricker, H.A., Masson-Delmotte, V., Naish, T.R., Siegert, M.J., Xavier, J.C. (2018) Choosing the future of Antarctica. Nat. 558, 233–241.

[11] Siegert, M. (2016) Glaciology: vulnerable Antarctic ice shelves. Nat. Clim. Chang. 7, 11–12.

[12] Sperna, W., Van, B., Kwadijk, J., Bierkens, M. (2010) The ability of a GCM-forced hydrological model to reproduce global discharge variability. Hydrol. Earth Syst. Sci. 14.

[13] Sui, C., Zhang, Z., Yu, L., Li, Y., Song, M. (2017) Investigation of Arctic air temperature extremes at north of 60 °N in winter. Acta Oceanologica Sinica, 36, 51–60.

[14] You, Q., Jiang, Z., Wang, D., Pepin, N., Kang, S. (2017) Simulation of temperature extremes in the Tibetan Plateau from CMIP5 models and comparison with gridded observations. Clim. Dyn. 51, 355–369.

[15] Zhang, X., Alexander, L., Hegerl, G.C., Jones, P., Klein Tank, A., Peterson, T.C., Trewin, B., Zwiers, F.W. (2011) Indices for monitoring changes in extremes based on daily temperature and precipitation data. WIREs: Clim. Chang. 2, 851–870.

# Adaptive Hydropower Reservoir Management under Climate Change in the Lancang-Mekong River Basin


TANG Qiuhong[1,3], YUN Xiaobo[2]

[1] Key Laboratory of Water Cycle and Related Land Surface Processes, Institute of Geographic Sciences and Natural Resources Research, Chinese Academy of Sciences, Beijing, China

email: tangqh@igsnrr.ac.cn

[2] National Meteorological Center, China Meteorological Administration, Beijing, China

email: yunxiaobo17@mails.ucas.ac.cn

[3] University of Chinese Academy of Sciences, Beijing, China


## 1. INTRODUCTION

The Lancang-Mekong River, which traverses approximately 5,000 km in Asia, is an important international river flowing across six countries, that is, China, Myanmar, Lao, Thailand, Vietnam and Cambodia. The human livelihoods and ecosystem of the Lancang-Mekong River Basin (LMRB) rely heavily on the commonly shared water resources characterized by seasonal flood pulse. Flow dynamics along the Lancang-Mekong River and its tributaries are likely subject to a substantial change due to climate change and new dam construction. Climate change leads to higher temperatures and more extreme weather conditions in LMRB, which will likely accelerate the hydrological cycle and affect rainfall, snow melt, and river flows. At the same time, Hydropower dams are proliferating in LMRB driven by the pursuit of renewable electricity and societal resilience to flooding.

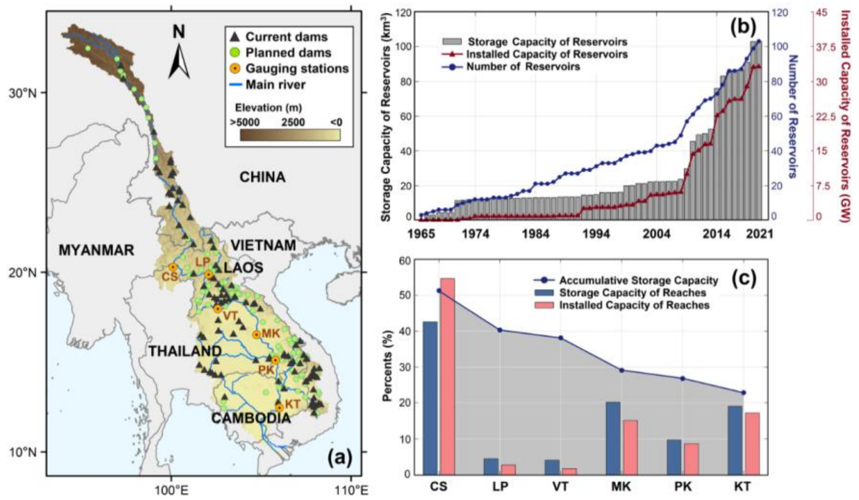


**Figure 1** (a) The Lancang-Mekong River Basin （LMRB） with the dams and streamflow gauging stations. (b) Changes in the number, installed capacity and storage capacity of reservoirs during 1965–2021 in LMRB. (c) Observed and simulated daily streamflow at CS stations in LMRB during 2008–2016.

Hydrological extremes both dry extremes and wet extremes can be exacerbated by climate change and threat water security in LMRB. Reservoirs can be managed effectively mitigate the risks of these extreme events. However, current knowledge about changes in hydrological extreme events under climate change and the effectiveness of reservoir regulation in LMRB remains limited, and the tradeoffs between hydropower production and extremes control are unclear in a changing environment. This study fills the knowledge gap by evaluating the effectiveness of reservoir regulation for changing hydrological extremes in the 21st century. The VIC-Reservoir hydrological model forced by the bias-corrected CMIP6 climate forcing data were used to project the future streamflow changes in LMRB, and the copula-based joint Standardized Streamflow Index (SSI) was adopted to identify basin-wide dry and wet hydrological extremes. Further more, we quantify the relative effects of climate change and reservoir operation on flooding and hydropower generation in LMRB.

## 2. MATERIALS AND METHODS

### *2.1 VIC model coupled with reservoirs*

The VIC model[1] coupled with reservoir (VIC-Reservoir)[2] was adopted to simulate the hydrology in LMRB. The soil data were acquired from the Harmonized World Soil Database (HWSD)[3], and the land cover data were obtained from the Global Land Cover Characterization (GLCC) dataset[4]. The reservoir and dam data were obtained from the GMDD and existing research[5]. The runoff in VIC was routed through a channel network at 0.25-degree spatial resolution[6]. The VIC-Reservoir model operates as follows: First, the topological relationship between the sub-basins located the reservoirs are determined according to streamflow directions. Second, the natural streamflow entering a reservoir is calculated, and then regulated streamflow is determined according to the reservoir operation rules. This operation is developed sequentially from upstream dams to downstream ones, ensuring that the simulated streamflow at any dam accounts for the impact of operations of all the upstream dams. The detailed data of the dams, including dam height, reservoir storage capacity, reservoir geometry, was used to estimate potential hydropower production.

### *2.2 SSI and Copula*

The standardized streamflow index (SSI)[7] is an index obtained by first calculating the distribution probability of river streamflow and then normalizing it. The magnitude of SSI can directly reflects the streamflow changes and the impact from climate change and reservoir regulation directly. Considering that LMRB is located in the monsoon area, a 3-month scale SSI (SSI-3) was selected to capture the seasonal characteristics. The generalized extreme value distribution was selected as the fitting function of SSI-3 because its best-fitting effect according to Kolmogorov-Smirnov test [8].

Basin-wide hydrological extreme events are described as a situation that both upstream and downstream experience concurrent dry extreme or concurrent wet extreme. Copula function is a connection function, which were used to estimate the joint probability of concurrent dry/wet hydrological extremes in LMRB. Two dependent time series $X$ and $Y$ have distributions $F_x(x)$ and $F_y(x)$, respectively. The joint distribution F(x, y) of $X$ and $Y$ is calculated as follows:

$$F(x, y) = P(X \leq x, Y \leq y) = C(F_X(x), F_Y(x))$$

In the whole basin, CS and KT stations (Figure 1) were selected to represent the upstream and downstream in LMRB respectively. Different copula types will affect the connection effect. A14 copula was selected from eight common copula types according to the copula weight theory[9].

## 3. RESULTS

### *3.1 Changes in hydrological extreme events[10]*

The distributed hydrological model forced by the future climate model from the Inter-Sectoral Impact Model Intercomparison Project 3b (ISIMIP3b) assessed the effectiveness of reservoir regulation for changing hydrological extremes in the 21st century. The results from three Shared Socio-economic Pathways (SSP) scenarios indicated that precipitation and temperature will continue to increase over the future period of LMRB, and the annual streamflow will show a trend of first decrease and then increase.

With the streamflow changes, hydrological extreme events also vary. We analyzed the changes in basin-wide and sub-basin extreme events by evaluating the changes of concurrent dry and wet hydrological extremes among different stations in LMRB. Figure 2 shows an increase in the basin-wide dry hydrological extreme during 2031-2060 and a threefold increase in the basin-wide wet hydrological extreme during 2071-2100. The properly operated 103 reservoirs in LMRB can regulate the seasonal streamflow and delay the propagation of extreme events from meteorological processes to hydrological processes, which will effectively mitigate the basin-wide dry hydrological extremes caused by climate change. However, reservoir operation has limited effect on the basin-wide wet hydrological extremes, which indicates that LMRB will face serious high flood risks by the end of the 21st century.

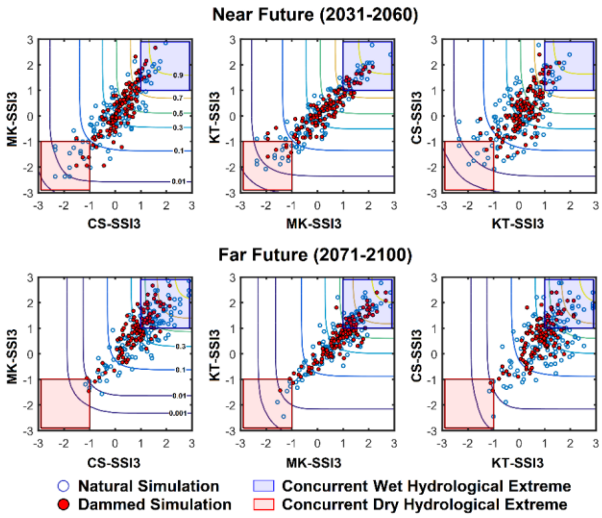


**Figure 2** Level curve of the joint probability distribution of the SSI-3 at different stations and for different periods in LMRB (SSP585 scenario)[10].

### *3.2 Reducing future floods through reservoir regulation[11]*

Considering the high future flood risk in LMRB by the end of the 21st century, we conducted an in-depth analysis of the changes in flood magnitude and flood frequency. The VIC model was coupled with an adjustable reservoir module to investigate the tradeoffs between different reservoir operation strategies of hydropower production and flood control under the combined impacts of climate change and reservoir operation in LMRB.

Results from figure 3 show that climate change would continue to increase flood magnitude and flood frequency by 9.0% ~ 31.2% and 17.7% ~ 44.1%, respectively, by the end of the 21st century. The adaptive reservoir operation can reduce flood magnitude by 5.6% ~ 6.4% and frequency by 17.1% ~ 18.9% at the cost of 9.8% ~ 14.4% of basin-wide hydropower generation. At the same time, changing reservoir operation strategies can postpone the upcoming high flood risk for at least 20 years. It is worth mentioning that Chinese large upstream reservoir will play an important role in downstream flood control at the cost of greater hydropower generation losses. Switching reservoir operation strategies will cause Chinese reservoirs to suffer an average 11.1% hydropower loss (16,677 GWh/yr), which is 5.4 times the hydropower loss (3,103 GWh/yr) of midstream and downstream reservoirs.

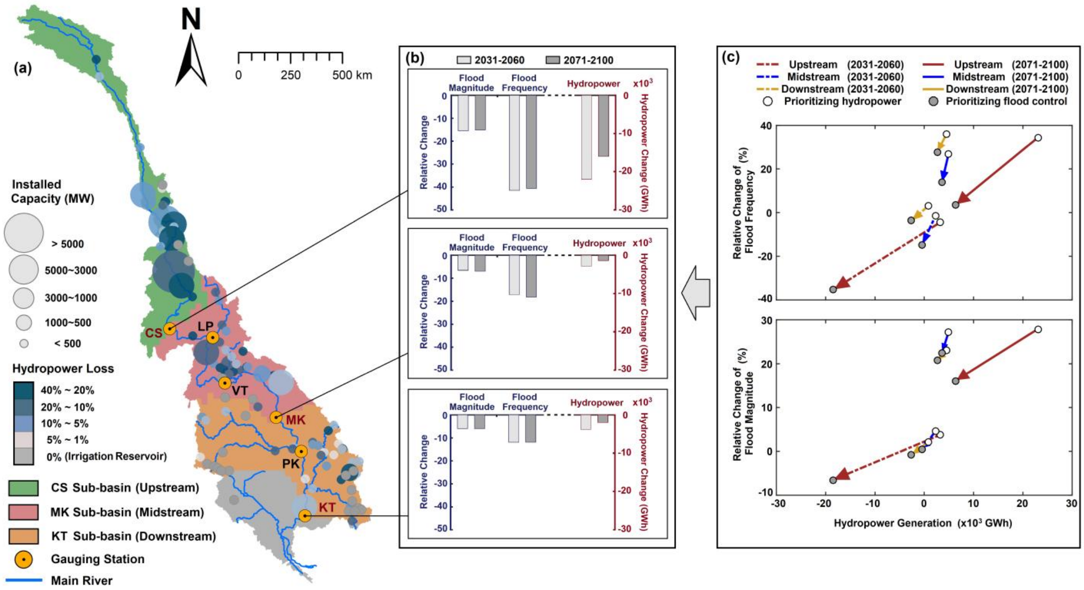

**Figure 3** (a) Average hydropower loss of different reservoirs during 2071–2100 in LMRB (SSP585 scenario). (b) Changes in flood magnitude, flood frequency and hydropower when switching between prioritizing hydropower generation and flood control strategies at three sub-basins during the near future period (2031–2060) and the far future period (2071–2100). (c) The tradeoffs between hydropower production and flood control at upstream, midstream, and downstream LMRB in 21st century.[11]

## 4. SUMMARY

Our results indicate that the LMRB will suffer more dry hydrological extremes (up to 33%)in the 2040s, and more wet hydrological extremes (up to 363%) by the end of the 21st century. Reservoir regulation can mitigate the basin-wide dry extreme events, but has limited effect on wet extreme. The lack of the reservoir storage capacity to deal with wet hydrological extreme poses a challenge to transboundary water management in the basin.

Further evaluation showed that while climate change would increase flood magnitude and frequency, adaptive reservoir operation can reduce flood magnitude by 5.6%–6.4% and frequency by 17.1%–18.9% at the cost of 9.8%–14.4% of basin-wide hydropower generation. Particularly, upstream reservoirs suffer more hydropower loss (5.4 times) than downstream ones when flood control is prioritized in reservoir regulation. Our findings have implications for integrated water and energy management at the transboundary river basin under climate change.

## References


[1] LIANG X, LETTENMAIER D P, WOOD E F, et al. 1994. A simple hydrologically based model of land surface water and energy fluxes for general circulation models. Journal of Geophysical Research, 99: 14415-14428.

[2] YUN X, TANG Q, WANG J, et al. 2020. Impacts of climate change and reservoir operation on streamflow and flood characteristics in the Lancang-Mekong River Basin. Journal of Hydrology, 590: 125472.

[3] FAO, et al. 2012. ISRIC-World Soil Information, Institute of Soil Science, Chinese Academy of Sciences (ISSCAS), Joint Research Centre of the European Commission (JRC), Harmonized World Soil Database, v1.21.

[4] LOVELAND T R, REED B C, BROWN J F, et al. 2000. Development of a global land cover characteristics database and IGBP DISCover from 1 km AVHRR data. International Journal of Remote Sensing, 21(67): 1303-1330.

[5] SHIN S, POKHREL Y, YAMAZAKI D, et al. 2020. High Resolution Modeling of River-Floodplain-Reservoir Inundation Dynamics in the Mekong River Basin. Water Resources Research, 56(5).

[6] LOHMANN D, NOLTE-HOLUBE R, RASCHKE E. 1996. A large-scale horizontal routing model to be coupled to land surface parametrization schemes. Tellus A, 48(5): 708-721.

[7] CHEN X, LI F wen, FENG P. 2018. Spatiotemporal variation of hydrological drought based on the Optimal Standardized Streamflow Index in Luanhe River basin, China. Natural Hazards, 91(1): 155-178.

[8] WILKS D S. 1999. Interannual variability and extreme-value characteristics of several stochastic daily precipitation models. Agricultural and Forest Meteorology, 93(3): 153-169.

[9] HUARD D, ÉVIN G, FAVRE A C. 2006. Bayesian copula selection. Computational Statistics & Data Analysis, 51(2): 809-822.

[10] YUN X, TANG Q, LI J, et al. 2021. Can reservoir regulation mitigate future climate change induced hydrological extremes in Lancang-Mekong River Basin?. Science of The Total Environment: 147322.

[11] YUN X, TANG Q, SUN S, et al. 2021. Reducing climate change induced flood at the cost of hydropower in the Lancang-Mekong River Basin. Geophysical Research Letters, 48(20).

# The Use of Multi-source Data to Support High-resolution Flood Modelling and Impact Assessment

LIANG, Qiuhua[1]; CHEN, Huili [1]; MING, Xiaodong[1,2]

[1] School of Architecture, Building and Civil Engineering, Loughborough University, Leicestershire, UK
[2] JBA Risk Management, Skipton, North Yorkshire, UK

Email: Q.Liang@lboro.ac.uk (for author 1)
Email: H.Chen2@lboro.ac.uk (for author 2)
Email: Xiaodong.Ming@jbarisk.com (for author 3)

## 1. INTRODUCTION

Flooding is the most wide-spread natural hazard that regularly threatens people's lives and properties in every country and region across the world, regardless of their development level (UNDRR, 2020). For example, the year of 2021 witnessed a series of catastrophic floods, such as the July extreme events occurred in the Europe and Henan Province of China that caused widespread damages and killed more than 230 and 300 people, respectively. Due to climate change, both the frequency and intensity of extreme precipitation are expected to increase, which will inevitably trigger more extreme flood events globally. The development of effective flood risk management strategies is therefore crucially important for every government to save lives and sustain economic development, especially in the low-to-middle income countries (LMICs) where disasters induced by flooding or other natural hazards can set back development for years and even decades.

With rapid development of computing technology and availabiligy of rich source of data from remote sensing in the last decades, numerical modelling has become an indispensable tool to support flood risk management. Hydrodynamic models that solve the full 2D shallow water equations (SWEs), especially those equipped with shock-capturing capability, still represent the state of the art and have been widely used for flood modelling and risk assessment. The coupling of this type of models with the latest high-performance computing technology, especially modern graphics processing units (GPUs), has allowed simulation of the whole process of flooding from rainfall to inundation across a large catchment or city at real time (e.g. Xia et al., 2019; Xing et al., 2019; Ming et al., 2020).

However, the application of hydrodynamic models in flood modelling and risk assessment requiers high-quality data of sufficient resolution that are not always available, especially in the data-scarce environment of LMICs. Even in a developed country where data are rich, e.g the UK, it is highly challenging to collect any in-event data for model calibration and validation. In a data-scarce environment, even the basic topographic and flood exposure data essential for high-resolution flood risk assessment are commonly not available, hindering the application of the latest modelling technologies to provide detailed risk information to inform decision-making. UNDRR recognises this important issue and identifies data as the bottle neck for disaster risk reduction in LMICs (UNDRR, 2019). To address the challenges, this paper explores data from multiple sources to improve the prractice of flood modelling and risk assessment in different contexts.

## 2. A HIGH-PERFORMANCE HYDRODYNANMIC MODEL FOR FLOOD SIMULATION

In this work, the High-Performance Integrated hydrodynamic Modelling System (HiPIMS) developed at Loughborough University (Xia et al., 2019) is integrated with data from multiple sources to support flood modelling and risk assessment in different contexts. HiPIMS solves the full 2D SWEs that can be written in a matrix form as

$$\frac{\partial \mathbf{q}}{\partial t} + \frac{\partial \mathbf{f}}{\partial x} + \frac{\partial \mathbf{g}}{\partial y} = \mathbf{R} + \mathbf{S}_{\mathrm{b}} + \mathbf{S}_{\mathrm{f}} \tag{1}$$

where $t$, $x$ and $y$ denote the time and the two Cartesian coordinates; $\mathbf{q}$, $\mathbf{f}$ and $\mathbf{g}$ are the vectors containing the conserved flow variables, and the fluxes in the $x$- and $y$-directions, respectively; $\mathbf{R}$, $\mathbf{S}_\mathrm{b}$ and $\mathbf{S}_\mathrm{f}$ contain the mass, slope and friction source terms. The vector terms are given by

$$\mathbf{q} = \begin{bmatrix} h \\ uh \\ vh \end{bmatrix}, \mathbf{f} = \begin{bmatrix} uh \\ u^2h + \frac{1}{2}gh^2 \\ uvh \end{bmatrix}, \mathbf{g} = \begin{bmatrix} vh \\ uvh \\ v^2h + \frac{1}{2}gh^2 \end{bmatrix} \tag{2}$$

$$\mathbf{R} = \begin{bmatrix} P + I + D \\ 0 \\ 0 \end{bmatrix}, \mathbf{S}_\mathrm{b} = \begin{bmatrix} 0 \\ -gh\frac{\partial b}{\partial x} \\ -gh\frac{\partial b}{\partial y} \end{bmatrix}, \mathbf{S}_\mathrm{f} = \begin{bmatrix} 0 \\ -\frac{\tau_{bx}}{\rho} \\ -\frac{\tau_{by}}{\rho} \end{bmatrix} \tag{3}$$

where $h$ is the water depth, $u$ and $v$ are the two depth-averaged velocity components in the $x$- and $y$-directions, $P$ represents the precipitation rate, $I$ is the infiltration rate, $D$ is the drainage rate, $\rho$ is the water density, $g$ is the gravitational acceleration, and $\tau_{bx}$ and $\tau_{by}$ are the frictional stresses estimated as follows:

$$\tau_{bx} = \rho C_f u\sqrt{u^2 + v^2} \text{ and } \tau_{by} = \rho C_f v\sqrt{u^2 + v^2} \tag{4}$$

where $C_f = gn^2/h^{1/3}$ is the friction coefficient with $n$ being the Manning coefficient.

HiPIMS solves the above governing equations using a shock-capturing Godunov-type finite volume scheme with improved source term discretization (Xia et al., 2017). The model has been widely applied to and tested against simulation of different types of flooding processes including flash floods induced by intense rainfall. To substantially improve its computational efficiency for large-scale simulations, HiPIMS is implemented for simulations on multiple GPUs to achieve high-performance computing (Xia et al., 2019).

## 3. APPLICATIONS AND RESULTS

To support high-resolution flood modelling using HiPIMS, a range of data analytics techniques have been developed and applied to improve data quality for model set up, validation and flood impact assessment. In the section, a couple of examples are presented to show some of these applications.

### *3.1 The use of crowd-source data for model validation*

In the first application, HiPIMS is applied to reproduce an urban flash flood in the ~ 400 km$^2$ Tyneside area in Northeast England, UK, created by a short-duration extreme rainfall event on June 28$^{th}$, 2012. Following the event, the Newcastle City Council reported £8m of damage and more than 500 homes being flooded. To support the flood simulation, high-quality spatial datasets including topographical data, land cover data, and radar rainfall data were made available from the UK Environment Agency and further processed by removing overhead bridges and re-inserting building layers to provide all necessary data for whole-process flood modelling at 2m resolution. The DEMs produced at different stages of processing are shown in Fig. 1.

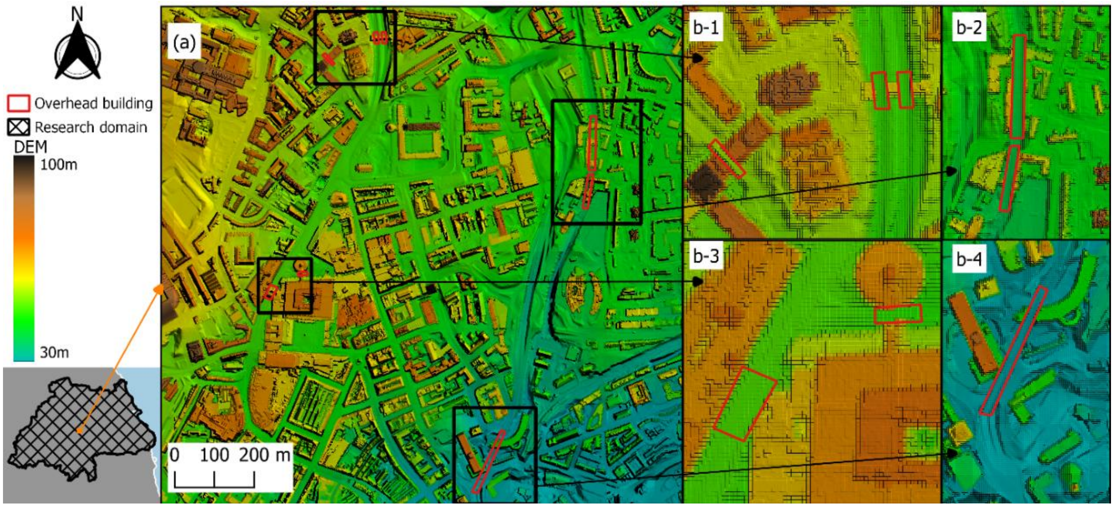


**Fig. 1.** Processing DEM for flood modoelling: (a) Hybrid DEM; (b) Rectified DEM after removing overhead buildings.

However, during such a short-duration extreme flood event, it is challenging to conduct any fieldwork to collect field data and so high-quality data are often unavailable for model calibration and verification. Nowadays, with the widespread use of smartphones, it has become common for public to share photos and other information on social media. An innovative data collection system was therefore developed to collect and analyse text messages, photos and other relevent flood information from Twitter and other online social networks to support flood forecasting and model validation (Smith et al., 2017). Particularly, photos may provide geo-referenced images recording useful flood information, including flood location, time, and extent, which can potentially provide important evidences for calibrating and validating flood models. For example, Fig. 9 compares the simulated and observed flood/dry extents at two locations, demonstrating the highly accurate simulation results produced by HiPIMS.

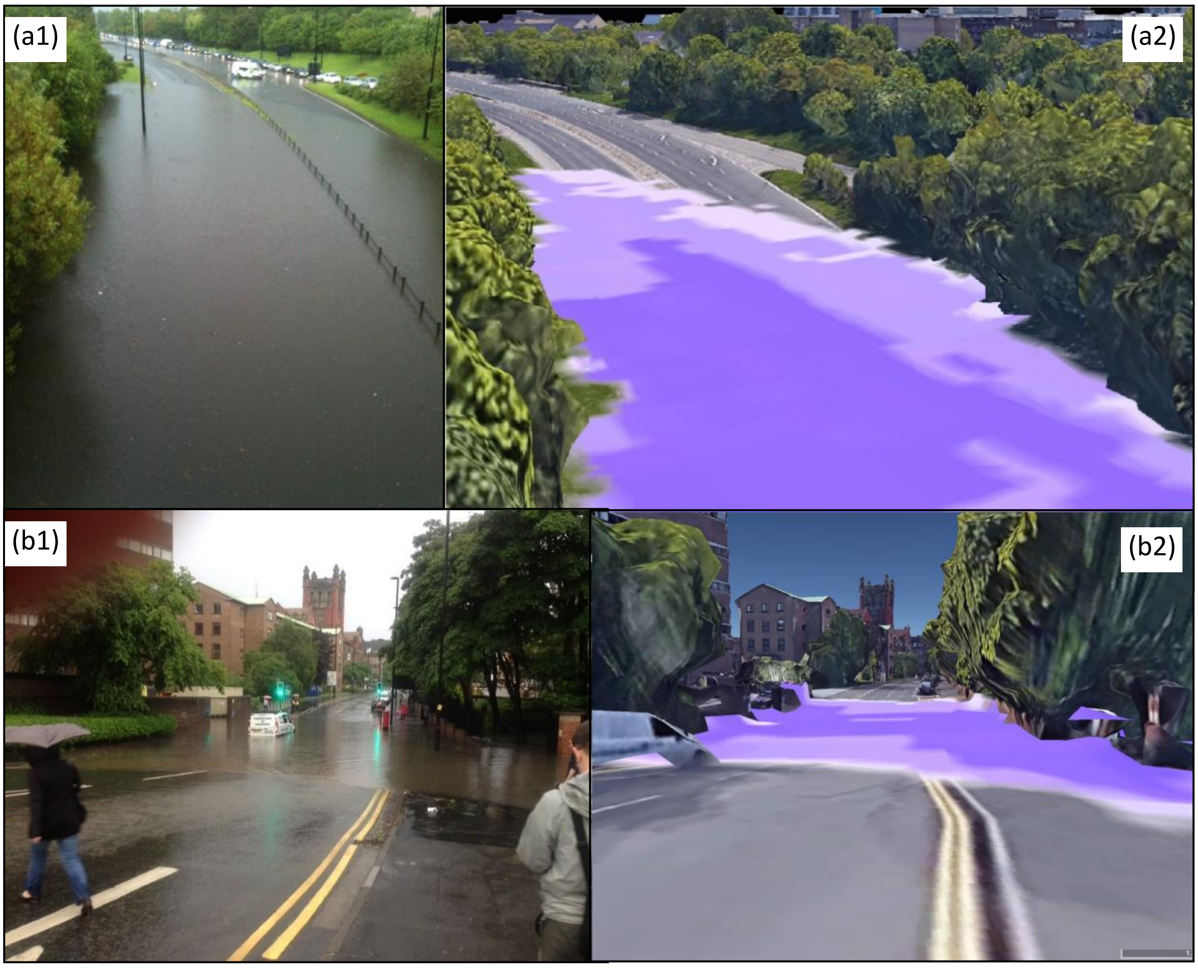

**Fig. 2.** Comparison between observed and simulated flood/dry extents at: (a) Central Motorway (Photo taken on an overhead bridge at 17:35); (b) Queen Victoria Road (Photo taken at 16:40), at Newcastle upon Tyne.

### *3.2 The use of data from multiple sources to support object-level flood impact assessment*

To demonstrate the application of HiPIMS for high-resolution flood modelling and impact assessment in data-scarce environments, glacier lake outburst floods (GLOFs) from the Tsho Rolpa Lake in Nepal are considered. In addition to integrating open spatial data including DEMs and land use data from multiple sources to improve data quality, an effective approach was developed to extract flood exposure and damage data from the OpenStreetMap (OSM) and other open data platform to support object-level flood impact assessment, allowing the analysis of potential flood impact on individual buildings and key public, health, traffic, worship, commercial and other facilities (Chen et al. 2022). Figure 9 shows the resulting inundation maps of three identified critical facilities (two hydropower plants and one airport) under the worst-case scenario to provide high-resolution details of their spatial exposure.

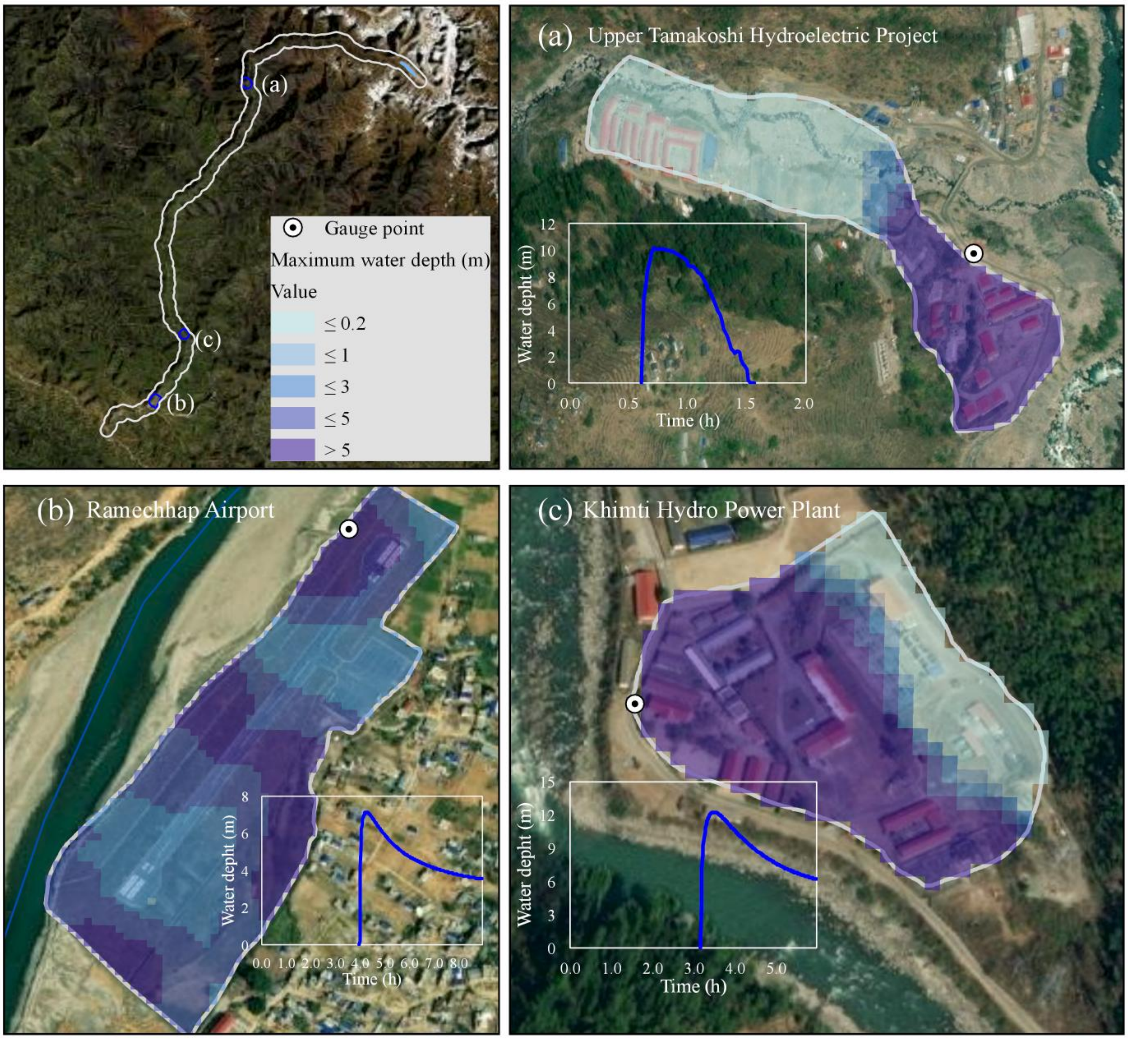


**Fig. 3.** Flood maps at three identified critical facilities (two hydropower plants and one airport). The embedded depth hydrographs are predicted at the marked gauge points.

## 4. SUMMARY

High-resolution flood modelling and risk assessment can provide detailed information to inform the development of effective flood risk management strategies. However, unavailability of high-quality data imposes a great challenge on the application of the latest high-performance flood models for this purpose, regardless of the development level of the case study under consideration. This paper introduces the recent developments in using data from multiple sources to address this issue and presents two examples to showcase the approaches developed for different contexts.

## References


[1] Chen H, Zhao J, Liang Q, et al. (2022) Assessing the potential impact of glacial lake outburst floods on individual objects using a high-performance hydrodynamic model and open-source data. *Science of the Total Environment*, 806(3): 151289.

[2] Ming X, Liang Q, Xia X, et al. (2020) Real-Time Flood Forecasting Based on a High-Performance 2-D Hydrodynamic Model and Numerical Weather Predictions. *Water Resour. Res.* 56: e2019WR025583.

[3] Smith L, Liang Q, et al. (2017) Assessing the utility of social media as a data source for flood risk management using a real-time modelling framework. *Journal of Flood Risk Management* 10(3): 370-380.

[4] UNDRR (2020) *The human cost of disasters: an overview of the last 20 years (2000-2019)*. UNFCCC Press Release.

[5] UNDRR (2019) *Global Assessment Report on Disaster Risk Reduction*. Geneva, Switzerland, UNDRR.

[6] Xia X, Liang Q, Ming X (2019) A full-scale fluvial flood modelling framework based on a high-performance integrated hydrodynamic modelling system (HiPIMS). *Adv. Water Resour.* 132: 103392.

[7] Xia X, Liang Q, Ming X, Hou J (2017) An efficient and stable hydrodynamicmodel with novel source term discretization schemes for overland flow and flood simulations. *Water Resour. Res.* 53, 3730–3759.

[8] Xing Y, Liang Q, et al. (2019) City-scale hydrodynamic modelling of urban flash floods: the issues of scale and resolution. *Nat. Hazards* 96: 473–496.

# Evaluating five intercalibration methods for generating consistent brightness temperatures from AMSR2 and FY-3D

TIANTIAN Wang[1,2], JIANGYUAN Zeng [1]

[1] State Key Laboratory of Remote Sensing Science, Aerospace Information Research Institute, Chinese Academy of Sciences, China
email: wangtiantian20@mails.ucas.ac.cn

[2] University of Chinese Academy of Sciences, China
email: zengjy@radi.ac.cn

## 1. INTRODUCTION

Geophysical parameters such as soil moisture, surface temperature, snow water equivalent are important parameters of the Earth system and play an important role in weather forecasting, climate simulation and prediction research. For many climate-related studies, long-term and consistent observations are required, which is difficult to achieve with a single sensor, while the combination of sensors can achieve this goal. As the second generation of Chinese polar-orbiting meteorological satellite, the Fengyun-3 (FY-3) series satellites provide multi-frequency brightness temperature (TB), which have attracted increasing attention in recent years [1]-[2]. The microwave radiometer imager (MWRI) carried on FY-3D launched in November 2017 has similar sensor configuration and overpass time to AMSR2 boarded on GCOM-W1. Therefore, it opens new opportunities to jointly use FY-3D and AMSR2 in various applications. However, due to small difference in sensor configuration (e.g., bandwidth and incidence angle), there still remains some bias between these two sensors, which can be reduced by the intercalibration.

There are generally three types of intercalibration approaches [3]: SNO (simultaneous nadir overpass), statistical intercalibration, and double-differencing methods. Among these three methods, the statistical intercalibration is best suited for two instruments with near simultaneous observations and similar configuration [4], such as FY-3D MWRI and AMSR2. Several studies have carried out the intercalibration between FY-3 MWRI and AMSR-E/2. However, most previous studies focused on the regional scale, and the intercalibration in areas with high surface heterogeneity is worthy of further investigation. Additionally, the influence of different environment variables on the calibration accuracy is often ignored in previous studies which also deserves to be ascertained further.

In this study, a total of five intercalibration methods were compared based on FY-3D and AMSR2 TB from 2019 to 2020 over land at a global scale, including three methods used in previous studies, i.e., global linear regression, per-pixel linear regression joint global linear regression, and per-pixel linear regression joint inverse distance interpolation, as well as two newly introduced approaches, i.e., per-pixel linear regression joint nearest neighbor interpolation and global per-pixel linear regression., The impact of diverse environmental factors (land cover and its heterogeneity, climate types, water body fraction, terrain, and vegetation coverage) on the calibration accuracy was fully investigated.

## 2. MATERIALS AND METHODS

### *2.1 FY-3D MWRI and AMSR2 TB*

The AMSR2 level 3 (L3) TB, which served as a reference, and FY-3D MWRI L1 TB were used in this study. The H-pol and V-pol TB at five frequencies from 10.7 to 89 GHz during 1 January 2019 to 31 December 2020 was chosen for intercalibration. Since this study focuses on land surface, the TB in oceans as well as snow and ice covered areas were masked based on the IGBP land cover data. The FY-3D MWRI TB was synthesized into daily grid data and resampled to 0.25°, to be consistent with AMSR2 L3 TB.

### *2.2 Auxiliary environmental data*

A total of six environmental factors were used in this study to investigate their impact on calibration accuracy. These variables include [5]: the Global Land One-kilometer Based Elevation Digital Elevation

(GLOBE DEM); the MODIS IGBP land cover types and its derivation, the Gini–Simpson index (GSI) representing the land cover heterogeneity; climate types (tropical, arid, temperate, cold and polar) derived from Köppen–Geiger climate classification; NDVI data from MOD13Q1 and MYD13Q1 products; water body fraction preprocessed by ESA CCI soil moisture team with 0.25° spatial resolution. All the data were resampled (or aggregated) to the 0.25° grid resolution.

These six environmental factors were divided into different classification considering the number of samples and the representativeness of factors [5].

### *2.3 Intercalibration methods*

Five intercalibration methods were compared, which can be divided into two main categories: global intercalibration and per-pixel based intercalibration. The five methods are described as follows:

(1) global linear regression. For a specific channel, only one linear regression model was used for intercalibration. It is noteworthy that the pixels with correlation coefficient (*R*) of FY-3D and AMSR2 TB from 2019 to 2020 lower than 0.9 were not considered in the regression. The formula of linear regression is as follows:

$$y_{i,j} = ax_{i,j} + b \quad (1)$$

where $y$ is the reference data (i.e., AMSR2 TB); $x$ is the data to be intercalibrated (i.e., FY-3D TB); $a$ is the slope, and $b$ is the intercept of the linear equation; $i$ represents the row number of the pixel and its value ranges from 1 to 720; $j$ represents the column number of the pixel and its value ranges from 1 to 1440. That is to say, for global linear regression, the same $a$ and $b$ values are obtained for all the pixels.

(2) per-pixel linear regression joint global linear regression. Specifically, the linear regression was used for pixels with *R* value greater than 0.9 between FY-3D and AMSR2 TB on a per-pixel basis (i.e., one linear regression model per pixel), while the global linear regression model (i.e., obtained by the first intercalibration method) were applied for other pixels, and the formula is as follows:

$$y_{i,j} = a_{i,j}x_{i,j} + b_{i,j} \quad (2)$$

for per-pixel based linear regression methods, one specific $a$ value as well as one specific $b$ value are obtained for each pixel.

(3) per-pixel linear regression joint inverse distance interpolation. Equation (2) was applied for pixels with correlation coefficient greater than 0.9 between FY-3D and AMSR2 data on a per-pixel basis, while the coefficients (slope and intercept) of the linear models used in other pixels were interpolated by the inverse distance interpolation.

(4) per-pixel linear regression joint nearest neighbor interpolation. This method is similar to the third method, and the only difference is that the slope and intercept of the linear models used in the pixels where *R* between FY-3D and AMSR2 is lower than 0.9, were interpolated by the nearest neighbor interpolation.

(5) global per-pixel linear regression. Different from the previous four methods, the threshold of 0.9 is no longer used (i.e., pixels were not classified based on the *R* value between FY-3D and AMSR2 TB), and the linear equation (2) was applied to all pixels on a per-pixel basis.

## 3. RESULTS

### *3.1 Correlation coefficient (R) between FY-3D and AMSR2 TB*

The correlation coefficient between FY-3D and AMSR2 TB was calculated before intercalibration (not shown). The grids with correlation coefficient greater than 0.9 account for about 75% of the total. The grids with *R* value lower than 0.9 are mostly located in the densely vegetated areas and land-water mixed regions.

### *3.2 Intercalibration results*

The intercalibration coefficients (slope and intercept) of global linear regression method (i.e., the first method) for all FY-3D channels are listed in Table 1.

**Table 7.** Slope *a* and intercept *b* of global linear regression method for intercalibration.

| Channel | Ascending | | Descending | |
|---|---|---|---|---|
| | ***a*** | ***b*** | ***a*** | ***b*** |

| | | | | |
|---|---|---|---|---|
| 10.7GHz-H | 0.9214 | 22.4090 | 0.9346 | 19.5440 |
| 10.7GHz-V | 0.9171 | 26.1426 | 0.9202 | 25.0845 |
| 18.7GHz-H | 0.9404 | 14.8750 | 0.9359 | 11.8201 |
| 18.7GHz-V | 0.9123 | 25.2851 | 0.9177 | 23.7775 |
| 23.8GHz-H | 0.9509 | 15.4823 | 0.9609 | 12.9849 |
| 23.8GHz-V | 0.9434 | 18.8368 | 0.9498 | 17.1325 |
| 36.5GHz-H | 0.9267 | 22.4144 | 0.9425 | 19.3208 |
| 36.5GHz-V | 0.9427 | 19.1147 | 0.9489 | 17.6527 |
| 89GHz-H | 0.9626 | 10.6701 | 0.9709 | 9.2534 |
| 89GHz-V | 0.9668 | 10.6860 | 0.9689 | 10.2434 |

The intercalibration coefficients of per-pixel based intercalibration methods are shown great spatial difference. Fig.1 shows the intercalibration coefficients of global per-pixel linear regression as an example.

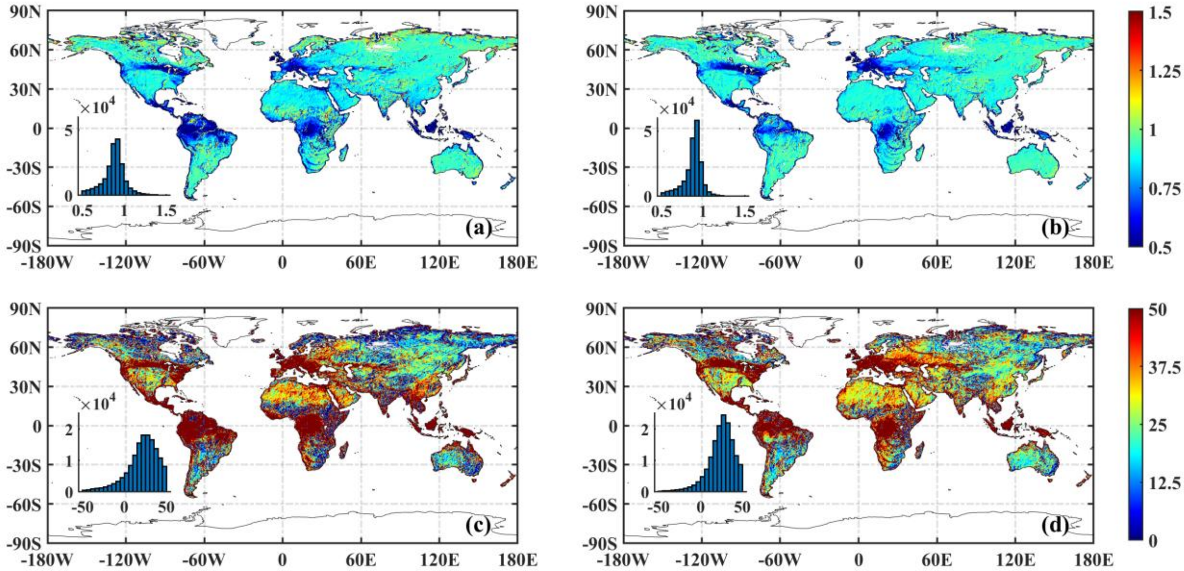


**Fig. 1**. Global distribution of the calibration coefficients using global per-pixel linear regression at 10.7 GHz at descending orbit from 2019 to 2020: (a) the slope value-*a* at H polarization, (b) the slope value-*a* at V polarization, (c) the intercept value-*b* at H polarization, and (d) the intercept value-*b* at V polarization.

Two error metrics, i.e., root mean square difference (RMSD) and Bias, were used to evaluate the accuracy of FY-3D TB at each channel before and after calibration. Bias at each channel was reduced to nearly 0 K and the results of RMSD are listed in Tables 2.

**Table 2.** RMSD (K) of FY-3D TB at each channel before and after calibration during 2019-2020. (1) belongs to global intercalibration, while (2) to (5) belong to per-pixel based intercalibration.

| Channel | Ascending | | | | | | Descending | | | | | |
|---|---|---|---|---|---|---|---|---|---|---|---|---|
| | before | global | per-pixel based | | | | before | global | per-pixel based | | | |
| | | (1) | (2) | (3) | (4) | (5) | | (1) | (2) | (3) | (4) | (5) |
| 10.7GHz-H | 7.34 | 6.33 | 5.29 | 4.45 | 5.19 | 2.93 | 7.95 | 6.38 | 5.37 | 4.19 | 5.15 | 2.69 |
| 10.7GHz-V | 6.20 | 3.93 | 3.26 | 2.82 | 3.09 | 1.95 | 6.46 | 3.91 | 3.22 | 2.65 | 3.11 | 1.72 |
| 18.7GHz-H | 5.69 | 5.37 | 4.45 | 4.10 | 4.39 | 2.79 | 4.99 | 4.85 | 4.03 | 3.58 | 3.94 | 2.49 |
| 18.7GHz-V | 4.00 | 3.20 | 2.67 | 2.54 | 2.65 | 1.88 | 3.86 | 2.82 | 2.35 | 2.16 | 2.29 | 1.60 |
| 23.8GHz-H | 5.35 | 4.31 | 3.59 | 3.43 | 3.51 | 2.60 | 4.96 | 3.49 | 2.87 | 2.72 | 2.84 | 2.16 |
| 23.8GHz-V | 4.79 | 2.83 | 2.39 | 2.32 | 2.35 | 1.91 | 4.78 | 2.20 | 1.85 | 1.77 | 1.80 | 1.51 |
| 36.5GHz-H | 7.24 | 5.71 | 4.88 | 4.46 | 4.81 | 3.43 | 7.10 | 4.11 | 3.49 | 3.30 | 3.51 | 2.69 |
| 36.5GHz-V | 5.80 | 3.97 | 3.40 | 3.24 | 3.35 | 2.75 | 5.56 | 2.77 | 2.35 | 2.27 | 2.32 | 2.03 |
| 89GHz-H | 6.39 | 6.15 | 5.50 | 5.17 | 5.25 | 4.78 | 4.73 | 4.14 | 3.70 | 3.63 | 3.68 | 3.50 |
| 89GHz-V | 5.62 | 5.12 | 4.59 | 4.39 | 4.39 | 4.22 | 4.27 | 3.49 | 3.15 | 3.10 | 3.14 | 3.05 |
| Average | 5.84 | 4.69 | 4.00 | 3.69 | 3.90 | 2.93 | 5.47 | 3.82 | 3.24 | 2.94 | 3.18 | 2.34 |

The above results demonstrate that the global per-pixel linear regression method (i.e., '(5)' in Table 2.) performs the best among the five intercalibration methods. Fig. 2 shows the global distribution of RMSD and Bias using the global per-pixel linear regression at 10.7 GHz at descending orbit. It can be seen the bias between calibrated FY-3D and AMSR2 observations is concentrated at nearly 0K and the RMSD of most regions is less than 3K.

### *3.3 Influencing factors of calibration accuracy*

The effects of environmental factors on calibration accuracy were investigated by taking the global per-pixel linear regression method as an example to display the results. Fig. 2 exhibits the RMSD of FY-3D V-pol TB at 10.7 GHz at descending orbit under different environment variables. The vegetation coverage has little influence on the calibration accuracy. The RMSD decreases with the increases of DEM and land cover heterogeneity (i.e., GSI). The water body fraction has the greatest influence on the calibration accuracy. The calibration accuracy in savannas and barren and in arid, cold and tropical climatic regions is better than that in other land cover and climate types.

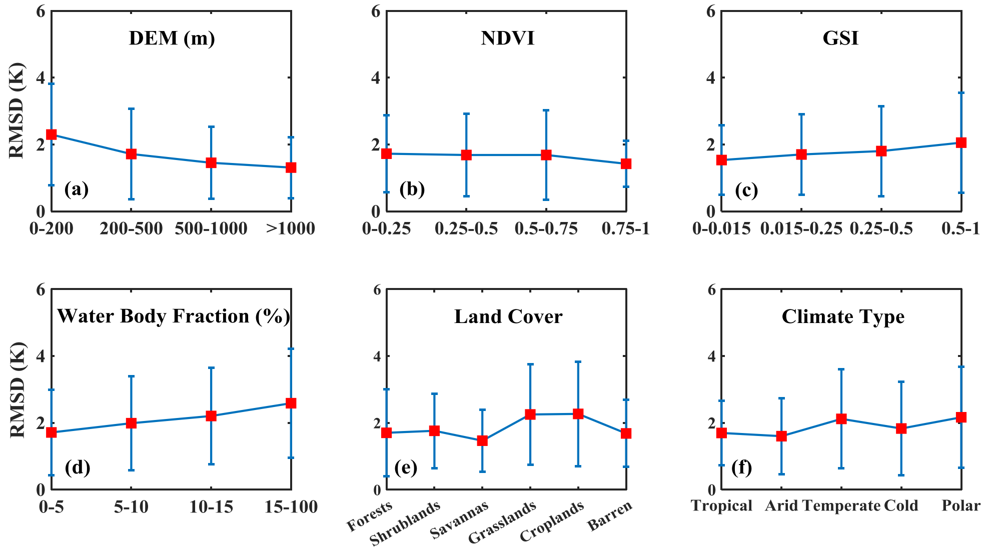


**Fig. 2**. Influence of environmental factors on RMSD (K) of FY-3D V-pol TB at 10.7 GHz at descending orbit from 2019 to 2020 calculated by the global per-pixel linear regression: (a) DEM, (b) NDVI, (c) GSI, (d) water body fraction, (e) land cover, and (f) climate types.

## 4. SUMMARY

The results demonstrate that the global per-pixel linear regression method performs the best among the five intercalibration methods. It can achieve satisfactory accuracy at all FY-3D channels ranging from 10.7 to 89 GHz with an averaged RMSD of 2.93 K and 2.34 K at ascending and descending orbits respectively, and the mean bias was also reduced to nearly 0 K. The most frequently used global linear regression performs the worst since it does not consider the spatial difference of the calibration coefficients of linear model under different ground conditions.

Among various environmental factors, the water body fraction exerts the largest impact on the calibration accuracy, followed by land cover heterogeneity and DEM, while vegetation coverage has little impact on it. The calibration accuracy is relatively lower in grasslands and croplands, as well as in temperate and polar climate zones than in other land cover and climate types.

The outcome of this study can offer a good reference for the intercalibration of satellites with similar configuration (not only for the multi-frequency satellites/sensors such as FY-3D and AMSR2, but also for the mono-frequency satellites such as SMAP and SMOS), to generate continuous and consistent data records.

## References

[1] Bormann N., Duncan D., English S., Healy S., Lonitz K., Chen K., Lawrence H., Lu Q. (2021) Growing operational use of FY-3 data in the ECMWF system, Advances in Atmospheric Sciences, 38 (8): 1285-1298.

[2] Zhang P., Lu Q., Hu X., Gu S., Yang L., Min M., Chen L., Xu N., Sun L., Bai W., Ma G., Xian D. (2019) Latest progress of the Chinese meteorological satellite program and core data processing technologies, Advances in Atmospheric Sciences, 36 (9):1027-1045.

[3] Chander G., Hewison T., Fox N., Wu X., Xiong X., Blackwell W. (2013) Overview of intercalibration of satellite instruments, IEEE Transactions on Geoscience and Remote Sensing, 51 (3):1056-1080.

[4] Du J., Kimball J., Shi J., Jones L., Wu S., Sun R., Yang H. (2014) Inter-calibration of satellite passive microwave land observations from AMSR-E and AMSR2 using overlapping FY3B-MWRI sensor measurements, Remote Sensing, 6 (9):8594-8616.

[5] Zeng J., Shi P., Chen K., Ma H., Bi H., Cui C. (2022) On the Relationship Between Radar Backscatter and Radiometer Brightness Temperature From SMAP, IEEE Transactions on Geoscience and Remote Sensing, 60: 4406116.

# Attributing Nitrogen & Carbon Emissions from Satellite Columns and a Model Free Method

COHEN Jason Blake[1]

[1]School of Environment and Spatial Informatics, China University of Mining and Technology, Xuzhou, China.
email: jasonbc@alum.mit.edu , jasonbc@cumt.edu.cn

## 1. INTRODUCTION

Human economic activities drive fluxes of emissions of climate altering species and air pollutants into the atmosphere. There is a subset of these species which fill both roles simultaneously: altering the climate system while also being source air pollutants. Presently, emissions are computed through various bottom-up methods, which use small samples of economic activity such as power generation, energy and emissions polluting activities like transportation, agriculture, etc. and combine these with small samples of measured emissions, to form emissions datasets[1]. However, using these bottom-up measurements in geophysical models and comparing them with remotely sensed measurements from multiple satellite platforms, we find that the emissions tend to be wrong[2]. Some species are overestimated, others are underestimated, and frequently there is a bias with urban areas and rural areas systematically over or underestimated[3]. This work instead adopts a new type of top-down approach to estimate emissions[4]. This type of approach is based on remotely sensed data from multiple satellites of Carbon and Nitrogen containing species at different spatial and temporal resolutions, both very fine spatial resolution and only a short duration, as well as much more coarse resolution but with upwards of 20 years of measurements[6]. This approach then uses a non-model-based approach, based on physical, chemical, thermodynamic principals, to invert the emissions in space and time[7]. This approach's terms are fit to match both the mean and variations in the input datasets, using "Medium-Data" and Big-Data approaches[8]. The computed emissions are made at the day-to-day and grid-to-grid scale, covering China and significant parts of South and Southeast Asia. An analysis of the magnitudes, day-to-day variation, and uncertainties is discussed. Impacts on energy consumption, energy efficiency, discovery of new sources and previously mis-located sources, geospatial maps of where to consider action, and impacts of these new emissions on both air pollution and climate change will also be mentioned.

## 2. MATERIALS AND METHODS

This work first takes column densities of NOx, CO, HCHO, and implied columns of BC, among others, from multiple satellites, in a quality-controlled manner. Next, on a grid-by-grid, and day-by-day basis, the pixels containing valid measurements are trained on a variance-maximized time-by-time grouped basis based on current a priori emissions databases. The constraints are made using machine learning fits, guided by a mass-conserving framework. These fitted values are then applied via bootstrap based on the PDFS generated in the fitting methods to produce emissions datasets. Since these emissions are derived in tandem with each other, the results are thermodynamically, chemically, and physically linked.

### *2.1 Remotely Sensed Data*

NO2 and HCHO are retrieved from both OMI and TROPOMI. CO is retrieved from both MOPITT and TROPOMI. BC is inferred using the multi-spectral core/shell inversion method, based on measurements from multiple aerosol platforms. AERONET and other ground-based networks are also used.

### *2.2 Analytical Techniques*

Variance maximization using EOF/PCA is used to decompose the underlying remotely sensed datasets into their components. Fits are made with the mass-conserving method using machine learning. Pixel-by-Pixel fits are made in a way that is consistent with the spatial and temporal fields from the variance maximization approach. Uncertainties are computed by applying the PCM method.

### *2.3 Equations*

Mass conservation equations of all species follow the general format shown in Eq.(1). The derivative and gradient terms are solved using in tandem with the nearest neighbors. The coefficients are fit using various machine learning approaches, over temporal scales constrained by the variance maximization approaches, where X is the species of interest, d/dt is the temporal derivative, $\nabla$ is the spatial gradient, $\alpha_1$, $\alpha_2$, and $\alpha_3$ are the fits for the physical, thermodynamic, and chemical terms.

$$E_X = \alpha_1 d([X])/dt - \alpha_2[X] - \alpha_3\nabla(u[X]) \qquad (1)$$

## 3. RESULTS

### *3.1 Mean Emissions Maps*

Results of the method when applied to $NO_2$ measured by OMI at moderate resolution over a decade is given in Figure 1. As observed, the new emissions on average are higher than the a priori emissions database. Although this is not true on each pixel-by-pixel basis. Second, the spatial distribution is different, with areas previously unidentified (including Hong Kong) identified, and with highly emitting sources frequently observed to be in different geospatial locations from the emissions inventories.

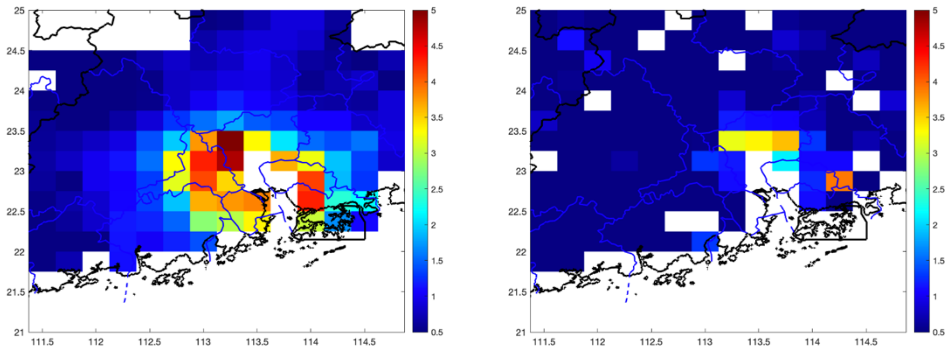


**Fig. 1.** Left is the mean emissions computed in this work. Right is the mean emissions given by the a priori MEIC database. All calculations are for the 5-year period from 2015 through 2019.

### *3.2 Uncertainty and Non-Linear Feedbacks*

One of the major advantages of this approach in addition to the fact that it is based on observations, is that it allows for a robust uncertainty analysis, consistent with underlying physical properties, and based upon advanced mathematical analysis. As observed in Figure 2, there is a robust error analysis performed on a grid-by-grid basis. It is clearly observed that areas with a significant amount of water or areas with a significant amount of recently changed vegetation fraction both have slightly higher error than areas which are relatively stable in terms of land use type. It is also observed that newly changing urban areas (not necessarily in the largest of urban centers) are further drivers of uncertainty. Analyzing the day-to-day variability on an urban-tier basis, it is observed that there is a significant amount of difference in the ratio of the variability to the mean on a day-to-day basis across different tiers of urban areas. This implies that effort to control emissions in different Tiers of cities should be targeted differently.

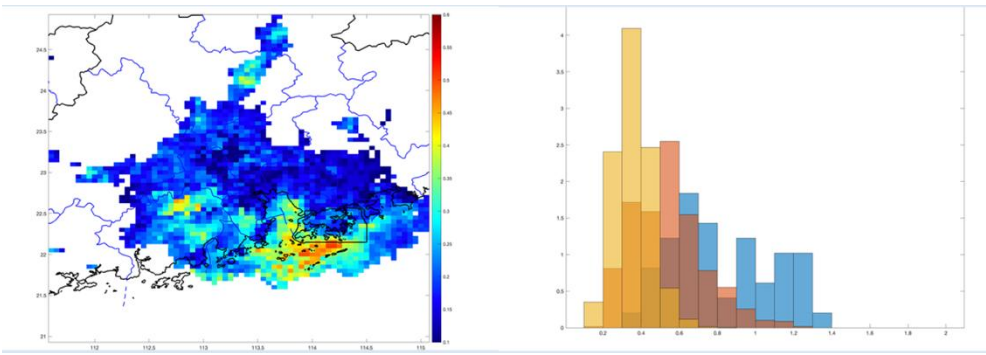

**Fig. 2.** Left is the average mean normalized error uncertainty (grid-by-grid). Right is the PDF of the daily variability of emissions over three different regions: orange is Tier 3 urban areas, red is Tier 2 urban areas, and blue is Tier 1 urban areas.

### *3.3 Source Identification and Attribution*

Due to its ability to strongly absorb ultraviolet radiation and visible radiation of different colors, BC is a carbon-containing emitted species which greatly impacts the climate system. The fact that this absorption is different across different colors in this range, has allowed a new technique to approximate the size, mixing state, and therefore source properties of BC. Here, the results of the size, shape, and mixing profiles, as well as emissions magnitude have been computed in the same manner. The set of results in Hong Kong are presented in Figure 3. First, it is observed that while on average the aerosol type is urban in nature, there are significant contributions from other types. Given that Hong Kong is a highly dense and urban city, such attribution is not found in the present-day emissions datasets of Hong Kong itself or the GBA in general. In specific, it is found that long range transport of aerosols from Southeast Asia and South Asia are prevalent during certain times of the year, and biomass burning aerosols from rural regions in Guangdong and Southeast Asia during other seasons of the year.

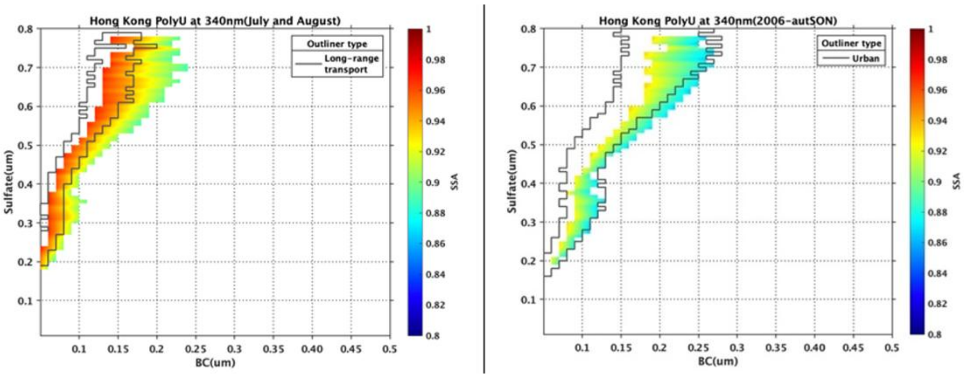


**Fig. 3. T**he size of BC (bottom) and shell (left), along with the SSA (color). As observed in July and August, the properties are a mixture of urban and long-range transported aerosols. However as observed in September, October, and November the conditions are a mixture of urban and biomass burning aerosols.

## 4. SUMMARY

The new emissions datasets indicate that there are significant underestimations on average in some of these species. However, more importantly, there are some bright spots, with local sources frequently reducing in top-tier urban areas also being observed. This means that current efforts to constrain well known emissions sources from highly polluting and non-mobile sources is working. However, the fact of the matter is that other species which are not well regulated, but also have a large impact on air pollution and climate are not as well controlled. Specific results of when, where, and what to control, from less efficient energy sources, from long-range and more out-of-city sources, and in surrounding nations are all identified and examined. It is hoped that this work can lead to improved emissions datasets and new approaches to continue to improve our knowledge of emissions at high spatial and temporal resolution, including uncertainties.

## References

[1] Cohen, J. B. and Prinn, R.G. (2011) Development of a fast, urban chemistry metamodel for inclusion in global models, *Atmos. Chem. Phys.*, 11, 7629-7656

[2] Cohen, J. B. and Wang C. (2013) An Estimate of Global Black Carbon Emissions Using a Top-Down Kalman Filter Approach. *J. Geophys. Res.*, 119, 1-17

[3] Cohen, J. B., Lecoeur, E., and Hui Loong Ng, D. (2017) Decadal-scale relationship between measurements of aerosols, land-use change, and fire over Southeast Asia, *Atmos. Chem. Phys.*, 17, 721-743

[4] Lin, C., Cohen, J. B., Wang, S., and Lan, R. (2020). Application of a combined standard deviation and mean based approach to MOPITT CO column data, and resulting improved representation of biomass burning and urban air pollution sources. *Remote Sensing of Environment*, 241, 111720

[5] Wang, S., Wang, X., Cohen, J. B., and Qin, K. (2021). Inferring Polluted Asian Absorbing Aerosol Properties Using Decadal Scale AERONET Measurements and a MIE Model. *Geophysical Research Letters*, https://doi.org/10.1029/2021GL094300

[6] Wang, S., Cohen, J. B., Deng, W., Qin, K., and Guo, J. (2021). Using a new top-down constrained emissions inventory to attribute the previously unknown source of extreme aerosol loadings observed annually in the monsoon Asia free troposphere. *Earth's Future*, *9*, e2021EF002167.
[7] Deng, W., Cohen, J. B., Wang, S., and Lin, C. (2021). Improving the Understanding between Climate Variability and Observed Extremes of Global NO2 Over the Past 15 Years. *Environmental Research Letters*, https://doi.org/10.1088/1748-9326/abd502
[8] Jian Liu, Jason Cohen. Quantifying the Missing Half of Daily $NO_x$ Emissions over South, Southeast and East Asia, 11 May 2022, https://doi.org/10.21203/rs.3.rs-1613262/v1

# Multiscale analysis of greenness trend over circumpolar arctic: uncertainties and implications for arctic greening and browning

LIU Caixia[1], XU Xiaoqing[2, 3]

[1] State Key Laboratory of Remote Sensing Science,

Aerospace Information Research Institute, Chinese Academy of Sciences, Beijing, P. R. China
email: liucx@radi.ac.cn

[2] School of Geospatial Engineering and Science, Sun Yat-Sen University, Guangzhou, P. R. China
[3] Peng Cheng Laboratory, Shenzhen, P. R. China
email: xuxq@pcl.ac.cn

## 1. INTRODUCTION

The Arctic is warming twice as fast as the global average [1]. Arctic warming has impacts on tundra ecosystem function because of its interactions with vegetation cover, wild life and human communities. Understanding the spatial distribution of Arctic greening and browning trends is important to evaluate the Arctic vegetation response to the changing climate or anthropogenic factors. Satellite-derived vegetation indices have been used for quantify these changes over high northern latitudes during the past four decades with coarse, moderate or high spatial resolution datasets. Increases in vegetation productivity have been completely observed by satellite observations over tundra ecosystems and those changes have been linked to shrub expansion and accelerated annual growth at locations throughout the Arctic [2-6]. However, the shrub expansion has been spatially uneven over the Arctic because of deer grazing [7,8]. The research on the influence of the Arctic warming amplification effect on the surface vegetation depends on the observation scale. High spatial resolution research on the greening of Arctic vegetation has been carried out in Alaska, Canada, and the Russian tundra for many years, but it is limited to the regional scale.

The finer resolution Landsat is a good complement to the AVHRR to evaluate long term tundra greenness trends and identify drivers of the changes. Both Landsat and AVHRR have almost the same observation period and the higher resolution of Landsat observations more closely matches the scale of field measurements and ecological changes than AVHRR observations. Although higher resolution data leads to the problem of increased data volume and high-speed computing power, the cloud computing platform Google Earth Engine (GEE) can help to facilitate scientific discovery by providing researchers with free access to the Landsat archive. To the best of our knowledge, most of these previous studies using Landsat datasets focus on regional or continental scales in the North American Arctic and here is still a gap in the understanding of vegetation greenness research in the entire Arctic tundra (north of the tree line).

## 2. MATERIALS AND METHODS

### *2.1 Study areas*

In the present study, we delimited the study area in the terrestrial Arctic. The terrestrial Arctic is defined as the northernmost part of the Earth characterized by tundra vegetation, an arctic climate and arctic flora, with the tree line and continental coastlines jointly determining the extent borders. Spatially, the present study covers an area of approximately 7.11 million km$^2$, overlapping with parts of six countries including Canada (CA), Denmark (Greenland, GR), Iceland (IC), Norway (NO), Russia (RU), and the United States (Alaska, AK).

### *2.2 Data and pre-processing*

Orthorectified top-of-atmosphere (TOA) reflectance data (L1T) Tier 1 from Landsat 5 TM, 7 ETM+ and 8 OLI sensors were used in this study. The TOA data rather than surface reflectance data were used because this is consistent with the existing studies on continental arctic greenness trends [9-11]. Landsat images have 30 m spatial resolution and all the used images were acquired during the melt season (1 July to 30 August) from 2000 to 2020. Unlike other existing greenness trend studies in the arctic area [12,13], we used all the available Landsat archive images during the melt season from 2000 to 2020 in the study area, including scenes with image contaminations due to clouds, ice/snow, aerosols, shadows, ETM+ scan line corrector (SLC) errors, etc. The use of contaminated images could increase the temporal resolution of observations. The number of Landsat observations during 2000-2020 in the Arctic is shown in Fig. 1. All of the Landsat data were acquired and processed with the help of GEE. The SimpleCloudScore algorithm implemented in the GEE, was used to evaluate cloud cover in the TOA reflectance images. We set the threshold score at 20 to exclude the high cloud cover images according to our visual interpretation because high cloud cover may lead to a decreased number of available ground control points and therefore the geolocation accuracy may decrease.

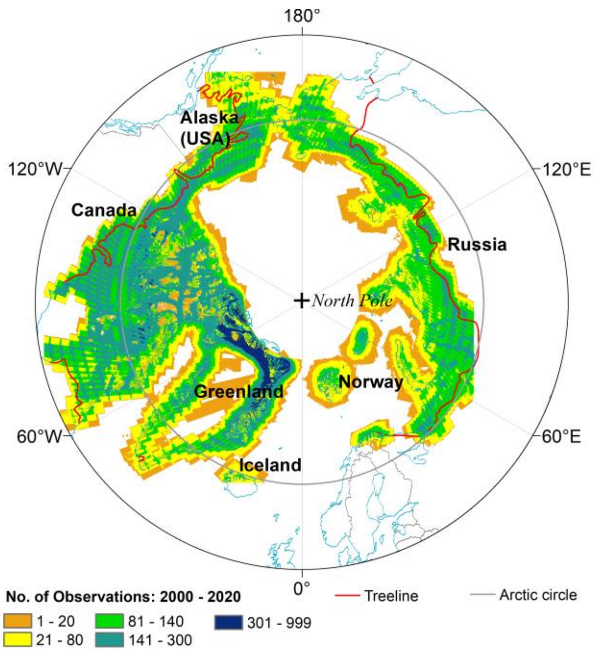


**Fig. 1.** Number of Landsat observations during the study period.

In order to compare spatial and trend differences, AVHRR GIMMS NDVI3g v3.1 time series (hereafter GIMMS) [14] was also used in this study. The GIMMS data are bi-monthly with a spatial resolution of 1/12 degrees (~8 km at the equator). A maximum NDVI composite in every year in July and August were derived and then used for trend calculation. The same regression method, TSR, was performed on this dataset over the same study period.

### *2.3 NDVI trend derivation*

The NDVI time series data during melt seasons were used for each land pixel except for non-water or non-snow locations. The values from Landsat 5, 7 and 8 were calibrated using equations from Roy et al. [15]. Valid time series were defined in that there were at least two observations in the study period or the NDVI trend was not calculated. Linear trends were conducted for the NDVI time series with non-parametric Theil–Sen regression (TSR) models within GEE, which were better than an ordinary least square regression analysis because a TSR is sensitive to outliers with a breakdown point of approximately 29% [16]. Additionally, a TSR has been successfully applied to the trend analysis of a Landsat NDVI time series across Alaska [11], a Landsat Tasseled Cap (TC) time series in the Canadian North-West and the Arctic Lena Delta in Russia [17-19]. Each pixel was observed to determine the slope between every data pair and the median value was then calculated. This slope of regression was set as the annual NDVI trend. The TSR prediction precision could be improved when the number of valid observations increased. A Student’s t-test was used to evaluate the significance of the trend. Trends with $p < 0.05$ were determined to be significant and only the changed pixels were retained in the final results. As prior studies have defined [9-11], a greening trend has a significant positive slope and a browning trend has a significant but negative slope.

## 3. RESULTS

### *3.1 Landsat NDVI trends over the decades*

The greening trend was significant across the entire circumpolar tundra biome for the 2000–2020 period (Fig. 2). The most significant greening occurred in the northern and southern parts of Russia's Yamal Peninsula and the central Gydan Peninsula, the northeastern Chukchi Peninsula, southeastern Canada, and northwestern Alaska. Browning mainly occurs in mountainous areas with undulating terrain and wetlands in central and eastern Russia. The average greening trend value was 0.003 NDVI units per year. The results show that the area with changes in vegetation greenness is 1.04 million $km^2$, accounting for 15.5% of the total area of the study area, of which the area with increasing greenness (greening) accounts for 94.7% and the area with decreasing greenness (browning) accounts for 5.3%.

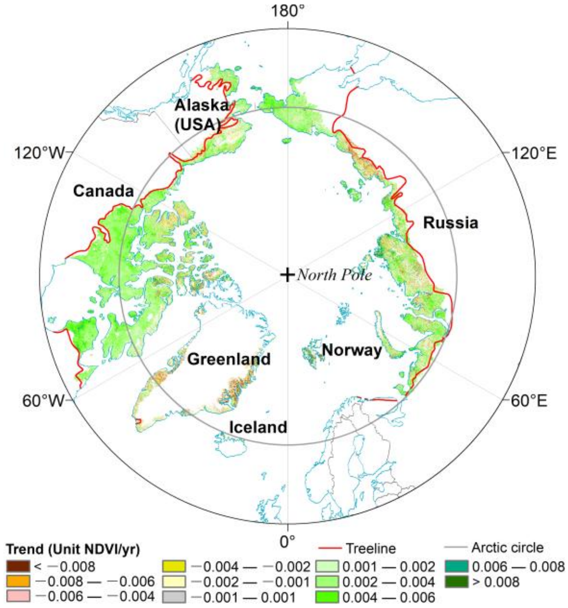


**Fig. 2.** The greenness trend map based on Landsat data.

### *3.2 Landsat NDVI trends and a comparison with AVHRR*

The greenness trend map derived from AVHRR GIMMS data is shown in Fig. 3. The average greening trend value was 0.003 NDVI units per year. Both the AVHRR and Landsat NDVI trends indicated an overall greening of the circumpolar tundra. However, the greening to browning ratio is very different between results. The ratio is 17.9:1 in Landsat results, but 1.6:1 in AVHRR results, indicating that the coarse-resolution remote sensing observations underestimate the difference between the two trends.

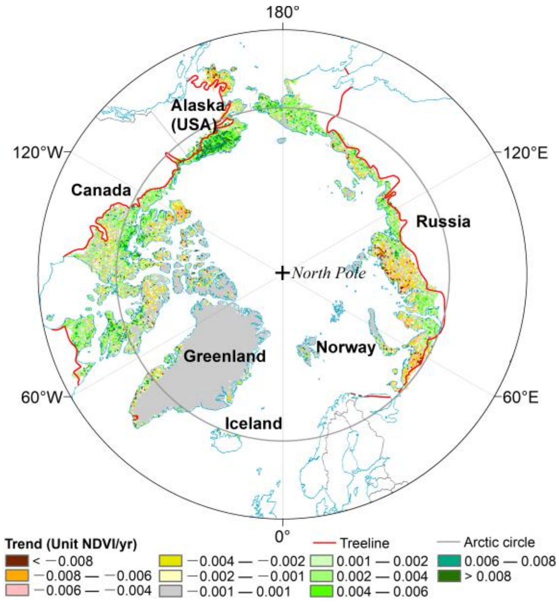


**Fig. 3.** The greenness trend map based on AVHRR GIMMS data.

There are also inconsistent geographic patterns of the NDVI trend between the two data sources for the study area. For example, for the areas of western Russia, AVHRR analysis indicated extensive browning, while in the Landsat analysis much of these areas did not show any statistically significant trends. As far as greening, for the areas of mountainous Alaska, AVHRR analysis indicated extensive greening, while in the Landsat analysis much of these areas did not show statistically significant trends.

## 4. SUMMARY

In short, we provide here continuous 30 m resolution greenness trend map during the past two decades over the entire arctic tundra, which help us to understand the response of arctic vegetation to climate change and anthropogenic disturbance. In contrast to coarse resolution trend maps (i.e., AVHRR), the pixel-by-pixel Landsat-based trend maps may contribute to more detailed change driver attribution in the context of climate warming and oil gas exploitation activities in northern permafrost. In order to help us improve understanding of vegetation greening in circumpolar areas in different vegetation types and geographic gradients, there is a high demand for higher spatial resolution observations in future research, as well as collecting field measurement data over focal scales and even the tundra biome scale.

## References

[1] Post, E.; Alley, R.B.; Christensen, T.R.; Macias-Fauria, M.; Forbes, B.C.; Gooseff, M.N.; Iler, A.; Kerby, J.T.; Laidre, K.L.; Mann, M.E. The polar regions in a 2 C warmer world. Science advances 2019, 5, eaaw9883.

[2] Berner, L.T.; Massey, R.; Jantz, P.; Forbes, B.C.; Macias-Fauria, M.; Myers-Smith, I.; Kumpula, T.; Gauthier, G.; Andreu-Hayles, L.; Gaglioti, B.V. Summer warming explains widespread but not uniform greening in the Arctic tundra biome. Nature communications 2020, 11, 1-12.

[3] Forbes, B.C.; Fauria, M.M.; Zetterberg, P. Russian Arctic warming and 'greening'are closely tracked by tundra shrub willows. Global Change Biol 2010, 16, 1542-1554.

[4] Frost, G.V.; Epstein, H.E.; Walker, D.A. Regional and landscape-scale variability of Landsat-observed vegetation dynamics in northwest Siberian tundra. Environmental Research Letters 2014, 9, 025004.

[5] Macias-Fauria, M.; Forbes, B.C.; Zetterberg, P.; Kumpula, T. Eurasian Arctic greening reveals teleconnections and the potential for structurally novel ecosystems. Nature Climate Change 2012, 2, 613-618, doi:10.1038/nclimate1558.

[6] Frost, G.V.; Epstein, H.E. Tall shrub and tree expansion in Siberian tundra ecotones since the 1960s. Global Change Biol 2014, 20, 1264-1277.

[7] Veselkin, D.; Morozova, L.; Gorbunova, A. Decrease of NDVI values in the southern tundra of Yamal in 2001–2018 correlates with the size of domesticated reindeer population. Modern problems of remote sensing of the Earth from space 2021, 18, 143-155.

[8] Verma, M.; to Bühne, H.S.; Lopes, M.; Ehrich, D.; Sokovnina, S.; Hofhuis, S.P.; Pettorelli, N. Can reindeer husbandry management slow down the shrubification of the Arctic? J Environ Manage 2020, 267, 110636.

[9] Ju, J.; Masek, J.G. The vegetation greenness trend in Canada and US Alaska from 1984–2012 Landsat data. Remote Sens Environ 2016, 176, 1-16.
[10] Pastick, N.J.; Jorgenson, M.T.; Goetz, S.J.; Jones, B.M.; Wylie, B.K.; Minsley, B.J.; Genet, H.; Knight, J.F.; Swanson, D.K.; Jorgenson, J.C. Spatiotemporal remote sensing of ecosystem change and causation across Alaska. Global Change Biol 2019, 25, 1171-1189.
[11] Liu, C.; Huang, H.; Sun, F. A Pixel-Based Vegetation Greenness Trend Analysis over the Russian Tundra with All Available Landsat Data from 1984 to 2018. Remote Sensing 2021, 13, 4933.
[12] Raynolds, M.K.; Walker, D.A.; Verbyla, D.; Munger, C.A. Patterns of change within a tundra landscape: 22-year Landsat NDVI trends in an area of the northern foothills of the Brooks Range, Alaska. Arctic, antarctic, and alpine research 2013, 45, 249-260.
[13] Raynolds, M.K.; Walker, D.A. Increased wetness confounds Landsat-derived NDVI trends in the central Alaska North Slope region, 1985–2011. Environmental Research Letters 2016, 11, 085004.
[14] Pinzon, J.E.; Tucker, C.J. A non-stationary 1981–2012 AVHRR NDVI3g time series. Remote Sensing 2014, 6, 6929-6960.
[15] Roy, D.P.; Kovalskyy, V.; Zhang, H.; Vermote, E.F.; Yan, L.; Kumar, S.; Egorov, A. Characterization of Landsat-7 to Landsat-8 reflective wavelength and normalized difference vegetation index continuity. Remote Sens Environ 2016, 185, 57-70.
[16] Fernandes, R.; Leblanc, S.G. Parametric (modified least squares) and non-parametric (Theil–Sen) linear regressions for predicting biophysical parameters in the presence of measurement errors. Remote Sens Environ 2005, 95, 303-316.
[17] Nitze, I.; Grosse, G. Detection of landscape dynamics in the Arctic Lena Delta with temporally dense Landsat time-series stacks. Remote Sens Environ 2016, 181, 27-41.
[18] Fraser, R.H.; Olthof, I.; Kokelj, S.V.; Lantz, T.C.; Lacelle, D.; Brooker, A.; Wolfe, S.; Schwarz, S. Detecting landscape changes in high latitude environments using landsat trend analysis: 1. Visualization. Remote Sensing 2014, 6, 11533-11557.
[19] Olthof, I.; Fraser, R.H. Detecting landscape changes in high latitude environments using Landsat trend analysis: 2. Classification. Remote Sensing 2014, 6, 11558-11578.

# Change analysis to the daily river ice fraction of the Yenisei River

Yixiao Zhang[1,2], Yubao Qiu[1*], Wenshan Liang[3], Jingtian Zhou[1,2], Guoqiang Jia[1]

[1]Aerospace Information Research Institute, Chinese Academy of Sciences, Beijing, China

Email: zhangyixiao211@mails.ucas.ac.cn (for author1)

Email: qiuyb@aircas.ac.cn (for author2)

Email: zhoujt@aircas.ac.cn (for author4)

Email: jiagq@aircas.ac.cn (for author5)

[2]College of Resources and Environment, University of Chinese Academy of Sciences, Beijing, China

[3]Scientific Institute of Pearl River Water Resources Protection, Guangzhou, China

Email: 276753683@qq.com

## 1. INTRODUCTION

River ice is an important component of the terrestrial cryosphere. In the northern hemisphere, approximately 60% of rivers are affected by ice in winter regularly or intermittently [1]. The development of river ice could change the physical, chemical, and biological conditions of rivers, influencing the freshwater ecosystem in winter [2]. Especially, the spatiotemporal change of river ice, which is controlled by atmospheric circulatory fluxes, can be an indicator of climate change [3]. In the context of global warming [4], the physical process of river ice has changed significantly, with the global river ice extent decreasing by 2.5 percentage points over the past 30 years [5]. Compared with global warming, the warming in the Arctic region is more intense [6], causing a reduction in river ice cover duration, a decrease of maximum river ice thickness, and a shifting of the date of ice break-up to earlier dates [7-11].

The Yenisei River is the second largest river in Russia, with a wide area and large river flow. Because of the low temperature, some river water is stored as river ice during the long winters [12]. And the contribution of individual rivers to the total ice volume of Arctic rivers is proportional to basin size [7]. Despite the research on river ice variability and the research on river ice phenology conducted in the Yenisei River [10, 11, 13], the data sources are limited to in-situ data. It should be noted that since mountains and plateaus account for over 90% of the basin area, observation sites are sparely distributed. And central Siberia is cold, remote, and inaccessible. These factors challenge the acquisition of data and make it difficult to achieve continuous spatiotemporal monitoring of river ice in the large river basin. The application of remote sensing provides a better choice. In this study, we estimate daily river ice coverage and analyze the spatiotemporal change in the Yenisei River for the period 2002-2021.

## 2. MATERIALS AND METHODS

### *2.1 Data Source*

Daily snow cover data products (MOD10A1/MYD10A1) were used to identify river ice, which are collected and generated by the Moderated Resolution Imaging Spectroradiometer (MODIS) on Terra and Aqua satellite. We used the river vector dataset prepared by Liang et al. [14], to determine the location of Yenisei River. The Landsat7(ETM+) and Landsat8(OLI) images were used for validation. We also used ERA5-Land data from the European Centre for Medium-Range Weather Forecasts (ECMWF).

### *2.2 Estimating river ice fraction*

We extracted river ice pixels from MODIS images using the classic Normalized Snow Index Algorithm (NDSI). Firstly, we assumed that river ice coverage doesn't change for a short time. Then based on the temporal and spatial continuity of rivers, cloud removal was carried out with reference to the algorithm of Qiu et al. [15]. Thirdly, the river ice coverage was calculated in unit of 12.5km grid. Some filters were applied to reduce the errors caused by clouds and polar night.

### *2.3 Validation*

The river ice coverage obtained by visual interpretation was deemed as ‘true value’ and used for validation [16]. We used quantitative accuracy as an indicator for accuracy verification, as shown in Eq (1) and Eq (2)。

$$Ki = 1 - |Li - Mi| \tag{1}$$

$$V = \sum_{i=1}^{n} Ki/n \tag{2}$$

Where i – grid number (i<n), Li – river ice coverage from Landsat, Mi – river ice coverage from MODIS, Ki – the accuracy of every grid, n – total number of selected grids, V – the accuracy of the river basin.

## 3. RESULTS

### *3.1 Validation of river ice*

The comparison with Landsat shows that the river ice coverage basin has an average accuracy of 86% in the Yenisei River. At Lower and Middle Yenisei River, the Pearson correlation coefficients of river ice coverage extracted from the two remote sensing data are 0.97 and 0.84, respectively, with accuracy of 94% and 87%. At Upper Yenisei River, the Pearson correlation coefficients and accuracy is 0.77 and 76%. During the melting season, river ice melt from upstream and gradually move toward downstream. Under the influence of dynamics and thermodynamics, the changes of river ice in the upper reaches are more intense.

### *3.2 Spatial-temporal distribution of river ice*

River ice covers widely in the Yenisei River. On average, river ice coverage in more than 65% of the region is higher than 0.60 every winter. Fig.1(a) depicts the spatial-temporal distribution of river ice coverage in winter (hereafter referred to as river ice coverage). River ice coverage in low latitude area is low and fluctuates greatly, while in high latitude area it is stable. This result indicates that the distribution of river ice is regional, corresponding to the distribution of air temperature in winter (Fig.1(b)).

### *3.3 Trend analysis*

The variation trend of river ice coverage was analyzed by Theil Sen's Slope statistical method and Mann-Kendall test method. Result shows that (Fig.2(a)), in 82.81% (3218 grids) of the Yenisei River basin, river ice coverage is decreased, and 21.91% (705 grids) of which passed the significance test. Only 26 grids show a statistically significant increasing trend. If we only inspect the direction of the trends (both significant and insignificant), the average rate of change in river ice coverage is -0.0028 $yr^{-1}$. And the average slope of air temperature in winter (hereafter referred to as air temperature) is 0.0878 ℃ $yr^{-1}$.

### *3.4 The correlation between river ice and air temperature*

The correlation analysis shows that there is a significant negative correlation between river ice coverage and air temperature in the Yenisei River basin, and the Pearson’s r is -0.69 Fig.3(a). The correlation between negative accumulated air temperature and river ice coverage is similar (Pearson’s r is -0.66). In other words, warm winter is not beneficial for the development of river ice. Although there is a strong correlation between river ice coverage and air temperature in winter, it was distinct in different latitudes. In the 45 °N~60 °N region, the correlation between river ice coverage and air temperature is obvious, but in the extremely cold region (north of 60 °N), no marked relationship is observed (Fig.3(b)).

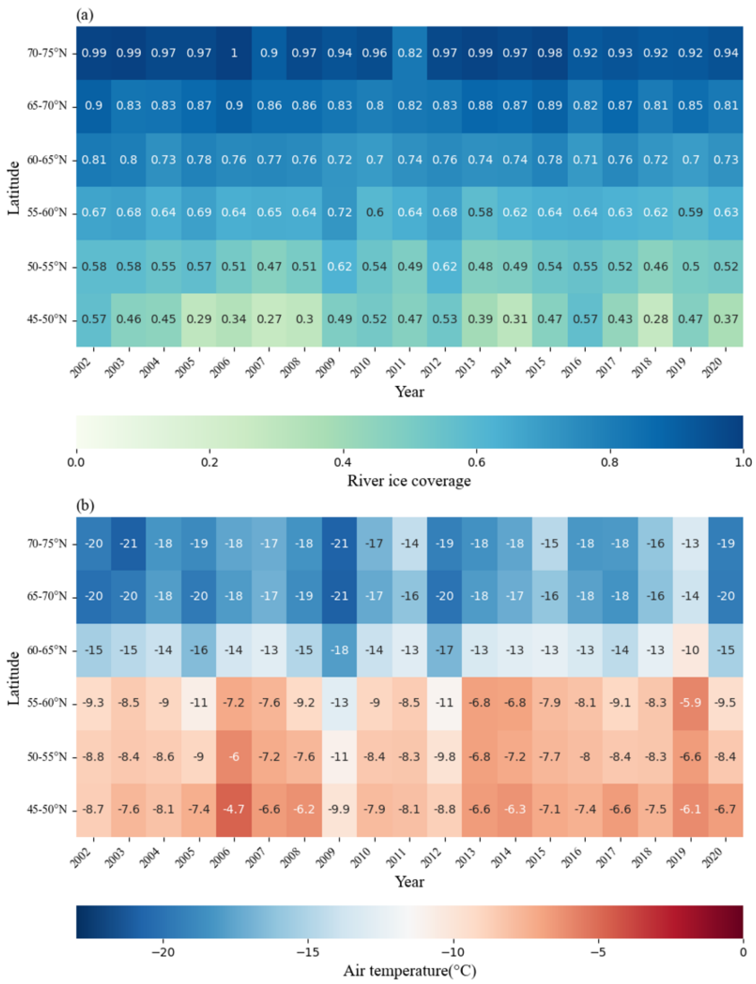


Fig.1.The spatial distribution of winter river ice(a) and air temperature(b) at different latitudes.

(Winter: Oct-May)

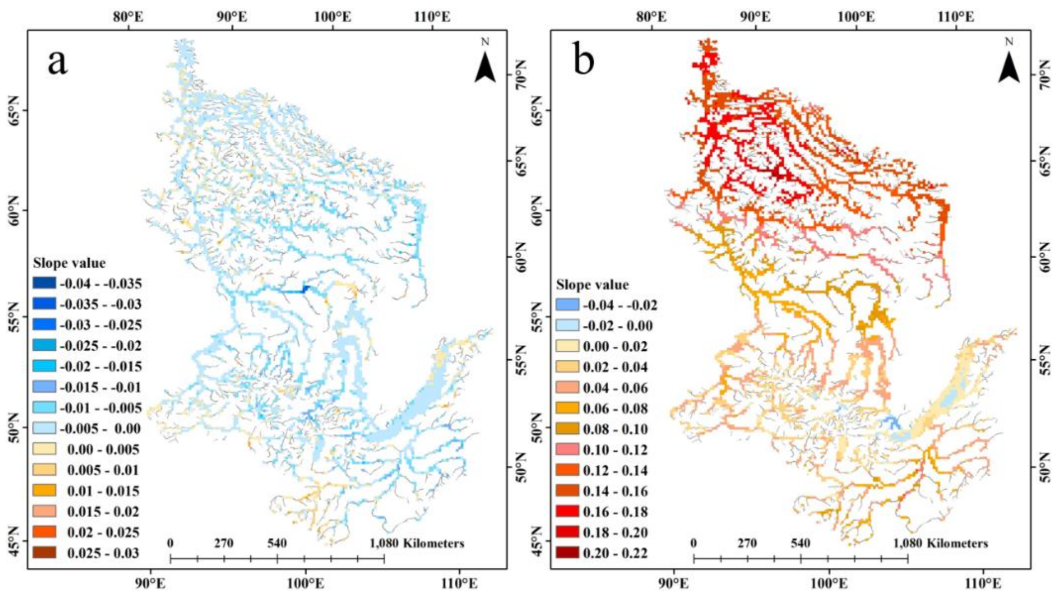


Fig.2. Winter river ice coverage(a) and air temperature(b) trends for the period 2002-2021.

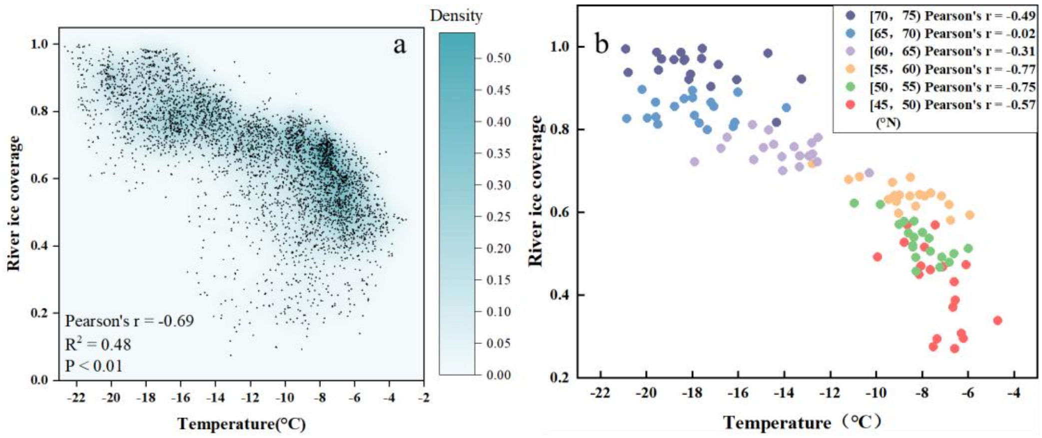


Fig.3.The correlation between winter river ice coverage and air temperature (multi-year) (a) and the correlation between winter river ice coverage and air temperature in different latitudes (b).

## 4. SUMMARY

In an attempt to further understand the change of river ice in the Yenisei River, we estimated daily river ice coverage in the grid scale. River ice coverage is characterized by spatial differences, which is associated with air temperature. Trend analysis suggests that river ice coverage is lessening slightly. Moreover, the correlation analysis verifies that river ice change is significantly driven by air temperature, which exhibits a strong latitude dependency. This study monitored the spatiotemporal variation of river ice in the Yenisei River basin, supporting investigations on the response of arctic great rivers to climate change.

## Funding

This study was supported by Strategic Priority Research Program of the Chinese Academy of Sciences [grant numbers XDA19070201 and XDA19070102] and the Multi-Parameters Arctic Environmental Observations and Information Services Project (MARIS) funded by Ministry of Science and Technology (MOST) [grant number 2017YFE0111700].

## Reference

[1] Prowse, T.D., *River-Ice Hydrology.* Encyclopedia of Hydrological Sciences, 2005.
[2] Lindenschmidt, K.-E., H.M. Baulch, and E. Cavaliere, *River and lake ice processes-Impacts of freshwater ice on aquatic ecosystems in a changing globe.* Water (Switzerland), 2018. **10**(11).
[3] Prowse, T., et al. *River-ice break-up/freeze-up: A review of climatic drivers, historical trends and future predictions*. 2007. International Glaciology Society.
[4] Serreze, M.C., et al., *Observational evidence of recent change in the northern high-latitude environment.* Climatic Change, 2000. **46**(1-2): p. 159-207.
[5] Yang, X., T.M. Pavelsky, and G.H. Allen, *The past and future of global river ice.* Nature, 2020. **577**(7788): p. 69-73.
[6] AMAP, *Arctic Climate Change Update 2021: Key Trends and Impacts. Summary for Policy-Makers*. 2021, Arctic Monitoring and Assessment Programme (AMAP) Tromsø, Norway.
[7] Park, H., et al., *Quantification of warming climate-induced changes in terrestrial Arctic river ice thickness and phenology.* Journal of Climate, 2016. **29**(5): p. 1733-1754.
[8] Marszelewski, W. and B. Pawlowski, *Long-Term Changes in the Course of Ice Phenomena on the Oder River along the PolishGerman Border.* Water Resources Management, 2019. **33**(15): p. 5107-5120.
[9] Chen, Y. and Y. She, *Long-term variations of river ice breakup timing across Canada and its response to climate change.* Cold Regions Science and Technology, 2020. **176**.
[10] Shiklomanov, A.I. and R.B. Lammers, *River ice responses to a warming Arctic - Recent evidence from Russian rivers.* Environmental Research Letters, 2014. **9**(3).
[11] Vuglinsky, V., *Assessment of Changes in Ice Regime Characteristics of Russian Lakes and Rivers under Current Climate Conditions.* Natural Resources, 2017. **08**(06): p. 416-431.
[12] Prowse, T.D., *River-ice ecology II: Biological aspects.* Journal of Cold Regions Engineering, 2001. **15**(1): p. 17-33.
[13] Prowse, T., et al., *Past and Future Changes in Arctic Lake and River Ice.* Ambio, 2012. **40**(S1): p. 53-62.
[14] Wenshan, L., et al., *Vector dataset for river systems originating in Eurasia to the Arctic Ocean.* IOP Conference Series: Earth and Environmental Science, 2020. **502**(1).
[15] Qiu, Y., et al., *MODIS-based daily lake ice extent and coverage dataset for Tibetan Plateau.* 2019. **3**(2): p. 170-185.
[16] Brown, D.R.N., et al., *Changing river ice seasonality and impacts on interior Alaskan communities.* Weather, Climate, and Society, 2018. **10**(4): p. 625-640.

# Multidimensional analysis and seasonal asymmetry of Arctic sea ice

Guo Yu[1,2,3,4], Wang Xiaoli [1,2,3 *], Hou Xiyong [1,2,3]

[1] CAS Key Laboratory of Coastal Environmental Processes and Ecological Remediation, Yantai Institute of Coastal Zone Research, Chinese Academy of Sciences, Yantai Shandong 264003, China
[2] Shandong Key Laboratory of Coastal Environmental Processes, Yantai Shandong 264003, China
[3] Center for Ocean Mega-Science, Chinese Academy of Sciences, Qingdao 266071, China
[4] University of Chinese Academy of Sciences, Beijing 100049, China
email: yguo@yic.ac.cn
email: xlwang@yic.ac.cn
email: xyhou@yic.ac.cn

## 1. INTRODUCTION

Arctic sea ice is not only recognized as an indicator but also an amplifier of global climate change, playing an important role in global climate system[1]. In recent decades, Arctic sea ice has undergone unprecedented changes[2-8]. Many scholars around the world have carried out numerous studies on sea ice in the aspects of spatial-temporal changes[2, 6, 9-13], prediction simulation[14-16] and driving mechanism [17-21]. Due to the long time scale and availability of sea ice concentration(SIC) data, sea ice area(SIA) and extent(SIE) calculated based on SIC have become the hot parameters of Arctic research. However, the long-term records of sea ice thickness (SIT) are difficult to obtain due to limited satellite observation time, leading to SIT less of a concern than other sea ice parameters. SIA and SIT are the parameters of sea ice in horizontal dimension and vertical dimension respectively. In order to better explore the variability of Arctic sea ice, the sea ice parameters should be comprehensively evaluated from different dimensions. Moreover, many studies have concluded that the largest sea ice reduction occurs in summer, but how sea ice changes in different seasons, especially in melt and freeze seasons, remains obscure. Therefore, this study aims to investigate the spatial-temporal variations of Arctic sea ice in the horizontal (SIA) and vertical (SIT) dimensions from 1979 to 2020. Then, the seasonal asymmetry in Arctic sea ice was further discussed, mainly focusing on the differences between melt season and freeze season.

## 2.MATERIALS AND METHODS

### *2.1 Data sources*

#### *2.1.1 SIC and SIA*

The SIC data from 1979 to 2020 is obtained from the National Snow and Ice Center (NSIDC; https://nsidc.org/data), with a spatial resolution of 25 km×25 km. SIA is the cumulative area of ice cover[6], which can be calculated through the sum of the grid cell areas multiplied by the SIC (at least 15%).

#### *2.1.2 SIT*

The Pan-Arctic Ice Ocean Modeling and Assimilation System(PIOMAS) is a coupled ice-ocean model assimilation system[22], which can be applied to assess changes of SIT over long time series. To improve simulation accuracy, the system constrains the model solution by assimilating observational data such as sea ice concentration and sea surface temperature[15].

### *2.2 Methods*

Based on satellite and assimilation data, the variations of Arctic sea ice from multiple spatial and temporal scales are analyzed in this study. The long-term trends of SIA and SIT are analyzed on monthly, seasonal and annual scales. Seasonally, January – March, April – June, July – September and October – December are widely regarded as the winter, spring, summer and autumn in the Arctic[23]. To further explore the seasonal asymmetry of sea ice, this study defines the melt season as the month between the maximum and minimum values of sea ice in the current year, while the freeze season is defined as the month between the minimum (previous year) and maximum values (current year) of sea ice. Moreover, the

Arctic is divided into twelve subregions to explore the spatial differences of sea ice. For trend detection, the linear regression and M-K trend method is used to explore the spatial-temporal variation trends of SIA and SIT.

## 3.RESULTS

### *3.1 Multidimensional analysis of Arctic sea ice*

The spatial-temporal variations of sea ice in the horizontal dimension and vertical dimension are shown in Figure 1 and 2. In the horizontal dimension, there were large declining trends of SIA in the Barents Sea, Kara Sea, East Siberian Sea, with rates of more than $-5.0 \times 10^3$ $km^2$/yr; In the horizontal dimension, there were large declining trends of SIT in the Beaufort Sea, Chukchi Sea, East Siberian Sea, Canadian Archipelago, with rates of more than -2.4 cm/yr. However, the subregions with large reduction trends of SIA (at least $-5.0\times10^3 km^2$/yr) do not show the same significant trends of SIT (at least -2.4cm/yr); and vice versa. The greatest thinning occurs where the ice is initially thickest.

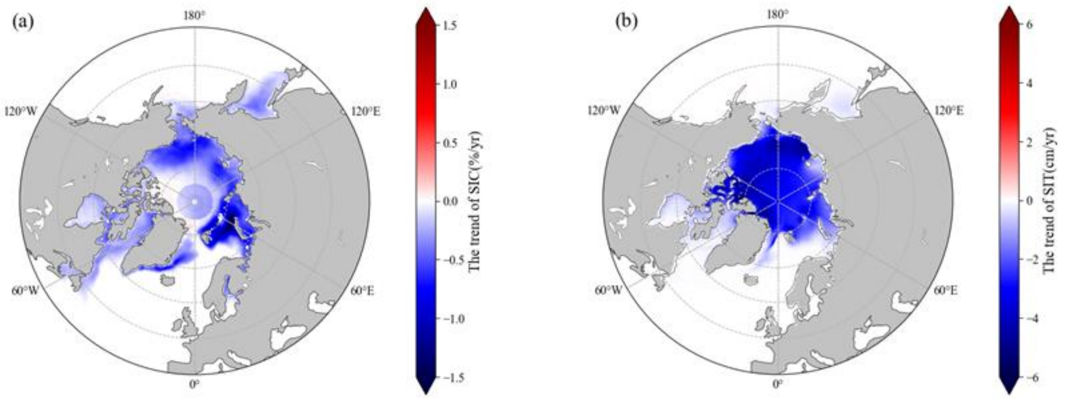


**Fig. 1.** Spatial variation trends of Arctic sea ice concentration(a) and thickness(b) from 1979 to 2020

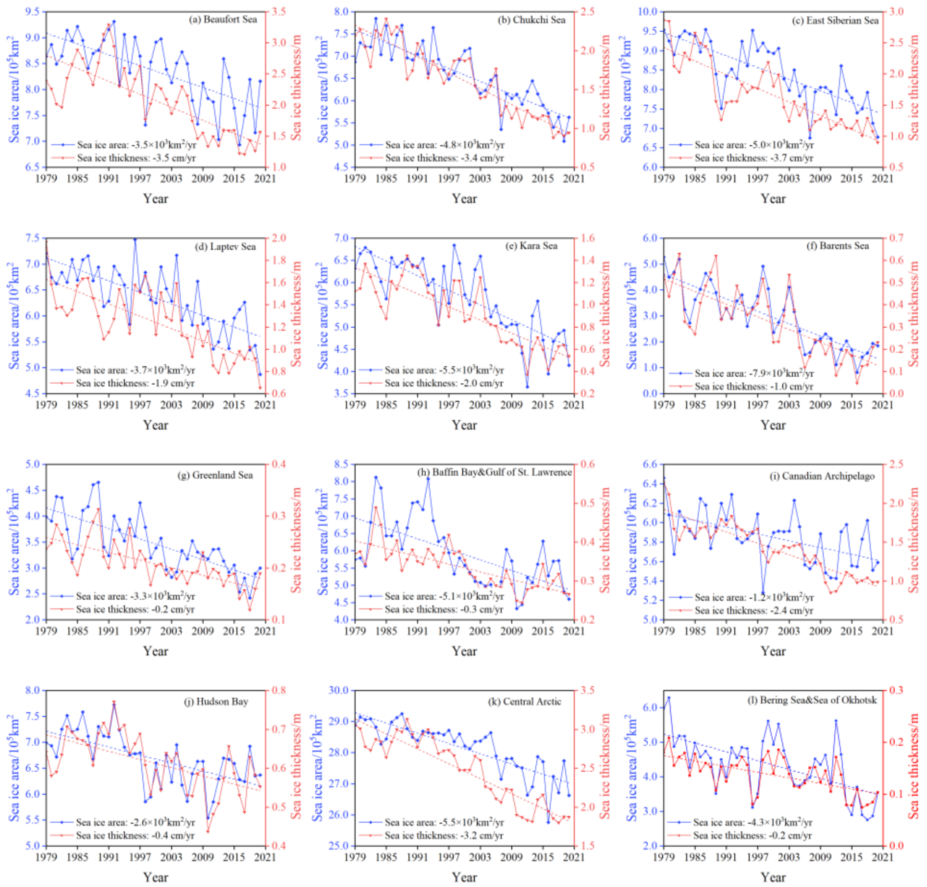


**Fig. 2.** The interannual variations of sea ice area and thickness in the 12 subregions(a-l) from 1979 to 2020

### *3.2 Asymmetry of sea ice freezing and melting*

Figure 2 indicated that sea ice variations have obvious seasonal asymmetry, that is, there exists differences between the melt season and freeze season of Arctic sea ice. In terms of the melting season, SIA began to melt in March or April, while that of SIT began in April or May. Obviously, the melting season of SIA was longer and earlier than SIT. In terms of the freezing season, SIA and SIT began to refreeze in September, but there were differences in their freezing rates. In the vertical dimension, sea ice froze slowly in all subregions. In the horizontal dimension, sea ice rapidly froze within two or three months, with representative regions including the Beaufort Sea, Chukchi Sea, East Siberian Sea, Laptev Sea, Kara Sea, Canadian Archipelago, Hudson Bay and Central Arctic. Unlike the above regions, the freezing rates of SIA and SIT are similar in Barents Sea, Greenland Sea, Baffin Bay & Gulf of and Bering Sea &Sea of Okhotsk, which share a common feature of external ocean connectivity. Overall, in the horizontal dimension, SIA was characterized by early melting and rapid freezing; in the vertical dimension, SIT was characterized by late melting and slow freezing.

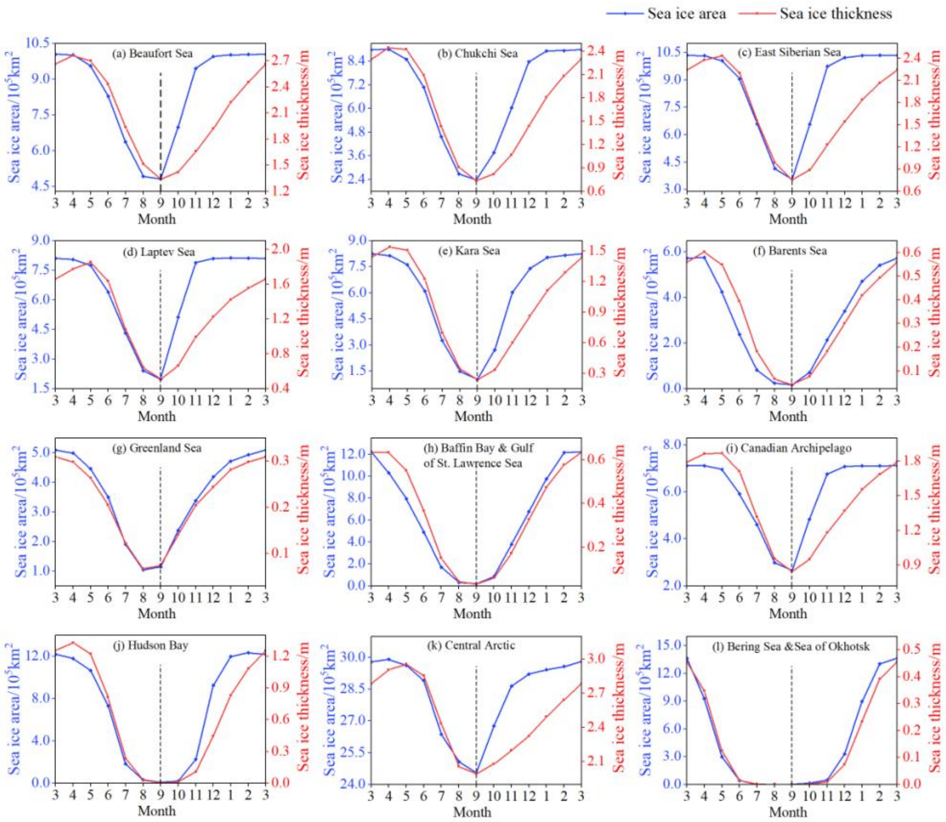


**Fig. 3.** The monthly variations of sea ice area and thickness in the 12 subregions(a-l) from 1979 to 2020

## 4.SUMMARY

The study investigated the spatial-temporal variations of Arctic sea ice in the horizontal (SIA) and vertical (SIT) dimensions from 1979 to 2020. Results indicated that Arctic sea ice was declining at an unprecedented rate, with the trend of $-5.4\times10^4$km$^2$/yr in SIA and -2cm/yr in SIT. In the horizontal dimension, the Kara Sea, Barents Sea and East Siberian Sea showed large declining trends of SIA, which was mainly affected by the North Atlantic warm current and transpolar drift stream. In the horizontal dimension, the Beaufort Sea, Chukchi Sea, East Siberian Sea, and Canadian Archipelago showed large declining trends of SIT. Under the influence of growth-thickness feedback, the greatest thinning occurred where the ice was initially thickest. Thus, SIA is more regulated by external factors, while SIT depends mainly on its own thermodynamic properties. This study also reveals that global temperature is the main driver of long-term Arctic sea ice decline, while interannual oscillations and spatial variability of sea ice are mainly regulated by ocean-atmosphere factors and own thermodynamic properties. Moreover, Arctic sea ice variability is characterized by obvious seasonal asymmetry, which is not only reflected in the length of melt season and freeze season, but also in the rate of sea ice melting and freezing. In the horizontal dimension, SIA is characterized by early melting and rapid freezing. However, in the vertical dimension, SIT is characterized by late melting and slow freezing.

## References

[1] Cai Q., Wang J., Beletsky D., et al. (2021) Accelerated decline of summer Arctic sea ice during 1850–2017 and the amplified Arctic warming during the recent decades. Environmental Research Letters, 16(3).

[2] Kumar A., Yadav J. & Mohan R. (2021) Spatio-temporal change and variability of Barents-Kara sea ice, in the Arctic: Ocean and atmospheric implications. Sci Total Environ, 753: 142046.

[3] Xiao F., Zhang S., Li J., et al. (2021) Arctic sea ice thickness variations from CryoSat-2 satellite altimetry data. Science China-Earth Sciences, 64(7): 1080-1089.

[4] Wang Z., Li Z., Zeng J., et al. (2020) Spatial and Temporal Variations of Arctic Sea Ice From 2002 to 2017. Earth and Space Science, 7(9).

[5] Peng G. & Meier W. N. (2018) Temporal and regional variability of Arctic sea-ice coverage from satellite data. Annals of Glaciology, 59(76): 191-200.

[6] Parkinson C. L., Cavalieri D. J., Gloersen P., et al. (1999) Arctic sea ice extents, areas, and trends, 1978-1996. Journal of Geophysical Research-Oceans, 104(C9): 20837-20856.

[7] Chen J. L., Kang S. C., Meng X. H., et al. (2019) Assessments of the Arctic amplification and the changes in the Arctic sea surface. Advances in Climate Change Research, 10(4): 193-202.
[8] Arthun M., Eldevik T. & Smedsrud L. H. (2019) The Role of Atlantic Heat Transport in Future Arctic Winter Sea Ice Loss. Journal of Climate, 32(11): 3327-3341.
[9] Onarheim I. H., Eldevik T., Smedsrud L. H., et al. (2018) Seasonal and Regional Manifestation of Arctic Sea Ice Loss. Journal of Climate, 31(12): 4917-4932.
[10] Duan C., Dong S., Xie Z., et al. (2019) Temporal variability and trends of sea ice in the Kara Sea and their relationship with atmospheric factors. Polar Science, 20: 136-147.
[11] Chen P. & Zhao J. P. (2017) Variation of sea ice extent in different regions of the Arctic Ocean. Acta Oceanologica Sinica, 36(8): 9-19.
[12] Blanchard-Wrigglesworth E. & Bitz C. M. (2014) Characteristics of Arctic Sea-Ice Thickness Variability in GCMs. Journal of Climate, 27(21): 8244-8258.
[13] Arthun M., Onarheim I. H., Dorr J., et al. (2021) The Seasonal and Regional Transition to an Ice-Free Arctic. Geophysical Research Letters, 48(1).
[14] Peng G., Matthews J. L. & Yu J. T. (2018) Sensitivity Analysis of Arctic Sea Ice Extent Trends and Statistical Projections Using Satellite Data. Remote Sensing, 10(2).
[15] Schweiger A., Lindsay R., Zhang J., et al. (2011) Uncertainty in modeled Arctic sea ice volume. Journal of Geophysical Research-Oceans, 116.
[16] Huang F., Zhou X. & Wang H. (2017) Arctic sea ice in CMIP5 climate model projections and their seasonal variability. Acta Oceanologica Sinica, 36(8): 1-8.
[17] Eisenman I. (2010) Geographic muting of changes in the Arctic sea ice cover. Geophysical Research Letters, 37.
[18] Dorr J., Arthun M., Eldevik T., et al. (2021) Mechanisms of Regional Winter Sea-Ice Variability in a Warming Arctic. Journal of Climate, 34(21): 8635-8653.
[19] Bitz C. M. & Roe G. H. (2004) A mechanism for the high rate of sea ice thinning in the Arctic Ocean. Journal of Climate, 17(18): 3623-3632.
[20] Petty A. A. (2018) A Possible Link Between Winter Arctic Sea Ice Decline and a Collapse of the Beaufort High? Geophysical Research Letters, 45(6): 2879-2882.
[21] Lukovich J. V., Stroeve J. C., Crawford A., et al. (2021) Summer Extreme Cyclone Impacts on Arctic Sea Ice. Journal of Climate, 34(12): 4817-4834.
[22] Zhang J. L. & Rothrock D. A. (2003) Modeling global sea ice with a thickness and enthalpy distribution model in generalized curvilinear coordinates. Monthly Weather Review, 131(5): 845-861.
[23] Stroeve J. & Notz D. (2018) Changing state of Arctic sea ice across all seasons. Environmental Research Letters, 13(10).

# Ice flow velocity mapping based on high-resolution COSMO-SkyMed data, Amery Ice Shelf, East Antarctica

K. Lin [1,2], G. Qiao [1,2], L. Wang [1,2], Z. Yu [1,2], R. Li [1,2]

[1] Center for Spatial Information Science and Sustainable Development Applications, Tongji University, 1239 Siping Road, Shanghai, China
email: 985864430@qq.com

[2] College of Surveying and Geo-Informatics, Tongji University, 1239 Siping Road, Shanghai, China
email: qiaogang@tongji.edu.cn
email: (lijuan_wang, yuzeran, rli)@tongji.edu.cn

## 1. INTRODUCTION

Ice flow velocity is closely related to the mass balance of ice sheets and ice shelves in Antarctica. It is an important input parameter for calculating ice flux and an indicator for describing the state and characteristics of ice flow [1]. The likely response of ice shelves to a warming climate is increased surface and basal melting, leading to increased ice flow velocity. Therefore, estimating ice flow velocity is vital for understanding the movement of glaciers in Antarctica. The Amery Ice Shelf (AIS) is the largest ice shelf in the East Antarctic, draining about 12.5% of the water of Antarctica and 16% of the mass from the interior of Antarctica to the ocean [2], making it a sensitive indicator in mass balance estimation of East Antarctic. Moreover, AIS is also an important ice flux-gate for monitoring the majority of ice mass redistribution in Antarctica [3]. The emergence of Synthetic Aperture Radar (SAR) provides a conventional, low-cost, high-frequency and large-space coverage means for monitoring ice flow velocity. However, the conventional DInSAR technique relies on the coherence between the two images and is less sensitive to the displacement in the azimuth direction, which limits its application range [4]. Regardless of whether the coherence is preserved, the offset tracking technique can directly estimate the glacier displacement in the range and azimuth direction, and has become an alternative to measuring glacier motion by DInSAR [5]. Moon et al. used offset tracking technology to extract the ice velocity of David Glacier from sentinel data, proving the reliability of the method [6]. However, the accuracy of offset tracking is usually lower than that of DInSAR, which is mostly meter-level accuracy [7]. How to improve the accuracy of offset tracking has become a problem that needs to be solved. The advent of high-resolution SAR images such as TerraSAR-X and COSMO-SkyMed (CSK) provides more options and possibilities to solve this issue. These high-resolution images make the estimation error of offset tracking less than 10 cm [8], which makes the observations in high ice flow regions feasible and credible. In this paper, we collected 26 pairs of CSK images and derived the ice flow velocity of AIS by using offset tracking approach. The feasibility of monitoring rapidly changing glacier movement by using CSK data was verified. Finally, the error of the ice flow velocity map was analyzed in detail.

## 2.MATERIALS AND METHODS

### *2.1 Data*

Compared with the early radar satellite systems, the CSK satellite has greatly improved the spatial resolution. In spotlight mode, images with a resolution of up to 1 meter and a width of 10 kilometers can be obtained; in HIMAGE mode, images with a width of 40 kilometers and a resolution of 3 meters can be obtained, which provides a basis for high-precision radar mapping. In addition, the large-area image acquisition capability of CSK is unmatched by other satellite systems. It is a constellation of four X-band radar satellites that operate at 9.6 GHz. It has left-right look capability, which can double the shooting efficiency. In addition, the rapid response capability of CSK satellites can meet the real-time needs of users. The CSK satellite can collect data 8 times a day in the same area, and the shortest imaging interval is about 18 minutes. It makes CSK images continuous over a long period of time in the same area. Therefore, using the CSK data, the ice flow velocity in the AIS can be extracted with a large area, high definition and high precision. We have collected 26 pairs of CSK images from June to August, 2019, to extract ice flow velocity (Table 1). We introduced Bedrock Mapping Project 2 (BEDMAP-2) DEM data to remove topographic effects for co-registration of SAR images.

**Table 8.** Details of CSK data used in the study

| Image ID | Acquisition date | Acquisition mode | Polarization | CSK-satallite | Incidence angle | Look dir. |
|---|---|---|---|---|---|---|
| 20F01110-10 | 2019.08.04/08.20 | HIMAGE | HH | 4 | 29.543 ° | Right |
| 20F01110-13 | 2019.06.02/06.18 | HIMAGE | HH | 2 | 29.557 ° | Right |
| 20F01110-15 | 2019.07.14/07.30 | HIMAGE | HH | 1 | 29.795 ° | Right |
| 20F01110-43 | 2019.06.12/06.28 | HIMAGE | HH | 2 | 29.532 ° | Right |
| 20F01110-44 | 2019.06.12/06.28 | HIMAGE | HH | 2 | 29.521 ° | Right |
| 20F01110-49 | 2019.06.06/06.22 | HIMAGE | HH | 2 | 29.579 ° | Right |
| 20F01110-50 | 2019.06.06/06.22 | HIMAGE | HH | 2 | 29.591 ° | Right |
| 20F01110-52 | 2019.06.06/06.22 | HIMAGE | HH | 2 | 29.613 ° | Right |
| 20F01110-53 | 2019.06.06/06.22 | HIMAGE | HH | 2 | 29.626 ° | Right |
| 20F01110-54 | 2019.06.06/06.22 | HIMAGE | HH | 2 | 29.638 ° | Right |
| 20F01110-55 | 2019.06.06/06.22 | HIMAGE | HH | 2 | 29.648 ° | Right |
| 20F01110-56 | 2019.06.09/06.25 | HIMAGE | HH | 1 | 29.914 ° | Right |
| 20F01110-57 | 2019.06.09/06.25 | HIMAGE | HH | 1 | 26.925 ° | Right |

### *2.2 Method*

Due to the high ice flow velocity of the AIS, the SAR images in this area are often incoherence during the InSAR process. In addition, AIS lacks of ground control points for phase calibration, so extracting velocity using DInSAR technique in AIS is inappropriate. Offset tracking method was introduced as an alternative to overcome the limitations of large deformation and low coherence. Offset tracking can use a normalized cross-correlation algorithm to estimate the offset of two SAR images in range and azimuth directions. The principle is to select a specific patch in the master image and match it within a search window in the slave image. Then, the cross-correlation coefficient for each pixel between the two images is calculated. Finally, the offset between two pixels is estimated with the largest cross-correlation coefficient in a window.

In this paper, the implementation flowchart of offset tracking is shown in Fig. 1. First, we established the mapping relationship between the SAR reference image and DEM, and that between the SAR slave image and DEM. The two mapping relationships were combined to obtain an initial co-registration look-up table. Second, the pixel offset between master image and slave image was estimated by a search window. Determination of window size is very important in offset tracking process. After trial and error, the size of the search window was set to 256 × 256 pixels, equivalent to an area of about 512 × 512 m on the ground. Then, the offset with a cross-correlation coefficient less than 0.1 should be eliminated due to the low correlation. Finally, we projected the pixel offset to the WGS 1984 Antarctic Polar Stereographic (APS) projection through the geocoding process to obtain the image mosaic of ice flow velocity.

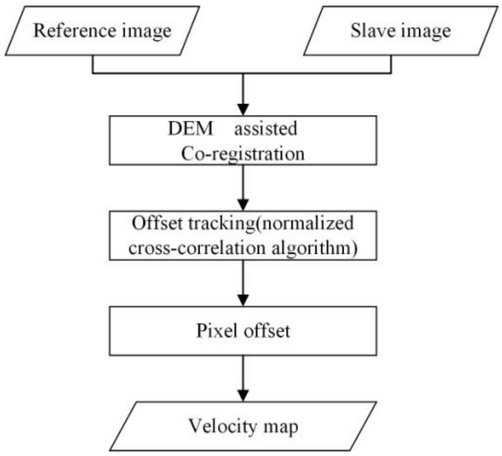


**Fig. 1.** Flowchart of the offset tracking method.

## 3.RESULTS

### *3.1 Ice flow velocity of AIS*

The velocity in the line-of-sight direction on the CSK image was successfully extracted. Assuming that the glacier surface is horizontal, range and azimuth velocities are then combined to represent ice flow velocity. The displacement is geocoded into the BEDMAP-2 DEM geometric model to obtain the velocity mosaic of AIS (Fig. 2).

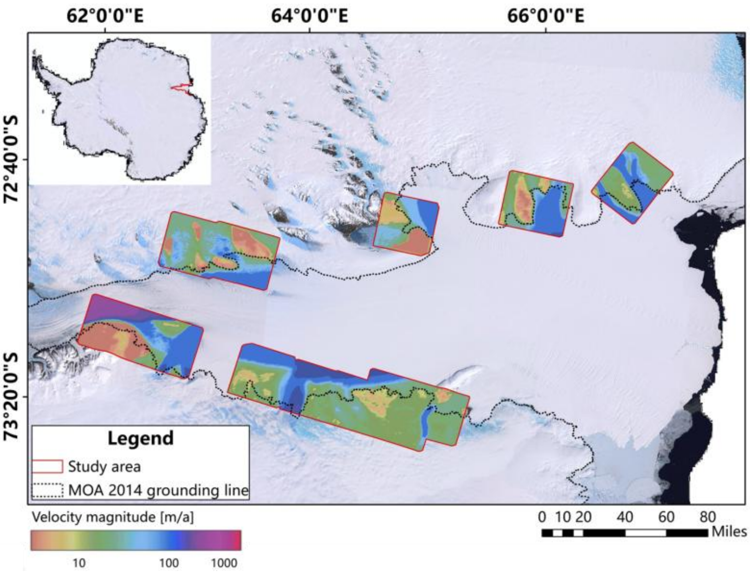


**Fig. 2.** AIS ice flow velocity extracted by offset tracking based on CSK data.

### *3.2 Error analysis*

In order to analyze the accuracy of our result, we introduced the MEaSUREs InSAR-Based Antarctica Ice Velocity Map, Version 2 (MEaSUREs) [9] in 2019, and plotted the difference between our ice flow velocity and MEASUREs' (Fig. 3a). It can be seen that our velocity is within 10 m/a of that from MEASUREs in the region of low flow velocity (velocity smaller than 60 m/a). The difference between the two in the region with high flow velocity (velocity greater than 60 m/a) is also within -50 m/a to 50 m/a, which proves that our method is reliable in mapping the ice flow velocity in AIS.

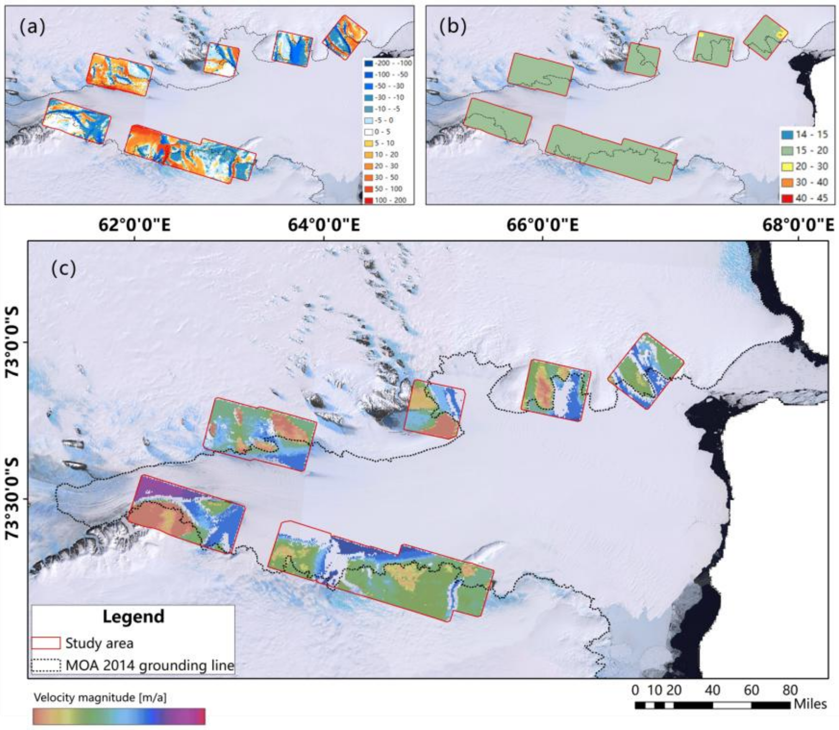


**Fig. 3.** Error analysis chart. (a) is the difference map between our velocity and MEASUREs'. (b) is the MSE map obtained by calculating the root mean square of theoretical error of COSMO data and theoretical error of MEASUREs data. (c) is the part where our velocity differs from the MEASUREs' by no more than twice MSE.

Errors in offset tracking are mainly caused by ionospheric delay, co-registration, geocoding, and topography. The use of high-resolution external DEM (Bedmap 2) can help to reduce the topographic error and achieve high-precision co-registration in the glacier region. The mean residual of the co-registration is about 0.03 pixel in range direction and 0.02 pixel in azimuth direction, which accounts for an error of ~11.7 m/a for the flow velocity in AIS. The azimuth offset between azimuth spectral sub-band images may be related to ionospheric delays [10]. We used the bandpass filter bpf to separate single look complex (SLC) data. To display the offset in the azimuth direction, we extracted the imaginary part of the offset. Then, we came to the conclusion that the ionospheric delay is an azimuth offset of 0.01 pixels, whose contribution to the ice flow velocity error is 9.1 m/a. Therefore, the velocity error of CSK data does not exceed 15 m/a. Combining our error with that of MEaSUREs, the mean square error (MSE) is roughly distributed between 15-20 m/a (Fig. 3b). Finally, we filtered out the part where our velocity differs from the MEaSUREs' by more than double MSE. It can be seen that 80% of the ice flow velocity is within the error range (Fig. 3c).

## 4.SUMMARY

Ice flow velocity is an important parameter for understanding glacier motion, which indicates the mass transport from the interior of Antarctica to the ocean and assesses the stability of an ice shelf. AIS is one of the glaciers with the fastest ice flow velocity in East Antarctica. It plays an important role in the mass balance of the entire Antarctica. Therefore, monitoring the ice flow velocity of AIS is of great significance for studying the mass balance and estimating the movement of glaciers in Antarctica. In rapidly changing areas, offset tracking technology is more appropriate, but the accuracy is inferior to DInSAR. CSK data has the advantages of high resolution, continuous image, and wide monitoring range, which can largely solve the problem of low accuracy of offset tracking in mapping the ice flow velocity. Using the high-resolution CSK images from June to August 2019, we extracted the ice flow velocity of AIS by the offset tracking approach. We discovered that the ice flow velocity from MEaSUREs and this study fit each other quite well, and the error was found to be under 15 m/a. It demonstrates the advantages of high-resolution CSK images in mapping the ice flow velocity in Antarctica.

## References

[1] Thakur, P. K., Swain, A. K., Dhote, P. R., Kumar, P., Kaushik, S., Gajbhiye, D., ... & Kumar, A. S. (2021). Satellite and ground based estimates for ice surface velocities in the part of central Dronning Maud Land, East Antarctica: Implications for ice flux calculations. Polar Science, 30, 100737.
[2] King, M. A., Coleman, R., Morgan, P. J., & Hurd, R. S. (2007). Velocity change of the Amery Ice Shelf, East Antarctica, during the period 1968–1999. Journal of Geophysical Research: Earth Surface, 112(F1).
[3] Fricker, H. A., Warner, R. C., & Allison, I. (2000). Mass balance of the Lambert Glacier–Amery Ice Shelf system, East Antarctica: a comparison of computed balance fluxes and measured fluxes. Journal of Glaciology, 46(155), 561-570.
[4] Tomar, K. S., Kumari, S., & Luis, A. J. (2021). Seasonal ice flow velocity variations of Polar Record Glacier, East Antarctica during 2016–2019 using Sentinel-1 data. Geocarto International, 1-16.
[5] Wang, Q., Zhou, W., Fan, J., Yuan, W., Li, H., Sousa, J. J., & Guo, Z. (2017). Estimation of Shie Glacier surface movement using Offset Tracking technique with cosmo-skymed images.
[6] Moon, J., Cho, Y., & Lee, H. (2021). Flow Velocity Change of David Glacier, East Antarctica, from 2016 to 2020 Observed by Sentinel-1A SAR Offset Tracking Method. Korean Journal of Remote Sensing, 37(1), 1-11.
[7] Nakamura, K., Aoki, S., Yamanokuchi, T., Tamura, T., & Doi, K. (2022). Validation for Ice Flow Velocity Variations of Shirase Glacier Derived From PALSAR-2 Offset Tracking. IEEE Journal of Selected Topics in Applied Earth Observations and Remote Sensing, 15, 3269-3281.
[8] Milillo, P., Rignot, E., Rizzoli, P., Scheuchl, B., Mouginot, J., Bueso-Bello, J. L., ... & Zink, M. (2021, March). TanDEM-X Surface Elevation Changes and Synergies with COSMO-SkyMed for Cryosphere Monitoring. In EUSAR 2021; 13th European Conference on Synthetic Aperture Radar (pp. 1-6). VDE.
[9] Rignot, E., Mouginot, J., & Scheuchl, B. (2017). MEaSUREs InSARBased Antarctica Ice Velocity Map, Version 2, Boulder, Colorado USA, NASA National Snow and Ice Data Center Distributed Active Archive Center.
[10] Wegmuller, U., Werner, C., Strozzi, T., & Wiesmann, A. (2006, July). Ionospheric electron concentration effects on SAR and INSAR. In 2006 IEEE International Symposium on Geoscience and Remote Sensing (pp. 3731-3734). IEEE.

# SDG 14 (Life Below Water): Blue Innovation for the Delivery of the SDGs

# Spatial assessment of coastal flood risk due to sea level rise in China's coastal zone through the 21st century

Xu He[1,2,3,4], Hou Xiyong [1,3,4]

[1]Yantai Institute of Coastal Zone Research, Chinese Academy of Sciences, Yantai, Shandong, P.R. China

[2]University of Chinese Academy of Sciences, Beijing, P.R. China

[3]CAS Key Laboratory of Coastal Environmental Processes and Ecological Remediation, Yantai Institute of Coastal Zone Research, Chinese Academy of Sciences, Yantai, Shandong, P.R. China

[4]Shandong Key Laboratory of Coastal Environmental Processes, Yantai, Shandong, P.R. China

## 1. INTRODUCTION

In the context of climate warming, coastal flooding caused by sea level rise (SLR) has become one of the major risks worldwide, with substantial effects on socio-economic development and natural ecosystems in the coastal area[1,2]. For example, it can not only destroy the infrastructure by inundation, such as buildings and roads, and damage the tourism and fishery, causing huge economic losses and human casualties[3-5], but also lead to the serious damage to the ecological environment of coral reefs, mangroves, and coastal wetlands[6]. In the past decades, the frequent occurrence of severe coastal floods has gained widespread attentions[7-10], such as those in the U.S. Atlantic and Gulf coasts[11], northwestern Europe[12], southeastern Australia[13], and East Asia[14]. As climate change progresses and sea level rises, the coastal flood risk (CFR) is expected to become more serious across the planet in the future[15]. According to the "China's Sea Level Bulletin 2020", the series of reports from the Intergovernmental Panel on Climate Change (IPCC), and the United Nations Office for Disaster Risk Reduction (UNISDR)[16-19], the rate of SLR in China's adjacent seas was higher than the global average in history and will continue to rise in the future, which means CFR will be significantly increased accordingly in China's coastal zone (CCZ). The CCZ is recognized as an important population and economic center in China, e.g., over 40% of China's population lives in coastal provincial administrative regions, and the region contributes nearly 60% of the national gross domestic product (GDP)[20]. Obviously, coastal flooding poses a serious threat to coastal societies [14]. Therefore, it is crucial to analyze the future impacts of coastal flooding in China at different levels of SLR under socio-economic change scenarios, which is beneficial for policy-makers to draw up proper coastal urban planning and formulate scientific disaster prevention and mitigation policies in the future and contributes to the realization of the United Nations Sustainable Development Goal (SDG) 14.2.

## 2. MATERIALS AND METHODS

### *2.1 Study area*

The study area is selected based on the administrative divisions of prefecture-level cities along the eastern coast of mainland China. Due to the absence of demographic and economic data, Hong Kong, Macao, Taiwan, and the islands in the South China Sea are excluded from the CFR assessment. Therefore, this study area covers a total of 11 coastal provinces. In addition, the six prefecture-level cities those are close to the coastline but not directly adjacent to the sea (which are more influenced by the sea), such as Anshan, Dezhou, Linyi, Huzhou, Foshan, and Yulin, are included in the study area.

### *2.2 Methods*

the assessment framework of CFR in the CCZ is referred to Nguyen, *et al.* (2019)[21] and incorporated a series of sub-indicators adapted from Yin, *et al.* (2013)[22], Weis, *et al.* (2016)[23], and Zhang, *et al.* (2021)[24] to measure the degree of CFR under future multi-scenarios(Fig. 1). The CFR assessment follows these steps: firstly, the CFR assessment indicators are selected based on their availability and attribute characteristics; secondly, the value of each indicator is reclassified and normalized to establish the spatial database based on a Geographic Information System (i.e., ArcGIS software); thirdly, Analytic Hierarchy Process- Entropy Weight (AHP-EW) combined method is used for calculating the combined weight of each indicator layer; finally, the indicators are weighted and stacked for obtaining the values of the hazard, exposure & sensitivity, and adaptive capacity, respectively, and further weighted by 50%, 30%, and 20% for hazard, exposure & sensitivity, and adaptive capacity, respectively, to calculate the CFR values. In addition, based on the values of CFR, five ranked levels e.g., “Very low” (0-0.2), “Low” (0.2-0.3), “Medium” (0.3-0.4), “High” (0.4-0.5), and “Very high” (>0.5) are designated. Moreover, the CFR map is visualized using ArcGIS software to represent the spatial distribution of the five CFR levels.

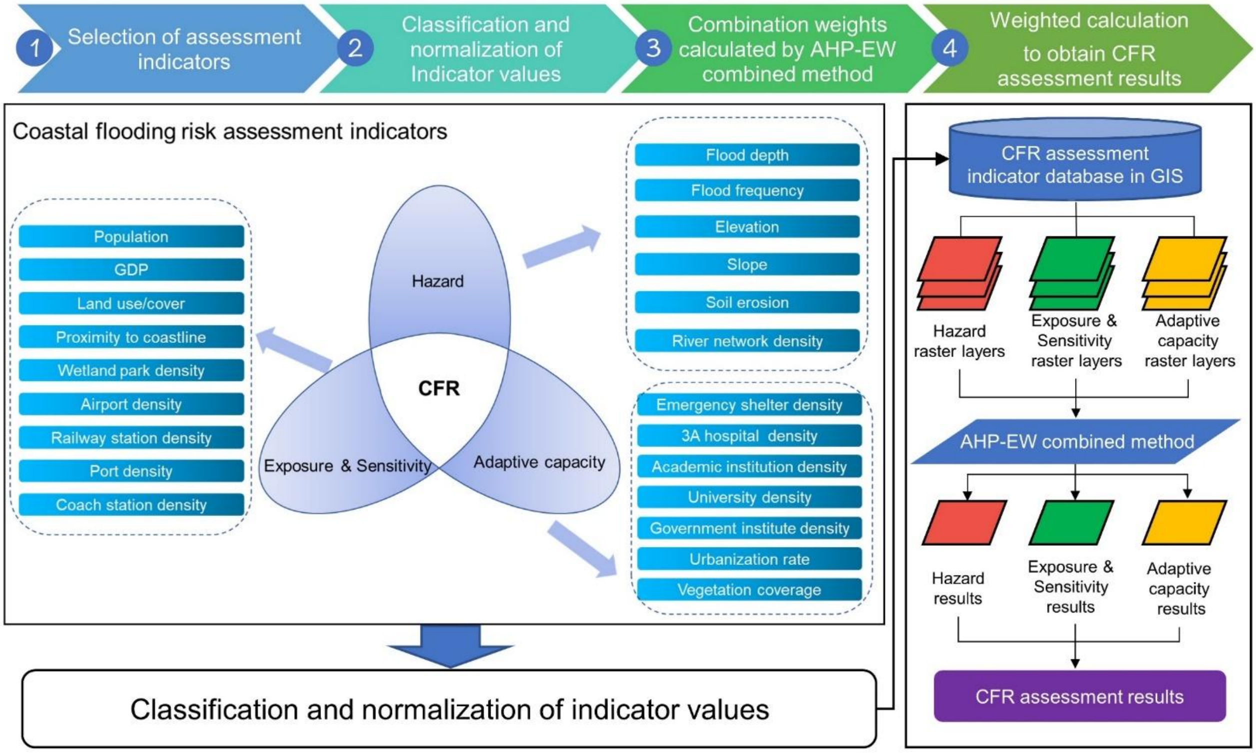


**Fig. 1.** An assessment framework for coastal flood risk caused by SLR in the CCZ.

## 3. RESULTS

### *3.1 Temporal and spatial characteristics of CFR*

Fig. 2 shows the spatial distribution of CFR in 2030, 2050, and 2100 under RCP2.6-SSP1, RCP4.5-SSP2, and RCP8.5-SSP5, respectively. Overall, the spatial patterns of CFR in the CCZ are similar among scenarios and years. The regions with “High” level are mainly distributed around the regions with “Very high” level. And they are mainly distributed in the southern coastal area of Liaoning, the coastal area from eastern Hebei to northwestern Shandong, the Jiaozhou Bay area in southeastern Shandong, the northern to central Jiangsu, the Yangtze River Delta (southern Jiangsu, Shanghai, and northern Zhejiang), and the Pearl River Delta (southeast Guangdong), which are low-lying coastal areas with densely populated, economically developed, or industrially diverse. By contrast, the CFR level in inland mountainous or hilly areas with higher elevations is “Very low”, such as the northeastern part of the coastal zone in Liaoning, the western part of the coastal zone in Zhejiang and Fujian, and the southern part of Hainan. Moreover, the regions with “Low” CFR level are primarily concentrated in the coastal areas of Hebei and Tianjin, the eastern part of the coastal area in Shandong and Zhejiang, the central part of the Guangxi coastal zone, and the northeastern part of Hainan. In addition, the regions with “Medium” CFR level are mainly distributed in the central part of the Liaoning coastal area, the northwestern part of

Shandong, the southwestern part of the Jiangsu coastal area, and the central part of the Zhejiang coastal zone.

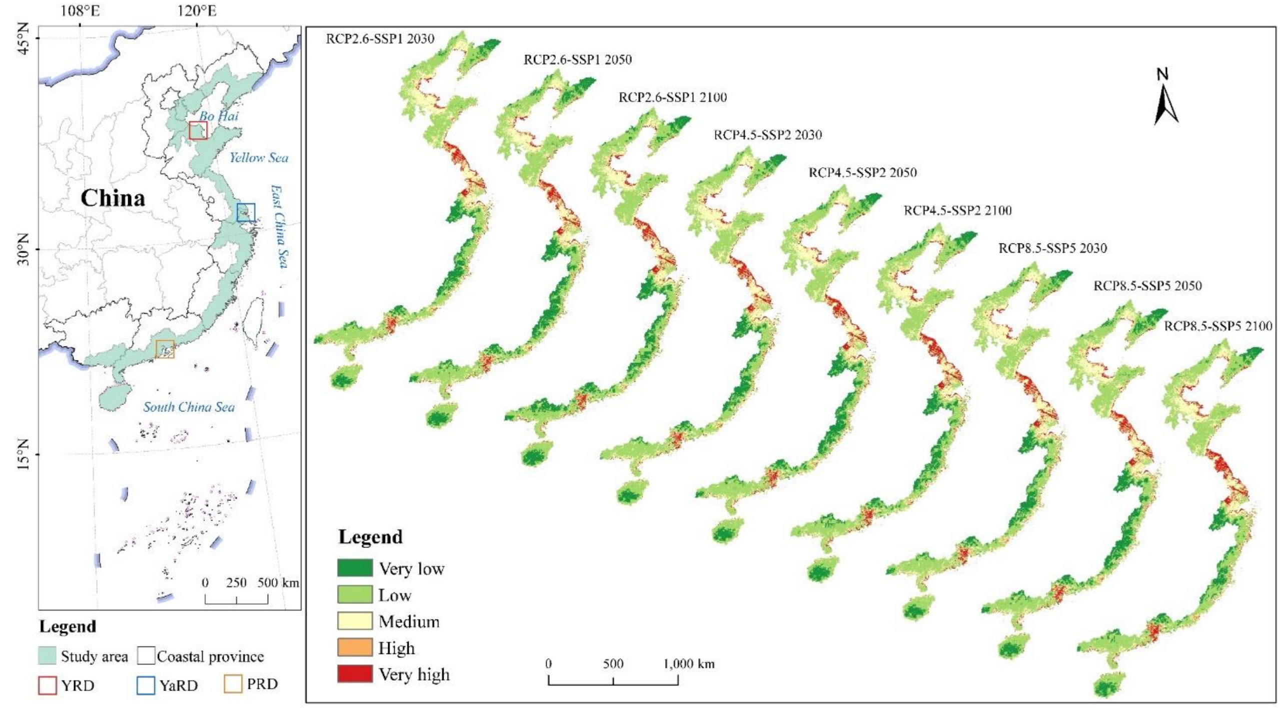


**Fig. 2.** Spatiotemporal distribution of the CFR in 2030, 2050, and 2100 under RCP2.6-SSP1, RCP4.5-SSP2, and RCP8.5-SSP5, respectively. YRD, YaRD, and PRD represent the Yellow River Delta, Yangtze River Delta, and Pearl River Delta, respectively.

### *3.2 Potentially affected population and GDP in typical CFR areas*

In the assessment of CFR, the risk areas of "High" and "Very high" are needed for special attention (called the typical CFR areas). The potentially affected population and GDP in the typical CFR areas of the 11 coastal provinces among scenarios and years are shown in Fig. 3. In general, Guangdong's population and GDP are expected to be the most affected in the coastal provinces, with an affected GDP of 7914.96 billion USD (RCP8.5-SSP5 2100) and an affected population of 68.30 million (RCP2.6-SSP1 2050), followed by Zhejiang. Moreover, Guangxi and Hainan have the lowest expected effects on population and GDP in the coastal provinces among scenarios and years.

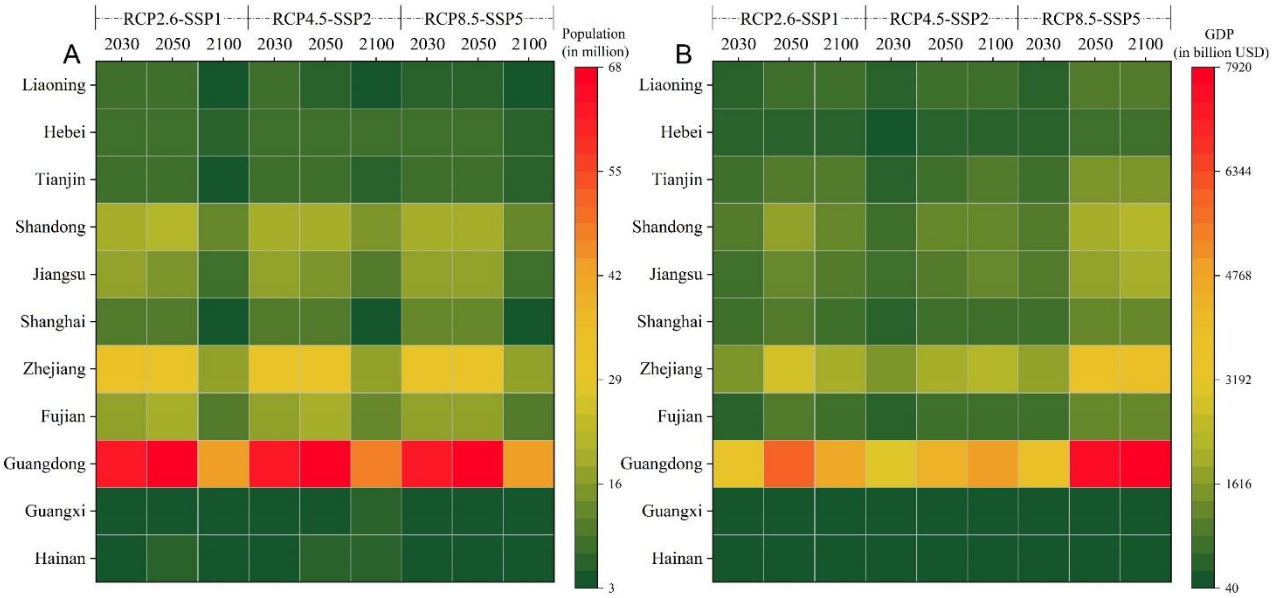

**Fig. 3.** Number of potentially affected population and GDP in typical CFR areas of the 11 coastal provinces in 2030, 2050, and 2100 under RCP2.6-SSP1, RCP4.5-SSP2, and RCP8.5-SSP5, respectively. (A) is the number of the expected population affected in the typical CFR areas of 11 coastal provinces. (B) is the number of the expected GDP affected in the typical CFR areas of 11 coastal provinces.

### *3.3 Expected LULC losses in typical CFR areas*

Further analysis of the expected LULC losses in the area of “High” and “Very high” CFR areas is shown in Fig. 4A and 4B. As can be seen from the figures, in the “High” CFR area, the types of expected LULC losses are similar among scenarios and years. The LULC with the highest area proportion is built-up, whose area proportions exceeded 40% among all scenarios and years, followed by the farmland (which exceeded 30%). By contrast, in the “Very high” CFR area, the types of expected LULC losses are significantly different among scenarios and years. For example, under RCP2.6-SSP1, the constructed wetland, built-up, and coastal wetland become the third major loss type in 2030, 2050, and 2100, respectively; Under RCP4.5-SSP2, built-up overtakes constructed wetland as the third major loss type in 2050. Under RCP8.5-SSP5, built-up overtakes inland freshwater as the second major loss type, and inland freshwater as the third major loss type after 2050. In addition, the area proportions of farmland are the highest and exceeded 30% among scenarios and years, followed by the inland freshwater or built-up.

Fig. 4C shows the area change of each type of expected LULC loss in the typical CFR areas of 11 coastal provinces among scenarios and years. It is found that the total area of the typical CFR areas in Jiangsu is the largest among scenarios and years, and its LULC losses type with the largest area is mainly farmland, followed by inland freshwater and built-up. Although Guangdong’s total areas of typical CFR areas are slightly smaller than Jiangsu’s, the main type of expected LULC losses is built-up, followed by farmland and inland freshwater, and the area loss of built-up in Guangdong is the largest in all coastal provinces, followed by Jiangsu, Shandong, and Zhejiang. In addition, the expected loss of constructed wetland in Shandong is the largest in all coastal provinces among scenarios and years.

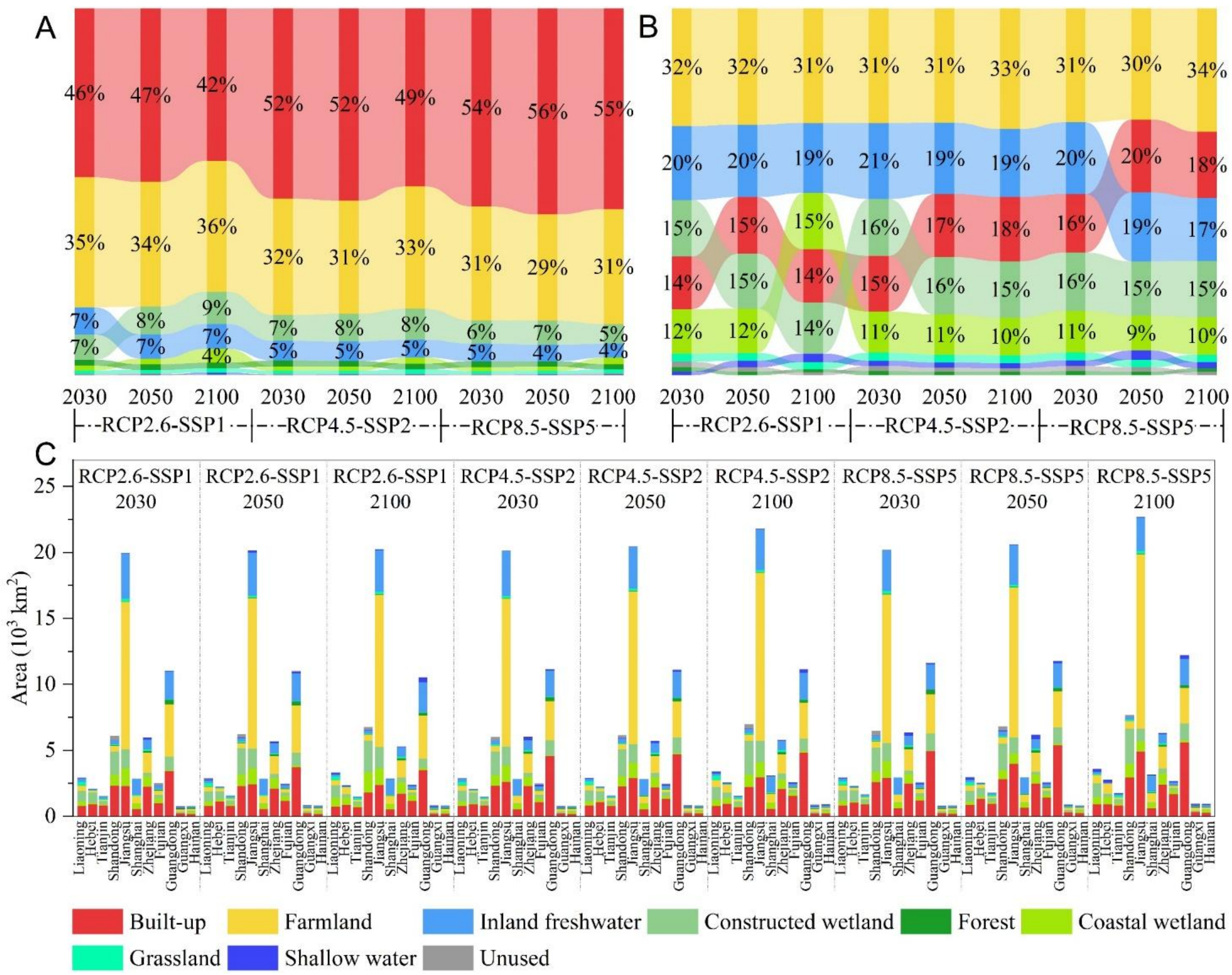


**Fig. 4.** Area proportion and area of expected LULC losses in the typical CFR areas in 2030, 2050, and 2100 under RCP2.6-SSP1, RCP4.5-SSP2, and RCP8.5-SSP5, respectively. (A) is the area proportion of expected LULC losses in the "High" CFR area. (B) is the area proportion of expected LULC losses in the "Very high" CFR area. (C) is the area of expected LULC losses in the typical CFR areas of 11 coastal provinces.

## 4. SUMMARY

Among the climate change-induced threats to coastal regions, coastal flooding caused by sea level rise (SLR) is considered one of the most serious and presents an intensifying trend over time. The negative impacts and risks associated with coastal flooding are difficult to visualize spatially and cause great inconvenience to policy-makers in understanding the distribution of different risk levels and developing adaptation policies. Therefore, the spatial assessment of coastal flood risk (CFR) has been the subject of scarce research. Our study proposes a framework for CFR based on the hazard, exposure & sensitivity, and adaptive capacity of China's coastal zone (CCZ) and maps the spatial distribution of CFR by GIS in 2030, 2050, and 2100 under RCP2.6-SSP1, RCP4.5-SSP2, and RCP8.5-SSP5, respectively. Our results reveal that (1) low-lying coastal areas with densely populated, economically developed, or industrially diverse are faced with serious coastal flood risks, such as the Yellow River Delta, the Yangtze River Delta, the Pearl River Delta, and the coastal areas in Jiangsu. (2) The coastal area of Guangdong is significantly faced with the massive potentially affected population and GDP due to CFR among scenarios and years. (3) As threatened by CFR mostly, built-up and farmland are particularly required to guard against the negative impact of coastal flooding, especially in Guangdong and Jiangsu. Results in this study are expected to provide the intuitive information and basis for governments, policy-makers, and local communities in addressing the increased CFR over the CCZ, which contribute to the realization of SDG 14.2.

## References


[1] Nicholls, R.J.; Cazenave, A. **2010** Sea-level rise and its impact on coastal zones. *Science*, *328*, 1517-1520, doi:https://doi.org/10.1126/science.1185782.

[2] Tadesse, M.G.; Wahl, T. **2021** A database of global storm surge reconstructions. *Sci. Data*, *8*, 10, doi:10.1038/s41597-021-00906-x.

[3] Vousdoukas, M.I.; Mentaschi, L.; Voukouvalas, E.; Verlaan, M.; Jevrejeva, S.; Jackson, L.P.; Feyen, L. **2018** Global probabilistic projections of extreme sea levels show intensification of coastal flood hazard. *Nat. Commun.*, *9*, 1-12, doi:https://doi.org/10.1038/s41467-018-04692-w.

[4] Fang, Y.; Yin, J.; Wu, B. **2016** Flooding risk assessment of coastal tourist attractions affected by sea level rise and storm surge: a case study in Zhejiang Province, China. *Nat. Hazards*, *84*, 611-624, doi:https://doi.org/10.1007/s11069-016-2444-4.

[5] Hallegatte, S.; Green, C.; Nicholls, R.J.; Corfee-Morlot, J. **2013** Future flood losses in major coastal cities. *Nat. Clim. Chang.*, *3*, 802-806, doi:https://doi.org/10.1038/nclimate1979.

[6] Lovelock, C.E.; Cahoon, D.R.; Friess, D.A.; Guntenspergen, G.R.; Krauss, K.W.; Reef, R.; Rogers, K.; Saunders, M.L.; Sidik, F.; Swales, A. **2015** The vulnerability of Indo-Pacific mangrove forests to sea-level rise. *Nature*, *526*, 559-563, doi:https://doi.org/10.1038/nature15538.

[7] Gornitz, V. **1991** Global coastal hazards from future sea level rise. *Paleogeogr. Paleoclimatol. Paleoecol.*, *89*, 379-398, doi:https://doi.org/10.1016/0921-8181(91)90118-G.

[8] Thumerer, T.; Jones, A.P.; Brown, D. **2000** A GIS based coastal management system for climate change associated flood risk assessment on the east coast of England. *Int. J. Geogr. Inf. Sci.*, *14*, 265-281, doi:https://doi.org/10.1080/136588100240840.

[9] Nadal, N.C.; Zapata, R.E.; Pagan, I.; Lopez, R.; Agudelo, J. **2010** Building damage due to riverine and coastal floods. *J. Water Resour. Plan. Manage.-ASCE*, *136*, 327-336, doi:https://doi.org/10.1061/(asce)wr.1943-5452.0000036.

[10] Toimil, A.; Losada, I.J.; Nicholls, R.J.; Dalrymple, R.A.; Stive, M.J.F. **2020** Addressing the challenges of climate change risks and adaptation in coastal areas: A review. *Coastal Engineering*, *156*, doi:10.1016/j.coastaleng.2019.103611.

[11] Sajjad, M.; Lin, N.; Chan, J.C.L. **2020** Spatial heterogeneities of current and future hurricane flood risk along the U.S. Atlantic and Gulf coasts. *Sci. Total Environ.*, *713*, 136704, doi:https://doi.org/10.1016/j.scitotenv.2020.136704.

[12] Ganguli, P.; Paprotny, D.; Hasan, M.; Güntner, A.; Merz, B. **2020** Projected Changes in Compound Flood Hazard From Riverine and Coastal Floods in Northwestern Europe. *Earth Future*, *8*, e2020EF001752, doi:https://doi.org/10.1029/2020EF001752.

[13] Asbridge, E.F.; Low Choy, D.; Mackey, B.; Serrao-Neumann, S.; Taygfeld, P.; Rogers, K. **2021** Coastal flood risk within a peri-urban area: Sussex Inlet district, SE Australia. *Nat. Hazards*, *109*, 999-1026, doi:https://doi.org/10.1007/s11069-021-04865-9.

[14] Fang, J.; Lincke, D.; Brown, S.; Nicholls, R.J.; Wolff, C.; Merkens, J.L.; Hinkel, J.; Vafeidis, A.T.; Shi, P.; Liu, M. **2020** Coastal flood risks in China through the 21st century - An application of DIVA. *Sci. Total Environ.*, *704*, 135311, doi:https://doi.org/10.1016/j.scitotenv.2019.135311.

[15] Woodruff, J.D.; Irish, J.L.; Camargo, S.J. **2013** Coastal flooding by tropical cyclones and sea-level rise. *Nature*, *504*, 44-52, doi:https://doi.org/10.1038/nature12855.

[16] IPCC. **2019** *IPCC Special Report on the Ocean and Cryosphere in a Changing Climate* Cambridge University Press: Cambridge, UK and New York, NY, USA.

[17] IPCC. **2021** *Climate Change 2021: The Physical Science Basis. Contribution of Working Group I to the Sixth Assessment Report of the Intergovernmental Panel on Climate Change*; Cambridge University Press: Cambridge, UK and New York, NY, USA.

[18] UNISDR. **2017** *National Disaster Risk Assessment*; United Nations Office for Disaster Risk Reduction: https://www.undrr.org/publication/words-action-guidelines-national-disaster-risk-assessment.

[19] MNR. China's Sea Level Bulletin 2020. Available online: http://gi.mnr.gov.cn/202104/t20210426_2630186.html (accessed on 2021-04-26).

[20] Du, P.; Hou, X.; Xu, H. **2022** Dynamic Expansion of Urban Land in China’s Coastal Zone since 2000. *Remote Sens.*, *14*, doi:https://doi.org/10.3390/rs14040916.

[21] Nguyen, K.-A.; Liou, Y.-A.; Terry, J.P. **2019** Vulnerability of Vietnam to typhoons: A spatial assessment based on hazards, exposure and adaptive capacity. *Sci. Total Environ.*, *682*, 31-46, doi:https://doi.org/10.1016/j.scitotenv.2019.04.069.

[22] Yin, J.; Yin, Z.; Xu, S. **2013** Composite risk assessment of typhoon-induced disaster for China's coastal area. *Nat. Hazards*, *69*, 1423-1434, doi:https://doi.org/10.1007/s11069-013-0755-2.

[23] Weis, S.W.M.; Agostini, V.N.; Roth, L.M.; Gilmer, B.; Schill, S.R.; Knowles, J.E.; Blyther, R. **2016** Assessing vulnerability: an integrated approach for mapping adaptive capacity, sensitivity, and exposure. *Clim. Change*, *136*, 615-629, doi:https://doi.org/10.1007/s10584-016-1642-0.

[24] Zhang, Y.; Wu, T.; Arkema, K.K.; Han, B.; Lu, F.; Ruckelshaus, M.; Ouyang, Z. **2021** Coastal vulnerability to climate change in China's Bohai Economic Rim. *Environ. Int.*, *147*, 106359, doi:https://doi.org/10.1016/j.envint.2020.106359.

# Marine Sustainable Development Goals and coral reef ecosystem management-- Taking Sanya Coral Reef Reserve as an example

WU Hongrong [1], ZHU Lanwei [2]

[1] School of Earth Sciences, Yangtze University, Wuhan 430000，China
email: wuhr2022@163.com

[2] Aerospace Information Research Institute,Chinese Academy of Sciences, Beijing 100000，China
email: zhulw@aircas.ac.cn

## 1. INTRODUCTION

Marine resources are an important guarantee for the economic development of human society. To a large extent, the Marine resources possessed and controlled by a country determine the level of its Marine economic development, and even the level of national economy and welfare. Therefore, attaching importance to the ocean, sustainable development and utilization of Marine resources, and ensuring the sustainable development of China's oceans have become important issues to be solved [1]. Coral reef ecosystems in the highest biological diversity and productivity of all the Marine ecology, its value and services account for 2.85% of the Marine ecosystem, but the coral reef ecosystems have a vulnerable side, easily affected by various external factors and be destroyed, but once the damage is hard to recover within a short period of time. Therefore, when utilizing coral reef resources, it is necessary to properly handle the relationship between economic development and coral reef protection, so as to achieve the maximum efficiency and sustainable utilization of resources [2].

Sanya is a famous Marine tourist resort, besides beautiful panoramic beaches, there are coral reef ecological resources. Coral reef ecosystem is an essential ecosystem in the Marine ecosystem and plays an important role in the survival of Marine organisms such as fish and other biota. Due to the offshore industry, agriculture, mining, tidal flats pond farming and other human activities led to the offshore heavy metals and persistent organic pollutants (pops) problems such as pollution, eutrophication and acidification, changed the water quality and Marine biological community structure, Marine biogeochemistry cycle, and ultimately affect the Marine ecosystem services function and health [3]. This paper first introduces the concept of coral reef sustainable development, analyzes the sustainable development mode of coral reef in Sanya and the pressure of sustainable development, and puts forward the way to realize the sustainable development of coral reef in Sanya, so as to maintain the stability of coral reef resources in Sanya and its important role in regional social and economic development.

## 2. CONCEPTS RELATED TO CORAL REEFS

### *2.1 Coral reefs*

Coral reef is a beautiful underwater landscape built by the bone accumulation of stony coral growing in the tropical ocean and other reef-building organisms, reef-attaching organisms and algae living in it after a long life and death. According to their morphological characteristics, corals can be divided into reef-building corals and non-reef-building corals. Reef-building corals have a rapid calcification rate due to the symbiosis of zooxanthellae with single cells. Reef-building corals secrete calcium carbonate to form exoskeletons, and they grow from generation to generation, eventually reaching the low tide line to form a reef, a sea-floor uplift with anti-wave properties. According to the relationship between reef and shoreline, it can be divided into fringing reef, barrier reef and atoll.

### *2.2 Coral reef ecosystems*

Coral reef ecosystems are collections of living corals, skeletons of dead corals, and other reef life. Coral reef ecosystems are known as "tropical rainforests of the sea" and are among the most biodiverse on earth. Coral reefs cover less than 0.2 percent of the world's ocean, but coral reef ecosystems support a quarter of all Marine life, including more than 40,000 species. Coral reef ecosystems also make a significant contribution to humanity, supporting 10 per cent of all Marine fisheries.

### *2.3 Sustainable development of coral reefs*

Sustainable development of coral reefs can be defined as the ability of reef-related activities to be carried out in a manner that takes into account the relationship between humans and coral reef ecosystems in order to maintain the health of coral reefs and continue to provide coral reef products and services for future generations. The ecological environment on the basis of the existing reefs, don't destroy the coral reef ecosystem, improving economic efficiency of coral reefs and the harmonious development of human society and nature as the goal, gradually realize the ecological protection and economic development in harmony, make the sustained development of coral reef resources, sustained economic growth, people are harmonious with coral reefs, environmental resources and economic promote each other. The sustainable development of coral reef includes three aspects: sustainable coral reef ecology, sustainable coral reef economy and sustainable coral reef social development.

## 3. SANYA CORAL REEF

### *3.1Sanya Coral Reef*

Sanya Coral Reef Nature Reserve, covering an area of about 8500 hectares, was formally established in 1989 and became a national Marine nature reserve in 1990. The nature reserve is composed of three parts from east to west: Yalong Bay area, Luhuitou Peninsula-Yulin Jiao Area and East and west Daimao Area(Figure 1). Representative stations were selected to observe the coral reefs in this area, and important data and data were obtained, such as the distribution of coral reefs, coral species, living coral coverage rate and dominant species, and death and harm of rocky coral reefs, and the threats to coral resources in Sanya were further analyzed.

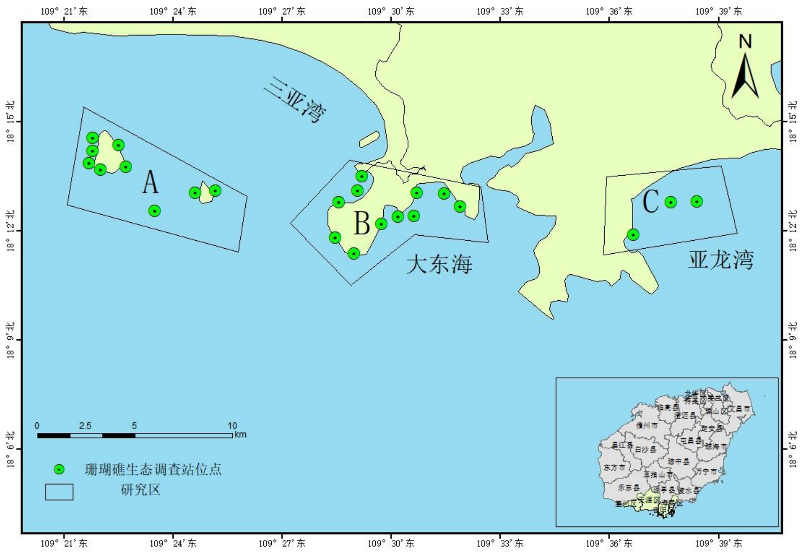


**Fig. 1.** Coral study areas and locations of observaion stations

### *3.2 Pressure on coral reefs in Sanya*

#### *3.2.1The natural pressure*

Natural pressures on the Sanya coral Reef Reserve come from global warming, ocean acidification and typhoons. Most of these factors are large-scale, that is, regional or even global. Coral reefs have harsh habitat requirements, such as high temperature, high radiation, low temperature, high (low) salinity, toxic pollutants, viruses and the combination of these factors can cause coral bleaching.

#### *3.2.2The natural pressure*

Sanya Coral Reef Reserve is affected by human activities, mainly overfishing, destructive fishing, pollutant discharge, sediment threat and biological erosion, etc. These factors are mostly local and small-scale. In addition, the impact of local construction projects and the discharge of oily sewage from fishing boats, as well as domestic sewage discharged from the island, on the reef environment cannot be underestimated.

## 4.STATUS QUO OF CORAL REEF ECOLOGICAL PROTECTION IN SANYA

### *4.1Ecological management of coral reefs based on Marine Protected Areas (MPA)*

Coral reef ecological protection is to establish a coordinated, stable, sustainable and ecologically beneficial coral reef ecosystem with scientific and ecological management methods. Marine protected Areas (MPA) are considered to be the best tool for protecting coral reef habitats and biodiversity, providing fisheries, jobs and increasing tourism revenues. Marine reserves can not only protect biodiversity within the area, but also contribute greatly to the improvement of biodiversity in adjacent areas through the export of larvae, the migration of adults and the protection of breeding populations.Although some studies suggest that there is no significant increase in coral cover within MPAs, it is clear that MPAs are at least effective in reducing coral loss compared to unprotected reefs.

### *4.2 Problems existing in ecological protection of coral reef in Sanya*

The reasons why some Marine reserves in developing countries are not achieving the desired results include: lack of public support; Users are unwilling to comply with regulations and are difficult to implement due to the lack of obligations and the support of economic and technical resources; In addition, in the traditional developing countries, Marine protected areas strictly restricted access to fail to take effect, and because of the local community dependence on coral reef resources is very heavy, they have no other alternative sources of economic life, so you must help to find alternative sources of economy, local residents can't strictly set the access section at the same time, and should adopt a broader concept, including more, Such as temporary closed areas.

### *4.3 Suggestions on coral reef ecological protection in Sanya*

Although Sanya coral reef Protection Zone has been designated long ago, the current institutional setting is not sound, there is no staffing, coral protection related work, no signs and indicators. Therefore, in order to protect the health and growth of regional coral reef ecosystem, the following suggestions are made:

1) In accordance with national and local laws, regulations and regulations on nature reserves and in light of the situation of Sanya nature Reserves, a protection management system has been formulated to institutionalize and standardize the protection management. In order to achieve the effectiveness of management by objectives, it is necessary to formulate mid - and long-term development plans or management plans, and formulate annual work implementation plans according to the mid - and long-term development plans or management plans, so as to make routine management work orderly.

2) the reasonable division of function, functional partition of sanya bay waters planning only within the scope of the experimental area for tourism development activities, strict control development projects, development intensity and scope of development, make full use of existing facilities and natural resources reasonable allocation of resources and the spatial layout, realize the sustainable utilization of the tourism resources. At the same time, artificial coral restoration should be carried out in coral degraded areas to prevent the continuous degradation of coral reef ecosystem.

3) To control the pollution of Marine water environment, monitor the quality of water environment in the waters around Sanya Bay, analyze and identify the main causes of water pollution; We will strengthen the monitoring and management of pollution discharge sources, and treat or relocate key pollution sources.

4) Promote community co-management. With the enhancement of coral reef protection and management in Sanya, the rights of surrounding community residents to use Marine resources have been limited and changed to a certain extent, and such contradictions cannot be fundamentally alleviated by simple measures. Promoting community co-management is a feasible way to alleviate this problem. Promote community co-management to promote the transformation of local resource utilization and industrial structure adjustment, strengthen cooperation with local government and community residents, common management, common development.

## 5.SUMMARY

In recent years, due to the interference of natural and human factors, there have been many problems in the products and services of coral reef ecosystem, which have obviously affected the sustainable development of coral reef resources utilization. Although the coral reef nature reserve has been established in Sanya to protect coral reefs, the model still needs to be optimized and improved gradually, and needs to be adjusted with the change of the utilization of coral reefs in Sanya.

Due to the lack of in-depth understanding of the structure and function of coral reef ecosystem, it is difficult to develop and utilize coral reef resources according to the law of sustainable development, and to establish reasonable and effective management and control system. Therefore, the study of coral reef dynamics is the focus of the present and future.

## References

[1] Chen Shang, Ren Dachuan, Li Jingmei, et al. Chinese journal of ecology,2010,30(23): 623-6330. (in Chinese with English abstract)

[2] Zhao Meixia, Yu Quanfu, Zhang Qiaomin, et al. Journal of tropical oceanography,2011,30(02):74-80. (in Chinesewith English abstract)

[3] Yuan Jingjing, Lv Yonglong, HE Guizhen. Acta ecologica sinica,2017,37(24):8139-8147. (in Chinese with English abstract)

[4] Shi Y W. Research on ecological protection measures of coral reefs in Guangdong Province [D]. Guangdong Ocean University,2018. (in Chinese with English abstract)

[5] An X H. Comprehensive analysis and research on coral reefs and their ecosystems in China [D]. Ocean University of China,2003.(in Chinese with English abstract)

[6] Zhao Huanting, Wang Lirong, Yuan Jiayi. Tropical geography,2016,36(01):55-65.

# An iterative space-quality-based interpolation on dissolved oxygen using Argo $O_2$ profiles

YUE Linfeng[1,2], XUE Cunjin[3,1]

[1] Key Laboratory of Digital Earth Science, Aerospace Information Research Institute, Chinese Academy of Sciences, Beijing 100094, PR China
email: yuelinfeng20@mails.ucas.ac.cn

[2] University of Chinese Academy of Sciences, Beijing 100049, PR China

[3] International Research Center of Big Data for Sustainable Development Goals, Beijing 100094, PR China
xuecj@aircas.ac.cn

Acknowledgments: This research was supported by the Strategic Priority Research Program of the Chinese Academy of Sciences (No. XDA19060103)

## 1.INTRODUCTION

Dissolved oxygen is an important factor in ocean health, and global ocean deoxygenation is a consensus and a critical issue worldwide[1]. There is an urgent need to understand the spatial and depth distribution and trends of global ocean dissolved oxygen[2]. The availability of $O_2$ observations in international databases does not allow a comprehensive quantitative assessment of the severity of hypoxia at seasonal and interannual scales[3]. Argo is the only real-time observation system for three-dimensional observation of the upper ocean[4-5], which aims to obtain three-dimensional, wide-area, real-time, multi-element integrated hydrographic profiles through the deployment of floats. Currently, Biogeochemical Argo (BGC-Argo) provides 240,000 dissolved oxygen profiles worldwide and adds about 20,000+ profiles per year. It provides an important data base for understanding and analyzing the current characteristics and trends of dissolved oxygen in the global ocean. As Argo has unprecedented advantages in temporal resolution, spatial coverage and vertical resolution[6], this paper designs a marine dissolved oxygen interpolation method based on the spatial characteristics and quality flags of the dissolved oxygen data. This paper aims to develop a global spatial grid of dissolved oxygen at the monthly scale of the climatic state at standard depth to serve the global marine ecological health assessment.

## 2.MATERIALS AND METHODS

### *2.1 Data source*

In this paper, we use dissolved oxygen observations of Argo floats from 2010 to 2021, in which the Argo $O_2$ profiles from January 1 to January 31 are obtained for the climatological January dissolved oxygen concentration profiles, and the climatological monthly data of marine dissolved oxygen concentration from February to December are obtained by analogy. These data have been subjected to real-time quality control and delayed quality control by national Argo data centers, mainly including profile position and time check, temperature and salinity extremes check, drift velocity check, pressure check, burr check, gradient check and density inversion check, etc[7-8]. However, due to human factors such as the limited effort invested by national Argo data centers and the systematic errors in floats measurements, there are still some data with large errors included in the Argo floats observations submitted to GDAC[9]. According to the data quality flags provided in the Argo user's manual, the unusable and obviously erroneous data are eliminated and finally screened out dissolved oxygen data with different flags of quality.

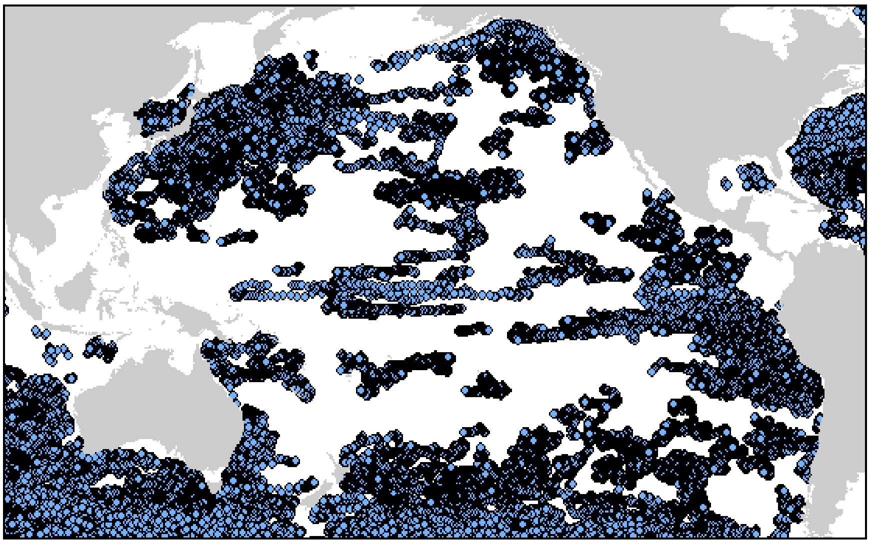

**Figure 2.** Spatial Distribution of Argo $O_2$ profiles

### *2.2 Standard level interpolation in depth*

The dissolved oxygen observed by the Argo floats in depth are discrete and irregular. Therefore, the dissolved oxygen observations in depth need to be interpolated to the standard levels. Since the shallow layer of the ocean is influenced by seawater activity and the deep layer of the ocean is relatively stable, the standard levels with unequal intervals is used to combine the characteristics and practical needs of Argo floats. The specific vertical interpolation method adopts Akima method[10], which is based on the known data points to establish a cubic polynomial curve with first-order derivatives, and can fit the discrete data points to form a smooth and natural function curve[11]. Using the Akima interpolation method, the fitting function between dissolved oxygen concentration and depth is established. Finally, the ocean dissolved oxygen concentration at the depth of any ocean observation standard level can be obtained by inputting the depth of that observation level.

### *2.3 Methods*

The gridding method of marine dissolved oxygen studied in this paper is based on the ideas of direct insertion method and stepwise iterative method. The so-called direct insertion method is a simple replacement of the gridded model field by the observed data. This method needs to ensure that the observed data are real and reliable and that there are enough observation points. The stepwise iterative idea was proposed by Cressman[12] in 1959. The method adopts the iterative idea to gradually correct the increment until the accuracy requirement is reached. The iterative formula is:

$$f_i = f_i^b + \Delta f \qquad (1)$$

$$\Delta f = \frac{\sum_{j=1}^{K} w_{ij}^2 (Doxy_j - f_i^b)}{\sum_{j=1}^{K} w_{ij}} \qquad (2)$$

Where $f_i$ denotes the final analytical value at grid i, $f_i^b$ is the initial value of the background field of dissolved oxygen concentration at grid i, and $Doxy_j$ denotes the j-th observation point within the influence radius R of the grid i, a total of K dissolved oxygen observations, and $w_{ij}$ is the weighting factor. The key point of the Cressman stepwise revision idea is the determination of the weighting function:

$$W_{ij} = \begin{cases} \frac{R^2 - d_{ij}^2}{R^2 + d_{ij}^2} & d_{ij} < R \\ 0 & d_{ij} > R \end{cases} \quad (3)$$

In this paper, a double-constrained stepwise iterative interpolation method based on the spatial characteristics and the quality flags of dissolved oxygen is proposed. The detailed process is shown in Figure 1. The weighting function used in this paper is designed by considering the spatial distance of the profiles and the quality flags:

$$W_{ij} = \begin{cases} w_{qc} * \frac{R^2 - d_{ij}^2}{R^2 + d_{ij}^2} & d_{ij} < R \\ 0 & d_{ij} > R \end{cases} \quad (4)$$

Not only the spatial distance between the Argo $O_2$ profiles and the points to be interpolated is considered, but also the quality flags of dissolved oxygen is taken into account. The spatial search radius is determined adaptively to ensure that there is enough data within the range for interpolation. And then a stepwise iterative revision of the marine dissolved oxygen is performed using equation (2). During the iterative process, the dissolved oxygen interpolation results are used to replace the initial values until a preset accuracy threshold is met.

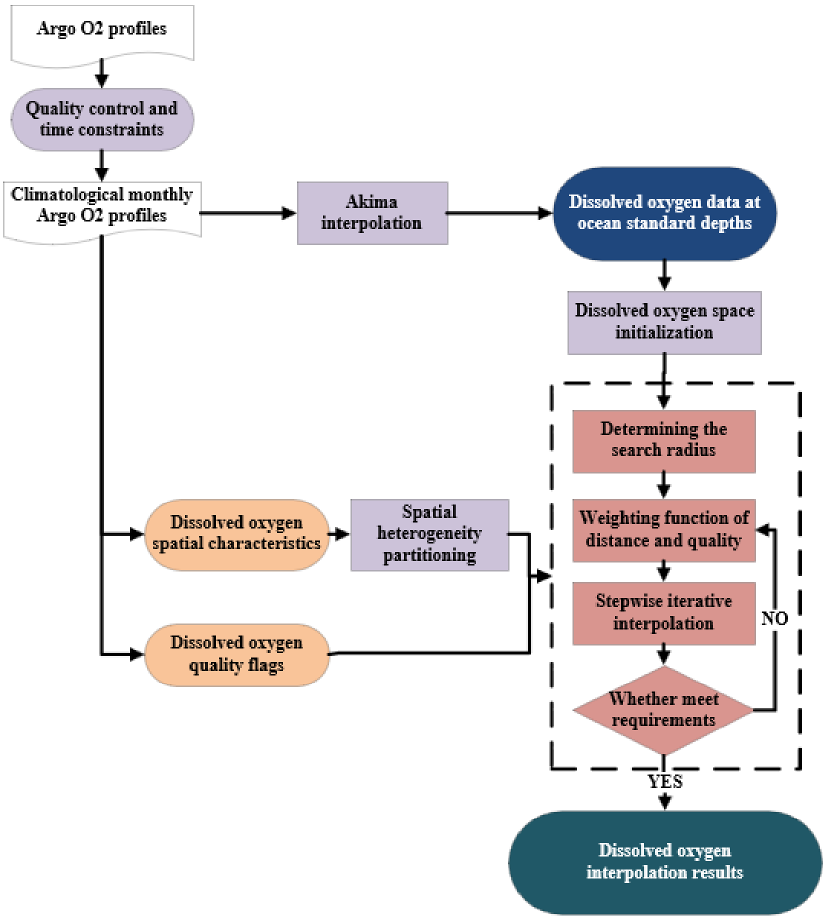


**Figure 1**. The Flow Chart of Interpolation Method

## 3.RESULTS

Applying the above method to the Argo $O_2$ profiles from 2005 to 2021. The monthly climatological dissolved oxygen raster data with a spatial resolution of 1 ° × 1 ° at each standard depth level were generated. Figure 3 shows the spatial distribution characteristics of global ocean dissolved oxygen concentration in four depth levels in January (winter) and July (summer). As can be seen from the figure, the spatial distribution of dissolved oxygen concentration at different depths basically maintains the characteristics of low concentration at low equatorial latitudes and high concentration at high polar latitudes. In the middle and high latitude regions of the northern Pacific Ocean, the area of dissolved oxygen low value zone gradually increases with increasing depth. The main low oxygen zones are located in the equatorial Pacific region, the Gulf of Mexico, the east-central part of the equatorial Atlantic Ocean, and the equatorial Indian Ocean region.

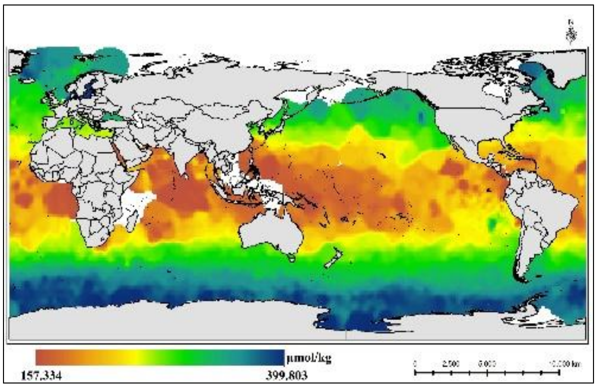

January, 10dbar

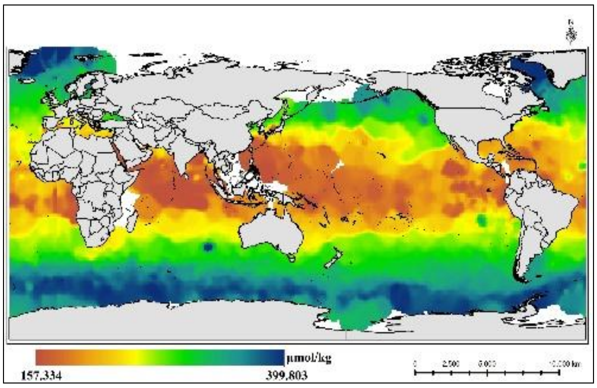

July, 10dbar

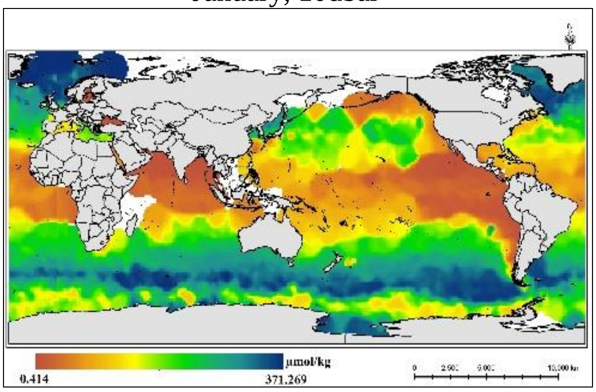

January, 200dbar

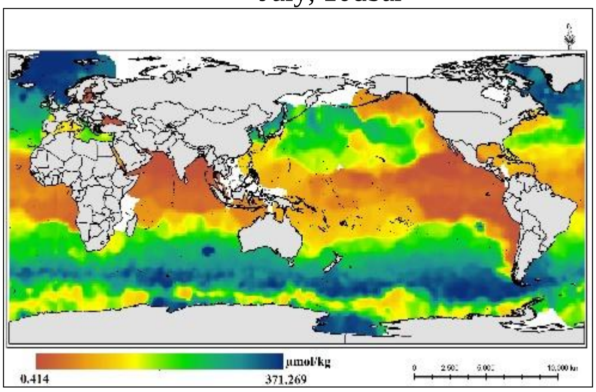

July, 200dbar

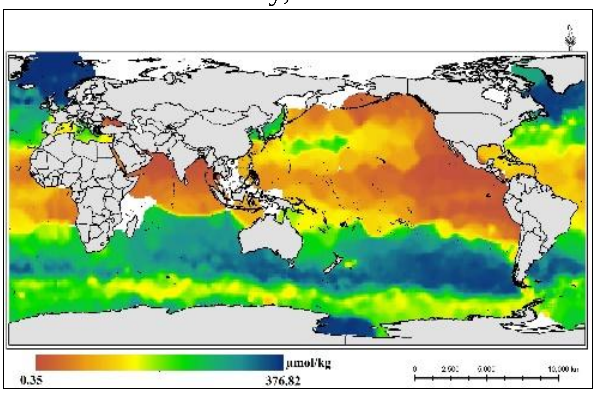

January, 500dbar

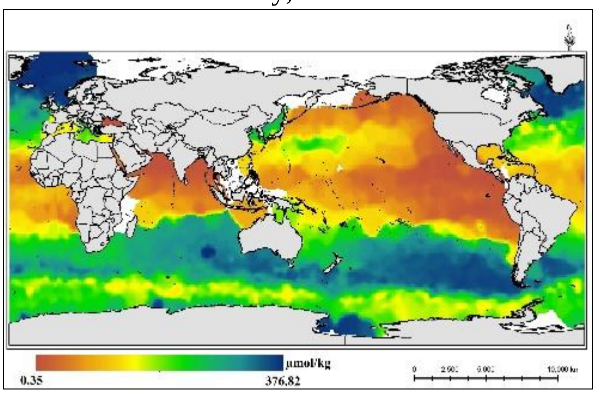

July, 500dbar

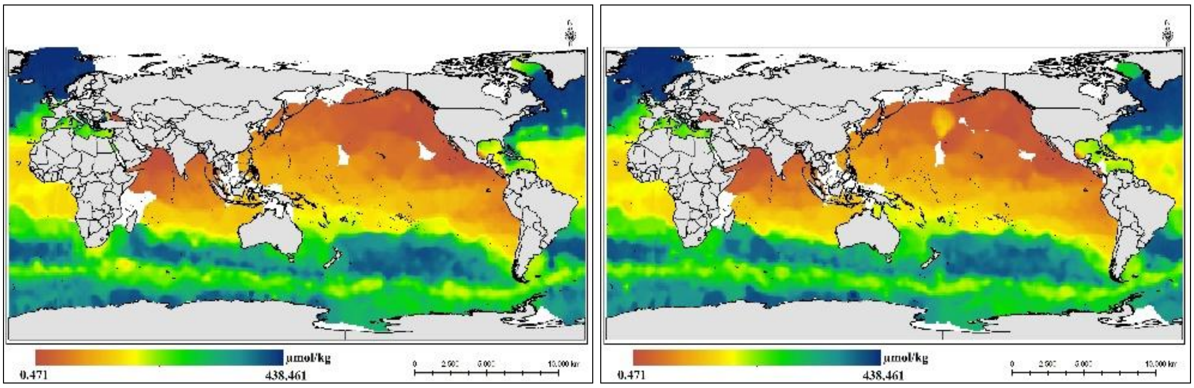


January, 100dbar July, 1000dbar

**Figure 3**. Global Dissolved Oxygen Concentration Distribution

In order to verify the feasibility of the dissolved oxygen interpolation method, a number of Argo $O_2$ profiles that were not involved in the interpolation in 2022 were randomly selected. In addition, Interpolation result is compared and analyzed with the relatively authoritative WOA18 datasets[13]. As shown in Table 1, the maximum absolute error between the interpolated results and the random profiles is less than 15 umol/kg, and the relative error is within 5%. The difference between the interpolated result and the WOA18 datasets in the same period and at the same depth is shown in Figure 4. The result shows that the percentage of regions with absolute errors less than 20 umol/kg was more than 85% globally.

**Table 9.** Result of random point comparison

| 编号 | 浮标 ID | 周期 | 观测值 (umol/kg) | 插值 (umol/kg) | 误差 (umol/kg) | 相对误差 (%) |
|---|---|---|---|---|---|---|
| **1** | 1902381 | 1 | 210.831 | 210.902 | 0.071 | 0.03 |
| **2** | 2902270 | 108 | | | | |
| **3** | 5904844 | 183 | 215.156 | 214.780 | -0.376 | -0.17 |
| **4** | 5905103 | 144 | 325.733 | 317.525 | -8.208 | -2.51 |
| **5** | 5905138 | 187 | 298.229 | 288.725 | -9.504 | -3.18 |
| **6** | 5905986 | 174 | 195.506 | 201.082 | 5.576 | 2.86 |
| **7** | 5906020 | 188 | 208.235 | 198.121 | -10.114 | -4.86 |
| **8** | 5906208 | 74 | 247.677 | 255.031 | 7.354 | 2.96 |
| **9** | 5906218 | 67 | 252.084 | 258.207 | 6.123 | 2.42 |
| **10** | 5906221 | 70 | 313.106 | 327.220 | 14.114 | 4.5 |
| **11** | 5906226 | 71 | 329.889 | 341.088 | 11.199 | 3.39 |
| **12** | 5906249 | 66 | 250.810 | 259.037 | 8.227 | 3.27 |
| **13** | 5906303 | 51 | 194.703 | 195.330 | 0.627 | 0.32 |
| **14** | 5906310 | 39 | 229.277 | 235.955 | 6.678 | 2.9 |
| **15** | 5906343 | 30 | 201.162 | 207.686 | 6.524 | 3.24 |
| **16** | 5906449 | 9 | 202.478 | 194.711 | -7.767 | -3.83 |
| **17** | 5906475 | 5 | 203.489 | 202.944 | -0.545 | -0.27 |
| **18** | 5906503 | 3 | 199.267 | 202.738 | 3.471 | 1.74 |
| **19** | 5906624 | 113 | 320.351 | 328.624 | 8.273 | 2.58 |
| **20** | 7900566 | 75 | 288.801 | 296.345 | 7.544 | 2.61 |

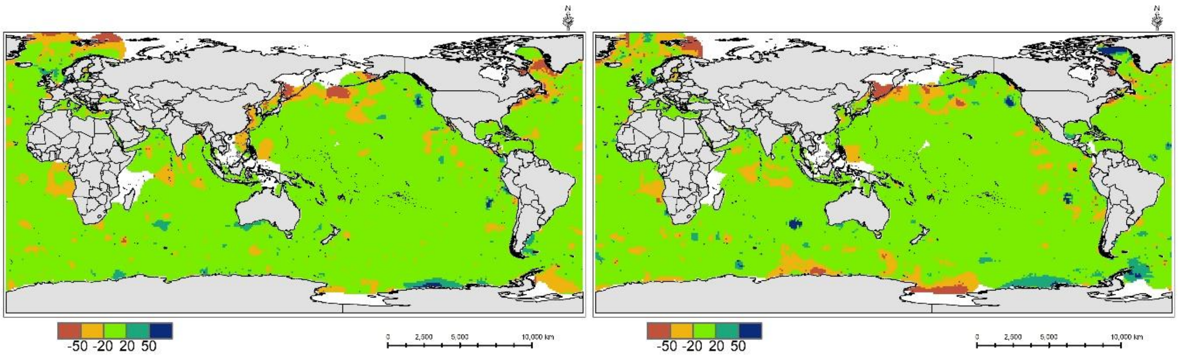


January, 10dbar                July, 10dbar

| umol/kg | <-50 | -50~-20 | -20~20 | 20~50 | >50 |
|---|---|---|---|---|---|
| 比例 | 1.7% | 10.3% | 85.9% | 1.8% | 0.3% |

| umol/kg | <-50 | -50~-20 | -20~20 | 20~50 | >50 |
|---|---|---|---|---|---|
| 比例 | 1.8% | 10.4% | 85.0% | 2.3% | 0.5% |

**Figure 4.** The Difference Results of Dissolved Oxygen

## 4.SUMMARY

Using the Argo $O_2$ profiles , we design a double-constrained iterative interpolation method based on the spatial characteristics and quality flags of dissolved oxygen. A comparative analysis was carried out with random Argo $O_2$ profiles and the WOA18 datasets. The main conclusions are as follows:

1. A double-constraint interpolation method was designed by integrating the spatial characteristics of Argo profiles and quality flags to ensure the optimal dissolved oxygen data participation interpolation and spatial interpolation unbiased issue.
2. Using the idea of stepwise iterative revision, a climatological monthly marine dissolved oxygen spatial grid product development method was designed to achieve the optimal ocean dissolved oxygen interpolation problem.
3. Along with the advantages of short Argo buoy collection period, wide coverage area and high vertical resolution[14], the gridding of marine dissolved oxygen based on Argo profiles will become more and more common. These products will help support ocean model assessments, improved formulation of indicators on climate and ocean health.

## References

[1] Limburg, K. E., Breitburg, D., Swaney, D., and Jacinto, G. (2020). Ocean deoxygenation: a primer. One Earth 2, 24–29. doi: 10.1016/j.oneear.2020.01.001

[2] Giglio D, Lyubchich V, Mazloff M R. Estimating Oxygen in the Southern Ocean using Argo Temperature and Salinity [J]. Journal of Geophysical Research: Oceans, 2018, 123(6): 4280-4297.

[3] Grégoire M, Garçon V, Garcia H, Breitburg D, Isensee K, Oschlies A, Telszewski M, Barth A, Bittig HC, Carstensen J, Carval T, Chai F, Chavez F, Conley D, Coppola L, Crowe S, Currie K, Dai M, Deflandre B, Dewitte B, Diaz R, Garcia-Robledo E, Gilbert D, Giorgetti A, Glud R, Gutierrez D, Hosoda S, Ishii M, Jacinto G, Langdon C, Lauvset SK, Levin LA, Limburg KE, Mehrtens H, Montes I, Naqvi W, Paulmier A, Pfeil B, Pitcher G, Pouliquen S, Rabalais N, Rabouille C, Recape V, Roman M, Rose K, Rudnick D, Rummer J, Schmechtig C, Schmidtko S, Seibel B, Slomp C, Sumalia UR, Tanhua T, Thierry V, Uchida H, Wanninkhof R and Yasuhara M (2021) A Global Ocean Oxygen Database and Atlas for Assessing and Predicting Deoxygenation and Ocean Health in the Open and Coastal Ocean. Front. Mar. Sci. 8:724913. doi: 10.3389/fmars.2021.724913

[4] Chen D K, Xu J P, Ma J R, et al. Argo global observation network and studies of upper ocean structure, variability and predictability[J]. Adv Earth Sci, 2008, 23: 1-7.

[5] Riser, S.C., Freeland, H.J., Roemmich, D., Wijffels, S., Troisi, A., Belbeoch, M., et al. (2016). Fifteen years of ocean observations with the global Argo array[J]. Nature Climate Change, 6(2), 145-153. DOI: 10.1038/nclimate2872.

[6] Breitburg, D., Levin, L.A., Oschlies, A., Gre´goire, M., Chavez, F.P., Conley, D.J., Garc¸on, V., Gilbert, D., Gutie´rrez, D., Isensee, K., et al. (2018). Declining oxygen in the global ocean and coastal waters. Science 359, eaam7240.

[7] Li H, Xu J, Liu Z, et al. Study on the establishment of gridded Argo data by successive correction[J]. Marine Science Bulletin, 2012, 5: 502-514.

[8] Thierry V, Bittig H. Argo quality control manual for dissolved oxygen concentration[J]. 2021.

[9] Bittig H C, Maurer T L, Plant J N, et al. A BGC-Argo guide: Planning, deployment, data handling and usage[J]. Frontiers in Marine Science, 2019, 6: 502.

[10] Akima H.,1970. A new method for interpolation and smooth curve fittingbased on local. Journal of the ACM，17（4）：589-602.
[11] Crisp M P, Jaksa M B, Kuo Y L. Framework for the optimisation of site investigations for pile designs in complex multi-layered soil[J]. Res. Rep. Sch. Civil Environ. Min. Eng, 2019.
[12] Cressman G P.,1959. An operational objective analysis system. Mon.Wea. Rev，87：367-372.
[13] Garcia H.E., T.P. Boyer, O.K. Baranova, R.A. Locarnini, A.V. Mishonov, A. Grodsky, C.R. Paver, K.W. Weathers, I.V. Smolyar, J.R. Reagan, D. Seidov, M.M. Zweng (2019). World Ocean Atlas 2018: Product Documentation. A. Mishonov, Technical Editor.
[14] Zhang C, Wang D, Liu Z, et al. Global Gridded Argo Dataset Based on Gradient-Dependent Optimal Interpolation[J]. Journal of Marine Science and Engineering, 2022, 10(5): 650.

# Ocean Big data in support of the sustainable development of the Maritime Silk Road

Tang Shilin

South China Sea Institute of Oceanology, Chinese Academy of Sciences

email: sltang@scsio.ac.cn

## 1. INTRODUCTION

The marine environment of the Maritime Silk Road is complex and changeable, and marine disasters occur frequently. The accelerated maritime activities of coastal countries along the Maritime Silk Road, port construction, resource development, navigation safety, and maritime rights protection have put forward new demands on marine data and its application capabilities. The sustainable development of the Maritime Silk Road faces large challenges. Two platforms, the South China Sea infrastructure for ocean & marine data interchange (data.scsio.ac.cn) and the Indian Ocean Big Data Sharing Infrastructure (io.scsio.ac.cn), are two intelligent digital platforms for the Maritime Silk Road. The two platforms are opened digital repositories to manage, access and share data, information, products, and knowledge originating from research cruises, new automatic observing systems, satellite remote sensing, and numerical models. The data cover all disciplines of marine science, including physical oceanography, marine chemistry, marine biology, and marine ecology. In this study, we proposed two cases based on the datasets. The first one is to use these data from the platforms to monitor changes in water environments in the ocean around the port of Colombo during the construction period. The results indicated that the impact of the construction of Colombo Port on the water environment can basically be restored to the preconstruction level within 4 months. Another case concerns the phytoplankton size variation in the northern Indian Ocean. The results indicate that tropical cyclones have a significant impact on the phytoplankton grain size structure.

## 2. MATERIALS AND METHODS

The Ocean Big data of the Maritime Silk Road platforms implement the policy of "Data Management of the South China Sea Institute of Oceanography, Chinese Academy of Sciences". It is continuously collecting scientific data from the Maritime Silk Road, and it is comprehensively developing scientific data resources based on the South China Sea Ocean Data Center. From cooperation with marine scientists, it produces a batch of ecological environment remote sensing and data assimilation data.

### *2.1 Two databases for maritime silk road*

The South China Sea infrastructure for ocean & marine data interchange（SCSOD) has federated open digital repositories to manage, access and share data, information, products, and knowledge originating from research cruises and new automatic observing systems. SCSOD includes the important issues of trust that are addressed in data-based research: security, confidentiality, ownership, assured provenance, authenticity, and the quality of the data and the metadata.

The Indian Ocean Big Data Sharing Infrastructure (IOBD) constructs the Maritime Silk Road three-dimensional comprehensive data observation network, integrates the Maritime Silk Road multisource remote sensing information source, establishes the marine environment forecast system for the Maritime Silk Road, and integrates the "data + computing power + algorithm" application to build the Maritime Silk Road Big Scientific and Intelligent Data Platform. At present, the platform has initially formed the new mechanism of data work that drives technological innovation and development by marine big data, promoted data services to run through the entire life cycle of scientific research activities, released multiple sets of numerical model products such as 30 years of wind, waves and currents in the Indian Ocean and South China Sea, and released remote sensing data products of the marine ecological environment with multiple resolutions in the Indian Ocean and South China Sea.

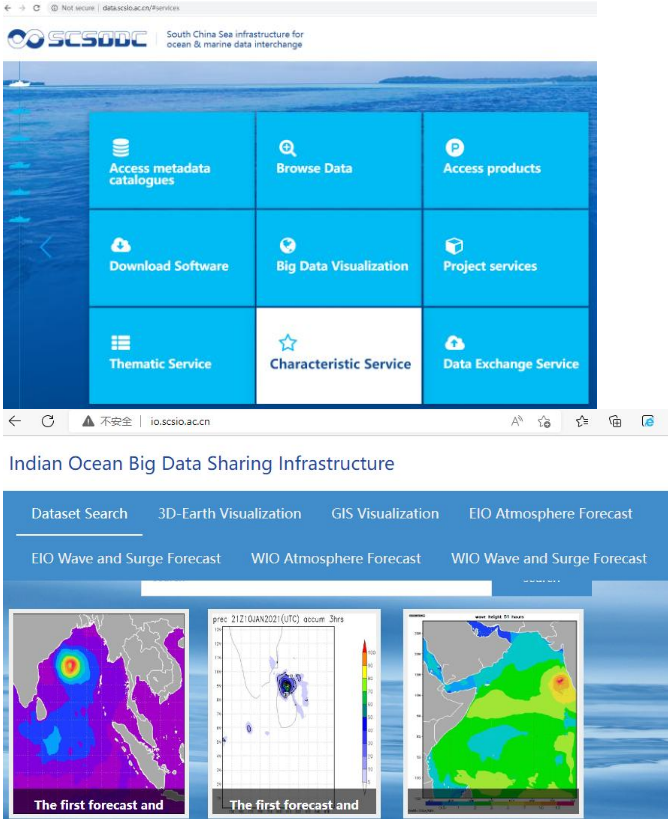


Figure 1. The webpage of the two platforms for the Maritime Silk Road

### *2.2 Usage of the big earth data*

For the first case, the Landsat OLI L1 data, including the visible light band and infrared band from Landsat 8 from 2013 to 2020, with a time resolution of 16 days and a spatial resolution of 30 m in Colombo Port, were processed to determine the chlorophyll a concentration (Chl a) and suspended sediment in our platform.

For the second case, the L3-level chlorophyll a concentration (Chla) data and photosynthetic active radiation (PAR) data of the Aqua and Terra fusion of MODIS from 2003 to 2022, with a temporal resolution of 1 day and a spatial resolution of 4 km, were used. The chlorophyll-a concentration from Bio-Argos in 2013-2022 was obtained from “the International Argo Program and the national programs”.

## 3. RESULTS

### *3.1 The water environment in the ocean around Colombo port*

The statistical analysis of the dynamic changes in the water environment near Colombo Port from 2013 to 2020 shows that the water environment in water near Colombo Port corresponding to SDG 14.1.1 presents an overall good trend.

On a spatial scale, the water environment variation caused by port construction was controlled in a range of <10 km and an area of <54 km$^2$. The northern coastal area of the port is adjacent to the river estuary and is the only export channel for port construction, while the middle and southern coastal areas of the port were closed by priority embankments at the beginning of construction. Therefore, the construction of Colombo port mainly affects the northern coastal area of the port (the increase in chlorophyll-a <1.2

mg/m$^3$, the increase in suspended sediment <1.5 g/m$^3$) and has little effect on the middle and southern coastal areas of the port (the increase in chlorophyll-a <0.06 mg/m3, and the increase in suspended sediment <0.03 g/m$^3$).

On time scales, the interannual changes in the overall water environment of Colombo port and the peaks of chlorophyll-a and suspended sediment were from the end of 2014 to the beginning of 2015, while the concentrations in other years were relatively stable. The seasonal characteristics were that the chlorophyll-a and suspended sediment were significantly higher in spring and winter than in summer and autumn. Although chlorophyll-a and suspended sediment increased in the initial stage of construction (from the end of 2014 to the beginning of 2015), these increases were able to basically be restored to the preconstruction level within 4 months. From a national perspective, China’s port construction can meet the goals of sustainable development by minimizing the impact of construction on the marine environment.

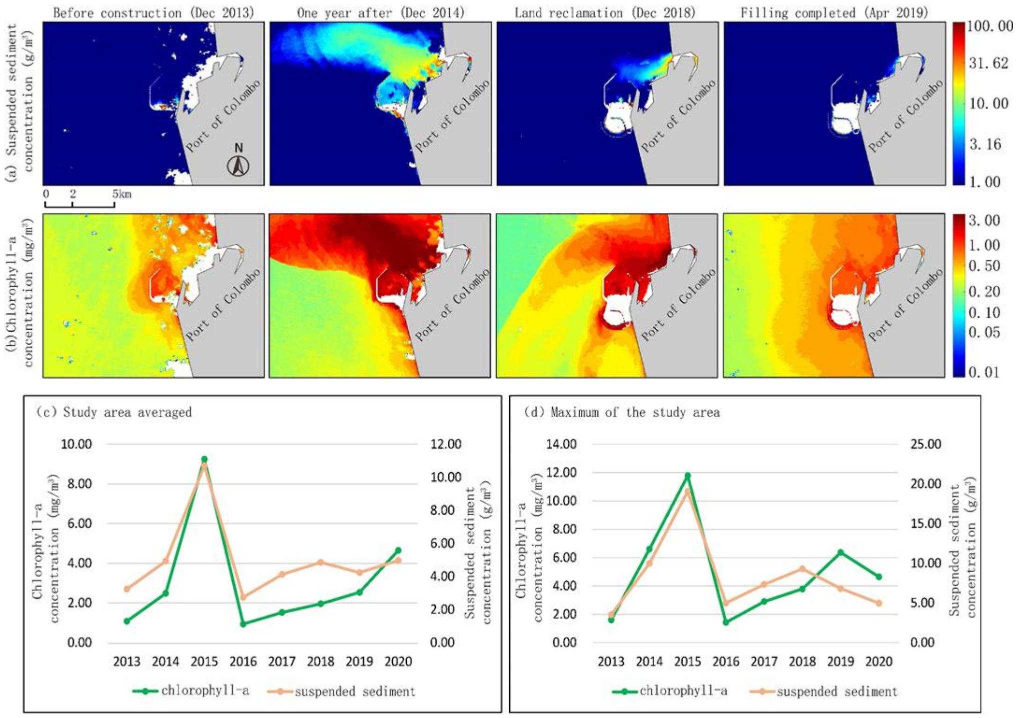


Figure 2. The spatial distribution of sea surface suspended sediment and chlorophyll concentrations and their area increments in nearshore water of Colombo port

### *3.2 Tropical cyclone on the particle size structure of phytoplankton*

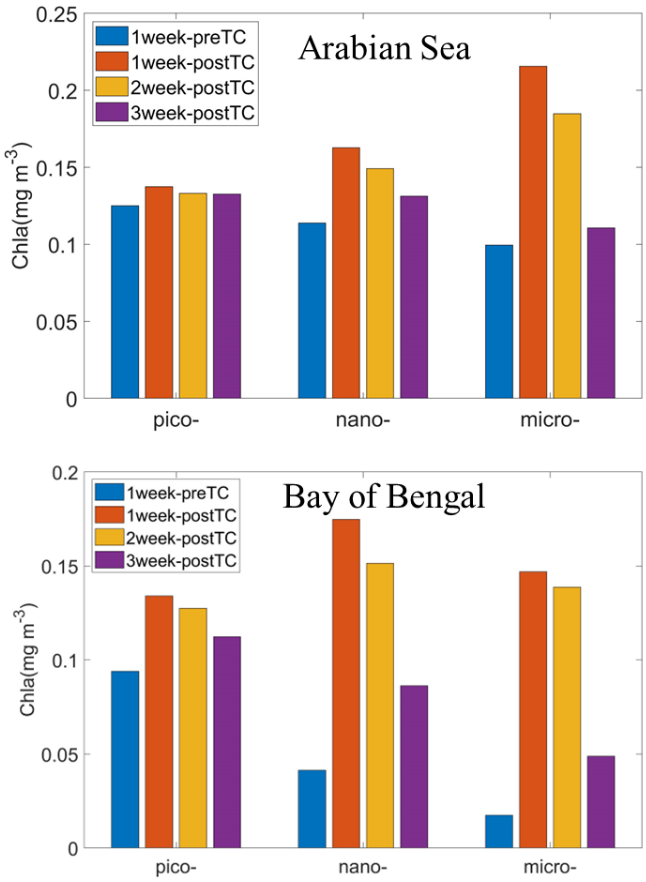


Figure 3 Changes in phytoplankton grain size structure caused by regional mean climatic tropical cyclones from 2003 to 2022 after the transformation of the central coordinate system of the tropical cyclone in the North Indian Ocean

Figure 3 shows the regional average phytoplankton grain size climatological distribution caused by tropical cyclones in the North Indian Ocean from 2003 to 2022. Before the passage of the tropical cyclone, the phytoplankton biomass in the Arabian Sea was higher than that in the Bay of Bengal, and the Bay of Bengal was dominated by picophytoplankton, while the proportion of microphytoplankton in the Arabian Sea was slightly higher than that of picophytoplankton and dominated. The transition of tropical cyclones will cause a significant increase in phytoplankton biomass of all sizes in the North Indian Ocean within 1-2 weeks, and the phytoplankton particles will be larger in size: the Arabian Sea is dominated by microphytoplankton to small phytoplankton. The Bay of Bengal will shift from picophytoplankton dominance to microphytoplankton dominance. The tropical cyclone basically returned to the pretransit level after 3 weeks. Therefore, the transition of tropical cyclones caused a larger proportion of phytoplankton in the northern Indian Ocean, where the Arabian Sea is usually dominated by microphytoplankton, while the Bay of Bengal is dominated by microphytoplankton.

# SDG 15 (Life on Land): Sustainable Use of Terrestrial Ecosystems

# Global high spatial resolution subclasses oil palm mapping

You Xu[1,2] , Dongjie Fu [2], Hao Yu[2], Rong Fan[2] , Bin He[2] , Fenzhen Su[2]

[1]Faculty of Geomatics, Lanzhou Jiaotong University, Lanzhou 730070, China.

email: xuyou160605@163.com

[2]State Key Laboratory of Resources and Environmental Information System, Institute of Geographic Sciences and Natural Resources Research, Chinese Academy of Sciences, Beijing 100101, China.

email: fudj@lreis.ac.cn
email: yuh@lreis.ac.cn
email: fanr@lreis.ac.cn
email: heb@lreis.ac.cn
email: sufz@lreis.ac.cn

## 1. INTRODUCTION

Oil palm was a crop with the highest oil yield compared to other oil producing crops including soybean, peanut(Cheng, Yu et al. 2018). Most of the previous studies focused on Southeast Asia and only classified oil palms in a single class with coarse spatial resolution. Expansion of oil palm cultivation has brought with it a series of environmental problems such as massive deforestation, loss of biodiversity, soil degradation and weakened climate regulation. Refined mapping of oil palm subclasses will provide scientific basis for the environmental impact evaluation caused by the expansion of oil palm cultivation. Moreover, the spatial resolution of the current products are not accuracy enough.

In tropical regions, there are often cloudy and foggy weather, and it is difficult to exclude these disturbances using optical satellite imagery data alone(Maskell, Chemura et al. 2021). Radar satellite imagery data has good penetration of clouds and fog and can accurately obtain information on ground objects, and SAR data has high sensitivity to feature contours and water content. The C-band SAR backscatter coefficients from Sentinel-1 are able to identify the canopy structure of oil palm well and distinguish oil palm from other land cover types(Danylo, Pirker et al. 2021).

In this study, we combined Planet & NICFI Basemaps (4.77 m), Sentinel-1/2 (10 m) from ESA, JRC Global Surface Water Mapping Layers and global mangrove distribution data. Moreover, we used spatial texture, tree age data , and this information is supposed to be helpful for the subclass oil palm classification. Furthermore, we use Google Earth Engine to process the global mapping of industrial mature oil palm(IMOP), industrial young oil palm(IYOP), smallholder mature oil palm(SMOP) and smallholder young oil palm(SYOP).

This study aims:i) to produce a 4.77m high-resolution global oil palm subclasses map; ii)to calculate the area and distribution of each oil palm subclass on global scale; and iii)to understand the current distribution of oil palm subclasses at different elevations and altitudes and the expansion trends of the oil palm.

## 2. MATERIALS AND METHODS

### *2.1 Candidate area of oil palm classification*

Oil palm is known to grow in humid, warm tropical regions and has been found in Southeast Asia, South Asia, West Africa, Central Africa and the Americas till 2020. Depending on the crop structure and economic policies, the area and type of oil palm cultivation varies from country to country. In combination with the 100km*100km grid used in the 'High-resolution global map of smallholder and industrial closed canopy oil palm plantations' study by Descals(Descals, Wich et al.). to determine the extent of existing oil palm plantations in 2019. the extent of non-oil palm plantations was removed by slope, elevation and protected area threshold settings using the selected 2020 oil palm subclasses sample sites.

### *2.2Sentinel-1 and Sentinel-2 satellite images pre-processing*

Although the Sentinel-1 data retrieved from Google Earth Engine has undergone thermal noise removal, radiometric calibration and terrain correction, it still lacks the necessary processing steps such as edge noise removal, streak removal, scatter filtering and local incidence angle normalization (Kaplan, Fine et al. 2021, Kustiyo, Rokhmatuloh et al. 2021). Sentinel-1 raw data has the presence of noise caused by its own factors, and noise can seriously interfere with the classification of features during supervised classification.

Sentinel-2 data are used to synthesize the spectral index information data in addition to their own raw band information in the classification of oil palm subclasses. The quality of the spectral index information data is greatly disturbed by the cloud factor, so cloud-removing operation must be carried out, and in this study the maximum cloud threshold was set at 5%.

### *2.3Mapping of global subclasses oil palm*

On a global scale, the following 3 steps will be carried out to reach the goal of producing a high resolution spatial distribution map of oil palm subclasses: i) The areas that are inaccessible to oil palm cultivation were removed, which include cities, water bodies, mangroves, protected areas, and areas that are beyond the elevation and elevation limits that should be met by oil palm cultivation; the corresponding study area was divided into a small grid of 100km * 100km. ii) Data fusion (Planet & NICFI and Sentinel-1/2 data) and supervise classification(classification and regression tree method, Cart) were used to classify the oil palm sub-classes in each grid area by sample points taken from Google Earth Pro and the area of oil palm subclasses were counted. iii) Post-processing methods were used to process the raw classification images for fine patches and to improve the classification accuracy and visual effect; non-oil palm sub-classes were masked out and the oil palm sub-classes were mapped.

## 3. RESULTS

### *3.1Spatial distribution patterns of global subclasses oil palm*

Figure 1 shows global oil palm cultivation in 2020 in 41 countries across Asia, Africa , Oceania and the Americas, including Indonesia and Malaysia(Fig.1).Ten countries including Indonesia, Malaysia, Cambodia, Nigeria and Colombia, four species of oil palm seeds are grown in each of these areas.The area planted with oil palm in Southeast Asia and Oceania is 54,187,000 hectares, accounting for 60% of global oil palm cultivations, with Indonesia and Malaysia planting oil palm intensively and the remaining countries planting oil palm more scattered;The second oil palm planting area is Africa,with a total amount of 19,850,000 hectares, which accounts for 22% of global oil palm cultivations; The oil palm planting area of America is 14,882,900 hectares, accounting for 17% of global oil palm cultivations; South Asia has 1,325,000 hectares oil palm, accounting for only 1% of global oil palm cultivations.

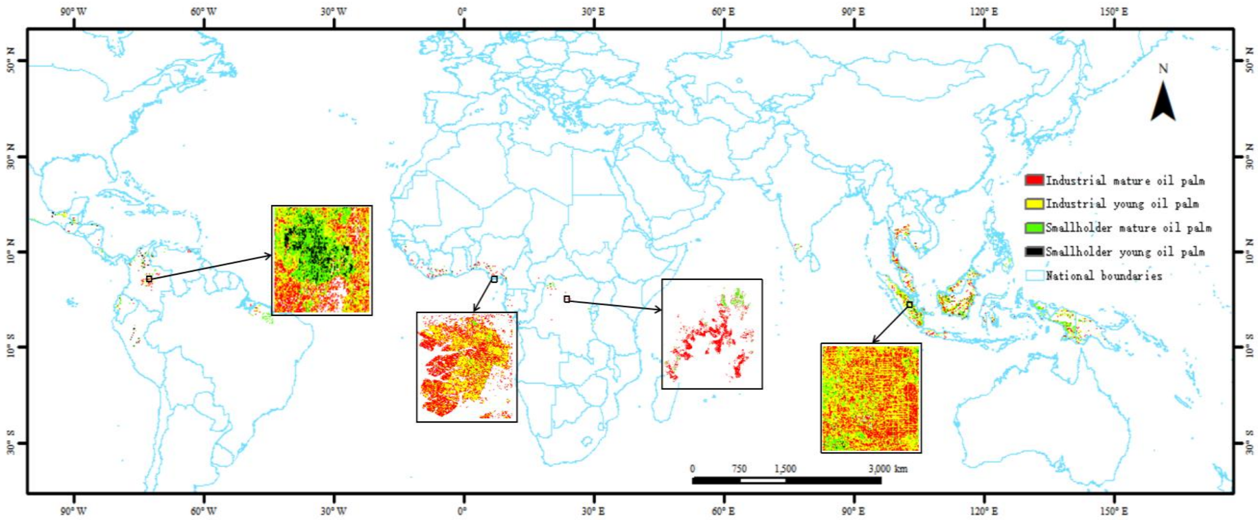

Fig. 1. Global spatial distribution map of oil palm subclasses

In different regions, due to the differences in topography, climate and the degree of development of oil palm cultivation, the distribution pattern of oil palm varies. In Indonesia and Malaysia, oil palm has a clear distribution pattern along the mountains in addition to being planted in the plains; However, in Africa and the Americas, oil palm cultivation is mainly distributed along plains and valleys.Figure 2, Figure 3 and Figure 4 show the spatial distribution of oil palm subclasses in Southeast Asia and Oceania, Africa, and the Americas respectively.

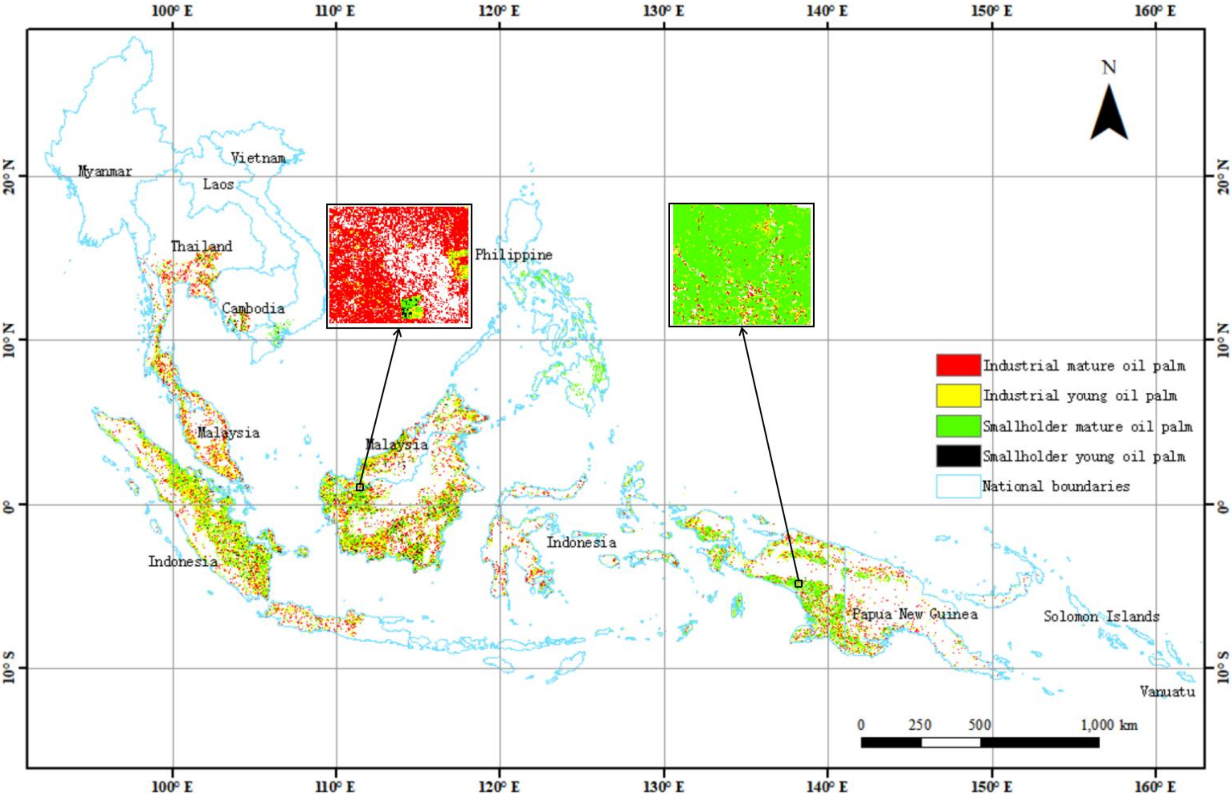


Fig. 2. Spatial distribution map of oil palm subclasses in Southeast Asia and Oceania

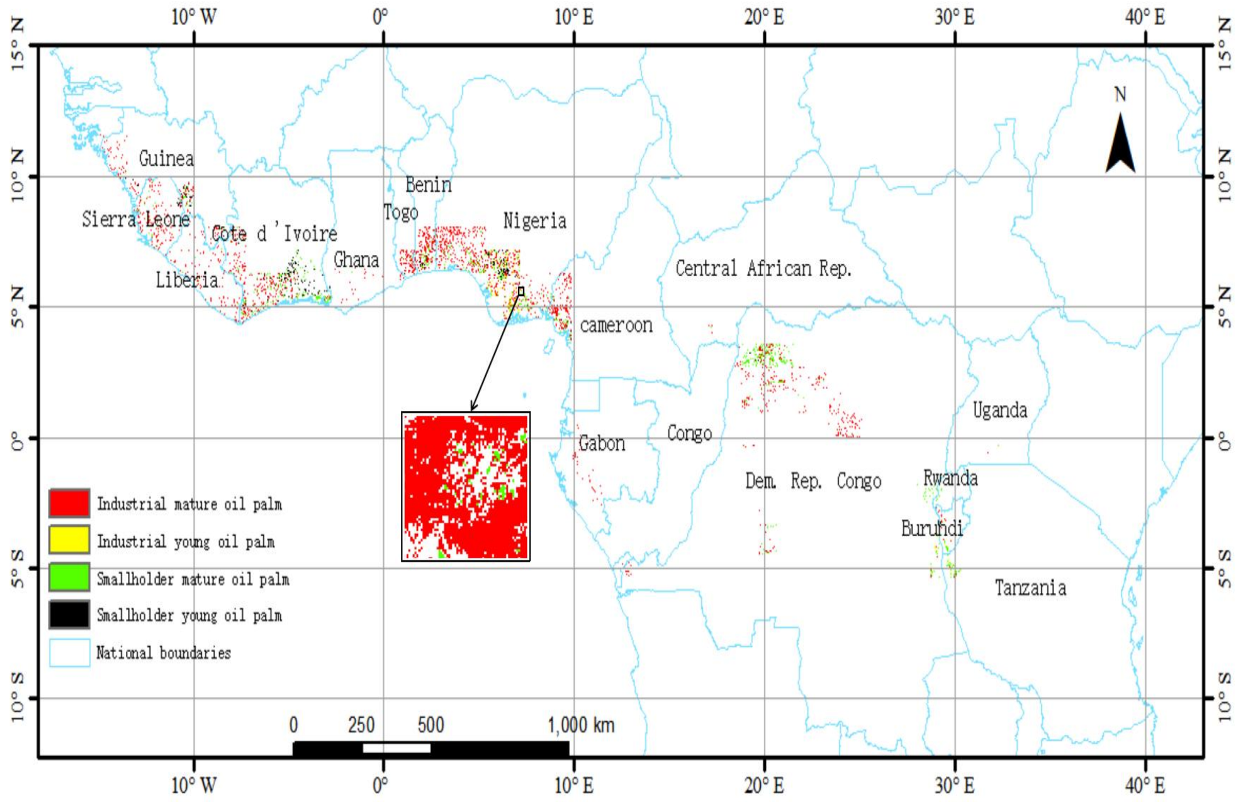


Fig. 3. Spatial distribution map of oil palm subclasses in Africa

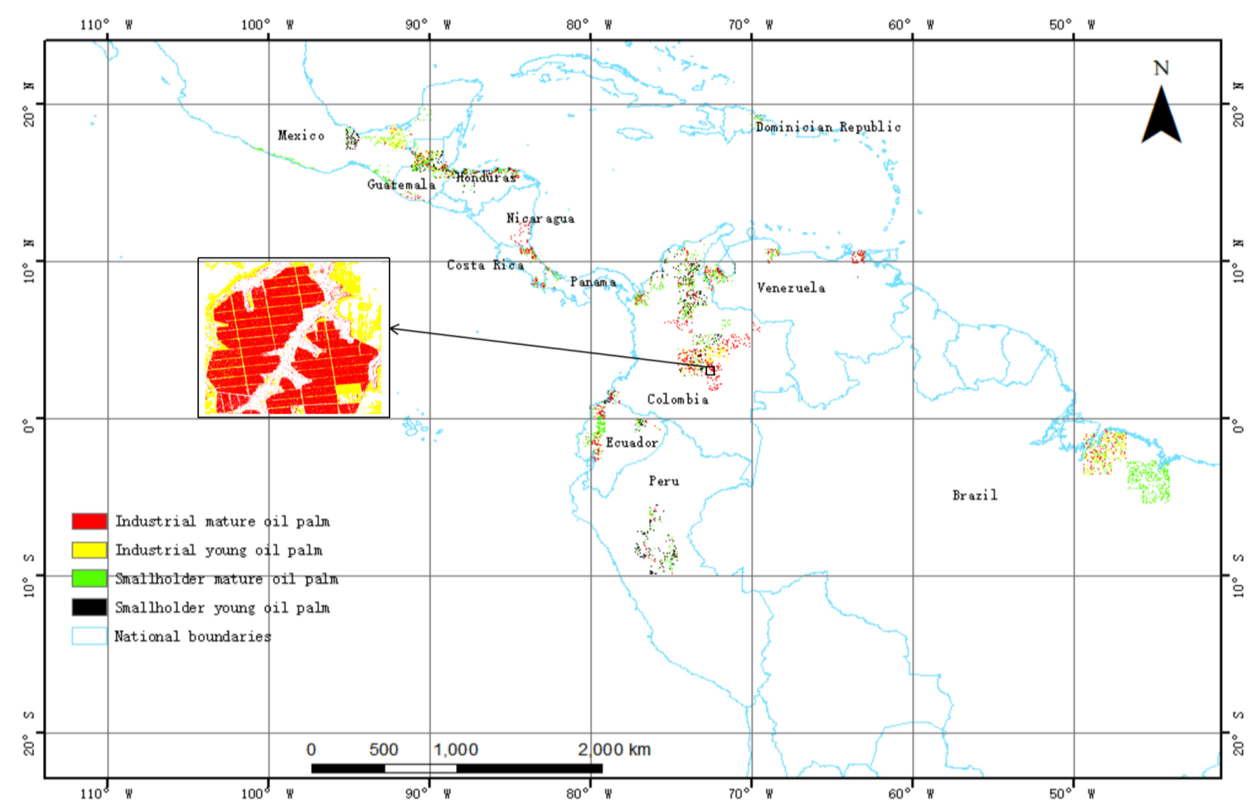


Fig. 4.Map of the spatial distribution of oil palm subclasses in the America

### *3.2Share of global oil palm subclasses*

Among the global oil palm subclasses, The area of IMOP , IYOP , SMOP and SYOP are 31.4038, 17.2767 , 31.0913 and 10.4732 million hectares, accounting for 35%, 19%, 34% and 12% of the total oil palm cultivation area, respectively. All four oil palm subclasses have the largest regional share of their respective oil palm subclasses in South East Asia. The IMOP planted in Southeast Asia accounts for 65% of the global IMOP, and the corresponding proportion of IYOP , SMOP and SYOP is 88%, 45% and 42%.

**Table 10.** Area under oil palm seeds in different regions

| (Mha) | Southeast Asia and Oceania | South Asia | Africa | America |
|---|---|---|---|---|
| Industrial mature oil palm | 2043.80 | 1.90 | 670.60 | 42.41 |
| Industrial young oil palm | 1528.10 | | 45.40 | 15.42 |
| Smallholder mature oil palm | 1397.50 | 130.60 | 871.70 | 70.93 |
| Smallholder young oil palm | 449.30 | | 397.30 | 20.07 |

### *3.3Global oil palm subclasses accuracy and analysis*

The producer accuracy (PA) and user accuracy (UA) for IMOP , IYOP, and SMOP are currently above 70%, while the PA and UA for SYOP are lower, which is in between 65% and 70%. Compared to the 2019 Descals et al. with IMOP and SMOP only mapping study, the classification accuracy is lower but the oil palm subclasses are more refined. Table 2 shows the global classification accuracy of the oil palm subclasses.

**Table 2.** Classification accuracy of global oil palm subcategories

| | Industrial mature oil palm | Industrial young oil palm | Smallholder mature oil palm | Smallholder young oil palm |
|---|---|---|---|---|
| PA(%) | 74.0 | 74.0 | 75.0 | 66.0 |
| UA(%) | 72.0 | 70.0 | 77.0 | 68.0 |

## 4. SUMMARY

In this study, we produce a global oil palm subclasses spatial distribution dataset for 2020 using an image-oriented classification approach with high-resolution Planet& NICFI (4.77m), Sentinel-2 optical remote sensing data and Sentinel-1 radar data, and propose a global oil palm subclass spatial distribution determination method. Compared to Descals et al.'s study, which added open canopy oil palm subclasses to the global mapping of oil palm subclasses; our study has a slightly lower taxonomic precision but a higher spatial resolution.Overall classification accuracy of 79.86% for forests, other categories (grassland, bare land, other agricultural land), and four categories of oil palm. This product will provide data to support the assessment of the environmental and social impacts of oil palm expansion, particularly in terms of deforestation and local regional climate change.

## References


[1]Cheng, Y., et al. (2018). "Towards global oil palm plantation mapping using remote-sensing data." International Journal of Remote Sensing **39**(18): 5891-5906.

[2]Danylo, O., et al. (2021). "A map of the extent and year of detection of oil palm plantations in Indonesia, Malaysia and Thailand." Sci Data **8**(1): 96.

[3]Descals, A., et al.(2021)."High-resolution global map of smallholder and industrial closed-canopy oil palm plantations."Earth System Science Data **13**(3):1211-1231.

[4]Kaplan, G., et al. (2021). "Normalizing the Local Incidence Angle in Sentinel-1 Imagery to Improve Leaf Area Index, Vegetation Height, and Crop Coefficient Estimations." Land **10**(7).

[5]Kustiyo, et al. (2021). "Speckle noise reduction of Sentinel-1 SAR data using fast fourier transform temporal filtering to monitor paddy field area." IOP Conference Series: Earth and Environmental Science **739**(1).

[6]Maskell, G., et al. (2021). "Integration of Sentinel optical and radar data for mapping smallholder coffee production systems in Vietnam." Remote Sensing of Environment **266**.

# Spatial-temporal variation and attribution of salinization in the Yellow River Basin

HONG Mengmeng[1,2], WANG Juanle [2]

[1] Shandong University of Technology, Zibo, China
email: hongmm@lreis.ac.cn

[2] Institute of Geographic Sciences and Natural Resources Research, Chinese
email: wangjl@igsnrr.ac.cn

## 1. INTRODUCTION

Soil salinization is a manifestation of land degradation, which mainly refers to the phenomenon or process of the accumulation of soluble salt in the soil surface, and is sometimes called salinization[1]. The occurrence of soil salinization will lead to the reduction of crop yield and even the death of crop, seriously restricting the development of agriculture [2]. The Yellow River basin as an important food reserves in our country, its ability to land use, crop yields important significance for national food safety, responded to an appeal by the state and improve local salinization land, promote the protection and restoration of the Yellow River as a whole and environmental governance, strive to build a development area in the Yellow River basin ecological protection and high quality is necessary. To carry out SDG15.3 land degradation research and use big data to analyze and excavate the spatial-temporal distribution and change of salinization in the Yellow River Basin is of great significance for the high-quality and sustainable development of the Yellow River Basin.

## 2. MATERIALS AND METHODS

### *2.1 Materials*

In this study, Landsat8_OLI (Operational Land Imager) time series image data with a spatial resolution of 30 meters in 2015 and 2020 were used in the Yellow River Basin, and the data were downloaded by GEE. The field observation data used for accuracy verification included 15 samples in 2015 and 40 samples in 2020. The sample data includes longitude, latitude, conductivity (EC), salt content and PH value of the sampling site. Based on GEE high-resolution images, 145 sample data were selected for accuracy verification according to the texture characteristics of salinization.

### *2.2 Methods*

1 Selection of inversion parameters

The indices that have influence on the inversion model of salt spatial distribution mainly include surface Albedo, vegetation cover index, salt index and iron oxide content.

Albedo refers to the ability of objects on the earth's surface to reflect solar radiation. The surface Albedo varies greatly with different spectral characteristics. As the salinization level changes, the surface texture will change and the surface reflectance will be different. Therefore, Albedo is one of the indicators to measure the salinization level, and its formula is as follows:

$$Albedo = 0.356B + 0.13R + 0.373NIR + 0.085SR1 + 0.072SR2 - 0.0018 \tag{1}$$

Where, B, R, NIR, SR1 and SR2 correspond to the reflectance values of blue wave band, red band, near infrared band, short infrared band 1 and short infrared band 2 of Landsat8 OLI multi-spectral images respectively.

Salt index reflects the spectral reflectance of salt crust on soil surface and plays an important role in measuring soil salinization. In this paper, SI, SI2 and SI3 salt indices are selected for analysis, and their formulas are as follows:

$$SI = \sqrt{B * R} \tag{2}$$

Where, B, R and G correspond to the reflectance values of blue band, red band and green band of Landsat8 OLI multispectral images respectively.

NDVI reflects the vegetation coverage. Different salinization levels lead to different vegetation growth on the surface, so THE VALUE of NDVI will have corresponding deviation.

$$NDVI = (NIR - R) / (NIR + R) \tag{3}$$

Where, NIR and R correspond to reflectance values of near-infrared band and red band of Landsat8 OLI multispectral images respectively.

2 Construction of feature space

NDVI, Albedo and SI pixel information in the study area were selected to construct three-dimensional feature space. Based on the trend of pixels, the fitting function of feature space was obtained, and the trend of pixels was shown in the figure:

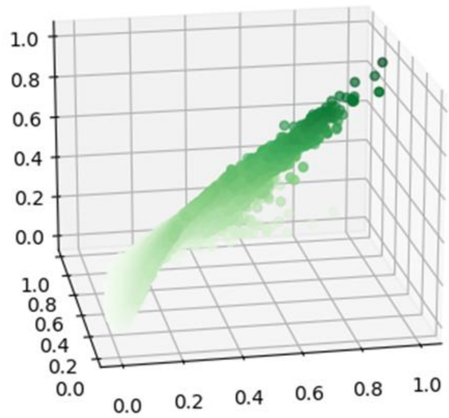


Fig. 1 Construction of feature space

Based on this, the feature space is constructed as follows:

$$ASN = \sqrt{(Albedo\text{-}1)^2 + (SI - 1)^2 + NDVI^2} \tag{3}$$

## 3. RESULTS

The results showed that the salinization area of the Yellow River basin decreased from 2015 to 2020. Saline soil and severe salinization are mainly distributed in the Yellow River Delta and Hetao area, while mild salinization is mainly distributed in the middle and upper reaches of the Yellow River and Shanxi Province, and there are some moderate salinization areas in the upper reaches of the Yellow River.

## 4. SUMMARY

Based on GEE data platform and Landsat 8 OLI multispectral data, this case dynamically detected the salinization change of the Yellow River Basin from 2015 to 2020 using the characteristic space model. It found that the salinization area in the study area decreased and the degree of salinization also showed a slightly decreased trend. The reasons include reasonable environmental management and agricultural production measures.

## References

[1 ]Bian, L, Wang, J, Liu, J, Han, B. M (2021). Spatiotemporal Changes of Soil Salinization in the Yellow River Delta of China from 2015 to 2019. Sustainability , 13, 822. DOI:https://doi.org/10.3390/su13020822

[2]Yuan G X, Chen D ,Xv Y Y et al. (2022). Review on extraction methods of soil salinization information. Journal of North China University of Water Resources and Electric Power，43，02，95101. DOI:10.19760/j.ncwu.zk.2022027.

# Spatial-Temporal Dynamic Pattern and Driving Mechanism of Desertification in the Selenga River Basin of Mongolia from 1990-2020

XU Shuxing[1], WANG Juanle [2],

State Key Laboratory of Resources and Environmental Information System, Institute of Geographic Sciences and Natural Resources Research, Chinese Academy of Sciences, Beijing 100101, China
email: Xusx@lreis.ac.cn

email: wangjl@igsnrr.ac.cn

## 1. INTRODUCTION

Desertification is one of the most serious eco-environmental and socio-economic problems in the world, endangering human survival and social stability[1,2]. In 2012, UNCCD pointed out that the goal of zero growth in land degradation should be achieved by 2030. In 2015, the United Nations made mitigation, containment and reversal of terrestrial ecosystem degradation as its 15th sustainable development goal (SDG15.3). Mongolia has a fragile ecological environment and serious land degradation, which is a hot spot of global desertification[3]. In 2007, more than 72 percent of Mongolia's land was affected by desertification, the scope of desertification is still expanding, and about 90 per cent of the land area will face the risk of desertification in the future[4]. As one of the three major basins in Mongolia, the Serenge River Basin is the main concentration area of agriculture and animal husbandry in the country. With the rapid growth of livestock and population in the basin, the problem of land degradation and desertification in the region is becoming more and more serious, which seriously restricts the sustainable development of agriculture and animal husbandry in Mongolia.

In recent years, remote sensing provides an important means for monitoring desertification on different temporal and spatial scales[5-10]. the main methods of remote sensing monitoring desertification are visual interpretation, remote sensing image classification and desertification index method. Compared with other methods, the feature space model is supported by strong knowledge of remote sensing mechanism, the method and calculation process are simple, and its result accuracy is high, especially in a certain region, it is most widely used in regular monitoring. However, due to the differences in geographical environment in different regions, it is necessary to select appropriate and accurate feature space construction indexes and methods to extract regular and rapid desertification information.

In this study, based on Landsat images from 1990 to 2020, four typical desertification indexes were obtained by inversion. According to the distribution patterns of pairwise indexes in 2D space, a point-point, point-line nonlinear characteristic space model or linear space model was constructed to establish an optimal feature space model suitable for normalized rapid desertification monitoring in Selenge river basin, and the spatio-temporal dynamic pattern and driving factors of desertification in this region were discussed in detail. The purpose of this paper is to provide scientific data for the sustainable development of animal husbandry in Selenge basin and the whole of Mongolia and to achieve the United Nations Sustainable Development goals (SDGs) in the suppression of land degradation.

## 2. MATERIALS AND METHODS

### *2.1 Study Area*

The Serenge River originates from the northern slope of the Han Gai Mountain in Mongolia, with a total length of 1024 kilometers and a basin area of 447060 square kilometers, accounting for 82% of the area of Lake Baikal. It is the largest tributary of Lake Baikal. This study selects the part of Mongolia, namely the Selenge River Basin, covering the capital Ulaanbaatar and 12 provinces such as the Central Province, Darhan Ula Province and Kusugur Province (Fig.1). The climate in the middle and upper reaches of Selenge basin belongs to mild and humid climate, while the climate in the middle and lower reaches belongs to dry and low temperature climate. The basin is the main agricultural and animal husbandry area in Mongolia. More than 60% of Mongolian agricultural products are produced in the Selenge River basin, and by 2020, the livestock volume in this basin will account for 58% of the country's total livestock in 2020. The Serenge River Basin is the main population gathering area of Mongolia, which accounts for about 79% of the total population of Mongolia.

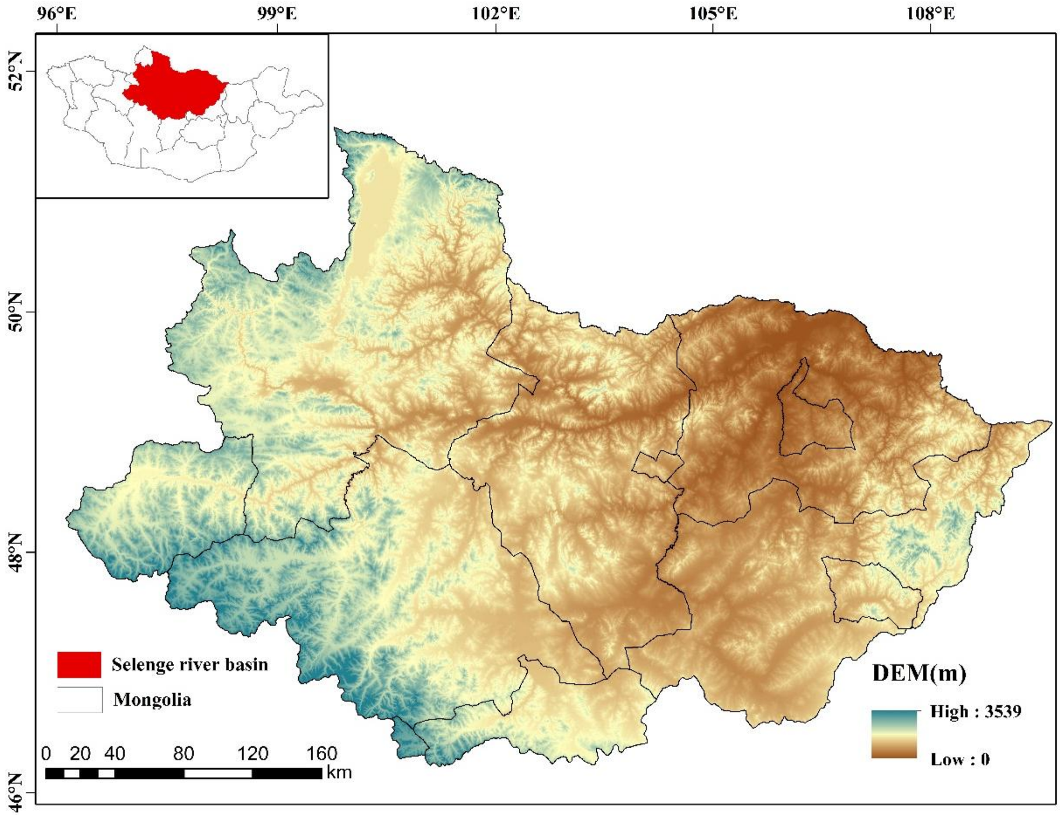


Fig.1 Geographic location of the study area

### *2.2 Data Sources*

In this study, Landsat images of 1990, 1995, 2000, 2005, 2010, 2015 and 2020 with 30 m spatial resolution were used to analyze the desertification information recognition and spatial pattern change of Selenge River Basin in Mongolia from June to September. The Landsat data are all from GEE platform, and the image pre-processing such as cloud removal, mosaic and cropping are completed on GEE platform, and seven periods of cloud-free high-quality images covering the whole Selenge River Basin in Mongolia are obtained.

In the feature space model, water bodies and urban construction areas will be mistakenly divided into desertification areas, so the global surface water data set [11] and artificial opaque water surface data set [12] of the Joint Research Center are used to eliminate water bodies and urban construction areas respectively.

The measured data of 128 outfield points in Mongolia and Google Earth online map obtained in 2015 are used to verify the accuracy of desertification recognition results, including longitude and latitude. Vegetation coverage, surface albedo and topsoil grain size data.

### *1.3 Feature Space Model*

In this study, normalized vegetation index, improved soil regulated vegetation index, surface albedo and surface soil grain size index were selected as the characteristic spatial index of desertification inversion in Selenge river basin, and each characteristic spatial index was calculated based on GEE platform. The calculation formula is as shown in (1)-(4):

$$\mathrm{NDVI} = (\mathrm{B_{NIR}} - \mathrm{B_{RED}})/(\mathrm{B_{NIR}} + \mathrm{B_{RED}}) \quad (1)$$

$$MSAVI = (2B_{NIR} + 1 - \sqrt{(2B_{NIR} + 1)^2 - 8(B_{NIR} - B_{RED})})/2 \tag{2}$$

$$TGSI = (B_{RED} - B_{BLUE})/(B_{RED} + B_{BLUE} + B_{GREEN}) \tag{3}$$

$$Albedo = 0.356B_{BLUE}+0.13B_{RED}+0.373B_{NIR}+0.085B_{SWIR1}+0.072B_{SWIR2}-0.0018 \tag{4}$$

$B_{nir}$、$B_{RED}$、$B_{BLUE}$、$B_{GREEN}$、$B_{SWIR1}$、$B_{SWIR2}$ refer to the surface reflectivity of near infrared band, red band, blue band, green band and shortwave infrared band, respectively.

According to the four typical desertification indexes of NDVI, MSAVI, Albedo, TGSI, five desertification inversion characteristic spaces are constructed by using ENVI 5.2 two-dimensional scatter map tool (Fig.2). According to the distribution patterns of typical desertification indexes in the feature space, the desertification index inversion methods divided in point-point, point-to-line and vertical direction are selected respectively.

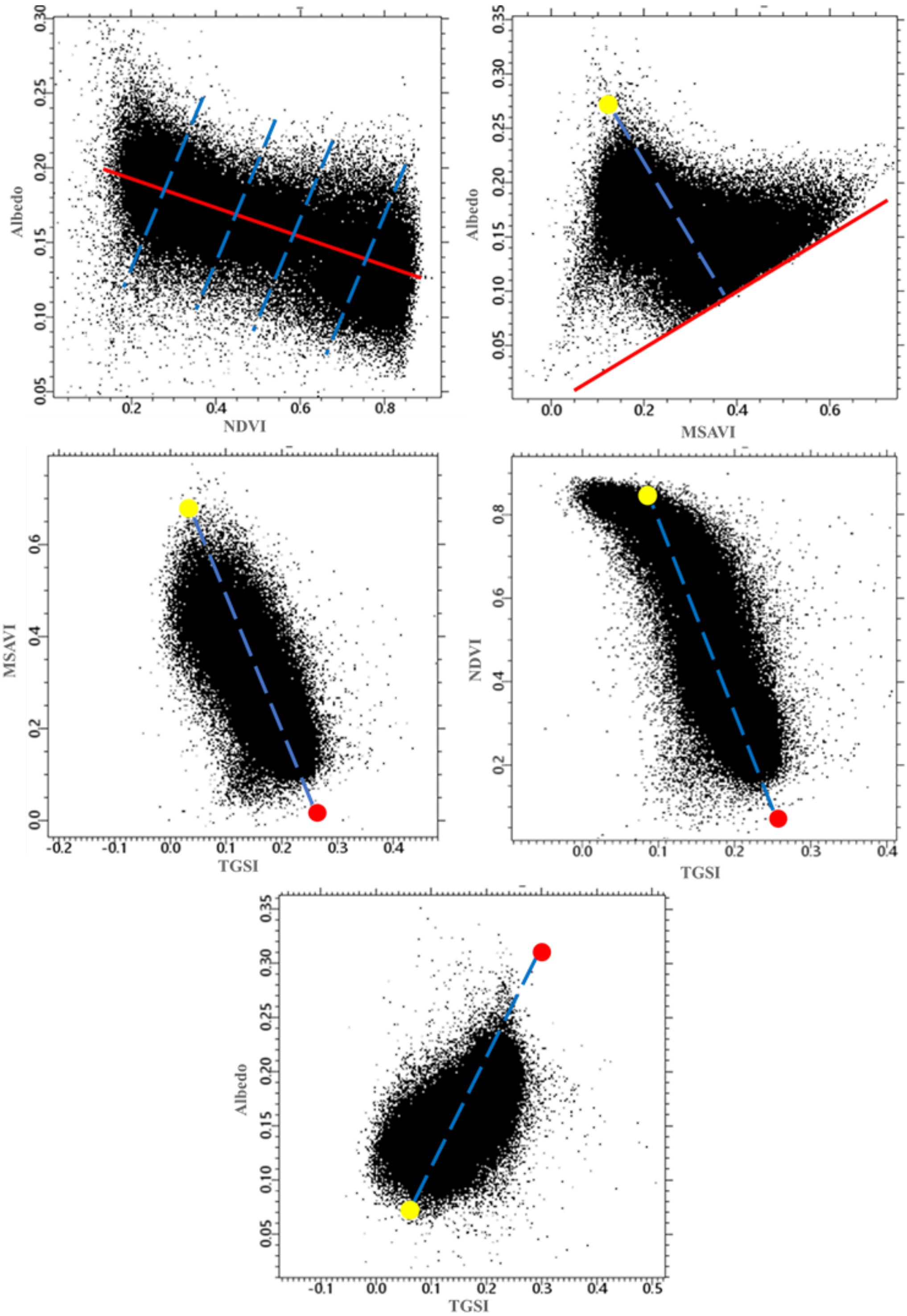


Fig.2 Feature Space

## 3. RESULTS

Fig.3 depicts the spatial distribution of different degrees of desertification in different periods. Extremely severe and severe desertification are mainly distributed in the central province in the southeast of Selenge basin and some areas of Ulaanbaatar, and show a trend of expanding to the middle and northwest as a whole. Moderate and mild desertification is mainly distributed in the northern grassland and southwestern regions. The non-desertification areas are mainly distributed in the forest areas of the north and northeast, and there is no obvious large-scale land desertification. At the same time, from 1990 to 2005, the severity of land desertification in the southeast and northwest increased rapidly, and the extremely severe desertification began to change from sporadic distribution to flaky continuous distribution. and from 2005 to 2015, the land with mild and moderate desertification was further transformed into land with severe and severe desertification, and from 2015 to 2020, the degree of desertification was alleviated in the northern grassland region and the central region. However, the situation of desertification in the southeast is still grim.

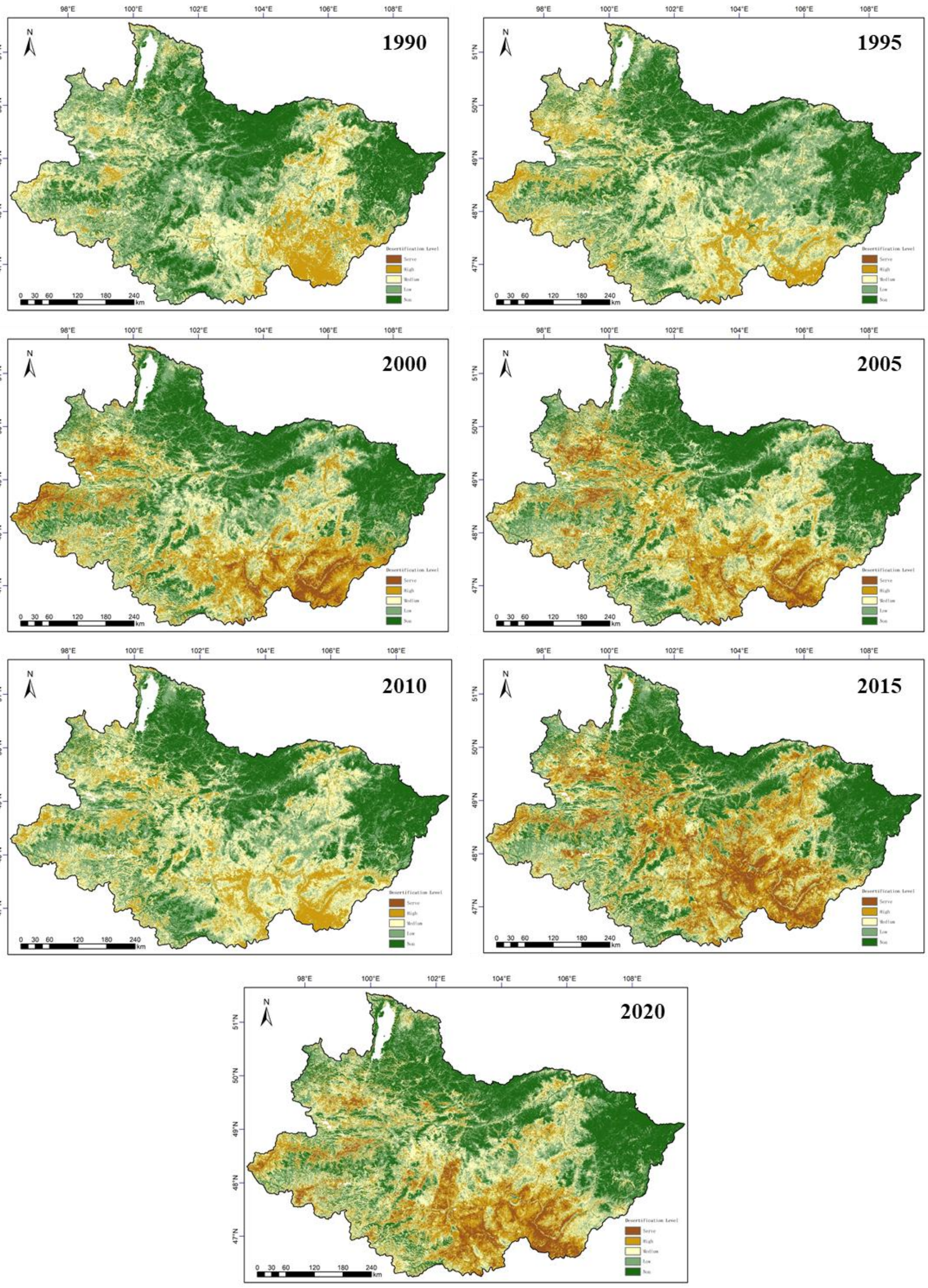


Fig.3 Temporal-Spatial Distribution of Desertification in Selenge River Basin of Mongolia from 1990 to 2020

## 4. SUMMARY

Extremely severe and severe desertification are mainly distributed in the central province in the southeast of Selenge basin and some areas of Ulaanbaatar, and show a trend of expanding to the middle and northwest as a whole. Moderate and mild desertification is mainly distributed in the northern grassland and southwestern regions. The non-desertification areas are mainly distributed in the forest areas of the north and northeast, and there is no obvious large-scale land desertification.

## References


[1] Wang Xinyuan, Yang Xiaopeng, Chen Xiangshun, Li Yulin, qu Hao, Peng Wen. Construction of desertification monitoring index system-- A case study of Gansu Province [J]. Ecological economy, 2016. 32 (7): 174-177.

[2] Oh K, Jeong Y, Lee D, et al. Determining development density using the urban carrying capacity assessment system[J]. Landscape and urban planning, 2005, 73(1): 1-15.

[3] Collado A D, Chuvieco E, Camarasa A. Satellite remote sensing analysis to monitor desertification processes in the crop-rangeland boundary of Argentina[J]. Journal of Arid Environments, 2002, 52(1): 121-133.

[4] Wang Tao, Zhu Zhenda. Some problems in the study of desertification in China-- 1. The concept and connotation of desertification [J]. China Desert, 2003 (03): 3-8.

[5] Eckert S , F Hüsler, Liniger H , et al. Trend analysis of MODIS NDVI time series for detecting land degradation and regeneration in Mongolia[J]. Journal of Arid Environments, 2015, 113:16-28.

[6] Dorj, O., Enkhbold, M., Lkhamyanjin, S., Mijiddorj, K.h., Nosmoo, A., Puntsagnamil, M.,Sainjargal, U., 2013. Mongolia: country features, the main causes of desertification and remediation efforts. In: Heshmati, G.A., Squires, V.R. (Eds.), Combating desertification in Asia, Africa and the Middle East: Proven Practices. Springer,Netherlands, Dordrecht, pp. 217–229.

[7] Current Status of Desertification in Mongolia; Research Center on Desertification, Institute of Ecological eography, Mongolian Academy of Sciences: Ulaanbaatar, Mongolia, 2007.

[8] Xue Z,Qin Z,Li H,et al.Evaluation of aeolian desertification from 1975 to 2010 and its causes in northwest Shanxi Province,China[J].Global&Planetary Change,2013, 107(7094):102-108.

[9] Wei Huidong, Xu Xianying, Ding Feng, et al. Dynamic monitoring of land desertification in Minqin oasis. Resources and Environment in Arid areas, 2007. 21( 10) : 12 − 17.

[10] Duan, H., Wang, T., Xue, X., Yan, C., 2019. Dynamic monitoring of Aeolian desertification based on multiple indicators in Horqin Sandy Land, China. Sci. Total Environ. 650, 2374–2388.

[11] Ajaj QM，Pradhan B，Noori AM，et al． Spatial monito-ring of desertification extent in western Iraq using Landsat images and GIS． Land Degradation ＆ Development，2017，28: 2418 − 2431.

[12] Pan Xia, Gao Yong, Wang Ji. Study on Land Desertification inversion in Alashan League based on Normalized vegetation Index [J]. Soil Bulletin, 2018. 49 (05): 1024-1033.

# Dynamic attribution and coping strategies of sandstorms in the Mongolian Plateau

Yu Zhang[1,2], Juanle Wang [2]

[1] College of Geoscience and Surveying Engineering, China University of Mining & Technology,

Beijing 100083, China;
email:yzhang@lreis.ac.cn

[2] State Key Laboratory of Resources and Environmental Information System, Institute of Geographic Sciences and Natural Resources Research, Chinese Academy of Sciences, Beijing 100101, China

## 1. INTRODUCTION

Mongolia is a close neighbor in northern China. The resources, environment and ecological problems of the Mongolian plateau are closely related to the ecological barrier in northern China. General Secretary Xi Jinping has stressed that the country's efforts to build an important ecological security barrier in the north.Mongolia jointly announced that China and Mongolia should strengthen cooperation in the ecological environment and desertification control[1], jointly tackle global climate change, and create a clean and beautiful ecological environment. Sandstorms raging, land degradation, desertification and other ecological and environmental problems restrict the sustainable development of this region.

Satellite remote sensing has become the most important means of monitoring sandstorms. Many scholars use the MODIS data of Terra and Aqua satellites, the AVHRR data of NOAA satellite, Fengyun satellite data and Himawari-8 satellite data to carry out qualitative and quantitative remote sensing research on dust weather.In the study of sandstorms in Mongolia Plateau, using the data of western Inner Mongolia meteorological station to study the spatial and temporal law of sandstorm, believe that the lower surface soil humidity is one of the important elements of the surface coverage type on sandstorms (1980-2000)[2]. Some scholars also used the data of the sandstorm observation station in the area of China-Mongolia border (1980-2014) to find that the Inner Mongolia sandstorm was mainly affected by southern Mongolia.It can be seen that in the research of Mongolian Plateau sandstorm, Mongolia and Inner Mongolia lack recent research sequence before 2000, and multiple data support (remote sensing, station, text, etc.)[3].It is difficult to reveal the spatial and temporal characteristics and change trend of the Mongolian plateau sandstorm on the macroscopic scale. This study mainly adopts the big data analysis method combining multi-source remote sensing and historical data. Based on the multi-source earth big data, we analyzed the spatial and temporal distribution characteristics, attribution and response strategies of the 21-year sandstorm in 2000-2021.

## 2. MATERIALS AND METHODS

In the present study, Mainly based on the MODIS LIB data, Using the relevant inversion dust model, Revert dust information year by year; Based on the Landsat TM data[4], Sortified land was extracted using the SEI model, The dynamic distribution of sandstorms in 21 years from 2000 to 2021 is obtained; Combining text mining data, station records, inversion data, To verify the results of the remote sensing interpretation, Analysis of spatial and temporal distribution of 2000-2021 Mongolian Plateau; Combining the local Mongolian plateau subcushion ecosystem data (such as land cover data) [5]and social media data (policies, news, etc.), To analyze the dust storm attribution, And give the relevant coping strategies.

### *2.1 Methods*

Visual interpretation: True color synthesis (B4, B3, B1); three-channel color synthesis histogram equilibrium enhancement method: (B7-B2-B1); (B1-B2-B20);

Domain value method: Normalized Difference Dust Index (NDDI): NDDI = (R7-R3) / (R7 + R3), The reference domain value is: dust image NDDI> 0.28; Thermal Infrared Dust Index (TDI):TDI=-

7.937+0.1227BT20+0.0260BT30-0.7068BT31+0.5883BT32; The reference threshold is: dust image TDI> 1; Brightness Temperature Difference(BTD):BTD=B31-B32; The reference threshold is: BTD<0.

No threshold method: Dust storm detection index (DSDI):

$$DSDI = \left\{ [(BT_{22} + BT_{34}) - (BT_{30} + BT_{31})] \times \left( \frac{R_4 - R_3}{R_{26}} \right) \right\} - b31_{emis}$$

For all dust pixels, the DSDI is> 0

## 3. RESULTS

### 3.1 DUST EXTRACTION RESULTS

The results show that, In the image of the 431-band combination in the visual interpretation method, Yellow-brown with feather texture for dust; In the 1,2, and 20-band combination, Blue and white with feather texture for dust; In the 7,2, and 1-band combinations, Dark reddish-brown with feather grain texture for dust; In the threshold method, The NDDI does not completely separate the dust area from the land surface; TDI cannot effectively separate dust storms from clouds in the study area; The extraction effect of the BTD method is relatively ideal; But these algorithms require to apply different thresholds for each event, To separate the dust feathers from the MODIS satellite images; yet, In most cases, These thresholds are different from the suggested values given by the algorithm provider. The results of the no-threshold method show that, by comparing with the original images, almost all dust images are extracted, and all dust image values are greater than 0, which effectively reduces the problem that other algorithms need to adjust the threshold value. However, its accuracy still needs further verification and analysis.

### *3.2 land useresults*

#### *3.2..1 Barren*

The barren area of the Mongolian Plateau is widely distributed throughout the Gobi region in central and western Mongolia. This region has severe weather conditions including very little precipitation, an extremely arid climate, and strong winds. In addition, it is a sandy area with sparse vegetation (Figure 11). The barren land area increased between 2000 and 2010 and decreased during other study periods, as shown in Figure 3h. The rate of increase was 1.30% from 2000 to 2010, and the greatest rate of increase occurred from 2010 to 2015, reaching 1.93%. Compared to 1990, barren land decreased by 109,517.53 km2 by 2020. The observed average rate of change over 30 years was −0.45%.

#### *3.2..1 Sand*

The sand areas on the Mongolian Plateau are concentrated in western Inner Mongolia and western Mongolia. These sand areas are distributed among the Badan Jaran, Tengger, and Ulan Bu deserts. Additional sand areas were also located within the Zabu Khan Province and the Gobi region in Mongolia (Figure 12). The total sand area increased between 1990 and 2020 (Figure 3i). The increase rate varied for each decade. The largest increase occurred from 2010 to 2015, when it reached 0.61%. Compared to 1990, the sand area increased by 11,488.36 km2 by 2020. The average observed rate of change over the past 30 years was 0.17%.

## References

[1].Buren, G. Research on the Status, Causes of Desertification and the Prospect of Grassland Animal Husbandry in Mongolia. Master's Thesis, Inner Mongolia University, Hohhot, China, 2011.

[2].Wang, Y.X. Empirical Study on Grassland Resource Degradation and Its Influencing Factors in Inner Mongolia.Master's Thesis. Inner Mongolia Agricultural University, 2010.

[3].Wei, Y.Q.; Li, X.; Gao, F.; Huang, C.L.; Song, X.Y.; Wang, B.; Ma, H.Q.; Wang, P.L. The United Nations 2030 Sustainable Development Goals Framework and the China Response Strategy. Earth Prog. 2018, 33, 1084–1093.

[4].Oyungerel, A. Sustainable Development of Animal Husbandry in Mongolia. Master's Thesis,Chinese Academy of Agricultural Sciences, Beijing, China, 2018.

[5].Yang, I. Research on Sustainable Animal Husbandry Development in Inner Mongolia. Master's Thesiss, Chinese Academy of Agricultural Sciences, Beijing, China, 2010.

# Estimating Fractional Cover of Photosynthetic and Non-photosynthetic Vegetation in the Arid and Semi-arid Areas of China

Cuicui JI[1], Xiaosong LI[2], Zhihai GAO[3], Xuemei YANG[4], Jianping PAN[1], Maolin Chen[1]

[1] School of Civil Engineering, Chongqing Jiaotong University, China
email:cuicuiji@whu.edu.cn; email:pjplj@126.com

[2] Key Laboratory of Digital Earth Science, Institute of Remote Sensing and Digital Earth, Chinese Academy of Sciences , China;email: lixs@radi.ac.cn

[3] Institute of Forest Resource Information Techniques, Chinese Academy of Forestry, China; email: zhgao@ifrit.ac.cn

[4] State Key Laboratory Breeding Base of Desertification and Aeolian Sand Disaster Combating, Gansu Desert Control Research Institute, Lanzhou, China;email: yxm9693@163.com

## 1. INTRODUCTION

Arid regions occupy over 30% of the global land surface, and desertification is especially severe in arid and semiarid zones, affecting more than two billion people. In arid regions, degradation of natural vegetation is a serious issue since it causes wind augmentation and sand invasion, and greatly endangers the ecological environment. Photosynthetic vegetation (PV) is defined as plant material including chlorophyll (e.g., green leaves and flowers), which is a significant plant factor in arid and semiarid regions. Non-photosynthetic vegetation (NPV) is plant material lacking chlorophyll (e.g., senescent plants, branches, and plant stubble), and it occupies a significant part of natural vegetation in arid and semiarid regions [1; 2]. PV and NPV are not only important indicators for changes of the ecological environment, but are also essential elements in surveying vegetation status and researching carbon storage in arid regions [3]. Therefore, acquiring fractional cover of PV ($f_{PV}$) and NPV ($f_{NPV}$) data synchronicity and quantification is very significant for vegetation productivity and the monitoring of desertification. It also provides important factors for different ecological and hydrological models (Fig.1).

**Fig. 1** Photosynthetic vegetation and Non-photosynthetic vegetation.

## 2. MATERIALS AND METHODS

### *2.1. Fractional-Cover Field Measurement*

There were 81 surveyed fractional-cover sites with field measurements in August 2017 in arid and semi-arid region (Fig. 2). The central position of each field site was recorded by Global Positioning System (GPS) with a WGS84 coordinate system. Following Guerschman, and Muir et al. [4; 5], for natural or pastoral vegetation communities, field measurements use three 30 m measuring tapes cross-distributed in a hexagonal shape at intervals of 60 degrees from the midpoint (Fig.3). For artificial vegetation in parallel rows, two 30 m tapes, orienting at 45 degrees and crossing the sowing lines, were used. The observer recorded the type of material at each meter, including the amount of green leaves, cryptogams, dry leaves, and different kinds of bare soil, such as crust and rocks. If there was middle (shrub)- and/or upper-layer (tree) vegetation, it recorded top-layer coverage by looking up the meter point. The cover percentage was calculated by dividing the count for a special type by the total count (90 or 60).

When records included plants with leaves still attached, the operator evaluated if it was photosynthetic vegetation on the basis of its colorings.

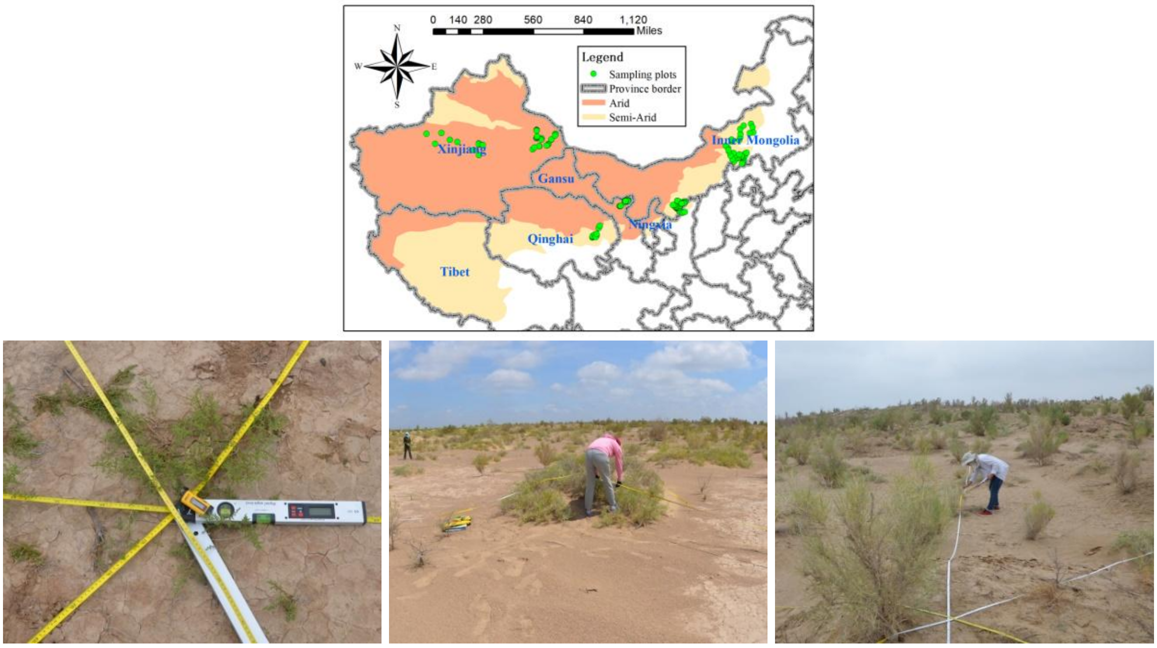


(a) (b) (c)

**Fig.2** Field observations. (a) Recordi ng central location by Global Positioning System (GPS); (b,c) field measurements of vegetation fractional cover.

### *2.2. Endmember Collection, Processing, and Selection*

All endmember spectra were acquired by a portable Analytic Spectral Device (ASD; Boulder, CO) spectroradiometer on 3–9 August 2016 in the field. A variety of PV, NPV, BS, and shadow endmember reflectance spectral measurements were acquired in full range (350–2500 nm). In this way, we built the pure endmember spectral library from each field as shown in Fig. 4. In view of endmember applicability and representativeness, it was required that the number of each endmember spectrum was no less than 10. A total of 84 reflectance spectra were collected, varying by 65 types of PV, 12 types of NPV, 10 types of bare soil, and 2 types of shadow.

## 3. RESULTS

### *3.1. Spectral Characteristics*

The spectra of different types of materials, including PV/NPV/BS/shadow endmembers, were collected by field-spectrum measurements in order to estimate $f_{PV}$ and $f_{NPV}$. Bands severely affected by water vapor were abandoned, and the spectral ranges of 350–1350, 1450–1750, and 2000–2350 nm were kept. All endmember spectra were convolved to Landsat 8 OLI bands. The average spectral value of each endmember was taken as the adopted PV/NPV/BS/shadow spectra by way of removing the effect of endmember variability concerning temporal and spatial data (Fig. 7). According to characteristics of the average PV–NPV–BS–shadow spectral curves (Fig. 8) corresponding to bands of the Landsat 8 OLI satellites.

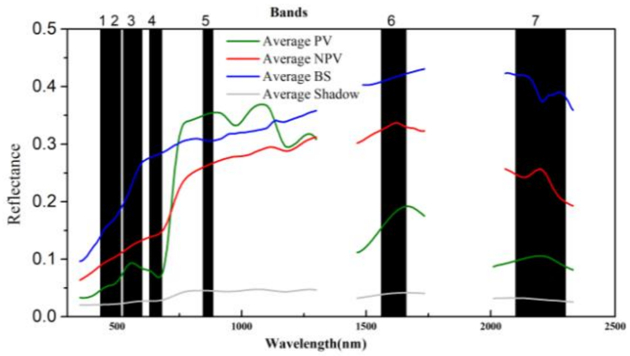


**Fig.3** Average reflectance of selected PV, NPV, BS, and shadow endmembers, and band position of Landsat 8 OLI sensor.

Fig.3 describes endmember spectra's spatial changeability. The spectral curve of healthy PV always shows characteristics of "peak and valley", the visible domain valley (blue and red at 450 and 670 nm) was mainly caused by the strong absorption of chlorophyll, and they were perceptibly different than the spectral characteristics of PV endmembers in the spectral-domain range of 750–1250 nm. Throughout the entire spectral curve, PV displayed noticeable disparities between red and near-infrared, but NPV and BS did not. Therefore, PV could be distinguished from NPV and BS. There were clear absorption features near shortwave infrared 2100 nm for NPV, mainly due to nonstructural components such as cellulose, hemicellulose, and lignin, but did not have such absorption characteristics for BS and PV. Because there was significantly different chlorophyll content for PV and NPV, PV and NPV could be distinguished according to the red edge position. Due to the influence of NPV type, humidity, and decomposition degree, the reflectance of the VIS–NIR spectral NPV may have been higher or lower than BS. Consequently, it was difficult to make a distinction between NPV and BS. Regardless of difficulty, the spectral characteristic of the NPV in 500–900 nm and around 2100 nm was significantly distinct from BS. A bow-shaped protuberance was shown in the 500–900 nm spectral range for BS [6]. The non-cellulose element of NPV resulted in spectral-absorption features at about 2100 nm [7]. Therefore, according to the unique characteristics of each endmember, endmember spectra within the specific spectral range could effectively distinguish between PV, NPV, and BS. Shadow reflectance was almost nonexistent and consistent throughout the whole spectral curve (Fig. 8), so shadows indicated noticeable variances with the three other endmembers.

### *4.2. Estimated Endmember fractions Accuracy Evaluation*

PV–NPV–BS–shadow endmembers were adopted for Landsat 8 OLI images on August 2017 to estimate $f_{PV}$ and $f_{NPV}$ with LSMM and AUTOMCU. The PV and NPV fractional cover map in the arid and semi-arid areas of China, produced have an overall accuracy of 87.72% and 88.74% for $f_{PV}$ and $f_{NPV}$ estimation, and $R^2$ were 0.83 and 0.62, respectively in the scatterplots. The model unmixing RMSE was 0.0101 for the surveyed sample in the study area.

The model unmixing RMSE was 0.0101 for the surveyed sample in the study area. It illustrated the endmember fraction map and unmixing RMSE map produced by Landsat-8 SR images in 2017. The meridional results (Fig. 10(a)) illustrate that there are two peak intervals for NPV fractional cover: 110°–120°E (east of china) and 106°–113°E (southeastern of China). The two peak values in the meridional direction are located in the northeastern of China. The zonal results illustrate that there is one peak intervals for NPV fractional cover: 23°–27°N, located in the southeastern of China. The nadir values for PV fractional cover are located in 103°E and 25°N in the meridional and zonal directions, respectively, while there are three peak intervals for PV fractional cover in the meridional direction:72-75°E, 97-102°E, 120°E. The PV and NPV fractional cover are complementary. The unmixing RMSE map (Fig. 10(b)) show the maximum RMSE in the middle area of the arid region for the low PV and NPV cover with sandy.

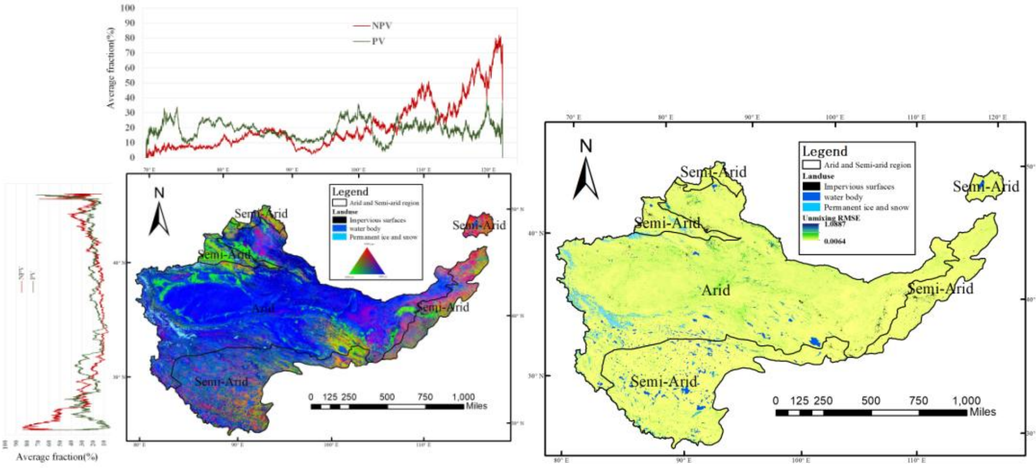


**(a)** **(b)**

**Fig.4** (a)Endmember fraction map with the meridional and zonal average $f_{\mathrm{PV}}$ and $f_{\mathrm{NPV}}$ in 2017, and (b)unmixing RMSE map based on Landsat-8 with six bands and 30 m spatial resolution by LSMM.

Taking all landcover class area except impervious surfaces, water body and permanent ice and snow in arid and semiarid region, the mean fractional cover are 16.16% and 18.85% for PV and NPV in 2017(Fig. 4). The PV fractional cover is less than 35% in the 80% of arid and semiarid area, while the NPV fractional cover is less than 33% in the 80% of study area. This indicates a qualitative agreement with the characteristics of vegetation in arid and semiarid area. And the NPV fractional cover is significantly lower than the PV fractional cover.

Above all, PV–NPV–BS–shadow endmembers were adopted for Landsat-8 sensor by LSMM with AUTOMCU and FCLS unmixing algorithm based on GEE cloud compute platform to produce PV and NPV fractional cover in the arid and semiarid area of China, which is feasible. The results illustrate that the PV and NPV fractional cover increased obviously in the past 8 years in arid and semi-arid areas of China, but the fNPV increased more significantly than fPV. In the process of ecological construction from 2013 to 2020, the NPV degradation became more and more serious following PV fractional cover increased.

## 4. SUMMARY

Based on the field spectra, and satellite data, we analyzed the performance of Landsat8 OLI sensors for the estimation of PV, NPV, and BS fractions in arid and semi-arid regions by the LSMM and AUTOMCU. Our conclusions are summarized as follows: (1)the results indicate that the PV and NPV fractional cover map produced by the PV–NPV–BS–shadow endmembers method by LSMM with AUTOMCU and FCLS unmixing algorithm is accurate and suitable for regional or global PV and NPV fractional cover applications.(2) a serial of 30 m PV and NPV fractional cover maps were produced by composited Landsat 8 Operational Land Imager (OLI) datasets of annual maximum NDVI using the GEE platform in arid and semi-arid areas of China.

## References

[1] J.P. Guerschman, M.J. Hill, L.J. Renzullo, D.J. Barrett, A.S. Marks, and E.J. Botha, Estimating fractional cover of photosynthetic vegetation, non-photosynthetic vegetation and bare soil in the Australian tropical savanna region upscaling the EO-1 Hyperion and MODIS sensors. Remote Sensing of Environment 113 (2009) 928-945.

[2] X.S. Li, G.X. Zheng, J.Y. Wang, C.C. Ji, B. Sun, and Z.H. Gao, Comparison of Methods for Estimating Fractional Cover of Photosynthetic and Non-Photosynthetic Vegetation in the Otindag Sandy Land Using GF-1 Wide-Field View Data. Remote Sensing 8 (2016) 800.

[3] J.F. Reynolds, D.M.S. Smith, E.F. Lambin, B. Turner, M. Mortimore, S.P. Batterbury, T.E. Downing, H. Dowlatabadi, R.J. Fernández, and J.E. Herrick, Global desertification: building a science for dryland development. Science 316 (2007) 847-851.

[4] J.P. Guerschman, P.F. Scarth, T.R. Mcvicar, L.J. Renzullo, T.J. Malthus, J.B. Stewart, J.E. Rickards, and R. Trevithick, Assessing the effects of site heterogeneity and soil properties when unmixing photosynthetic vegetation, non-photosynthetic vegetation and bare soil fractions from Landsat and MODIS data. Remote Sensing of Environment 161 (2015) 12-26.

[5] J. Muir, M. Schmidt, D. Tindall, R. Trevithick, P. Scarth, and J.B. Stewart, Field measurement of fractional ground cover:A technical handbook supporting ground cover monitoring for Australia., 2011.

[6] C. Ji, Y. Jia, Z. Gao, H. Wei, and X. Li, Nonlinear spectral mixture effects for photosynthetic/non-photosynthetic vegetation cover estimates of typical desert vegetation in western China. PLoS ONE 12 (2017) 1-22.

[7] T. Li, X.S. Li, and F. Li, Estimating fractional cover of photosynthetic vegetation and non-photosynthetic vegetation in the Xilingol steppe region with EO-1 hyperion data. Acta Ecologica Sinica 35 (2015) 3643-3652.

# Red List Assessment of Chinese Higher Plants

LI Liping [1], QIN Haining [2], ZHAO Lina [2], LIU Qingjie [1],

[1] Aerospace Information Research Institute, Chinese Academy of Sciences, China
email: liliping@aircas.ac.cn

email: liuqj@aircas.ac.cn

[2] Institute of Botany, Chinese Academy of Sciences, China
email: hainingqin@ibcas.ac.cn
email: zhaoln@ibcas.ac.cn

## 1.INTRODUCTION

The International Union for Conservation of Nature (IUCN) Red List of Threatened Species is central in biodiversity conservation [1]. In 1991, Chinese experts finished the *China Plant Red Data Book: Rare and Endangered Plants* [2] which is the first attempt of assessing large amount of plant species status. After this, systematically according to the IUCN method, China has made three assessments. The first assessment preliminarily assessed 4408 species. With 34450 and 39327 species assessed, the second and third assessments fully assessed the almost all higher plants of China. This provided a good opportunity of the comparison of the values of Red List Index (RLI).

## 2.MATERIALS AND METHODS

### *2.1 Data sources*

The assessment result of 2013 was from the released document of Chinese government (http://www.mee.gov.cn/gkml/hbb/bgg/201309/t20130912_260061.htm);

The assessment result of 2020 was mainly from the book [3] and the further research;

The IUCN assessment results of plants distributed in China were searched and downloaded from the website of IUCN (www.iucnredlist.org).

### *2.2 Data analysis*

RLI was mainly calculated according to the recommended method of IUCN [4,5]. Two kinds of assigned weights were used to calculate the RLI, which are equal steps weights and extinction risk weights. The weight values were listed here in Table 1.

**Table 1**. The IUCN Red List and two types of weights

| Status | Equal steps method | Extinction risk method |
|---|---|---|
| Extinct (EX) | 5 | 1 |
| Extinct in the Wild (EW) | 5 | 1 |
| Regional Extinct (RE) | 5 | 1 |
| Critically Endangered (CR) | 4 | 0.5 |
| Endangered (EN) | 3 | 0.05 |
| Vulnerable (VU) | 2 | 0.005 |
| Near Threatened (NT) | 1 | 0.0005 |
| Least Concern (LC) | 0 | 0 |

## 3.RESULTS

### *3.1 The assessment result of 2013 and 2020*

There were 32054 species assessed both in year 2013 and 2020. The species numbers in each status were listed in Table 2.

**Table 2**. The assessment result of 2013 and 2020

| | 2020 | | | Species / Total species (%) | 2013 | | | Species / Total species (%) |
|---|---|---|---|---|---|---|---|---|
| Status | Family | Genus | Species | | Family | Genus | Species | |
| EX | 18 | 20 | 20 | 0.06 | 34 | 47 | 50 | 0.16 |
| CR | 124 | 296 | 543 | 1.69 | 119 | 294 | 552 | 1.72 |
| EN | 182 | 549 | 1225 | 3.82 | 190 | 566 | 1224 | 3.82 |
| VU | 212 | 780 | 1911 | 5.96 | 209 | 748 | 1739 | 5.43 |
| NT | 230 | 901 | 2565 | 8.00 | 201 | 809 | 2549 | 7.95 |
| LC | 391 | 2798 | 22256 | 69.43 | 389 | 2797 | 22121 | 69.01 |
| DD | 250 | 942 | 3534 | 11.03 | 261 | 976 | 3819 | 11.91 |
| Total | 444 | 3376 | 32054 | 100.00 | 444 | 3376 | 32054 | 100.00 |

Note: DD represents Data Deficient; EX here is the combination of EX, EW and RE which all indicate the extinction status of species in different scales.

### *3.2 Red List Index*

Based on the equal steps method, we obtained the result of RLI being 0.9151 and 0.9139 in 2013 and 2020, respectively. This slight decreasing pattern indicates a slight decline in plant diversity in China over the past decades, especially for species not threatened. While with the method of extinction risk which gives relatively higher weights of threatened species, the RLI being 0.9864 and 0.9872 in 2013 and 2020, respectively. This slight increasing pattern shows the efforts of China’s plant conservation reversed the deterioration of species threatened. We suggest that besides the threatened species, attentions should also be given to the common species.

## 4. SUMMARY

Our study systematically analyzed the the last two red list assessments of higher plants in China, compares the threatened status of plants in 2013 and 2020 by using the RLI. This research provides an important scientific basis for the evaluation of SDG15.5.1 in China.

## References


[1] Cazalis V., Marco M., Butchart S., Akakaya H., González-Suárez M., Meyer C., Clausnitzer V., Bhm M., Zizka A., Cardoso P., et al. (2022) Bridging the research-implementation gap in IUCN Red List assessments. Trends in Ecology & Evolution. 37: 359-370.

[2] Fu L, Jin, J. (1991) China Plant Red Data Book: Rare and Endangered Plants Volume 1, Science press, Beijing, 736pp.

[3] Qin H. (2020) Seed Plants of China: Checklist, Uses and Conservation Status. Hebei Science and Technology Publishing House, Shijiazhuang. 4 volumes.

[4] Butchart S., Stattersfield A., Bennun L., Shutes S., Akcakaya H., Baillie J., Stuart S., Hilton-Taylor C., Mace G. (2004) Measuring global trends in the status of biodiversity: Red List Indices for birds. PLOS Biology, 2(12): e383.

[5] Butchart S., Akçakaya H., Chanson J., Baillie J., Collen B., Quader S., Turner W., Amin R., Stuart S., Hilton-Taylor C. (2007) Improvements to the Red List Index. PLOS ONE, 2(1): e140.

**Mining the drivers of forest change in the upper Indus Valley, high Asia region from 1990 to 2020**

Xinrong Yan [1, 2], Juanle Wang [1, 2, 3, 4, *], Xiaotong Liu [5], Hongyu Zhao [6] and Yuxin Wu [1]

1 State Key Laboratory of Resources and Environmental Information System, Institute of Geographic Sciences and Natural Resources Research, Chinese Academy of Sciences, Beijing 100101, China
2 University of Chinese Academy of Sciences, Beijing 100049, China
3 China-Pakistan Earth Science Research Center, Islamabad 45320, Pakistan
4 Jiangsu Center for Collaborative Innovation in Geographical Information Resource Development and Application, Nanjing 210023, China
5 Academy of Inventory and Planning, National Forestry and Grassland Administration, 100714 Beijing, China
6 State Key Laboratory of Earth Surface Processes and Resource Ecology, Beijing Normal University, Beijing 100875, China.
***** Correspondence: wangjl@igsnrr.ac.cn; Tel.: (+86-010-6488-8016) Address: 11A, Datun Road, Chaoyang District, Beijing, 100101, China

**Abstract:** The High Asia region is the water tower for many river valleys in East and South Asia, which has vital significance for regional environmental conservation and ecological security. In the upper Indus Valley, the role of forests is often overlooked, and their loss will lead to a reduction in ecological services, such as water conservation and disaster prevention, and will indirectly affect the water and food security of 230 million people in South Asia. Quantifying the drivers of forest change is a prerequisite for ensuring sustainable development in the upper Indus Valley. This study used forest disturbance and recovery data, history fire data, topographic data, and land use data to construct a decision tree model for mining the of drivers of forest change. Classification of the drivers of forest disturbance and recovery was achieved in the upper Indus Valley. The results showed that (1) disturbance mainly occurred in the central region of the upper Indus Valley, where forest degradation was the main driver accounting for 68.97%, and agricultural transfer was the secondary driver accounting for 21.58%; commercial cultivation and deforestation drivers both disturbed about 4% of the area, and fire, human activities, and natural hazards disturbed only a small area of forest accounting for less than 1%; (2) the spatial distribution of recovery was basically consistent with the disturbance, with natural recovery being the main driver of forest recovery, accounting for 60.08%, and cultivated recovery being the secondary driver, accounting for 39.92%; (3) relevant governance measures or forest conversation policies in the Indus Valley were recommended, such as increasing the supply of non-biomass energy, controlling the scale of livestock, and establishing friendly land use policies, to maintain the growth and balance of forest area and quality.

**Keywords**: Forest Change; disturbance and recovery; driving force; upper Indus Valley, high Asia region

## 1.INTRODUCTION

Forest ecosystems form the natural environmental conditions that sustain human survival and have many important ecological services, including water conservation, soil conservation, carbon sequestration and oxygen release, nutrient accumulation, atmospheric purification, and biodiversity conservation [1]. Forest change includes both dynamic processes of disturbance and recovery due to differences in management policies, the intensity of human activities, and the effects of climate change. Forest disturbances include deforestation and loss, with deforestation being the abrupt transition from a forested to a non-forested state, and forest loss being the loss of parts of forest cover, such as forest degradation, selective logging, and anthropogenic forest management activities. Forest recovery is a reverse process of forest disturbance, a process by which forest cover increases under improved hydrothermal conditions or artificial nurturing.

The upper Indus Valley located in the High Asia region, an important water tower in the Asian and European subcontinents, with diverse and fragile forest ecosystems [2, 3]. The mountain range has created diverse geographies and has given origin to several important rivers. The Indus Valley has the largest continuous irrigation system in the world, and the Indus and its tributaries provide an important water supply within the basin [4]. The instability of the upstream forest ecosystem can lead to frequent flooding of the downstream plains and threaten agricultural production. Upstream forest ecosystem security guarantees downstream water and food security for 230 million people in South Asia. For example, deforestation was one of the major causes of massive floods in Pakistan in 2010 [5]. The disaster destroyed almost all cotton and sugarcane in Punjab and Sindh, reduced rice production by 40 percent, and caused severe losses in wheat production [6]. Forests can effectively prevent soil erosion, sequester carbon, release oxygen, and provide important and stable ecological services for downstream water and energy supply. However, it is worth noting that in these regions, climate change and anthropogenic activities have led to significant changes in the basin forests [2]. Rapid reduction in forest area and frequent disturbances increase the risk of mega-floods in the basin [7]. A clear understanding and knowledge of forest change forms the basis for developing regional sustainable development policies. Previous studies have monitored forest resources in parts of the upper Indus and obtained information on the temporal and spatial distributions of forest change [2, 8]. However, understanding forest change in the upper Indus Valley requires not only discovering the temporal and spatial distribution of forest change, but also quantifying and identifying the causes of forest change in the region, which is central to formulating and adjusting sustainable development strategies. Forest change drivers are diverse and complex, and include multiple types of environmental change and human activities.

Remote sensing technology can monitor forest resources at different scales, and long time-series image data can also be used to obtain temporal and spatial information on forest changes [9, 10]. However, a comprehensive description of forest dynamics requires not only the discovery of spatial and temporal information but also an understanding of the causes of change. In natural-influenced forest change processes, the drivers include natural disasters such as fires or landslides, while in human-influenced change processes, the drivers include human activities such as urban development or inappropriate forest management. Clarifying the factors of forest disturbance and recovery has important implications for forest management; however, it is difficult to identify and describe the specific causes through automated methods from a remote sensing monitoring perspective [11]. Several studies have attempted to map the factors that cause forest disturbance [12-14]. The drivers of forest disturbance and recovery can be classified into manual and semi-automated extraction methods. Manual interpretation is a combination of remote sensing imagery as the data source and human-computer interaction to obtain the driving factors of forest change. There are several disturbance-specific monitoring programs in the United States to assess forest damage caused by fires, pests, and diseases. The Monitoring Trends in Burn Severity (MTBS) project used Landsat data to map the annual fire area and severity in the United States and Alaska from 1984 to the present [15]. The Aerial Detection Survey (ADS) project maps the forest damage caused by pests and diseases [16]. Manual interpretation provides important knowledge for understanding forest changes and enhancing forest management but requires intensive computer work and specialized knowledge of image interpretation. The semi-automated extraction method is based on manual interpretation, incorporating algorithmic models and a prior knowledge to achieve change in driver information extraction. These studies can be classified into two categories: one using attributes such as spectral, texture, and topography of the detected disturbance patches [17, 18], and the other directly derived from a prior knowledge of Landsat spectral-temporal metrics and causal event types [14, 19-21]. The spectral characteristics of pixels or patches affected by perturbations can be obtained from satellite data and combined with other auxiliary data for attribution analysis with classifiers such as random forests and regression trees [22-25]. These methods usually result in high overall classification accuracy (>90%) [22, 23]; however, the perturbation category is usually relatively homogeneous. Huo et al. (2019) established a semi-automatic method for describing high-intensity (50% forest cover loss) forest disturbance driver analysis, using forest change products and Landsat data to obtain training datasets from data sources such as high-resolution imagery, and using a random forest classifier to obtain a map of forest disturbance types in adjacent areas of the United States [26].

Only a few previous studies qualitatively described the causes of forest change in the upper Indus Valley, and most of them described only a single driver of change, lacking global, long time series, and quantitative results of drivers of change. This study focused on the drivers of forest change in the upper Indus Valley, with the main objectives of (1) mapping the drivers of forest disturbance and recovery change and obtaining spatial and temporal perceptions of the distribution of drivers; (2) quantifying the contribution of different drivers to forest disturbance and recovery and analyzing the differences in the drivers of forest change in different administrative regions from the perspective of forest management; and (3) proposing recommendations for sustainable development of the basin. We expect that this study will increase the knowledge and understanding of the drivers of forest change in this ecologically sensitive area of the upper Indus and provide a corresponding knowledge base for regional environmental policy development for forests.

## 2.MATERIALS AND METHODS

### *2.1. Study Area*

The Indus River Basin is located between 24°-37°N and 66°-82°E (Figure 1). It is northeast of the Karakorum Mountains and Himalayas, southeast of the Thar Desert of India, northwest of the Hindu Kush Mountains of Afghanistan, southwest of the Baluchistan Plateau, and south of the Arabian Gulf. The climate of the Indus Valley is subtropical, with obvious monsoonal characteristics; however, due to the influence of the high mountain ranges in the northeast, the climate is usually between dry and semi-dry, tropical, and subtropical. The Indus River is one of the 50 rivers with the highest average annual flow in the world, and includes many important tributaries distributed in China, Afghanistan, Pakistan, and India.

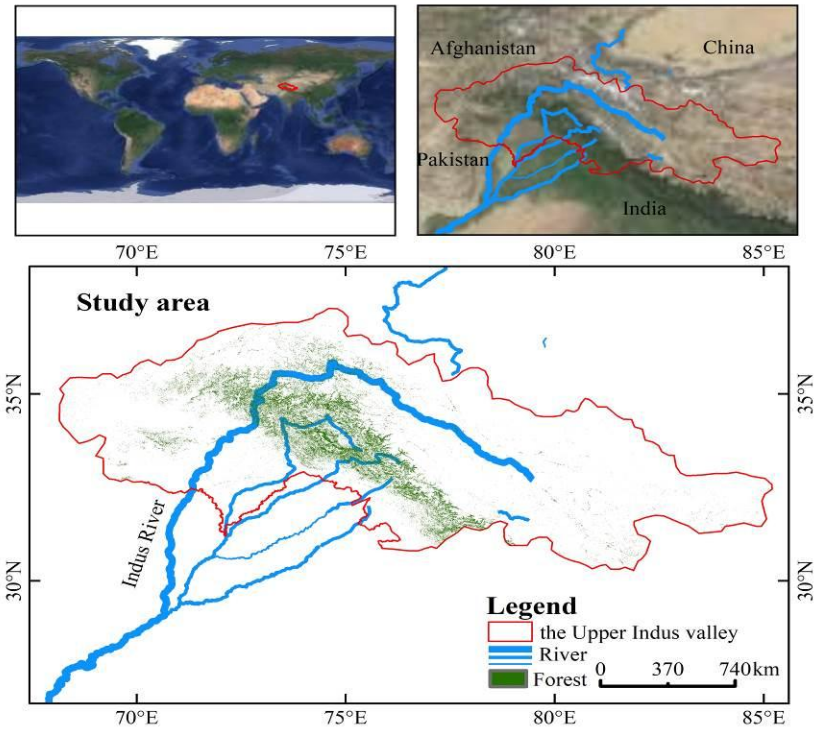


Figure 1. The Upper Indus Valley Location

### *2.2. Data Preprocessing*

Table 1 shows the data used in this study, including forest disturbance and restoration data, land use data, Google Earth imagery, topographic data, and the FireCCI51 fire dataset ( MODIS Fire_cci Burned Area Pixel Product version 5.1).

Table 1. Datasets used in this study

| Name | Data source | Data description |
|---|---|---|
| Forest disturbance and recovery data | Previously published research [2] | The forest disturbance and recovery data were obtained using the LandTrendr spectral-temporal segmentation algorithm, combined with 8203 scenes of Landsat imagery and multi-source remote sensing data analysis. The data record information on the time, magnitude, and duration of forest disturbance and recovery occurring in the upper Indus Valley from 1990 to 2020. The spatial resolution of the data is 30 m.<br>The overall accuracy of the forest change data was 86.01% with a kappa coefficient of 0.73. This dataset was used as the initial input data in this study to explore the driving forces of forest change. |
| Land Use Data | Globaland30 | GlobeLand30 is a 30-meter spatial resolution global land cover data developed by China with 10 primary types: agricultural land, forests, grassland, shrubland, wetland, water, tundra, artificial surface, bare land, glacier and permanent snow [27] (http://www.globallandcover.com/home.html?type=data, Access date: April 10, 2022)<br>In this study, this dataset was used to construct a decision tree model of the drivers of forest change. |
| FireCCI51 | MODIS Fire_cci Burned Area Pixel Product | FireCCI51 is a month-by-month 250 m spatial resolution dataset containing burned area information and ancillary data. It is based on surface reflectance in the near-infrared band from the MODIS instrument on the Terra satellite and active fire information from the |

| | | |
|---|---|---|
| | | same sensor on the Terra and Aqua satellites [28].<br>This dataset was used to identify disturbances caused by forest fires. |
| Topographic data | The Shuttle Radar Topography Mission (SRTM) digital elevation data [29] | SRTM is the most complete and highest resolution digital elevation model of the earth. It was produced in 2000 as a joint effort of NASA, the National Geospatial-Intelligence Agency, and the German and Italian Space Agencies. |
| Sample data on forest disturbance and recovery drivers | Google Earth Pro Software, Visual UI Interpretation | Sample data of forest disturbance and recovery drivers are generated from multi-source remote sensing data, combined with visual interpretation. The data are used to evaluate the accuracy of the driver analysis results.<br>Disturbance driver samples were (1) collected from Global Fire Atlas with Characteristics of Individual Fires data and the Terra and Aqua combined MCD64A1 Version 6 Burned Area data product [30]; (2) Google Earth high spatial resolution image sampling (3) interactive sampling of Landsat image visualization interface (https:// emaprlab.users.earthengine.app/view/lt-geepixel-time-series) to obtain samples of disturbed event drivers.<br>Recovery drive samples were obtained through Google. Earth has high spatial resolution image sampling and interactive sampling of the Landsat image visualization interface. |

### *2.3. Mapping relationships between forest change types and driving forces*

In this study, we propose a decision tree model based on multisource remote sensing imagery to identify the driving forces of forest disturbance and recovery. In our conceptual model, forests were transformed into other land use types after disturbance. We can analyze the potential drivers of forest change through the transformation of land use types after disturbance. The mapping relationships between the types of land use after disturbance and the driving forces are shown in Table 2. There were six driving forces of forest disturbance in this study: agricultural transfer, commercial planting, forest degradation, construction activities, deforestation, and natural hazards. Forest recovery is divided into natural recovery and cultivated forest recovery. In areas with good water and heat conditions, forest recovery can be completed by ecosystem self-healing after disturbance. In areas where human activities are involved, forest recovery can also be completed by plantation and commercial forest cultivation.

Table 2. Mapping relationship between forest change in 1990-2020 and land use in 2020

| Change class | Type of land use in 2020 | Possible drivers of change | High resolution image cases (left is before, right is after) |
|---|---|---|---|
| Disturbance | Cultivated land | Agricultural transfer | 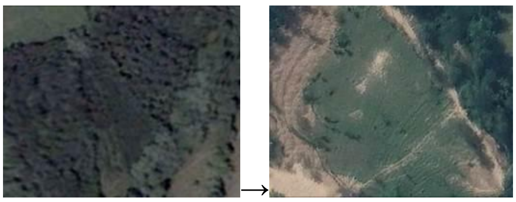<br>74 °50'5.13"E 33 °56'50.38"N |
| | Forest | Commercial planting<br>(Disturbances were detected, and the land use type remains forest in 2020, a process of change for commercial planting.) | <br>*74 °47'51.47"E 33 °40'10.02"N* |

| | | | |
|---|---|---|---|
| | | | <br>(75 °15'51.33"E,33 °47'31.24"N) |
| | Grassland, shrubland, wetland | Forest degrenradation<br>( Significant reduction in forest density, or death, or reduction in greenness ) | 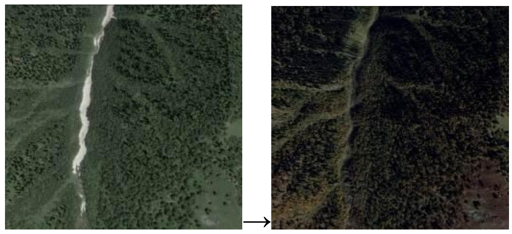<br>( 74 °39'22.36"E, 34 °43'32.00"N) |
| | Artificial surfaces | Human activities<br>( Urbanization, mining) | <br>75 °0'27.13"E 33 °55'23.46"N |
| | Bare land | Deforestation | <br>74 °27'37.39"E 32 °53'2.86"N |
| | Permanent snow and ice | Natural hazards | <br>74 °24'37.53"E 32 °54'50.29"N |
| Recovery | / | Cultivated forest | <br>74 °51'48.89"E, 33 °43'2.94"N |
| | / | Nature Recovery | 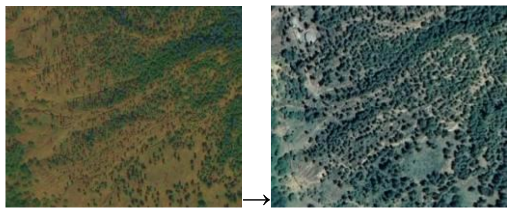 |

### 2.4 Decision tree model based on multi-source remote sensing data

We propose a decision tree model based on multisource remote sensing data to distinguish the driving forces of forest change (Figure 2). The model is divided into the following steps as well as several steps according to different data sources.

(1) Classification of data inputs. 1990-2020 spatial and temporal distribution information of forest disturbance and restoration is the main data source, which is divided into 3 bands, which records the "year", "duration," and "level" information of forest change. The level is the magnitude classification of disturbance and recovery, which is divided into light, moderate, and serious. Fire, land use, and topographic data were recorded as auxiliary data at different locations in the decision-tree model.

(2) Identification of fire-initiatiated-induced disturbances. Using a temporal matching method, the input disturbance data were matched with the FireCCI51 data in terms of time and space. If matching can be accomplished in both time and space, these areas are recorded as fire-induced disturbances.

(3) Identification of other disturbance drivers. Forest degradation, commercial cultivation, agricultural transfer, human activities, and natural hazard disturbances were identified through established mapping relationships using land-use data.

(4) Identification of recovery drivers. Natural and artificial recovery were judged using two thresholds. One is the distance between the recovery area, the artificial surface, and the cultivated land. The second is the slope of the recovery area.

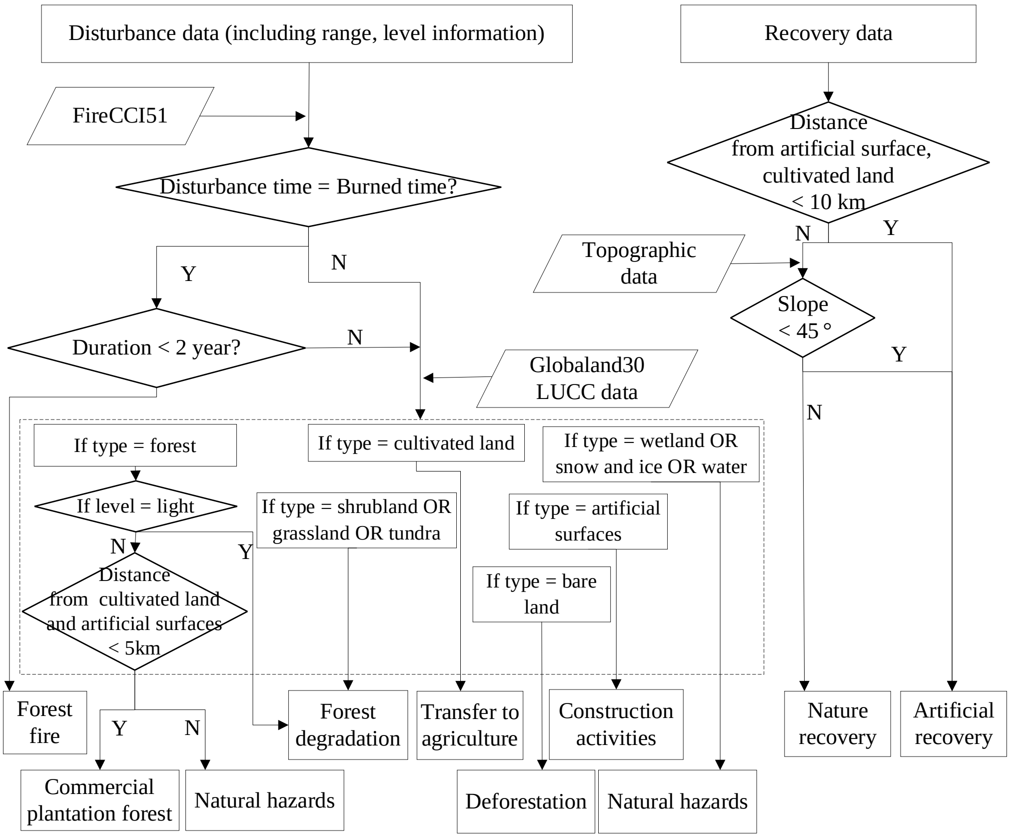


Figure 2. Decision Tree Model for Forest Change Driver Analysis.

### 2.5 Accuracy assessment

The accuracy of the decision tree model for classifying drivers was analyzed using a sample of driver events collected interactively from high-resolution remote sensing images and time-series remote sensing images. The confusion matrix, also called the error matrix, was used to evaluate the classification accuracy by comparing the drivers of the validation samples with those classified by the decision tree model. The overall classification accuracy, user accuracy, producer accuracy, and Kappa coefficient were used to evaluate the final classification results.

## 3.RESULTS

### *3.1. Spatial characteristics of disturbance and recovery drivers*

Figure.3 shows the spatial distribution of the drivers of forest disturbance in the upper Indus Valley from 1990 to 2020. Disturbances occur mainly in the central region of the upper Indus Valley, which is also the main distribution area of the forest. In terms of spatial extent, agricultural transfer occurs mainly in the southern Himalayan region where it meets the plains and on the eastern side of the Kashmir valley. In both regions, agricultural shifts are located in the transition zone between the plains and the mountains. Commercial cultivation is mainly found on the southern slopes of the Himalaya and in the southeastern region of the upper Indus valley, with a small portion in the Kashmir Valley and the western edge of the Hindu Kush. The forest degradation is mainly distributed on the northern side of the Himalayas, the southern side of the Hindu Kush and the eastern side of the Kashmir Valley, with dispersed distribution in the areas bordering Pakistan and Afghanistan. Disturbances caused by natural hazards are not distributed over a large area, but mainly near the high Himalayan mountains and around the high mountain valleys.

Areas disturbed by forest fires are widespread but very small in size, mainly in the low hills north of Islamabad and a small part of the western Kashmir valley. Human activities causing forest disturbance are concentrated in the central Kashmir Valley, and the surrounding areas of Islamabad and Srinagar, mainly due to construction activities (in cities and towns) and production activities (mining in high mountain areas), with a small area of distribution. Disturbances due to deforestation are not widespread and are mainly found on both sides of the Srinagar Valley (plain-alpine transition zone), around towns, and in the south-eastern region of the upper Indus Valley.

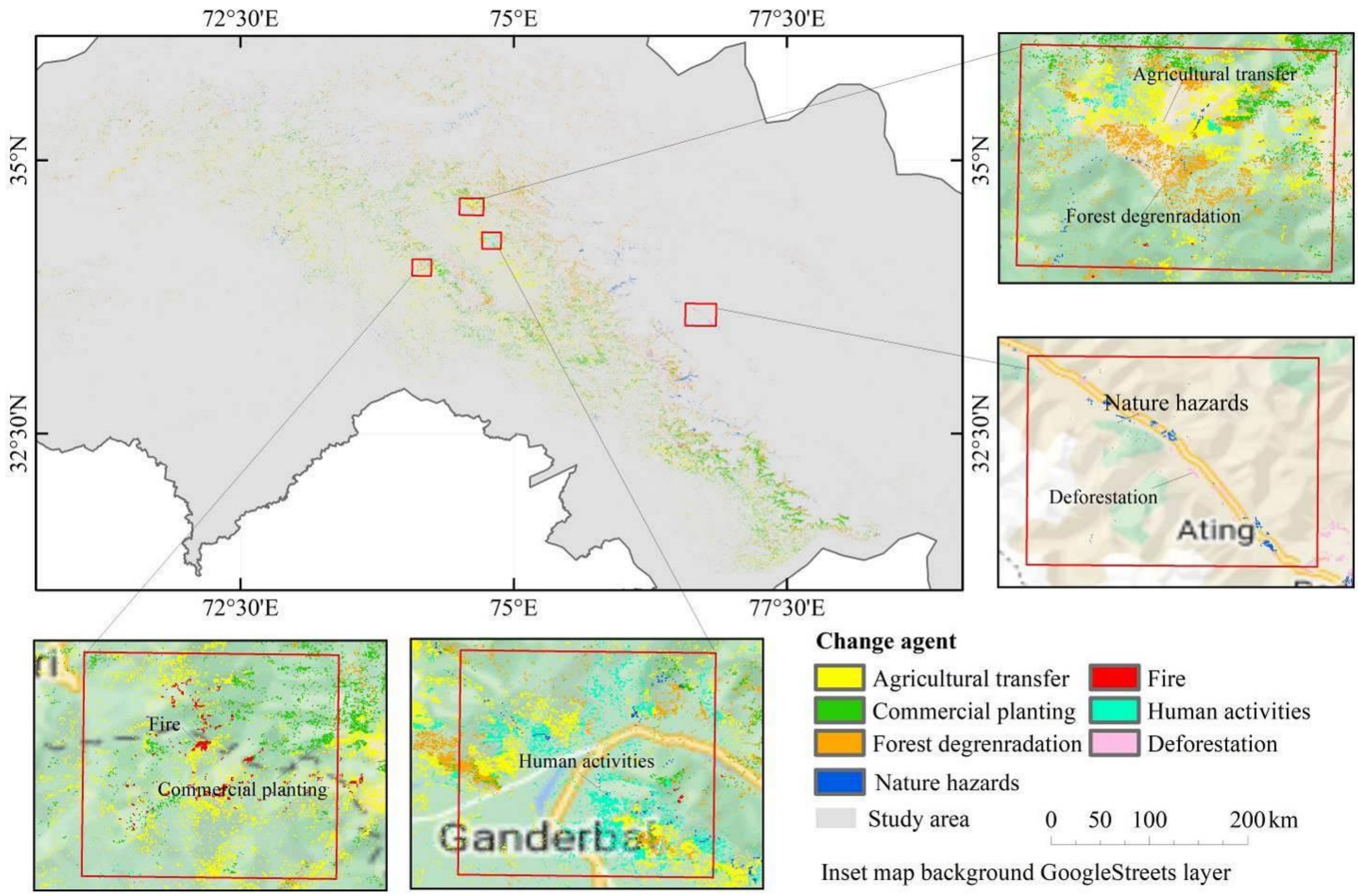

Figure 3. Spatial distribution of agents of forest disturbance in the upper Indus Valley. The overall distribution of the seven disturbance types from 1990-2020 is shown in the main figure, with examples of each type highlighted in the inset.

The spatial distribution of the drivers of forest recovery in the upper Indus Basin from 1990-2020 is shown in Figure 4. The recovered areas were highly consistent with the distribution of disturbed areas. Most of the recovery area is located in the eastern Hindu Kush and western Himalayas, with lesser distribution in the eastern and northwestern parts of the upper Indus Valley. The two drivers of artificial and natural recovery showed significant differences. Artificial recovery is mainly located in the Hindu Kush, the western side of the Himalayas, and the Kashmir Valley, with a small area in the Tibetan areas of China. Natural recovery is concentrated on the eastern side of the Himalayas and alpine areas of the Kashmir Valley.

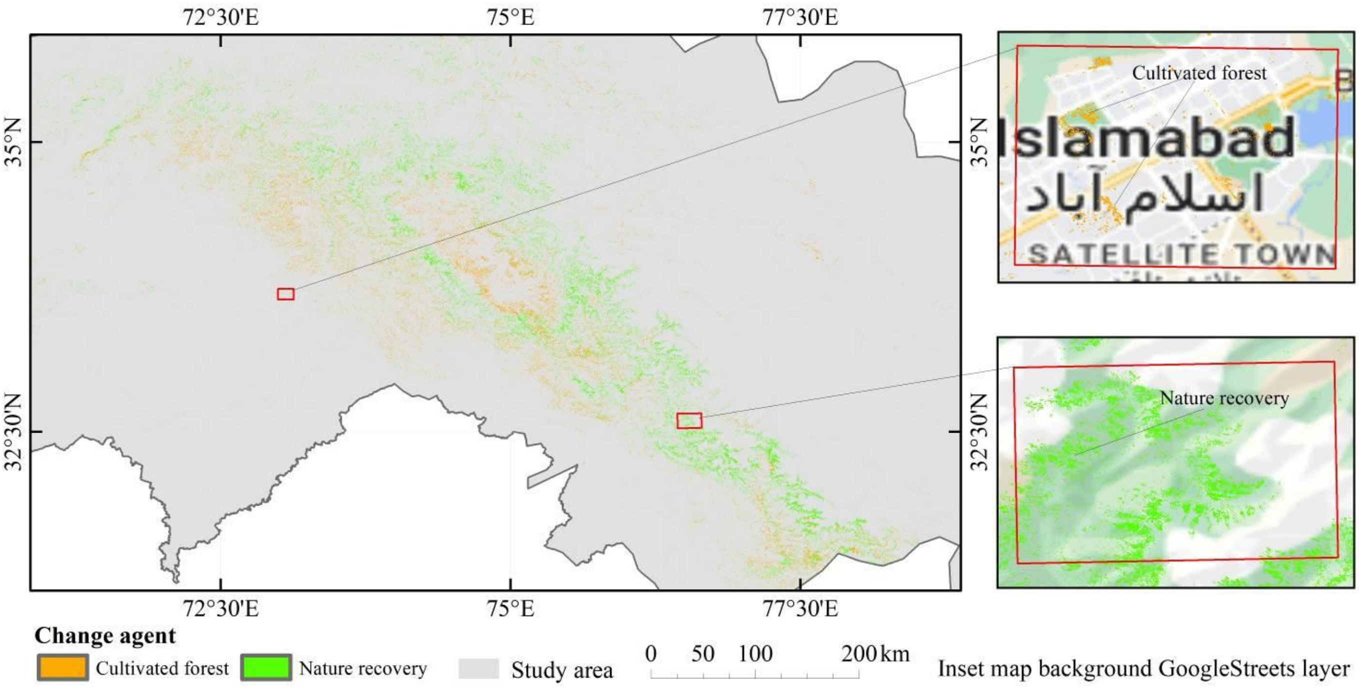


Figure 4. Spatial distribution of forest recovery drivers in the upper Indus Valley. The overall distribution of the two recovery drivers is shown in the main figure, with examples of each type highlighted in the inset.

### *3.2 Characteristics of the temporal distribution of drivers of forest change*

In our previous study, we obtained a total forest disturbance area of 13,233.55 km$^2$ in the upper Indus Valley between 1990 and 2020 [2]. In this study, the results of our classification of different disturbance drivers showed that forest degradation was the main cause of forest disturbance with a total area of 9125.95 km$^2$, accounting for 68.97% of the disturbed forest, and the average value of the disturbed area was 294.38 km$^2$ per year (Figure 5). The second main reason is the agricultural transfer, with a total area of 2854.97 km$^2$, accounting for 21.58% of the disturbed forest, and an average disturbance area of 92.09 km$^2$ per year. Commercial cultivation and deforestation were the smaller drivers of forest disturbance, both accounting for 4% of the total disturbed forest area, with mean values of 17.77 km$^2$ and 17.17 km$^2$ per year, respectively. The area of forest fires, human activities and natural hazards were the minimal drivers of forest disturbance, with an area of less than 80 km$^2$ over 31 years, accounting for less than 1% of the total disturbed forest area, with mean values of 2.52 km$^2$, 1.58 km$^2$ and 1.32 km$^2$ per year, respectively.

The interannual variability characteristics of the different disturbance events showed large differences in the performance of the different disturbance drivers (Figure 5). The overall trend of forest degradation decreased yearly, mainly in 1990-2000, accounting for 67.17% of the 31 years. There was a small peak in forest degradation drivers between 2006 and 2008, and after 2009, the average forest degradation area decreased to 100 km$^2$/year. The area of the agricultural transfer driver fluctuated and decreased with time. From 1994 to 1998, there was a peak in the area of disturbance in the agricultural transfer driver, reaching a peak of 311.2 km$^2$ in 1997. The second small peak occurred from 2004 to 2008, and after 2009 there was a significant decrease in the area of agricultural transfer. The overall trend in the disturbance area of the commercial planting driver fluctuated. The disturbance was concentrated between 1990-2002, with 67% of the disturbed area in all 13 years. 2005-2008 showed a second small peak in commercial planting, after which the disturbed area significantly decreased. Deforestation also shows a fluctuating decreasing trend, with a significant decrease from 2001-2004, and a small increase from 2006-2007. After 2008, the area has been maintained at 10km$^2$ / year. Forest fire drivers showed a gradually decreasing trend, mainly distributed between 1990-2002. The disturbed area during these 13 years accounted for 68.56% of the total fire area. After 2006, the overall trend of forest fires was unstable, with fires in 2012, 2016, and 2017 covering an area greater than 2 km$^2$ and occurs in recent years covering an area less than 1 km$^2$. The main forest disturbance caused by urban construction and mining in human activity drivers has been decreasing yearly, mainly between 1990 and 1998. After 1999, the disturbed area covered < 1 km$^2$. The overall trend of disturbance by natural hazards was stable, with a larger disturbance area of more than 1 km$^2$ in 1990-2000 and 2006-2008. In subsequent years, the differences in area were small.

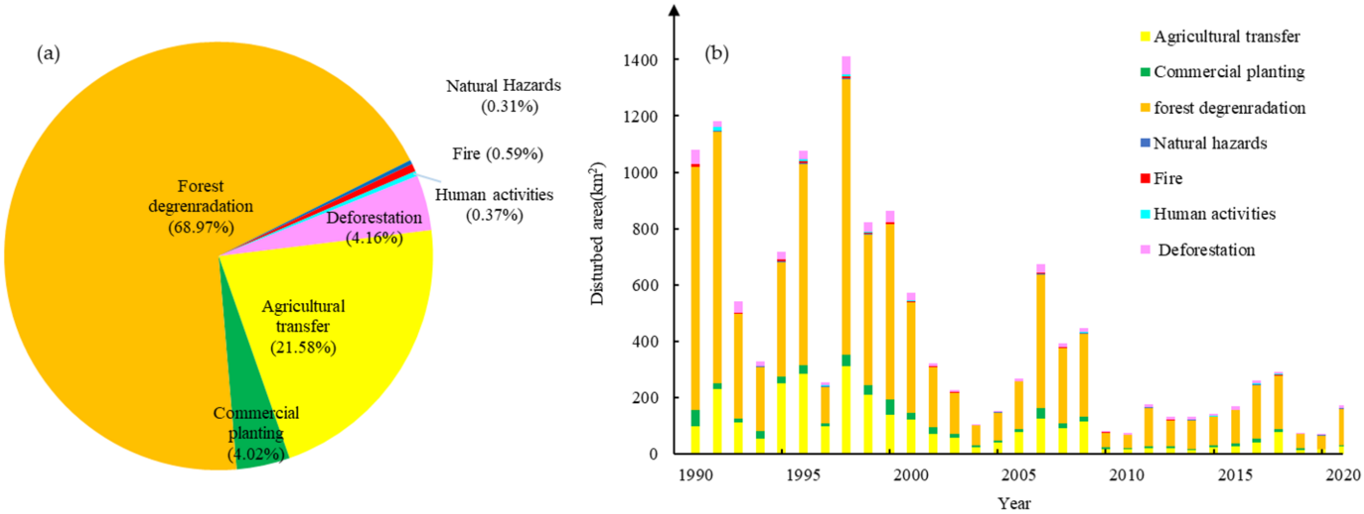


Figure 5. Characteristics of temporal changes in different drivers of disturbance in the upper Indus Valley from 1990 to 2020. (a) Total area of different disturbance drivers as a percentage of the total disturbed area; (b) quantitative characteristics of the interannual variation of different disturbance drivers.

From the overall situation of forest recovery in the upper Indus Valley from 1990 to 2020, the total area of natural recovery is 8233.6 km$^2$, accounting for 60.08%, and the area of cultivated forest recovery is 2764.65 km$^2$ less than that of natural recovery, accounting for 39.91% (Figure 6). The interannual variation of natural recovery drivers is characterized by an increase then decrease, approaching the trend of a normal distribution. The area gradually increased from 1993 and decreased after reaching a peak of 829.93 km$^2$ in 2000. The naturally restored area was the largest in the interval from 1999 to 2010, accounting for 61.45% of all naturally restored areas. From 2010 to 2016, the area of the natural recovery drivers was relatively stable, with an average of 129.58 km$^2$ / year. After 2016, there was a gradual increase in the recovery of the natural forests. The interannual trends of the cultivated forest drivers were similar to those of natural recovery, but with some differences. The two main time periods of cultivated forest recovery were 1990-1993 and 2000-2011, which accounted for 75.74% of the total area. The proportion of cultivated forests has gradually increased since 2014.

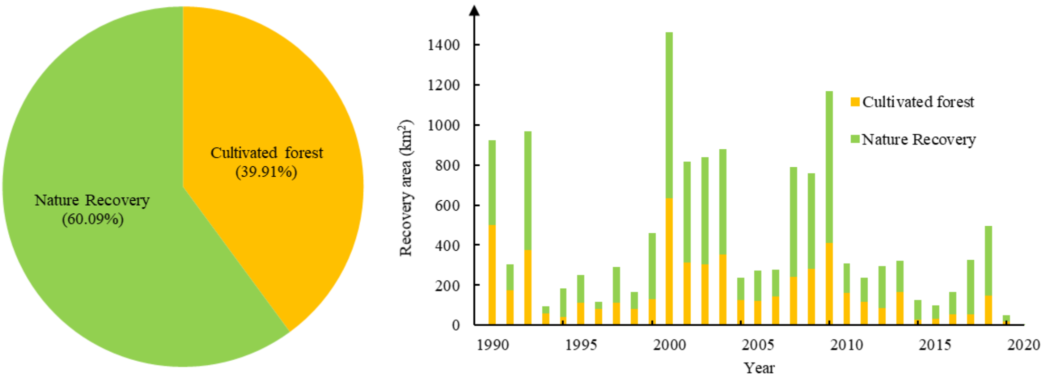


Figure 6. Characteristics of temporal changes in different drivers of recovery in the upper Indus Valley from 1990 to 2020. (a) Total area of different recovey drivers as a percentage of the total recoverd area; (b) quantitative characteristics of the interannual variation of different recovery drivers.

### *3.3 Accuracy Assessment*

Validation samples generated from multi-source remote sensing imagery were used for accuracy of the decision tree model classification of the drivers results. The accuracy assessment results showed that the method used in this study can effectively distinguish forest change drivers (Tables 3 and 4). The different forest change (disturbance and recovery) drivers showed high producer and user accuracy.

From the identification results of the disturbance drivers, the overall accuracy was 81.56%, and the Kappa coefficient was 0.75. In terms of the user and producer accuracy of disturbance drivers, the highest user accuracy of 87.84% was found for the forest degradation driver. The three drivers of forest fire, agricultural transfer, and commercial planting all have user accuracies above 80%, whereas those of natural disasters, deforestation, and human activities are lower, but all are above 63%. Fire had the highest producer accuracy of 92.53%; forest degradation and human activity drivers also achieved high producer accuracy of 88.19% and 88.4%, respectively; and deforestation had the lowest producer accuracy of 55.79%. From the results of the recovery driver identification, the overall accuracy was 85.28%, and the Kappa coefficient was 0.69. Both the cultivated forest and natural recovery drivers achieved high producer and user accuracy.

Table 3. The result of accuracy assessment of disturbance drivers

| | Reference data: validation dataset (pixels) | | | | | | | |
|---|---|---|---|---|---|---|---|---|
| | Fire | Agricultural transfer | Commercial planting | Forest degrenradation | Human activities | Deforestation | Natural hazards | User accuracy |
| Fire | 260 | 0 | 0 | 52 | 0 | 0 | 0 | 83.33% |
| Agricultural transfer | 3 | 524 | 35 | 64 | 0 | 0 | 0 | 83.71% |
| Commercial planting | 6 | 130 | 664 | 0 | 0 | 5 | 0 | 82.48% |
| Forest degrenradation | 0 | 46 | 85 | 1524 | 36 | 32 | 12 | 87.84% |
| Human activities | 0 | 51 | 32 | 74 | 358 | 45 | 0 | 63.93% |
| Deforestation | 12 | 2 | 36 | 7 | 5 | 106 | 0 | 63.10% |
| Potential natural disasters | 0 | 0 | 0 | 7 | 6 | 2 | 36 | 70.59% |
| Producer accuracy | 92.53% | 69.59% | 77.93% | 88.19% | 88.40% | 55.79% | 75.00% | |
| Overall accuracy | 81.56% | | | | | | | |
| Kappa | 0.75 | | | | | | | |

1

Table 4. The result of accuracy assessment of recovery drivers

| | Reference data: validation dataset (pixels) | | |
|---|---|---|---|
| | Cultivated forest | Nature recovery | User accuracy |
| Cultivated forest | 2113 | 232 | 90.11% |
| Nature recovery | 362 | 1327 | 78.57% |
| Producer accuracy | 85.37% | 85.12% | |
| Overall accuracy | | 85.28% | |
| Kappa | | 0.69 | |

## 4.DISCUSSION

### *4.1. Forest Disturbance and Recovery in Different Regions*

In this study, we combined multisource remote sensing data and decision tree models to obtain data on the drivers of disturbance and restoration. The contribution of each driver to forest change was counted and quantified, and differences in the drivers of forest change in terms of administrative regions were explored. Table 5 shows the statistics for forest change attribution in this region at the administrative level.

Forest degradation occurs in all the administrative districts of the Upper Indus Valley. Jammu & Kashmir, Himachal Pradesh and Khyber Pakhtunkhwa are the three districts with the highest area of forest degradation with an area of 3199.21 km$^2$, 2645.69 km$^2$, and 1126.95 km$^2$ respectively. Forests in the high Asia region are strongly affected by climate change, and drought caused by climate change is an important cause of forest degradation [31]. Seasonal droughts, floods or consequent pests and diseases are possible causes of forest degradation. The delayed arrival and early retreat of the southwest monsoon can lead to reduced precipitation and increased risk of high temperatures in the South Asian subcontinent. The resulting droughts can cause thermal stress on forests and lead to the degradation of healthy forests [32]. Wild animals such as Asiatic black bears also wreak havoc in forests, often feeding on the skins of certain trees and triggering forest degradation [33].

Agricultural transfer drivers occurred in 19 administrative districts of the upper Indus Valley, mainly in India and Pakistan. Jammu & Kashmir and Khyber Pakhtunkhwa have the most disturbed forests by agricultural shifts, with an area of 1277 km$^2$ and 659.89 km$^2$. In many areas of Pakistan, India, and Afghanistan, a large amount of former agricultural land in river valleys has been converted to non-agricultural land due to population growth and lack of management policies. This has led to a shift in agriculture to forested areas on both sides of river valleys [34].

Commercial planting has taken place in 16 provinces in five countries, mainly involving urban greening and economic forest cultivation around river valleys and farmlands. Himachal Pradesh and Jammu and Kashmir have the largest commercial planting areas, 231.6 km$^2$ and 95.69 km$^2$ respectively. In recent years, there has been evidence that subtropical fruit cultivation in the Himachal Pradesh area has developed rapidly, which has led to the reduction of the original forest [35]. In addition, Himachal Pradesh has introduced horticultural plantations on a large scale, and the main types of cultivated forests include chir pine, cultivation, and khair forests [36]. Afghanistan also has a small portion of commercial planting; Konarha is planted with an area of 10.69 km$^2$.

Forest fires occurred in 12 provinces, with larger areas in India and Pakistan. Specific climatic conditions and human activities were the main causes of forest fires in these two regions. Previous studies have pointed out that the Kashmir Valley has a complex climatic environment with hotter local microclimates than other regions, irregular precipitation in winter, and dry summers and autumns, which are favorable conditions for burning to occur [37, 38]. Also, the summer capitals of Jammu and Kashmir, Srinagar, and the surrounding satellite towns attract a large population, and increased human activity is an important cause of forest burn.

Human activity-induced forest disturbance occurred in 11 provinces, mainly due to construction and mining activities. Overall, the disturbed area in each province was less than 10 km$^2$, and five of them were less than 1 $km^2$. Pakistan and India are the two countries with the highest forest loss, with population growth, infrastructure development, urbanization, and rapid development of satellite towns being the main causes [39].

Deforestation occurred in 25 provinces in five countries, recorded in areas converted from forest to bare land. India has the largest deforested area, accounting for 66.67% of the total deforested area. Biomass energy, especially fuelwood, is the main source of energy for cooking and water heating in rural areas. The growth of populations and livestock has led to deforestation [40]. In Himachal Pradesh, the annual direct demand of the local population for wood is 31,063 $m^3$, and the indirect demand amounts to 3,646,348 tons [41]. In outer regions of Himachal Pradesh, forest resources are under the same condition, with degradation and deforestation linked to the heavy reliance of local populations on biomass for energy. It is worth noting that although the areas of forests and disturbed areas in Afghanistan are not large compared to other countries, the area of deforestation in Afghanistan as a percentage of the disturbed area of forests in the country is much higher than other countries, and is mainly in the Konarha Province. Previous studies have also noted that in eastern Afghanistan, the annual deforestation rate was estimated to be 0.06% from 1975 to 1990, with a significant decrease from 2005 to 2014 [42].

Natural hazard-induced deforestation occurred in 13 provinces—mainly geologically vulnerable areas in India, Pakistan, and China. Landslides and erosion caused by construction activities and earthquakes have all led to increased vulnerability of forest ecosystems in the upper Indus Valley, resulting in the disturbance or loss of forest [43]. Road construction increases mountain instability and the resulting natural hazard is an important causal factor for forest loss [44].

The recovery of cultivated forests occurs in 26 provinces; Jammu and Kashmir and Khyber Pakhtunkhwa are the two provinces with the largest area of 2194.97 $km^2$ and 1285.34 $km^2$ respectively. These two provinces are also representative of other provinces in India and Pakistan, which have gradually focused on forest conservation in the upper Indus Valley in recent years. According to relevant media reports, it can be found that both countries have developed a considerable amount of planted forest recovery plans in this region. In particular, since 2015, the area of forests to be planted is still growing rapidly, but it still takes some time to discover these areas through satellite observations. India's Jammu and Kashmir Province has developed an afforestation program for a certain area in the annual plan of operations (APOs) each year. Khyber Pakhtunkhwa Province in Pakistan has implemented the Billion Trees Afforestation Program with good socioeconomic benefits [45]. In addition to public-benefit plantations, commercial plantations are an important factor in plantation recovery. The widespread use of agroforestry complex systems and planting of plantation species with short forest rotation (<7 years), such as poplar (Populus deltoides), are the main drivers of forest recovery in northwestern India [46]. It is worth noting that planted forests were also restored at high altitude in Ali, Tibet, China, with an area of 20.17 $km^2$. China officially launched a biological sand control project in the Shiquanhe Town Basin in 1994 with a cumulative planting of 15.17 $km^2$, which is consistent with the results of this study (*http://www.xizang.gov.cn/xwzx_406/dsdt/202108/t20210805_253265.html, Accessed Daate: April 14, 2022*). For nature-recovered forests, we also recognize that this is the opposite of forest degradation. That is, there is no anthropogenic disturbance, but only a process of forest greenness reduction or death change due to climatic and environmental conditions, such as drought, pests, and diseases. When hydrothermal conditions improve, degraded forests are transformed back to a normal state.

Table 5. Forest area changes influenced by different driving forces of the upper Indus Valley ($km^2$)

| | | Disturbance | | | | | | | Recovery | |
|---|---|---|---|---|---|---|---|---|---|---|
| Country | Province | Agricultural transfer | Commercial planting | Forest degrenradation | Natural hazards | Fire | Human activities | Deforestation | Cultivated forest | Nature recovery |
| Afghanistan | Bamian | 0.04 | 0.00 | 0.05 | 0.00 | 0.00 | 0.00 | 0.00 | 0.05 | 0.03 |
| | Badakhshan | 0.41 | 0.01 | 1.03 | 0.02 | 0.00 | 0.00 | 0.06 | 1.25 | 0.96 |
| | Baghlan | 1.17 | 0.00 | 3.57 | 0.00 | 0.00 | 0.00 | 0.17 | 1.57 | 1.98 |
| | Ghazni | 0.02 | 0.00 | 0.08 | 0.00 | 0.00 | 0.00 | 0.00 | 0.07 | 0.01 |
| | Kabol | 0.62 | 0.00 | 0.44 | 0.00 | 0.00 | 0.10 | 0.04 | 2.07 | 0.15 |
| | Kapisa | 7.76 | 0.00 | 4.12 | 0.00 | 0.06 | 0.00 | 0.29 | 11.92 | 1.22 |
| | Konarha | 13.88 | 10.69 | 148.02 | 0.38 | 4.40 | 0.00 | 33.41 | 49.80 | 160.67 |
| | Laghman | 2.58 | 0.82 | 15.99 | 0.04 | 0.00 | 0.00 | 2.43 | 8.69 | 11.73 |
| | Lowgar | 0.97 | 0.00 | 0.70 | 0.00 | 0.00 | 0.00 | 0.09 | 3.02 | 0.19 |
| | Nangarhar | 1.25 | 2.98 | 26.83 | 0.01 | 0.32 | 0.01 | 3.37 | 4.64 | 22.87 |
| | Paktia | 2.20 | 17.88 | 37.84 | 0.00 | 0.43 | 0.00 | 6.56 | 14.56 | 28.52 |
| | Paktika | 0.91 | 4.85 | 7.93 | 0.00 | 0.00 | 0.00 | 1.40 | 2.22 | 5.40 |
| | Parvan | 4.95 | 0.00 | 6.15 | 0.00 | 0.00 | 0.00 | 0.54 | 9.75 | 1.56 |
| | Vardak | 1.57 | 0.00 | 4.86 | 0.00 | 0.00 | 0.00 | 0.26 | 4.90 | 1.43 |
| China | Xinjiang | 0.00 | 0.00 | 2.57 | 0.02 | 0.00 | 0.20 | 0.01 | 0.00 | 1.77 |
| | Xizang | 0.72 | 0.15 | 191.33 | 2.41 | 0.00 | 0.00 | 8.92 | 20.17 | 302.59 |
| India | Himachal Pradesh | 350.36 | 231.60 | 2645.69 | 4.46 | 19.66 | 1.15 | 164.57 | 818.24 | 2250.94 |
| | Haryana | 0.04 | 0.00 | 0.01 | 0.00 | 0.00 | 0.00 | 0.00 | 0.06 | 0.00 |
| | Jammu & Kashmir | 1277.62 | 91.33 | 3199.21 | 8.20 | 20.42 | 32.80 | 202.36 | 2194.97 | 2607.47 |
| | Punjab | 3.08 | 0.05 | 0.69 | 0.14 | 0.06 | 0.20 | 0.02 | 5.79 | 0.10 |
| | Uttar Pradesh | 298.16 | 5.45 | 47.54 | 0.00 | 0.00 | 0.00 | 0.37 | 0.00 | 47.65 |
| Nepal | Karnali | 0.00 | 0.0 | 1.12 | 0.00 | 0.00 | 0.00 | 0.01 | 0.00 | 1.56 |
| Pakistan | Azad Kashmir | 0.00 | 23.20 | 610.17 | 2.94 | 8.94 | 1.93 | 5.42 | 478.41 | 642.44 |
| | Federally Administered Tribal Areas | 17.75 | 12.18 | 119.31 | 0.00 | 6.81 | 0.05 | 6.29 | 116.66 | 118.27 |
| | Gilgit Baltistan | 163.72 | 32.86 | 893.77 | 3.09 | 0.57 | 3.20 | 29.48 | 336.02 | 752.88 |
| | Khyber Pakhtunkhwa | 659.89 | 95.69 | 1126.95 | 19.09 | 14.56 | 5.82 | 82.94 | 1285.34 | 1264.57 |
| | Punjab | 45.34 | 2.66 | 29.96 | 0.25 | 1.91 | 3.66 | 1.99 | 98.79 | 6.65 |
| Total | | 2854.98 | 532.40 | 9125.95 | 41.05 | 78.15 | 49.11 | 551.01 | 5468.96 | 8233.60 |

### *4.2 Implications of the spatial and temporal distribution of forest drivers for future sustainable development in the Indus Basin from 1990-2020*

We obtained for the first time, the spatial and temporal distribution of the drivers of forest change in the upper Indus River basin from a watershed-scale analysis. Unlike previously reported or localized studies, we characterized these driving forces more quantitatively in time and space in the upper Indus Valley. For the overall trend of forest change, the rate of forest disturbance is slowing down and the rate of forest recovery is gradually increasing, but still faces the potential impacts of human activities and climate change on forest ecosystem stability [47].

Figure 7 illustrates the proportion of disturbed forest areas with different drivers in the 27 provinces of the Upper Indus Valley. This result demonstrates that forest changes in the upper Indus Basin were dominated by forest degradation in all provinces. The specific climate of the high Asia region leads to instability of forest ecosystems. The impact of other driving forces on forest ecosystem stability cannot be ignored; for example, in Afghanistan, India, and northeastern Pakistan, where agricultural transfer accounts for a significant proportion. Previous studies have shown that in eastern Pakistan and west-central India, the expansion of forests to cropland is mainly due to the expansion of cropland in areas with low soil productivity (due to soil degradation and lack of irrigation) and the overdependence on forest resources in rural areas [5, 48].

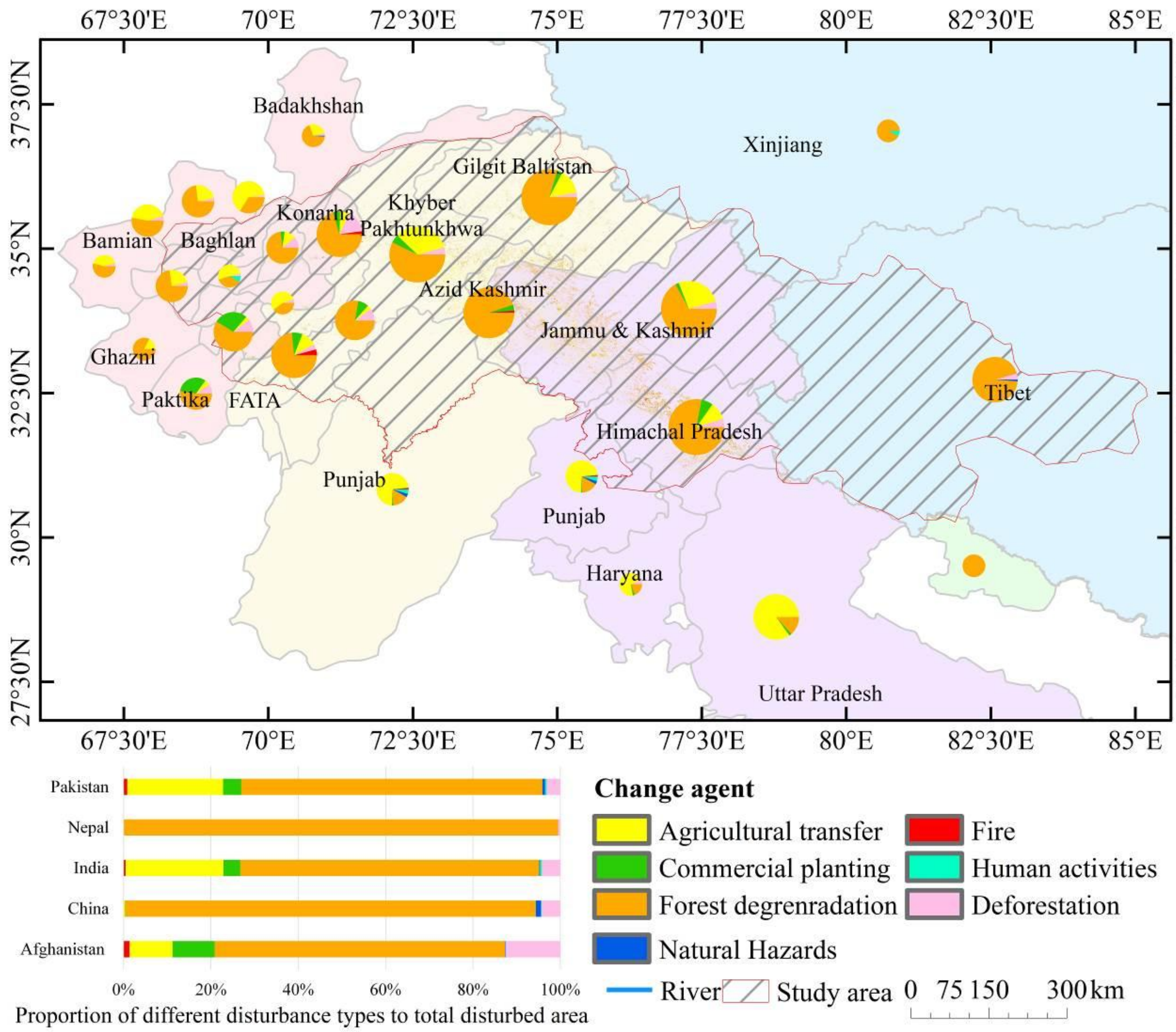


Figure 7. The proportion of disturbed area of different drivers to the regional forest disturbed area; the pie chart shows the proportion of disturbed forest area of different drivers to the total disturbed area in each province; The bar chart shows the proportion of the area of forest disturbed by different drivers to the total area of forest disturbed in different countries. A uniform legend is used for the pie and bar charts.

The trend of forest change over the past 31 years has been positive, but we should also recognize that forest disturbance, especially anthropogenic disturbance, can destabilize the original forest ecosystem and biodiversity. In the context of global warming, irregular monsoons, reduced precipitation, and frequent high-temperature heat waves have led to increased vulnerability of forest ecosystems, and forests in high Asia are facing progressively worse environmental threats [49]. From the perspective of forest change in the upper Indus Valley and future sustainable development of the entire basin, the ecological security of the upper and lower Indus Valley should be considered together. Deforestation, forest degradation, and ecological imbalances due to changes in forest species composition may cause irreversible damage to unstable and fragile mountainous regions, such as the Indian Himalayas and Indus River Plain. The instability of the upstream forest ecosystem will lead to the weakening of forest ecosystem services, such as water conservation and wind and sand control. Instability or reduction of forest ecosystem services can threaten water security in the mainstem and tributaries of the Indus River, as observed in Pakistan in 1992 and 2010, leading to catastrophic floods for which deforestation was an important cause [5]. Floods threaten the security of food production in the Indus Valley and the survival of 230 million people in the basin; based on this, the countries and regions concerned should take full action to ensure the ecological security of the

Indus River Valley. To achieve sustainable development in the Indus River Basin, we listed the priorities for forest conservation in conjunction with our research findings.

(1) Increase the supply of non-biomass energy in rural areas, especially in Himachal Pradesh, Jammu and Kashmir, Khyber Pakhtunkhwa, and Afghanistan. The government should provide low-cost, non-biomass energy as an alternative to biomass energy. Reduce the heavy dependence of rural village populations on forest resources and protect existing natural and planted forests.

(2) Control the scale of animal husbandry and establish strict protection policies. In natural forest distribution areas, especially in the Kashmir Valley and the southwest slopes of the Himalayas, a stricter policy of mountain closure and reforestation is implemented to reduce the disturbance of forests by human activities and grazing. Afghanistan and Kashmir Valley should strictly limit the size of commercial economic forests and protect natural forests. In areas of transition between agriculture and forests, such as Afghanistan, eastern Pakistan, and northwestern India, the monitoring of land resources should be strengthened to prevent forest loss.

(3) Reasonable land-use planning to reduce encroachment of construction land and farmland on forestland. For deforestation in the construction of roads, residential areas, and satellite towns, a corresponding forest area should be planted in ecologically fragile areas for ecological compensation. The transfer of forest land on slopes to agricultural land should be strictly controlled to prevent further soil erosion. In Afghanistan and Pakistan, fire monitoring and early warning systems should be strengthened to reduce fire-induced forest damage.

(4) Accelerate the economic paradigm shift to reduce the economy's dependence on direct forest use. The countries concerned can accelerate the transformation of the agricultural model and development of tourism to reduce the dependence of economic activities on forest resources.

### *4.3. Method Limitations and Its Application*

Our results show that the classification of forest change drivers can be effectively accomplished using multi-source remote sensing data and decision tree models. We also note that a relatively high attribution accuracy can be obtained by combining machine learning methods with elements such as spectral textures before and after disturbance events [50]; however, this also places higher demands on data processing, especially when image data are created. At the same time, we recognize that 30 years of remote sensing images are insufficient for natural forest change monitoring. This is because forest biomass and accumulation growth are slow in the specific physical geography of the high Asia region. It was also observed through multiple remote sensing data that satellite observations from 1990-2020 were insufficient to monitor forest disturbances; more disturbances may have occurred in years before 1990, when many satellite observations were missing. Although our results indicate that the area of forest recovery is larger than the disturbed area from 1990-2020, the forest condition in the upper Indus valley should be a matter of concern to the countries concerned on a long-term scale.

## 5.SUMMARY

This study combined forest disturbance and recovery data, multi-source remote sensing data, and a decision tree classification model to successfully map the attribution of drivers of forest change in the upper Indus Valley. Our results quantitatively characterized the spatial and temporal characteristics of the different drivers of forest change in the upper Indus Valley. During the last 30 years, the combined pressures of climate change and human activities have left the upper Indus forests in a precarious state, with forest degradation as the primary driver; agricultural expansion and commercial cultivation as secondary drivers; and fire, natural hazards, and deforestation affecting only a small portion of the forests. For forest recovery, the upper Indus Valley forests were primarily initiated by ecosystem self-healing. Although the overall forest trend over the 30-year period was positive, we should also recognize that forest disturbance, especially anthropogenic disturbance, can destroy the stability and biodiversity of the original forest ecosystem. The relevant countries in the Indus Basin should actively adopt policies to maintain an increase in forest area and quality to promote the sustainable development of the basin.

## References

1. Huang, L., B. Wang, X. Niu, *et al.* (2019). Changes in ecosystem services and an analysis of driving factors for China's Natural Forest Conservation Program. Ecology and Evolution. **9**(7): 3700-3716.
2. Yan, X. and J. Wang. (2022). The Forest Change Footprint of the Upper Indus Valley, from 1990 to 2020. **14**(3): 744.
3. Immerzeel, W.W., A.F. Lutz, M. Andrade, *et al.* (2020). Importance and vulnerability of the world's water towers. Nature. **577**(7790): 364-369.
4. Qureshi, A.S. (2011). Water Management in the Indus Basin in Pakistan: Challenges and Opportunities. Mountain Research and Development. **31**(3): 252-260.
5. Zeb, A., A. Hamann, G.W. Armstrong, *et al.* (2019). Identifying local actors of deforestation and forest degradation in the Kalasha valleys of Pakistan. Forest Policy and Economics. **104**: 56-64.
6. Pacetti, T., E. Caporali, and M.C. Rulli. (2017). Floods and food security: A method to estimate the effect of inundation on crops availability. Advances in Water Resources. **110**: 494-504.
7. Mehmood, A., S. Jia, A. Lv, *et al.* (2021). Detection of Spatial Shift in Flood Regime of the Kabul River Basin in Pakistan, Causes, Challenges, and Opportunities. Water. **13**(9).
8. Ahmad, A., S.R. Ahmad, H. Gilani, *et al.* (2021). A Synthesis of Spatial Forest Assessment Studies Using Remote Sensing Data and Techniques in Pakistan. Forests. **12**(9).
9. Zhu, Z., C.E. Woodcock, and P. Olofsson. (2012). Continuous monitoring of forest disturbance using all available Landsat imagery. Remote Sensing of Environment. **122**: 75-91.
10. Meigs, G.W., R.E. Kennedy, A.N. Gray, *et al.* (2015). Spatiotemporal dynamics of recent mountain pine beetle and western spruce budworm outbreaks across the Pacific Northwest Region, USA. Forest Ecology and Management. **339**: 71-86.
11. Attiwill, P.M. (1994). THE DISTURBANCE OF FOREST ECOSYSTEMS - THE ECOLOGICAL BASIS FOR CONSERVATIVE MANAGEMENT. Forest Ecology and Management. **63**(2-3): 247-300.
12. Pickell, P.D., T. Hermosilla, N.C. Coops, *et al.* (2014). Monitoring anthropogenic disturbance trends in an industrialized boreal forest with Landsat time series. Remote Sensing Letters. **5**(9): 783-792.
13. Kennedy, R.E., Z. Yang, J. Braaten, *et al.* (2015). Attribution of disturbance change agent from Landsat time-series in support of habitat monitoring in the Puget Sound region, USA. Remote Sensing of Environment. **166**: 271-285.
14. Hermosilla, T., M.A. Wulder, J.C. White, *et al.* (2015). Regional detection, characterization, and attribution of annual forest change from 1984 to 2012 using Landsat-derived time-series metrics. Remote Sensing of Environment. **170**: 121-132.
15. Pflugmacher, D., W.B. Cohen, and R.E. Kennedy. (2012). Using Landsat-derived disturbance history (1972-2010) to predict current forest structure. Remote Sensing of Environment. **122**: 146-165.
16. Meddens, A.J., J.A. Hicke, and C.A.J.E.A. Ferguson. (2012). Spatiotemporal patterns of observed bark beetle-caused tree mortality in British Columbia and the western United States. **22**(7): 1876-1891.
17. Shimizu, K., O.S. Ahmed, R. Ponce-Hernandez, *et al.* (2017). Attribution of Disturbance Agents to Forest Change Using a Landsat Time Series in Tropical Seasonal Forests in the Bago Mountains, Myanmar. Forests. **8**(6).
18. Schleeweis, K.G., G.G. Moisen, T.A. Schroeder, *et al.* (2020). US National Maps Attributing Forest Change: 1986-2010. Forests. **11**(6).
19. Schroeder, T.A., K.G. Schleeweis, G.G. Moisen, *et al.* (2017). Testing a Landsat-based approach for mapping disturbance causality in US forests. Remote Sensing of Environment. **195**: 230-243.
20. Oeser, J., D. Pflugmacher, C. Senf, *et al.* (2017). Using Intra-Annual Landsat Time Series for Attributing Forest Disturbance Agents in Central Europe. Forests. **8**(7).
21. Moisen, G.G., M.C. Meyer, T.A. Schroeder, *et al.* (2016). Shape selection in Landsat time series: a tool for monitoring forest dynamics. Global Change Biology. **22**(10): 3518-3528.
22. Hermosilla, T., M.A. Wulder, J.C. White, *et al.* (2015). Regional detection, characterization, and attribution of annual forest change from 1984 to 2012 using Landsat-derived time-series metrics. **170**: 121-132.
23. Kennedy, R.E., Z. Yang, J. Braaten, *et al.* (2015). Attribution of disturbance change agent from Landsat time-series in support of habitat monitoring in the Puget Sound region, USA. **166**: 271-285.
24. Oeser, J., D. Pflugmacher, C. Senf, *et al.* (2017). Using intra-annual Landsat time series for attributing forest disturbance agents in Central Europe. **8**(7): 251.
25. Meddens, A.J., C.A. Kolden, and J.A.J.R.S.o.E. Lutz. (2016). Detecting unburned areas within wildfire perimeters using Landsat and ancillary data across the northwestern United States. **186**: 275-285.
26. Huo, L.-Z., L. Boschetti, and A.M. Sparks. (2019). Object-Based Classification of Forest Disturbance Types in the Conterminous United States. **11**(5): 477.
27. Jun, C., Y. Ban, and S. Li. (2014). Open access to Earth land-cover map. Nature. **514**(7523): 434-434.
28. Lizundia-Loiola, J., G. Oton, R. Ramo, *et al.* (2020). A spatio-temporal active-fire clustering approach for global burned area mapping at 250 m from MODIS data. Remote Sensing of Environment. **236**.
29. Farr, T.G., P.A. Rosen, E. Caro, *et al.* (2007). The shuttle radar topography mission. Reviews of Geophysics. **45**(2).
30. 
31. Mahmood, T., S. Mirza, S. Gulzar, *et al.* (2020). Pakistan's Timberline Forest Ecosystem Dynamics vis-a-vis Changing Climate Across Three Provinces (KPK, AJK and GB) Using GIS/RS Techniques. Revista de Chimie. **71**: 86-98.
32. Bhuiyan, C., A.K. Saha, N. Bandyopadhyay, *et al.* (2017). ADVANCES IN REMOTE SENSING AND GIS-BASED DROUGHT MONITORING Analyzing the impact of thermal stress on vegetation health and agricultural drought - a case study from Gujarat, India. Giscience & Remote Sensing. **54**(5): 678-699.
33. Ullah, Z., S. Mahmood, Z. Iqbal, *et al.* (2021). Damages to Himalayan White Pine (Pinus wallichiana) by Asiatic Black Bear (Ursus thibetanus) in Kaghan Valley, Pakistan. Forests. **12**(8).
34. Ahmad, A. and S.M. Nizami. (2015). Carbon stocks of different land uses in the Kumrat valley, Hindu Kush Region of Pakistan. Journal of Forestry Research. **26**(1): 57-64.
35. Ahmad, R., B. Hussain, and T. Ahmad. (2021). Fresh and dry fruit production in Himalayan Kashmir, Sub-Himalayan Jammu and Trans-Himalayan Ladakh, India. Heliyon. **7**(1).

36. Shah, S. and D.P. Sharma. (2015). Land use change detection in Solan Forest Division, Himachal Pradesh, India. Forest Ecosystems. **2**(1): 26.
37.
38. Tomar, J.S., N. Kranjcic, B. Durin, *et al.* (2021). Forest Fire Hazards Vulnerability and Risk Assessment in Sirmaur District Forest of Himachal Pradesh (India): A Geospatial Approach. Isprs International Journal of Geo-Information. **10**(7): 19.
39. Chettry, V. and M. Surawar. (2021). Assessment of urban sprawl characteristics in Indian cities using remote sensing: case studies of Patna, Ranchi, and Srinagar. Environment Development and Sustainability. **23**(8): 11913-11935.
40. Prasad, R., S. Maithel, and A. Mirza. (2001). Renewable energy technologies for fuelwood conservation in the Indian Himalayan region. Sustainable Development. **9**(2): 103-108.
41. Uniyal, S.K. and R.D. Singh. (2012). Natural resources assessment and their utilization Analyses from a Himalayan state. Environmental Monitoring and Assessment. **184**(8): 4903-4919.
42. Reddy, C.S. and K.R.L. Saranya. (2017). Earth observation data for assessment of nationwide land cover and long-term deforestation in Afghanistan. Global and Planetary Change. **155**: 155-164.
43. Kanwar, N. and J.C. Kuniyal. (2022). Vulnerability assessment of forest ecosystems focusing on climate change, hazards and anthropogenic pressures in the cold desert of Kinnaur district, northwestern Indian Himalaya. Journal of Earth System Science. **131**(1).
44. Gardner, J.S. (2002). Natural hazards risk in the Kullu District, Himachal Pradesh, India. Geographical Review. **92**(2): 282-306.
45. Khan, N., S.J. Shah, T. Rauf, *et al.* (2019). Socioeconomic Impacts of the Billion Trees Afforestation Program in Khyber Pakhtunkhwa Province (KPK), Pakistan. Forests. **10**(8).
46. Rizvi, R.H., S.K. Dhyani, R.S. Yadav, *et al.* (2011). Biomass production and carbon stock of poplar agroforestry systems in Yamunanagar and Saharanpur districts of northwestern India. Current Science. **100**(5): 736-742.
47. Haughan, A.E., N. Pettorelli, S.G. Potts, *et al.* Determining the role of climate change in India's past forest loss. Global Change Biology.
48. Meiyappan, P., P.S. Roy, Y. Sharma, *et al.* (2017). Dynamics and determinants of land change in India: integrating satellite data with village socioeconomics. Regional Environmental Change. **17**(3): 753-766.
49. Bacha, M.S., M. Muhammad, Z. Kilic, *et al.* (2021). The Dynamics of Public Perceptions and Climate Change in Swat Valley, Khyber Pakhtunkhwa, Pakistan. Sustainability. **13**(8).
50. Li, Y., Z. Wu, X. Xu, *et al.* (2021). Forest disturbances and the attribution derived from yearly Landsat time series over 1990-2020 in the Hengduan Mountains Region of Southwest China. Forest Ecosystems. **8**(1).

# Using 'Big Data' to Measure Desertification for SDG Target 15.3

GRAINGER Alan

School of Geography, University of Leeds, Leeds LS2 9JT, UK.

email: a.grainger@leeds.ac.uk

## 1. INTRODUCTION

Since drylands cover such a large proportion of global land surface area, accurate measurements of the extent and rate of change of desertification are essential to monitor compliance with the Land Degradation Neutrality (LDN) Target 15.3 of the Sustainable Development Goals (SDGs). Owing to the limited amount of national measurement of desertification, previous research has strongly recommended the use of 'big data', and particularly satellite data, to monitor national and global compliance with the LDN Target [1].

## 2. MATERIALS AND METHODS

This presentation, based on research published earlier this year [2], outlines a set of seven rules for constructing reliable information about global environmental change phenomena through planetary measurement: (i) define a phenomenon clearly and appropriately; (ii) specify the minimum number of attributes to measure, to completely characterize a phenomenon; (iii) disaggregate measurement of a phenomenon, to represent the full diversity of its spatial distribution; (iv) minimize spatial systematic errors, by using sensors whose spatial resolution matches the areal variability of a phenomenon and whose spectral resolution matches its most distinctive property; (v) minimize temporal systematic errors, by choosing a monitoring frequency consistent with the turnover time of a phenomenon; (vi) minimize the systematic and random errors associated with the method used to classify satellite images; and (vii) minimize the systematic and random errors associated with the algorithm used to combine estimates of the various attributes of a phenomenon. It then uses these rules to critically evaluate previous proposals for using big data to monitor compliance with the LDN Target.

## 3. RESULTS

The presentation will report four main findings. First, previous proposals have neglected to mention that existing global information on desertification is inadequate. Second, existing reviews of research in this field give the impression that the potential for using big data to measure the actual status of land degradation for the SDGs has been extensively evaluated, but this is not supported by the evidence. Indeed, some of the papers cited only estimate the potential hazard of desertification rather than its actual status. Third, of the 3 papers whose proposed methods can be evaluated, all three are underspecified, two are not fully disaggregated, and two use proxy indicators only loosely linked to the ideal variables for measuring particular attributes of land degradation. Fourth, it is possible to use big data to measure desertification, though until remote sensing methods are devised to monitor two of the seven attributes of desertification - wind erosion and soil compaction - estimates will remain underspecified.

## References

[1] Allen C., Smith M., Rabiee M. and Dahmm H., 2021. A review of scientific advancements in data sets derived from big data for monitoring the Sustainable Development Goals. *Sustainability Science* **16**: 1701–1716.

[2] Grainger A., 2022. Are global environmental uncertainties inevitable? Measuring desertification for the SDGs. *Sustainability* **14**, 4063.

# Research on sensitive parameters of oil species identification based on microwave experiment

MA Jing [1,2,3], GUO Jie [1,2]

[1] CAS Key Laboratory of Coastal Environmental Processes and Ecological Remediation, Yantai Institute of Coastal Zone Research, Chinese Academy of Sciences, Yantai Shandong 264003, P.R. China;
email: jma@yic.ac.cn

[2] Shandong Key Laboratory of Coastal Environmental Processes, Yantai Shandong 264003, P.R. China;
email: jguo@yic.ac.cn

[3] University of Chinese Academy of Sciences, Beijing, 100049, China

## 1. INTRODUCTION

The development of maritime trade and the development and transportation of offshore oil resources have increased the number of marine oil spill pollution accidents. In order to minimize the environmental impact of oil spills, it is necessary to take rapid emergency response to deal with oil spills. Correctly identifying the types of oil spills is of great significance for quick disposal of oil spills[1].Satellite remote sensing technology has a wide range of dynamic observation capabilities, and SAR plays a major role in the process of remote sensing monitoring of oil spills on the sea surface with its all-day, all-weather advantages[2].SAR relies on the backscattering formed by the roughness of the sea surface to image. The oil film on the sea surface suppresses the capillary gravitational waves on the sea surface and reduces the roughness of the sea surface, thereby weakening the backscattering and forming dark spots on the SAR image[3].The damping effect of the oil film depends on the physical properties of the oil film, and the damping caused by different oil films is also different[4].Based on this theory, scholars have carried out research on oil species identification based on SAR.

This paper selects four kinds of oils: diesel, crude oil, oil-water mixture and palm oil, and carried out the C-band full polarization scatterometer oil spill observation experiment. The sensitive characteristic parameters of microwave identification of oil film were explored and applied to SAR images obtained from offshore oil film experiments for oil species identification.

## 2. MATERIALS AND METHODS

### *2.1 Experimental oil and instruments*

Four kinds of oil were selected for the experiment, namely (1) diesel oil; (2) crude oil, whose asphalt content was 0.73% and density was 0.92 g/mL; (3) oil-water mixture; (4) palm oil, whose density was 0.85 g/mL. This experiment is located in the oil boom set up in the land-based seawater pool (45 m×40 m×2 m) of Nanjiang Wharf in Laoshan District, Qingdao. The size of the oil boom area is 6.8 m×3.2 m, C-band full-polarization scatterometer (VV, HH, VH/HV polarization) is set on the steel plate platform beside the pool, and scans at 5°intervals within the range of 25°-60°incident angle.

### *2.2 Experimental process*

The time of this field experiment is from September 26th to September 29th, 2021. After measuring the seawater temperature on September 26th, the C-band full polarization scatterometer was used to first scan the NRCS(Normalized Radar Cross Section) of the seawater, and then pour diesel oil into the oil boom in 12 times with oil temperature measurement. After the diesel test is completed, clean the oil film. NRCS measurements for other oils are similar to diesel.

### *2.3 Characteristic Parameters*

Polarization difference (PD) is the difference between the NRCS of VV polarization and HH polarization , and the calculation formula is shown in (1). The PD value is greatest when the sea surface is clean, and gradually decreases as the impact of oil spills increases [5].

$$PD = \sigma_{VV}^{0} - \sigma_{HH}^{0} \qquad (1)$$

Damping Ratio (DR) can quantitatively describe the damping effect of oil film on ocean wave spectrum, and is defined as the ratio of NRCS for oil-free seawater and for the oil-covered sea surface, and its calculation formula is shown in (2).

$$DR = \sigma^{0,\mathrm{Water}} / \sigma^{0,Oil} \qquad (2)$$

Polarization Ratio (PR) is the ratio of NRCS for HH polarization and for VV polarization. The calculation formula is shown in (3).

$$PR = \frac{\sigma_{HH}^{0}}{\sigma_{VV}^{0}} \qquad (3)$$

where $\sigma_{VV}^{0}$ –NRCS of VV polarization, $\sigma_{HH}^{0}$ –NRCS of HH polarization, $\sigma^{0,Water}$ –NRCS for oil-free water surface , $\sigma^{0,,\mathrm{Oil}}$ –NRCS for oil-covered water surface.

## 3. RESULTS

### *3.1 Variation analysis of oil film characteristic parameters*

Taking 30 °incidence angle as an example, the calculation of each characteristic parameter is shown in the figure 1. As a derivative of crude oil, the PD value of diesel oil is close to that of crude oil, and the PD value of palm oil is quite different from other oil films, which can be effectively distinguished. The PR values of the four types of oil films are close, and there is no significant difference. Similar to PD, the DR values of diesel and crude oil are close, and the DR value of palm oil is the smallest. Due to the influence of emulsification and environmental factors, the NRCS increased, and the DR of the oil-water mixture showed a larger trend of increasing.

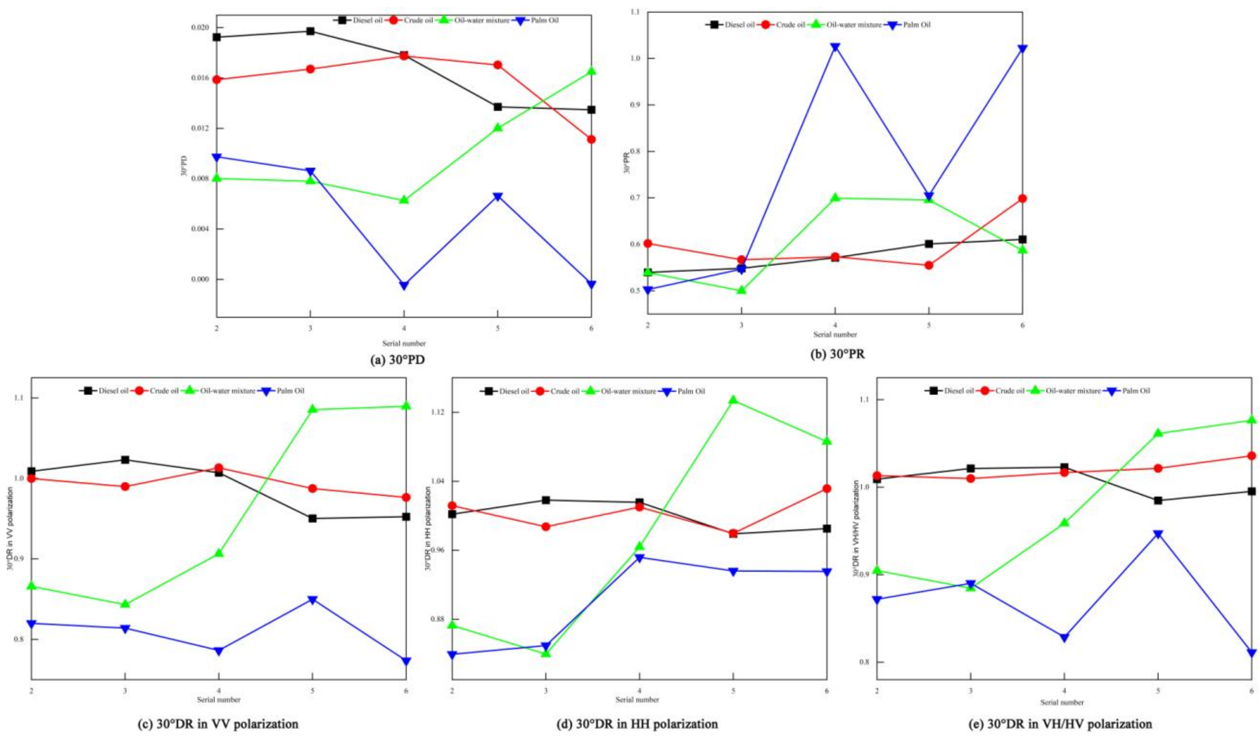


Figure.1 Parameter variation of different sequences at 30 °incident angle

### *3.2 Mean statistics of characteristic parameters*

The mean value of each parameter under the incident angle of 30 °is calculated, and the result is shown in Figure 2. It can be seen from the figure that the PD values of diesel and crude oil are similar, but there are differences between the PD values of crude oil, oil-water mixture and palm oil, which have the potential to distinguish. The DR in different polarization is different between palm oil and mineral oil, and the difference of mean value between mineral oil in VH/HV polarization is large. The palm oil of PR is the largest, and the difference between it and mineral oil is large.

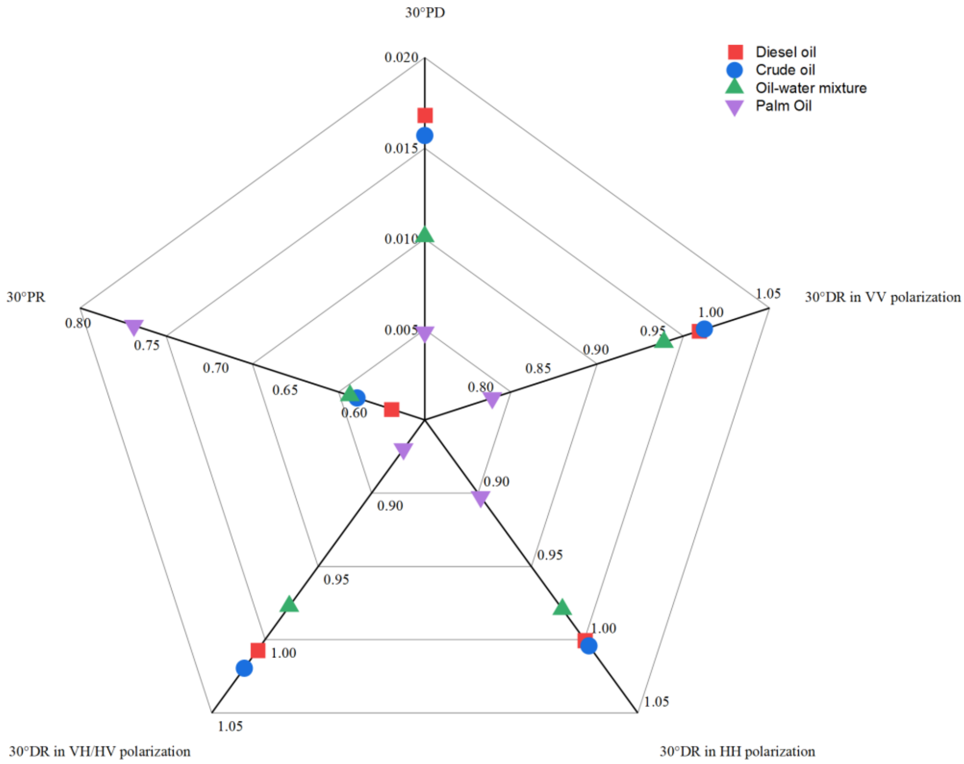


Figure.2 Mean of different parameters at 30 °incidence angle

## 4. SUMMARY

It can be seen from the field experiments that PD is more effective for the identification of crude oil, emulsified oil and plant oil, DR is effective for the identification of plant oil and mineral oil, and DR in VH/HV polarization is effective for the identification of crude oil and emulsified oil. This conclusion is applied to the spaceborne SAR image to verify the validity of the oil species identification.

## ACKNOWLEDGEMENT

This work was supported by National Natural Science Foundation of China, No.42076197 and NSFC-Shandong Joint Fund, No.U2106211, Shandong United Key Fund, U1906217.

## References

[1]Lu Yingcheng, Liu Jianqiang, Ding Jing, et al. (2019) Optical remote identification of spilled oils from the SANCHI oil tanker collision in the East China Sea, Chinese Science Bulletin, 64(31):3213-3222.
[2]Xu Chenqi, Guo Jie, Yang Qixia, et al. (2021) Identification of crude oil and emulsified crude oil based on microwave scattering experiment, Marine Sciences, 45(04): 13-21.
[3]Li Yu, Chen Jie, Zhang Yuanzhi. (2019) Progress in Research on Marine Oil Spills Detection Using Synthetic Aperture Radar, Journal of Electronics & Information Technology, 41(03): 751-762.
[4]Zheng H, Zhang J, Khenchaf A, et al, 2021. Study on Non-Bragg Microwave Backscattering from Sea Surface Covered with and without Oil Film at Moderate Incidence Angles[J]. Remote Sensing, 13(13).

# Effects of land cover change on water heat fluxes in the Yellow River Delta

NING Jicai, GAO Zhiqiang

Yantai Institute of Coastal Zone Research, Chinese Academy of Sciences, Yantai 264003, China
email: jcning@yic.ac.cn
email: zqgao@yic.ac.cn

## 1. INTRODUCTION

Research on climate change and water demand has increased over the past years because of dramatic environmental changes. One of the long term solutions lies in understanding of how water use efficiency can be improved to reduce wastage.1 Quantitative predictions of regional water balances, management of water resources, irrigation scheduling, and climate and weather prediction require accurate quantification of evapotranspiration (ET)[1,2]. As an essential component of the hydrologic cycle, ET drives energy and water exchanges between the hydrosphere, atmosphere, and biosphere[3]. ET is one of the fundamental parameters of the hydrologic cycle at all scales, and is influenced by many factors, such as air temperature, soil moisture, and vegetation type[4]. Accurate observation and estimation of ET are extremely important to increase our understanding of global climate change, land–atmosphere interactions, water cycle, and ecological studies[5,6]. Development of remote sensing technology has made it possible to estimate land surface evapotranspiration at the regional or basin scale[7]. Bastiaanssen et al.[8,9] developed the Surface Energy Balance Algorithm for Land (SEBAL), a remote sensing model that maps evapotranspiration, biomass growth, water deficit, and soil moisture. The SEBAL model is based on the surface energy balance equation and has been widely used.

The Yellow River Delta (YRD) has received increasing attention from scientists, engineers, and environmental planners, because of its critical role in wildlife protection, energy production, and agriculture. Like many of the large deltas around the world, the YRD is facing increasing risks of degradation due to anthropogenic and natural forces. With the expansion of reclamation activities, natural systems, especially wetland ecosystems, in the Yellow River Delta area have been suffering from severe disturbances in recent years[10,11]. The objective of this article is to examine how ET responded to changes in land cover in the Yellow River Delta over the past 30 years based on a map of the ET distribution retrieved using the SEBAL model.

## 2.MATERIALS AND METHODS

### *2.1 Data*

Landsat images of the same day in different years were selected as the data source for a comparative study of ET and vegetation indexes in the Yellow River Delta. To obtain better inversion results, images from the dry season were selected and combined with data of local meteorological conditions. We used Landsat 5 TM (June 5, 1986) and Landsat 8 OLI/TIRS (June 5, 2015) data (from the USGS http://earthexplorer.usgs.gov/). After atmospheric and radiometric correction to remove data noise, the remote sensing data were used as basic source data for the retrieval of LST and ET. Meteorological data including temperature, wind speed, relative humidity, and precipitation was obtained from fourteen internal and peripheral meteorological stations from the China Meteorological Data Network (http://data.cma.cn/). All data were geo-referenced to a common UTM coordinate system (WGS_1984_UTM_Zone_50N) and re-sampled using a nearest neighbor algorithm with a pixel size of 30 m × 30 m. Atmospheric correction of Landsat TM/ETM data should be carried out by combining a look-up table (LUT) and dark-object method (DOM), in order to obtain accurate reflectance data[12].

***2.2 Retrieval of LST***

The development of the mono-window algorithm for LST retrieval from the thermal band data of Landsat TM/ETM is based on the premise that the at-satellite brightness temperature can be computed from the thermal band. According to the radiance transfer equation, Taylor's expansion to the Planck function has to be applied. Qin et al. derived an approximate expression for LST retrieval, suitable for the thermal bands of TM/ETM+ data by simplifying the relationship between radiance and brightness temperature using a linear regression, as expressed below[13]:

$$T_s = \{a_6(1-C_6-D_6)+[b_6(1-C_6-D_6)+C_6+D_6]T_6-D_6T_a\}/C_6 \quad (1)$$

in which $T_s$ is the LST [K]; $T_6$ is the brightness temperature [K] (band 6 for Landsat 5, band 10 for Landsat 8); $a_6$ and $b_6$ are the regression coefficients between $T_6$ and $C_6$; and $T_a$ is the average effective mean atmospheric temperature [K]. In practice, the possible temperature range of LST is 0–70 ℃, $a_6$ = −67.35535 and $b_6$ = 0.458608.

***2.3 Retrieval of ET***

The SEBAL model, which is designed based on traditional surface heat balance equations, can integrate multi-source and multi-sensor data to estimate land surface water and heat fluxes, employing the advantages of remote-sensing technologies. The equations are based on the theory that incoming net solar radiation drives all energy exchanges on the Earth's surface. The surface energy balance equation is as follows[14]:

$$LE = Rn - G - H \quad (2)$$

where LE is the latent heat flux [W $m^{-2}$]; Rn is the net radiation [W $m^{-2}$]; G is the soil heat flux [W $m^{-2}$]; and H is the sensible heat flux [W $m^{-2}$]. As one of the residual methods of the energy budget, the SEBAL model was developed based on the energy balance principle and aerodynamic turbulence theory.

In Eq. (2), the net radiation, which is the summation of soil heat flux, sensible heat flux, and latent heat flux, can be calculated based on the land surface radiation as follows:

$$R_n = (1-\alpha)R_s\downarrow + \varepsilon_s\sigma(\varepsilon_a T_a^4 - T_s^4) \quad (3)$$

where $R_s\downarrow$ is the incident solar short-wave radiation, also known as the total solar radiation [$\mathrm{W\,m^{-2}}$]; $\alpha$ is the surface albedo [dimensionless]; $\varepsilon_s$ is the surface emissivity [dimensionless]; $\sigma$ is the Stefan–Boltzmann constant [$5.6696\times10^{-8}\mathrm{W\,m^{-2}\,K^{-4}}$]; $T_s$ is the LST [K], retrieved from remote-sensing data; $T_a$ is the air temperature [K] of reference height [Z2]; and $\varepsilon_a$ is the atmospheric emissivity [dimensionless], which can be calculated by an empirical formula. In this study, we followed the evaporative fraction method to extend the calculation from instantaneous ET to daily ET.

$$ET_{24} = 24\times60\times60\times\Lambda_{24}\times\frac{R_{n24}-G_{24}}{\lambda\cdot\rho_w}\times10^3 \quad (4)$$

Where $R_{n24}$ is the 24 h net radiation [W $m^{-2}$]; G is the 24 h soil heat flux [W $m^{-2}$]; $\rho_w$ is the density of water [1.0×103kg $m^{-3}$], $\lambda$ is the latent heat of water vapor [$\lambda = [2.501-0.00236(T_s-273.15)]\times10^6, \mathrm{J\,Kg^{-1}}$], $\Lambda_{24}$ is the 24 h average evaporative fraction, which is approximately equal to the instantaneous evaporative fraction Λ. Λ can be calculated by:

$$\Lambda = \frac{LE}{R_n - G} \quad (5)$$

Where LE, $R_n$ , and G are variable explained above.

***2.4 Calculation of FVC***

Fractional Vegetation Cover (FVC) is an important biophysical parameter describing vegetation quality and reflecting ecosystem changes. It is also a controlling factor in transpiration, photosynthesis, and other terrestrial processes. The calculation of FVC is based on NDVI values, which may be calculated using spectral reflectance data. FVC was computed as expressed below:

$$FVC = \frac{NDVI - NDVI\max in}{NDVI\max ax - NDVI} \times 100\% \tag{6}$$

where $FVC$ is the fractional vegetation cover [%]; Normalized Difference Vegetation Index (NDVI) is the NDVI value at each pixel [dimensionless]; $NDVI\,max$ is the NDVI value that corresponds to 100% vegetation cover [dimensionless]; and $NDVI\,min$ is the NDVI of bare soil [dimensionless].

## 3.RESULTS

### *3.1 Analysis of the Spatial-Temporal Pattern of ET*

Daily ET was determined using the SEBAL model (Fig. 1). It can be seen from the profile that the daily ET first decreases and then increases inwards from the coast. This was closely related to the spatial distribution of land cover types. High ET values occurred in the salterns and culture ponds in the coastal region because of sufficient water sources. In the large farmland areas in the inland region, high vegetation cover contributed to high evapotranspiration. Most of the transitional zones between the farmland and culture ponds were less developed grassland and saline-alkali land, therefore the evapotranspiration was low in these areas. Compared to 1986, 2015 saw an increase in ET, suggesting that with increasing development, the salterns and culture ponds increased in area, while the saline-alkali land cover decreased. As a result, the overall regional ET increased. It was concluded that land use changes affected the variation in ET.

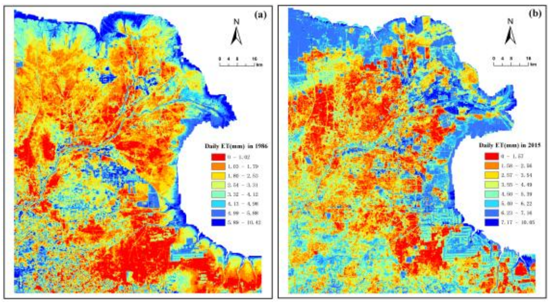

**Fig. 1.** Daily ET distribution maps in (a) 1986 and (b) 2015.

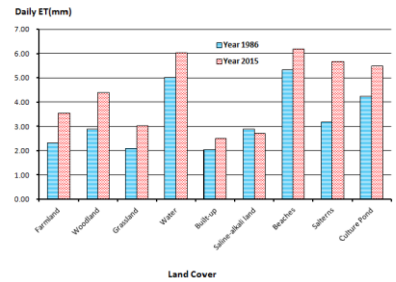


**Fig. 2.** Daily ET values for different land covers.

Different land cover structures affected every aspect of evapotranspiration, therefore ET changed due to the difference in land cover type. It was evident from Fig. 1 that ET was high for the water region, salterns, culture ponds, and beaches, and this was closely related to adequate water supply. By contrast, ET was low in the built-up region, saline-alkali land, and grassland, because most energy was lost through sensible heat exchange. Comparing ET values for different land cover types showed a similar pattern for each year, suggesting that daily ET was closely related to land cover type (Fig. 2). Nearly every land cover type had a higher daily ET in 2015 than in 1986. An analysis of the LST indicated that a higher LST in 2015 enhanced the heat exchange and thus increased the ET values.

### *3.2 Analysis of Land Cover Effects on ET*

The analyses above indicated that there was a close correlation between LST and ET. We overlaid LST and ET distribution maps and developed a linear regression for LST and ET. LST was discretized in 1-degree intervals, and the average evapotranspiration value for a certain temperature was calculated by determining the spatial overlap of the ET distribution map. A close, negative correlation existed between LST and ET (Fig. 3). When the surface temperature increases, the sensible heat flux prevails in the surface energy balance causing less ET. Similarly, when the surface temperature decreases, the cooling effect of the latent heat is apparent due to higher ET. The correlation coefficient was -0.9868 in 1986 and -0.9752 in 2015.

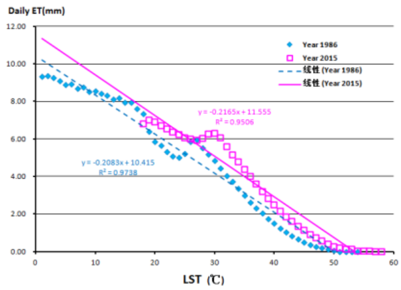

**Fig. 3.** Correlation between daily ET and LST.

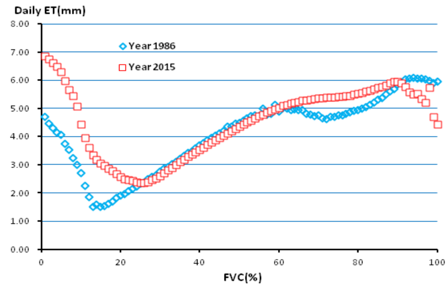

**Fig. 4.** Scatter plots between the mean daily ET and the FVC.

A linear solution to ET and LST for the two years can help derive their linear equations. These two equations had nearly the same slope and similar intercepts, and R2 values were 0.9738 and 0.951, respectively. A synthesis of the data for both years resulted in the following linear equation for LST and ET [p=0.00018].

$$ET=-0.2326LST+11.595 \quad (R^2=0.9588) \qquad (7)$$

where ET denotes daily evapotranspiration [mm], and LST denotes land surface temperature [°C]. Eq. 7 can be used for approximate calculation of daily ET if there is a lack of data for ET calculation, and LST values are available. Land cover status affects the distribution of LST and influences the spatial distribution of ET. We used FVC to research the relationship between ET and land cover types. We overlaid maps of ET distribution and FVC at 1% intervals, as shown in Fig. 4.

FVC was closely related to LST, as well as to daily ET (Fig. 4). An FVC value of 14% was the inflection point in 1986 (25% in 2015). Daily ET and FVC were negatively correlated when FVC was between 1% and 14% in 1986 (1% and 25% in 2015), and the correlation coefficient was -0.99 in 1986 (-0.96 in 2015). Daily ET and FVC were positively correlated when FVC was between 14% and 94% in 1986 (26% and 90% in 2015), and the correlation coefficient was 0.95 in 1986 (0.97 in 2015). When the FVC value exceeded 94% in 2015, daily ET and FVC were negatively correlated.

## 4.SUMMARY

From 1986 to 2015, the overall land area increased by 205.81 km$^2$ in the Yellow River Delta due to sea-land interaction and the influence of sediment deposition by the river. The analysis of land cover change indicated that compared with 1986, 3,947.22 km$^2$ of land cover changed in 2015, accounting for 35.03% of the total land area in 1986.Different types of land covers were converted in different ways. Despite an increase in the total area, large areas of farmland and grassland were converted into salterns and culture ponds. The diversity of wetland conversion demonstrated the fragility of wetland ecosystems. The development of saline-alkali land was one of the major types of land cover conversion in the area. Overall, land cover conversion occurred mainly from less developed into highly developed land cover types.

Land use and land cover affect ET, but there are differences in ET for different vegetation and land cover types. ET can be adequately determined at leaf and plant levels; however, ET is one of the least understood aspects of the hydrologic cycle at large scales. This is, in part, due to the difficulty associated with assessing ET at a regional scale. For a given spatial-temporal condition, there is a close relationship between vegetation index and ET. However, a vegetation index is a reflection of vegetation form, structure, soil regime, and other relevant essential factors, and specific site conditions should be taken into consideration when vegetation indices are used for assessing changes in ET. In this study, we only discussed the linear relationship between evapotranspiration and surface temperature, and the correlation between FVC and evapotranspiration. Many additional complicating factors can affect the results.

## References

[1] Jiang L., et al., (2009) A satellite-based daily actual evapotranspiration estimation algorithm over South Florida, Global & Planetary Change, 67(1):62-77.

[2] Mu Q., Zhao M., Running S. W., (2011) Improvements to a MODIS global terrestrial evapotranspiration algorithm, Remote Sensing of Environment, 115(8):1781-1800.

[3] Katul G. G. et al., (2012) Evapotranspiration: A process driving mass transport and energy exchange in the soil plant atmosphere climate system, Reviews of Geophysics, 50(3):185-201.

[4] McMahon T., et al., (2013) Estimating actual, potential, reference crop and pan evaporation using standard meteorological data: A pragmatic synthesis, Hydrology and Earth System Sciences 17(11):4503-4503.
[5] W. J. Shuttleworth, Putting the 'vap' into evaporation, Hydrology & Earth System Sciences 11(1), 210-244 (2007).
[6] Wang K., Dickinson R. E., (2012) A Review of Global Terrestrial Evapotranspiration: Observation, Modeling, Climatology, and Climatic Variability, Reviews of Geophysics, 50(2):93-102.
[7] Yang J. Y., et al., (2015) Water consumption in summer maize and winter wheat cropping system based on SEBAL model in Huang-Huai-Hai Plain, China, Journal of Integrative Agriculture, 14(10):2065-2076.
[8] Bastiaanssen et al. W. G. M., (1998) A remote sensing surface energy balance algorithm for land (SEBAL) - 1. Formulation, Journal of Hydrology, 212: 198-212.
[9] Bastiaanssen W. G. M. et al., (1998) The surface energy balance algorithm for land (SEBAL): part 2 validation, Journal of Hydrology, 212(98):801-811.
[10] Jin Y. W., et al., (2016) Effects of seashore reclamation activities on the health of wetland ecosystems: A case study in the Yellow River Delta, China, Ocean & Coastal Management, 123:44-52.
[11] Bi N. H., Wang H. J., Yang Z. H., (2014) Recent changes in the erosion-accretion patterns of the active Huanghe (Yellow River) delta lobe caused by human activities, Continental Shelf Research 90:70-78.
[12] Liang S., Fang H., Chen M., (2001) Atmospheric correction of Landsat ETM+ land surface imagery-Part I: Methods, IEEE Transactions on Geoscience & Remote Sensing, 39(11):2490-2498.
[13] Qin Z., et al., (2001) Mono-window Algorithm for Retrieving Land Surface Temperature from Landsat TM6 data, Acta Geographica Sinica, 56(4):456-466.
[14] Gao Z. Q., et al., (2011) A coupled remote sensing and the Surface Energy Balance with Topography Algorithm (SEBTA) to estimate actual evapotranspiration over heterogeneous terrain, Hydrology and Earth System Sciences, 15(1): 119-139.

# Digital Technology: Digital Transformation Changing the World

# Remote Sensing Ore-prospecting Using the Improved Computer Vision Methodology in the Northern Altun Mountain,China

Qinjun Wang[1,2,3,4], Jingjing Xie[1,2,3], Peng Liu[1,2,3], Dingkun Chang[1,2,3], Zhichao Li[4]

[1] International Research Centre of Big Data for Sustainable Development Goals, China;

wangqj@radi.ac.cn(Q.W.); xiejingjing19@mails.ucas.ac.cn (J.X.); liup@aircas.ac.cn(P.L.); changdingkun20@mails.ucas.ac.cn (D.C.); 1006320484@qq.com(Z.L.)

[2]Key Laboratory of Digital Earth Science, Aerospace Information Research Institute, Chinese Academy of Sciences (CAS), China;

[3]Yanqi Lake Campus of University of Chinese Academy of Sciences, China;

[4]Key Laboratory of the Earth Observation of Hainan Province, Hainan Aerospace Information Research Institute, China

## 1. ABSTRACT

Accurate extraction of ore-indicating info is the key to improve the accuracy of remote sensing ore prospecting. However, due to the influence of spatial and spectral resolution, there are two problems existed in the remote sensing ore-prospecting: (1) the weak ore-indicating info is easy to be omitted; (2) spectral indexes are easy to enhance non-mineralized objects, such as shadows. To solve these two problems, this paper proposed an improved computer vision methodology and made two innovations: (1) using the spectral distance to replace the orientations difference to make the extracted results focused on a target. The results showed that its accuracy was 96.5% and thus improving the ability of ore-indicating info extraction; (2) a remote sensing ore-prospecting model named "rock masses + structures + altered minerals" in the Northern Altun Mountain was established to predict 28 prospecting areas. Field verification on the Hongliugou prospecting area in Xinjiang province, China showed that the model was effective in the delineation of the prospecting areas and thus providing a reference for remote sensing ore-prospecting in "high altitude, deep cutting and uninhabited mountainous areas".

## 2. INTRODUCTION

Mineral resources are the basic materials for the sustainable development of national economy and society. Therefore, the exploration of mineral resources plays an important role in national economic development. Before the appearance of satellite remote sensing, they were mainly investigated using the airborne magnetometers, gravimeters and field investigation. These data laid a solid foundation for people to carry out mineral resources exploration in the future.

Since the appearance of satellite remote sensing in the 1970s, it has been used in the mineral resource explorations. It is a technical means to extract the ore-indicating info in the study area by remote sensing with the characteristics of non-contact detection, macroscopic, multi-spectral and multi-spatial resolution. Since the late 1980s, remote sensing ore-prospecting works based on airborne imageries have been carried out. Minerals have been directly identified according to their remote sensing features. For example, in the 1980s, Chile used aerial photography to interpret mineralized alteration zones and discovered Martai and Lobo gold mines. From the late 1990s to the beginning of the 21st century, the resource remote sensing satellites developed quickly. In 1999, Japan launched the TERRA satellite with the advanced spaceborne thermal emission and reflection radiometer (ASTER). It has the highest spatial resolution of 15m and has been widely used in remote sensing ore-prospecting by setting the sensitive bands to mineral resources in the near-infrared and short-wave infrared wavelengths (Q. J. Wang, 2006; S. L. Chattoraj et al., 2020). In 2000, the United States launched the Earth Observation Satellite 1, which carried the Hyperion sensor and marked the remote sensing ore-prospecting entering the satellite hyperspectral era. In addition to hyperspectral remote sensing satellite, the United States also launched IKONOS, QuickBird, Worldview, Geoeye and other high spatial resolution satellites in about 2000, which opened the sub-meter remote sensing ore-prospecting era (Y. Q. Sun, et al., 2017). In about 2000, China launched the resource satellite series, such as the China-Brazil Earth Resources Satellites (CBERS) and applied them to ore-prospecting successfully (X. F. Dong et al., 2020).

With the rapid development of remote sensing satellites, remote sensing ore-prospecting technologies also developed significantly. Because of the difficulty in acquiring hyperspectral data, multispectral remote sensing imageries are still the main data sets in the remote sensing ore-prospecting.

In multispectral remote sensing, the commonly used methods, such as band ratios are easy to enhance the non-mineralized info, such as shadows, which interfere seriously with the effects of mineralized info extraction (T. T. Sun, 2020).

How to introduce the computer vision methodology into the intelligent ore-indicating info extraction becomes the key to improve the accuracy of remote sensing ore-prospecting. The computer vision model proposed by Itti et al. in 1998 is a bottom-up visual attention model based on "feature integration theory". Its basic principle is to extract the intensity, colors, and directions of the input imagery under different scales. A centre-surround operator is used to make the saliency map, and the winner-take-all competition mechanism in biology is also used to extract the saliency objects from the imagery (L. Itti et al., 1998).

However, the ore-indicating info, such as the altered minerals, is so weak in the remote sensing imageries that it is difficult to be highlighted using the traditional computer vision methodology. Therefore, improving the computer vision methodology to make it suitable for ore-indicating info extraction becomes a problem to be solved in the intelligent ore-prospecting.

## 3. MATERIALS AND METHODS

### *2.1 The study area*

As shown in Fig.1., the study area is located in the Ruoqiang County, southeastern Xinjiang province, China. The Xiangyun gold mine and the Beiketan gold mine are developed in this area. Besides the volcanic rocks and the tectonic zones controlling their metallogenic locations, minerals near the known ore sites, such as the silicification, limonite and potash feldspar on the ground are the ore-indicating info for detecting the gold mines (B. Wang, 2017; Y. Yang, 2003).

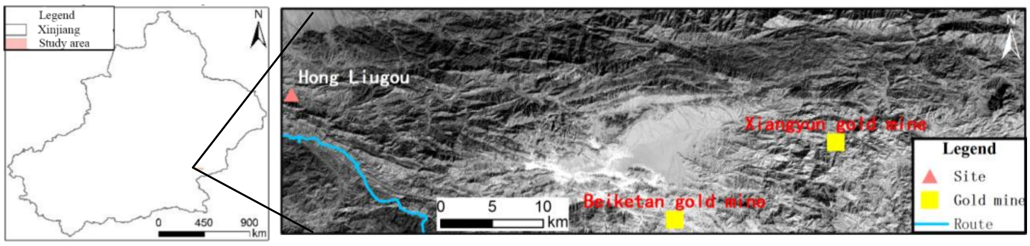


**Fig. 1.** Location map of the study area

### *2.2 Materials*

Shown in table 1, one ASTER imagery and one geological map of the Solcuri with a scale of 1:500,000 were acquired.

**Table 1.** Data list of the study area

| Data type | Name | Spatial resolution /scale |
|---|---|---|
| Geological map | Solcuri | 1:500000 |
| ASTER | AST_L1T_00303032008045010_20150523075313_97942 | 15m |

### *2.3 Methods*

#### *2.3.1 The traditional computer vision methodology*

Shown in Fig.2., Itti proposed the computer vision methodology in 1998 (L. Itti, et al., 1998). In which, the multiscale imagery features were combined into a single saliency map. A dynamical neural network then selected attended locations in the order of decreasing saliency. It broke down the complex problem of scene understanding by rapidly selecting in a computationally efficient manner.

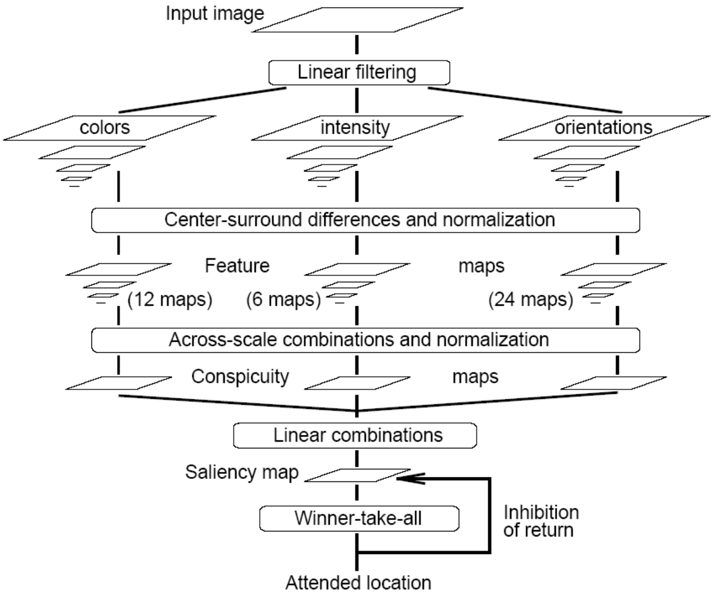


**Fig.2.** Architecture of the traditional computer vision methodology.

### *2.3.2 The improved computer vision methodology*

The principle of the traditional computer vision methodology is to make a saliency map using a center-surround operator (L. Itti, 1998). The extracted objects are usually saliency relative to surroundings, while their features cannot be determined due to the lacking of the target info. To solve this problem, this article improved the Itti's computer vision methodology by introducing the target spectrum, whose architecture is shown in Fig. 3.

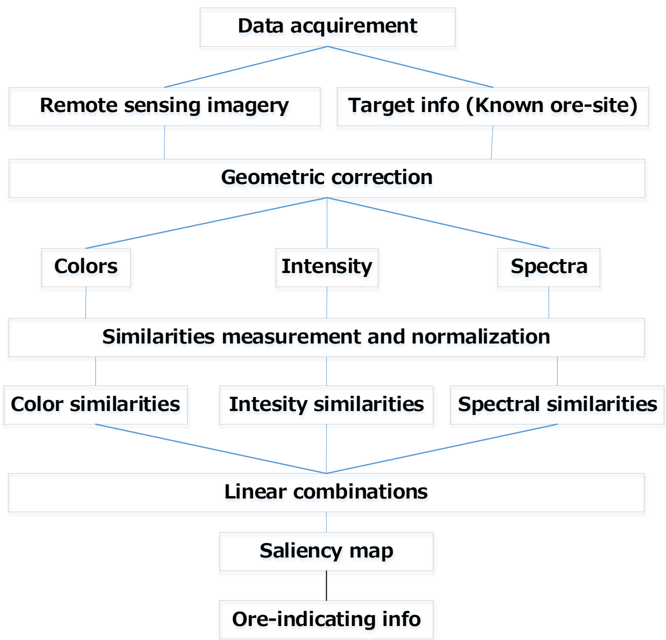


**Fig. 3.** Architecture of the improved computer vision methodology

## 4. RESULTS

Research showed that the silicification, potash feldspar, and limonite were so commonly existed in the gold mines that they could be used as the ore-indicating info in the study area. (Y. Yang, 2003). As to ASTER, band 13, band 6 and band 3 are sensitive to these altered minerals. Therefore, taking the Xiangyun gold mine as the known gold site with above altered minerals, we firstly extracted the reference spectrum with 14 bands from its location on the imagery. Then, we extracted the ore-indicating info by combining the color similarity (band 13, band 6 and band 3 of the spectrum represented R, G, B respectively), intensity similarity and spectral similarity (with 14 bands) from the reference spectrum and the pixel spectrum using the "improved computer vision methodology" and the results were shown in Fig. 4. From which, we can see that the intensity of the ore-indicating info is strong near the Xiangyun gold mine and the EW orientated faults of the northern Altun Mountain, especially at the intersections between EW orientated structures and the NE or NW orientated structures. Therefore, the intensity map of the ore-indicating info provides a good scientific evidence for delineating the prospecting areas as shown in Fig.5.

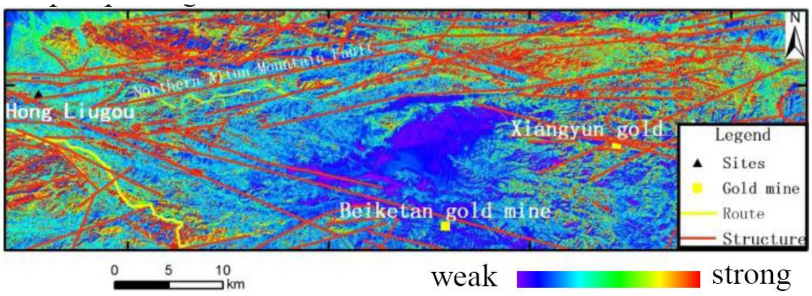


**Fig. 4.** Intensity map of the ore-indicating info

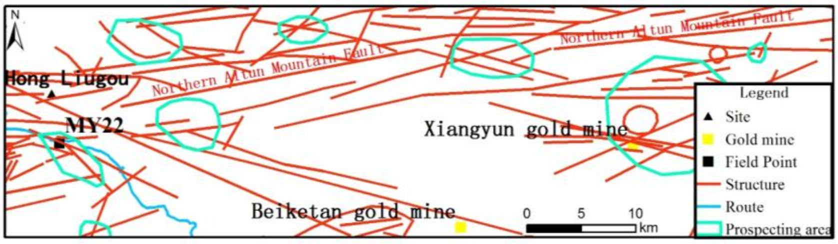


**Fig. 5.** Prospecting areas in the study area

Along the route in Fig.5, we carried out a field investigation from August 13 to 27, 2019 and found malachite and pyrite on the point of MY22, which had not yet actually been mined now in Hongliugou. Their pictures are shown in Fig. 6. In which, the blue-green colored samples on the left were the malachites and the needled yellowish-white ones on the right were the pyrites. The content of copper and arsenic was 6.3% and 28ppm respectively tested by the INNOV-X portable mineral (alloy) element analyzer C8200. Combined with the close relationship between malachite and copper, pyrite, arsenic and gold, we delineated it as the "Hongliugou copper-gold prospecting area".

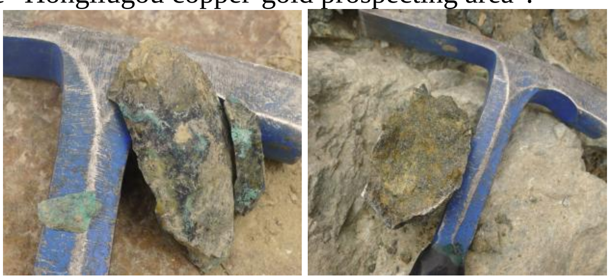

**Fig.6** Malachites and pyrites in point MY22

## References

[1] Q. J. Wang, Q. Z. Lin. (2006) A new target detection algorithm:spectral sort encoding algorithm, Geology and prospecting, 42(3):91-96,.

[2] S. L. Chattoraj, S.R.U. Prasad, P.K. Champati ray, F.D. Van der Meer, G. Arindam, A. B. Pour. (2020) Integration of remote sensing, gravity and geochemical data for exploration of Cu-mineralization in Alwar basin, Rajasthan, India, Int J Appl Earth Obs Geoinformation, https://doi.org/10.1016/j.jag.2020. 102162.

[3] Y. Q. Sun, S. F. Tian, B. G. Di. (2017) Extracting mineral alteration information using WorldView-3 data, Geoscience Frontiers, 8:1051-1062.

[4] X. F. Dong, F. P. Gan, N. Li, B. K. Yan，L. Zhang，J. Q. Zhao，J. C. Yu, R. Y. Liu, Y. N. Ma. (2020) Fine mineral identification of GF-5 hyperspectral image, Journal of Remote Sensing(Chinese), 24(4):454-464.

[5] T. T. Sun, J. Y. Si, D. L. Lu. (2020) Application of remote sensing interpretation in the Cha Xiaoma area, Qinghai, Mineral exploration, 11(1):190-194.
[6] L. Itti, C. Koch and E. Niebur. (1998)A Model of Saliency-based Visual Attention for Rapid Scene Analysis, Pattern Analysis and Machine Intelligence, IEEE Transactions on, 20:1254-1259.
[7] B. Wang. (2017)Geological and geochemical characteristics of Orogenic gold deposits in the Northern Margin of the Altun Tagh--By the example of Beiketan gold deposit, M.S. thesis, Dept. Geological engineering, China University of Geosciences (Beijing), Beijing, China.
[8] Y. Yang. (2003) Rb-Sr isotope age of the mineralization of Dapinggou gold deposits in Altun, Xinjiang geology,21(3):303-306.

# Dynamic changes of synergy and trade-off between global SDG goals from 2000 to 2020

Yue Li[1,2,3], Min Cao[1,2,3], Min Chen[1,2,3], Yuying Bai[1,2,3], Lijiao Chang[1,2,3]

[1] Key Lab of Virtual Geographic Environment, Ministry of Education of PRC, Nanjing Normal University

[2]State Key Laboratory Cultivation Base of Geographical Environment Evolution (Jiangsu Province)

[3]Jiangsu Center for Collaborative Innovation in Geographical Information Resource Development and Application

Contact Author: Min Cao, caomin@njnu.edu.cn

The 2030 Agenda for Sustainable Development proposes 17 SDGs containing 169 targets covering a wide range of social, economic and environmental areas [1]. The implementation of the 2030 Agenda needs to focus on the interlinkages between the goals and targets [2], and it is generally considered that if the promotion of one goal can contribute to the development of other goals, such a relationship is called synergy, while the opposite is considered a trade-off. Most studies currently focus on the study of synergy or trade-off relationships that exist among the 17 SDGs and 169 targets [3-4], focusing on whether there are synergy and trade-off relationships among SDGs [5] or whether there is a clear direction of interactions among goals [6-7]. Understanding the changes in synergy and trade-off relationships among SDGs and their directions can help strengthen the synergy among SDGs and inhibit the negative interactions among SDGs to help policy makers formulate reasonable policies.

We collected data on 85 indicators for 47 targets under 17 goals for 192 countries worldwide from 2000 to 2020, and normalized the data with reference to the 2021 Sustainable Development Report [8]. After testing the data for multicollinearity, we removed 6 targets and 20 indicators, taking into account the degree of certainty and credibility of the data. Based on the SDR 2021 report, the world was divided into seven sub-regions (192 countries in total), taking into account geographical location, economic income level, etc.

After the temporal smoothness test and spatial autocorrelation test, the relationship between the indicators of the explanatory variables and the indicators of the independent variables was obtained using the spatio-temporal geographically weighted regression, and the coefficient matrix of global countries from 2000 to 2020 was constructed using the spatio-temporal geographically weighted regression coefficients to describe the relationship between the SDG explanatory variables and the SDG independent variables.

The constructed spatio-temporal geographically weighted regression equation：

$$Y_i = \beta_0(u_i, v_i, t_i) + \textstyle\sum_k \beta_k(u_i, v_i, t_i) X_{ik} + \varepsilon_i \tag{1}$$

where $Y_i$ is the explanatory variable at point $i$ of the sample; $u_i$ is the longitude coordinate of point $i$; $v_i$ is the latitude coordinate of point $i$; $t_i$ is the time coordinate of point $i$; $(u_i, v_i, t_i)$ are the coordinates of the spatio-temporal dimension of point $i$ of the sample; $\beta_0(u_i, v_i, t_i)$is the constant term for point $i$ of the sample; $\beta_k(u_i, v_i, t_i)$ is the regression coefficient of the kth explanatory variable at point $i$ of the sample; $X_{ik}$ is the kth explanatory variable for point $i$ of the sample; $\varepsilon_i$ is the random error.

The centrality metric in network science provides a quantitative measure of the relative importance of different nodes. Where degree centrality provides a good reflection of the importance of a node, intermediate centrality of edges reflects the ability of the edges of two nodes to control the information transmission in the whole network. Therefore, we use degree centrality and intermediate centrality of edges to better understand the synergy and trade-off relationships among SDG goals.

The study shows that the number of synergistic goals is greater than the number of trade-offs for most countries globally in 2020, and a small number of countries such as Mongolia, Korea, and sub-Saharan Gabon have fewer synergistic targets than trade-offs and need to improve the trade-offs between goal pairs; the larger values for most OECD countries indicate that the number of synergistic goals is greater and that it is more beneficial to promote sustainable development in these countries themselves through greater cooperation (Fig 1).

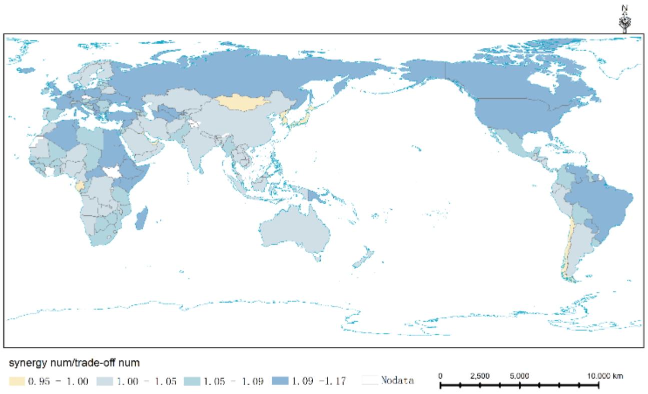


Fig.1 Spatial distribution of global synergy/trade-off quantitative ratios in 2020

The number of synergistic indicator pairs decreases in most countries in the world from 2000 to 2020, while the number of synergistic indicator pairs in China, the United States and Brazil shows a more obvious upward trend (Figure 2.a). The number of synergistic indicator pairs in Central Africa and Turkey shows a decreasing trend (Figure 2.b).

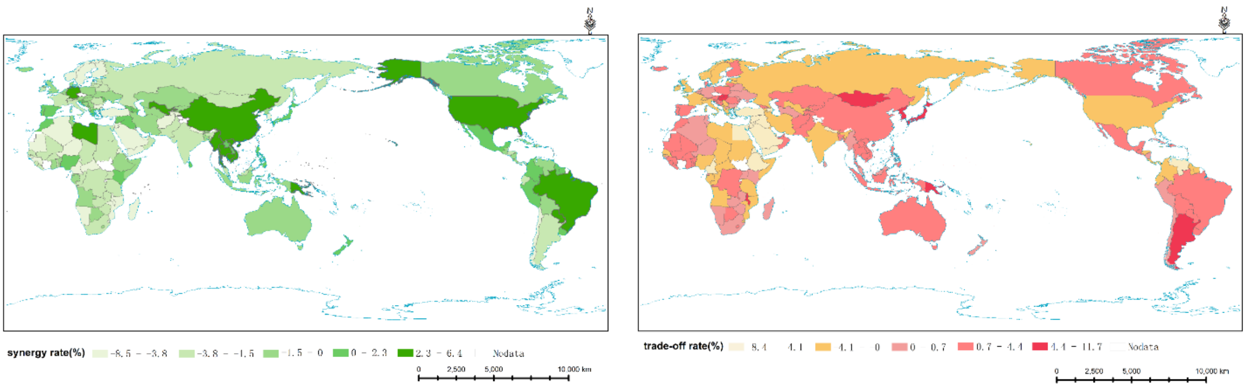


（a） Synergistic Network （b） Trade-off Network

Fig 2 Rate of change of global indicator pairs, 2000-2020

## References

[1] United Nations (2015). Transforming our world: The 2030 Agenda for Sustainable Development A/RES/70/1. New York: United Nations General Assembly.

[2] Nilsson M, Griggs D, Visbeck M (2016) Map the interactions between sustainable development goals. Nat News 534:320.

[3] International Council for Science (ICSU), International Social Sciences Council (ISSC) (2015) Review of the sustainable development goals: the science perspective. International Council for Science (ICSU), Paris.

[4] Le Blanc D (2015) Towards integration at last? The sustainable development goals as a network of targets. UN Department of Economic & Social Afairs, DESA Working Paper No. 141

[5] Sachs J, Schmidt-Traub G, Kroll C, Lafortune G, Fuller G (2019) Sustainable Development Report 2019: G20 and large, Countries. Bertelsmann Stiftung and Sustainable Development Solutions Network (SDSN), New York.

[6] Pham-Trufert M, Metz F, Fischer M, Ruef H, Messerli P (2020b) Interactions among sustainable development goals: knowledge for identifying multipliers and virtuous cycles. Sustain Dev 1-15

[7] Dawes JHP (2020) Are the sustainable development goals self-consistent and mutually achievable? Sustain Dev 28:101–117.

[8] SDG Indicators (2021) https://unstats.un.org/sdgs/indicators/indic ators-list/. Statistics Division, Department of Economic and Social Afairs, UN. Accessed 15 March.

# Technology-enabled solutions for biodiversity conservation—China Nature Watch Program

Cheng Chen[1], Yu Mengjiao[1], Wei Chunyue[1], Wang Ning[1], Chen Anyu[1], Luo Mei[2], Xiang Chun[3], Liu Chunlei[4]

[1] Shan Shui Conservation Center, China
email: chengchen@shanshui.org

[2] Center for Nature and Society, College of Life Sciences, Peking University
[3] GREEN DATA
**4** Shanghai Minhang District Qingyue Environmental Protection IT Service Center

## 1.INTRODUCTION

The survival and growth of human society depend on biodiversity, whose preservation is crucial for mitigating and adapting to climate change as well as for accomplishing Sustainable Development Goals (SDGs). Human activities, especially those led by enterprises have been causing a big percent of biodiversity loss. To identify such biodiversity risks and conserve biodiversity, biodiversity data collection is needed to identify threats to biodiversity conservation and land use gaps. However, traditional methods lack efficient data collection mechanisms, are difficult to adapt to application scenarios, and are no longer applicable to today's biodiversity conservation needs.

Currently, technology is booming like never before, and the integration of big data, cloud computing and artificial intelligence is accelerating, a force that is increasingly helping traditional industries to develop efficiently. The empowerment of digital technology is important for biodiversity conservation. Biodiversity conservation relies on a robust and complete data base, which includes two parts of spatial-based data: on one hand, wildlife distribution data based on field surveys must be obtained, and on the other hand, threats to biodiversity need to be clarified, including the location of enterprises and business activities such as construction projects. The use of technology can greatly enhance the data collection, not only by support timely collection of the latest biodiversity data, but also by making good use of the data base to promote data-driven ecological and environmental decision-making, which leads to new methods and pathways to achieve a high level of ecological conservation. Currently, these two parts of the database are developing rapidly and have achieved good results, however, there are also some problems and shortcomings that need to be addressed in a targeted manner.

Camera trap, a commonly used species survey method, is an important source of species distribution data, especially for elusive and rare species. In the past, large amounts of camera trap data were organized and processed manually, which took months to convert the raw data into usable data results. The current application of artificial intelligence techniques has brought a breakthrough solution for camera trap species identification [1][2], somehow helping species distribution data to be quickly obtained from infrared cameras. However, AI has to be trained for specific species fauna; also AI models need to be setup in data process workflow, and translated into user-friendly tools so that to be friendly for conservationists.

Environmental Impact Assessment (EIA) policy is important for preventing biodiversity risks and mitigating environmental damage. Besides the ecological impact assessed by the EIA reports, construction project locations in the reports show where enterprises' activities change land use, and potentially have impacts on biodiversity. Thus, the development of EIA big data plays a crucial supporting role in environmental management decisions. In recent years, the development of EIA big data has made great progress, and frameworks such as data centers, collection systems, and service platforms have been built [3]. However, such systems do not analyze the text in EIA reports to extract their key information such as geographic location effectively, nor do they integrate them into usable databases that can be applied to prevent biodiversity impacts in data decision making.

The current bottlenecks come from the difficulty of collecting biodiversity and enterprise location data in the traditional way and the delay in updating data, as well as the lack of an integrated database for multiple types of data and interactive platform for data use. It leads to difficulties for various biodiversity stakeholders to make biodiversity-friendly decision basing on data.

To address the above problems, based on years of data collection and long-term research and conservation practice, this study has collected and integrated multi-source database, applied new technology to establish a continuous and more efficient data collection system, and developed a data tool to support data use of multi stakeholders. We hope the study explores a digital solution for data-driven biodiversity-sustainable development, so that to promote cross-field collaborations to raise conservation awareness in business, and the mainstreaming of biodiversity conservation in China society.

## 2.MATERIALS AND METHODS

### 2.1 Data collection and Database

#### 2.1.1 AI for Species Data Collection

A systematic overview of the current camera trap data workflow and areas for improvement with digital technology was generated after interviews with conservationists working with camera traps in field (both in remote areas and in cities) and exploration of existing camera trap data management systems (e.g., eMammal, Wildlife Insights). We collected and evaluated relevant demands to identify how AI in workflow could assist in preliminary data screening and improve the speed of obtaining species data from camera trap.

For the key steps of data acquisition like field data collection and data processing, this project developed a series of auxiliary tools and designed an integrated platform including animal detection model and species identification model. For the animal detection model, after preliminary investigation, the Mega Detector model (Microsoft AI) was selected as the model candidate, for which a thorough performance test was conducted using more than 200,000 camera trap images representing ecosystems ranging from alpine meadow, forests, to wetland. For the species identification model, collaborating with technical partners, models were trained with over 15,000 camera trap images containing 19 species on the Qinghai-Tibetan Plateau, which were continuously improving with new training data input.

#### 2.1.2 Tech for enterprises' activity locations Collection

Through desktop research, we analyzed the EIA policy system, information disclosure, and EIA report formats and features, and established a methodology for structured EIA report extraction. We cooperated with GREEN DATA, who obtained all the EIA report URLs since 2013 through a crawler, and docked them to us through an API to obtain a more comprehensive data source of EIA report texts.

Based on the above methodology and data sources, a python-based distributed EIA data crawling and storage system was established. The system contains crawling, extraction and structured storage functions. Using the Scrapy framework, we obtained millions of EIA reports including all provinces in China through web crawlers, then extracted the latitude and longitude information of construction projects from the EIA reports, cleaned the data using pandas and NumPy, and stored them to a PostgreSQL database after structuring. The data was visualized using tableau and the crawler was deployed on Docker. The EIA database was formed to provide a data base for further application of the data to ecological risk assessment, etc.

#### 2.1.3 Data integration - Biodiversity conservation oriented database

In response to the need of sustainable biodiversity decision-making, it is necessary to construct a database that includes biodiversity conservation targets and enterprise pressures to assess the degree of threat to biodiversity. Multiple types of data are assessed and integrated into one database to support scientific biodiversity conservation. The database includes biodiversity baseline data and corporate construction data.

The biodiversity baseline data includes species and protected areas. With the help of artificial intelligence and cloud computing technology, species data are efficiently analyzed and extracted to form key information with species names and locations that can be aggregated into a database. Using GIS technology, photographic data from National Nature Reserve are transformed into vector data, resulting in data that can be used in conjunction with other data. Enterprise Pressure databases include data on the location of construction projects, mining and pollution emissions. The application of crawler and cloud storage technologies enabled the extraction of corporate location information in a structured manner, creating a database of construction project locations. We also obtained the Mining Discharge Permission, Sewage Discharge Permission from GREEN DATA and Corporate Sewage Monitoring Data from Shanghai Minhang District Qingyue Environmental Protection IT Service Center, to form a complete enterprise database.

The data form and content of these three types of data are different, but the fields, access methods and interfaces of these three types of data are integrated into the same dimension through their common spatial and temporal attributes. The data is stored in a PostgreSQL database for efficient retrieval and referencing. By integrating and transforming the data to form a nature observation database, a complete data base is obtained for biodiversity data utilization.

### 2.2 Data application and interaction

#### 2.2.1 Corporate Biodiversity Pressure Assessment

Multiple types of data in Nature Watch Database need to be tested and used to explore the efficacy of the database and further improve it, the project attempts to apply the data to assess the biodiversity pressure on companies[4]. A random sampling method was used to draw a group of listed companies in industries with key impacts on biodiversity. Using the biodiversity data in the database, as well as data on the location of commercial activities in the EIA reports, pollutant discharge permits and mining permits of construction projects, the direct pressures on national protected areas and natural habitats from the operations and construction activities of these companies were identified, as well as the pressures on biodiversity from negative events of the companies. By identifying and weighting the different pressure categories, we derived the pressure levels of the enterprises on biodiversity.

#### 2.2.2 Biodiversity Impact Assessment Tool

The Biodiversity Impact Assessment Tool (BIA) [5]works by overlaying and analyzing biodiversity data, such as wildlife distribution, ecosystems, and nature reserves, with selected locations or the locations of construction projects， investigate if the site or region is within certain distance (e.g., 3 km, 5 km) from and may cause impact on endangered species habitat and/or protected areas.

These functions and data are integrated into the mobile application platform and website to enable automated and instantaneous biodiversity impact assessment queries so that the database can be used and queried by a wider audience, providing a professional data tool for different stakeholders.

## 3. RESULTS

### 3.1 Data collection and Database

#### 3.1.1 Camera Trap Data Assistant Tools

Animal detection model testing: MegaDetector model performs the best in forest ecosystems with only less than 1% of animal images undetected (i.e., false negative). In alpine meadow and urban wetlands, about 5-7% of animals were missed by the model, most of which were small animals like birds and rodents. Such missing rates are acceptable since research and stakeholders' interests mainly lie in large and medium size animals (e.g., felids, ungulates). Therefore, MegaDetector helps filter out about 75% blank photos (i.e., false positive) from human identification, which accounts for over half of total photos, hence saving approximately 40% of conservationists' time in the species identification process.

#### 3.1.2 Tech for enterprises' activity locations Collection

The information will be extract from the EIA report and store it in a structured way, turning the data scattered in the report into a resource that can be used in multiple application scenarios. We also summarize and refine key fields and data structure to form data dictionaries and data specifications according to the type, structure and hierarchy of EIA-related data. We applied the technology to the construction of EIA big data and achieved a distributed crawler system for environmental impact assessment. It improves data efficiency, promotes orderly accumulation of data, and establishes a database in order to be applicable to more application scenarios.

**3.1.3 Data Integration**

The Nature Watch database maintains baseline biodiversity data collected from multiple data sources, including species records (2,591 species, 1.35 million records) and protected areas (6 national parks, 474 national reserves, etc.), as well as an Enterprise Pressure databases, include construction projects from environmental impact assessment reports (183,000 construction projects), Mining Discharge Permission, Sewage Discharge Permission and Corporate Sewage Monitoring Data from partners. This integration has revitalized the existing databases, broken through the conversion problem between various databases, and achieved interoperability between databases.

### 3.2 Data application and interaction

**3.2.1 Corporate Biodiversity Pressure Assessment**

To overview the current status of enterprises caused impacts and risks on biodiversity, we performed the Biodiversity Pressure Assessment research. Through developing an evaluation framework and workflow, and integrating multi-sourced data, for the first time, we distinguished potential impact of listed corporates on high-biodiversity-value-areas. Includes identified direct pressure on national protected areas and natural habitats from companies' operational and construction activities, and find out the corporate's negative incidents about the environment exert considerable pressure on biodiversity.

**3.2.2 Biodiversity Impact Assessment Tool**

The Biodiversity Impact Assessment (BIA) tool attempts to promote more scientific land use and business decisions by using the Nature Watch database developed as an interactive tool to effectively identify whether development and construction are encroaching on wildlife habitats or nature reserves. Until now, the BIA tool has provided interactive and visualized biodiversity impact assessment inquiry services to more than 1260 construction project planners and other stakeholders, businesses and corporates can use it to avoid biodiversity risks, facilitating biodiversity-friendly decision making, eventually raising awareness of protection and promoting biodiversity mainstreaming.

## 4. SUMMARY

Biodiversity conservation is of great importance to human and society. However human land use is currently causing the main threat to biodiversity. A **data-driven biodiversity-sustainable development** needs to be promoted to support evidence-based conservation, in which to build up and apply database of biodiversity and land use is crucial. However, currently such data base is insufficient and there are gaps in data collection. Digital technology is urgently needed to help build up to solve the problems. To this end, this study has explored a systemic digital solution for biodiversity conservation based on technology and data as a pilot research, through using technology to improve the efficiency of species and land use data collection, producing a complete set of integrative databases, and trying to apply the databases to alarm biodiversity risks in land use. By creating a digital infrastructure in the field of biodiversity and providing solutions for sustainable biodiversity decision-making, we hope to help achieve the goal of mainstreaming biodiversity conservation.

## References

[1] Willi, M., Pitman, R. T., Cardoso, A. W., Locke, C., Swanson, A., Boyer, A., Veldthuis, M., & Fortson, L. (2019). Identifying animal species in camera trap images using deep learning and citizen science. Methods in Ecology and Evolution, 10(1), 80–91. https://doi.org/10.1111/2041-210X.13099

[2] Norouzzadeh, M. S. , Morris, D. , Beery, S. , Joshi, N. , Jojic, N. , & Clune, J. . (2021). A deep active learning system for species identification and counting in camera trap images. Wiley(1).

[3] Pan P, Zhao XH, Liang P, et al. Progress and prospect of environmental impact assessment big data construction[J]. Environmental Impact Assessment. 2017,39(6):19-22,30. DOI:10.14068/j.ceia.2017.06.005.
[4] Shan Shui Conservation Center. (2022) Corporate Biodiversity Pressure Assessment, Report, (in progress)
[5] Shan Shui Conservation Center. (2020) BIA Biodiversity Impact Assessment Tool. Available: bia.hinature.cn

# SDG Big Data Platform

CHEN Can[1]

[1] Computer Network Information Center, CAS, China
email: chencan@cnic.cn

## 1.BACKGROUND

The Sustainable Development Goals, i.e., SDGs, introduced by United Nations (UN) and committed by 193 countries, are the blueprint to achieve a better and more sustainable future for all people on the planet. SDGs address the global challenges we face, including poverty, inequality, climate change, environmental degradation, peace and justice [1-3], and the goals cover all three key development pillars: economic, social, and environment, as well as enablers such as institutional coherence, policy coherence, and accountability [4-8].

UN developed the measurement framework for the UN Agenda 2030 for Sustainable Development [9], comprised of 232 indicators designed to measure the 17 Sustainable Development Goals (SDGs) and their respective 169 targets [10-12], which would be “action oriented, global in nature and universally applicable”, thus, quantifying progress towards achieving the SDGs is essential to track global efforts towards sustainable development and guide policy development and implementation[8], [13].

Big Earth Data is big data in the field of Earth science with spatial attributes, especially the massive Earth observation data generated by space technology. Such data is mainly produced at a large spatial scale by scientific devices, detection equipment, sensors, socio-economic observations, and computer simulation processes. Similar to other types of big data, Big Earth Data is massive, multi-sourced, heterogeneous, multi-temporal, multi-scaled, and non-stationary. But more than just that, it has strong spatiotemporal and physical correlations, and the data generation methods and sources are controllable. Big Earth Data science is interdisciplinary, encompassing natural sciences, social sciences, and engineering. It systematically studies the correlation and coupling of the Earth system based on data analysis. Earth is observed and studied as a whole by simultaneously employing big data, artificial intelligence, and cloud computing, so as to understand the complex interactions and development processes between Earth's natural system and the human social system. Big Earth Data can make an important contribution to the realization of SDGs.

The CASEarth Big Earth Data system can support the implementation of SDGs by converting Big Earth Data to relevant information, providing policy-making support, constructing and integrating an index system, and studying the relationships and couplings between various SDG targets from the perspective of the Earth system. It can also support the monitoring and evaluation of SDG indicators through data-sharing platforms and cloud infrastructure by providing data, online calculations, and visual presentations.

## 2.SDG BIG DATA PLATFORM CONSTRUCTION PROGRESS

At FBAS 2021, we released the SDG big data platform, which provides a comprehensive and integrated display of SDGs-oriented data, resources, and achievements for three service scenarios: researchers, decision makers, and the public. The platform provides online access to resources, SDG workbench and decision support visualization system in both Chinese and English.

Over the past year, based on the users’ feedback, we have upgraded and improved the platform in terms of cloud environment infrastructure, earth big data resources, computational analysis engine, SDG scientific research workbench and other aspects.

We expanded the capabilities of the CASEarth cloud environment. The demonstration of the distributed platform construction plan and the Huairou platform expansion plan have been completed. The research and development of computing function file list viewing, downloading, and pre-processing and post-processing functions has been completed. The platform continues to run stably and serves special applications. In 2022, 72,000 computing jobs will be completed, consuming 30.7 million CPU hours.

We completed the classification system of big earth data and SDG classification system to provide computing-oriented data products and sharing services, and realize the introduction and production of satellite data on the cloud. We developed 35 global SDG big data products, 41 global regional SDG big data products, 18 SDG big data products in China, and 11 SDG big data products in typical regions of China.

We launched the standard OpenAPI service interface for remote sensing data; completed the sorting and storage of LDN product production data. We improved the non-functional indicators of the Earth Data Miner system to provide stable cloud services. We added guided automatic learning service and RetinaNet target detection algorithm based on TensorFlow2.0 in Deeplearning Cloud System.

Based on the cloud native technology architecture, we have reconstructed the SDGs workbench. Users only need to use a browser to complete the entire process of scientific research activities.

## 3.SDGS WORKBENCH

Cloud native [14] technologies empower organizations to build and run scalable applications in modern, dynamic environments such as public, private, and hybrid clouds. Containers, service meshes, microservices, immutable infrastructure, and declarative APIs exemplify this approach.

These techniques enable loosely coupled systems that are resilient, manageable, and observable. Combined with robust automation, they allow engineers to make high-impact changes frequently and predictably with minimal toil.

Based on the cloud native technology architecture, we have reconstructed the SDGs workbench. Figure 1 shows the system architecture. We have built a cloud-native environment composed of multiple container clusters on the CASEarth Cloud, including two service clusters and one management cluster, providing cloud-native databases, cloud-native programming environments, machine learning model training, data visualization, container image repository, code repository, DevOps and other services.

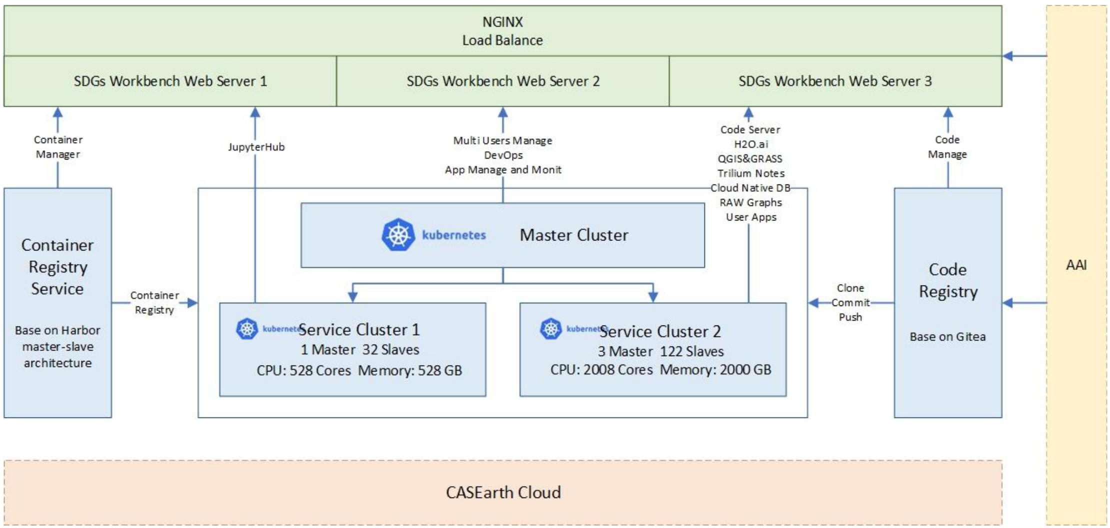

*Figure 2 SDGs Workbench*

We have integrated the existing research tools such as SDG indicator calculation, SDG data product production, Earth Data Minor, and deep learning cloud service platform on the SDGs workbench; support users to access and use various shared data directly in the code. So as to provide users with one-stop resource integration and application services, users only need to use a browser to complete the entire process of scientific research activities.

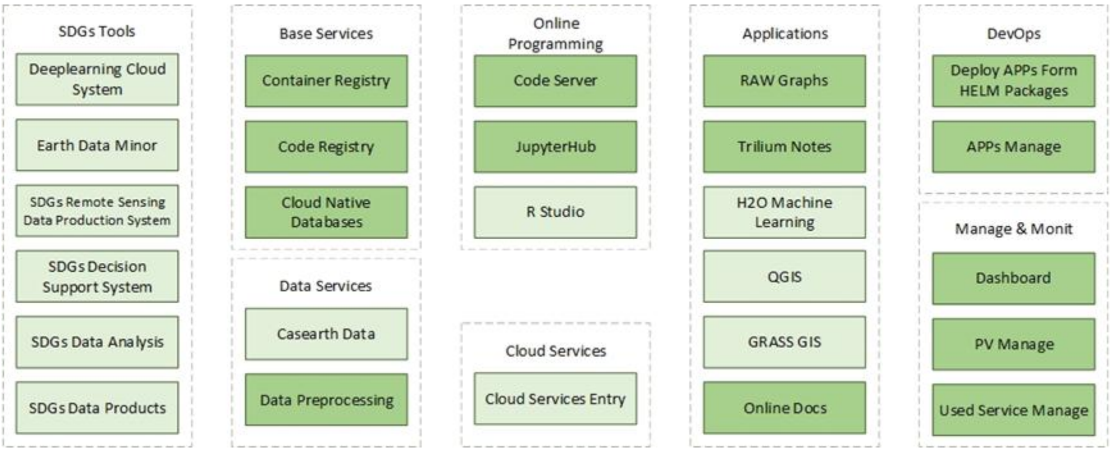


*Figure 3 Services in SDGs Workbench*

## 4.FORECAST

In the next step, we will build a data lake platform with metadata management as the bus. For structured, semi-structured, and unstructured data for SDG, we will provide data integration tools, and use object storage and HDFS clusters to store the data and metadata, and provide data analysis engines to provide big data analysis and processing capabilities.

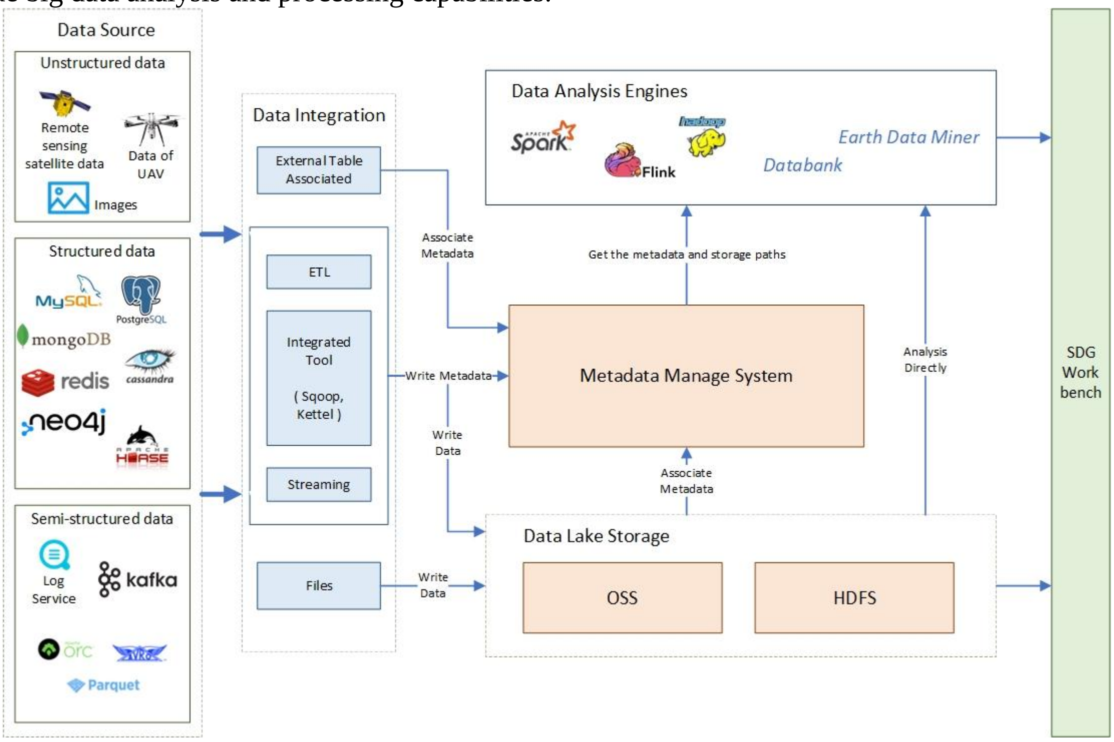


*Figure 4 SDGs Workbench Forecast*

## References

[1] P. Caballero, “The SDGs: Changing how development is understood,” Global Policy, vol. 10, pp. 138–140, 2019.
[2] T. Hák, S. Janoušková, and B. Moldan, “Sustainable Development Goals: A need for relevant indicators,” Ecological Indicators, vol. 60, pp. 565–573, Jan. 2016, doi: 10.1016/j.ecolind.2015.08.003.
[3] S. Morton, D. Pencheon, and N. Squires, “Sustainable Development Goals (SDGs), and their implementationA national global framework for health, development and equity needs a systems approach at every level,” British medical bulletin, pp. 1–10, 2017.
[4] N. Kanie and F. Biermann, Governing through goals: Sustainable development goals as governance innovation. mit Press, 2017.
[5] P. P. Walsh, E. Murphy, and D. Horan, “The role of science, technology and innovation in the UN 2030 agenda,” Technological Forecasting and Social Change, vol. 154, p. 119957, 2020.

[6] M. King, “Broadening the global development framework post 2015: Embracing policy coherence and global public goods,” The European Journal of Development Research, vol. 28, no. 1, pp. 13–29, 2016.
[7] M. Elder, M. Bengtsson, and L. Akenji, “An optimistic analysis of the means of implementation for sustainable development goals: Thinking about goals as means,” Sustainability, vol. 8, no. 9, p. 962, 2016.
[8] S. MacFeely, “Measuring the sustainable development goal indicators: An unprecedented statistical challenge,” Journal of official statistics, vol. 36, no. 2, pp. 361–378, 2020.
[9] U. N. S. Division, “Discussion paper on principles of using quantification to operationalize the SDGs and criteria for indicator selection.” United Nations Statistics Division New York, 2015.
[10] R. Bandura, “A survey of composite indices measuring country performance: 2008 update,” New York: United Nations Development Programme, Office of Development Studies (UNDP/ODS Working Paper), 2008.
[11] E. Rametsteiner et al., “Analysis of national sets of indicators used in the National Reform Programmes and Sustainable Development Strategies,” Luxembourg: Eurostat & Office for Official Publications of the European Communities, 2007.
[12] T. Tasaki, Y. Kameyama, S. Hashimoto, Y. Moriguchi, and Hideo Harasawa, “A survey of national sustainable development indicators,” International Journal of Sustainable Development, vol. 13, no. 4, pp. 337–361, Jan. 2010, doi: 10.1504/IJSD.2010.038173.
[13] “Big Data for Development: Opportunities and Challenges - White Paper • UN Global Pulse.” https://www.unglobalpulse.org/document/big-data-for-development-opportunities-and-challenges-white-paper/ (accessed Jul. 17, 2022).
[14] CNCF Cloud Native Definition v1.0, https://github.com/cncf/toc/blob/main/DEFINITION.md

# Data Ownership and Pricing in Distributed Machine Learning

Chao Wu[1]

Zhejiang University, China
email: chao.wu@zju.edu.cn

## 1. INTRODUCTION

It has been widely believed that great value can be mined from data, especially with modern modeling methods like deep learning. With the rapid growing amount of data, along with the expanding applications of data-driven technologies, so called "Data Economy" has been a phenomenal social-economic form.

To establish data economy based on valuable data requires as a framework of economic principles and practical rules, such as data valuation, pricing, ownership integration, and property trading. As the data economy is still in its early stage, such principles and rules are not yet fully developed.

To provide a foundation of building an efficient, fair, and sustainable eco-system to support data economy, we focus on two basic topics in this work: data valuation and ownership. These two related topics need urgently to be investigated since lots of actions in current data economy build upon them. The vagueness in current data valuation and ownership makes the top data economy actions difficult to be measured and promoted.

We need to understand, although many efforts have been paid to investigate data valuation and ownership, especially from big tech companies, these two topics are quite challenging, due to the following reasons:

1. Non-linear and unpredictable value of data;

2. Near zero replication cost of data;

3. Difficulty in protecting data ownership;

4. The tension between data ownership protection and data utilization (data sharing and transparency).

## 2.MATERIALS AND METHODS

Data has value, but as we mentioned before, the value we can get from data is non-linear and unpredictable. Below are the reasons: 1) The utility of a data-driven product or service depends not only on the data, but also on the model upon data, therefore, before modeling, it's difficult to understand the value of data; 2) The value of data can be augmented with other data, in a non-linear manner; 3) The utility of a data-driven product of service also depends on the user of it.

Therefore, we propose that the realization of data value extraction needs a workflow, within which extra resources (external data, modeling, analytics, etc.) are augmented and the final data product (e.g., a predictive model) is used to generate utilities and benefits. And it's at the end of workflow, we are able to value the data. We name such workflow as "data chain", or "data value-added chain".

To valuate the actions in a data chain, we assume at the time, the payoff for the whole data chain is given. Then the problem is how to allocate the profit to all the participating providers in the data chain. To achieve this, we propose a revised version of Shapley Value [2] - Shapley Value for Data Chain (SVDC).

For an action, we define a baseline provider, which is the provider with no extra cost to serve the baseline function. For example, for data providers, the baseline provider can be the open data with no cost; and for data modeling, the baseline provider can be the open sourced pre-trained model without extra cost for model training.

The Shapley value calculation can be further applied to members in a sub-provider (if it has multiple collaborative members), and thus forms a tree hierarchy. Once the final payoff is determined, it can be divided to all providers in the tree, from the root to leafs. As we mentioned before, such calculation suffers the issue in real case decision making ("Join first, Result Later", as shown in the Figure). Therefore, it's desired to estimate the payoff before establishing the data chain.

Our data pricing framework considers the contribution of data to the model, as well as the contribution of preprocessing and algorithm to the model. We regard the data, preprocessing and algorithm as agents in the cooperative game model, and construct a Multi-Agent Reinforcement Learning Model for evaluation.

Referring to the CTDE (centralized training with decentralized execution) [3] algorithm in QMIX [4] and QPLEX [5] papers, a Multi-Agent Reinforcement Learning Model from data collection to preprocessing and algorithm process is preliminarily constructed to improve the fair distribution between data and algorithm.

(1) Each element on the data chain is regarded as an agent in the Multi-Agent Reinforcement Learning Model. We believe that the best data pricing strategy is to maximize the Q function of each agent in the data chain. This is consistent with the assumption of CTDE method based on value decomposition in Multi-Agent Reinforcement learning problem, that is, IGM principle, which asserts the consistency between joint and local greedy action selections in the joint action value and individual action values.

(2) Agents make actions according to the policy network in their respective action space. For example, each data owner has two actions: providing data set and not providing data set. The algorithm agent provides free and charged algorithms as actions. Take the model obtained from the joint action of the data chain as the state, and the policy will continuously optimize the model (finetune) to maximize the benefit of the data pricing model. We believe that the value function of each agent can fairly measure the contribution of all agents in the data chain, and we distribute income accordingly.

(3) In the Multi-Agent Reinforcement Learning Model, we represent reward as a function of the accuracy of the model obtained through the data chain on the test set, and take into account the cost of data collection, data preprocessing, and data modeling.

It is too expensive to make a contract that clearly stipulates that the parties pay and act in every observable state. Oliver Hart's theory holds that integration does not change the cost of entering into a full contract, but rather distributes residual ownership, that is, the right to control all aspects of an asset that are not specified by the contract. Therefore, in order to maximize the value of data in the market, I propose to integrate data ownership and compensate the consolidated parties based on their utility. Our work propose that one agent should integrate the other agents in the data chain. This idea is inspired by modern property rights theory [1], which is based on the idea that ownership formed in cooperation should belong to the party that contributes most to the output after integration.

Our framework uses the least core to ensure that each integrated provider is compensated for at least its expected value. Contrast with the Shapley value, which confers only a generic notion of “importance”, the core gives a viable range to make agents in the coalitions. And this will allow the agents prefer not to leave the grand coalition.

## 3.SUMMARY

We propose a new way of conducing data valuation and ownership identification, considering these challenges. The contributions of this work includes:

1. The methodology is for the so called "Data Chain", which considers the data value extraction as a comprehensive value-added process. The proposed valuation fit for all the steps of the whole data chain, instead of just for data collection;

2. The proposed data valuation and ownership integration can support decision making support in real cases, which means the valuation and integration is done beforehand, so the decision maker can get the expectation before participating the data chain.

3. We propose a new ownership integration and compensation method based on modern property theory, and thus facilitate the better utilization of data, compared with current narrow definition of data ownership.

## References


[1] Nicita, Antonio, Matteo Rizzolli, and Maria Alessandra Rossi. "Towards a theory of incomplete property rights." Available at SSRN 1067466 (2007).

[2] Shapley, Lloyd S. "A value for n-person games." Classics in game theory 69 (1997).

[3] Lowe, Ryan, et al. "Multi-agent actor-critic for mixed cooperative-competitive environments." Advances in neural information processing systems 30 (2017).

[4] Rashid, Tabish, et al. "Qmix: Monotonic value function factorisation for deep multi-agent reinforcement learning." International conference on machine learning. PMLR, 2018.

[5] Wang, Jianhao, et al. "Qplex: Duplex dueling multi-agent q-learning." arXiv preprint arXiv:2008.01062 (2020).

# SDG 18: The Missed Keystone of Sustainability

EREMCHENKO Eugene[1]

[1] Lomonosov Moscow State University, Russia
email: e.eremchenko@geogr.msu.ru

## 1. INTRODUCTION

Sustainable Development is a fundamental priority for all mankind, recognized by the United Nations since 2015. Currently, the concept of Sustainable Development, based on a deep and comprehensive analysis of modern challenges, is formulated in the form of a set of 17 Sustainable Development Goals (SDGs) [1], detailed in the form of 169 targets [2]. Each of these goals sets guidelines for ensuring crisis-free development in specific aspects of the general well-being of peoples and humanity as a whole. The achievement of each of these goals is declared as the ultimate development guidelines for each of the countries. It is assumed that the implementation of all 17 SDGs will ensure synergy, assure eternal sustainability and prevent regional and global crises.

Unfortunately, reality is not so optimistic. The declaration of SDGs did not bring sustainable development to the world. On the contrary, civilization is getting into deeper and deeper crises. Even more dangerous is that they have a hybrid nature and can have severe and unpredictable long-term consequences. A typical example of such a crisis was the COVID-19 pandemic, which had not been overcome by the time of this study. Currently, it is not even known whether the catastrophic consequences of the pandemic are the result of the insufficient development of any SDGs, or, instead, originated from excessive activity to overcome it. In any case, the pandemic is a serious challenge to the concept of Sustainable Development.

Ensuring the resilience of modern civilization to new threats naturally raises the question of the integrity of the existing SDGs. It may be necessary to adapt the list of goals to take into account the growing understanding of the problems faced by civilization. This raises the question of the need to search for possible factors contributing to systematic management errors due to the imbalance of the current SDGs. The study of such factors requires an interdisciplinary approach. To do this, in particular, it is necessary to consider the semiotic and cybernetic features of the information used today in global governance. Regular revision of the SDG list and its possible expansion are seen as desirable.

An important element of such a study may be the analysis of the implementation of the Digital Earth as a universal system of global governance, seamlessly linking all hierarchical tiers of decision-making together and thereby avoiding discrepancies caused by inter-scale inconsistency of information.

## 2. MATERIALS AND METHODS

### *2.1 Methodology*

The high interdisciplinarity of the issue under study requires the involvement of a broad and versatile methodological base. Within the framework of the existing gradation of the orders of cybernetics [3, 4], modern global civilization should be considered as a cybernetic system of the highest, third order [5], that “involves an active-interactive element in a circuit that enables it to redirect itself in order to adapt to its context" [4]. The content of any cybernetic system is information that is represented by signs and, therefore, should be investigated by methods of semiotics as a science of signs addressed to control [6].

### *2.2 Research and Discussion*

The modern management system, being cybernetic in nature, is embedded in the existing economic architecture, implemented with the help of economic tools and actually identified with it. Both cybernetics and economics are defined as control systems. Naturally, each control system circulates its own specific information. It can be classified semiotically by the types of signs used in it as parameters. In economics, any information is mediated by “cost” as a control parameter. A characteristic feature of the cost is that it is a scalar, non-negative and discrete quantity. Economics can be defined as "a management mode based on the use of a single scalar value as a control parameter – cost." [7]. Economics is unique because it uses only scalar values expressed in money, which are the least functional parameter for use in management systems. Thus, we can say that from the point of view of semiotics, economics is the worst management model theoretically possible.

On the contrary, real-world entities should be represented by values of different types. A small part of them can be represented as scalar, discrete and non-negative quantities. Some require much more advanced semiotic tools – vectors, tensors, etc. The absolute majority of entities cannot be represented by any values at all (for example, fractals). The use of inadequate parameters to measure values that do not correspond to them generates errors in decision-making, the consequence of which is the development of crises. This dependence of the quality of management on the parameters used to control systems is fully realized in the modern world, and the so-called "digital economy" is thought of as a means of solving it. It is assumed that saturation of the control system with heterogeneous indicators will improve the quality of system management.

However, from the semiotics point of view, the digital economy not only does not solve management problems, but also brings them to the utmost acuteness, since such parameters are also scalar, discrete and not negative – and as such are identical to units of cost, money. The most well-known such tools are all kinds of ratings [8]. Thus, the digital economy is not only unable to resolve the management crisis generated by the semiotic limitations of the economy, but also further aggravates it by including in the management of a variety of diverse, but semiotic identical to money tools. It is no accident that the digital economy generates chaos in management, global crises become permanent, flowing into one another. Moreover, completely new types of global confrontation are being formed. Thus, the COVID-19 pandemic turned into a completely new type of world war – a war not between states, but between different industries [9]. In this war, a number of industries (microbiology, pharmaceuticals, etc.) diverted huge funds from other industries (tourism, passenger transportation, etc.), which suffered a crushing defeat with long-term consequences. This marked a conflict, for example, between SDG3 (Good Health and Well-Being) and SDG8 (Decent Work and Economic Growth). The old formats of global confrontation have not disappeared, but new ones are appearing in addition to them. Probably, this process of hybridization of global crises will continue, and humanity will become the arena of qualitatively new types of confrontations. In the SDG vision, this will mean growing contradictions between the 17 existing SDGs. Their prevention may require the introduction of new SDGs.

Geospatial information plays a fundamental role in management, and it is this information that is particularly susceptible to disorganization due to the use of non-optimal signs for this. Maps are a source of data that is critical for making managerial decisions (area of territory, length of coastline, length and area of inland reservoirs, etc.). However, most of these parameters, in principle, do not and cannot have any numerical expression due to their fractal nature and are generated in the process of representing real entities using scale-dependent cartographic signs. Moreover, many of these quantities not only do not have values that are invariant for maps of different scales – they do not even have a limit to which their value could aspire (coastline paradox [10, 11]).

For example, the continent of Antarctica exists in reality, and it has a coastline. But this coastline does not have a certain length, because the length appears only when the real coastline is mediated by its polyline sign, and the length of this polyline on maps of different scales will be different and will not tend to any particular value.

## 3. RESULTS

The representation of geodata in the form of signs in general and scalar signs in particular is the primary source of divergences that destroy global and state governance. The most significant consequence of the incorrect representation of reality for management was the segmentation of the management system on a large–scale basis into different levels – for example, global, continental, state, regional, municipal, etc. It can be shown that such a division, expressed in the form of a tiered decision-making architecture and located is space entities separated by borders (states), is not a natural form of organization of human society. It was generated in the distant past by the adaptation of signs as a tool for representing space using maps. Maps are necessarily scale-dependent, so managing complex structures requires the use of maps of different scales with different, incompatible representations of the geospatial context. The appearance of maps led to vertical (tiering) and horizontal (entities separated by borders) segmentation of a single civilization and its management system. With the development of technology and until recently, this segmentation has been aggravated by the appearance of more and more new maps. The invention of maps initiated the segmentation of society. It led to the segmentation of control systems. Maps are used to generate scalar parameters necessary for control (for example, the length of the coastline). But such parameters are massively dependent and lead to an aggravating disorganization of management, giving rise to more and more complex hybrid crises. The inadequacy generated by the representation of the situation with the help of signs is a fundamental cause of unstable development and a prerequisite for crises.

The way out of this impasse was marked by the Digital Earth – a new mode of representation of geospatial space, which allows to realize both three-dimensionality and large-scale independence due to the underlying new scientific principle [12]. The concept of the Digital Earth was proposed by Albert Gore in the 1990s [13] and in the next decade it was put into practice – the most striking milestone of this was the Google Earth project and the pioneering TerraVison system that preceded it a decade earlier [14]. Despite its indisputable scientific novelty, the idea of the Digital Earth as a magical horizon and the ultimate goal of the development of geography has long been felt [15].

Digital Earth has made it possible to eliminate the mismatch between different-scale replicas of the global situation and thereby eliminate the fundamental cause of inefficient management on all levels, manifested in contradictions between individual SDGs. This ensured the implementation of situational awareness mode, which assumes "Situational awareness is the perception of the elements in the environment within a volume of time and space, the comprehension of their meaning and the projection of their status in the near future" [16]. This result was achieved by presenting the geospatial context in an unsigned form, using mosaic of high resolution satellite images draping the global model of the Earth.

Digital Earth became the first global information system that uses, along with signs, also an unsigned representation of the situation [17]. In general, it can be said that in the Digital Earth, an unsigned representation of the geospatial context is mainly used, while user information immersed in it is represented using ordinary signs. This synergy of the two approaches makes it possible to ensure high reliability of the perception of situation and high quality of the decisions made. In the future, perhaps, such an approach to the presentation of information will evolve in accordance with scientific and technological development.

The emergence and use of Digital Earth has shown that the exclusion of aberrations in the perception of the situation is a mandatory factor in preventing crises and, accordingly, in ensuring sustainable development. Aberrations of perception and understanding of the situation are responsible for inconsistencies in achieving individual SDGs, and overcoming the natural causes of such grounds is a prerequisite for ensuring sustainable development. The importance of such a goal and its specificity are obvious. Therefore, it can be recommended to formulate the next Sustainable Development Goal:

**SDG 18. Undistorted and Unmediated Vision of Earth.** Elimination of systematic distortion in the perception of the situation due to the use of semiotically incorrect parameters, such as the scalar parameter "cost".

## 4. SUMMARY

The list of 17 SDGs needs to be supplemented with a specific goal – the exclusion of errors in decision-making caused by the use of incorrect management parameters of their description. The most characteristic reason for them is the use of a scalar parameter – cost. In this case, the Digital Earth is a complementary addition to the digital economy. It is necessary to put into control the entire dynamic range of means of representing the situation, including images not mediated by signs. This task has already been solved in the Digital Earth concept. It can be formulated in the form of a specific SDG #18 – Undistorted and Unmediated Vision of Earth. To achieve it, it is necessary to share and implement Digital Earth Vision as ultimate framework for global information.

## References


[1] UN Department of Economic and Social Affairs (2022) Do you know all 17 SDGs? United Nations. Available: https://sdgs.un.org/goals (15-07-2022)

[2] UN General Assembly (2015) Resolution adopted by the General Assembly on 25 September 2015, United Nations. Available: https://www.un.org/ga/search/view_doc.asp?symbol=A/RES/70/1&Lang=E (15-07-2022)

[3] Styopin V.S. (2003) Selfdeveloping Systems and Post-Nonclassical Rationality, Voprosy Filosofii, 8, 5–17.

[4] Yolles M. (2021) Metacybernetics: Towards a General Theory of Higher Order Cybernetics, Systems, 9, 34. https://doi.org/10.3390/ systems9020034

[5] Lepskiy V. (2018) Evolution of Cybernetics: Philosophical and Methodological Analysis, Kybernetes, 47, 249–261.

[6] Lind M. (2002) Semiotics and Intelligent Control. In: Liu, K., Clarke, R.J., Andersen, P.B., Stamper, R.K., Abou-Zeid, ES. (eds) Organizational Semiotics. IFIP — The International Federation for Information Processing, vol 94. Springer, Boston, MA. https://doi.org/10.1007/978-0-387-35611-2_18

[7] Eremchenko E., Tikunov V., Nikonov O., Moroz V., Massel L, Zakharova A., Dmitrieva V., Panin A. (2018) Digital Earth and digital economy, Geocontext. 5(5):. 40-54. URL: http://www.geo-context.org/index.php/geocontext/article/view/33 (15-07-2022)

[8] Van Moere A. (2013) Raters and Ratings. In Antony J Kunnan (Ed.), The Companion to LanguageAssessment, John Wiley and Sons.

[9] Angelina A., Eremchenko E. (2021) Tourism and Global Confrontation: Lessond from COVID-19 Pandemic, Proceedings of the 3rd International Scientific and Practical Conference, Irkutsk, pp. 121-124.

[10] Mandelbrot, B.(1983) The Fractal Geometry of Nature, W.H. Freedman and Company. New York. P. 468. (Updated and Augmented Edition).

[11] Husain A., Reddy J., Bisht D., Sajid M. (2021) Fractal dimension of coastline of Australia, Springer Nature Scientific Reports, 11:6304.

[12] Liu Z., Foresman T., van Genderen J., Wang L. (2020) Understanding Digital Earth. In: Guo, H., Goodchild, M.F., Annoni, A. (eds) Manual of Digital Earth. Springer, Singapore. https://doi.org/10.1007/978-981-32-9915-3_1

[13] Gore A. (1999) The Digital Earth: understanding our planet in the 21st Century. Photogramm Eng Remote Sens 65(5):528–530

[14] TERRAVISION (1994) ART+COM Studios. Available: https://artcom.de/en/?project=terravision (15-07-2022)

[15] Eremchenko E. (2019) Prehistory of the Digital Earth Concept, Geocontext, 7 (1): 44-53. Available: https://geo-context.org/index.php/geocontext/article/view/47 (15-07-2022)

[16] Endsley M. (1995) Toward a Theory of Situation Awareness in Dynamic Systems, Human Factors, 37(1):32-64.

[17] Eremchenko E. (2020) What is and What is not the Digital Earth, CEUR-WS Proceedings, (2744):47. Available: http://ceur-ws.org/Vol-2744/paper47.pdf (15-07-2022)

# Youth Innovation: Sharing for the Future

# Tropical cyclone risk assessment for Pacific Small Island Developing States

YANG Hongyu[1], YANG Xiaofeng [1*], Du Yanlei [1], WANG Sheng [1]

[1] State Key Laboratory of Remote Sensing Science, Aerospace Information Research Institute, Chinese Academy of Sciences, Beijing, 100101, China.
email: yhyxzx@outlook.com
email: yangxf@radi.ac.cn
email: duyanlei@aircas.ac.cn
email: wangsheng@radi.ac.cn

## 1. INTRODUCTION

Since the United Nations included "build resilient infrastructure" and "make cities and human settlements inclusive, safe, resilient and sustainable" in goal 9 and goal 11 [1] of the 2030 agenda for sustainable development, the sustainable development of Small Island Developing States (SIDS) has attracted more and more attention from the international community. SIDS are internationally recognized as a group of 58 countries, which are distributed in three regions: the Pacific Ocean, the Caribbean Sea, AIMS (i.e. Africa, the Indian Ocean, the Mediterranean, and the South China Sea). SIDS generally encounter the challenge of sustainable development due to factors such as small territory, population growth, and weak resistance to natural disasters. Tropical cyclone (TC) is one of the most important natural disasters threatening Pacific SIDS. In order to formulate appropriate mitigation strategies under the condition of extremely imperfect historical loss records, it is necessary to assess the tropical cyclone risk of Pacific SIDS.

Risk refers to the probability of loss (or potential loss) for a specific cause (hazard) at a specific location and within a specific time period, and it is generally interpreted as a function of vulnerability, exposure, and hazard [2]. Based on the multiplicative risk model expressing risk, exposure and vulnerability, this paper uses the best track data from the Joint Typhoon Warning Center (JTWC) to carry out the hierarchical cyclonic buffer analysis, constructs a tropical cyclone hazard coefficient model and quantitatively evaluate the risk level of Pacific SIDS threatened by tropical cyclones.

## 2. MATERIALS AND METHODS

### *2.1 Materials*

This paper uses the tropical cyclone track data archive from JTWC, which is usually called the "best track". It records the main parameters of tropical cyclones in the Northwest Pacific (WP), the Central Pacific (CP), the Northern Indian Ocean (IO), and the Southern Hemisphere (SH) from the 1950s to now, and integrates the best track data set according to the division of sea areas.

Besides, this paper uses the 2020 world population density map with the resolution of 3 arcs (about 100m at the equator) released by Worldpop. The world population density map released by Worldpop is the most accurate population density data set at present, so it has been cited and studied by many organizations in recent years.

### *2.2 Mathods*

#### *2.2.1 Improved wind speed buffer model*

The wind speed buffer zone refers to the area surrounding the cyclone path that exceeds a certain wind speed, which plays an important role in the post-disaster analysis of tropical cyclones. It can describe the scope and strength of the impact of tropical cyclones, and provide an important basis for governments, international organizations, or scientific researchers in disaster reduction and disaster assessment [3,4].

This paper uses the tropical cyclone track data set from JTWC to build a hierarchical wind speed buffer database in the study area. In the data recorded after 2004, various parameters of a tropical cyclone will be recorded every 6 hours for a tropical cyclone process. In this paper, the central longitude and latitude and the four-quadrant radius of 34 knots, 50 knots, and 64 knots wind speed are used to construct the hierarchical wind speed buffer.

After data preprocessing, this paper constructs the wind speed buffer in three steps: 1) construct a single-point wind speed buffer, 2) make single-point wind speed buffers denser, 3) merge and smooth whole-process buffers.

Finally, a database containing 521 34-knots wind speed buffers, 409 50-knots wind speed buffers, and 318 64-knots wind speed buffers is obtained, with a time span from 2004 to 2020.

*2.2.2 National Tropical Cyclone risk assessment*

Many pieces of literatures discussing natural disasters have proposed risk assessment equations [5,6], and appropriate equations should be selected according to specific problems. In this paper, the multiplicative model of danger, exposure, and vulnerability is used to evaluate the risk, whose rationality is that if any component is equal to zero, the risk is zero [2]. Due to the special vulnerability of Pacific SIDS, this paper regards vulnerability as a constant, and the risk assessment equation is simplified to the form of Eq. (1).

$$Risk = Hazard \cdot Exposure \tag{1}$$

After widely investigating the existing standards for measuring the damage potential of different wind speeds [7-10], this paper chooses the dissipation rate per unit area D proposed by Emanuel[11] as a parameter to quantify the hazard, as shown in the Eq. (2).

$$D = \rho C_D V^3 \tag{2}$$

where $\rho$ – air density, $V$ – a characteristic wind speed at low levels, $C_D$ – surface drag coefficient.

Because the surface of the marine area involved in this paper is relatively homogeneous, the difference in air density has little effect on the results and $D$ can be regarded as proportional to the third power of $V$. According to the previously constructed hierarchical wind speed buffer database, this paper divides the wind speed into three levels: 34~50 knots, 50~64 knots, and more than 64 knots. The third power of the ratio of the left value of the interval is calculated respectively to weight the TC frequency to illustrate the relative contribution to the hazard. Ultimately, the danger at a certain point in space is given by Eq. (3).

$$Hazard = Times_{34-50} + 3.18 Times_{50-64} + 6.64 Times_{>64} \tag{3}$$

where $Hazard$ – tropical cyclone hazard at a certain point, $Times_{34-50}$ – the number of times this point has been covered by 34~50 knots wind speed buffer, $Times_{50-64}$ – the number of times this point has been covered by 50~64 knots wind speed buffer, $Times_{>64}$ – the number of times this point has been covered by wind speed buffer of more than 64 knots.

According to Eq. (3), the hazard layer can be obtained by the operation of the raster layer, as shown in Fig.1. The hazard level is classified into 10 levels from low to high.

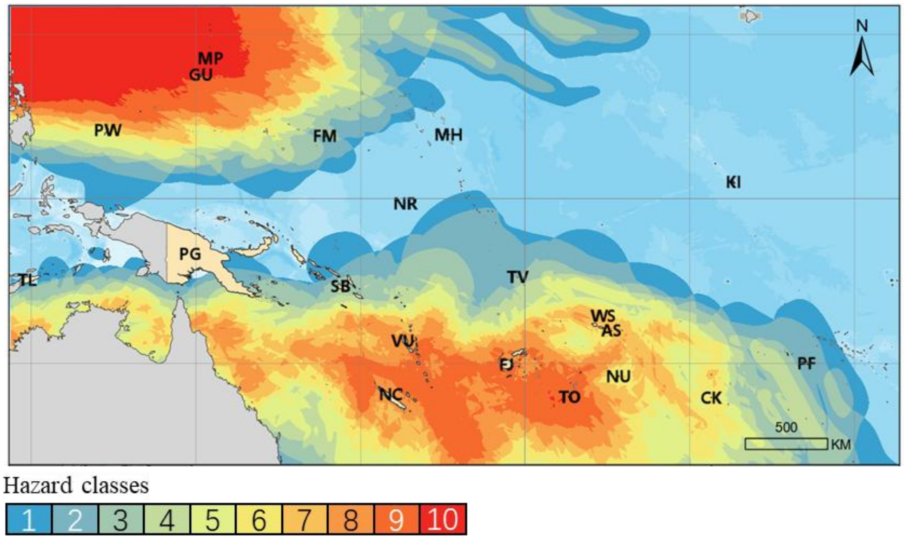


**Fig. 1.** Tropical cyclone hazard map

This paper prepares the constrained 3-arc (~100m near the equator) resolution 2020 world population density map published by WorldPop as the exposure layer here and multiplies it with the hazard layer to draw the final risk map.

To evaluate TC risk at the country level, the cumulative value of risk pixels from within each country was recorded as the country cumulative TC risk, and the ratio of this cumulative value to the total country population was recorded as the per capita risk. The combination of the two dimensions was used to evaluate TC risk in Pacific SIDS, which has the advantage of avoiding a decisive influence of the country population on the results. This paper classifies each of the two into five classes and uses the mean of two classes to measure the final country's TC risk.

## 3. RESULTS

Fig.2 shows the national-level tropical cyclone risk rating for each Pacific SIDS derived from the risk map by spatial analysis, which is evaluated in two dimensions: national cumulative risk and per capita risk. Among Pacific SIDS, Fiji has the highest national cumulative risk and the Northern Mariana Islands has the highest per capita risk. Together with Guam, they are evaluated at the highest risk level of 4. Fiji is located in the South Pacific and has a large population with high levels of exposure and hazard, while Guam and the Northern Mariana Islands have the highest level of TC hazard among all countries. New Caledonia, Vanuatu, and Tonga, located in the South Pacific, have close TC hazard and exposure levels, and the final TC risk was evaluated as level 3. It is worth mentioning that Nauru, Kiribati, and the Marshall Islands, which have almost no TC risk, are almost coincident with the origin in this figure and are recorded as level 0. This result provides a reference basis for the rational allocation of resources and the proposal of mitigation options.

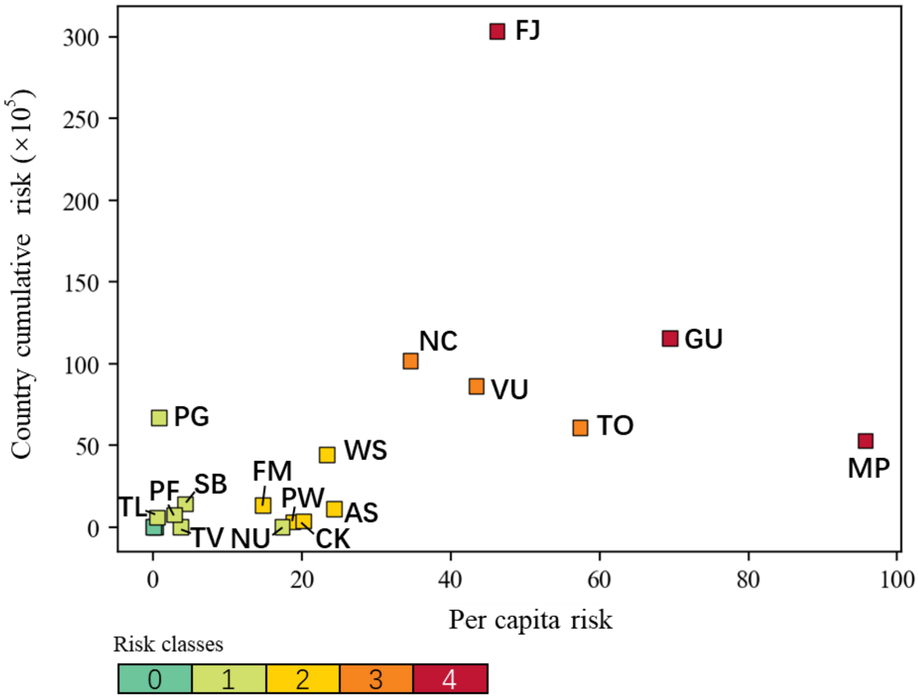


**Fig. 2.** TC risk classes of Pacific SIDS

## 4. SUMMARY

Risk assessment of Pacific SIDS is a pressing issue, and hazard mapping is one of the most critical issues. In this paper, we improve the method of constructing wind speed buffers and build a wind speed buffer database using historical TC data as a way to produce hazard layers and perform a risk assessment for Pacific SIDS.

There are still limitations to this study. One of the main drawbacks is the insufficient wind speed buffer data, which is because the well-documented wind radius information from JTWC started in 2004, and this problem will be solved in the future with the continued increase of best track data with recorded wind radius information. Second, this study doesn't consider the effects of events such as extreme rainfall and storm surge caused by tropical cyclones [12,13], which can be introduced into the risk assessment model in future studies.

## References

[1] UN. 2015 Transforming Our World: The 2030 Agenda For Sustainable Development, Report.
[2] Peduzzi P, Chatenoux B, Dao H, et al. 2012 Global trends in tropical cyclone risk, Nature Climate Change, 2(4): 289-294.
[3] Pascal Peduzzi. 2005 Cyclone Database Manager-A tool for converting point data from cyclone observations into tracks and wind speed profiles in a GIS, Report.
[4] Mishra M, Kar D, Debnath M, et al. 2022 Rapid eco-physical impact assessment of tropical cyclones using geospatial technology: a case from severe cyclonic storms Amphan, Natural Hazards, 110(3): 2381-2395.
[5] Hoque M A A, Pradhan B, Ahmed N, et al. 2019 Tropical cyclone risk assessment using geospatial techniques for the eastern coastal region of Bangladesh, Science of The Total Environment, 692: 10-22.
[6] Lin C Y, Shieh P Y, Wu S W, et al. 2022 Environmental indicators combined with risk analysis to evaluate potential wildfire incidence on the Dadu Plateau in Taiwan, Natural Hazards.
[7] Weatherford C L, Gray W M. 1988 Typhoon Structure as Revealed by Aircraft Reconnaissance. Part I: Data Analysis and Climatology, Monthly Weather Review, 116(5): 1032-1043.
[8] Croxford M, Barnes G M. 2022 Inner Core Strength of Atlantic Tropical Cyclones, Monthly Weather Review, 130(1): 127-139.
[9] Businger S, Businger J A. 2001 Viscous Dissipation of Turbulence Kinetic Energy in Storms, Journal of the Atmospheric Sciences, 58(24): 3793-3796.
[10] Kantha L. 2006 Time to replace the Saffir-Simpson hurricane scale, Eos, Transactions American Geophysical Union, 87(1): 3-6.

[11] Emanuel K A. 1999 The power of a hurricane: An example of reckless driving on the information superhighway, Weather, 54(4): 107-108.
[12] Deo A, Chand S S, Ramsay H, et al. 2021 Tropical cyclone contribution to extreme rainfall over southwest Pacific Island nations, Climate Dynamics, 56(11-12): 3967-3993.
[13] Krishneel K S, Danielle C V, Andrew D M. 2021 A decision tree approach to identify predictors of extreme rainfall events – A case study for the Fiji Islands. Weather and Climate Extremes, 34: 100405.

# The spatial variability of glacier mass budget in the Upper Indus Basin during the early 21st century

Kunpeng Wu[1], Shiyin Liu[1], Zongli Jiang[2]
[1]Institute of International Rivers and Eco-Security, Yunnan University, Kunming, 650091, China
[2]Hunan University of Science and Technology, Xiangtan, 411201, China

## 1. INTRODUCTION

Anomalous behaviour of glaciers in the Karakoram was suspected since the nineteenth century (Godwin-Austen, 1864; Hayden, 1907). Balanced mass budgets were estimated for Karakoram glaciers in the past decades (Brun et al., 2017; Shean et al., 2020). However, the changes of mass balance for Karakoram glaciers in the early 21st century are rare. Brun et al. (2017) reported mass budgets of -0.06 ± 0.19 m w.e. a-1 and 0.05 ± 0.19 m w.e. a-1 in the entire Karakoram for the periods of 2000–2008 and 2008–2016, respectively. Hence, it may be assumed that Karakoram glaciers are in different mass budget conditions in the early twenty-first century. The Indus River originating from the Hindu Kush – Karakoram – Himalaya (HKH) mountain ranges depends significantly for its annual flows (as high as 50–80%) on the contribution from glacier and snow meltwater (Immerzeel et al., 2010). A lot of large valley glaciers developed in the Upper Indus River Basin (UIB) (Hewitt, 2007) (Fig. 1).

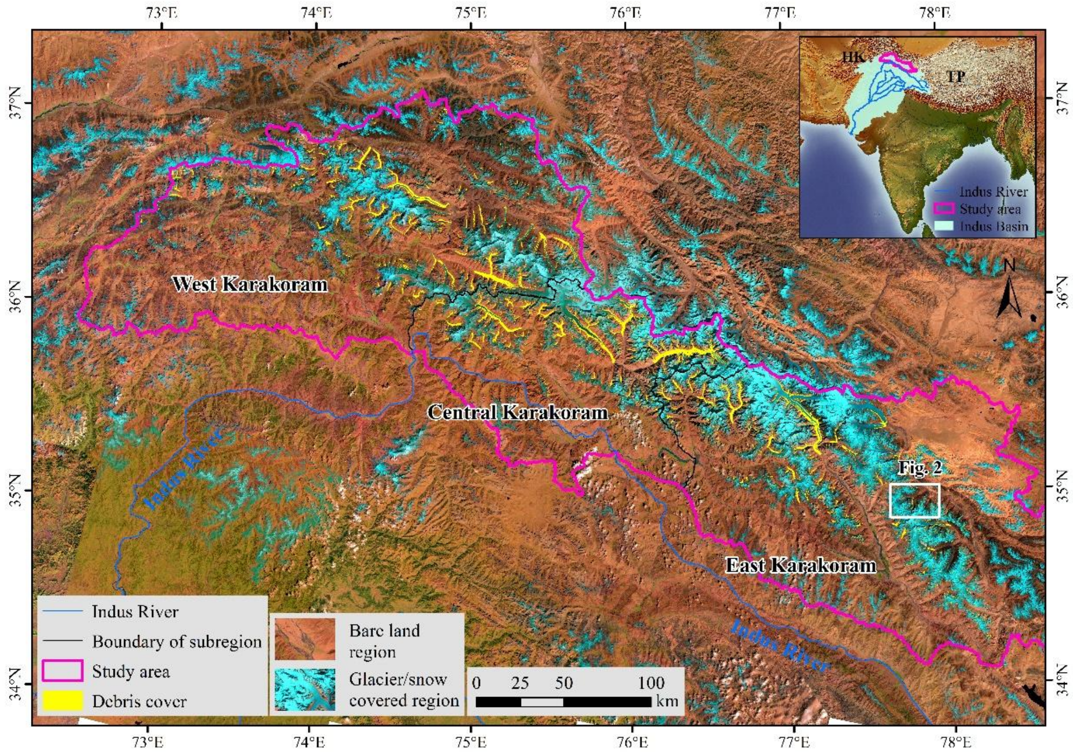


Figure 1. Regional overview of the study area with boundaries of investigated sub-regions, glacier cover and debris cover.

## 2. MATERIALS AND METHODS

### *2.1 Materials*

For glacier mass balance calculations, DEMs and glacier outlines covering the glacierized area of the UIBKK were used in our study. Three DEMs were employed to estimate the changes of glacier surface elevation in the UIBKK. The SRTM C-band DEM was provided by U.S. Geological Survey (Farr et al., 2007). The DEM for the early 2010s was extracted from fifteen pairs of TSX/TDX images, which acquired from the German Aerospace Center (DLR) (Krieger et al., 2007). The latest DEM was extracted from ZY3-02 stereo images.

### *2.2 Glacier height changes*

Based on the method of Differential InSAR (DInSAR), glacier height changes in the periods of 2000 – 2013 and 2013 – 2019 were derived from TSX/TDX and reference DEMs (here ZY3-02 and SRTM DEM). First, by means of InSAR method, the bistatic interferogram was generated from TSX/TDX image and reference DEMs. The bistatic interferogram contain topographic phase, topographic residual phase and flat earth. Next, the topographic phase and flat earth simulated by the orbital information from TSX/TDX image and reference DEMs were removed from the bistatic interferogram. Thus, the topographic residual phase, induced by the glacier height change, was converted to a differential interferogram. Finally, the map of glacier height changes was generated from unwrapped differential interferogram (Wu et al., 2018).

Glacier height changes from 2000 – 2019 were acquired by DEM differencing with SRTM DEM and ZY3-02 DEM (Nuth & Kääb, 2011). Employed the cosinusoidal relationship between elevation difference, terrain slope and terrain aspect in non-glaciated regions, relative horizontal and vertical shift between SRTM DEM and ZY3-02 DEM were corrected.

## 3. RESULTS

In total, no significant mass changes were found in the UIBKK. The average change of glacier elevation for the study area was -1.90 ± 0.34 m in the early 21st century. Glaciers in the UIBKK experienced a slight thinning of -0.10 ± 0.08 m a-1 or a mass balance of -0.09 ± 0.07 m w.e. a-1 (Fig. 2). The average changes of glacier surface elevation varied from ~ -5.03 to 4.41 m a-1 in the UIBKK, while more than 90% of the glaciers (99% of the glacier area) fall in the elevation change category of -1 to 1 m a-1.

The rate of glacier mass loss in the UIBKK has decreased slightly. Glaciers experienced an average thinning of -0.14 ± 0.18 m a-1 or a mass loss of -0.12 ± 0.16 m w.e. a-1 during 2000 – 2013, then it decreased to -0.07 ± 0.23 m a-1 or -0.06 ± 0.21 m w.e. a-1 during 2013 – 2019.

A polarization of glacier mass balances was estimated over the study area in the early 21st century. The most negative mass balance of -0.25 ± 0.08 m w.e. a-1 was measured in the West UIBKK from 2000 to 2019, and an accelerated mass loss was found from -0.09 ± 0.07 m w.e. a-1 in 2000 – 2013 to -0.64 ± 0.17 m w.e. a-1 in 2013 – 2019. Glaciers in the Central UIBKK experienced a moderate mass loss with -0.07 ± 0.09 m w.e. a-1 from 2000 to 2019, and homogeneous mass losses were found in the periods of 2000 – 2013 and 2013 – 2019. Glaciers in the East UIBKK experienced a slight mass gain or balanced mass budget with +0.01 ± 0.19 m w.e. a-1 from 2000 to 2019, while a shifted glacier mass balances from negative to positive were found in the periods of 2000 – 2013 and 2013 – 2019, with means of -0.14 ± 0.14 m w.e. a-1 and +0.27 ± 0.29 m w.e. a-1 respectively.

## 4. SUMMARY

In our study, the spatiotemporal pattern of glacier mass balances in the Karakoram region of Upper Indus Basin (UIBKK) have been estimated, by employing the ZY3-02 stereo images, TerraSAR-X/TanDEM-X images, SRTM DEM and for the early 21st century (2000–2019). Glaciers in the UIBKK experienced a polarization of mass balances from 2000 to 2019. The spatiotemporal pattern of glacier mass balance in the UIBKK showed that mass balances shifted from negative to positive from West to East, respectively, along longitude. Glacier mass loss decelerated from -0.12 ± 0.16 m w.e. a-1 in 2000–2013 to -0.06 ± 0.21 m w.e. a-1 in 2013–2019. An accelerated mass loss was found in the West UIBKK, while mass budgets in the East UIBKK shifted from negative to positive from 2000–2019.

The spatiotemporal patterns of mass balances in the UIBKK were consistent with the tendencies of winter precipitation and summer temperature. Climate warming may play more important role in glacier changes in the UIBKK.

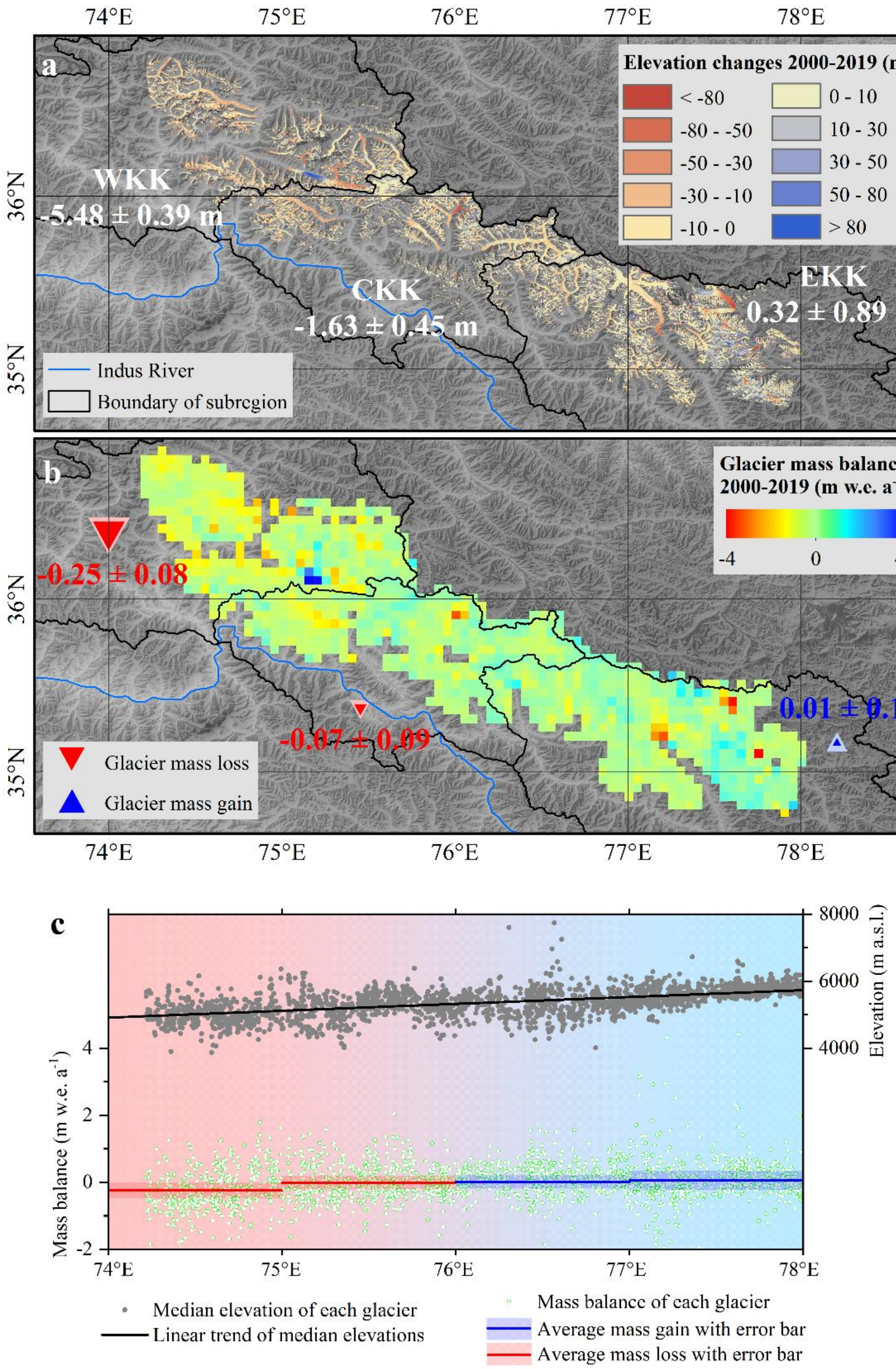


Figure 2. The spatial pattern of glacier mass budget in the UIB in the early 21st century.

## References


[1] Brun, F., Berthier, E., Wagnon, P., Kaab, A., & Treichler, D. (2017), A spatially resolved estimate of High Mountain Asia glacier mass balances, 2000-2016, Nat Geosci, 10(9), 668-673.

[2] Farr, T. G., Rosen, P. A., Caro, E., Crippen, R., Duren, R., Hensley, S., et al. (2007), The shuttle radar topography mission, Reviews of geophysics, 45(2).

[3] Godwin-Austen, H. H. (1864), The glaciers of the Muztagh Range, Proceedings of the Royal Geographical Society, 34, 19-56.

[4] Hayden, H. H. (1907), Notes on certain glaciers in Northwest Kashmir, Records of the Geological Survey of India, 35, 127-137.
[5] Hewitt, K. (2007), Tributary glacier surges: an exceptional concentration at Panmah Glacier, Karakoram Himalaya, Journal of Glaciology, 53(181), 181-188.
[6] Immerzeel, W. W., van Beek, L. P. H., & Bierkens, M. F. P. (2010), Climate Change Will Affect the Asian Water Towers, Science, 328(5984), 1382-1385.
[7] Krieger, G., Moreira, A., Fiedler, H., & Hajnsek, I. (2007), TanDEM-X: A Satellite Formation for High-Resolution SAR Interferometry, Geoscience and Remote Sensing, IEEE Transactions on, 45, 3317-3341.
[8] Nuth, C., & Kääb, A. (2011), Co-registration and bias corrections of satellite elevation data sets for quantifying glacier thickness change, The Cryosphere, 5(1), 271-290.
[9] Shean, D. E., Bhushan, S., Montesano, P., Rounce, D. R., Arendt, A., & Osmanoglu, B. (2020), A Systematic, Regional Assessment of High Mountain Asia Glacier Mass Balance, Frontiers in Earth Science, 7.
[10] Wu, K., Liu, S., Jiang, Z., Xu, J., Wei, J., & Guo, W. (2018), Recent glacier mass balance and area changes in the Kangri Karpo Mountains from DEMs and glacier inventories, The Cryosphere, 12(1), 103-121.

# Impacts of COVID-19 on SDGs revealed by satellite remote sensing: a bibliometric analysis

CHEN Xuejuan[1], Xu Zheping[1], Jiang Tian[1], Zeng Yan[1]

[1] National Science Library, Chinese Academy of Sciences, China
email: chenxuejuan@mail.las.ac.cn (author 1)
email: xuzp@mail.las.ac.cn (author 2)
email: jiangtian@mail.las.ac.cn (author 3)
email: zengy@mail.las.ac.cn (author 4)

## 1. INTRODUCTION

The global community is at a critical moment in its pursuit of the Sustainable Development Goals (SDGs). However, the COVID-19 pandemic has affected many aspects of human life, and is threatening the implementation of the 2030 Agenda for Sustainable Development[1,2].

Big earth data is a new key to explore the earth, playing an important role in supporting the SDGs. Under the COVID-19 pandemic, big earth data can be used to monitor the impacts of COVID-19 on the economy, society, environment, etc. [3,4]. The European Space Agency (ESA) launched the announcement of funding “Space in response to COVID-19 outbreak” [5]. ESA and the European Commission have worked closely together to create the ‘Rapid Action Coronavirus Earth observation’ dashboard, which uses Earth observation satellite data to measure the impacts of the coronavirus lockdown and monitor post-lockdown recovery [6]. In addition, NASA, ESA, and the Japan Aerospace Exploration Agency (JAXA) have jointly created the “COVID-19 Earth Observation Dashboard” [7,8,9], which combines satellite data to monitor key environmental parameters – such as air and water quality changes, climate change, economic and human activities including industry, shipping, construction, traffic, as well as agricultural productivity during COVID-19 pandemic, and study how epidemic control measures affect these conditions.

At present, a lot of researches about COVID-19 have been published, with more than 18,300 papers in CNKI database, more than 300,000 articles in Web of Science-Core collection database, and more than 600,000 publications in World Health Organization (WHO) literature platforms[10]. Based on these published researches, identify and analyze publications that used satellite remote sensing data and method help understand the importance of remote sensing in monitoring and evaluating the impacts of COVID-19. Therefore, this study focuses on the researches about COVID-19 with using satellite remote sensing date and methods. The purpose is to reveal the research hotspots and the impacts of COVID-19 on SDGs.

## 2.MATERIALS AND METHODS

### *2.1 Data sources and search strategies*

In this study, we obtained publications about COVID-19 from the Web of Science Core Collection (hereinafter referred to as WOS). The search strategies were set as follows: (ALL=covid-19 OR ALL=covid OR ALL=coronavirus OR ALL=sars-cov-2 OR ALL=2019.ncov OR ALL="novel coronavirus") AND PY>= 2019. The search results, which counts to 323802, contain many publications that mentioned COVID-19 as a background but not as research themes. Since the World Health Organization has established a data platform to collect COVID-19 literature, we selected publications from WOS that also were collected by World Health Organization as a raw dataset, totally counting to 304938.

### *2.2 Data processing*

In order to select the publications that research COVID-19 by using remote sensing methods, we built a vocabulary about satellites and sensors. By identifying words about satellites and sensors in the abstract, there are 616 publications identified.

In order to analyze the impact of COVID-19 pandemic on SDGs, we also download publications on Dimensions platform which has indexed the corresponding SDGs on publications.

Therefore, the final dataset we use in this study contains 616 publications with title, keywords, authors, nationalities, publication dates, journals, affiliations, satellite type, the corresponding SDGs, and so on.

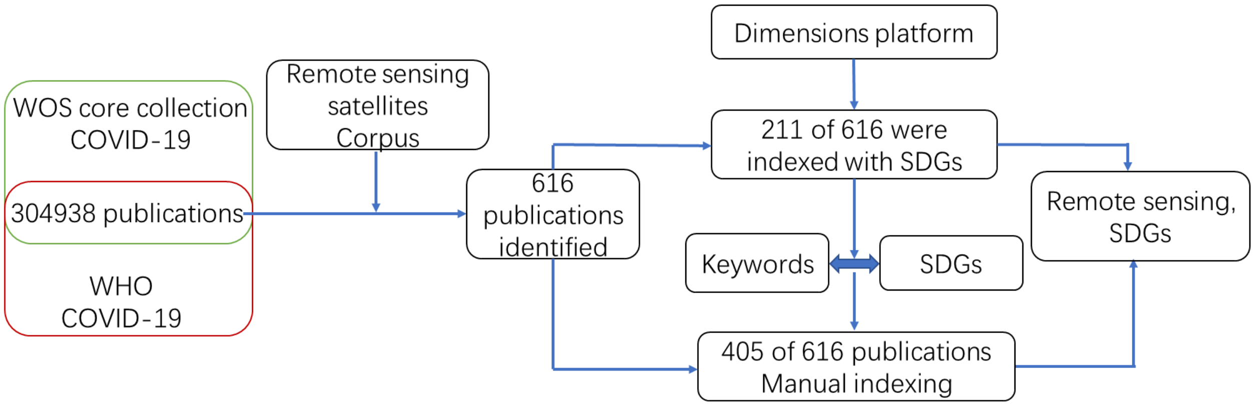


**Fig. 1**. The detailed process of screening and identifying for researches about SDGs with remote sensing methods under COVID-19 pandemic.

### *2.3 Bibliometric analysis*

Bibliometric analysis was mainly conducted by MySQL and VOSviewer. Data from WOS were exported to MySQL. The statistical analysis by MySQL contains the distribution of countries, research fields and SDGs, *etc*. VOSviewer is a knowledge visualization software. It can generate a variety of co-occurrence diagrams, especially keywords co-occurrence diagram which is usually used to study hotspots and analyze research frontiers in this field.

## 3.RESULTS

### *3.1 Statistical Analysis on literature*

We analyzed the journals and research fields of these publications. Remote Sensing ranked first with 47 articles, followed by the Aerosol and Air Quality Research with 27 and Science of the Total Environment with 26. By statistics of the papers published in each research field, we found that the number of publications in Environmental Sciences was the most. Other research fields includes Remote Sensing; Geosciences, Multidisciplinary; Meteorology & Atmospheric Sciences; Imaging Science & Photographic Technology; Multidisciplinary Sciences; Public, Environmental & Occupational Health; Green & Sustainable Science & Technology, which indicates that remote sensing can be used to study the impacts of COVID-19 on a wide range of research areas on the earth.

**Table 11.** Distribution of journals and research fields.

| Journal | Publications | Research field | Publications |
|---|---|---|---|
| Remote Sensing | 47 | Environmental Sciences | 313 |
| Aerosol and Air Quality Research | 27 | Remote Sensing | 103 |
| Sci Total Environ | 26 | Geosciences, Multidisciplinary | 93 |
| Atmospheric Chemistry and Physics | 20 | Meteorology & Atmospheric Sciences | 84 |
| Geophysical Research Letters | 18 | Imaging Science & Photographic Technology | 72 |
| Atmosphere | 11 | Multidisciplinary Sciences | 39 |
| Environ Res | 11 | Public, Environmental & Occupational Health | 33 |
| Environmental Research Letters/Scientific Reports/Frontiers in Marine Science/Sustainability/Remote Sensing Applications: Society and Environment | 9 | Green & Sustainable Science & Technology | 24 |

| | | |
|---|---|---|
| | Engineering, Electrical & Electronic | 19 |
| | Environmental Studies/ Geography, Physical | 17 |

### *3.2 Analysis of Research Hotspots*

Fig.2 shows the co-occurrence of keywords. In general, except for words with the same meaning of COVID-19, the hot keywords in these publications including lockdown, air quality, air pollution, remote sensing, $NO_2$, TROPOMI, emissions, ozone, PM2.5, aerosols, AOD, etc.

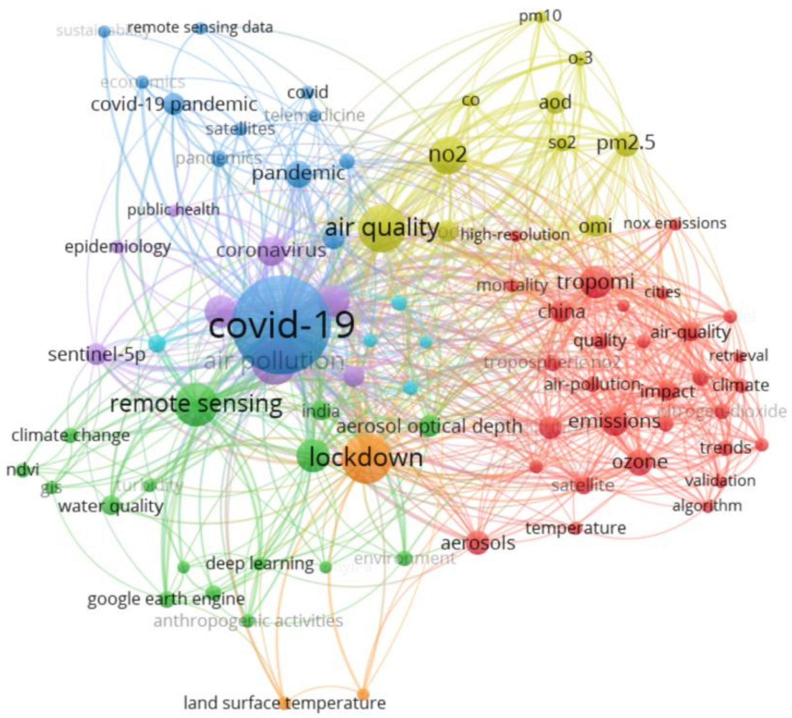


***Fig. 2 Co-occurrence of keywords in publications about COVID-19 with remote sensing method***

By identifying the SDGs for each article, it was found that the top 5 SDG were SDG11, SDG13, SDG3, SDG7, SDG2. Among them, the number of publications of SDG11 was the most, and the hot keywords in SDG11 include: air pollution, lockdown, air quality, NO2, particulate matter, PM2.5, aerosols, remote sensing, AOD, ozone, emissions, etc. Among the top 4 SDGs by the number of published articles, their hot keywords all include air quality/air pollution. Air quality is closely related to many aspects of human beings, including climate change, human health, energy, sustainable cities and communities, which is drawing increasing attention. The satellites/sensors used to carry out the researches include: MODIS, Sentinel, TROPOMI, Landsat, OMI, VIIRS, EMI, IASI, Pleiades, CALIPSO, GOSAT, OCO-2, GF-2, CALIP, etc.

The above analysis shows that, researchers are most concerned about the impacts on air quality under the COVID-19 pandemic and the lockdown measures.

**Table 2.** Hot keywords and satellites/sensors for SDGs.

| SDGs (TOP 5) | Keywords (TOP 10) | Satellites/Sensors |
|---|---|---|
| 11 Sustainable Cities and Communities | air pollution, lockdown, air quality, $NO_2$, particulate matter, PM2.5, aerosols, remote sensing, AOD, ozone, emissions | MODIS, Sentinel, TROPOMI, Landsat, OMI, VIIRS, EMI, IASI, Pleiades, CALIPSO |
| 13 Climate Action | emissions, aerosols, lockdown, air pollution, air quality, climate change, remote sensing, carbon emission, $NO_2$, resolution | TROPOMI, Sentinel, OMI, GOSAT, VIIRS, CALIPSO, OCO-2 |
| 3 Good Health and Well Being | air pollution, air quality, lockdown, mortality, $NO_2$, health impact, human health, ozone, fine particulate matter, aerosol | Sentinel, MODIS, TROPOMI, OMI |

| | | |
|---|---|---|
| | optical depth | |
| 7 Affordable and Clean Energy | lockdown, energy consumption, air quality, aerosol, carbon emission, social carbon cost, containment efficacy, public health, air pollution, biomass burning | MODIS, OMI, Sentinel, CALIPSO, GF-2, CALIP |
| 2 Zero Hunger | remote sensing, precision agriculture, proximal sensing, cereals, drones, citizen science, low-cost sensors, IoT, food security, water management | MODIS, Landsat, Sentinel |

## 4.SUMMARY

In this study, we identified a total number of 616 publications about the research on COVID-19 with using satellite remote sensing data and methods. Researches published in the journal - Remote Sensing were the most, and the journal - Aerosol and Air Quality Research ranked second.

Satellite remote sensing is widely used to study the impacts of COVID-19 and the lockdown measures on earth and human life. Most publications that studied COVID-19 with satellite remote sensing data and methods concern about SDG11. Air quality is a hotspot, which is closely related to climate change, human health, energy, sustainable cities and communities, etc.

## References


[1] The Sustainable Development Goals Report (2021), Report, http://opendbar.casearth.cn/file//sdg_report/The-Sustainable-Development-Goals-Report-2021.pdf

[2] Big Earth Data in Support of the Sustainable Development Goals 2021 (2021), Chinese Academy of Sciences, Report, http://opendbar.casearth.cn/file//sdg_report/Big%20Earth%20Data%20in%20Support%20of%20the%20Sustainable%20Development%20Goals%202021-ZN.pdf

[3] COVID-19: how can satellites help? https://www.esa.int/Applications/Observing_the_Earth/COVID-19_how_can_satellites_help

[4] Satellites provide crucial data on crops during COVID-19, https://www.esa.int/Applications/Observing_the_Earth/Satellites_provide_crucial_data_on_crops_during_COVID-19

[5] Space in response to COVID-19 outbreak, ESA, https://www.esa.int/Applications/Telecommunications_Integrated_Applications/Space_in_response_to_COVID-19_outbreak. (2022.07.18)

[6] 'Rapid Action Coronavirus Earth observation' dashboard now available, ESA, https://www.esa.int/Applications/Observing_the_Earth/Rapid_Action_Coronavirus_Earth_observation_dashboard_now_available. (2022.07.18)

[7] The COVID-19 Earth Observing Dashboard, https://www.eodashboard.org/. (2022.07.18)

[8] Join the 2021 Earth Observation Dashboard Hackathon, https://earthdata.nasa.gov/learn/articles/eo-dashboard-hackathon. (2022.07.18)

[9] Space agencies join forces to produce global view of COVID-19 impacts, https://www.esa.int/Applications/Observing_the_Earth/Space_agencies_join_forces_to_produce_global_view_of_COVID-19_impacts. (2022.07.18)

[10] COVID-19 Global literature on coronavirus disease, World Health Organization, https://search.bvsalud.org/global-literature-on-novel-coronavirus-2019-ncov/

# DBAR-Digital Technology for Agricultural Monitoring and Food Security

# Incidence Angle Aided Active Pairwise Constraint Learning for Time-Series Clustering Based Crop Mapping of UAVSAR Imagery

Qin Xingli [1], Wu Bingfang [1], Yang Jie [2], Zhao Lingli [3], Li Pingxiang [2], Sun Kaimin [2]

[1] State Key Laboratory of Remote Sensing Science, Aerospace Information Research Institute, Chinese Academy of Sciences, China
email: qinxl@aircas.ac.cn

[2] State Key Laboratory of Information Engineering in Surveying, Mapping and Remote Sensing, China
3 School of Remote Sensing and Information Engineering, Wuhan University, China

## 1. INTRODUCTION

Airborne PolSAR is an important data source for the fine classification of crops, and has important applications in agricultural monitoring and food safety. However, the wide range of incidence angles of airborne PolSAR imagery leads to the significant difference between the backscattering coefficients of crops in the near range and the far range, thus reducing the accuracy of crop mapping using the time-series clustering technique. In this paper, constrained clustering methods are introduced to solve the incidence angle effects. Constrained clustering (which is also known as semi-supervised clustering) can introduce background knowledge (also known as side information) to guide a clustering algorithm [1]. To achieve reliable crop mapping from airborne PolSAR images via constrained time-series clustering, we propose an active pairwise constraint learning method (APCL). The proposed method integrates the batch-mode active learning method (BMAL), the information contained in the incidence angle, and the characteristics of the crops' time-series curves to learn informative instance-level constraints. The method was designed for PolSAR images with a wide range of incidence angles and was verified in the experiments conducted in this study, where we mapped crops from UAVSAR images using several constrained clustering methods and time-series similarity measures.

## 2. MATERIALS AND METHODS

### *2.1 Study Area and Experimental Data*

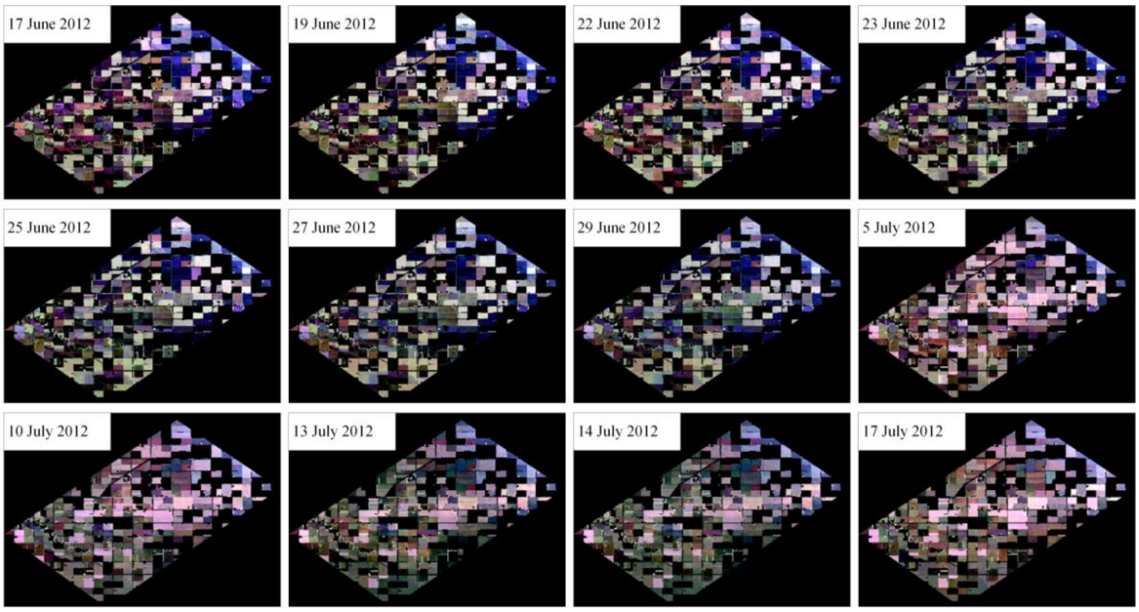


Figure 1. Pauli RGB images of the UAVSAR time-series images.

The study area located in the southwest of Winnipeg, Manitoba, Canada, is covered by various crops. Four types of crops were considered in the crop mapping experiments: oat, corn, canola, and soybean. The reference map for the crop distribution was made according to the land-cover classification map produced by the NASA National Snow and Ice Data Center Distributed Active Archive Center (NSIDC DAAC) [2]. The data used in this study were the UAVSAR images obtained during the Soil Moisture Active Passive Validation Experiment 2012 (SMAPVEX2012). The SMAPVEX12 campaign lasted 43 days (June 7–July 19, 2012) during which time the soil moisture and vegetation conditions changed significantly. By the end of the campaign, 13 days of UAVSAR data were acquired [3]. In this study, 12 UAVSAR images of the same flight line were used for the crop mapping, as shown in Figure 1. The images were ground range projected and multi-looked data (GRD), whose preprocessing processes include radiometric calibration, geometric correction (WGS-84) and multi-looks processing (15 pixels in range and 60 pixels in azimuth directions). To reduce the time spent in the experiment, these images were resampled from 1134×795 (pixels) to 378×265 (pixels).

### *2.2 Methods*

The constrained clustering methods using instance-level constraints were introduced to improve the reliability and stability of time-series clustering results. However, the effectiveness of pairwise constraints from the commonly used random sampling remains uncertain. Therefore, in view of the characteristics of UAVSAR time-series images, we propose a new method for generating informative pairwise constraints, which we call "active pairwise constraint learning (APCL)". The flowchart of APCL is shown in Figure 2, which consists of two main steps: 1) extraction of the candidate sample set; and 2) construction of the pairwise constraints.

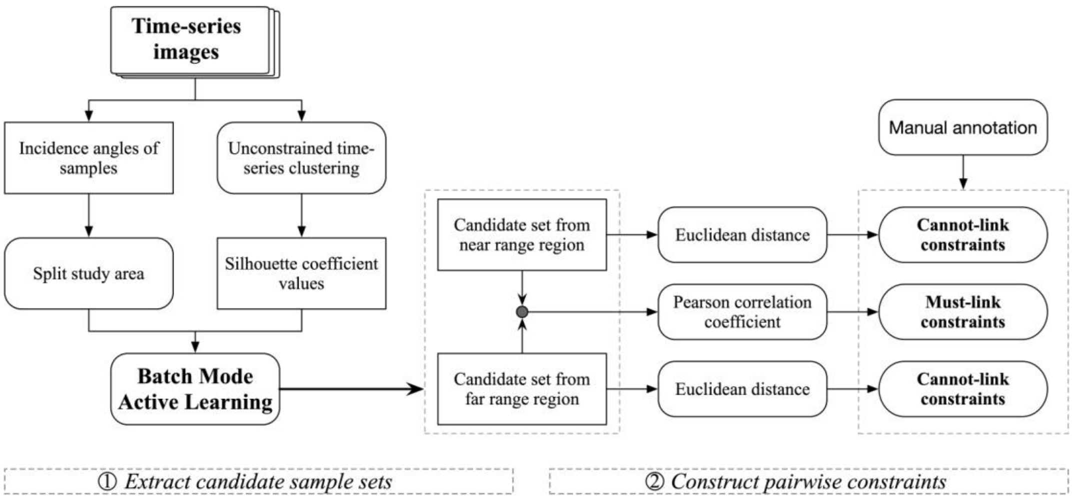


Figure 2. Flowchart of the proposed active pairwise constraint learning method.

### (1) Extraction of the Candidate Sample Set

The objective of this step is to extract a group of samples with rich information. Active learning is commonly used in classification tasks, where it regards the samples which are the most helpful to improve the performance of the classifier as the informative samples [4]. However, conventional active learning techniques select only a single sample at each iteration for manual labeling and retrain the prediction model [5-8], which is inefficient and not applicable to the clustering task of the paper. To address these limitations, we consider batch-mode active learning (BMAL) technique, in which a batch of samples are selected for manual annotation simultaneously at each round. The key issue of BMAL is to select the most informative batch of samples with as little redundancy as possible, so that they can provide the highest possible information to the prediction model [5, 7, 9, 10]. It should be noted that, different from the BMAL in the classification task, the proposed method only performs the sample selection process once. To extract informative candidate sample set, both the uncertainty criterion and diversity criterion are considered in the proposed method.

### (2) Construction of the Pairwise Constraints

When learning the pairwise constraints, two characteristics of the crops in the UAVSAR time-series images are taken into account: 1) the time-series curves of the same type of crops from the near range and far range may have high shape similarity but large spatial distances; and 2) the time-series curves of the different types of crops with small differences of incidence angle may be close to each other in the feature space, thus leading to misclassification. Consequently, we construct the must-link constraints (MLC) based on the first characteristic, and construct the cannot-link constraints (CLC) based on the second characteristic.

## 3. RESULTS

In order to evaluate the effectiveness of APCL, all the samples (the total number is 30605) of the study area were used for time-series clustering, and PC-KMeans was used as the constrained clustering algorithm. The three time-series similarity criteria (ED, DTW and Pearson) and the two constraints generation methods (RSRIA and random sampling) were also used for comparison. The total number of MLCs and CLCs was 12000 (40% of the total of samples), and the number of initial cluster centroids was set to eight. In addition, the results of PC-KMeans with zero constraints were used as the baseline to evaluate the accuracy improvement effect of the constrained clustering. After obtaining the clustering results, for each cluster, the number of samples of each class was counted according to the reference map, then the class label with the largest number of samples was assigned to the cluster (In practice, the process of labeling clusters should be done manually). Each experiment was repeat five times, and the result closest to the average accuracy was taken for analysis. The crop classification maps are shown in Figure 3.

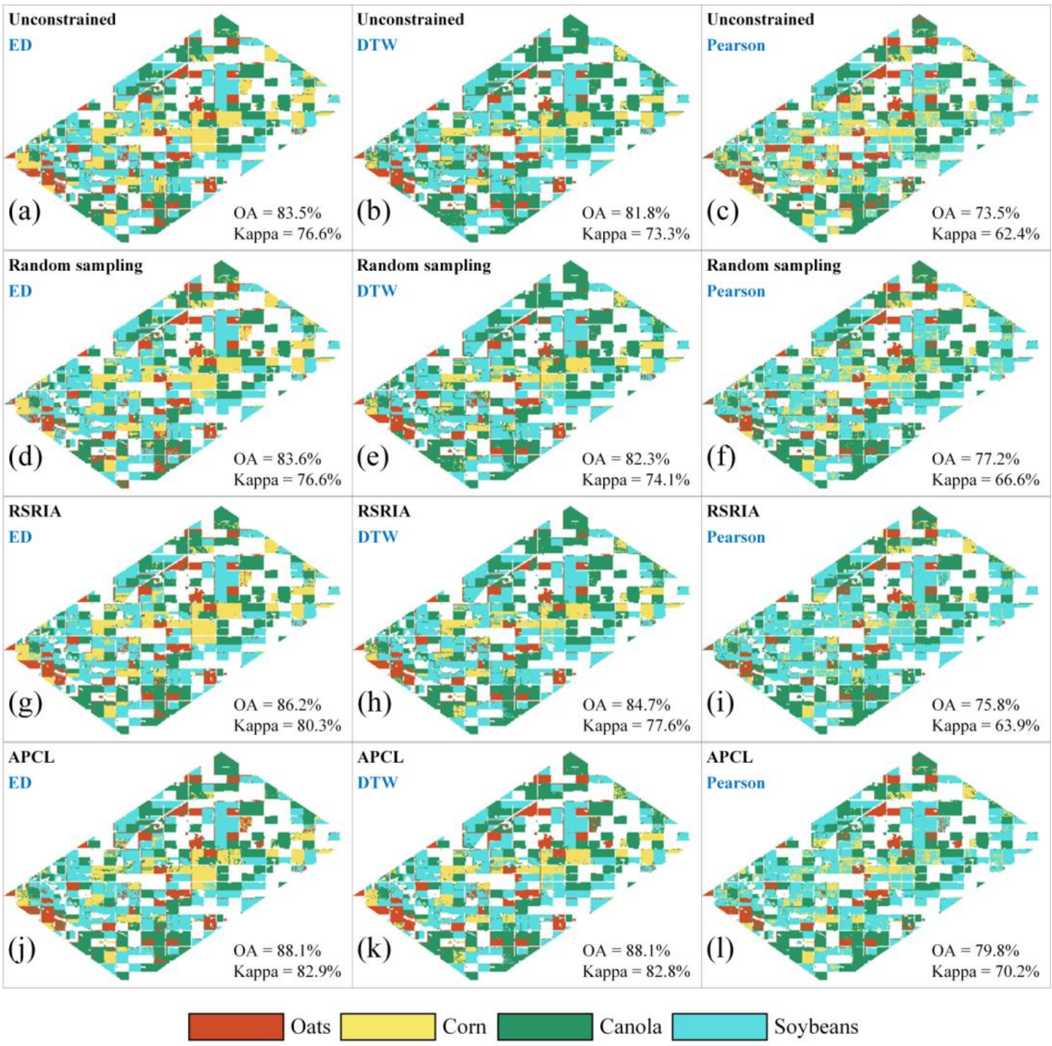

Figure 3. Crop classification maps: (a), (b), and (c) are results of unconstrained clustering; (d), (e), and (f) are the results of random sampling; (g), (h), and (i) are results of RSRIA; (j), (k) and (l) are the results of APCL. For each row, the first image is obtained using ED, the second is obtained using DTW, and the last is obtained using Pearson.

The crop classification maps show that unconstrained clustering achieved its highest accuracy (kappa = 76.6%) when using ED as the similarity criterion, the best accuracy of random sampling is 77.6% when using DTW as the similarity criterion, and the best accuracy of RSRIA is 80.3% when using ED as the similarity criterion. The accuracies of APCL are significantly better than the above results when using ED and DTW, with the kappa being 82.9% and 82.8%, respectively. All the four methods have poor accuracies when using Pearson, however, the accuracy of APCL (kappa=70.2%) is still better than that of the other methods.

## 4. SUMMARY

In this paper, in consideration of the large differences in the backscatter coefficients between crops in the near range and the far range of airborne PolSAR images, an active pairwise constraint learning method has been proposed to generate informative instance-level constraints for time-series clustering. The experimental results using UAVSAR images not only show the necessity for constrained clustering in improving the crop mapping accuracy, but also highlight the effectiveness of the proposed method compared to the commonly used random sampling method.

As a semi-supervised clustering technique, constrained clustering also needs some supervised information to aid the clustering process. However, supervision by instance-level constraints is more general and more realistic than specific class labels. By using knowledge, even when the class labels may be unknown, a user can specify whether pairs of samples belong to the same cluster or not. In addition, the usage of the information contained in the incidence angles by the proposed method has a certain reference value for future study.

## References

[1] Lampert, T., et al., *Constrained distance based clustering for time-series: a comparative and experimental study.* Data Mining and Knowledge Discovery, 2018. **32**(6): p. 1663-1707.
[2] McNairn, H., J. Powers, and G. Wiseman, SMAPVEX12 Land Cover Classification Map, Version 1. [June to July 2012]. Boulder, Colorado USA. NASA National Snow and Ice Data Center Distributed Active Archive Center., 2014.
[3] McNairn, H., et al., The Soil Moisture Active Passive Validation Experiment 2012 (SMAPVEX12): Prelaunch Calibration and Validation of the SMAP Soil Moisture Algorithms. IEEE Transactions on Geoscience and Remote Sensing, 2015. 53(5): p. 2784-2801.
[4] Schein, A.I. and L.H. Ungar, Active learning for logistic regression: an evaluation. Machine Learning, 2007. 68(3): p. 235-265.
[5] Demir, B., C. Persello, and L. Bruzzone, Batch-Mode Active-Learning Methods for the Interactive Classification of Remote Sensing Images. IEEE Transactions on Geoscience and Remote Sensing, 2011. 49(3): p. 1014-1031.
[6] Chakraborty, S., V. Balasubramanian, and S. Panchanathan, Adaptive Batch Mode Active Learning. IEEE Transactions on Neural Networks and Learning Systems, 2015. 26(8): p. 1747-1760.
[7] Li, H., et al., Batch mode active learning via adaptive criteria weights. Applied Intelligence, 2020.
[8] Patra, S. and L. Bruzzone, A cluster-assumption based batch mode active learning technique. Pattern Recognition Letters, 2012. 33(9): p. 1042-1048.
[9] Wang, Z., et al., A batch-mode active learning framework by querying discriminative and representative samples for hyperspectral image classification. Neurocomputing, 2016. 179: p. 88-100.
[10] Chang, C. and H. Huang, Automatic Tuning of the RBF Kernel Parameter for Batch-Mode Active Learning Algorithms: A Scalable Framework. IEEE Transactions on Cybernetics, 2019. 49(12): p. 4460-4472.

# Winter wheat identification by integrating spectral and temporal information

ZHANG Xiwang[1], LIU Jianfeng[2]

[1] Key Laboratory of Geospatial Technology for the Middle and Lower Yellow River Regions (Henan University), Ministry of Education, P.R.China
email: zhangxiwang@vip.henu.edu.cn

[2] Yellow River Conservancy Technical Institute, P.R.China
email: liujianfeng@yrcti.edu.cn

## 1. INTRODUCTION

The key to global food security is sustainable agriculture, and improved agricultural practices require current, spatially explicit information on crops [1-2]. Timely information on crop acreage at regional and national scales is essential for accurately predicting yields, optimizing spatial patterns, and agricultural planning [3-4]. Remote sensing has proven to be an effective and widely used tool in the agricultural field, for applications such as mapping and monitoring, for many decades [5-6], by providing positive solutions to pressing agricultural problems [7-8]. Spatial and temporal resolutions of remote sensing products are the two main features to consider when extracting information [9]. In practical applications, there is generally a trade-off between temporal and spatial resolutions, as current sensors rarely have both high spatial resolution and high temporal resolution [10]. This trade-off generally leads to non-ideal results. Therefore, optimal results are obtained by combining the spatial features of finer spatial resolution remote sensing images and the temporal frequency of coarser spatial resolution images [11]. This combination can provide a feasible and economical solution [12], especially when ideal finer spatial resolution images cannot be obtained. In current studies which integrate fine and coarser spatial resolution images, either the fine resolution data is only used to provide endmembers for pixel unmixing [13], or the identification results from the fine resolution images are used to build regression models with coarser resolution vegetation index series[14]. The results of either approach are usually coarse resolution abundance without sufficient spatial detail about the individual components [15]. Limited attention has been paid to the spatial relationships between the pixels from these two kinds of images. In this paper, we propose a new method for expressing the quantitative relationship between the MODIS NDVI time series and actual crop acreage, and use it to determine the spatial distribution of sub-pixels within the coarse resolution pixel.

## 2. MATERIALS AND METHODS

### *2.1 Datasets and preprocessing*

In this paper, the data include Landsat TM, time series MODIS NDVI, land use, and field investigation data. The Landsat TM image is resampled using a 25 m resolution, and then each 250 m MODIS pixel will correspond to $10\times10$ TM pixels. 56 stratified random samples of $250\times250$ m were selected to create Winter wheat acreage fraction samples. Five-hundred validation points and statistical yearbook data were used to validate the winter wheat planting area

### *2.2 General research ideas*

This research consists of three parts: (1) analyze the growth of major vegetation by MODIS NDVI time series, select the ideal phenological stages for regression analysis, and assess winter wheat abundance; (2) calculate the membership for winter wheat based on Bayesian rules; and (3) propose an AM model integrating abundance and membership to identify winter wheat. The overall methods used in this study are presented as a flowchart in Fig. 1.

### *2.3 Abundance assessment from MODIS time series*

In order to more clearly observe the differences within a season, the MODIS NDVI curves of each land cover type are extracted and they are plotted together for the 2009–2010 growing season in Fig. 2.

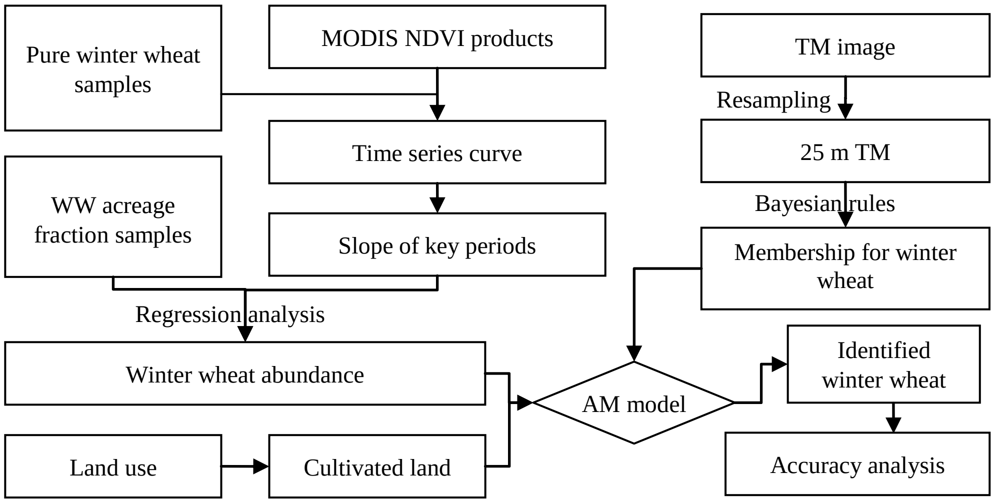


**Fig. 1.** Flowchart for identifying winter wheat in this study. WW means winter wheat, and AM means Abundance-Membership model.

The distinctive features captured in the time series can usually be used to identify crop types [15]. Analogous to the principle of atmospheric windows in earth surface reflectance data, the peaks at points B and E can be considered as reflection peaks, while the points A, C and F are absorption troughs. Like the vegetation index's highlighting of vegetation information, the slope of the time series curve indicates the acreage fraction within a pixel. For example, in the period from point C to point D, if the acreage proportion of winter wheat in a MODIS pixel is closer to 100%, then its NDVI time series curve should be more similar to pure winter wheat. A MODIS pixel with winter wheat mixed with other types will result in a lower slope, and the larger the proportion of other types, the smaller the slope. Therefore, the winter wheat acreage proportion in each MODIS pixel has a significant positive correlation with the slope of period CD.

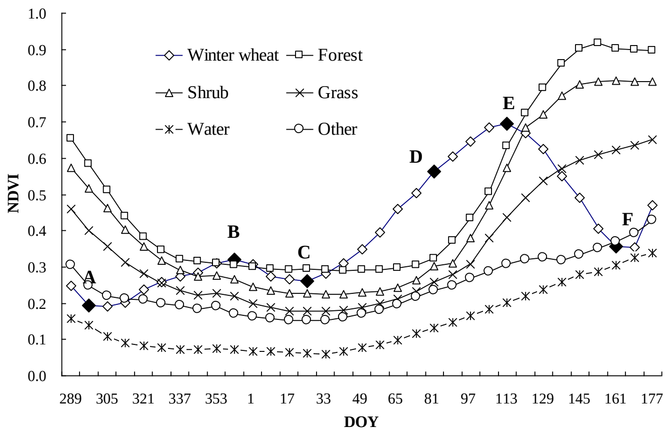


**Fig. 2**. Normalized difference vegetation index (NDVI) time series curves of each land cover type during the 2009–2010 growing season. A-F, the key feature points in the time series curve of winter wheat; DOY, the day of a year.

Based on the above analysis, a regression analysis is employed to assess the abundance of winter wheat at the MODIS scale using temporal information. First, a correlation analysis is performed between abundance samples and time series curve slopes to rationally choose the periods for optimal abundance assessment. Then, the periods with significant correlation coefficients are selected to build regression models.

### *2.4 Membership calculation based on bayesian rules*

The calculation method for membership based on Bayesian rules adopted in this study is a typical, commonly used method.

### *2.5 Winter wheat identification model*

In this section, we design an Abundance-Membership (AM) model to identify winter wheat by integrating the assessed abundances from temporal information and the membership for winter wheat from spectral information. Because the MODIS 250 m data and TM 25 m are strictly registered, each MODIS pixel corresponds to 10×10 TM pixels in the space. Assuming the MODIS data has *m* rows and *n* columns in this study area, the abundance image is processed as follows:

$$PAI = Int(100 \cdot AI) = Int\left(100 \cdot \begin{pmatrix} AI_{11} & \cdots & AI_{1n} \\ \cdots & \cdots & \cdots \\ AI_{m1} & \cdots & AI_{mn} \end{pmatrix}\right) \tag{1}$$

Where, *PAI* is the Processed Abundance Image at the MODIS scale; *AI* is the original Abundance Image; $AI_{ij}$ is the original abundance value of the pixel at the *i*th row and *j*th column, $0 \le AI_{ij} \le 1$; and *Int* is a function for a rounding operation. Then, $PAI_{ij}$ is the pixel value of the processed abundance images at the *i*th row and *j*th column, $0 \le PAI_{ij} \le 100$.

For the processed abundance image, the corresponding pixel membership matrix (10×10 membership pixels at 25 m scale) of each MODIS pixel is processed as follows:

$$CT_{ij} = Matrixrank(PAI_{ij}, P_{ij}) = Matrixrank\left(PAI_{ij}, \begin{pmatrix} P_{ij11} & \cdots & P_{ij1k} \\ \cdots & \cdots & \cdots \\ P_{ijk1} & \cdots & P_{ijkk} \end{pmatrix}\right) \tag{2}$$

Where, $CT_{ij}$ is the calculated threshold for the membership matrix corresponding to the abundance pixel at the *i*th row and *j*th column; $P_{ij}$ is the membership matrix corresponding to the abundance pixel at the *i*th row and *j*th column; $P_{ijhl}$ is the membership value at the *h*th row and *l*th column in this membership matrix, $k$=10, $1 \le h, l \le k$; and *Matrixrank* is a function that sorts 100 membership values in descending order within the matrix $P_{ij}$, and outputs the $PAI_{ij}$th membership value.

Based on the spatial relationship between the abundance and membership data, winter wheat pixels are identified according to the relative sizes of the membership values in the corresponding matrix. In each matrix, winter wheat is identified by the Eq. (3):

$$RES_{ijhl} = \begin{cases} 1 & P_{ijhl} \ge CT_{ij} \\ 0 & P_{ijhl} < CT_{ij} \end{cases} \tag{3}$$

where $RES_{ijhl}$ is the value of the identified pixel at the *h*th row and *l*th column in the membership matrix which corresponds to the abundance pixel at the *i*th row and *j*th column.

## 3. RESULTS

After the winter wheat abundance is processed according to Eq. (1), the abundance value F implies that there are F pixels belonging to winter wheat in the corresponding 10×10 TM pixels. The membership was calculated and it indicates the probability of winter wheat. The processed abundance image and membership image are spatially operated using the *Matrixrank* function to produce a threshold image. Finally, Eq. (3) is used to identify winter wheat according to the threshold image and corresponding membership matrix. The identified result of winter wheat distribution is shown in Fig. 3.

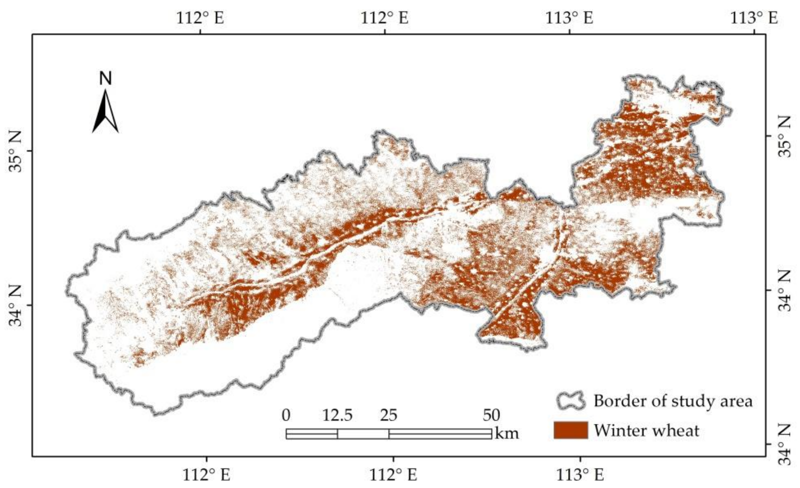


**Fig. 3.** The identification result of winter wheat in the study area

The total acreage of identified winter wheat in this study area is 155,538.63 ha. Using the 500 random validation points, confusion matrices of the three methods are produced. Compared to maximum likelihood classification (MLC) and random forest classification (RFC), overall accuracy of the proposed method is increased by 6.75% and 2.80%, respectively. The Kappa coefficient is also significantly improved.

## 4. SUMMARY

Undoubtedly, higher spatial resolution remote sensing images will generally result in higher crop identification accuracy. However, it is difficult to acquire high-quality images covering an entire study area of interest in a specified short time period because of cloud cover and other weather conditions. Intraclass differences will approach interclass differences when only remote sensing images of non-ideal period can be obtained, and the traditional spectral-based methods do not perform well. To solve this problem, this study proposes a solution for winter wheat identification. The abundance derived from key temporal change features of time series MODIS NDVI is combined with the membership derived from spectral information of Landsat TM. In addition, the separability of targets is improved by narrowing the discriminant space. These results are significantly higher than those obtained MLC and RFC using the same images. This study demonstrates the feasibility of improving identification accuracy by adding temporal information and limiting the size of the discriminant space. Furthermore, it also provides a new perspective and enriches research ideas for crop-type identification and acreage estimation using multi-source remote sensing data.

## References

[1] Conrad C, Dech S, Dubovyk O, et al. **(**2014**)** Derivation of temporal windows for accurate crop discrimination in heterogeneous croplands of Uzbekistan using multitemporal RapidEye images. *Computers and Electronics in Agriculture*, **103**, 63–74.

[2] Zhang X, Zhang Q. (2016)Monitoring interannual variation in global crop yield using long-term AVHRR and MODIS observations. *ISPRS Journal of Photogrammetry and Remote Sensing*, **114**, 191–205.

[3] Wu B, Li Q. (2012) Crop planting and type proportion method for crop acreage estimation of complex agricultural landscapes. *International Journal of Applied Earth Observation and Geoinformation*, **16**, 101–112.

[4] Zhang X, Qiu F, Qin F. (2019) Identification and mapping of winter wheat by integrating temporal change information and Kullback–Leibler divergence. *International Journal of Applied Earth Observation and Geoinformation*, **76**, 26–39.

[5] Bolton D K, Friedl M A. (2013) Forecasting crop yield using remotely sensed vegetation indices and crop phenology metrics. *Agricultural and Forest Meteorology*, **173**, 74–84.

[6] Potgieter A B, Lawson K, Huete A R. (2013) Determining crop acreage estimates for specific winter crops using shape attributes from sequential MODIS imagery. *International Journal of Applied Earth Observation and Geoinformation*, **23**, 254–263.

[7] Gallego J, Bamps C. (2008) Using CORINE land cover and the point survey LUCAS for area estimation. *International Journal of Applied Earth Observation and Geoinformation*, **10**, 467–475.

[8] Xiao F, Li Y, Du Y, et al. (2014) Monitoring Perennial Sub-Surface Waterlogged Croplands Based on MODIS in Jianghan Plain, Middle Reaches of the Yangtze River. *Journal of Integrative Agriculture*, **13**, 1791–1801.

[9] Li X, Ling F, Foody G M, et al. (2017) Generating a series of fine spatial and temporal resolution land cover maps by fusing coarse spatial resolution remotely sensed images and fine spatial resolution land cover maps. *Remote Sensing of Environment*, **196**, 293–311.

[10] Zhang Y, Foody G M, Ling F, et al. (2018) Spatial-temporal fraction map fusion with multi-scale remotely sensed images. *Remote Sensing of Environment*, **213**, 162–181.

[11] Gao F, Masek J, Schwaller M, et al. (2006) On the blending of the Landsat and MODIS surface reflectance: predict daily Landsat surface reflectance. *IEEE Transactions on Geoscience and Remote Sensing*, **44**, 2207–2218.

[12] Gao F, Anderson M C, Zhang X, et al. (2017) Toward mapping crop progress at field scales through fusion of Landsat and MODIS imagery. *Remote Sensing of Environment*, **188**, 9–25.

[13] Pan Y, Li L, Zhang J, et al. (2012) Winter wheat area estimation from MODIS-EVI time series data using the Crop Proportion Phenology Index. *Remote Sensing of Environment*, **119**, 234–242.

[14] Potapov P, Hansen M C, Stehman S V, et al. (2008) Combining MODIS and Landsat Imagery to Estimate and Map Boreal Forest Cover Loss. *Remote Sensing of Environment*, **112**, 3708-3719.

[15] Tao J, Wu W, Zhou Y, et al. (2017) Mapping winter wheat using phenological feature of peak before winter on the North China Plain based on time-series MODIS data. *Journal of Integrative Agriculture*, **16**, 348–359.

# DBAR-Data Sharing for Sustainable Development Goals

# Open Data Policies and Strategies Roadmap towards Sustainable Development Goals.

Mogire[1], Wafula[2], Waweru[3]
[1]South Eastern Kenya University, P.O. Box 170, Kitui, 90200, Kenya
email: omogire@seku.ac.ke
[2,3]Jomo Kenyatta University of Agriculture and Technology, P.O. Box 62,000, Juja, 00200, Kenya
email: [2]muliaro@icsit.jkuat.ac.ke, email [3]waweru_mwangi@icsit.jkuat.ac.ke

## ABSTRACT

For a decade now, open data has been painted the "magic bullet", if well leveraged has the potential to accelerate achievements of vision 2030 agenda, whose goal is to build peaceful, resilient, equitable, inclusive and sustainable societies. Open data, can be used to implement, measure and track the progress of all the 17 SDGs. Open data can fight corruption which is the biggest road block to 2030 agenda. Contrary, for a decade now, majority of open data initiatives seam to be voluntary and politically instigated, and as such they are resting on shaky foundations with no or weak legislation, policies and strategies; and as such, the initiatives risk stalling or collapsing if political goodwill and community pressure subsides. To fully harness the fruits of open data, data revolution initiatives must be rooted in strong and inclusive data legislation, synergised by political benevolence with consistent global data management as exemplified in Mexico, Korea, Japan and Canada that have shown firm progress in their four barometer rankings. If not the case, open data initiatives will extinct once the political wind subsides as seems to have happened in Kenya, Ghana, Rwanda, Costa Rica and Ecuador which initially had shown positive progress, but the dying political enthusiasm has seen them succumb. In order to actualise the Global goals, there is an urgent need to mobilize data revolution without leaving anyone behind, anchored in sound data legislation and policies. From research literature and case studies, synthesis of findings, we proposes a novel conceptual open data policy and strategies framework towards this course. The output seeks to cement open data initiatives grounded in sound data legislation for governments and policy makers in the path to new sustainable development agenda as envisaged 17 SDGs.

Keywords: Big Data; Open Data; Policies; Strategies; Sustainable; 17 SDGs,

## 1. INTRODUCTION

The world is facing conspicuous societal, economic, political and environmental challenges today. As such, there is synergies to have interventions that can lead to the achievement of 17 SDGs. The 17 SDGs is the UN 2015-2030 vision unveiled in 2015 and presents a holistic approach to global sustainability by embracing economic, political, social and environmental developments through building peaceful, resilient, equitable and inclusive societies [1]. Open data that has been baptized many words like; "oil", "gold", "lifeblood", "currency", "sexiest", "magic bullet" has gain traction globally for a decade now with more than 50% of countries joining open data revolution for various reasons [2]. Data that was once the sanctuary of statisticians and academicians, has now become a developmental cause being embraced by everyone from grassroots to international forums. The UN recognized vitality of open data by embodying data revolution principles which emphasizes availability, equal and universal access to data towards achieving development goals [1]. Open data is digital data that is made available with the technical and legal characteristics necessary for it to be freely used, re-used, and redistributed by anyone, anytime and anywhere [3]. The open data FAIR principles that have now been adopted globally requires that open data be Findable, Accessible, Interoperable and Reusable[4] .With open data a decade old now, its roots can be traced to Obama Open Government Directive of 2008 with synergies from Open Government Partnership, European Commission open data initiatives, G8 Open Data, Open data charters, G20 Anti-Corruption Open Data Principles, 2015 UN SDGs endorsement on data revolution, Africa Data Consensus of 2015 and International champions like ICSU, CODATA, IAP, TWAS, ISSU, WDS ,RDA and AOSP. Research findings shows that open data can help to identify political, social, economic, and environmental trends and support the 17 Sustainable Development Goals [1]. Common known benefits of opening data in political and social trend include; transparency, accountability, fighting corruption, building trust in government, citizen participation, self-empowerment, innovation, Improvement of policy-making processes, stimulation of knowledge developments; economic benefits like economic growth, stimulation of innovation through re-use of data, Improved products and/or services and efficiency[5] . Yet many open data movements are voluntary and politically instigated hence resting on shaky foundations of legislation, week or lack of data policies and as such, the initiatives risk stalling or collapsing if such political goodwill and community pressure subsides. Therefore, to meet the new sustainability agenda, its calls for an urgent need in mobilizing data revolution globally in order to implement, track and monitor progress, hold governments to account, fight corruption and foster sustainable development agenda. Such data is not only an essential but versatile resource to the success of the 17 goals to make the world a better place[1,3,5] . This study sought to review literature in open data revolution, open data legislation and the UN sustainable development agenda. The Analysis of the findings is then used to propose a novel open data policy and strategy framework for vision 2030 agenda. The research output adds to the existing body of knowledge about open data as well as catalyzing sustainable development agenda and beyond.

## 2. METHODOLOGY

The research methodology of reviewing current literature on the aforementioned research aim and questions globally was followed. Various open data initiatives, open data policies, opportunities, challenges and the 17 SDGs were investigated as visualized in Fig. 1. Based on the inputs obtained from literature review and case studies, a conceptual open data policy and strategy framework to underpin open data readiness, implementation, monitoring and evaluation of open data initiatives towards 2030 agenda is developed. We also build upon, remix and reinterpreted data from the four open data barometer findings [2] as secondary data with questions on open data initiatives, legislation, open data policies, strategies and the 17 SDGs in relation to data revolution as demonstrated in Fig 2.

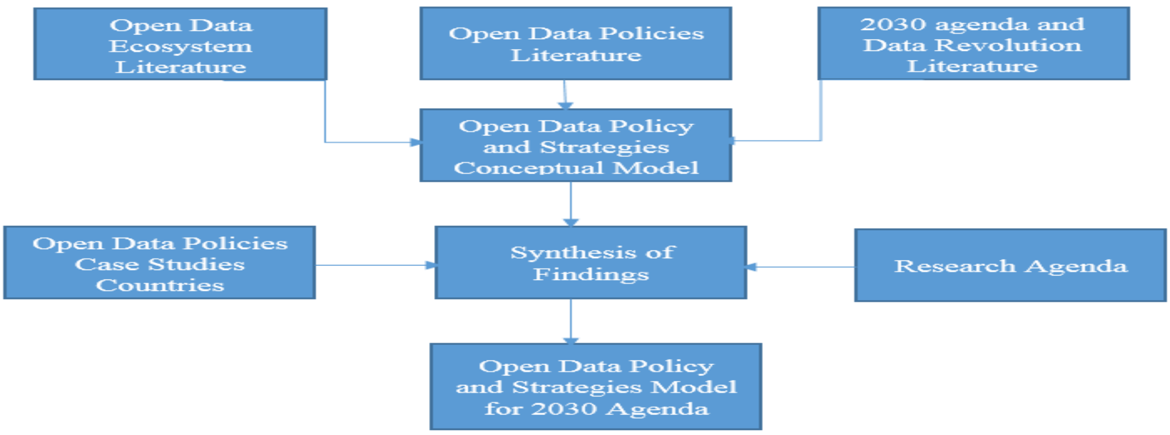


*Fig. 1.* Research Methodology adopted for coming up with the open data policy and strategies.

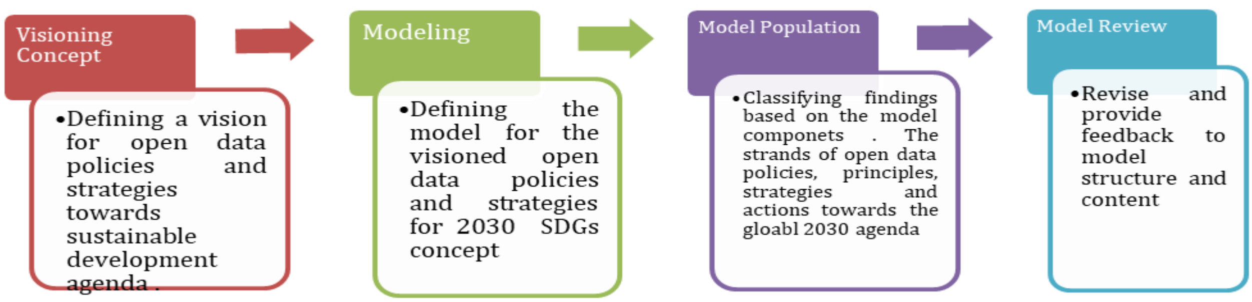

*Fig. 2.* Methodology for building open data policies and strategies for vision 2030 agenda.

## 3. DATA REVOLUTION FOR 2030 AGENDA

The world is facing extreme societal, economic, political and environmental challenges today. To address these challenges, in 2015, the world unveiled 17 SDGs that presents a holistic approach to global sustainability in four the strands of development; economic, political, social and environmental that will build peaceful, resilient, equitable and inclusive societies [1]. Given that Africa has borne the brunt of these challenges as its population continues to soar, in addition to 17 SDGs, Africa Union (AU) unveiled for the continent agenda 2063, an African dream that envisions creating Peaceful, Prosperous and Integrated continent by 2063. Both UN 2030 and AU 2063 visions urgently calls everyone to join data revolution without leaving anyone behind in order to monitor progress, hold governments to account and foster sustainable development. Towards this end, the UN principles towards 2030 agenda, embodies data revolution which emphasizes on data release, data use and value addition to tackle 17 SDGs [1,5]. At the same time Africa recognizing that it requires systematic and sustained research to arrive at data driven decisions to these challenges, AU adopted African Data Consensus 2015; a roadmap towards improving data standards as well as availability in a region that has notoriously struggled to capture even basic information such as birth registration [6]. According to the World Bank Group, open data can be used to identify political, social and economic trends of a country, improve private and public service, build trust in governance, and promote economic development, support development in all areas that relate to the 17 SDGs. Consequently, the Global Partnership for Sustainable Development Data and the International Open Data Charter were launched at the same time as the SDGs were unveiled in 2015. Yet research shows that much more remains to be done to unlock the full potential of open data as a SDGs accelerator. Only a small portion of countries provide open and free online access to datasets critical to the SDGs, such as public spending, health, education, maps, or census data. Table 2 shows the type of open data and the corresponding SDGs such open data can support towards 2030 agenda. To guarantee that open data revolution will be available for a long period of time and to be used to deliver vision 2030 agenda, it should not be entrenched in countries laws with sound data legislation and policies, strategies, principles and actions together with political synergies. Long-term policies, strategies, principles and actions that comprehensively addresses legal, political, social, economic, institutional, operational and technical challenges is the cornerstone to open data impediments [5]. Therefore with the SDGs still high on the political agenda of many countries, recognition of data’s importance to development is at an all-time high. Until all these factors are in place, open data cannot be a true SDG accelerator and If we allow this moment to slip away, open data could fade into a ghost town of abandoned houses, outdated data portals, and unused apps.

### *3.1 Open Data Legislation Gap*

Many countries open data policies lack legislative backing. Legislation emphasizes the need for open data legislation, freedom of information act, open data policies, open government data directives, open data memorandums and declarations. With open data now a decade old, it is time for governments to move beyond open data rhetoric and open data portals initiatives to put the fundamental policies, strategies, principles and actions in place to support a sustainable open data culture if agenda 2030 is to be realized as visualized in Fig 3. Although the amount of data openly available continue to increase, there are still many open data challenges related to data management, licensing, interoperability and exploitation. There is a need to evolve policies, strategies, principles, practices, action points and ethics around closed, shared, and open data (GODAN). Leading governments are generally advancing towards the same, but have yet to introduce the reforms required to make open data a part of day-to-day governance. They must now start investing significant resources to build the infrastructure, policies and practices necessary to drive this transformation agenda if they do not, the open data movement will stagnate [7].

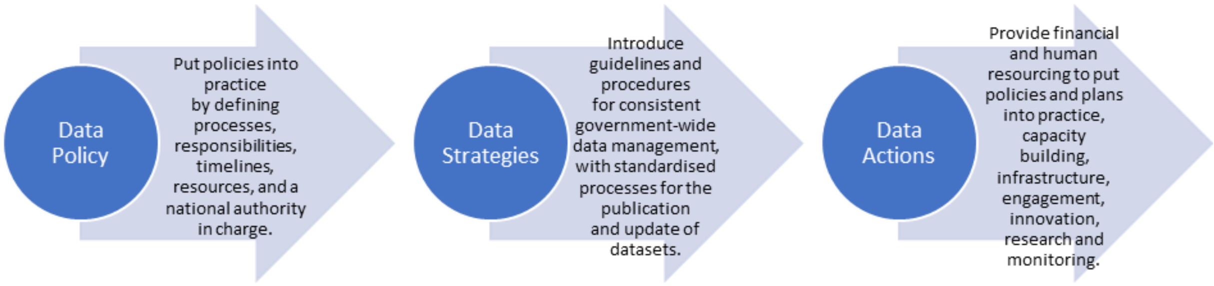


*Fig. 3.* Open data road from policies, to guidelines, to actions to truly FAIR open data.

Over the last ten years now, open data initiatives have spread so fast but with weak policies and legislation in place and as such no progress on the number of truly open datasets around the world. Less than 10% of all the datasets are open and governments have been reluctant to publish the datasets that can most benefit citizens. And when available, this data is incomplete and of poor quality [8]. Such weak legislation and policies normally impede open data revolution. Further, absence of strong Right to Information (RTI) laws prevents citizens from using open data to hold government to account. At the same time, weak or absence of data protection laws have more often than not undermined citizen confidence in open government data initiatives [8].

## 4. PROPOSED NOVEL OPEN DATA POLICY AND STRATEGY FRAMEWORK FOR 2030 SDGS.

A Policy is a purposive course of action followed by an actor or set of actors in dealing with a problem or matter of concern [9]. When applied to the field of open data, open data policies and strategies will spur readiness, opening, implementation and impact assessment in open data ecosystem [8]. Besides from ensuring the process of opening data, open data policies aim to achieve a certain impact on the society as does any policy. In developing open data policies, governments envisage to stimulate and guide the publication of government data and to gain advantages from its use. Current policies are rather inward looking. They note that open data policies can be improved by cooperating with other organizations, focusing on the impact of the policy, stimulating the use of open data and looking at the need to create a culture in which publicizing data is incorporated in daily working processes. It follows that countries needs to learn from each other to improve on policies and strategies. [5] . Successful open data policy requires three pillars: Policy content, Policy context and Policy impact [10] as illustrated in fig.4. While Fig 5 shows Migration path to sustainable development agenda of 2030.

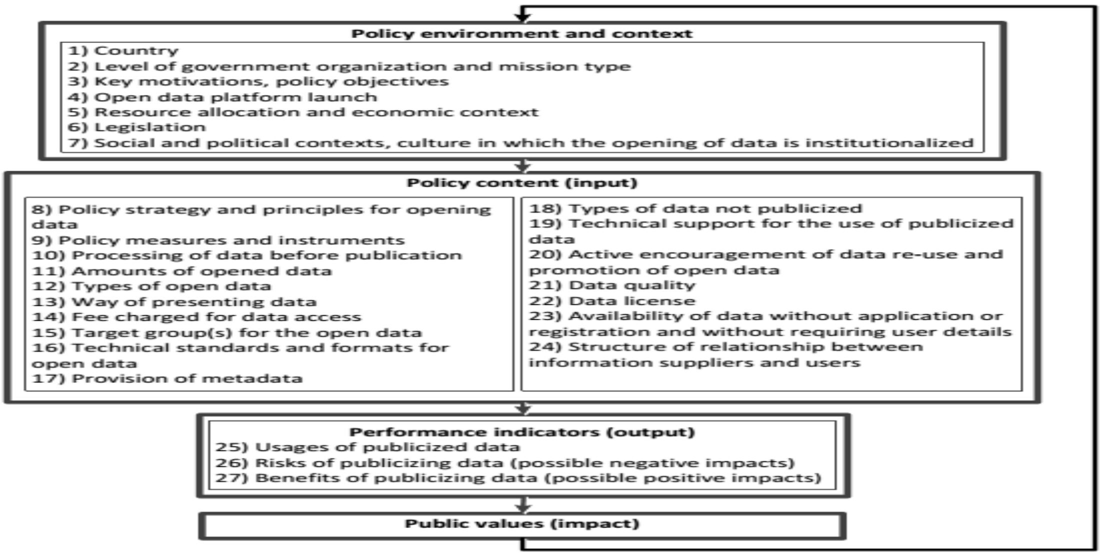


*Fig. 4.* open data policy context, content and impact (Zuiderwijk & Janssen, 2014)

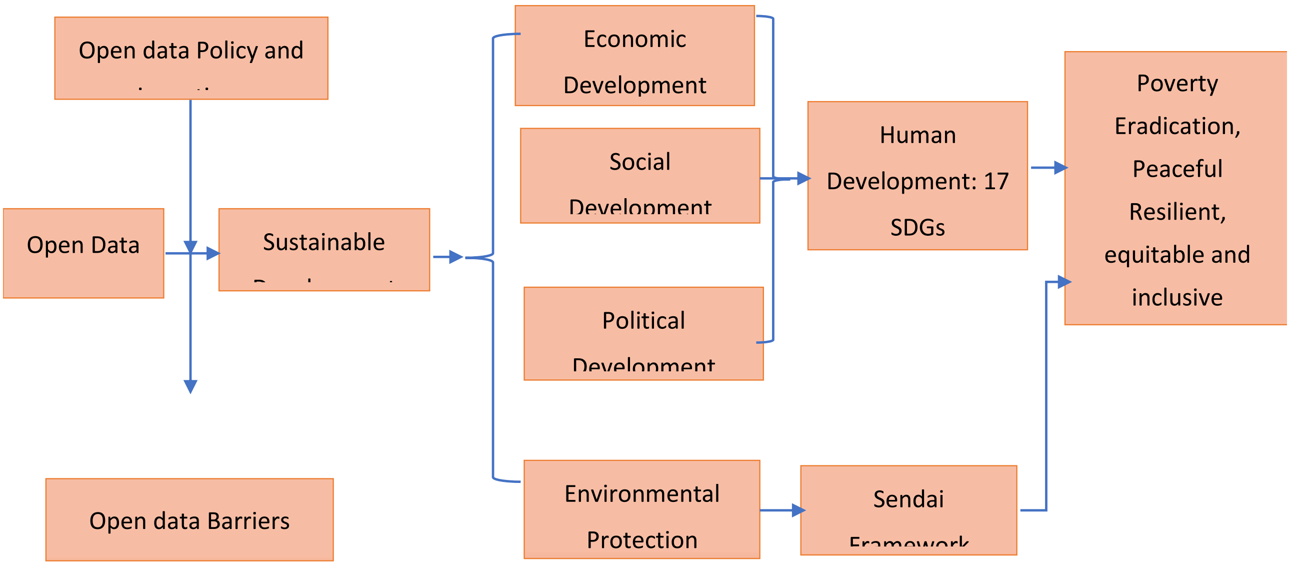


*Fig.5.* Migration path to sustainable development agenda of 2030.

## 5. SUMMARY

Open Data has been painted as the "magic bullet" that can accelerate the achievements of vision 2030, whose agenda is to build peaceful, resilient, equitable and inclusive societies by monitoring the progress and impact of 17 SDGs at the same time holding governments to account. There no doubt that effective deployment and use of open data will lead to informed decision making at all levels of governance towards smart and sustainable development agenda. From a systematic review of variety of literature and numerous open data dashboards and expert reviews reveals that despite the many open data initiatives and its associated paybacks, open data must be rooted in strong and sound data legislation synergized by political commitments and consistent global data management as epitomized in Mexico, Korea, Japan and Canada that have achieved steady progress in their Barometer rankings. Otherwise, open data initiatives without policy will die when the political momentum dwindles as seems to have happened in Kenya, Rwanda, Costa Rica and Ecuador where positive progress was initially made on open data revolution, but now dying political enthusiasm has seen them succumb to the former. The above proposed novel policy and strategies framework has strands that include ICT infrastructure, organization and Governance to guide open data towards 2030 agenda and beyond.

## REFERENCES

[1] United Nations. (2015) The UN Sustainable Development Goals. Available at:http://www.un.org/sustainabledevelopment/summit/ (accessed 16 January 2018)
[2]World Wide Web Foundation. (2015) Open Data Barometer Global Report (Second Edition) http://www.opendatabarometer.org(accessed 16 January 2018)
[3] International Open Data Charter. (2015). https://opendatacharter.net/wp-content/uploads/2015/10/opendatacharter-charter_F.pdf (accessed 4 March 2022)
[4]Bell, D., & Gajera, J. (2020). Findable accessible interoperable reusable data principles (FAIR). Radiopaedia.Org. https://doi.org/10.53347/rid-81680
[5] Rininta Putri Nugroho Anneke Zuiderwijk Marijn Janssen Martin de Jong , (2015),"A comparison of national open data policies: lessons learned", Transforming Government: People, Process and Policy, Vol. 9 Iss 3 pp. 286 – 308
[6] Africa data consensus(2015).Final version adopted by the high level, https://repository.uneca.org/handle/10855/22669(Retrieved August 4, 2020)
[7] Janssen, M., Charalabidis, Y. and Zuiderwijk, A. (2012). Benefits, adoption barriers, and myths of open data and open government, Information Systems Management, Vol. 29 No. 4, pp. 258-268
[8] Open Data Barometer 4th Edition (2017). Global Report, The World Wide Web Foundation. https://opendatabarometer.org/doc/4thEdition/ODB-4thEdition-GlobalReport.pdf(accessed March, 2022)
[9] Anderson, C. (2010). Presenting and Evaluating Qualitative Research. American Journal of Pharmaceutical Education, 74, 141. https://doi.org/10.5688/aj7408141
[10] Zuiderwijk, A., & Janssen, M. (2014). Open data policies, their implementation and impact: A framework for comparison. Government Information Quarterly, 31(1), 17–29. doi:10.1016/j.giq.2013.04.003

# DBAR-Digital Technology for Environmental Change Assessment and Sustainable Development

# Future land-use impacts on terrestrial carbon pools under SDG scenarios, China

Ya Tian[1,2*], Kai Wu[2,3], Min Cao[2,3], Min Chen[2,3], Hui Lin[1,4]

[1]School of Geography and Environment, Jiangxi Normal University, Nanchang 330022, China.
email: ygxinxity@whu.edu.cn

[2]Key Laboratory of Virtual Geographic Environment, Ministry of Education of PRC, Nanjing Normal University, Nanjing 210023, China

[3]Jiangsu Center for Collaborative Innovation in Geographical Information Resource Development and Application, Nanjing 210023, China

[4]Key Laboratory of Poyang Lake Wetland and Watershed Research, Ministry of Education, Jiangxi Normal University, Nanchang, 330022, China

Email: ygxinxity@whu.edu.cn (Ya.Tian) kwu@nnu.edu.cn (Kai Wu) caomin@njnu.edu.cn (Min Cao) chenmin0902@163.com (Min.Chen) huilin@cuhk.edu.hk (Hui.Lin)

## 1.INTRODUCTION

Land-use change has complex interactions with the economy, society, and environment and plays an important role in regulating climate, food security, and the carbon cycle[1–5]. Land-use change leads to habitat loss and threatens biodiversity[6], affects terrestrial carbon storage[7], leads to loss of high-quality cultivated land and threatens food security[5,8]. Global urbanisation offsets 30 % of climate-driven terrestrial net primary productivity growth, with cities contributing to more than 70 % of anthropogenic greenhouse gas emissions[9,10]. Forest reduction and afforestation are important factors that affect terrestrial carbon sinks and regulate climate change[2]. In the United Nations 2030 Agenda, sustainable development goals (SDGs), such as food security (SDG2), economic growth (SDG8), sustainable urban development (SDG11), and environmental-friendly development (SDG15), are the most important parameters that can help global economies achieve sustainable developemnt[5,11–13]. Therefore, it is important to correctly understand how future land-use change can affect the realization of multiple SDGs, such as SDG2, SDG8, and SDG15. In this study, we present spatially explicit projections of global land-use change from 2016 to 2030, discuss their impacts on terrestrial carbon pools.

Projections of land-use patterns require established scenarios that represent possible future socio-economic and environmental conditions[14]. Scenario-based simulations support the analysis of potential land-use changes in uncertain futures[15]. Several previous studies have formulated guiding frameworks for the future use of land resources. Some scholars have studied future land-use prediction under different representative concentration pathways (RCPs)[16], shared socio-economic pathways (SSPs)[17,18], and SSP-RCP scenarios[19,20]. Some studies have modelled a global urban map for 2030, based on the United Nations population and economic projections[21]. The climate scenarios developed by the Intergovernmental Panel on Climate Change (IPCC) have also been used to simulate future changes in global land covers[1,22,23]. However, in different SDG scenarios, the effects of land-use change on terrestrial carbon pools remain unclear. The United Nations 2030 Agenda for sustainable development (hereinafter referred to as the 2030 Agenda) set up a comprehensive and integrated framework of 17 goals, 169 targets, and 231 unique indicators [13], which were designed to guide the progress of sustainable development till 2030[23]. The 17 SDGs integrate the three dimensions of development goals: economy, society and environment[13]. Using a system that considers the interaction between SDGs and analyses the relationship between the speed of their progress and the land use in different regions is a hot topic in sustainable development research[24]. Some scholars have constructed indicator systems and methods[25–30], proposed a framework for evaluating the interaction between the SDG indicators[31–33], and explored the synergy and trade-off effects between these indicators[34,35]. In this study, we built a new multi-social, economic environment scenario to simulate future land-use change, analysed future urban expansion patterns, and investigated the impacts of these changes on terrestrial carbon pools, based on the SDGs.

Based on the interaction between land use and the key targets of SDGs, we considered the following scenarios: reference (REF), economic sustainable (ECO), grain sustainable (GRA), and environmentally sustainable (ENV), energy sustainable （EGY）. In these scenarios, we consider seven SDG indicators: gross domestic product (GDP) growth rate (SDG 8.1.1), cereal yield (SDG2.3.1), the prevalence of undernourishment (SDG2.1.1), and annual average particulate matter of less than 2.5 microns in diameter ($PM_{2.5}$) (SDG 11.6.2), Red List Index (SDG15.5.1), Mountain Green Cover Index (SDG15.4.2), Share of total final energy consumption (SDG7.2.1), Ratio of population with access to electricity (SDG7.1.1). The threshold was set based on the Sustainable Development Report 2020 (SDR 2020) colour dashboard[36,37]. The Development rate of the indicator to 2030 is set separately and the impact of the COVID-19 epidemic is comprehensively considered.

In this study, we built system dynamics (SD) models for different regions of China to predict future land demand under SDGs scenarios. The system dynamics (SD) model is based on the feedback control theory and is an effective method for studying complex system behaviour and feedback mechanisms, using a combination of qualitative and quantitative methods[38]. It is widely used to simulate land-use changes influenced by socio-economic and climate change factors. Many scholars use cellular automata (CA), combined with SD, to simulate future land-use changes driven by a variety of factors. Based on the SDG scenarios, we integrated the SD and CA models and considered the socio-economic and climatic factors, to predict future land-use changes[39–41] in China, for 2015-2030. We calculated the changes in terrestrial carbon storage caused by urban expansion and forest change in China, using the Integrated Valuation of Ecosystem Services and Trade-offs (InVEST) and Integrated Biosphere Simulator (IBIS) models for 2020–2030 while considering SDGscenarios[42,43]. Notably, our study provides a new perspective for exploring future land-use changes and their impacts on terrestrial carbon storage under the SDG framework.

## 2.MATERIALS AND METHODS

### *2.1 SDGs relationships between targets and identification of key targets*

We collect data on indicators of economic, social and environmental aspects involved in SDGs targets, and analyze the relationship between SDGs using statistical methods such as Geographical and temporal weighted regression (GTWR) in conjunction with the current situation of socio-economic development[44]. GTWR is a comprehensive consideration of temporal and spatial heterogeneity, which can explore the relationship between SDGs indicators in spatial and temporal dimensions. China was separated into sub-regions based on economic, climatic and natural factors, and the relationship between SDG indicators under different sub-regions was explored. The GTWR modeling of SDGs indicators in different sub-regions was performed separately, and the regression coefficients of different spatio-temporal indicators were analyzed; regression coefficients greater than 0 could be considered as synergistic relationships, and regression coefficients less than 0 were considered as trade-off relationships between targets. Through GTWR modeling and correlation analysis, significant indicator variables were obtained to analyze the relationship between SDG indicators. The key goals involving economy, environment, energy, and food are selected as the basis for scenario setting.

### *2.2 SDGs Scenarios Setting*

We set SDG scenarios based on SDG trends that may be generated in the future. The SDG trend dashboards indicate whether a country is on track to achieve a particular goal by 2030, based on its recent performance on given indicators. The SDG dashboard provide a visual representation of each country's performance on 17 SDGs. The"traffic light" colour scheme (green, yellow, orange, and red ) illustrates how far a region is from achieving a particular goal, which is on track or maintaining SDG achievement, moderately improving, stagnating, decreasing, respectively[36]. In this study, we considered four SDG scenarios: REF, ECO, GRA, ENV， EGY. In SDG scenarios, we consider seven SDG indicators: GDP growth rate (SDG 8.1.1), cereal yield (SDG2.3.1), the prevalence of undernourishment (SDG2.1.1), and annual average concentration of $PM_{2.5}$ (SDG 11.6.2), Red List Index (SDG15.5.1), Mountain Green Cover Index (SDG15.4.2), Share of total final energy consumption (SDG7.2.1), Ratio of population with access to electricity (SDG7.1.1). For the seven SDG indicators, we obtained the thresholds for different development trends based on SDG trend dashboards. The development trends of the SDG indicators were set separately under different SDG scenarios. In this study, we aggerated the China into different sub-regions. We set the indicator trends for four SDG scenarios in sub-regions based on regional development characteristics.

### *2.3 Calculation of the impact of land use change on terrestrial carbon pools*

We analysed the carbon storage change in China. The calculated data for 2020 included seven types of carbon density data (cLeaf, cWood, cRoot, cLitter, cSoil, and cRootLitter) obtained by the Integrated Biosphere Simulator (IBIS) model [45]. The IBIS model is a vegetation dynamics model that expresses land surface biophysics, terrestrial carbon fluxes, and global vegetation dynamics through an independent, naturally continuous framework structure. It is designed to deepen the study of the interactions between biosphere processes and to improve the study of the effects of land use, climate change and increasing atmospheric $CO_2$ on the structure and function of ecosystems, with processes related to water balance, phenology, carbon and nitrogen cycles, and vegetation dynamics. The model integrates a wide range of biophysical, physiological, and ecological processes, and this model framework can be directly coupled with General Circulation Models (GCMs).

Because the process of the carbon cycle includes the transition from atmospheric to ground carbon pools, and then, to soil and litter carbon pools (through photosynthesis and respiration), we re-classified the seven types of carbon density data in 2020 into four types of carbon density data (C_above, C_below, C_soil, and C_dead)[44]. Then, the land-use data in 2020 simulated by cellular automata and artificial neural networks (CA-ANNs) model was input into the Integrated Valuation of Ecosystem Services and Trade-offs (InVEST) model, to estimate the carbon stocks of different land types (cultivated land, forest and grass). The original carbon density data for 2000-2020, output from the Integrated Biosphere Simulator (IBIS) model, only considered climate change and the $CO_2$ fertilisation effect, while ignoring land-use change. Therefore, we assumed that the average carbon density of different land types will remain unchanged in 2030. Then, the land-use data simulated for the SDGs scenarios were input into the InVEST model, from 2020 to 2030. We obtained the predictions for the carbon storage for all the scenarios in 2020-2030. And we calculated the changes in forest carbon stocks and carbon losses in different regions from 2020 to 2030 under different scenarios, due to urban expansion in China.

### *2.4 Study Workflow*

This study analyzed the relationship between provincial-scale SDGs and the impact of land use change on terrestrial carbon pools in China. This study analyzed the relationship between provincial-scale SDGs and the impact of land use change on terrestrial carbon pools in China. Firstly, the study area was allocated to sub-regions, and the sub-regions were based on integrated consideration of natural and socio-economic factors. Secondly, GTWR models for different sub-regions were established to analyze the synergistic trade-offs between regional indicators and to select regional key SDG indicators. Based on the selected key SDG indicators, five SDG scenarios are constructed. Based on the SDR2022 color indicator board, the development rates of different indicators in different regions are set. Under the SDGs scenarios, different subsystems are constructed in different sub-regions, such as economy, food, energy, population, etc. The SD models are built to project the land demand under different scenarios and spatialize the future land use using CA-ANNs model, 2022-2030. The data set of spatial distribution of carbon density calculated from IBIS model to 2021 in China with the predicted future land use data under different scenarios is input to InVEST model to calculate carbon stock of different land classes from 2022-2030. The specific calculation process is shown in the Fig.1.

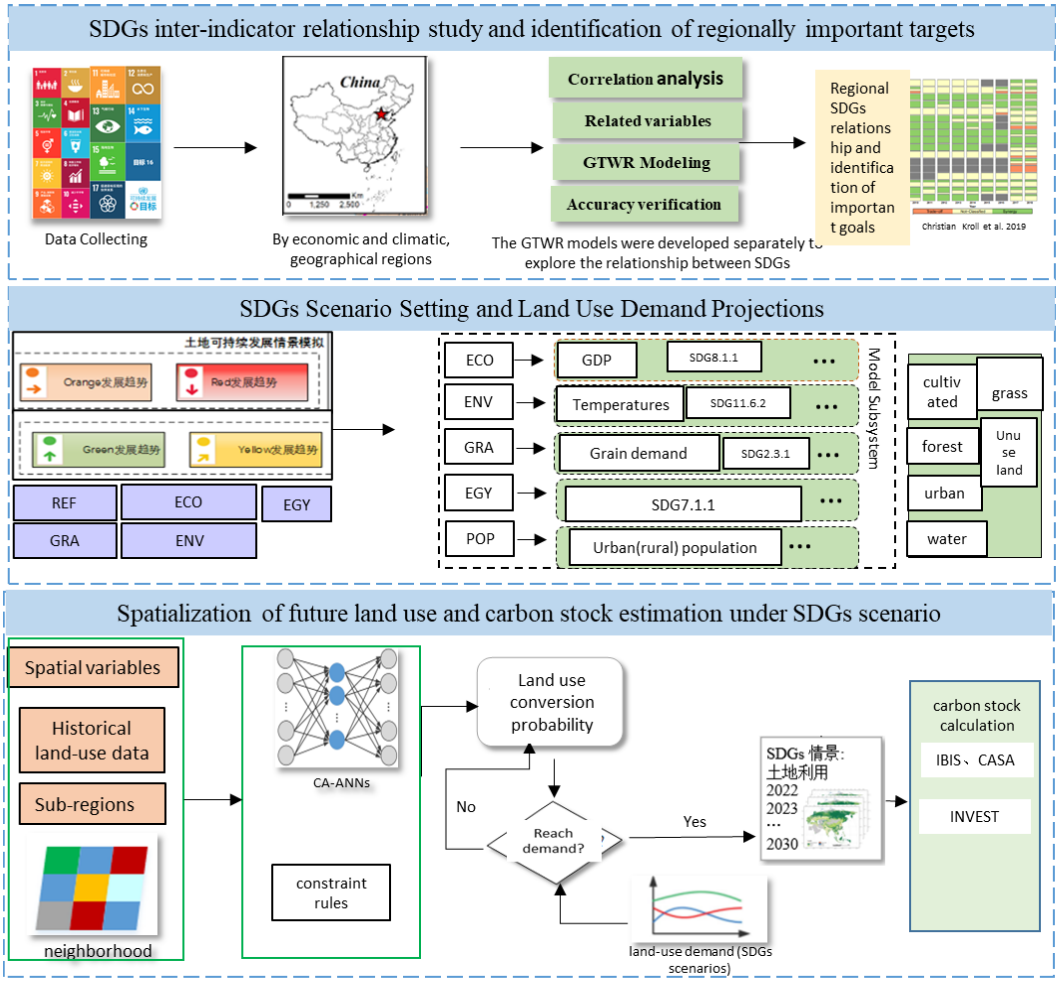


Fig.1. **Study workflow for future land use impacts on terrestrial carbon pools under SDG scenarios, China.** Abbreviations: economic sustainable (ECO), grain sustainable (GRA), environmentally sustainable (ENV), energy sustainable (EGY) and reference (REF).

## 3.RESULTS

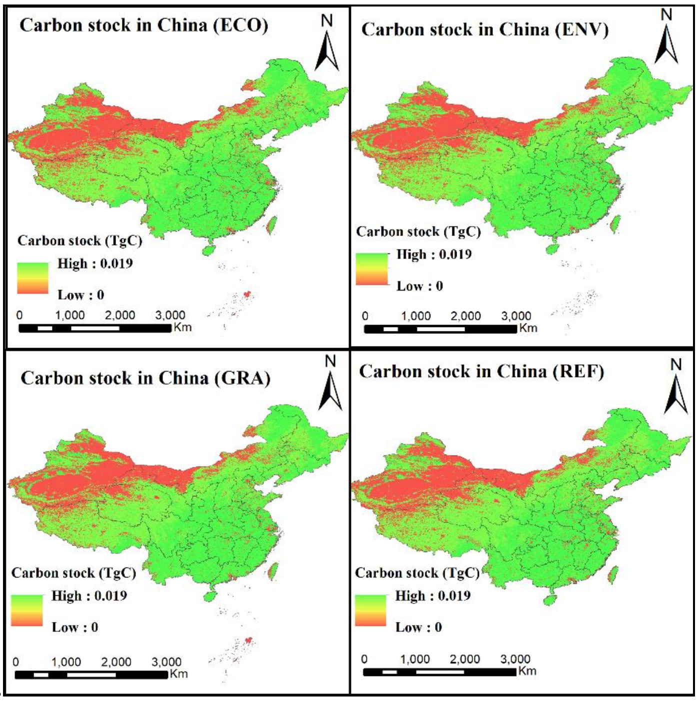


Fig.2. **Spatial distribution of terrestrial carbon stocks in China on 2030, under SDGs scenarios.**

Abbreviations: economic sustainable (ECO), grain sustainable (GRA), environmentally sustainable (ENV) and reference (REF).

## 4.SUMMARY

The study aims to achieve the identification of regional key SDGs and to explore the methods of localizing SDGs indicators. To explore the interaction between land use and economic and natural factors under different development paths in sub-regions, and to predict future land demand. A dataset of future land use in China (resolution:300m) under different SDGs scenarios is obtained based on the CA-ANNs model, and the impact on terrestrial carbon pools under different scenarios is analyzed. Setting a variety of SDGs scenarios, balancing the development needs of energy, economy, environment, and food security, and exploring the path to scientifically achieve SDGs goals. Identify key SDGs indicators based on actual regional development, promote synergy and suppress trade-offs, and truly provide decision-making suggestions for achieving regional sustainable development, enhancing regional innovation dynamics, creating new sustainable cities, and exploring the future development of the region.

## References


[1] Li, X. et al. A New Global Land-Use and Land-Cover Change Product at a 1-km Resolution for 2010 to 2100 Based on Human–Environment Interactions. Ann. Am. Assoc. Geogr. 107, 1040–1059 (2017).

[2] Harper, A. B. et al. Land-use emissions play a critical role in land-based mitigation for Paris climate targets. Nat. Commun. 9, (2018).

[3] Foley, J. A. et al. Global consequences of land use. Science (80-. ). 309, 570–574 (2005).

[4] Seto, K. C., Sánchez-Rodríguez, R. & Fragkias, M. The new geography of contemporary urbanization and the environment. Annu. Rev. Environ. Resour. 35, 167–194 (2010).

[5] Fujimori, S. et al. A multi-model assessment of food security implications of climate change mitigation. Nat. Sustain. 2, 386–396 (2019).

[6] Li, G. et al. Global impacts of future urban expansion on terrestrial vertebrate diversity. Nat. Commun. 13, 1–12 (2022).

[7] Yue, C., Ciais, P., Houghton, R. A. & Nassikas, A. A. Contribution of land use to the interannual variability of the land carbon cycle. Nat. Commun. 11, 1–11 (2020).

[8] Bren, C. et al. Future urban land expansion and implications for global croplands. 114, (2017).

[9] Hopkins, F. M. et al. Mitigation of methane emissions in cities: How new measurements and partnerships can contribute to emissions reduction strategies. Earth's Futur. 4, 408–425 (2016).

[10] Liu, X. et al. Global urban expansion offsets climate-driven increases in terrestrial net primary productivity. Nat. Commun. 10, (2019).

[11] Wu, X. et al. Decoupling of SDGs followed by re-coupling as sustainable development progresses. Nat. Sustain. (2022) doi:10.1038/s41893-022-00868-x.

[12] UNSD. SDG Indicators: Global indicator framework for the Sustainable Development Goals and targets of the 2030 Agenda for Sustainable Development. United Nations Statistics Division (2018).
[13] Transforming Our World: The 2030 Agenda for Sustainable Development. A New Era in Global Health (2018) doi:10.1891/9780826190123.ap02.
[14] Chen, G. et al. Global projections of future urban land expansion under shared socioeconomic pathways. Nat. Commun. 11, 1–12 (2020).
[15] Sohl, T. L. et al. Spatially explicit land-use and land-cover scenarios for the Great Plains of the United States. Agric. Ecosyst. Environ. 153, 1–15 (2012).
[16] Marcotullio, P. J., Keßler, C. & Fekete, B. M. The future urban heat-wave challenge in Africa: Exploratory analysis. Glob. Environ. Chang. 66, (2021).
[17] Riahi, K. et al. The Shared Socioeconomic Pathways and their energy, land use, and greenhouse gas emissions implications: An overview. Glob. Environ. Chang. 42, 153–168 (2017).
[18] Popp, A. et al. Land-use futures in the shared socio-economic pathways. Glob. Environ. Chang. 42, 331–345 (2017).
[19] Liao, W. et al. Projections of land use changes under the plant functional type classification in different SSP-RCP scenarios in China. Sci. Bull. 65, 1935–1947 (2020).
[20] Dong, N., You, L., Cai, W., Li, G. & Lin, H. Land use projections in China under global socioeconomic and emission scenarios: Utilizing a scenario-based land-use change assessment framework. Glob. Environ. Chang. 50, 164–177 (2018).
[21] Seto, K. C., Güneralp, B. & Hutyra, L. R. Global forecasts of urban expansion to 2030 and direct impacts on biodiversity and carbon pools. Proc. Natl. Acad. Sci. U. S. A. 109, 16083–16088 (2012).
[22] Sohl, T. L., Wimberly, M. C., Radeloff, V. C., Theobald, D. M. & Sleeter, B. M. Divergent projections of future land use in the United States arising from different models and scenarios. Ecological Modelling vol. 337 281–297 (2016).
[23] Li, X. et al. A cellular automata downscaling based 1 km global land use datasets (2010–2100). Sci. Bull. 61, 1651–1661 (2016).
[24] Bali Swain, R. & Ranganathan, S. Modeling interlinkages between sustainable development goals using network analysis. World Dev. 138, 105136 (2021).
[25] Zhu Jing,Sun Xin-zhang, H. Z. Research on China's sustainable development evaluation indicators in the framework of SDGs. China's population, resources and environment vol. 28(12) 9–18 (2018).
[26] Xu, Z. et al. Assessing progress towards sustainable development over space and time. Nature 577, 74–78 (2020).
[27] Wei, Y. et al. The United Nations Sustainable Development Goals (SDG) and the Response Strategies of China. Journal of Earth Science vol. 33 1084–1093 (2018).
[28] Costanza, R. et al. Modelling and measuring sustainable wellbeing in connection with the UN Sustainable Development Goals. Ecol. Econ. 130, 350–355 (2016).
[29] Chen, J., Peng, S., Zhao, X., Yuejing, G.E., Zhilin, L.I., Beijing, T., 2019. Measuring regional progress towards SDGs by combining geospatial and statistical information. Acta Geodaetica et Cartographica Sinica 48, 473-479. 10.11947/j.AGCS.2019.20180563.
[30] Allen, C., Metternicht, G. & Wiedmann, T. National pathways to the Sustainable Development Goals (SDGs): A comparative review of scenario modelling tools. Environ. Sci. Policy 66, 199–207 (2016).
[31] Weitz, N., Carlsen, H., Nilsson, M. & Skånberg, K. Towards systemic and contextual priority setting for implementing the 2030 agenda. Sustain. Sci. 13, 531–548 (2018).
[32] Nilsson, M. et al. Mapping interactions between the sustainable development goals: lessons learned and ways forward. Sustain. Sci. 13, 1489–1503 (2018).
[33] Nilsson, M., Griggs, D. & Visbeck, M. Policy: Map the interactions between Sustainable Development Goals. Nature 534, 320–322 (2016).
[34] Warchold, A., Pradhan, P. & Kropp, J. P. Variations in sustainable development goal interactions: Population, regional, and income disaggregation. Sustain. Dev. 29, 285–299 (2021).
[35] Pradhan, P., Costa, L., Rybski, D., Lucht, W. & Kropp, J. P. A Systematic Study of Sustainable Development Goal (SDG) Interactions. Earth's Futur. 5, 1169–1179 (2017).
[36] Sachs, J., Schmidt-Traub, G., Kroll, C., Lafortune, G. & Fuller, G. Sustainable Development Report 2020. Sustainable Development Report 2020 (2021) doi:10.1017/9781108992411.
[37] Schmidt-Traub, G., Kroll, C., Teksoz, K., Durand-Delacre, D. & Sachs, J. D. National baselines for the Sustainable Development Goals assessed in the SDG Index and Dashboards. Nat. Geosci. 10, 547–555 (2017).
[38] Tian, H. et al. Simulating Multiple Land Use Scenarios in China during 2010-2050 Based on System Dynamic Model. Tropical Geography vol. 37 547–561 (2017).
[39] Lauf, S., Haase, D., Hostert, P., Lakes, T. & Kleinschmit, B. Uncovering land-use dynamics driven by human decision-making - A combined model approach using cellular automata and system dynamics. Environ. Model. Softw. 27–28, 71–82 (2012).
[40] Gu, C., Guan, W. & Liu, H. Chinese urbanization 2050: SD modeling and process simulation. Sci. China Earth Sci. 60, 1067–1082 (2017).
[41] Cao, M. et al. Spatial Sequential Modeling and Predication of Global Land Use and Land Cover Changes by Integrating a Global Change Assessment Model and Cellular Automata. Earth's Futur. 7, 1102–1116 (2019).
[42] Sharp, R. et al. InVEST user's guide. The Natural Capital Project, Stanford (2014).
[43] Friedlingstein, P., Jones, M. W., O'Sullivan, M., Andrew, R. M., Bakker, D. C., Hauck, J., ... & Zeng, J. (2022). Global carbon budget 2021. Earth System Science Data, 14(4), 1917-2005.
[44] Fotheringham, A. S., Crespo, R. & Yao, J. Geographical and Temporal Weighted Regression (GTWR). Geogr. Anal. 47, 431–452 (2015).

# DBAR-Digital Technology for Urban Sustainability

# A Comprehensive Assessment Report of the Urbanisation Development of World Cultural Heritage Sites in co-cooperating "the Belt and Road Initiative" Partnership Countries and their Neighbouring Countries

Luyang Pan[1,2,3], Linlin Lu[2,3], Xinyuan Wang[2,3], Fulong Chen[2,3]

[1] College of Geodesy and Geomatics, Shandong University of Science and Technology, Qingdao 266590, China

[2] International Research Center of Big Data for Sustainable Development Goals, Beijing 100094, China

[3] Key Laboratory of Digital Earth Science, Aerospace Information Research Institute, Chinese Academy of Sciences, Beijing 100094, China

email: panluyangyyy@163.com (for author 1)

email: lull@radi.ac.cn (for author 2)

email: wangxy@aircas.ac.cn (for author 3)

email: chenfl@aircas.ac.cn (for author 4)

## 1.INTRODUCTION

As for SDG 11.4, the United Nations proposed to "make further efforts to protect and safeguard the world's cultural and natural heritage" and put forward the index calculation method of SDG11.4.1 "Total expenditure per capita (public and private) for the conservation, protection, and preservation of all cultural and natural heritage " however, the index only includes financial inputs to heritage sites [1]. The cultural heritage sites with different environments, scales, types, and materials require extra protection efforts and schemes. Through a comprehensive analysis of the natural and androgenic risks faced by world heritage and a scientific understanding of the protection needs of world heritage, the protection guidance and implementation of world heritage can be carried out differently and pertinently [2-3].

## 2.MATERIALS AND METHODS

We chose 286 cultural heritage sites near the urban area in cities and towns along the Belt and Road region. Considering the artificial and natural risks faced by the heritage site, six types of earth big data products (population density, built-up land, nighttime light, NO2 column concentration, land surface temperature, and precipitation) are selected to measure the urban development in the surrounding areas of the heritage site. Standardized processing and spatial analysis were performed based on the big-earth data products in 2010, 2015, and 2020. The 1000m, 3000m, and 5000m buffer zones centered on the heritage site were created to calculate the values of indicators and obtain the changes of heritage site indicators in time and space. Based on the mean value of standardized indicators, the comprehensive urban development index (CUDI) [4] around the heritage site is obtained (see Eq.1). Finally, the time and spatial change characteristics of the surrounding cities in the cultural heritage sites and their influence on the cultural heritage sites were analyzed.

$$\mathrm{CUDI} = \frac{1}{N}\sum_{K=1}^{N}\frac{X_K - \min_K}{\max_K - \min_K} \tag{1}$$

where N represents the total number of sub-indicators, $X_K$ represents the mean value of the K-th sub-indicator in the buffer zone of a heritage site, and $\min_k$ and $\max_k$ represent the minimum and maximum values of the K-th indicator in the heritage site, respectively.

## 3.RESULTS

The results showed that the mean value of CUDI increased from 0.2763 in 2010 to 0.3007 in 2015, and decreased slightly from 0.2995 in 2020. The average values of the four indicators of population, nighttime light, carbon dioxide emission, and built-up land are increasing. At the same time, the concentration of nitrogen dioxide column representing the air pollution decreased significantly. The area with the largest change in night lighting index is Strasbourg, France, which increased from 0.003 in 2010 to 0.654 in 2020. The area with the largest change in population index is near Kathmandu, Nepal, which has increased from 0.190 in 2010 to 0.793 in 2020, and the CUDI change rate around it is also the largest.Among the selected heritage sites, there are 53 regions with rapid growth (change rate ≥ 20%), 99 regions with 0~10% change rate of CUDI, and 56 regions with change rate less than 0.

## 4.SUMMARY

The number of cultural and mixed heritage in the Belt and Road region accounts for 84.4% of the world and has important research value [5]. According to the temporal and spatial distribution characteristics of the world cultural heritage, this research considers the potential natural and human risks caused by the urbanization of the cultural heritage sites. It proposed the CUDI as a new tool for monitoring urban development and the environment around the cultural heritage sites. Overall, the adverse factors around the world heritage sites are gradually eliminated, but there are still unbalanced and insufficient problems in protecting cultural heritage sites. The evaluation results can suggest countermeasures and measures for cultural heritage protection and provide scientific reference for United Nations Educational, Scientific, and Cultural Organization (UNESCO) and relevant countries and regions to achieve the sustainable development goal of "further efforts to protect and defend the world cultural and natural heritage" at the macro level.

## REFERENCES：

[1] United Nations. (2015). Transforming our world: The 2030 Agenda for Sustainable Development. Division for Sustainable Development Goals: New York, NY, USA. https://sustainabledevelopment.un.org/post2015/transformingourworld.

[2] Hadjimitsis D, Agapiou A, Alexakis D, Sarris A. (2013). Exploring natural and anthropogenic risk for cultural heritage in Cyprus using remote sensing and GIS. International Journal of Digital Earth, 6(2), 115-142.

[3] Luo L, Wang X, Guo H, Lasaponara R, Zong X, Masini N, et al. (2019). Airborne and spaceborne remote sensing for archaeological and cultural heritage applications: A review of the century (1907–2017). Remote Sensing of Environment, 232, 111280.

[4] Lu L, Weng Q, Guo H, Feng S, Li Q. (2019). Assessment of urban environmental change using multi-source remote sensing time series (2000–2016): A comparative analysis in selected megacities in Eurasia. Science of The Total Environment, 684, 567-77.

[5] Guo, H. D. (2018). Steps to the digital Silk Road [J]. Nature 554:5-27.

# A comprehensive evaluation of SDG11 indicators using geospatial big data

Liying Han[1,2,3], Linlin Lu[2,3*], Shuangcheng Zhang[1*], Penglong Wang[4], Qingting Li[5]

[1] College of Geological Engineering and Geomatics, Chang'an University, Xi'an 710054, China
email: 2020226024@chd.edu.cn

email: Shuangcheng369@ chd.edu.cn

[2] International Research Center of Big Data for Sustainable Development Goals, Beijing 100094, China
email: lull@radi.ac.cn

[3]Key Laboratory of Digital Earth Science, Aerospace Information Research Institute, Chinese Academy of Sciences, Beijing 100094, China

[4]Northwest Institute of Eco-Environment and Resources，Chinese Academy of Sciences，Lanzhou 730000, China

[5] Airborne Remote Sensing Center, Aerospace Information Research Institute, Chinese Academy of Sciences, Beijing, 100094, China

## 1. INTRODUCTION

The " Agenda 2030 for Sustainable Development" proposed by the United Nations in 2015 covers 17 Sustainable Development Goals (SDGs) and 169 specific goals, helping the international community to make a real and scientific understanding and accurate judgment on the sustainable development of global / regional cities, thereby affecting their practical actions and effective prevention and control [1]. However, as of April 2022, indicators 11.2.1 and 11.3.1 under SDG11 belong to Tier II, with clear concepts, internationally recognized methods and standards, but lack of regular compilation data [2]. Facing these challenges and obstacles, this paper uses high-resolution satellite images, population grid data and geospatial big data, evaluates the changes of traffic accessibility and land use efficiency in the main urban area of Guilin, China, from 2013 to 2020. Using the information provided in this paper, decision makers can make progress in achieving the sustainable development goals.

## 2. MATERIALS AND METHODS

### *2.1 SDG11.2.1*

First, through ArcGIS network analysis, the road network model is established. Secondly, calculate the 500m service area along the bus station road and the 1km service area along the railway station road. Finally, calculate the service population of each public transport station according to Eq. (1).

$$P_i = \sum_{j=1}^{n} P_{ij}$$

(1)

Where $P_{ij}$ – the population of a population area obtained by the complete or partial intersection of a service area (expressed as i) and multiple population areas j (j = 1... n), $P_i$ – the total population served by public transport stations in service area i.

Finally, calculate the SDG 11.2.1 for 2013, 2015 and 2020 according to Eq. (2), and analyze the change trend of public transport accessibility in Guilin.

$$\text{Percentage of population with convenient transportation services\%} = \frac{\text{Population with convenient transportation services}}{\text{Total urban population}} \times 100$$

(2)

### *2.2 SDG11.3.1*

The random forest classification method is used to classify land use. According to the classification results, analyze the urban boundaries and land use changes in each period, and calculate the land consumption rate (LCR) according to Eq. (3).

$$LCR = \frac{\ln\left(\frac{Urb_{t+n}}{Urb_t}\right)}{n} \quad (3)$$

Where $Urb_t$ – the total area covered by the urban building area in the initial year [$m^2$]; $Urb_{t+n}$ – the total area covered by the urban construction area in the last year [$m^2$]; N is the number of years between two measurement periods.

The global population distribution data set with landscan1km resolution is used to count the population in the study area in the corresponding year, and the population growth rate (PGR) is calculated according to Eq. (4).

$$PGR = \frac{\ln\left(\frac{Pop_{t+n}}{Pop_t}\right)}{n} \quad (4)$$

Where $Pop_t$ – the total population in the urban area in the initial year; $Pop_{t+n}$ – the total population in the urban area in the last year; n – the number of years between two measurement periods.

Combined with the change of construction land and population growth data, calculate the land utilization rate (LCRPGR) of Guilin functional urban area according to Eq. (5).

$$LCRPGR = \frac{LCR}{PGR} \quad (5)$$

In addition, the per capita land consumption, the percentage change rate of per capita land consumption and the percentage change rate of urban density are calculated according to Eq. (6), Eq. (7) and Eq. (8).

$$LCPC_{t1} = \frac{Urb_{t1}}{Pop_{t1}} \quad (6)$$

$$Change\ in\ LCPC_{(t1-t2)} = \frac{LCPC_{t2} - LCPC_{t1}}{LCPC_{t1}} \quad (7)$$

$$Change\ in\ Urban\ Infill = \frac{Urb_{t21} - Urb_{t1}}{Urb_{t1}} \times 100 \quad (8)$$

Where $Urb_{t21}$ – the total building area at time t2 within the city boundary at time t1 [$m^2$]; $Urb_{t1}$ – the total building area within the city boundary at time t1 [$m^2$].

## 3. RESULTS

The research results show that the accessibility of public transport in the main urban areas of Guilin has gradually improved from 2013 to 2020, and the index value of SDG11.2.1 has increased from 42.08% in 2013 to 52.31% in 2020. The expansion of construction land area does not match the population growth. The expansion speed of construction land is faster than the increase of population, and the per capita construction land area continues to increase.

## 4. SUMMARY

In view of the lack of SDG11 evaluation data, Taking Guilin City, an innovative demonstration area of the sustainable development agenda, as an example, the dynamic changes of SDG indicators 11.2.1 and 11.3.1 are comprehensively evaluated using high-resolution satellite images, population grid data and geographic big data. The results show that the accessibility of public transport in the main urban area of Guilin has gradually improved from 2013 to 2020. The expansion of construction land area does not match the population growth. This study proves the applicability of earth observation and geographic open big data in accurately and dynamically quantifying urban sustainable development indicators and targeted planning.

## References

[1] United Nations. (2015) Transforming our World: The 2030 Agenda for Sustainable Development, United Nations: New York, NY, USA. Available: http://www.un.org/ga/search/view_doc.asp?symbol=A/RES/.70/1&Lang=E(accessed on 30 June 2022).
[2] Guo, H. (2019) Big Earth data in support of the sustainable development goals (2019), EDP Sciences: 2021.

# Monitoring and projecting sustainable transitions in urban land use using remote sensing and scenario-based modelling in a coastal megacity

Luo Ke[1] ,Lu Linlin[2,3], Qureshi Salman[4], Chen Fang[2,3] ,Shu Lei[2,3]

[1] College of Geological Geomatics and Geoinformation, Guilin University of Technology,541004, China
email: luoke@glut.edu.com

[2] Key Laboratory of Digital Earth Science, Aerospace Information Research Institute, Chinese Academy of Sciences,100094, China
email: lull@radi.ac.cn
email: chenfang@radi.ac.cn

email: 8703az@gmail.com

[3] International Research Center of Big Data for Sustainable Development Goals, 100094, China

[4] Institute of Geography, Humboldt University of Berlin, 12489, Germany
email: salman.quireshi @ geo.hu-berlin.de

## 1. INTRODUCTION

The assessment of SDG11.3.1 indicator played an import role in understanding sustainable transitions in urban land use from local to regional and global scales. Based on remote sensing and scenario modeling, this study attempts to develop an approach for monitoring and making projections of the urban land use efficiency indicator to inform urban management and planning. Taking the coastal megacity of Tianjin, China as a case study, the spatial patterns of urban land use change were first mapped using multi-temporal satellite datasets and an urban sprawl matrix method. Then, the urban land use changes for the periods up to 2025 and 2030 under an environmental protection scenario were predicted by integrating local policy constraints into a cellular automata–Markov (CA–Markov) model using analytic hierarchy process and multi-criteria evaluation methods. Finally, values of the urban land use efficiency indicator SDG11.3.1 were derived for the period 2000 to 2030.

## 2. MATERIALS AND METHODS

### *2.1 Materials*

Eighteen Landsat images with path/row numbers 122/32, 122/33, 123/32 or 123/33 that covered the study area were selected for land use and land cover classification.Radiometric calibration and atmospheric correction were performed on all of the Landsat imagery. Other auxiliary data used in this study included topographic, road network and demographic data. Slope data were calculated from a digital elevation model. All of the datasets were converted to the WGS_ 1984_ UTM_ Zone_ 50N coordinate system.

### *2.2 Methods*

The workflow for sustainable transition analysis mainly consisted of three main steps. The land use and land cover were first classified using Landsat images covering the study area that were acquired in seven different years: 1990, 1995, 2000, 2005, 2010, 2015 and 2020. A random forest classifier was used and the seven categories were built-up land, agricultural land, forest, grassland, bare land, rivers and lakes, and oceans. In addition to the original Landsat images, spectral features including the Normalized Difference Water Index (NDWI)[1], Normalized Difference Vegetation Index (NDVI)[2], Normalized Difference Built-up Index (NDBI)[3] and topographic features such as elevation and slope were extracted from the original data for use as input data to the random forest classifier.

Based on the land use classification map, an urban sprawl matrix method was used to analyze the changes in the urban spatial patterns in the study area[4].Then, projections of future land use up to the years 2025 and 2030 were made using a CA–Markov model[5].Finally, the urban land use efficiency in the study area for the period 2000–2030 was analyzed using the urban land use efficiency indicator. The functional urban boundary was constructed by expanding the urban core area by 25% to create a buffer zone. The values of the SDG11.3.1 indicators were then calculated based on the urban land use and population changes within this boundary. The population growth rate (PGR), land consumption rate (LCR) and the ratio of the land consumption rate to the population growth rate (LCRPGR) were calculated using the following equations：

$$\begin{cases} PGR = \dfrac{\ln\left(Pop_{t+n}/Pop_t\right)}{n} \\ LCR = \dfrac{\ln\left(Urb_{t+n}/Urb_t\right)}{n} \\ LCRPGR = \dfrac{LCR}{PGR} \end{cases} \qquad (3)$$

Here, $Pop_t$ represents the population in year t, $Pop_{t+n}$ represents the population in year t + n, $Urb_t$ is the area of built-up land in year t and $Urb_{t+n}$ is the area of built-up land in year t + n.

## 3. RESULTS

In this study, we found that built-up area in Tianjin in 2020 doubled compared with 1990 and that 63.95% of the newly increased built-up land was converted from agricultural lands. The model prediction results indicate that the expansion of built-up land is more concentrated and land consumption and population growth tend to be more closely correlated when constrained by environmental protection measures. Extensive growth of built-up areas predicted in coastal areas might increase ecological and disaster risks, and should be strictly planned. The land use change modeling and analysis framework can be applied to growing coastal cities in other regions to inform sustainable land use planning.

## 4. CONCLUSIONS

In this study, the spatial patterns of land use and land cover change in the coastal megacity of Tianjin, China over the past 30 years were investigated and the dynamics of land use up to 2025 and 2030 were predicted. Based on the land use mapping and prediction results, the changes in urbanization sustainability were evaluated using the indicator of urban land use efficiency. The land use type most affected by the increase in the built-up land over the period 1990 to 2020 was agricultural land. The expansion of the built-up land in Tianjin was characterized by a radial pattern around the central urban area together with a strip shape of newly built-up land along the coastline in the Binhai New Area. Under the strict implementation of existing ecological protection regulations, it is predicted that the amount of land use conversion in Tianjin will slow down over the next ten years and that the characteristics of urban growth in the city will gradually change from extensive sprawl to efficient growth; the urbanization of the population and land will then tend to happen in a more coordinated way. However, according to the results of this study, the amount of land reclamation along the coast is expected to increase significantly, which may increase ecological risk and stress the marine ecosystem. Strict conservation and management policies should be implemented to promote sustainable use of the coastal areas. The land use change monitoring and prediction methods described in this paper can be applied to other growing coastal cities to promote sustainable urban development and environmental planning.

## References


[1] McFeeters S. K. (1996) The use of the Normalized Difference Water Index (NDWI) in the delineation of open water features, International Journal of Remote Sensing, 17: 1425-1432.

[2] Lu L., Kuenzer C. (2015) Evaluation of Three MODIS-Derived Vegetation Index Time Series for Dryland Vegetation Dynamics Monitoring, Remote Sensing, 7.

[3] Lu L., Wang Z. (2014) Dynamic and Static Combination Analysis Method of Slope Stability Analysis during Earthquake, Mathematical Problems in Engineering, 2014: 573962.

[4] Sahana M., Hong H. (2018) Analyzing urban spatial patterns and trend of urban growth using urban sprawl matrix: A study on Kolkata urban agglomeration, India, Science of The Total Environment, 628-629: 1557-1566.

[5] Mas J.-F. o., Kolb M. (2014) Inductive pattern-based land use/cover change models: A comparison of four software packages, Environmental Modelling & Software, 51: 94-111.

# DBAR-Climate Action and Sustainable Development in High Mountain Asia and Arctic Region/PEEX SDG13 Side Event

# A dataset of Landsat 8 snow coverage in the Himalayas from 2013 to 2020

SHI Lijuan[1,2], QIU Yubao[1,2,*], Li Yang[1,2], DING Lei[3], HE Siyu[1,2], LIU Zirui[1,2], LEMMETYINEN Juha[4], LI Qinghuan[1,2]

[1] Key Laboratory of Digital Earth Science, Aerospace Information Research Institute (AIR), Chinese Academy of Sciences (CAS), Beijing 100094, China. email: shilj@aircas.ac.cn; qiuyb@radi.ac.cn

[2] International Research Center of Big Data for Sustainable Development Goals (CBAS), Beijing 100094, China

[3] Xi'an Jiaotong-Liverpool University, Shanghai,215123, China

[4] Finnish Meteorological Institute P. O. Box 503, Fin-00101 Helsinki Finland.

Located on the southern edge of the Tibetan Plateau, the Himalayas are the highest mountain system in the world, and their snow cover and changes affect the regional climate, water resources and ecological environment. In order to better understand the changes of snow cover in this area and overcome the problems of insufficient detailed description of snow cover monitoring in mountainous areas with complex terrain by medium and low resolution remote sensing, we carried out snow cover monitoring by using Landsat 8 clear sky condition data with a spatial resolution of 30m. Due to the complex terrain of the mountainous area, in view of the general overestimation problem of the normalized snow cover index method in the Himalayas, we used the support vector machine (SVM) classification method to select the snow cover characteristic training samples of different terrain, shadow and other conditions on a scene-by-scene basis for snow accumulation. Combining with auxiliary data such as glacial lakes, surface water bodies and other auxiliary data and spatial neighborhood analysis for data post-processing, we constructed a 30m-resolution snow cover dataset in the Himalayas from 2013 to 2020. By comparing the high-resolution snow cover classification of Sentinel-2 within a grid of 900×900m, the correlation coefficient of snow cover rate is above 0.95, and the root mean square error is about 0.1%. The snow cover identification results constructed by the two results are highly consistent with each other. The snow cover dataset includes a total of 995 scenes covering the whole Himalayas for 8 years, mainly distributed in the winter snow season from October of the current year to April of the following year. This dataset can provide a basis for verification and optimization of snow cover spatiotemporal and characteristic analysis, and low-and-medium-resolution snow cover data, and provide support for studies on climate change, water resources management, and ecological benefits in the Himalayas and downstream regions.

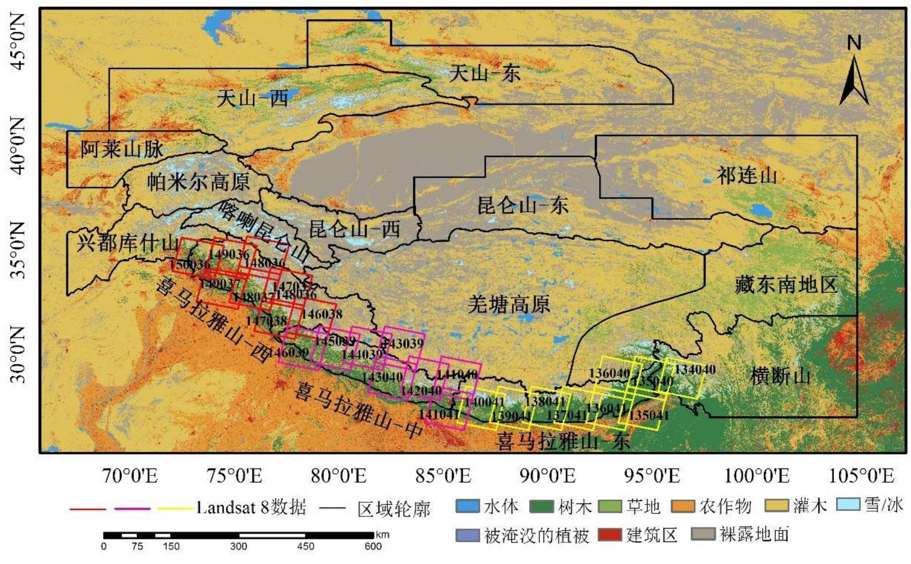


**Fig. 1.** Overview map of the study area (the bottom map is the global 10-meter land cover in 2020)

**Table 1.** Landsat 8 data of Himalayas from 2013 to 2020

| Mon-th | Year | | | | | | | | | | | | | | | | | | | | | | | |
|---|---|---|---|---|---|---|---|---|---|---|---|---|---|---|---|---|---|---|---|---|---|---|---|---|
| | 2013 | | | 2014 | | | 2015 | | | 2016 | | | 2017 | | | 2018 | | | 2019 | | | 2020 | | |
| | E | M | W | E | M | W | E | M | W | E | M | W | E | M | W | E | M | W | E | M | W | E | M | W |
| **1** | / | / | | 6 | 8 | 4 | 5 | 4 | 7 | 4 | 8 | 6 | 7 | 5 | 4 | 6 | 8 | 12 | 5 | 5 | 2 | 5 | 6 | 5 |
| **2** | / | / | | 6 | 8 | 4 | 1 | 4 | 3 | 3 | 8 | 4 | 5 | 6 | 4 | 2 | 5 | 6 | 2 | 5 | 4 | 7 | 1 | 10 |
| **3** | | | 1 | 1 | 8 | 1 | 1 | 6 | 3 | 4 | 2 | 4 | 1 | 5 | 5 | 2 | 6 | 7 | 1 | 10 | 3 | 1 | 7 | 6 |
| **4** | | | 3 | | 5 | 6 | | 3 | 8 | 2 | 4 | 2 | 1 | 6 | 6 | | 3 | 6 | 1 | 2 | 7 | | 2 | 3 |
| **5** | | 2 | 5 | | 4 | 2 | | 4 | 4 | | 3 | 4 | 1 | 3 | 3 | | 3 | 2 | | 5 | 5 | | | 2 |
| **6** | | | 6 | | 1 | 7 | | 2 | 2 | | | 1 | | 2 | | | 2 | 2 | | 1 | 2 | | | 2 |
| **7** | | | 2 | | | 3 | 1 | | 1 | | | | | | | | | | | | | | | |
| **8** | | | | | | 3 | | | 1 | | | 1 | | | 1 | | | | | | | | 1 | |
| **9** | 2 | 1 | 2 | | 2 | 6 | 1 | 5 | 3 | | 1 | | | 2 | 4 | 1 | 4 | 2 | | | 5 | | | 6 |
| **10** | 2 | 6 | 4 | 2 | 6 | 6 | 2 | 9 | 9 | 4 | 10 | 8 | 3 | 11 | 7 | 2 | 11 | 4 | | 5 | 8 | 2 | 2 | 12 |
| **11** | 10 | 10 | 11 | 1 | 12 | 4 | 8 | 11 | 6 | 8 | 15 | 5 | 7 | 11 | 8 | 5 | 9 | 8 | 4 | 7 | 1 | 7 | 2 | 1 |
| **12** | 7 | 10 | 3 | 6 | 6 | 7 | 4 | 12 | 8 | 9 | 9 | 8 | 8 | 7 | 8 | 6 | 9 | 5 | 2 | 7 | 8 | 6 | 2 | 4 |
| **total** | 87 imagers | | | 135 imagers | | | 138 imagers | | | 137 imagers | | | 141 imagers | | | 138 imagers | | | 107 imagers | | | 112 imagers | | |
| | 995 imagers | | | | | | | | | | | | | | | | | | | | | | | |

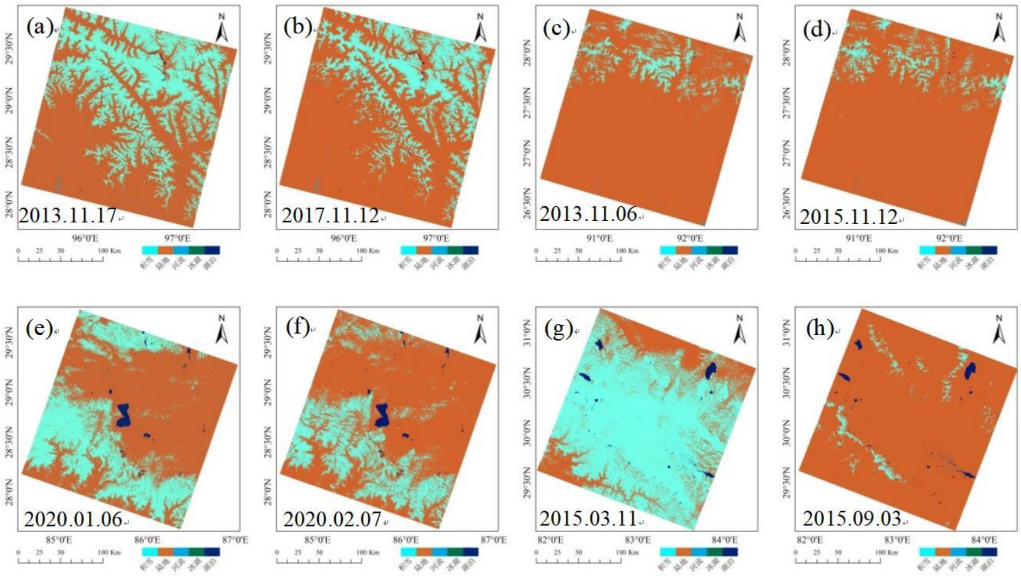


**Fig. 2.** Product samples in the snowy range of the Himalayas

## References:

[1] Qiu Y, Guo H, Chu D et al. MODIS daily cloud-free snow cover products over Tibetan Plateau. China Scientific Data 1 (2016), DOI: 10.11922/csdata.170.2016.0003

[2] He Siyu, Qiu Yubao, Shi Lijuan, Ding Lei, Zhao Quanhua, Liu Lijing. Snow cover monitoring data of Landsat 8 in the central and eastern Himalayas from 2013 to 2020 [J/OL]. China Scientific Data, 2022. DOI: 10.11922/11-6035.csd.2022.0005.zh

[3] Y. Wang, L. Wang*, J. Zhou, T. Yao, W. Yang, X. Zhong, R. Liu, Z. Hu, L. Luo, Q. Ye, N. Chen, H. Ding (2021). Vanishing Glaciers at Southeast Tibetan Plateau Have Not Offset the Declining Runoff at Yarlung Zangbo. Geophysical Research Letters, 48(21), 2021

# Mapping evaluation of GF-3 and Sentinel-1 satellite for sea ice margin

HUANG Lin [1,2,3], QIU Yubao [1,2]

[1] Key Laboratory of Digital Earth Science, Aerospace Information Research Institute, Chinese Academy of Sciences, Beijing 100094, China
email: huanglin@aircas.ac.cn
email: qiuyb@aircas.ac.cn
[2] International Research Center of Big Data for Sustainable Development Goals, Beijing 100094, China
[3] University of Chinese Academy of Sciences, Beijing 100049, China

## ABSTRACT

Sea ice remote sensing monitoring with high precision is important for ship navigation and marine service. The monitoring accuracy is often low in the sea ice edge area. Synthetic aperture radar (SAR) is a useful means to observe the sea ice with high spatial resolution. Sentinel-1 and GF-3 are located on orbit SAR satellites. Based on these two data, the monitoring differences and characteristics of sea ice and open water in marginal sea ice zone are compared and statistically analyzed. Nine pairs of samples with different ice-water ratios in the 2021 ice-melting period in the Kara Sea area were selected to carry out comparative analysis of backscattering between GF-3 and Sentinel-1 in the sea ice edge area under 500-m grids. The data are processed by radiometric calibration, incident angle normalization and resampling. The results show that GF-3 has a stronger resolution capability for sea ice and open water than Sentinel-1. Threshold segmentation or K-means clustering method was used from scatterplots of these two SAR sample pairs to obtain the ice and water classification results. It shows that the combination of the two data has the strongest distinction for ice and water, followed by GF-3, which the segmentation threshold is -17. Sentinel-1 samples are the weakest in distinguishing ice and water, visual interpretation is required can make a better distinction, the best threshold is around -23 to -25. In addition, HH polarization images combining the two data is more discriminative for ice and water than HV polarization from the scatter plots. From the density histograms, GF-3 shows a big difference between ice and water especially in ice edge area, and the histogram shows double peaks, but the difference of Sentinel-1 is not obvious, even the histogram of HV-pol shows a single peak shape, indicating that Sentinel-1 is not as good as GF3. The contrast error may be caused by the difference in imaging time between the two SAR images, leading to the displacement or deformation of the sea ice, thus the pixels cannot be completely matched.

**Key words:** Sea ice, SAR, GF-3, Mapping evaluation

***Figures***

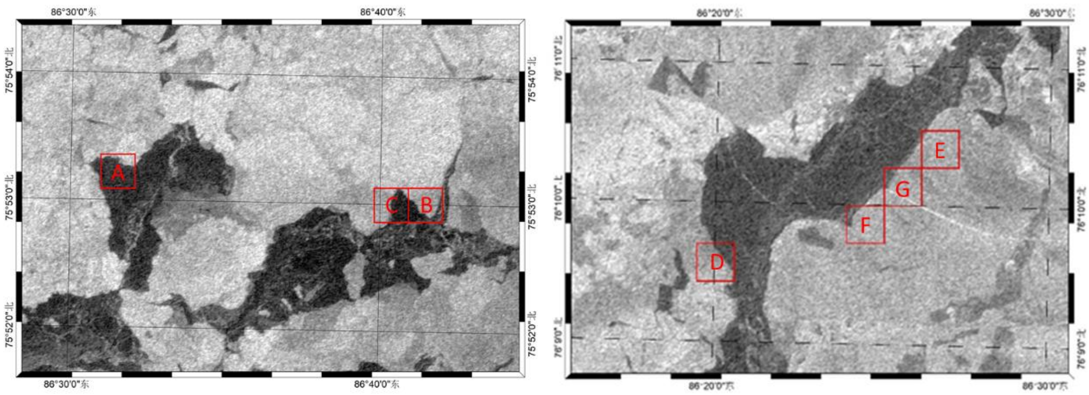


GF-3 Samples

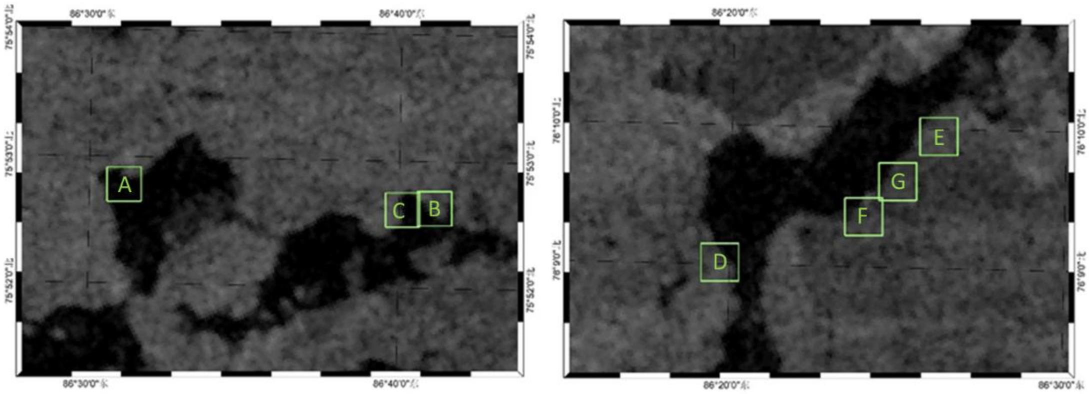


Sentinel-1 Samples

**Fig. 1.** SAR samples distribution in the Kara sea area

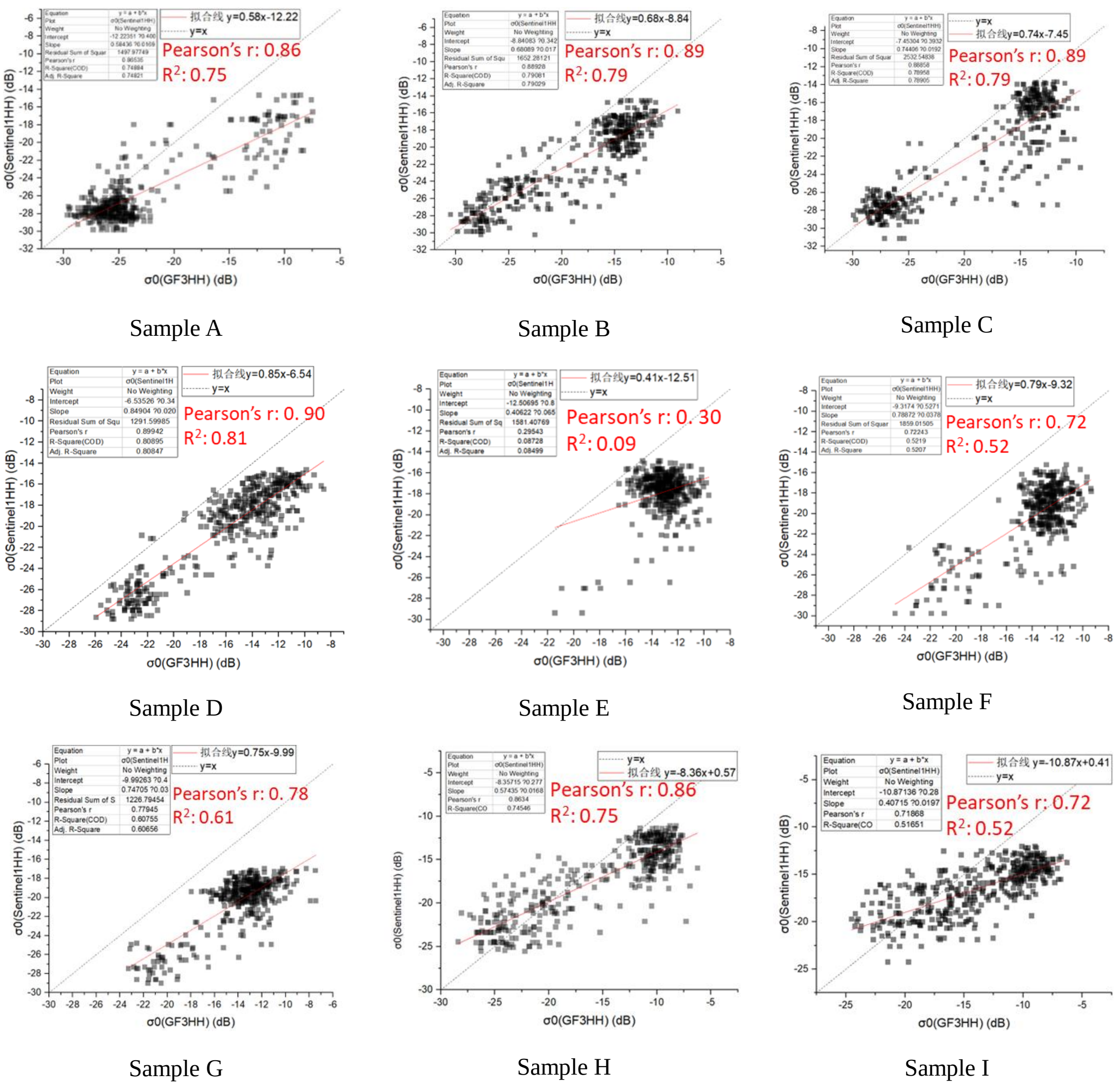


**Fig. 2.** Scatterplots of backscattering coefficient value for GF-3 HH-pol and Sentinel-1 HH-pol. Black lines denote the identity line. Red lines denote the linear regression of the respective value pairs between GF-3 and Sentinel-1 SAR samples. Linear regression equations are in the top left of the scatterplots.

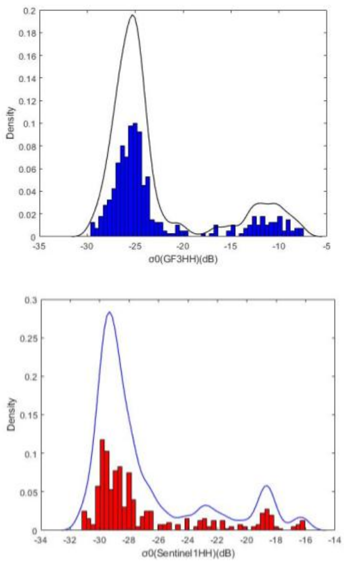


Sample A

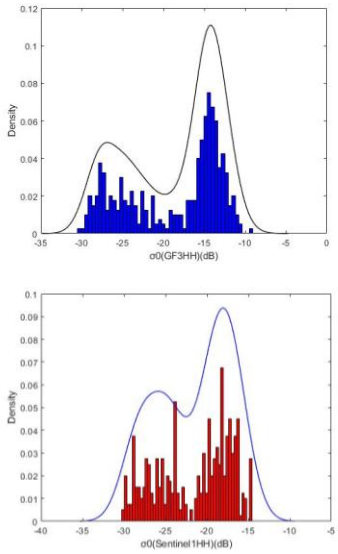


Sample B

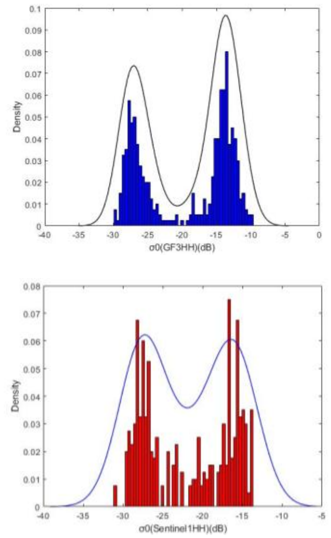


Sample C

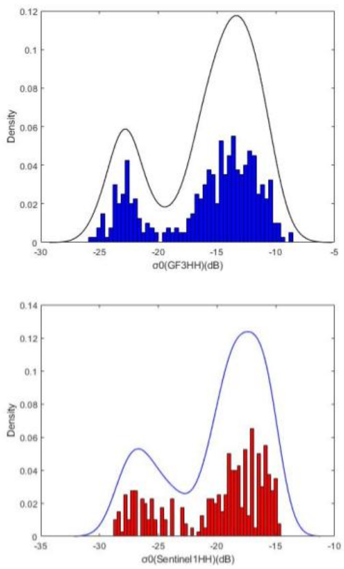


Sample D

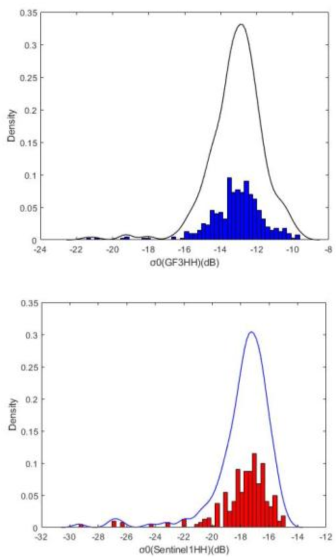


Sample E

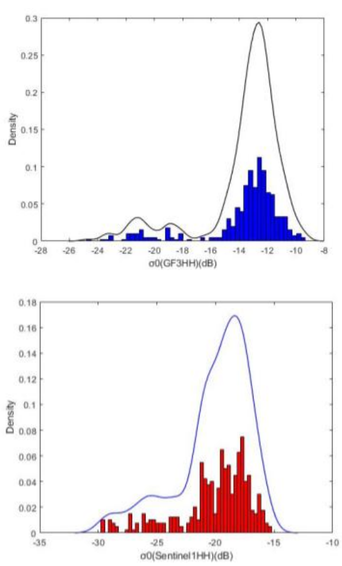


Sample F

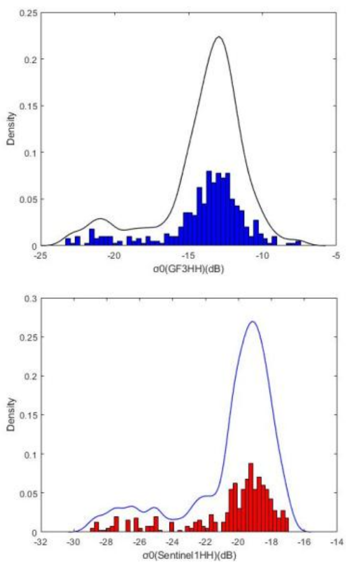


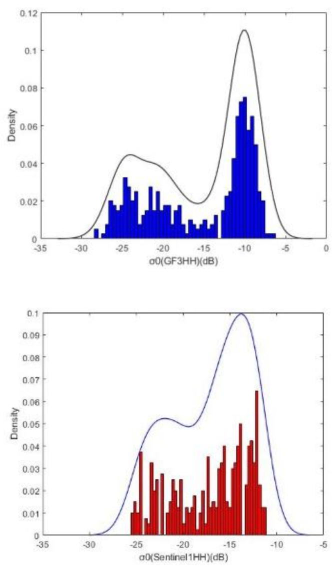


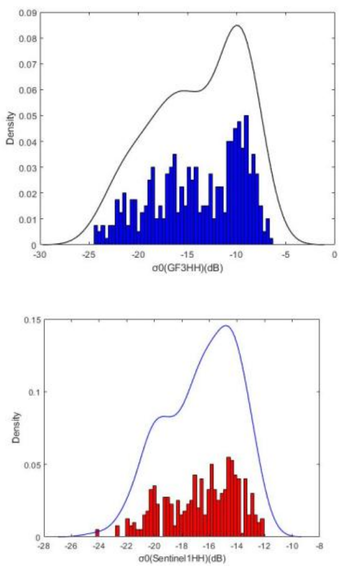

Sample G Sample H Sample I

**Fig. 3.** Density histograms of backscattering coefficient value of GF-3 and Sentinel-1 HH-pol data. The blue histograms denote the frequency histogram distribution of the backscatter coefficient values of GF-3 samples; the red histograms denote Sentinel-1 samples.

# DBAR-Digital Technology in Support of Water and Land Management for Sustainable Development

# Simulation of land use change along the Silk Road under the constraint of sustainable development goals

Kai Wu [1*], Tian Ya [2] Min Cao [1], Min Chen [1], Songshan Yue [1]

[1] Key Laboratory of Virtual Geographic Environment, Ministry of Education of PRC, Nanjing Normal University, Nanjing 210023, China.

[2] School of Geography and Environment, Jiangxi Normal University, Nanchang 330022, China.

email: kwu@nnu.edu.cn

## 1.INTRODUCTION

The Sustainable Development Goals (SDGs) are a call for action by all countries to promote prosperity while protecting the planet [1], and the United Nations has established 17 SDGs calling on the entire world to work together to end poverty, safeguard the environment, and improve the lives and futures of all people [2]. Land is an important aspect of natural resource since they provide the foundation for human exploitation and consumption of the land as well as the acquisition of living materials [3]. The sustainable use of land resources is critical for the economy, society, and environment to flourish in a way that is sustainable. This study analysed the land use changes along the Silk Road between 2001 and 2015, and presented the scenarios projection of land use change in the future under the constraint of multiple SDGs indicators. First of all, we divided the 66 countries along the Silk Road according to the economic and climatic conditions. Then we analysed the historical development trend of land use change along the Silk Road. At the same time, four sustainable development scenarios (reference, environmental protection, economic development and grain production) were set according to the Sustainable Development Report 2020 released by the United Nations [4]. A system dynamics model integrating socioeconomic and natural factors was used to predict land use change in 2030. The results show that different sustainable development scenarios have significant impacts on different types of land resources. The area of urban land will expand the fastest under the economic development scenario, while the cultivated land will decline more slowly under the grain production scenario and the forest land will decrease more slowly the environmental protection scenario, respectively. This study can provide a basis for judging the land sustainability of countries along the Silk Road.

## 2.MATERIALS AND METHODS

### *2.1: Defining the sub-regions along the Silk Road*

We aggerated the countries along the Silk Road into nine sub-regions, based on the geopolitical and socio-economic regions from the Shared Socioeconomic Pathways (SSPs) database and the agro-ecological zones (AEZs) developed by the Food and Agricultural Organization (FAO) and International Institute for Applied Systems Analysis (IIASA) [5]. The 9 sub-regions are defined as follows: China (CHN), Central and Western Asia (CWS), Eastern Europe (EEU), Europe high-income countries (EU-H), Europe middle-income countries (EU-M), Middle East high-income countries (MEA-H), Middle East middle-income countries (MEA-M), Other Asia countries (OAS) and Russia (RUS).

### *4.1 Sustainable development scenarios set*

We set the sustainable development scenarios by using four indicators from sustainable development report 2020(SDR) which analyzes the data from 193 UN member states to conduct a comprehensive and systematic assessment of each country's distance from achieving the Sustainable Development Goals (SDGs). The four sustainable development indicators are GDP growth rate (%), cereal yield and incidence of undernourishment, and $PM_{2.5}$ concentration, respectively which could represent the economic, food and environment aspects of a country. For each indicator, the SDR2020 provides color bands to quantitively measure its progress, while green, yellow, orange to red color bands indicates that the distance from the realization of the SDG indicator is increasing. Then we created four sustainable scenarios which called the Reference scenario (REF), Economic development scenario (ECO), Grain production scenario(GRA) and Environmental protection scenario (ENV). The reference scenario represents that the four sustainable development indicators will change following existing trend. In economic development scenario, the GDP growth will achieve the green threshold, which means the GDP growth will move towards optimization. In the Grain sustainable scenario, the Cereal yield and the Prevalence of undernutrition will achieve the green threshold.

### *2.3 System dynamics (SD) model build*

We used system dynamics (SD) model to express the complex interactions between the variables of sustainable development indicators and different land types [6]. Firstly, we divided the silk road into nine sub-region according by climate and socio-economic statistic each type of land area in each region along the Silk Road. Then for each sub-region, we employed the historical data from 2001 to 2015 to forecast the land use demand from 2015 to 2030. The land use demand will be driven by the trends of sustainable development indicators in sustainable development scenarios. Such as, the GDP growth will affect the area change of cultivated land and urban land by fixed asset investment. The cereal yield and prevalence of undernourishment will impact the area change of cultivated land by grain demand as well. Finally, we try to find some relationship between land use with natural environment and human society, Such as precipitation, temperature, Technological progress and Livestock production index. the interactions of sustainable, land and socio-economic constitutes the feedback closed-loop of the whole system.

## 3.RESULTS

### *4.2 Cultivated land demand under grain production scenario*

We compared the growth rate of cultivated land from 2015 to 2030 between the reference and grain production scenarios. We find that most of regions along the Silk road are show decreasing trends, but the decreasing speed will be significantly slower under the grain production scenario. Especially, in OAS sub-region under the grain production scenario, the trend of cultivated land will turn the decrease into increase, which may due to the large populaion in the sub-region. But in RUS subregion, there are no significantly difference between four sustainable development scenarios. It suggest that as latitude decreases, the variability between scenarios becomes greater.

### *4.3 Forest demand under environmental protection scenario*

We compared the growth rate of forest from 2015 to 2030 between the reference and environmental protection scenarios. We find most of regions along the Silk Road are show decreasing trends, but the decreasing speed will be significantly slower under the environmental protection scenario. The forest of the Silk Road is concentrated in the south of CHN sub-region, OAS and RUS sub-regions. Among them, the forest of CHN sub-region will increase under the environmental protection scenario which explains the necessity of the policy of returning farmland to forests adopted by China.

### *4.4 Urban under economic development scenario*

We compared the growth rate of forest from 2015 to 2030 between the reference and economic development scenarios. We find most of regions along the Silk Road are show increasing trends, and the increasing speed will be significantly faster under the economic development scenario. But in Europe, the rate of urban expansion in the EEU region has been slow down significantly after 2010, and there are no significantly difference between reference and economic development scenarios.

## 4.SUMMARY

The SDGs represented by a high number of interlinked goals, targets, and indicators could affect the social, environment and economic[7]. In this study, we proposed a method of land use forecasting under the constraints of multiple SDG indicators framework. The reference scenario and three others focus on economic development, grain production and environmental protection were set by assigning the corresponding SDG indicators to reach the green threshold range in 2030 according to the color indicator dashboard in the SDR 2020. Then we use system dynamics(SD) model to predict the land use demand along the Silk Road by 2030. Finally, we find different trends of SDG indicators will affect the land use area of a country, which has shown the interaction between the sustainability and land use. So SDGs will constrain the trends of land use change which may be beneficial to policy designation.

## References


[1] Nations, U., 2015. Transforming our world: the 2030 Agenda for Sustainable Development.

[2] Pradhan, P., Costa, L., Rybski, D., Lucht, W., Kropp, J.P., 2017. A Systematic Study of Sustainable Development Goal (SDG) Interactions. Earth's Future 5, 1169-1179.

[3] Ahmad, W., Iqbal, J., Nasir, M.J., Ahmad, B., Adnan, S., 2021. Impact of land use/land cover changes on water quality and human health in district Peshawar Pakistan. Sci. Rep.-UK 11, 16526.

[4] Sachs, J., Schmidt-Traub, G., Kroll, C., Lafortune, G. & Fuller, G. Sustainable Development Report 2020. Sustainable Development Report 2020 (2021).

[5] Jansen, L.J.M., Gregorio, A.D., 2000. Land Cover Classification System (LCCS): Classification Concepts and User Manual. Fao.

[6] You, S., Kim, M., Lee, J., Chon, J., 2018. Coastal landscape planning for improving the value of ecosystem services in coastal areas: Using system dynamics model. Environ. Pollut. 242, 2040-2050

[7] Breuer, A.; Janetschek, H.; Malerba, D., 2019. Translating Sustainable Development Goal (SDG) Interdependencies into Policy Advice. Sustainability, 11, 2092